Ultrasound in Obstetrics and Gynecology

Vol. 2: Gynecology

Eberhard Merz

2nd edition, fully revised

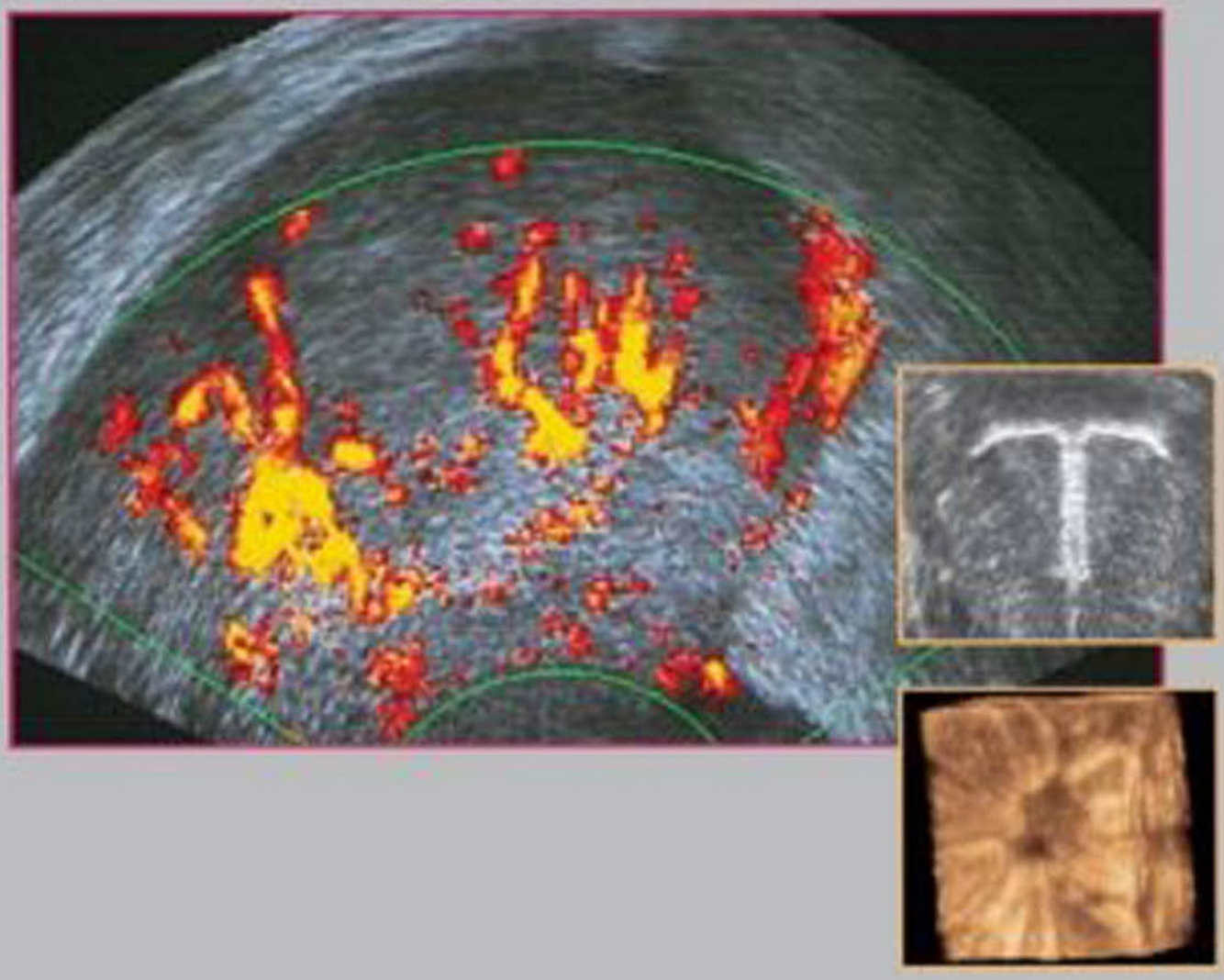

Thieme

مرکز خدمات فرهنگی سالکان

همگام با توسعه علمی و فرهنگی جهان معاصر و استفاده روزافزون کامپیوتر در بین جوامع بشری خصوصاً رشته های مختلف علوم و استفاده بهینه از آخرین یافته های پزشکی دنیا و ارائه این یافته ها در قالب نرم افزار پزشکی (Multimedia ، DVD &VCD ،e-book) ما را بر آن داشت که با گردآوری و ارائه این یافته ها گامی کوچک در راه ارتقاء سطح علمی متخصصین کلیه رشته های پزشکی کشور بصورت سمعی و بصری برداریم. امید است مشوق ما در این راه باشید.

لذا علاقمندان میتوانند برای دریافت هریک از محصولات ارائه شده به ازاء هر CD یا DVD مبلغ ۵۰۰۰ هزار تومان به حساب سپهر به شماره: ۰۳۰۶۵۰۰۱۰۰۰۰۳ بانک صادرات ایران (قابل واریز در سراسر کشور) بنام جواد شبرنگ واریز و پس از فکس فیش فوق بهمراه نشانی دقیق خریدار نسبت به خرید اقلام و دریافت کالای مورد نظر خود اقدام نمایند.

جهت مشاهده لیست محصولات به آدرس سایت www.Salekan.ir مراجعه فرمائید.

نشانی مرکز: تهران - میدان انقلاب -کارگر شمالی - ابتدای خیابان نصرت غربی - پلاک ٥٦ - طبقه اول

تلفن : ٤-٦٦٥٦٥٠٢٣ تلفکس: ٦٦٥٦٥٠٢٤ همراه: ۰۹۱۲۱۳۷۲۳۶۱

Thieme

Ultrasound in Obstetrics and Gynecology

Volume 2: Gynecology

Eberhard Merz, MD
Professor and Director
Dept. of Obstetrics and Gynecology
Hospital Nordwest
Frankfurt/Main, Germany

With contributions by

F. Bahlmann
F. Degenhardt
W. Goldhofer
E.-M. Grischke
V. Jaspers
S. Kupesic
A. Kurjak
H. Madjar
A. Oberstein
G. Weber

1025 illustrations

2nd edition, revised and updated

Thieme
Stuttgart · New York

Library of Congress Cataloging-in-Publication Data is available from the publisher.

1st German edition 1988
1st English edition 1991
2nd German edition 1997

This book is an authorized and revised translation of the German edition published and copyrighted 1997 by Georg Thieme Verlag, Stuttgart, Germany. Title of the German edition: Sonographische Diagnostik in Gynäkologie und Geburtshilfe, Lehrbuch und Atlas in 2 Bänden, Band 1 Gynäkologie.

Translator: Terry Telger, Translations for the Health Sciences, Waco, Texas, USA

Illustrators: Barbara Gay, Stuttgart, Germany; Katharina Schumacher, Munich, Germany

Important note: Medicine is an ever-changing science undergoing continual development. Research and clinical experience are continually expanding our knowledge, in particular our knowledge of proper treatment and drug therapy. Insofar as this book mentions any dosage or application, readers may rest assured that the authors, editors, and publishers have made every effort to ensure that such references are in accordance with **the state of knowledge at the time of production of the book.**

Nevertheless, this does not involve, imply, or express any guarantee or responsibility on the part of the publishers in respect to any dosage instructions and forms of applications stated in the book. **Every user is requested to examine carefully** the manufacturers' leaflets accompanying each drug and to check, if necessary in consultation with a physician or specialist, whether the dosage schedules mentioned therein or the contraindications stated by the manufacturers differ from the statements made in the present book. Such examination is particularly important with drugs that are either rarely used or have been newly released on the market. Every dosage schedule or every form of application used is entirely at the user's own risk and responsibility. The authors and publishers request every user to report to the publishers any discrepancies or inaccuracies noticed. If errors in this work are found after publication, errata will be posted at www.thieme.com on the product description page.

© 2007 Georg Thieme Verlag,
Rüdigerstrasse 14, 70469 Stuttgart, Germany
http://www.thieme.de
Thieme New York, 333 Seventh Avenue,
New York, NY 10001, USA
http://www.thieme.com

Typesetting by OADF, Holzgerlingen
Printed in Germany by Grammlich, Pliezhausen
10-ISBN 3-13-754402-5 (GTV)
13-ISBN 978-3-13-754402-9 (GTV)
10-ISBN 1-58890-146-7 (TNY)
13-ISBN 978-1-58890-146-0 (TNY)

1 2 3 4 5 6

Some of the product names, patents, and registered designs referred to in this book are in fact registered trademarks or proprietary names even though specific reference to this fact is not always made in the text. Therefore, the appearance of a name without designation as proprietary is not to be construed as a representation by the publisher that it is in the public domain.

This book, including all parts thereof, is legally protected by copyright. Any use, exploitation, or commercialization outside the narrow limits set by copyright legislation, without the publisher's consent, is illegal and liable to prosecution. This applies in particular to photostat reproduction, copying, mimeographing, preparation of microfilms, and electronic data processing and storage.

Preface

Ultrasound technology has advanced dramatically since 1986, when the first edition of this book appeared. Given the wealth of new sonographic applications and findings, it was necessary to separate our material into an obstetric volume and a gynecologic volume when creating a second edition.

In the gynecologic sector, a number of techniques have greatly broadened the spectrum of diagnostic imaging: transvaginal ultrasound, perineal and introital ultrasound, breast ultrasound, Doppler and color Doppler ultrasound, power Doppler imaging, ultrasound contrast hysterosalpingography, and 3D/4D ultrasound. Progress in diagnostic ultrasound has been driven by the development of various new and improved transducers for specialized applications and by rapid advances in the field of computer technology.

Resolution and image quality have also been greatly improved, enabling sonographers to define smaller structures within organs. Modern ultrasound scanners also feature significant ergonomic advances, making them easier and more comfortable to use on a daily basis.

In the field of gynecology, the ultrasound examination has become an important part of the diagnostic algorithm in both clinical and office settings. Gynecologic ultrasound has gained an established place in preoperative investigations as well as in preventive medicine.

By incorporating up-to-date advances in ultrasound technology, this book is designed to present an overview of gynecologic ultrasonography as it is practiced today.

Transvaginal ultrasound has greatly expanded the diagnostic options available to gynecologists for examining the true pelvis. As a result, considerable space has been devoted to this examination technique in the present volume. Although transvaginal ultrasound has supplanted transabdominal ultrasound for many applications, this book does not overlook the fact that abdominal ultrasound still has a significant role. Readers who have little or no experience with transvaginal ultrasound can still learn about the normal and abnormal findings in the female pelvis that can be revealed by transabdominal scanning. Moreover, transabdominal ultrasound still has definite indications that include the investigation of large lower abdominal masses and the exploration of the mid- and upper abdomen in the diagnosis and follow-up of cancer patients. Because intra-abdominal complaints may result from gastrointestinal, hepatic and urologic disorders as well as gynecologic problems, the book also touches on these "fringe areas" that gynecologists must deal with on a daily basis.

Moreover, this edition also covers intraoperative ultrasound, perineal and introital scanning, ultrasound contrast hysterosalpingography, Doppler and color Doppler ultrasound, transvaginal 3D/4D ultrasound, and breast ultrasound (2D and 3D/4D).

Color Doppler ultrasound has gained an established place in the evaluation of gynecologic tumor perfusion and benign–malignant differentiation. It is also used as an adjunctive diagnostic tool in reproductive medicine. Breast ultrasound is not only useful in differentiating between cystic and solid masses but can also provide a supplement or even an alternative to conventional mammograms. There are cases in which the preoperative ultrasound investigation of a breast mass can provide more accurate benign–malignant differentiation than mammography.

With the continuing development of 3D and 4D ultrasound technology there is no doubt that these techniques have reached a stage where they not only can be used in routine examinations but also provide us with images that cannot be achieved with 2D ultrasound. Therefore the chapters on 3D/4D ultrasound in gynecology and 3D/4D ultrasound in the breast have been included in this book.

The principal findings, differential diagnoses, and explanations in this book are reviewed in figures and tables at the end of each chapter. This is designed to give the examiner a concise overview and assist him or her in formulating a differential diagnosis. An effort has been made to present illustrative images for virtually any finding that may be encountered in the practice of diagnostic ultrasound. For both abdominal and vaginal ultrasound, the preoperative sonographic images are correlated with intraoperative or postoperative findings for a number of lesions that were surgically investigated.

While all of my coauthors have endeavored to present their material in a clear, complete and authoritative manner, it is inevitable that some points will not be covered exhaustively or will be viewed differently by different examiners. With this in mind, I invite my readers to contact me regarding any points that may be unclear or in dispute and to offer criticisms that may improve the accuracy of this book.

I am grateful to all my coauthors, whose expert contributions were instrumental in creating such a comprehensive work on gynecologic ultrasound. I also thank our photographer, Mr F. Feyrer, for his skillful photographic work and Dr Slovacek for her valuable help in researching the literature. I extend special thanks to the staff at Thieme Publishers for their outstanding guidance and support during the editorial planning and production of this book; in particular to Dr M. Becker for his work on the German edition, and to Dr Cliff Bergman, Mr Stephan Konnry, and Ms Elisabeth Kurz for making the English edition of this book possible.

Eberhard Merz

Contributors

Franz Bahlmann, MD
Buergerhospital Frankfurt
Frankfurt/Main, Germany

Friedrich Degenhardt, MD
Professor
Department of Gynecology
St. Franziskus Hospital Bielefeld
Bielefeld, Germany

Werner Goldhofer, MD
Center for Ultrsound in Obstetrics and Gynecology
Mainz, Germany

Eva-Maria Grischke, MD
Professor
Municipal Hospital Munich-Schwabing
Munich, Germany

Volker Jaspers, MD
Augusta Krankenanstalt Bochum
Bochum, Germany

Sanja Kupesic, MD
Department of Obstetrics and Gynecology
Medical School University of Zagreb
Sveti Duh Hospital
Zagreb, Croatia

Asim Kurjak, MD
Professor
Department of Obstetrics and Gynecology
Medical School University of Zagreb
Sveti Duh Hospital
Zagreb, Croatia

Helmut Madjar, MD
Professor
German Diagnostic Clinic
Wiesbaden, Germany

Eberhard Merz, MD
Professor and Director
Department of Obstetrics and Gynecology
Hospital Nordwest
Frankfurt/Main, Germany

Anna Oberstein, MD
Department of Obstetrics and Gynecology
Hospital Nordwest
Frankfurt/Main, Germany

Gerald Weber, MD
Center for Ultrasound in Obstetrics and Gynecology
Mannheim, Germany

Contents

General ... 1

1 Criteria for Describing an Ultrasound Mass ... 2
E. Merz

Localizing the Mass to a Specific Organ ... 2
Size of the Mass ... 2
Shape of the Mass ... 2
Internal Echo Pattern ... 3
Margins ... 4
Delineation ... 4
Mobility ... 4
Compressibility ... 4
Acoustic Shadowing and Acoustic Enhancement ... 4
Detecting Movement within a Mass ... 4
Uncertainties in the Description of Findings ... 4
Benign–Malignant Differentiation ... 4

Abdominal Ultrasound ... 5

2 Areas of Application and Examination Technique ... 6
E. Merz

Areas of Application ... 6
Examination Technique ... 6

3 Anatomy of the Female Pelvis ... 10
E. Merz

Uterus ... 10
Vagina and Bladder ... 10
Ovaries ... 10
Vessels ... 11
Abdominal Wall ... 11

4 Ovarian and Endometrial Changes during the Menstrual Cycle ... 17
E. Merz

Ovarian Changes during the Menstrual Cycle ... 17

5 Congenital Anomalies of the Genital Tract ... 23
E. Merz

6 Pelvic Inflammatory Diseases ... 25
E. Merz

7 Vaginal Masses ... 30
E. Merz

8 Uterine Masses ... 32
E. Merz

Benign Uterine Tumors (Myomas) ... 32
Malignant Uterine Tumors ... 32

9 Ovarian Masses ... 41
E. Merz, W. Goldhofer

Benign Ovarian Masses ... 41
Malignant Ovarian Tumors ... 42

10 Tubal Masses ... 56
E. Merz

Benign Tubal Masses ... 56
Tubal Carcinoma ... 56

11 Secondary Changes Associated with Gynecologic Tumors ... 57
E. Merz

12 Ultrasound Abnormalities in the Mid- and Upper Abdomen ... 60
E. Merz

Urinary Tract ... 60
Liver and Gallbladder ... 61
Spleen ... 61
Intestinal Tract ... 61

13 Localization of Intrauterine Contraceptive Devices ... 67
E. Merz

Correct Position ... 67
Lost IUD ... 67
Complications Associated with IUDs ... 69

14 Needle Procedures Guided by Abdominal Ultrasound ... 70
E. Merz

15 Postoperative Abdominal Ultrasound ... 72
Investigation of Postoperative Complications ... 72
Residual Urine Determination ... 72
E. Merz

16 Ultrasound in the Monitoring of Treatment Response ... 75
E. Merz

Intraoperative Ultrasound ... 79

17 Technical Aspects and Applications of Intraoperative Ultrasound ... 80

E. Merz, F. Bahlmann, and G. Weber

Technical Aspects ... 80
Applications in Gynecology ... 80

Perineal and Introital Ultrasound ... 85

18 Evaluation of the Lower Urinary Tract with Perineal and Introital Ultrasound ... 86

E.-M. Grischke

Sonographic Methods for Evaluating the Lower Urinary Tract ... 86
Perineal Ultrasound ... 86
Introital Ultrasound ... 87
Clinical Uses of Perineal and Introital Ultrasound ... 88

Transvaginal Ultrasound ... 91

19 Development and Current Role of Transvaginal Ultrasound ... 92

E. Merz

Historical Development ... 92
Current Role ... 92

20 Ultrasound Probes, Image Orientation, and Examination Technique ... 96

E. Merz

Ultrasound Probes ... 96
Scan Planes and Image Orientation ... 97
Examination Technique ... 97
Applications of Transvaginal Ultrasound in Gynecology ... 98

21 Anatomy of the Female Pelvis in Transvaginal Ultrasound ... 101

E. Merz

Vagina ... 101
Uterus ... 101
Uterine Biometry ... 101
Ovaries ... 105
Fallopian Tubes ... 105
Bladder ... 105
Ureters ... 108
Cul-de-Sac ... 108
Bowel ... 108
Pelvic Walls ... 108
Vessels ... 108
Lymph Nodes ... 108

22 Uterine and Ovarian Changes during the Menstrual Cycle ... 113

E. Merz

Uterine Changes during the Menstrual Cycle ... 113
Cervical Changes during the Menstrual Cycle ... 114
Ovarian Changes during the Menstrual Cycle ... 114
Sonographically Detectable Ovarian Changes ... 114

23 Sonographic Changes in the Stimulated Cycle and the Detection of Menstrual Disorders ... 120

E. Merz

The Endometrium in the Stimulated Cycle ... 120
Follicular Growth in the Stimulated Cycle ... 120
Monitoring Oocyte Maturation in an IVF Cycle ... 120
Abnormalities of Follicular Development ... 121

24 Genital Tract Anomalies ... 124

E. Merz

Uterine Anomalies ... 124
Vaginal Aplasia ... 124

25 Pelvic Inflammatory Disease ... 127

E. Merz

26 Vaginal Masses ... 130

E. Merz

Benign Vaginal Masses ... 130
Malignant Vaginal Tumors ... 130
Secondary Vaginal Malignancies ... 130

27 Uterine Masses ... 132

E. Merz, G. Weber

Benign Masses in the Uterine Corpus ... 132
Benign Masses in the Uterine Cervix ... 136
Malignant Uterine Tumors ... 136

28 Ovarian Masses ... 148

E. Merz

Benign Adnexal Tumors ... 149
Potentially Malignant Ovarian Tumors ... 153
Malignant Ovarian Tumors ... 159
Ultrasound Screening for Ovarian Carcinoma ... 162

29 Tubal Masses ... 164

E. Merz

Benign Tubal Masses ... 164
Tubal Carcinoma ... 164

30 Extragenital Masses ... 166

E. Merz

31 Ultrasound in the Follow-Up of Gynecologic Cancers ... *169*
G. Weber, E. Merz

Goals of Cancer Follow-Up Care ... *169*
Gynecologic Ultrasound Examination ... *169*

32 Localization of Intrauterine Devices ... *171*
E. Merz

Correct Position of the IUD ... *171*
IUD Mimics ... *171*
Lost IUD ... *172*
Other Complications Associated with IUDs ... *172*

33 Hysterosalpingo-contrast Sonography ... *174*
F. Degenhardt

Prerequisites and Preparations ... *174*
Indications for Ultrasound Tubal Assessment ... *174*
Examination Technique ... *175*
Evaluating the Uterus and Uterine Cavity ... *176*
Evaluating the Fallopian Tube and Ovary ... *176*
Adjunctive Techniques ... *180*
Advantages of Hysterosalpingo-contrast Sonography in Routine Applications ... *180*

34 Use of Transvaginal Ultrasound to Guide Needle Procedures in the True Pelvis ... *183*
E. Merz

Puncture Technique ... *183*
Transvaginal Follicular Aspiration ... *183*
Transvaginal Aspiration of Cysts ... *184*
Transvaginal Aspiration of Ascites ... *184*
Transvaginal Tissue Biopsy ... *184*

35 Transvaginal Ultrasound in the Investigation of Postoperative Complications ... *188*
G. Weber, E. Merz

Ultrasound Diagnosis ... *188*

36 Transvaginal Ultrasound in the Assessment of Treatment Response ... *191*
E. Merz

Myoma Reduction ... *191*
Endometriosis ... *191*

37 Transvaginal Ultrasound in Planning the Radiotherapy of Gynecologic Cancers ... *193*
V. Jaspers

Transvaginal Doppler Ultrasound (Color Doppler and Pulsed Doppler) ... *197*

38 Basic Principles and Practical Application of Transvaginal Doppler Ultrasound in Gynecology ... *198*
F. Bahlmann, E. Merz

Doppler Effect ... *198*
Pulsed Doppler Ultrasound, Pulsed-Wave (PW) Doppler ... *198*
Doppler Parameters ... *198*
Color Doppler Ultrasound ... *198*
Specific Vessels ... *199*
Power Doppler Imaging ... *199*

39 Transvaginal Doppler Ultrasound in the Evaluation of Infertility and Gynecologic Tumors ... *204*
A. Kurjak, S. Kupesic

Ovary ... *204*
Uterus ... *205*
Color Doppler Examination of the Ovary and Uterus and its Value in Infertile Patients ... *205*
Color Doppler Studies in Tumors ... *206*
Pitfalls and Artifacts ... *219*

Transvaginal 3D and 4D Ultrasound ... *221*

40 Transvaginal 3D/4D Ultrasound and its Applications in Gynecology ... *222*
E. Merz

Development of Transvaginal 3D Ultrasound ... *222*
Technical Aspects of 3D Ultrasound ... *222*
Advantages of Transvaginal 3D Ultrasound ... *223*
Problems in Transvaginal 3D Ultrasound ... *224*
Technical Aspects of 4D Ultrasound ... *224*
Applications of 3D and 4D Ultrasound ... *225*
Critical Appraisal and Outlook ... *226*

Transrectal Ultrasound ... *241*

41 Transrectal Ultrasound: Technique and Applications ... *242*
E. Merz

Development of Transrectal Ultrasound ... *242*
Probes ... *242*
Preparation ... *242*
Normal Anatomy ... *242*
Applications in Gynecology ... *243*
Obstacles in Transrectal Ultrasound ... *243*

Transuterine Ultrasound ... 247

42 Transuterine Ultrasound: Technique and Applications ... 248

E. Merz, V. Jaspers

Breast Ultrasound ... 251

43 Ultrasound Diagnosis of Breast Diseases ... 252

H. Madjar

Epidemiology of Breast Cancer ... 252
Results of Mammographic Screening ... 252
Role of Ultrasound ... 252
Examination Technique ... 253
Evaluation of Breast Masses ... 253

Breast Ultrasound ... 265

44 3D and 4D Breast Ultrasound ... 266

E. Merz, A. Oberstein

Introduction ... 266
Examination Technique ... 266
Display Options in 3D and 4D Breast Ultrasound ... 267
Applications ... 273
Advantages and Problems of 3D Breast Ultrasound ... 292
Critical Appraisal and Outlook ... 293

Appendix ... 297

45 Normal Organ Dimensions and Hemodynamic Values in Gynecologic Ultrasound ... 298

E. Merz

Normal Doppler Indices in the Vessels of the Internal Genitalia ... 299

Index ... 300

General

1 Criteria for Describing an Ultrasound Mass

An accurate description of the sonographic findings using standard nomenclature [1,2] is the basis for careful interpretation of any ultrasound examination. Particularly in the case of gynecologic masses, it would be incorrect to classify a lesion as a "myoma" or as an "ovarian cyst" on the basis of its initial appearance. A more rigorous method is to make a detailed description of the mass based on the assessment of various sonographic criteria (Table 1.1). After reviewing all of these criteria, the examiner can then proceed to interpret the findings and make a differential diagnosis.

Table 1.1 Criteria for describing an ultrasound mass

1 Affected organ
2 Size (in mm or cm)
3 Shape
- Round
- Oval
- Oblong
- Scalloped

4 Internal echo pattern (structure)
- Simple (homogeneous)
- Complex (nonhomogeneous)

A Cystic mass, cystic area
Evaluating the internal echoes
- Location of the internal echoes
  - No internal echoes
  - Peripheral
  - Central
  - Ubiquitous
- Size of the internal echoes
  - Fine
  - Moderately coarse
  - Coarse
- Intensity of the internal echoes (echogenicity)
  - Low-level
  - Medium-level
  - High-level
  - Extremely high-level (hyperechoic)
- Spacing of the individual echoes
  - Loose
  - Moderately dense
  - Dense
- Distribution of the internal echoes
  - Uniform distribution
  - Nonuniform distribution
  - Number of compartments
  - Wall thickness (in mm)
  - Septal thickness (in mm)

B Solid mass, solid area, solid echo complex
a) Intensity (echogenicity, see above)
b) Distribution of the internal echoes (see above)
c) Location, size, and shape of the solid area/echo complex

5 Margins
- Smooth
- Irregular

6 Delineation
- Well delineated
- Poorly delineated
- Nondelineated

7 Mobility
- Very mobile relative to adjacent organs
- Limited mobility
- Immobile

8 Compressibility
9 Acoustic shadowing or enhancement
10 Detecting movement within the mass

It is important to consider the technique of the ultrasound examination, especially in gynecologic ultrasound, because the scanning approach that is used (abdominal, vaginal, rectal, or perineal) as well as the transducer frequency will determine how well the internal echo characteristics of a gynecologic mass can be defined.

It should also be emphasized that accurate diagnosis requires optimum equipment settings. For example, it is extremely difficult to detect internal echoes if the instrument gain is set too low, whereas setting the gain too high will cause reverberations that mimic an internal echo pattern.

Localizing the Mass to a Specific Organ

During the initial part of the examination, an effort should be made to localize an ultrasound abnormality to a specific organ. This is best accomplished by following a systematic routine based on designated planes of section.

It is not always possible to identify the affected organ. This can be particularly difficult if the lesion has disrupted the normal organ boundaries, for example, or when one is dealing with an inflammatory conglomerate mass in which several organs are matted together. In other cases, closely adjacent structures may have such a similar ultrasound appearance that they are easily confused with each other (e.g., a pedunculated subserous myoma versus an ovarian tumor).

It can also be difficult to localize a lesion to the right or left side. For example, an adnexal mass does not necessarily involve the side on which it is detected, because a mobile adnexal mass may become displaced to the opposite side. A large adnexal mass often occupies a midline position and cannot be definitely assigned to the right or left side unless the contralateral adnexa can be clearly visualized.

If the mass cannot be definitely assigned to a specific organ, it should at least be localized to a particular region (e.g., the left adnexal region or the cul-de-sac).

Size of the Mass

A mass should always be imaged and measured in three planes in order to define its full extent. Its length, height, and width should be measured as outer-to-outer dimensions, in each case taking the maximum diameter in each plane of section.

Shape of the Mass

A mass may present a uniform or nonuniform shape. A *uniform mass* may be described as round, oval, pear-shaped, or oblong, or it may be compared to some other familiar geometric shape. *Masses with a nonuniform shape* are described as "scalloped."

Internal Echo Pattern

A mass may present a simple or complex internal echo pattern, depending on its contents. A *simple mass* is one that has a uniform or homogeneous sonographic appearance. A homogeneous mass may be devoid of internal echoes (a unilocular cyst) or may contain internal echoes (a cyst with floating particles or a solid tumor). A *complex mass*, on the other hand, has a nonuniform or nonhomogeneous appearance. A nonhomogeneous mass may be a multilocular cystic mass, a mixed cystic and solid mass, or a solid tumor that contains areas of contrasting echogenicity.

Internal echoes found within a *cystic mass* are evaluated with regard to their location, size, and intensity. The spacing and distribution of the echoes are also assessed, and the number of compartments, wall thickness, and maximum septal thickness are determined.

With a *mixed cystic and solid mass*, the cystic portion of the mass is described as noted above. In addition, the solid portion of the mass is characterized as having a regular or irregular shape, and its echogenicity is assessed. The same criteria are used in evaluating an intracystic mural nodule.

With a *purely solid tumor*, the echo pattern (regular/irregular) and echogenicity of the lesion are described. Particular attention is given to echogenicity, noting whether the echo amplitudes are uniform throughout the tumor or whether there are areas of contrasting echogenicity.

Cystic Mass, Cystic Area

Internal Echoes

If a mass or a certain area is devoid of internal echoes, it is described as echo-free (or anechoic). But if internal echoes are present, they are evaluated with regard to their location, size, intensity, spacing, and distribution.

Location of the internal echoes. Location refers to where the echoes are located within a cystic area—i.e., whether they are *peripheral*, *central*, or *ubiquitous*.

Size of the individual echoes (Fig. 1.1). Echo size refers to the surface area of the individual echoes in the B-mode ultrasound image. Small echoes are described as fine, medium-size echoes as moderately coarse, and large echoes as coarse.

Intensity level of the individual echoes (Fig. 1.2). The intensity level indicates the strength or amplitude of the echoes. *Low-level echoes* have a low amplitude, *medium-level echoes* have a moderate amplitude, and *high-level echoes* have a high amplitude. Internal echoes of extremely high amplitude can be described as *hyperechoic*.

Spacing of the individual echoes. Echo spacing refers to the density of the internal echoes—i.e., the number of echoes that are displayed per unit area. Echoes are described as *scattered* if they are spaced far apart, *moderately dense* if they are spaced somewhat far apart, and *dense* if they are spaced close together.

Distribution of the individual echoes (Fig. 1.1). Echoes are described as having a uniform or nonuniform distribution. This pertains to the size of the echoes as well as their spacing.

Number of Compartments

The number of compartments can be determined in multilocular cystic masses. The compartments may be described separately or jointly, depending on whether their internal echo patterns are different or the same.

Wall Thickness

Wall thickness can be measured only in cystic masses and is stated in millimeters. If the wall thickness varies at different sites, the maximum wall thickness is determined.

Septal Thickness

Septal thickness is determined in the same way as wall thickness. If sites of circumscribed thickening are seen, the maximum septal thickness is determined.

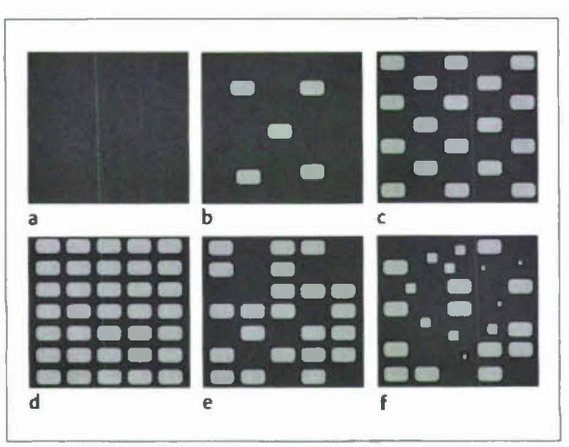

1

Fig. 1.1 The spacing of individual echoes and the uniformity of the echo distribution.
a Uniform echo pattern, echo-free.
b Uniform echo pattern, scattered internal echoes.
c Uniform echo pattern, moderately dense internal echoes.
d Uniform echo pattern, dense internal echoes.
e Nonuniform echo pattern with echoes of equal sizes.
f Nonuniform echo pattern with echoes of different sizes (fine, moderately coarse, coarse).

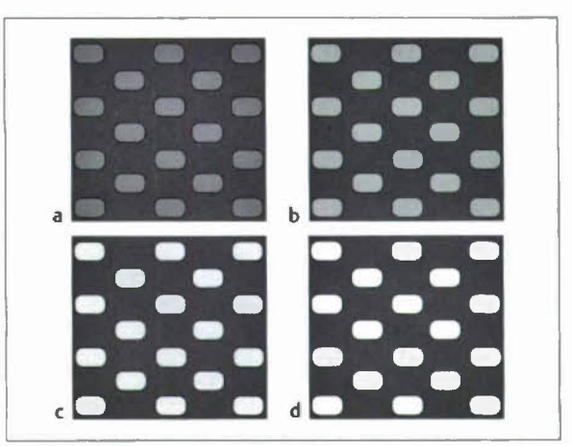

2

Fig. 1.2 Intensity levels of internal echoes.
a Low-level echoes.
b Medium-level echoes.
c High-level echoes.
d Hyperechoic.

Solid Tumor, Solid Area, or Solid Echo Complex

The internal echo pattern of a *purely solid tumor* is evaluated on the basis of the intensity and distribution of the echoes. If a *complex mass* is found to contain a solid area or an isolated echo complex (e.g., a papillary wall structure), the location, size and shape of the solid area should be assessed in addition to the echogenicity and echo distribution.

Margins

The margins of a mass are described as smooth or irregular.

Delineation

The delineation of a mass refers to how clearly the mass is demarcated from its surroundings: well delineated, poorly delineated, or undelineated.

Mobility

By applying pressure with the transducer, the examiner can determine how mobile a mass is in relation to neighboring organs. The mass may be very mobile relative to its surroundings, it may show limited mobility, or it may be immobile (fixed).

Compressibility

In transvaginal sonography, it is possible to apply direct pressure to the mass with the endovaginal probe. The degree of compressibility will vary depending on whether the lesion is a soft cystic mass, a tense cystic mass, or a firm solid tumor, and in this way the examiner can evaluate the consistency of the mass.

Acoustic Shadowing and Acoustic Enhancement

Acoustic Shadowing

Acoustic shadowing refers to the sound attenuation that occurs behind a mass as a result of physical effects (absorption, reflection, scattering, diffraction, refraction). The mass may cast a *complete shadow* that is devoid of any echoes or an *incomplete shadow* in which some echoes are still present. An acoustic shadow is produced by solid areas.

Acoustic Enhancement

Acoustic enhancement is present when the echoes returned from the area behind a mass are of greater amplitude than those returned from adjacent areas. It occurs when the mass itself absorbs less sound energy than its surroundings or functions in much the same way as a light-gathering lens [3]. The presence of acoustic enhancement always indicates a cystic structure.

Detecting Movement within a Mass

The great advantage of ultrasonography is that it is not a static examination; it can detect movement. This is useful in cases in which it is important to differentiate a gynecologic mass, for example, from a distended loop of bowel. While a true gynecologic mass will not change its appearance, a distended bowel loop can be recognized by noting movement of its contents during prolonged observation.

Uncertainties in the Description of Findings

Ultrasound findings cannot always be described with precision. If there are any uncertainties in describing a lesion, they should be noted in writing, with the finding being described as "*indeterminate*" or "*equivocal*." If an organ cannot be visualized at ultrasound, it should be reported as "currently not seen."

Benign–Malignant Differentiation

When the above criteria are applied, a mass can be classified as benign or malignant with reasonable confidence on the basis of its sonographic features. It should be considered, however, that the ultrasound evaluation of a mass is a macroscopic impression and not a microscopic analysis. As such, it can never replace a histologic examination.

A three-part classification scheme is recommended for the benign–malignant differentiation of masses by ultrasound: *benign*, *indeterminate*, and *malignant*.

References

1 Bönhof JA. Richtig benennen – besser erkennen. Ein Beitrag zur Terminologie der Sonogrammbeschreibung. Ultraschall Klin Prax 1987:2:178–84.
2 Merz E. Beschreibung auffälliger sonographischer Befunde. In: Merz E. Vaginosonographie. Stuttgart: Enke, 1992: 20–4.
3 Ziskin MC, LaFollette PS Jr, Radecki PD, Villafana T. The retrolenticular afterglow: an echo enhancement artifact. J Ultrasound Med 1986:5:385–9.

Abdominal Ultrasound

2 Areas of Application and Examination Technique

Areas of Application

Imaging modalities such as ultrasonography, computed tomography, and magnetic resonance imaging have become increasingly important in gynecologic diagnosis. In comparison with the more costly and complex modalities of computed tomography and magnetic resonance imaging, ultrasonography provides a simple, economical method for visualizing the abdominal organs.

Real-time sector transducers and curved-array probes have become the instruments of choice for transabdominal ultrasound scanning (Fig. 2.**1**). Their beam angle provides a better lateral view into the true pelvis than that afforded by real-time linear-array scanners.

When the normal sonographic anatomy of the true pelvis and the limitations of ultrasound technology are understood, sonography not only provides a useful, easily available adjunct to the bimanual examination but is often superior to it for determining the size of pelvic masses and localizing masses to specific organs. But at the same time, gynecologic ultrasound requires considerable experience on the part of the examiner, due to the extreme variability of normal and pathologic findings and the potential for misinterpretation. Moreover, abdominal ultrasound will not yield a satisfactory examination in some gynecologic patients due to the impact of abdominal-wall thickness and tissues on the quality of the ultrasound image. Especially in very obese patients, the value of abdominal ultrasound may be seriously compromised by the limited penetration depth and poor image quality.

While there has been a marked trend in recent years toward the greater use of transvaginal sonography in gynecologic diagnosis and treatment, there are many areas in which abdominal sonography can still be used and still has routine applications (Tables 2.**1**, 2.**2**).

In the majority of patients, ultrasound evaluation of the true pelvis is done to investigate a mass that was noted during the manual examination. There are several goals that the ultrasound examination should accomplish in cases of this kind:

- Define and localize the mass (unilateral or bilateral).
- Determine the size of the mass.
- Localize the mass to a specific organ.
- Differentiate the mass: cystic, solid, or mixed cystic/solid; smooth or indistinct margins; no internal echoes, homogeneous or nonhomogeneous internal echo pattern.
- Assess the mobility of the mass.
- Detect or exclude additional criteria for malignancy in suspicious cases (e.g., ascites, hepatic metastases).

When an abnormal mass is present in the true pelvis, abdominal ultrasound can detect it in almost 90% of cases [1–6] and is clearly superior to a manual pelvic examination [3,6]. On the other hand, even sonography is only 60–70% accurate in localizing a mass to a specific organ [7].

The major advantage of ultrasound lies in its ability to differentiate between solid and cystic masses. Often this distinction can be made solely on the basis of the sound-absorption characteristics of the lesion. Because solid tumors absorb sound waves, the wall of the mass facing the transducer tends to be clearly defined, while the far wall is often obscured by *acoustic shadowing*. However, sound absorption does not occur in cystic masses, owing to the good sound conductivity of the cystic fluid. As a result, the far wall of the cyst and the tissues behind it show increased echogenicity relative to their surroundings. This phenomenon is called *posterior acoustic enhancement*.

Table 2.1 Possible diagnostic applications of abdominal ultrasound in gynecology

- Monitoring follicular growth as part of an infertility evaluation
- Investigation of genital anomalies
- Investigation of lower abdominal pain and inflammatory changes, especially in patients with muscular guarding or rigidity
- Investigation of pelvic masses
- Checking the placement of intrauterine contraceptive devices
- Residual urine determination
- Detection of secondary tumor signs (ascites, hepatic metastases, urinary tract obstruction)
- Follow-up of functional cysts, monitoring response to medical endometriosis therapy or oncologic treatment
- Postoperative investigations (postoperative bleeding, hematoma, lymph cyst, cul-de-sac abscess, urinary stasis)

Table 2.2 Possible therapeutic applications of abdominal ultrasound in gynecology

- Ultrasound-guided follicular aspiration as a prelude to in-vitro fertilization
- Ultrasound-guided aspiration of cysts
- Ultrasound-guided drainage of ascites
- Ultrasound-guided drainage of a lymph cyst

With the advent of *gray-scale imaging* [8,9], it became possible to make a differentiated evaluation of the internal structure of masses. But even with this technology, diagnostic problems can still arise due to incorrect equipment settings or in cysts with a dense internal echo pattern. A well-perfused solid tumor or a tumor that has undergone cystic degeneration may be mistaken for a cyst if the gain is set too low. Conversely, a cyst with internal bleeding or a distended bowel loop may have an internal echo pattern that mimics that of a solid tumor. Often these doubts can be resolved by palpation, which also makes it possible to assess the consistency of the lesion.

Ultrasound cannot reliably distinguish between benign and malignant lesions. However, it can display irregularities in the contour and echo pattern of a mass or detect the presence of secondary changes, such as ascites or hepatic metastases, that provide a high index of suspicion for a malignant tumor.

On the whole, sonography is a valuable addition to the gynecologic examination and in many cases can furnish a specific diagnosis when interpreted within the context of the patient's history, pelvic examination, and laboratory findings.

Examination Technique

The prerequisite for any gynecologic ultrasound examination is a well-distended urinary bladder [10,11]. When the bladder is empty, the uterus and adnexa are obscured by overlying bowel loops, which hamper or prevent their visualization. But when the bladder fills with urine, it displaces the bowel out of the true pelvis, creating an acoustic window and a "water path" through which the pelvic organs can be scanned. In practice, the patient is given 1 L of a noncarbonated liquid to drink approximately 1 h before the examination. The examination begins when the patient feels definite pressure on her bladder. The bladder is ideally

distended when it just covers the full length of the uterus. An overdistended bladder may displace organs out of the true pelvis or press them against the pelvic wall, making them difficult to evaluate. If the bladder is inadequately distended, the uterine fundus and adnexal regions will be poorly visualized. In situations requiring an acute diagnosis, such as a suspected ectopic pregnancy, the bladder can be distended in retrograde fashion by instilling 300–400 mL of saline solution (0.9%) through a disposable catheter using an aseptic technique.

Besides a full bladder, an empty bowel is important in pelvic ultrasound examinations, because bowel loops filled with solid or liquid material can mimic a cystic or solid adnexal or cul-de-sac mass, depending on their contents. Gas-filled bowel loops, on the other hand, will reflect 100% of incident sound waves and prevent the scanning of underlying tissues.

Transabdominal scanning of the female pelvis is carried out with the patient supine. The examiner usually sits on the patient's left side (Fig. 2.**2**). The study begins with a longitudinal midline scan over the lower abdomen to confirm adequate bladder filling and establish the location and size of the uterus and cul-de-sac (scan plane I; Figs. 2.**2**, 2.**3**, 2.**7**). The transducer is moved to a more lateral, parallel plane to obtain a longitudinal section of the ovary (scan plane II, Figs. 2.**2**, 2.**4**, 2.**7**). The initial longitudinal scans are followed by a series of transverse scans beginning at the suprasymphyseal level (scan planes III–VIII, Figs. 2.**2**, 2.**5**, 2.**8**). The transducer can be angled or moved cranially as needed in order to obtain adequate views of the various pelvic levels and pelvic walls (Figs. 2.**7**, 2.**8**). Occasional oblique scans may also be necessary for optimal visualization of certain lesions (scan plane IX, Figs. 2.**2**, 2.**6**, 2.**7**).

To obtain *standard sonographic views*, the transducer should always be oriented in such a way that the left side of the longitudinal image is cranial and the right side is caudal (Fig. 2.**9**). On transverse scans, the right side of the patient should be displayed on the left side of the image, and the left side should be displayed on the right side of the image, conforming to an anatomical view (Fig. 2.**10**, Table 2.**3**).

If the ultrasound examination is done as part of a tumor work-up, the pelvic scans should be followed by views of the kidneys and urinary tract, the para-aortic region, and the liver in order to detect or exclude secondary changes such as urinary tract obstruction, para-aortic lymphoma, ascites, and hepatic metastases.

Table 2.**3** Image orientation in abdominal ultrasound

Sagittal scans	
Top of image	Anterior
Bottom of image	Posterior
Right side of image	Caudal
Left side of image	Cranial
Transverse scans	
Top of image	Anterior
Bottom of image	Posterior
Right side of image	Left
Left side of image	Right

References

1 Fleischer AC, James AE JR, Millis JB, Julian C. Differential diagnosis of pelvic masses by gray scale sonography. AJR Am J Roentgenol 1978;131:469–76.
2 Lawson TL, Albarelli JN. Diagnosis of gynecologic pelvic masses by gray-scale ultrasonography: analysis of specificity and accuracy. AJR Am J Roentgenol 1977;128:1003–6.
3 Nellen HJ, Hansmann M. Ultraschall in der gynäkologischen Tumordiagnostik. Arch Gynäkol 1973;214:275–9.
4 Queenan JT, Kubarych SF, Douglas DL. Evaluation of diagnostic ultrasound in gynecology. Am J Obstet Gynecol 1975;123:453–65.
5 Requard CK, Mettler FA Jr, Wicks JD. Preoperative sonography of malignant ovarian neoplasms. AJR Am J Roentgenol 1981;137:79–82.
6 Zanke S, Meinhold P, Eichhorn KH. Präoperative Differentialdiagnose von gynäkologischen Tumoren durch Ultraschall. Zentrabl Gynäkol 1980;102:990–9.
7 Hansmann M, Hackelöer BJ, Staudach A. Ultraschalldiagnostik in der Geburtshilfe und Gynäkologie. Lehrbuch und Atlas. Berlin: Springer, 1985.
8 Burckhardt CB. Technische Grundlagen der Grauwertdarstellung. Ultraschall 1980;1:242–6.
9 Kratochwil A. Ultraschall-Grauwerttechnik. Ultraschall 1980;1:232–41.
10 Donald I. Ultrasonic echo sounding in obstetrical and gynecological diagnosis. Am J Obstet Gynecol 1965;93:935–41.
11 Kratochwil A. Ultraschalldiagnostik in der Gynäkologie. Gynäkologie 1976;9:166–80

Fig. 2.1 Probes for abdominal gynecologic ultrasound examinations. *Left:* sector probe. *Right:* curved array.

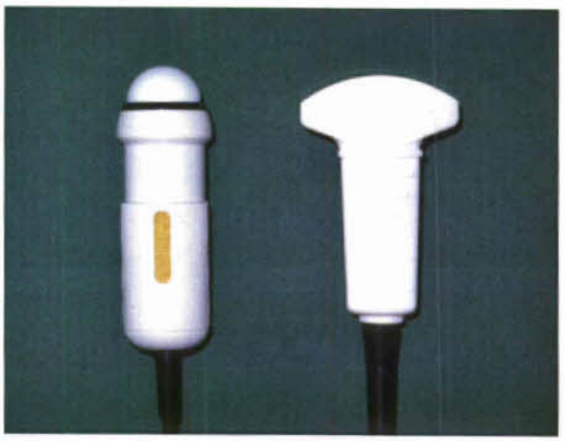

1

Fig. 2.2 Set-up for an abdominal ultrasound examination. The examiner sits to the left of the patient, and the examiner and patient each have their own monitor. I = Midsagittal scan, II = parasagittal scan, III–VIII = suprasymphyseal transverse scans, IX = oblique scan.

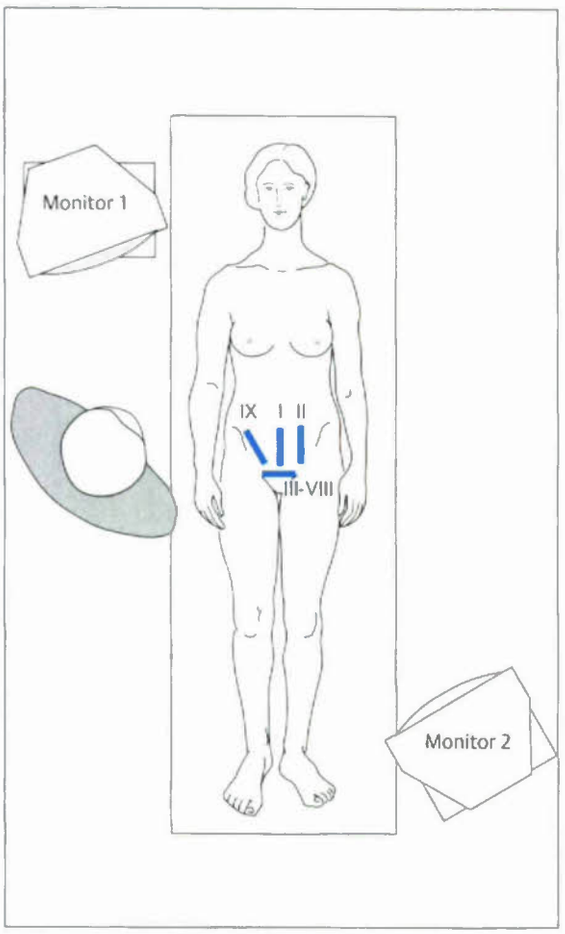

2

Fig. 2.3 Probe placement for a midsagittal scan.

3

Fig. 2.4 Probe placement for a left parasagittal scan.

4

Fig. 2.5 Probe placement for a suprasymphyseal transverse scan.

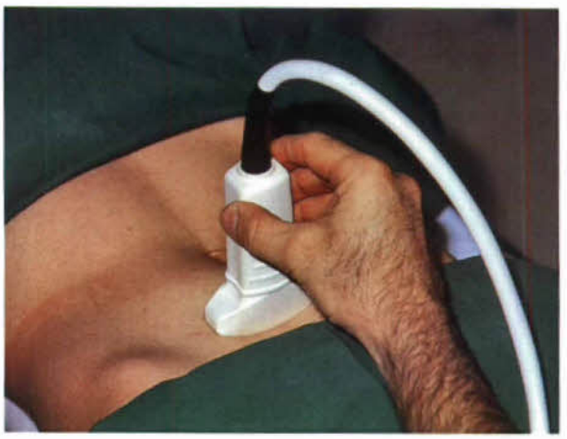

5

Fig. 2.6 Probe placement for an oblique scan through the right pelvic wall.

6

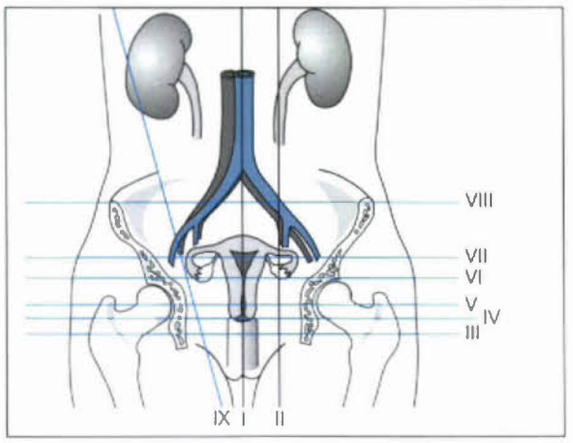

7

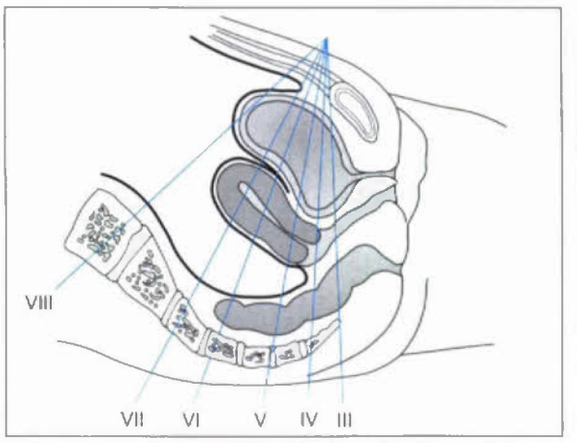

8

Fig. 2.7 Scan planes used in gynecologic ultrasound, anterior view.

Fig. 2.8 Scan planes used in gynecologic ultrasound, lateral view.

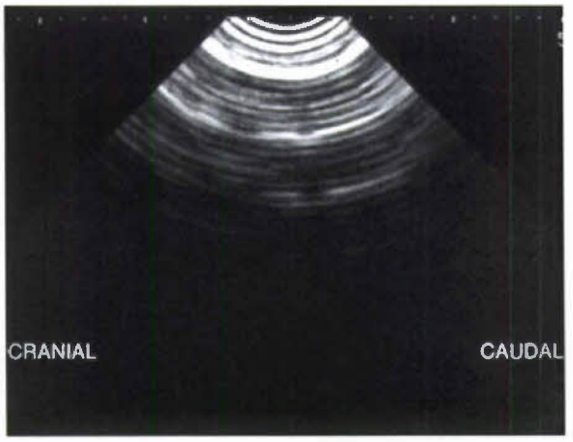

9

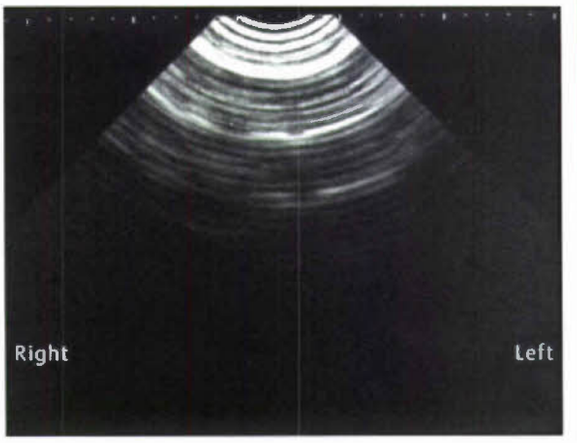

10

Fig. 2.9 Correctly oriented display of a longitudinal sonogram.

Fig. 2.10 Correctly oriented display of a transverse sonogram (conforms to anatomy).

3 Anatomy of the Female Pelvis

The female true pelvis contains the uterus, both adnexa, the vagina, the urinary bladder and ureters, and the rectum (Figs. 3.**1**, 3.**2**) [1]. All of these organs except the ureters can be visualized with abdominal ultrasound when the bladder has been adequately distended.

Uterus

In the longitudinal midline survey scan (plane I, Fig. 3.**3**), the uterus can be seen just behind the filled bladder, appearing as a pear-shaped, hypoechoic organ consisting of a corpus (body), isthmus, and cervix (Fig. 3.**1**). The size and appearance of the uterus vary markedly according to the patient's age and parity (Figs. 3.**4**–3.**15**) [1,2].

Bundscherer and Freundl [2] state that the uterus, which is estrogen-stimulated at birth, initially undergoes a rapid involution and remains relatively constant from the second to the eighth year of life. The prepubertal growth phase of the uterus begins during the ninth year of life (Table 3.**1**) [2]. According to Bernaschek et al. [3], however, the sonographic size of the uterus (uterine length × corpus depth × corpus width) increases almost linearly from 2.4 × 0.8 × 1.0 cm at 1 year of age to 4.0 × 1.2 × 1.6 cm at 13 years of age. The uterus measures approximately 7 × 3 × 4 cm in the sexually mature nullipara (Figs. 3.**4**, 3.**12**) and can measure up to 10 × 5 × 6 cm in multiparous women. Piiroinen [4] determined an average uterine length of 7.6 ± 0.7 (1 SD) cm in nulliparae and an average AP diameter of 2.9 ± 0.4 (1 SD) cm. For women who have born one child, he reports corresponding dimensions of 8.9 ± 0.9 (1 SD) cm and 3.8 ± 0.6 (1 SD) cm.

The uterus varies in size during the ovulatory cycle, reaching its smallest size on day 12 of the cycle and its largest size on day 27, according to serial sonographic measurements [5].

After menopause, the uterus again decreases in size (Figs. 3.**7**, 3.**14**, 3.**15**) and may shrink to approximately 4.5 × 1.5 × 2.0 cm.

When the urinary bladder is empty or only slightly distended, the uterus tends to assume a position of marked anteversion and anteflexion (Fig. 3.**16**). As the bladder fills with urine, the angle between the uterine axis and vaginal axis increases, and the uterus may straighten if the bladder is strongly distended (Fig. 3.**17**). In the retroflexed uterus (Figs. 3.**18**, 3.**19**), the uterine corpus is bent backward into the cul-de-sac. With severe retroflexion it may be difficult to evaluate the uterus and particularly the fundal part due to its greater distance from the transducer. The uterus itself has smooth borders and appears as a homogeneous, relatively hypoechoic structure with a central, linear endometrial echo, whose intensity varies on different days of the menstrual cycle (see pp. 47 ff.).

The suprasymphyseal transverse scan can be angled to demonstrate the different segments of the uterus. Directing the beam perpendicular to the abdominal wall or angling it slightly cephalad (plane V, Fig. 3.**20**) will display the cervix and parametrial connective tissue (Fig. 3.**21**). The scan plane can be angled farther cephalad (plane VI, Figs. 3.**22**, 3.**23**) to define the central portion of the uterine corpus.

Angling the scan plane even farther cephalad (plane VII, Fig. 3.**20**) will provide a transverse view through the upper portion of the uterine corpus (Fig. 3.**24**). Normally, the fallopian tubes and uterine round ligaments have about the same echogenicity as their surroundings and are not delineated, but they can be identified when pathologic changes are present such as ascites or changes in the organs themselves (e.g., hydrosalpinx).

Table 3.**1** Physiologic changes in uterine dimensions with aging (after Bundscherer and Freundl [2])

Age group	n	Length mm (SD)	Height mm (SD)	Width mm (SD)
Week 1–4	26	40 (5)	11 (2)	16 (4)
Month 2–6	14	35 (4)	9 (2)	12 (3)
Month 7–12	5	28 (5)	7 (1)	11 (1)
Age 2	9	28 (3)	8 (2)	11 (3)
Age 3	8	30 (2)	7 (2)	9 (3)
Age 4–5	10	29 (3)	7 (2)	12 (2)
Age 6–7	11	29 (4)	7 (1)	11 (1)
Age 8	17	33 (5)	7 (1)	12 (1)
Age 9	13	36 (6)	7 (1)	12 (2)
Age 10	19	37 (4)	7 (2)	11 (2)
Age 11	28	41 (7)	9 (3)	15 (4)
Age 12	16	47 (9)	11 (4)	18 (6)
Age 13	26	57 (11)	17 (5)	28 (9)
Age 14	11	70 (10)	22 (5)	29 (6)
Age 15	18	70 (8)	25 (5)	35 (9)
Age > 15	20	67 (9)	23 (5)	37 (10)

With extreme distension of the urinary bladder, the spinal column with the psoas muscle and common iliac vessels (Fig. 3.**25**) can be identified in a transverse plane directly above the uterine fundus (plane VIII, Fig. 3.**20**).

Vagina and Bladder

The vagina can be identified in the longitudinal scan as an echogenic, anteriorly convex double line located just behind the bladder between the uterine corpus and pubic symphysis (Figs. 3.**1**, 3.**8**–3.**19**). Posterior to the vagina and uterus is the rectum (Figs. 3.**1**, 3.**8**–3.**19**), whose echogenicity varies with its degree of distension.

Positioning the probe transversely and directing the beam slightly caudad provides a scan (plane IV, Fig. 3.**20**) that demonstrates the trigone of the bladder with the two ureteral orifices (Fig. 3.**26**) and, just behind that, the upper third of the vagina. When the scan is directed at an even lower angle (plane III, Fig. 3.**20**), the urethra appears as a ring-shaped structure anterior to the vagina (Fig. 3.**27**).

Ovaries

If the ovaries are not too far away from the uterus, they can be imaged concurrently with the uterine corpus in a transverse scan (plane VI or VII, Figs. 3.**20**, 3.**28**). But because the ovaries are highly variable in their location, it is not always possible to display both ovaries in one plane of section, and it may be necessary to slide the transducer in the cranial or

caudal direction in order to define the second ovary. If the ovary is close to the pelvic wall or is quite high in the pelvis (Fig. 3.**29**), it may be concealed by overlying bowel. The same is true of the ovaries after menopause (Fig. 3.**30**), the small size of which often makes them very difficult to distinguish from surrounding loops of bowel.

Occasionally, a distended bowel segment can mimic an ovary, but observing the feature for several minutes with a real-time scanner will usually demonstrate peristaltic motion. If it is still uncertain whether the imaged area is the ovary, the examiner can obtain a paravertebral longitudinal scan (plane II, Figs. 3.**3**, 3.**31**) and look for the iliac vessels or the ovarian vessels in the ovarian suspensory ligament (Fig. 3.**32**) to confirm the identity of the feature [6].

Bernaschek et al. [3] report that the average ovarian volume is 0.26 cm^3 by 1 year of age and increases steadily to an average of 1 cm^3 by 13 years of age. In women of childbearing age, the sonographic size of the ovary is approximately 3.0 × 1.5 × 2.0 cm (length × height × width). The average ovarian volume is 4.33 ± 1.91 cm^3 (1 SD) according to Campbell et al. [7] and 4 cm^3 (1.8–5.7 cm^3) according to Sample et al. [8]. The ovarian volume is easily calculated from the three linear measurements by applying the simplified formula for an ellipsoid: V = 0.5 × length × height × width [8].

Vessels

A lateral longitudinal or oblique scan can define the common iliac vessels, which branch distally into the external and internal iliac vessels (Fig. 3.**33**). Visualization of the pelvic vessels is usually done for the diagnosis of paravascular lymph-node enlargement or for detecting or excluding suspected thrombosis of the pelvic wall.

Abdominal Wall

The abdominal wall cannot be satisfactorily imaged with conventional 3.5-MHz transducers, which are designed to image structures at greater depths. But a higher-frequency transducer (5–10 MHz) has a shorter focal zone that can delineate the individual layers of the abdominal wall (Figs. 3.**34**–3.**37**). Above the umbilicus, the rectus abdominis muscle is surrounded by the anterior and posterior layers of the rectus sheath (anterior layer = tendons of the internal and external oblique muscles; posterior layer = tendons of the internal oblique and transversus abdominis muscles). The inner layer is absent below the arcuate line, and the two rectus muscles at that level are bounded posteriorly only by the transversalis fascia. In the midline between the two rectus muscles is the linea alba, a tendinous band extending from the xiphoid process to the upper border of the pubic symphysis.

References

1 Netter FH. Farbatlanten der Medizin, vol. 3: Genitalorgane. 2nd ed. Stuttgart: Thieme, 1987.
2 Bundscherer F, Freundl K. Die Uterusentwicklung im Kindesalter. Sonographische Normalwerte und Vergleich mit klinischen Zeichen der pubertären Entwicklung. Ultraschall Klin Prax 1992;7:32–6.
3 Bernaschek G, Lubec G, Schaller, A. Sonographische Untersuchungen über das Wachstum von Uterus und Ovarien zwischen dem 1.–14. Lebensjahr. Geburtshilfe Frauenheilkd 1984;44:727–30.
4 Piiroinen O. Studies in diagnostic ultrasound: size of the nonpregnant uterus in women of childbearing age and uterine growth and fetal development in the first half of normal pregnancy. Acta Obstet Gynecol Scand Suppl 1975;46:1–60.
5 Piiroinen O, Kaihola HL. Uterine size measured by ultrasound during the menstrual cycle. Acta Obstet Gynecol Scand 1975;54:246–50.
6 Hackelöer BJ, Nitschke-Dabelstein S. Ovarian imaging by ultrasound: an attempt to define a reference plane. J Clin Ultrasound 1980;8:497–500.
7 Campbell S, Goessens L, Goswamy R, Whitehead M. Real-time ultrasonography for determination of ovarian morphology and volume. Lancet 1982;i:425–6.
8 Sample WF, Lippe BM, Gyepes MT. Gray-scale ultrasonography of the normal female pelvis. Radiology 1977;125:477–83.

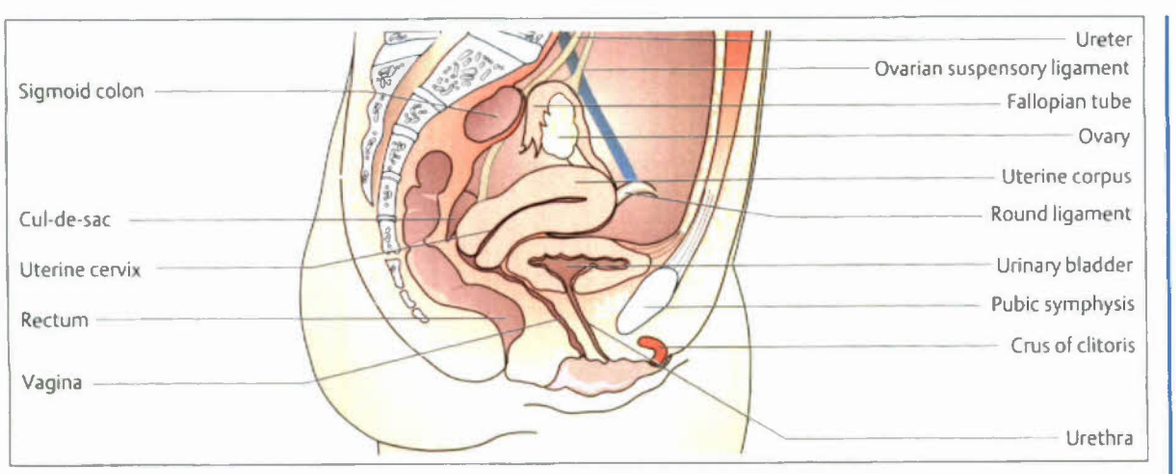

1

Fig. 3.**1** Anatomical longitudinal section through the female pelvis (after Netter [5]).

Fig. 3.2 Anatomical cross-section through the female pelvis.

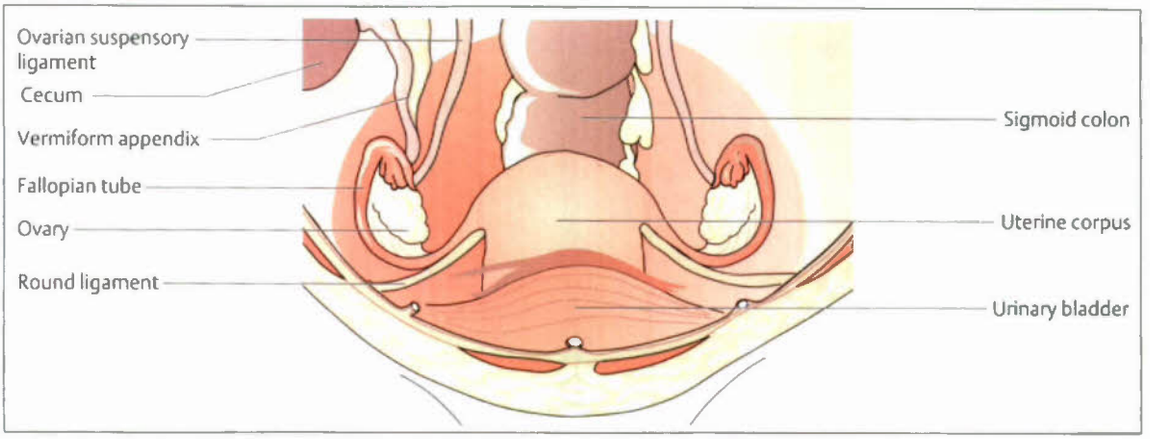

2

Fig. 3.3 Longitudinal and transverse scan planes used in abdominal ultrasonography: anterior aspect.

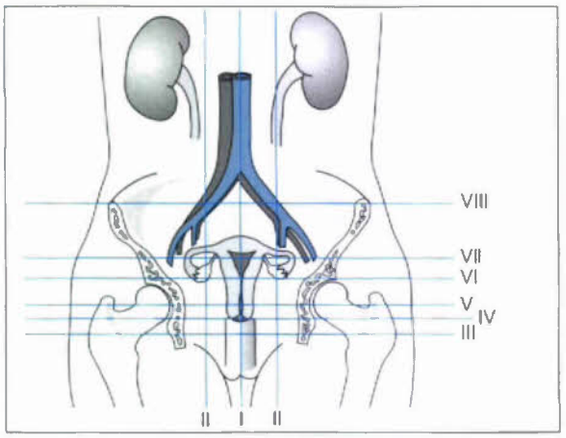

3

Fig. 3.4 Sonographic uterine length in childhood (mean ± 2 SD) (after Bundscherer and Freundl [2]).

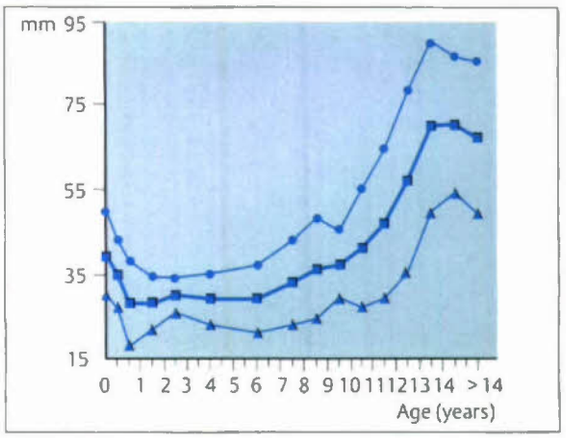

4

Fig. 3.5 Sonographic height of the uterine corpus in childhood (mean ± 2 SD) (after Bundscherer and Freundl [2]).

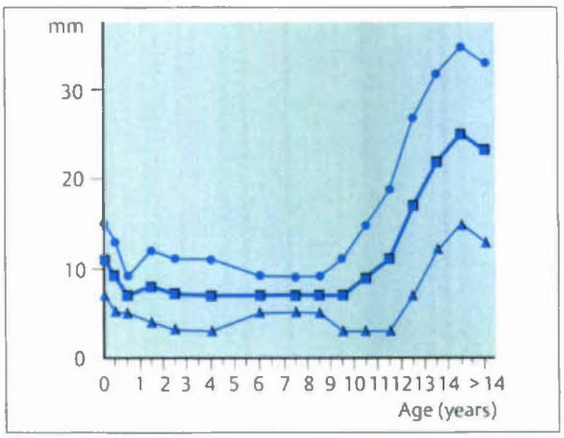

5

Fig. 3.6 Sonographic width of the uterine corpus in childhood (mean ± 2 SD) (after Bundscherer and Freundl [2]).

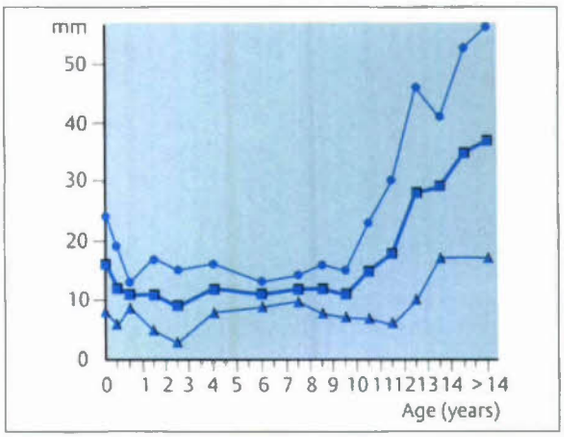

6

Fig. 3.7 Anatomical progression of uterine size from childhood to menopause (after Netter [5]).
a Uterus of a newborn.
b Uterus in the 4th year of life.
c Uterus at puberty.
d Uterus of a nulliparous adult.
e Uterus of a multipara.
f Uterus at menopause.

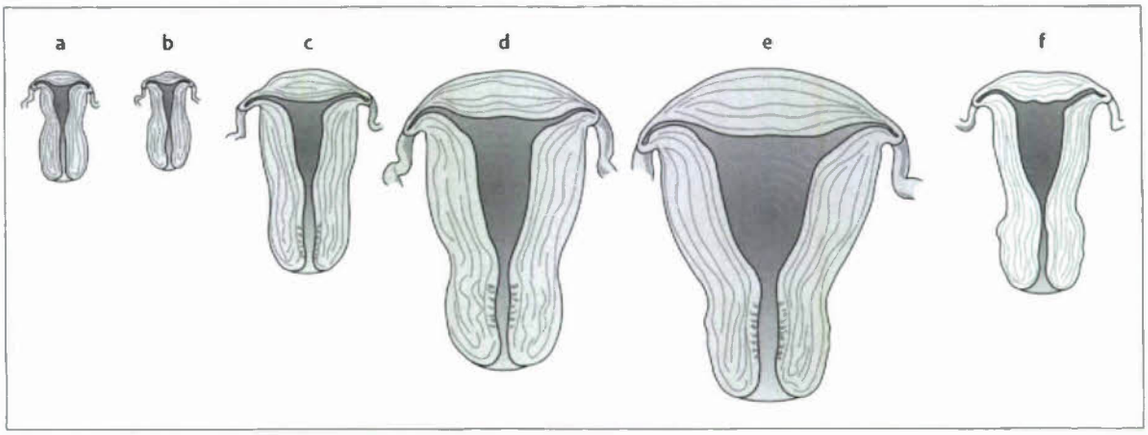

7

8

9

Vagina, Bladder, and Uterus

Fig. 3.8 Uterus of a 2-year-old girl, 2.9 × 1.1 × 1.2 cm (uterine length × corpus depth × corpus width). Midsagittal scan.

Fig. 3.9 Uterus of a 6-year-old girl, 2.9 × 1.0 × 1.2 cm (uterine length × corpus depth × corpus width). Midsagittal scan.

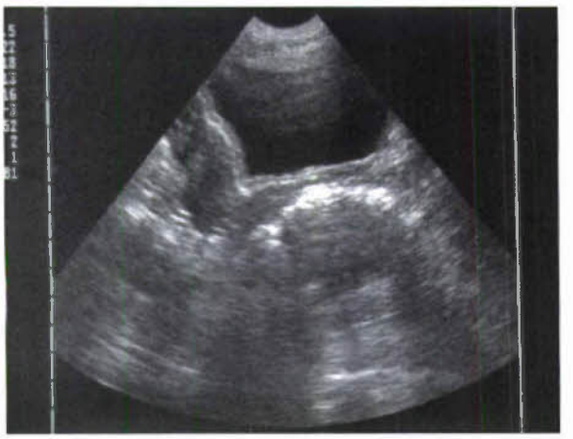

10

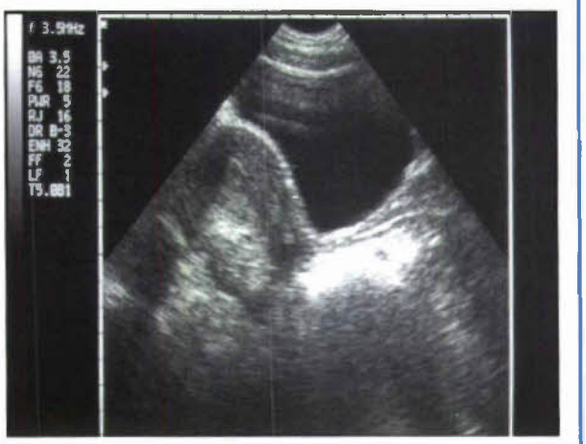

11

Fig. 3.10 Uterus of a 10-year-old girl, 4.0 × 1.2 × 2.0 cm (uterine length × corpus depth × corpus width). Midsagittal scan.

Fig. 3.11 Uterus of a 12-year-old girl, 5.0 × 2.1 × 2.8 cm (uterine length × corpus depth × corpus width). Midsagittal scan.

12

13

Fig. 3.12 Uterus of a sexually mature nullipara (uterine length 7 cm, corpus depth 3 cm, corpus width 4 cm). Longitudinal scan.
1 Full bladder
2 Uterine corpus
3 Cervix
4 Vagina
5 Rectum

Fig. 3.13 Uterus of a multipara (uterine length 10 cm, corpus depth 5 cm, corpus width 6 cm). Longitudinal scan.

14

15

Fig. 3.14 Atrophic uterus of a 75-year-old woman (uterine length 3.1 cm, corpus depth 1.7 cm, corpus width 2.3 cm).

Fig. 3.15 Atrophic uterus of a 75-year-old woman (uterine length 4.5 cm, corpus depth 2.3 cm, corpus width 2.4 cm).

16

Fig. 3.**16** Sharply anteflexed uterus with a minimally distended bladder. Longitudinal scan.

17

Fig. 3.**17** Uterus straightened by a fully distended bladder. Longitudinal scan.

18

Fig. 3.**18** Retroflexed uterus. Longitudinal scan.

19

Fig. 3.**19** Sharply retroflexed uterus. Longitudinal scan.

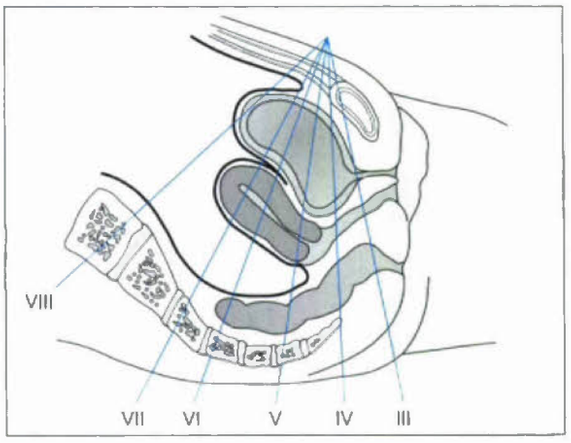

20

Fig. 3.**20** Transverse scan planes in abdominal ultrasound. Lateral aspect.

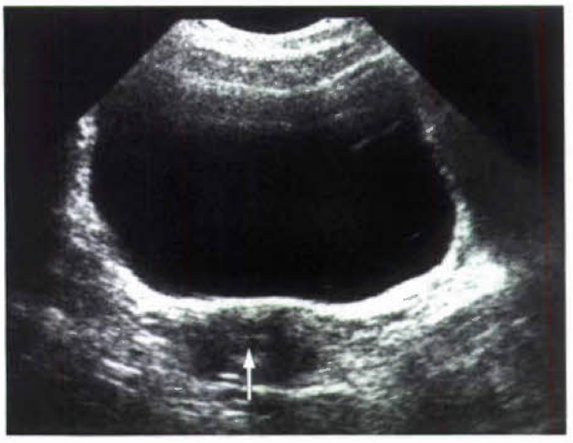

21

Fig. 3.**21** Transverse scan of the cervix and parametrial connective tissue. Cervical canal (—).

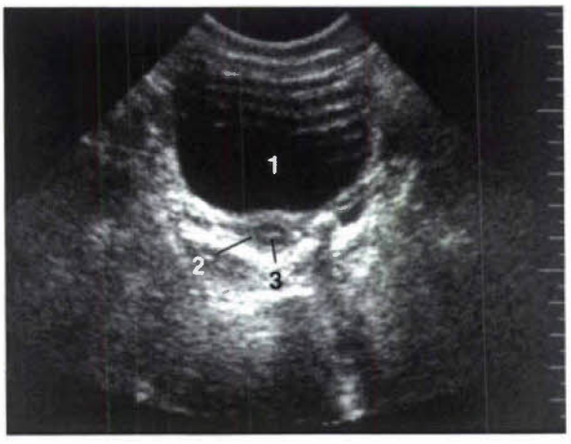

22

Fig. 3.**22** Transverse scan of the uterine corpus in a 4-year-old girl (width 2.3 cm).
1 Full bladder
2 Uterine corpus
3 Endometrium

23

Fig. 3.**23** Transverse scan of the uterine corpus in a 10-year-old girl.

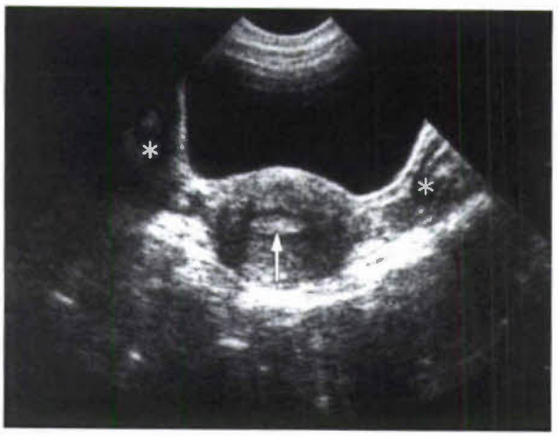

24

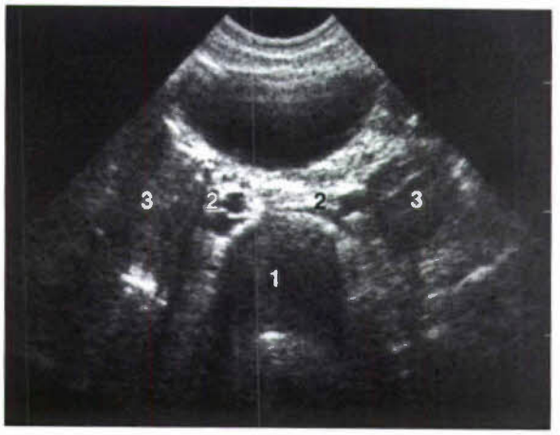

25

Fig. 3.**24** Transverse scan through the upper part of the uterine corpus. Note the central, linear endometrial echo (→). Psoas muscle (*).

Fig. 3.**25** Transverse pelvic scan above the uterus.
1 Spinal column
2 Common iliac vessels
3 Psoas muscle

Bladder and Urethra

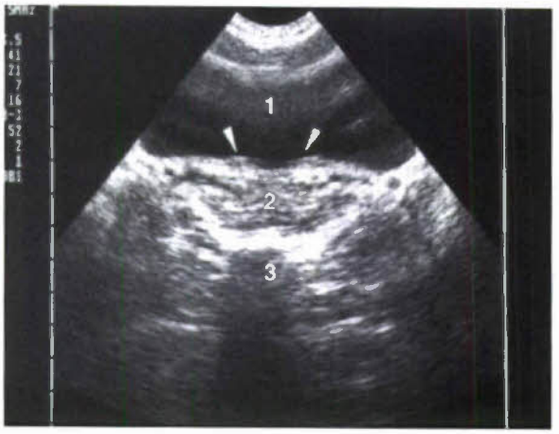

26

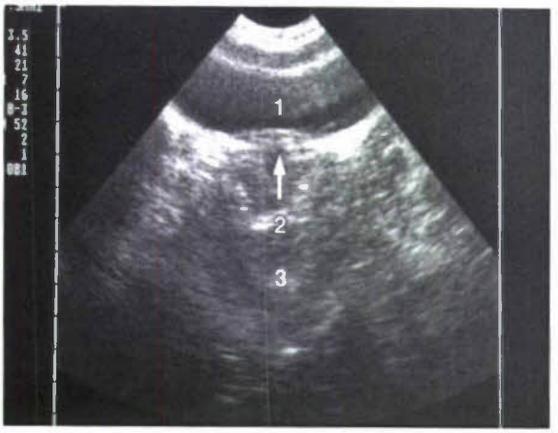

27

Fig. 3.**26** Transverse pelvic scan at the level of the bladder trigone (▶).
1 Full bladder
2 Vagina
3 Rectum

Fig. 3.**27** Transverse pelvic scan at the level of the anterior third of the vagina. The hypoechoic urethral lumen is visible in cross-section (→).
1 Full bladder
2 Vagina
3 Rectum

Ovaries

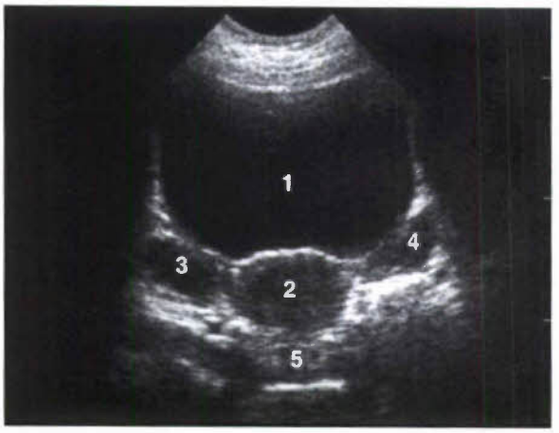

28

29

Fig. 3.**28** Transverse scan of the internal genitalia.
1 Full bladder
2 Uterine corpus
3 Right ovary
4 Left ovary
5 Colon

Fig. 3.**29** High ovaries in the pelvic wall region of a 10-year-old girl. Transverse scan through the true pelvis. The left ovary measures 2.4 × 0.9 × 1.7 cm.

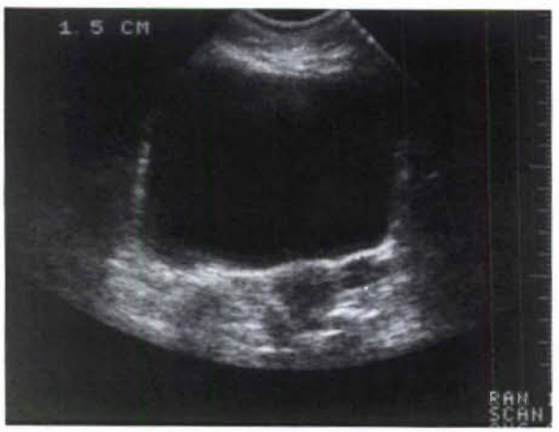

30

31

Fig. 3.**30** Transverse scan of the uterus and left ovary of a 57-year-old postmenopausal women. The left ovary measures 2.4 × 1.5 × 1.9 cm. Transverse scan through the true pelvis.

Fig. 3.**31** Longitudinal scan of the right ovary (plane II in Fig. 3.**3**).

Fig. 3.32 Right ovary (1) with associated ovarian vessels (2), which cross over the common iliac vessels (3). Lateral longitudinal scan.

Vessels

Fig. 3.33 Division of the common iliac vessels into the external (1) and internal (2) iliac vessels. Lateral longitudinal scan.

32

33

Abdominal Wall

Fig. 3.34 Anatomical structure of the abdominal wall.
a Above the umbilicus.
b Below the arcuate line.

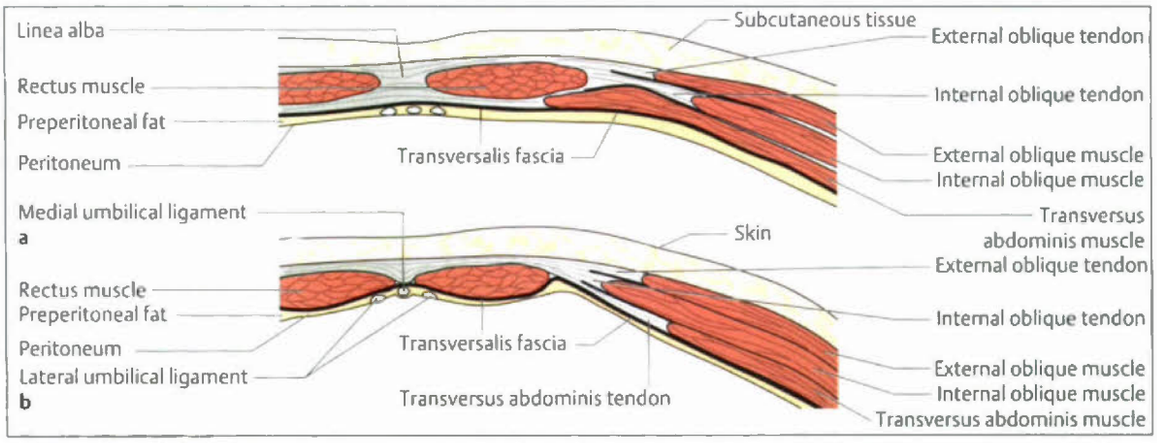

34

Fig. 3.35 Parasagittal longitudinal scan through the anterior abdominal wall.
1 Subcutaneous tissue
2 Right rectus abdominis muscle (▶◀)
— Transversalis fascia

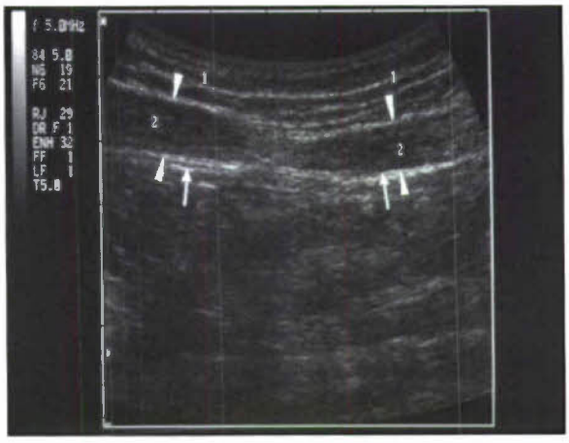

35

Fig. 3.36 Transverse scan through the anterior abdominal wall above the umbilicus.
1 Subcutaneous tissue
2 Right rectus abdominis muscle (▶◀)
3 Left rectus abdominis muscle (▶◀)
— Transversalis fascia

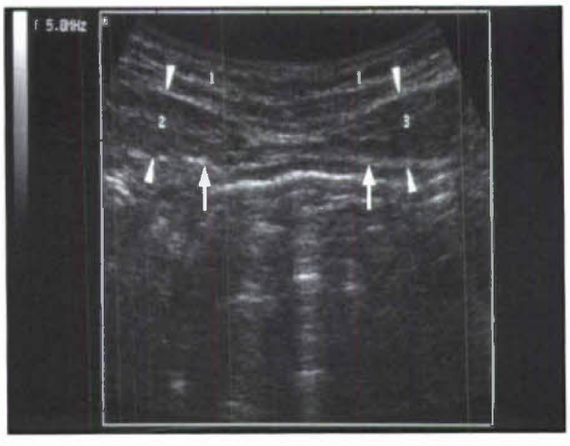

36

Fig. 3.37 Transverse scan through the anterior abdominal wall below the arcuate line.
1 Subcutaneous tissue
2 Right rectus abdominis muscle (▶◀)
3 Left rectus abdominis muscle (▶◀)
— Transversalis fascia

37

4 Ovarian and Endometrial Changes during the Menstrual Cycle

Serial ultrasound examinations of the organs of the true pelvis gave physicians their first noninvasive look at the physiologic changes that take place in the ovary and endometrium during the menstrual cycle. In recent years, sonographic monitoring of ovarian follicular growth has become particularly important in the evaluation and treatment of infertility. The traditional methods of basal body temperature (BBT) charting, mucus scoring, vaginal cytology, and serum hormone assays (estradiol, luteinizing hormone, progesterone) were certainly useful for detecting ovulation, but follicular maturation could be assessed only indirectly by means of relatively costly hormone assays, and it was not possible to ascertain the size and number of maturing follicles. Today, sonography provides an economical way to view the maturing follicle directly, determine its size, and confirm that ovulation has occurred. With the newer high-resolution scanners, moreover, it is usually possible to detect the endometrial changes that occur in association with follicular maturation.

Ovarian Changes during the Menstrual Cycle

Follicular Growth in the Normal Cycle

In the normal ovarian cycle, a single follicle begins to mature under the influence of the gonadotropic hormones FSH and LH. The follicle appears sonographically as a vesicular, echo-free structure on the ovary [1–6]. While several small follicles from 0.4 to 0.6 cm in diameter can usually be seen in both ovaries during the initial days of the cycle, a follicle on one of the ovaries becomes dominant starting on about day 10, enlarging to a diameter of approximately 1 cm (Fig. 4.**1**). That follicle grows at an almost linear rate of 2–3 mm per day over the next 4–5 days [2,5,7,8] (Figs. 4.**2**–4.**4**), reaching a size of 18–24 mm just before ovulation [1,2,9–12]. The follicle may have a somewhat elliptical shape initially, but the preovulatory follicle is generally round. Hackelöer et al. [2] found a good correlation between follicular size by ultrasound and the serum estradiol level.

The follicle is not always easy to define with ultrasound. Follicular detection can be difficult or even impossible in obese patients and in patients with extensive intra-abdominal adhesions, an inadequately distended bladder, or relatively high-sited ovaries. An overdistended bladder also hampers follicular evaluation by pushing the ovaries against the pelvic wall, where they are difficult to visualize. There are also structures that can mimic the sonographic appearance of a follicle, such as a blood vessel cut transversely by the image plane (especially in patients with adnexal varicosity, Fig. 4.**5**) or a fluid-filled bowel lumen. The latter can be identified as such by noting peristaltic motion, while a blood vessel can be identified by rotating the transducer 90° to display the vessel in a long-axis view.

In folliculometry, the follicular diameter is determined by measuring the internal diameter of the follicle in three planes (longitudinal, transverse, anteroposterior) and taking the average of those dimensions.

Sonographic follicular monitoring is started on about day 10 of the menstrual cycle, when the dominant follicle presumably has reached a minimum size of 1 cm. The scans are repeated at intervals of 1–2 days until ovulation is detected.

Occasionally, the cumulus oophorus can be identified with a high-resolution scanner shortly before ovulation [1,2,13]. It appears as a peripheral, circular feature within the follicular wall (Fig. 4.**4**). Normally, ovulation is not expected to occur until the follicle has reached a size of 1.7 cm [12] or 1.75 cm [1].

Once ovulation has occurred, various sonographic changes may be observed [1,11,14–17]:

- Complete disappearance of the cystic structure in the ovary
- Collapse of the cystic structure, with a decrease in its diameter (Fig. 4.**6**)
- A cystic mass with internal echoes (the corpus hemorrhagicum)
- The presence of follicular fluid in the cul-de-sac

Invasion of the ruptured follicle by blood vessels and the proliferation of granulosa lutein cells give rise to the corpus luteum, which appears sonographically as a hyperechoic structure located at the site of the former follicle [1] (Fig. 4.**7**). This feature is seen for only a few days, however, and afterward the ovary again becomes homogeneous. Occasionally, the development of a corpus luteum cyst may also be observed [7].

Serial ultrasound examinations can not only demonstrate normal follicular growth but can also detect abnormalities of follicular development. These include failure of the follicle to mature, deficient growth of the follicle, and luteinized unruptured follicle (LUF) syndrome [18,19]—i.e., premature luteinization of the follicle before it is fully mature. This disturbance is manifested on ultrasound by a loss of distinct follicular margins, the premature appearance of echogenic intrafollicular structures, and the absence of ovulation [18]. The development of a follicular cyst is occasionally observed and is confirmed by noting that the follicle has enlarged to more than 3 cm in size. Multiple small, peripheral follicles combined with ovarian enlargement are a feature of Stein–Leventhal syndrome (polycystic ovary syndrome) (Fig. 4.**8**).

Follicular Growth in the Stimulated Cycle

Sonographic monitoring of follicular growth has an important role in cycles stimulated by clomiphene citrate [20] and especially in gonadotropin-induced cycles [21–23], which are almost consistently associated with multifollicular growth (Figs. 4.**9**, 4.**10**). Indeed, it may be said that ultrasound has become an essential examination in these cases and that stimulation therapy should no longer be attempted without it. Hormone assays cannot provide specific information about the number and maturity of developing follicles in cases of multifollicular growth [22,23], and ultrasound is the only method that can promptly detect hyperstimulation with the development of giant follicular cysts (Fig. 4.**11**) or confirm the danger of multiple ovulation. If more than two mature follicles are identified, the therapy can be discontinued and the partners counseled with regard to temporary contraception. In our ultrasound-monitored patients with gonadotropin-stimulated cycles in whom BBT, cervical score, hormone levels (estradiol and progesterone), and follicular size are determined daily, we induce ovulation with human chorionic gonadotropin (HCG) when one or two follicles have reached a size of 1.8–2.0 cm. Preovulatory follicles in stimulated cycles measure an average of approximately 2.3 mm larger [24] than in spontaneous cycles.

Ultrasound has assumed special importance in candidates for in-vitro fertilization, where it is used both for the optimum timing of oocyte retrieval and increasingly for directing the follicular puncture and aspi-

ration of the follicular fluid and oocyte. However, the transabdominal–transvesical technique of oocyte retrieval guided by abdominal ultrasound [25,26] has been replaced completely by the transvaginal technique directed by an endovaginal transducer [27]. The advantage of transvaginal follicular aspiration is that it can be performed without general anesthesia and still provides an oocyte recovery rate comparable to that of laparoscopic follicular aspiration. Kemeter and Feichtinger [27] have reported an oocyte recovery rate of 79% for aspirations guided by transvaginal ultrasound.

A key advantage of transvaginal follicular aspiration over the transabdominal–transvesical method is that the aspirating needle only needs to travel a shorter distance, provided the ovaries are not situated too high. In addition, transvaginal sonography usually defines the follicles with greater sharpness and clarity than abdominal ultrasound [27].

Endometrial Changes during the Menstrual Cycle

Studies by several research groups [28–32] have shown that endometrial changes paralleling follicular maturation can be detected sonographically in both normal and stimulated cycles. As early as 1983, Bald and Hackelöer [29] used a high-resolution compound scanner to identify six different endometrial patterns that correlated well with follicular sizes and the appearance of the corpus luteum. To check the endometrial changes described by Bald and Hackelöer [29], we examined 73 of our own patients with a high-resolution sector scanner in both spontaneous and clomiphene-induced cycles [30]. We were able to observe corresponding cyclical changes in both groups (Figs. 4.**12**–4.**27**).

In the early proliferative phase, the endometrium appears only as a thin, continuous echogenic line (type 1; Figs. 4.**14**, 4.**15**). Later in the proliferative phase, starting on about day 8–10 of the cycle, the endometrial echo widens somewhat (type 2; Figs. 4.**16**, 4.**17**), and then widens further to a thickness of approximately 1 cm (type 3; Figs. 4.**18**, 4.**19**). Subsequent edema of the superficial cells leaves only a narrow, hyperechoic rim and a thin, high-level central echo separated by a hypoechoic zone (type 4; Figs. 4.**20**, 4.**21**). Approximately 1 day before ovulation, there is further dissolution of the central and marginal echoes, and little if any endometrial structure can be visualized (type 5; Figs. 4.**22**, 4.**23**). After ovulation has occurred, the *endometrial ring sign* described by Bald and Hackelöer [28] is observed (type 6; Figs. 4.**24**, 4.**25**). Because the type 6 pattern is never seen before ovulation in either normal or clomiphene-stimulated cycles, its appearance may be interpreted as evidence that ovulation has occurred [28].

A marked disturbance of endometrial development is found in anovulatory cycles. In a total of 12 anovulatory cases, we saw no instance in which endometrial development progressed beyond the type 4 pattern.

During the secretory phase of the cycle, the endometrium displays a markedly hyperechoic structure that resembles the type 3 pattern (Figs. 4.**26**, 4.**27**).

References

1 Hackelöer BJ, Robinson HP. Ultraschalldarstellung des wachsenden Follikels und Corpus luteum im normalen physiologischen Zyklus. Geburtshilfe Frauenheilkd 1978;38:163–8.
2 Hackelöer BJ, Fleming R, Robinson HP, Adam AH, Coutts JRT. Correlation of ultrasonic and endocrinologic assessment of human follicular development. Am J Obstet Gynecol 1979;135:122–8.
3 Hackelöer BJ, Dörfler R, Nitschke S, Buchholz R. Ultraschalldarstellung des Follikelwachstums und Basaltemperaturmessung – ein Vergleich zweier Methoden zur Ovulationsbestimmung. Ultraschall 1980;1:133–9.
4 Kratochwil A, Urban G, Friedrich E. Ultrasonic tomography of the ovaries. Ann Chir Gynaecol Fenn 1972;61:211–4.
5 O'Herlihy C, de Crespigny LJC, Robinson HP. Monitoring ovarian follicular development with real-time ultrasound. Br J Obstet Gynaecol 1980;87:613–8.
6 Smith DH, Pickert RH, Sinosisch M, Saunders DM. Assessment of ovulation by ultrasound and estradiol levels during spontaneous and induced cycles. Fertil Steril 1980;33:387–90.
7 Geisthövel E, Klosa W, Rabold B, Schillinger H, Breckwoldt M. Sonographische Kriterien der Ovarialfunktion in physiologischen Menstruationszyklen. Geburtshilfe Frauenheilkd 1984;44:225–32.
8 Renaud RL, Mader J, Dervain J, Ehret MC, Aron C, Plas-Roser S, et al. Echographic study of follicular maturation and ovulation during the normal menstrual cycle. Fertil Steril 1980;33:272–6.
9 Nitschke-Dabelstein S, Hackelöer BJ, Sturm G. Ovulation and corpus luteum formation observed by ultrasonography. Ultrasound Med Biol 1981;7:33–9.
10 O'Herlihy C, de Crespigny LJC, Lopata A, Johnston I, Hoult I, Robinson HP. Preovulatory follicular size: a comparison of ultrasound and laparoscopic measurements. Fertil Steril 1980;34:24–6.
11 Queenan JT, O'Brien GD, Bains LM, Simpson J, Collins WP, Campbell S. Ultrasound scanning of ovaries to detect ovulation in women. Fertil Steril 1980;34:99–105.
12 Terinde R, Baumeister A, Distler W, Freundl G, Herberger J, Kozlowski P. Sonographische Kontrolle der Ovulation. Ultraschall 1980;1:140–51.
13 Bomsel-Helmreich O, Bessis R, Huyen LV. Cumulus oophorus of the preovulatory follicle assessed by ultrasound and histology. In: Christie AD, editor. Ultrasound and infertility. Bromley: Chartwell-Bratt, 1982: 105.
14 De Crespigny LC, O'Herlihy C, Robinson HP. Ultrasonic observation of the mechanism of human ovulation. Am J Obstet Gynecol 1981;139:636–9.
15 Marinho AO, Sallam HN, Goessens LKV, Collins WP, Rodeck CH, Campbell S. Real-time pelvic ultrasonography during the periovulatory period of patients attending an artificial insemination clinic. Fertil Steril 1982;37:633–8.
16 Wetzels LCG, Hoogland HJ. Relation between ultrasonographic evidence of ovulation and hormonal parameters: luteinizing hormone surge and initial progesterone rise. Fertil Steril 1982;37:336–41.
17 Ylöstalo P, Rönnberg L, Jouppila P. Measurement of the ovarian follicle by ultrasound in ovulation induction. Fertil Steril 1979;31:651–5.
18 Coulam CB, Hill LM, Breckle R. Ultrasonic evidence for luteinization of unruptured preovulatory follicles. Fertil Steril 1982;37:524–9.
19 Jewelewicz R. Management of infertility resulting from anovulation. Am J Obstet Gynecol 1975;122:909–20.
20 Vargyas JM, Marrs RP, Kletzky OA, Mishell DR. Correlation of ultrasonic measurement of ovarian follicle size and serum estradiol levels in ovulatory patients following clomiphene citrate for in vitro fertilization. Am J Obstet Gynecol 1982;144:569–73.
21 Fink RS, Bowes LP, Mackintosh CE, Smith WI, Georgiades E, Ginsburg J. The value of ultrasound for maintaining ovarian responses to gonadotropin stimulant therapy. Br J Obstet Gynaecol 1982;89:856–61.
22 Geisthövel E, Skubsch U, Schillinger H, Breckwoldt M. Sonographische und endokrine Vergleichsuntersuchungen Gonadotropin-stimulierter Zyklen. Geburtshilfe Frauenheilkd 1982;42:819–23.
23 Hackelöer BJ, Nitschke S, Daume E, Sturm G, Buchholz R. Ultraschalldarstellung von Ovarveränderungen bei Gonadotropinstimulierung. Geburtshilfe Frauenheilkd 1977;37:185–90.
24 De Cherney AH, Romero R, Polan ML. Ultrasound in reproductive endocrinology. Fertil Steril 1982;37:323–33.
25 Feichtinger W, Kemeter P. Laparoscopic ultrasonically guided follicle aspiration for in vitro fertilization? In Vitro Fertil Embryo Transfer 1984;1:244–9.
26 Lenz S, Lauritsen JG. Ultrasonically guided percutaneous aspiration of human follicles under local anaesthesia: a new method of collecting oocytes for in-vitro fertilization. Fertil Steril 1982;38:673–7.
27 Kemeter P, Feichtinger W. Transvaginal oocyte retrieval using a transvaginal sector scan probe combined with an automated puncture device. Hum Reprod 1986;1:21–4.
28 Bald R, Hackelöer BJ. Neue sonographische Kriterien zur Darstellung der stattgehabten Ovulation. In: Kratochwil A, Reinold E, editors. Ultraschalldiagnostik 81. Stuttgart: Thieme, 1982: 224.
29 Bald R, Hackelöer BJ. Ultraschalldarstellung verschiedener Endometriumformen. In: Otto RC, Jann FX, editors. Ultraschalldiagnostik 82. Stuttgart: Thieme, 1983: 187.
30 Merz E, Schaller C, Hoffmann G, Pollow K. Ultrasonic evidence of endometrium in correlation to follicular development and hormonal parameters in patients stimulated with clomiphene citrate. Paper presented at the Eleventh World Congress of Gynecology and Obstetrics, Berlin 1985.
31 Nakano H, Sakamoto C, Koyanagi T, Kubota S. Endometrial images by ultrasound. Acta Obstet Gynaecol Jpn 1982;34:275–8.
32 Sakamoto C, Nakano H. The echogenic endometrium and alterations during menstrual cycle. Int J Gynaecol Obstet 1982;20:255–9.

1

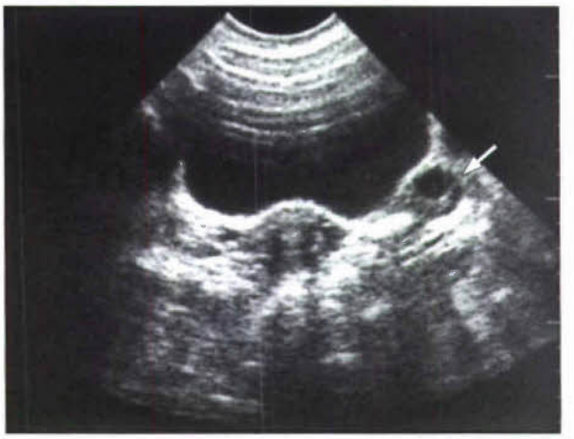

2

Follicular Growth in the Normal Cycle

Fig. 4.1 Follicular maturation (transverse scan), day 10 of the menstrual cycle. Multiple follicles measuring 0.8 cm or less are visible on the right ovary. The left ovary bears a dominant follicle 1.0 cm in size (→).

Fig. 4.2 Follicular maturation, day 11 of the menstrual cycle. Follicular diameter on the left ovary 1.3 cm (→).

3

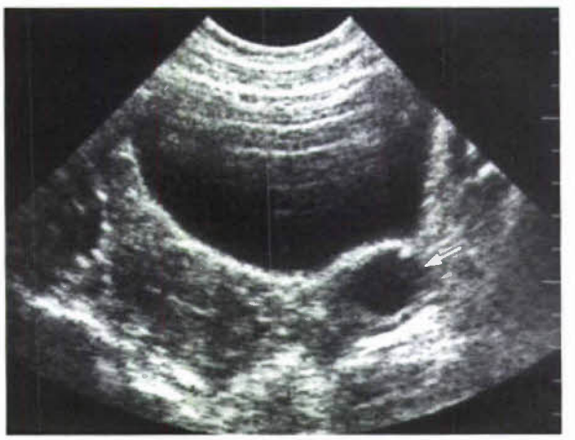

4

Fig. 4.3 Follicular maturation, day 14 of the menstrual cycle. Follicular diameter 1.9 cm (→).

Fig. 4.4 Follicular maturation, day 15 of the menstrual cycle. Mature follicle with a cumulus oophorus (→).

5

6

Fig. 4.5 Varicose veins in the right adnexal region mimicking the appearance of follicles (→). Transverse scan.

Fig. 4.6 Corpus luteum on the left ovary (→), day 16 of the menstrual cycle.

7

8

Fig. 4.7 Corpus luteum on the left ovary (→), day 19 of the menstrual cycle.

Fig. 4.8 Enlarged polycystic right ovary in Stein–Leventhal syndrome (polycystic ovary syndrome). Transverse scan. Several small follicles are visible in the cortical area.

Follicular Growth in the Stimulated Cycle

Fig. 4.9 Bilateral follicular maturation in response to clomiphene therapy, day 14 of the menstrual cycle. The follicular diameter is 2.2 cm on each side. Transverse scan.

9

Fig. 4.10 Multifollicular growth in response to treatment with human menopausal gonadotropin–human chorionic gonadotropin (HMG–HCG), day 16 of the menstrual cycle. Both ovaries are enlarged to 8 × 6 × 5 cm. Transverse scan.

10

Fig. 4.11 Hyperstimulation in response to treatment with human menopausal gonadotropin–human chorionic gonadotropin (HMG–HCG), with the development of giant follicular cysts. The right ovary measures 20 × 12 × 14 cm. Longitudinal scan.

11

Endometrial Changes during the Menstrual Cycle

Fig. 4.12 Endometrial patterns in longitudinal sonograms (after Bald and Hackelöer [29]). E = endometrial thickness.

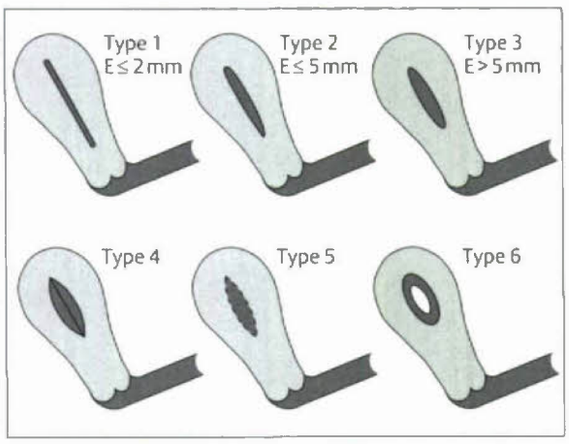

12

Fig. 4.13 Endometrial patterns in transverse sonograms.

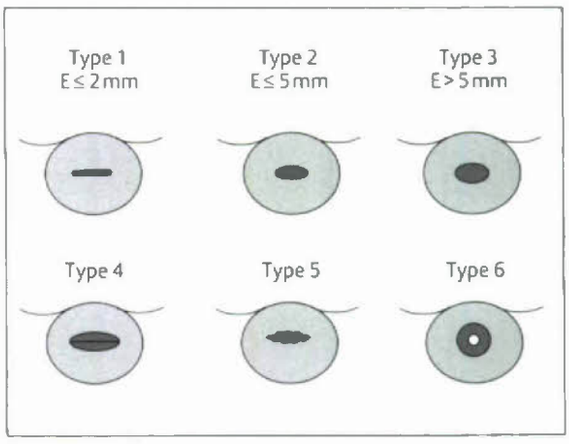

13

Fig. 4.14 Type 1 endometrium, day 4 of the menstrual cycle. The endometrial thickness is 2 mm. Midsagittal longitudinal scan.

14

Fig. 4.15 Type 1 endometrium. Transverse scan of the uterus.

15

16

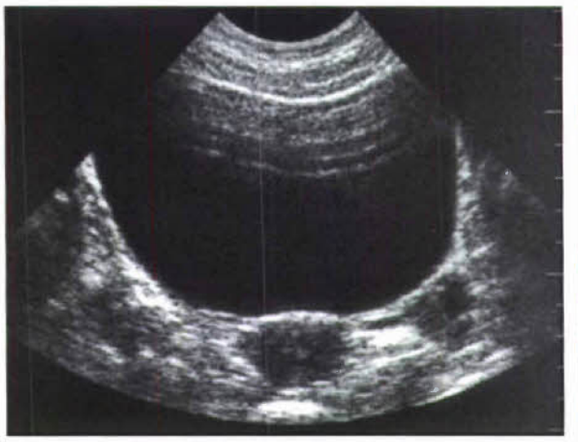

17

Fig. 4.16 Type 2 endometrium, day 8 of the menstrual cycle. The endometrial thickness is 3 mm. Midsagittal longitudinal scan

Fig. 4.17 Type 2 endometrium. Transverse scan of the uterus.

18

19

Fig. 4.18 Type 3 endometrium, day 11 of the menstrual cycle. The endometrial thickness is 0.7 cm. Longitudinal scan of the uterus.

Fig. 4.19 Type 3 endometrium. Transverse scan of the uterus.

20

21

Fig. 4.20 Type 4 endometrium, day 12 of the menstrual cycle. Note the narrow hyperechoic border and the thin, bright central echo, separated by a hypoechoic zone. Longitudinal scan of the uterus.

Fig. 4.21 Type 4 endometrium. Transverse scan of the uterus.

22

23

Fig. 4.22 Type 5 endometrium, day 13 of the menstrual cycle (preovulatory), marked by dissolution of the central echo and border. Longitudinal scan of the uterus.

Fig. 4.23 Type 5 endometrium. Transverse scan of the uterus. There is a mature follicle on the right ovary.

Fig. 4.**24** Type 6 endometrium, day 15 of the menstrual cycle. Note the typical wide, echogenic endometrial "ring sign" following ovulation. Longitudinal scan of the uterus.

24

Fig. 4.**25** Type 6 endometrium. The typical intrauterine ring sign is also appreciated in the transverse scan. Corpus luteum on the left ovary (—).

25

Fig. 4.**26** Thickened secretory endometrium, with a height of 1.0 cm. The endometrial structure resembles a type 3 pattern. Longitudinal scan of the uterus.

26

Fig. 4.**27** Secretory endometrium on day 22 of the menstrual cycle. Transverse scan of the uterus.

27

5 Congenital Anomalies of the Genital Tract

Congenital malformations of the female genital tract result from a failure of fusion of the müllerian ducts. The defect may involve part or all of the müllerian ducts, leading to a partial or complete duplication of the uterus. Müllerian duct anomalies are classified into three main groups based on the associated anatomical changes: agenesis, vertical fusion defects, and lateral fusion defects (Table 5.**1**).

Agenesis most commonly affects the uterus and vagina (Mayer–Rokitansky–Küster syndrome). Vertical fusion defects are based on a disturbance of fusion in the lower part of the müllerian ducts, while lateral fusion defects can lead to symmetrical as well as asymmetrical uterine anomalies.

Ultrasonography has become particularly important in the diagnosis of congenital malformations of the female genital tract [1–4]. As a noninvasive modality, it is used first before more invasive diagnostic procedures such as hysterosalpingography, hysteroscopy and laparoscopy. Children and adolescents in particular can be easily examined with this method.

Most genital anomalies involve the uterus (see Fig. 24.**2**); vaginal and adnexal anomalies are far less common. While pronounced uterine anomalies are easily detected on ultrasound images, there is a possibility that more subtle changes (e.g., an arcuate uterus) may be missed [5].

The best sonographic views of *uterine anomalies* such as uterus didelphys (Fig. 5.**1**) and uterus bicornis unicollis (Figs. 5.**2**, 5.**3**) are obtained with a partially distended bladder. In this state, the uterus is roughly perpendicular to the abdominal wall and is well delineated in the coronal plane. If an imperforate hymen is present in addition to the bicornate uterus, it leads to hematocolpos following the menarche, as menstrual blood collects in the vagina (Fig. 5.**4**). A subseptate uterus (Fig. 5.**5**) can be identified by demonstrating two separate endometrial echoes. Thicker septa can be clearly visualized in this way, but very thin intrauterine septa may be detectable only after the uterine cavity has been filled with physiologic saline solution.

Vaginal atresia may occur in isolation or may coexist with uterine aplasia (Mayer–Rokitansky–Küster syndrome). Sonography in this syndrome does not display the typical echogenic double contours of the normal vagina, and a uterus is not visualized (Figs. 5.**6**, 5.**7**). In its place there may be bowel, or at most a rudimentary uterine ridge.

Because malformations of the internal genitalia frequently coexist with urinary tract anomalies [6,7], every ultrasound examination should include scans of the renal fossae (Figs. 5.**8**, 5.**9**) to check for anomalies such as unilateral renal agenesis or a dystopic kidney (*pelvic kidney*) (Fig. 5.**10**).

Table 5.**1** Congenital anomalies of the female genital tract

• **Agenesis**	Uterine/vaginal aplasia (Mayer–Rokitansky–Küster syndrome)
• **Vertical fusion defects of the müllerian ducts**	Septum in the upper third of the vagina
• **Lateral fusion defects of the müllerian ducts**	Symmetrical and asymmetrical uterine anomalies

References

1 Funk A, Fendel H. Beitrag zur sonographischen Diagnostik kongenitaler Fehlbildungen. Z Geburtshilfe Perinatol 1988;192:77–82.
2 Jones TB, Fleischer AC, Daniell JF, Lindsey AM, James AE. Sonographic characteristics of congenital uterine abnormalities and associated pregnancy. J Clin Ultrasound 1980;8:435–7.
3 Schneider M, Crossman H. Sonography of the female child's reproductive system. Pediatr Ann 1980;9:180–6.
4 Valdes C, Malini S, Malinak LR. Ultrasound evaluation of female genital tract anomalies: a review of 64 cases. Am J Obstet Gynecol 1984;149:285–92.
5 Nicolini U, Bellotti M, Bonazzi B, Zamberletti D, Candiani GB. Can ultrasound be used to screen for uterine malformations? Fertil Steril 1987;47:89–93.
6 Gurin J, Leiter E. Anomalies of müllerian and wolffian ducts. South Med J 1981;74:805–8.
7 White JL, Lawson TL. Congenital uterine anomaly with renal agenesis. J Clin Ultrasound 1978;6:117–8.

1

2

Fig. 5.**1** Uterus didelphys in coronal section. Note the bilateral endometrial stripe (—).

Fig. 5.**2** Uterus bicornis unicollis in coronal section.

Fig. 5.3 Uterus bicornis unicollis in coronal section.
1 Right uterine horn
2 Left uterine horn
3 Common cervix

3

Fig. 5.4 Bicornuate uterus with pronounced hematocolpos (*). The two uterine horns overlie a grossly distended vagina.

4

Fig. 5.5 Subseptate uterus in transverse section. The uterine width is 5.4 cm. Note the two separate endometrial stripes (—).

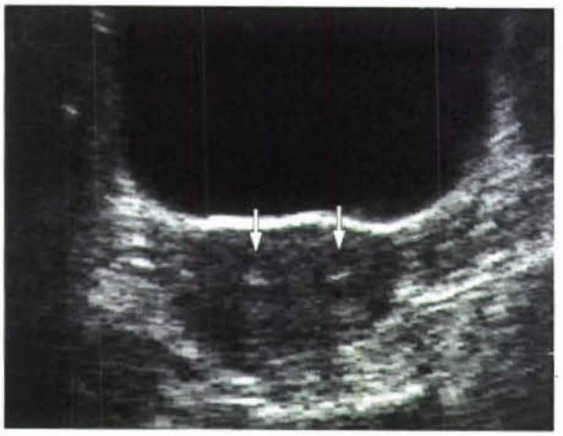

5

Fig. 5.6 Uterine and vaginal aplasia (in Mayer–Rokitansky–Küster syndrome). Midsagittal scan. The uterus and vagina cannot be defined with ultrasound.
1 Vaginal region
2 Uterine region

6

Fig. 5.7 Transverse scan of the case in Fig. 5.6.

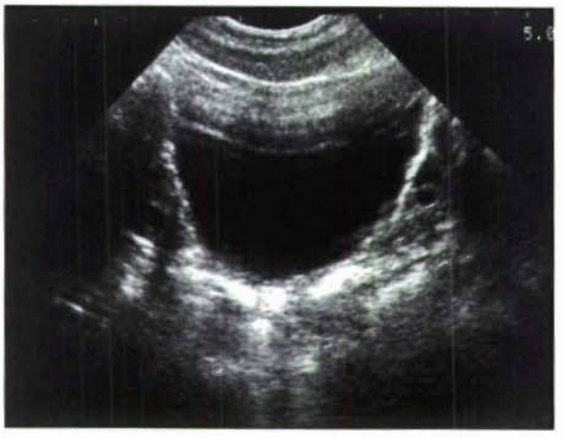

7

Fig. 5.8 Anatomically normal right kidney in a 10-year-old girl. Right upper abdominal longitudinal scan.

8

Fig. 5.9 Right renal aplasia in Rokitansky–Küster syndrome. Longitudinal scan.
1 Liver
2 Empty renal fossa

9

Fig. 5.10 Central pelvic kidney in Mayer–Rokitansky–Küster syndrome, mimicking a uterus.

10

6 Pelvic Inflammatory Diseases

The sonographic features of pelvic inflammatory disease are extremely varied, depending on the location, duration, and severity of the disease. While the early stages of pelvic inflammatory disease are unlikely to produce sonographic changes, a fully developed form of *acute adnexitis* is often associated with some degree of fluid collection in the cul-de-sac or fallopian tube, causing the latter to become visible at ultrasound [1] (Figs. 6.**1**–6.**3**). Adhesions obstructing the fimbriated end will produce some degree of tubal distension, depending on the nature and volume of the retained secretions, with the formation of a sactosalpinx that appears sonographically as a cystic mass located next to or behind the uterus.

A sactosalpinx that has no internal echoes is classified as a *hydrosalpinx* (Figs. 6.**4**–6.**6**). Unlike an ovarian cyst, which is usually round, a large hydrosalpinx is more pear-shaped with a narrow isthmus and a wider ampullary portion [2–4]. In some cases, however, the ampullary end may be distended into a spherical shape that mimics an ovarian cyst (Figs. 6.**7**, 6.**8**).

The presence of fine, diffuse internal echoes within the sactosalpinx means that the tube is filled with pus (*pyosalpinx*, Figs. 6.**9**–6.**11**) or blood (*hematosalpinx*). The changes are frequently bilateral [2,4].

Pelvic venous thrombosis may closely resemble a pyosalpinx or hematosalpinx on transverse scans (Fig. 6.**12**), but a longitudinal scan will clearly demonstrate its vascular structure and the hypoechoic thrombus (Figs. 6.**13**, 6.**14**).

With torsion of the sactosalpinx, the twisted tubal segments appear as adjacent cystic areas (Figs. 6.**15**, 6.**16**). The differential diagnosis should include the acute torsion of an ovarian cyst. The torsion in this case will cause an intracystic hemorrhage, marked by the presence of fine internal echoes within the cystic mass (Figs. 6.**17**, 6.**18**).

If the inflammation spreads to the ovary, it may incite the formation of a *tubo-ovarian abscess*, which has variable sonographic features depending on the degree of liquefaction and the amount of necrotic tissue present. Ultrasound usually demonstrates a unilocular or multilocular thick-walled mass located next to the uterus and containing diffusely scattered internal echoes [2–4] (Figs. 6.**19**–6.**21**). The cystic mass may contain a fluid level caused by the sedimentation of debris [5] (Fig. 6.**20**).

A severe inflammatory process will often spread from the adnexa to involve the bowel. This leads to the formation of an irregular *conglomerate mass* of variable echogenicity. Usually, the mass is poorly delineated from its surroundings.

If ultrasound raises suspicion of a tubo-ovarian abscess, differentiation is required from a number of noninflammatory changes in the true pelvis that have a similar ultrasound presentation (Table 6.**1**). In most cases, this differentiation can be accomplished by referring to the history, clinical findings, and laboratory parameters. However, diagnosis can be difficult in patients with *inflammatory bowel changes* such as those occurring with a perityphlitic abscess, diverticulitis, or Crohn's disease. These changes can mimic an inflammatory adnexal mass, especially when there is loss of intestinal peristalsis. The chronic inflammation in *Crohn's disease* can lead to thickening of the bowel wall, which creates a conspicuous target sign in transverse section [6] (Fig. 6.**22**).

If a *cul-de-sac abscess* develops, ultrasound will show a hypoechoic mass with indistinct margins located directly behind the uterus in the rectouterine pouch. The cul-de-sac abscess may have an echo pattern resembling that of a postoperative hematoma, but has been reported to be distinguishable from the latter by its finer internal echoes [7] (Fig. 6.**23**). If the inflammation is caused by gas-forming microorganisms, the tiny gas bubbles may heighten the echogenicity of the mass [8]. To exclude multifocal abscesses, it is always a good precaution to search the upper abdomen, especially the subphrenic and subhepatic spaces, for foci of abscess formation. A solitary cul-de-sac abscess can be selectively aspirated and drained under ultrasound guidance [9].

Table 6.1 Differential diagnosis of tubo-ovarian abscess

- Endometrioma
- Dermoid cyst
- Hemorrhagic corpus luteum cyst
- Torsion of an ovarian mass
- Pedunculated myoma
- Ectopic pregnancy
- Perityphlitic abscess
- Crohn's disease
- Diverticulitis
- Coproma

Preuterine *abscess formation*, whose causes include an iatrogenic perforation of the uterus during diagnostic curettage, can also be detected with ultrasound (Fig. 6.**24**).

Although ultrasound scanning in pelvic inflammatory disease is a valuable adjunct to the bimanual examination, which is usually painful and is often hampered by muscular guarding, the low specificity of ultrasound requires that sonographic findings always be interpreted within the context of the history, clinical examination, and laboratory findings [4]. Postinflammatory adhesions in the lesser pelvis can be directly visualized with ultrasound only if there is concomitant ascites (Fig. 6.**25**). Otherwise their presence can only be inferred from an atypical position of the uterine corpus. In the cervical region, marked thickening of the parametrial connective tissue and lateral displacement of the cervix may be noted as the result of a previous inflammatory process (Fig. 6.**26**).

References

1 Henkel B. Die ultrasonographische Diagnostik pathologischer Veränderungen der Tuba uterina. Ultraschall 1982;3:152–9.
2 Berland LL, Lawson TL, Foley WD, Albarelli JN. Ultrasound evaluation of pelvic infections. Radiol Clin North Am 1982;20:367–82.
3 Fleischer AC, James AE Jr, Millis JB, Julian C. Differential diagnosis of pelvic masses by gray scale sonography. AJR Am J Roentgenol 1978;131:469–76.
4 Lipsit ER. Inflammatory disease of the pelvis and postoperative fluid collections. In: Steel WB, Cochrane WJ, editors. Gynecologic ultrasound. Edinburgh: Churchill Livingstone, 1984: 85–104.
5 Uhrich PC, Sanders RC. Ultrasonic characteristics of pelvic inflammatory masses. J Clin Ultrasound 1976;4:199–204.
6 Seitz K. Sonographische Diagnostik beim Morbus Crohn. Ultraschall 1980;1:35–40.
7 Doust BD, Quiroz F, Stewart JM. Ultrasonic distinction of abscesses from other intra-abdominal fluid collections. Radiology 1977;125:213–8.
8 Kressel HY, Filly RA. Ultrasonographic appearance of gas-containing abscesses in the abdomen. AJR Am J Roentgenol 1978;130:71–3.
9 McArdle CR, Simon L, Kiejna C. Vaginal drainage of posthysterectomy abscess under direct ultrasonic guidance. Obstet Gynecol 1984;63(3 Suppl):90S–92S.

Fig. 6.1 Acute pelvic inflammatory disease with fluid in the cul-de-sac (→). Longitudinal scan.

1

Fig. 6.2 Acute bilateral pelvic inflammatory disease with a marked fluid collection in the cul-de-sac. Midsagittal scan.

2

Fig. 6.3 Acute bilateral pelvic inflammatory disease. Both fallopian tubes are distended by collected fluid. Transverse scan.
1 Uterine corpus
2 Right tube
3 Left tube
4 Bowel

3

Fig. 6.4 Pronounced hydrosalpinx (1) in longitudinal section. A portion of the uterus (2) is cut by the scan.

4

Fig. 6.5 Left hydrosalpinx. Transverse scan shows a pear-shaped dilation of the left fallopian tube to 8.1 × 5.2 × 6.2 cm.

5

Fig. 6.6 Surgical specimen corresponding to Fig. 6.5.

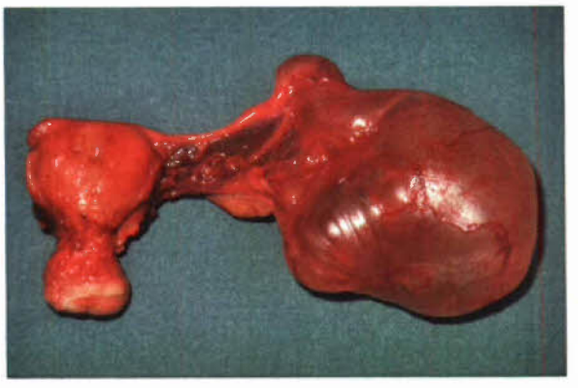

6

7

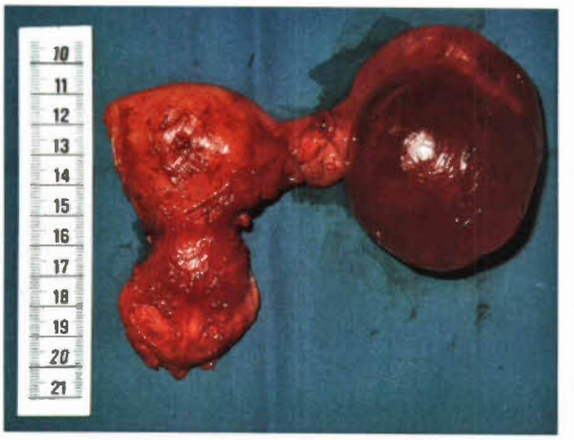

8

Fig. 6.7 Left sactosalpinx. Longitudinal scan. The ampullary portion of the tube is expanded to form a 6.4 cm globular mass, mimicking an ovarian cyst.

Fig. 6.8 Surgical specimen corresponding to Fig. 6.7.

9

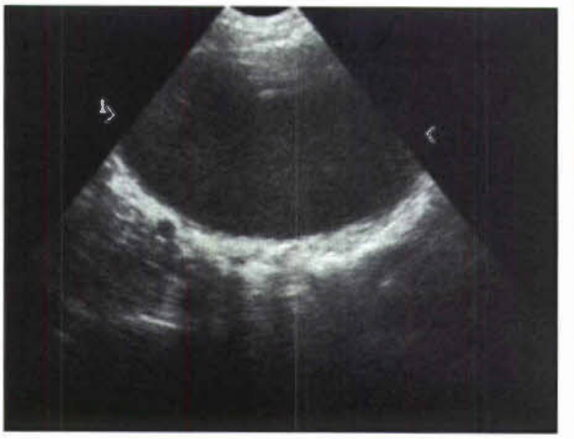

10

Fig. 6.9 Bilateral pyosalpinx. Transverse scan. The lumina of the fallopian tubes (→) are distended and contain fine, diffuse internal echoes.

Fig. 6.10 Massively distended pyosalpinx on the right side with fine, evenly distributed internal echoes in a patient with genital tuberculosis. The pyosalpinx is 11.2 cm long (> <).

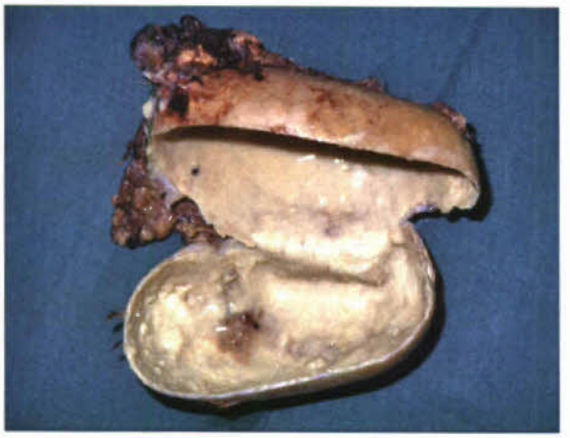

11

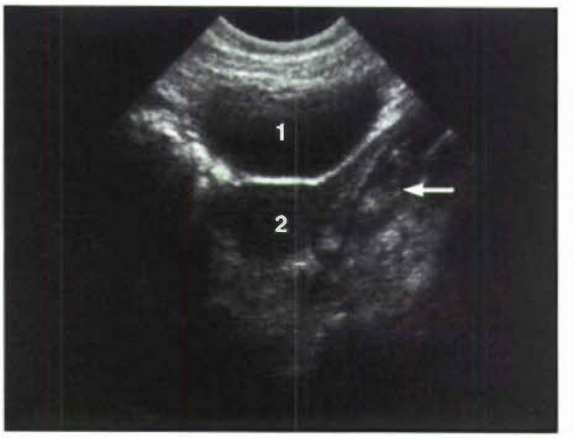

12

Fig. 6.11 Specimen corresponding to Fig. 6.10.

Fig. 6.12 Left iliac vein thrombosis. Transverse scan. A circumscribed, echogenic thrombus is visible in the left external iliac vein (→).
1 Urinary bladder
2 Uterine corpus

13

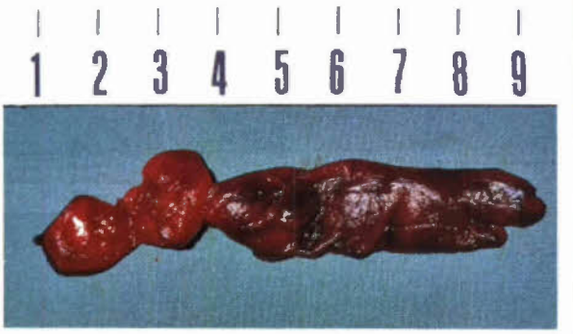

14

Fig. 6.13 Longitudinal scan of the iliac vein thrombosis in Fig. 6.12. A circumscribed, hyperechoic thrombus 2.1 cm in diameter is lodged in the vessel lumen (→).

Fig. 6.14 Surgical specimen corresponding to Figs. 6.12 and 6.13.

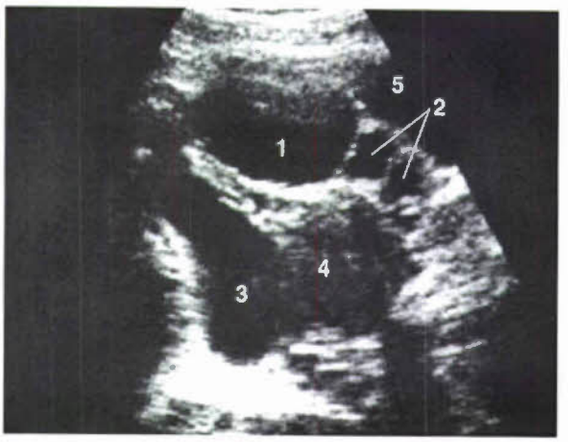

15

Fig. 6.**15** Bilateral sactosalpinx with torsion on the left side. Transverse scan.
1 Ampullary portion of left tube
2 Twisted isthmic portion of left tube
3 Distended ampullary portion of right tube
4 Uterine corpus
5 Urinary bladder

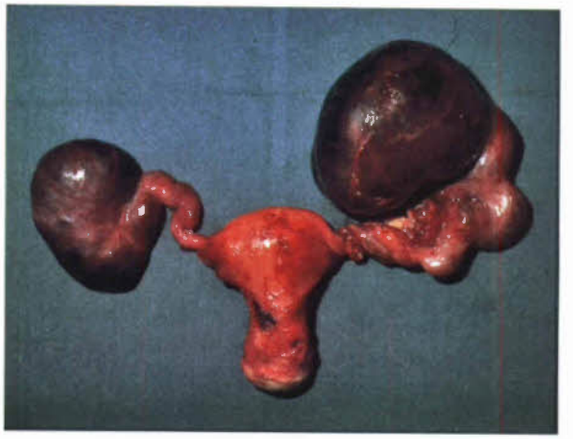

16

Fig. 6.**16** Surgical specimen corresponding to Fig. 6.**15**.

17

Fig. 6.**17** Loculated right ovarian mass with a twisted pedicle, poorly delineated from the uterus itself (*). Transverse scan.

18

Fig. 6.**18** Surgical specimen corresponding to Fig. 6.**17**.

19

Fig. 6.**19** This left tubo-ovarian abscess appears as a solitary, thick-walled mass above the uterus. The lower half of the cystic mass contains fine, diffuse internal echoes with a fluid level. Longitudinal scan with a 140° wide-angle transducer.

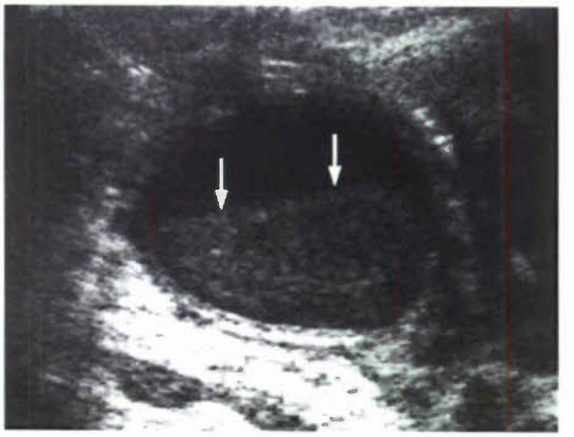

20

Fig. 6.**20** Magnified view of the mass in Fig. 6.**19** shows a conspicuous fluid level within the tubo-ovarian abscess (→). The abscess measures 7.4 × 5.1 × 6.4 cm. Longitudinal scan.

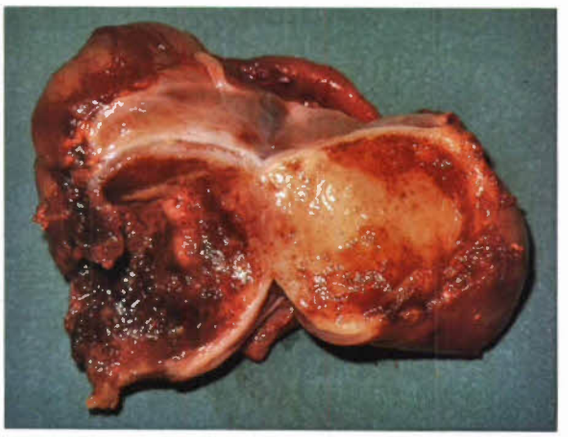

21

Fig. 6.**21** Surgical specimen corresponding to Fig. 6.**20**.

22

Fig. 6.**22** Target sign in the small bowel (→) in Crohn's disease mimics a right adnexal mass bordering the uterus (*). Transverse scan.

23

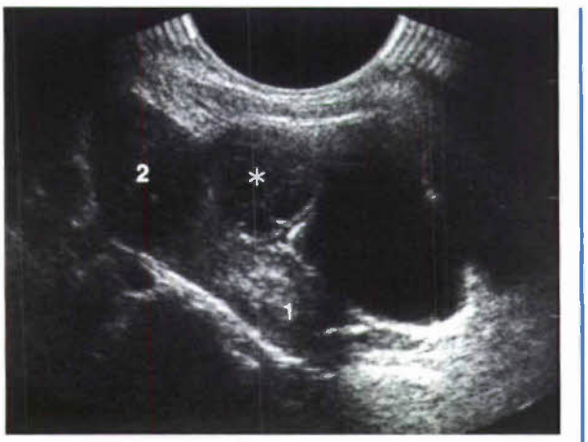

24

Fig. 6.**23** A large cul-de-sac abscess with diffuse internal echoes. Transverse scan.

Fig. 6.**24** Preuterine abscess secondary to an iatrogenic perforation during curettage. Longitudinal scan. Abscess cavity (*).
1 Cervix
2 Uterine corpus

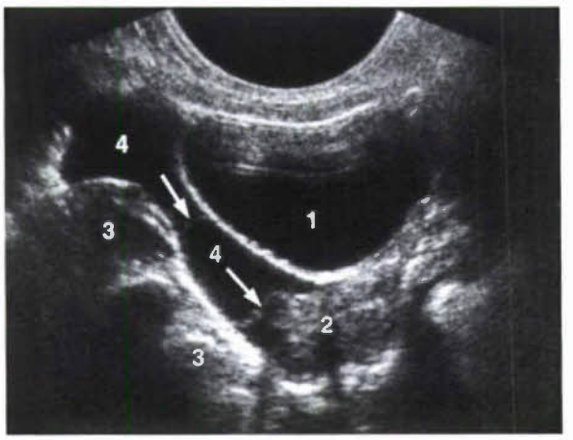

25

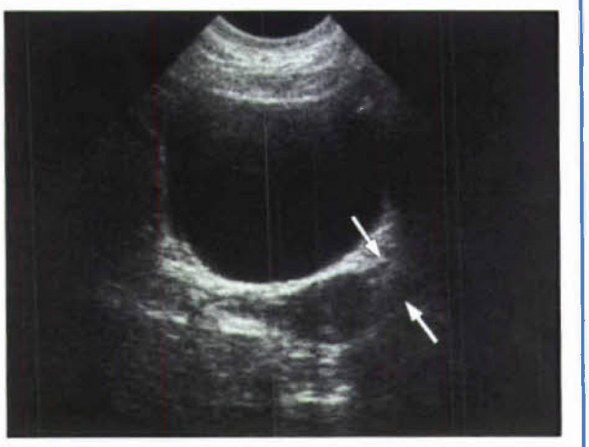

26

Fig. 6.**25** Adhesive bands (→) between the uterus, bladder, and colon in the presence of ascites. Longitudinal scan.
1 Urinary bladder
2 Retroflexed uterus
3 Colon
4 Ascites

Fig. 6.**26** The transverse scan shows the status after left parametritis. The cervix is markedly displaced toward the left side, and the left parametrium is thickened (→).

7 Vaginal Masses

Cystic structures are occasionally noted in the vaginal region during diagnostic ultrasound (Figs. 7.**1**–7.**8**). They may represent embryonic duct cysts derived from constrictions of the müllerian duct, or remnants of the Gartner duct. In addition to lesions of ontogenic origin, there is a large group of vaginal cysts that are caused by trauma, retention, invagination, or a parasitic infection [1]. Vaginal cysts have smooth margins on ultrasound scans. Depending on its contents, the cyst may be devoid of internal echoes (Figs. 7.**1**, 7.**2**), or echoes may diffusely line the interior of the cyst (Figs. 7.**4**, 7.**6**). A fluid level is sometimes visible inside the cyst (Fig. 7.**7**). With a Gartner duct cyst, it may be possible to define the lateral excretory duct in selected cases (Fig. 7.**2**).

Ultrasound can supplement the bimanual examination and speculum findings by determining the precise location of the cyst, defining its relationship to neighboring organs, and accurately delineating its size. This makes the ultrasound examination an important aid in preoperative risk assessment.

The differential diagnosis of vaginal cysts should include *hematocolpos* due to hymenal atresia (Fig. 7.**8**) and benign *connective-tissue tumors of the vagina*. The latter are derived from subepithelial mesenchymal tissue [2,3] and are considered very rare.

References

1 Mestwerdt W, Martius J. Gutartige Erkrankungen der Vagina. In: Mestwerdt W, editor. Gutartige gynäkologische Erkrankungen, I. Munich: Urban & Schwarzenberg, 1988.
2 Blaustein A, Sedlis A. Diseases of the vagina. In: Blaustein A, editor. Pathology of the female genital tract. New York: Springer, 1984: 59–98.
3 Dallenbach-Hellweg G. Weibliches Genitale. In: Remmele, W, editor. Pathologie, vol. 3. Berlin: Springer, 1984: 202–304.

Fig. 7.**1** An echo-free cyst at the center of the vagina (→). Longitudinal scan.

1

Fig. 7.**2** The transverse scan of the vaginal cyst in Fig. 7.**1** demonstrates an excretory duct in the left wall of the cyst (→).

2

Fig. 7.**3** Speculum view of the vaginal cyst in Figs. 7.**1** and 7.**2**.

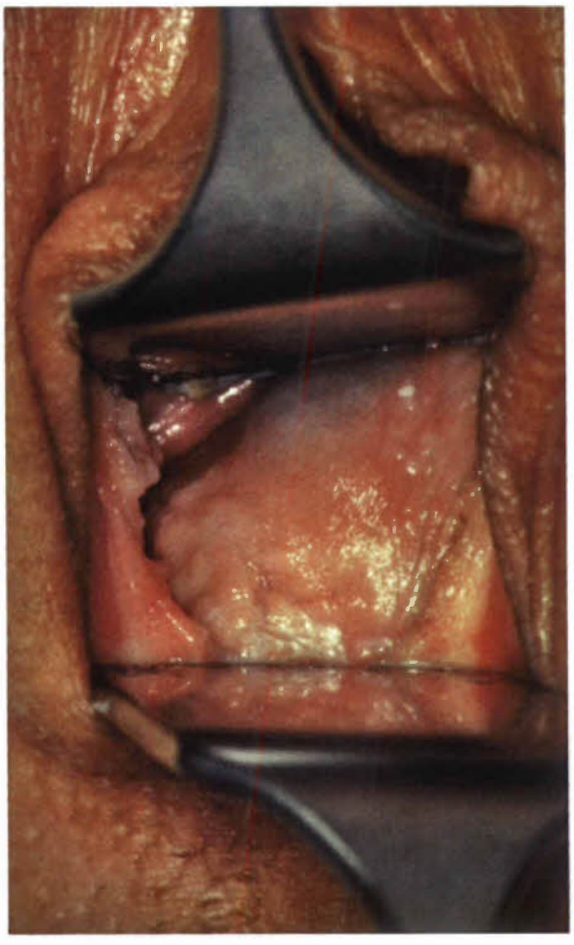

3

4

6

7

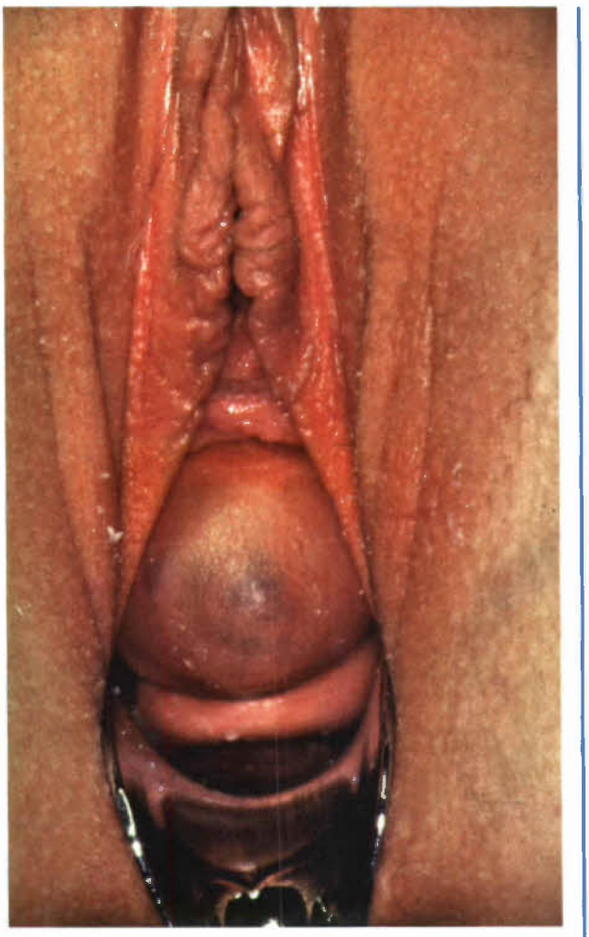

5

8

Fig. 7.4 Suburethral vaginal cyst with fine internal echoes (→). Longitudinal scan.

Fig. 7.5 Speculum view of the cyst in Fig. 7.4.

Fig. 7.6 A large Gartner duct cyst (diameter 8.7 cm) compressing the vaginal canal (→). Longitudinal scan. The cyst contains structures of varying echogenicity.

Fig. 7.7 A Gartner duct cyst with a fluid level (↓). Longitudinal scan.

Fig. 7.8 Hematocolpos in a 12-year-old girl with hymenal atresia.

8 Uterine Masses

Benign Uterine Tumors (Myomas)

Myomas (also known as leiomyomas or fibroids) are the most common benign neoplasms of the female genital tract. They are present in approximately 20% of women over 35 years of age. The great majority of these muscular tumors involve the uterine corpus, with only about 8% occurring in the cervical region [1]. Their sonographic features are extremely variable depending on their location, mode of extension, and degree of degenerative change (calcification, necrosis) [2–4]. At the onset of *intramural myoma growth*, usually the only initial change is a uniform expansion of the uterus, and ultrasound shows only a general uterine enlargement (Figs. 8.**1**, 8.**2**). However, as the nodule continues to grow, ultrasound reveals a round to oval, solid mass that deforms the uterine contours in varying degrees, depending on whether the tumor is intramural (Figs. 8.**3**–8.**8**), subserous (Figs. 8.**9**–8.**18**), intraligamentous (Fig. 8.**19**), or submucous (Figs. 8.**20**–8.**23**). Well-perfused myomas are markedly less echogenic than normal uterine tissue (Figs. 8.**3**, 8.**4**), while calcifications appear as hyperechoic areas that may cast an acoustic shadow (Figs. 8.**5**, 8.**27**).

Whereas most intramural and submucous myomas are easily detectable with ultrasound, *subserous myomas* in particular can be difficult to diagnose. Subserous myomas in the fundal region (Figs. 8.**10**, 8.**11**) may be hidden by bowel loops and may be poorly demarcated cranially. Pedunculated subserous myomas, especially those arising from the posterior uterine wall (Figs. 8.**16**–8.**18**), and intraligamentous myomas (Fig. 8.**19**) may be indistinguishable sonographically from a solid ovarian tumor [4] (Table 8.**1**) unless the pedicle of the myoma can be specifically defined (Fig. 8.**16**).

If the myoma has become soft and necrotic, its low-level internal echoes may simulate the appearance of an ovarian cyst (Fig. 8.**18**).

Pedunculated *submucous myomas* may cause distension of the uterine corpus or cervix, depending on their location (Figs. 8.**20**, 8.**21**), and a myoma projecting from the external os may present directly as a hypoechoic mass in front of the cervix (Figs. 8.**22**, 8.**23**). Cervical myomas that greatly distend the cervix (Figs. 8.**24**, 8.**25**) may be mistaken sonographically for a barrel-shaped cervical carcinoma, while a large myoma on the posterior cervical wall can mimic an ovarian or cul-de-sac mass (Table 8.**1**). Severe endometriosis should also be considered in the differential diagnosis of a myoma found on the posterior cervical wall (Fig. 8.**26**).

A *fibroid uterus* involved by multiple myomatous nodules appears sonographically as a lower abdominal mass with smooth margins but knobby contours. Zones of high echogenicity may coexist with hypoechoic areas depending on the degree of regressive change in the individual nodules (Fig. 8.**27**).

In the investigation of uterine myomas, ultrasound is helpful not only in objectifying palpable findings but also in establishing the number and exact location of the tumors. This is particularly important in cases in which surgical excision is being considered. Since the ultrasound examination also permits the size of the lesions to be determined more accurately and objectively than the manual examination, it is also useful in monitoring the growth of myomas over time. The detection of very rapid growth can provide an early warning sign of malignant sarcomatous transformation.

Table 8.1 Differential diagnosis between pedunculated subserous myoma and submucous myoma

Pedunculated subserous myoma
• Ovarian mass
• Tubal mass
• Focus of endometriosis
• Intestinal mass
Submucous myoma
• Mucosal polyp
• Endometrial or cervical carcinoma
• Metastasis (e.g., from breast carcinoma)

Malignant Uterine Tumors

Ultimately, histologic examination is the only way to prove the diagnosis of a uterine malignancy. Nevertheless, ultrasound is helpful in its ability to detect structural irregularities as well as local and generalized organ enlargement. Especially after menopause, changes of this kind are important in directing suspicion toward the presence of a malignant uterine tumor.

Endometrial Carcinoma

As a rule, the early stages of endometrial carcinoma are not detectable with ultrasound [4–6]. However, an abnormal-appearing endometrial pattern, especially in postmenopausal women, should raise the possibility of adenomatous hyperplasia, an endometrial polyp (Figs. 8.**28**, 8.**29**), or even an early endometrial carcinoma. On the other hand, significant endometrial thickening in a premenopausal patient may be nothing more than benign cystic hyperplasia (Fig. 8.**30**).

Advanced endometrial carcinoma presents at ultrasound with a nonhomogeneous pattern of mixed hyperechoic and hypoechoic areas in the uterine cavity (Figs. 8.**31**–8.**37**). The disease may be extensive enough to markedly distend the uterine corpus (Figs. 8.**33**–8.**37**) [7], making it difficult to distinguish from various benign changes [6,8] (Table 8.**2**).

It is not uncommon for a myoma to coexist with endometrial carcinoma. Consequently, the entire endometrium should be closely scrutinized whenever a "fibroid uterus" is found.

Table 8.2 Differential diagnosis of endometrial carcinoma

• Primary cervical carcinoma with endometrial involvement
• Glandular cystic hyperplasia
• Adenomatous hyperplasia
• Endometrial polyp
• Submucous myoma with regressive changes
• Hydatidiform mole

The depth of uterine wall invasion and the extent of disease (i.e., whether the tumor is confined to the corpus or has already spread to the cervix) are difficult to determine accurately with abdominal ultrasound. Endosonographic methods such as transvaginal sonography or even transuterine sonography [9–11] are more promising in this regard.

If the tumor obstructs the cervical canal, leading to hematometra (Fig. 8.**38**) or pyometra (Fig. 8.**39**), the fluid-filled uterine corpus will appear sonographically as a cystic mass in the lower midabdomen. Fine, diffuse internal echoes are found in both hematometra and pyometra.

Cervical Carcinoma

Early diagnosis of cervical carcinoma usually occurs during routine gynecologic examinations. Abdominal ultrasound can detect cervical carcinoma only if tumor degeneration has led to the formation of a cervical cavity (Figs. 8.**40**, 8.**41**) or to significant cervical distension (Figs. 8.**42**–8.**48**). If the tumor has spread to surrounding structures, the predominantly hypoechoic tumor masses may appear as solid, irregular exophytic nodules (Figs. 8.**44**–8.**48**). Extension into the bladder is demonstrated particularly well by ultrasound (Figs. 8.**44**, 8.**46**–8.**48**). The differential diagnosis includes primary bladder cancer and endometriosis of the bladder (Figs. 8.**49**, 8.**50**, Table 8.**3**).

Preoperative detection of parametrial involvement is difficult [2,5,6] because subtle lesions are not detectable sonographically and ultrasound cannot distinguish reliably between inflammatory and malignant infiltration [12,13] (Fig. 8.**51**). Nor has it been possible to make this differentiation with endosonographic methods such as transrectal scanning [14,15]. Similar problems arise in the detection of involved pelvic and para-aortic lymph nodes, which often are obscured sonographically by overlying bowel. Computed tomography appears to be superior to ultrasound in its ability to detect parametrial involvement and lymph-node metastases [16,17]. Ultrasound is definitely valuable, however, for detecting tumor-related urinary stasis (Figs. 8.**52**, 8.**53**) and excluding tumor recurrence after surgery [6].

Table 8.3 Differential diagnosis of cervical carcinoma

- Primary endometrial carcinoma with cervical involvement
- Primary bladder carcinoma infiltrating the cervix
- Rectal carcinoma infiltrating the cervix
- Parametritis
- Endometriosis of the bladder

References

1 Stegner E. Gynäkologie und Geburtshilfe. Stuttgart: Enke, 1984.
2 Fleischer AC, Walsh JW, Jones HW, Shaff MI, James AE. Sonographic evaluation of pelvic masses. Radiol Clin N Am 1982;20:397–412.
3 Gross BH, Silver TM, Jaffe M H. Sonographic features of uterine leiomyomas. J Ultrasound Med 1983;2:401–6.
4 Kratochwil A. Ultraschalldiagnostik in der Gynäkologie. Gynäkologe 1976;9:166–80.
5 Hansmann M, Hackelöer BJ, Staudach A. Ultraschalldiagnostik in Geburtshilfe und Gynäkologie. Lehrbuch und Atlas. Berlin: Springer, 1985.
6 Sanders RC. Ultrasound in pelvic malignancy. In: Steel WB, Cochrane WJ, editors. Gynecologic ultrasound. Edinburgh: Churchill Livingstone, 1984: 139–156.
7 Requard CK, Wicks JD, Mettler FA Jr. Ultrasonography in the staging of endometrial adenocarcinoma. Radiology 1981;140:781–5.
8 Fleischer AC, James AE Jr, Millis JB, Julian C. Differential diagnosis of pelvic masses by gray scale sonography. AJR Am J Roentgenol 1978;131:469–76.
9 Hotzinger H, Becker H, Becker V. Intrauterine Ultraschalltomographie (IUT): Vergleich mit makroskopischen Präparatschnitten. Geburtshilfe Frauenheilkd 1984;44:219–24.
10 Obata A, Akamatsu N, Sekiba K. Ultrasound estimation of myometrial invasion of endometrial cancer by intrauterine radial scanning. J Clin Ultrasound 1985; 13:397–404.
11 Popp LW, Lueken RP, Müller-Holve W, Lindemann HJ. Gynäkologische Endosonographie: erste Erfahrungen. Ultraschall 1983;4:92–7.
12 Bernardino ME, Dodd GD. Imaging of the pelvic contents in the female oncologic patient. Cancer 1981;48(2 Suppl):504–10.
13 Kurtz AB, Rubin CS, Kramer FL, Goldberg BB. Ultrasound evaluation of the posterior pelvic compartment. Radiology 1979;132:677–82.
14 Bernaschek G, Janisch H. Eine Methode zur Objektivierung des Parametrienbefundes beim Zervixkarzinom. Geburtshilfe Frauenheilkd 1983;43:498–532.
15 Zaritzky D, Blake D, Willard J, Resnick M. Transrectal ultrasonography in the evaluation of cervical carcinoma. Obstet Gynecol 1979;53:105–8.
16 Ginaldi S, Wallace S, Jing BS, Bernardino ME. Carcinoma of the cervix: lymphangiography and computed tomography. AJR Am J Roentgenol 1981;136:1087–91.
17 Walsh JW, Amendola MA, Konerding KF, Tisando J, Hazra TA. Computed tomographic detection of pelvic and inguinal lymph node metastases from primary and recurrent pelvic malignant disease. Radiology 1980;137:157–66.

Benign Uterine Masses

1

Fig. 8.1 Diffuse myomatosis in an anteflexed uterus. Uterine length is 8.2 cm, corpus depth 7.4 cm, corpus width 8 cm. The thin endometrial stripe is clearly defined (→). Longitudinal scan.

2

Fig. 8.2 Surgical specimen corresponding to Fig. 8.1.

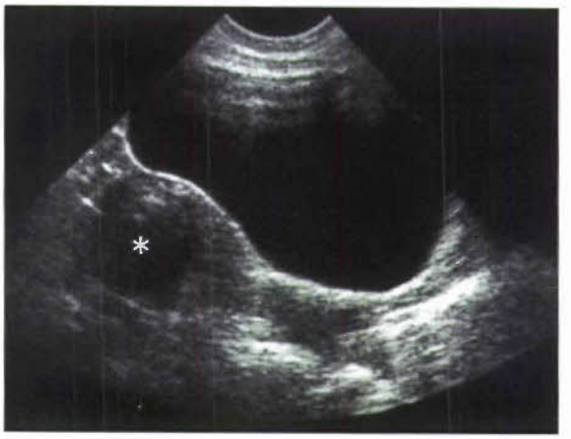

3

Fig. 8.3 Hypoechoic intramural myoma of the posterior uterine wall (*), 4 cm in diameter. Longitudinal scan.

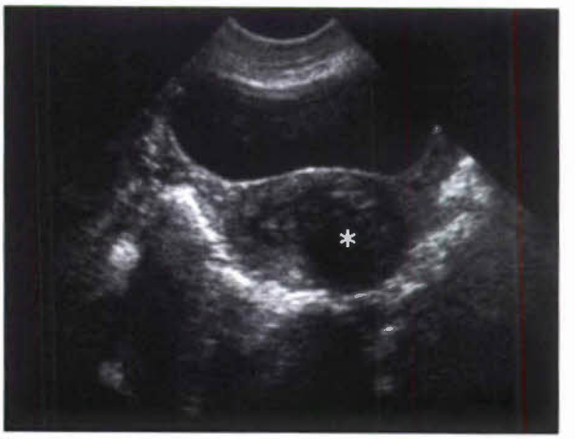

4

Fig. 8.4 Transverse scan of the myoma in Fig. 8.3. The tumor appears to occupy the left half of the uterine corpus (*).

5

Fig. 8.5 Large intramural myoma of the posterior uterine wall containing hypoechoic zones of calcification (—). Typical acoustic shadows are seen behind the calcifications.

6

Fig. 8.6 Intramural posterior wall myoma 12 cm in diameter, causing globular expansion of the uterus. Longitudinal scan.

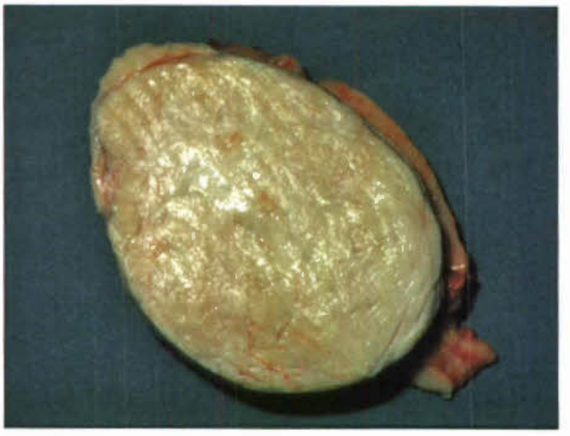

7

Fig. 8.7 Surgical specimen corresponding to Fig. 8.6.

8

Fig. 8.8 Transverse scan of the myoma in Figs. 8.6 and 8.7.

9

10

Fig. 8.9 Subserous anterior wall myoma 3.6 cm in diameter (→) indenting the urinary bladder. Longitudinal scan.

Fig. 8.10 Subserous fundal myoma 4 cm in diameter (→). Longitudinal scan.

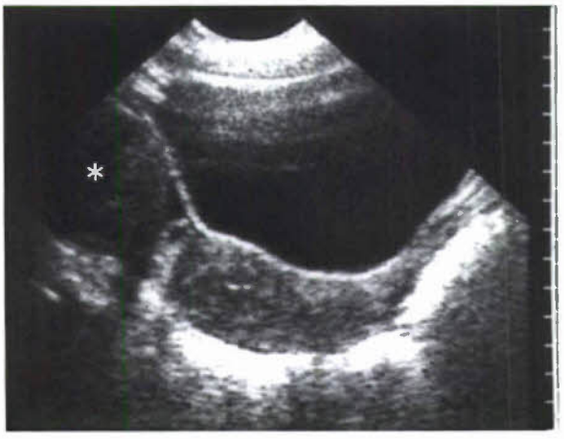

11

Fig. 8.11 Pedunculated subserous fundal myoma (*) in an otherwise normal-sized uterus. Longitudinal scan.

12

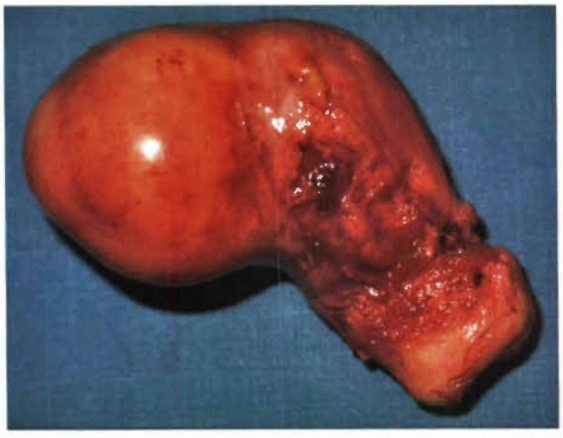

13

Fig. 8.12 Subserous posterior wall myoma 4.8 cm in diameter (*). Longitudinal scan.

Fig. 8.13 Surgical specimen corresponding to Fig. 8.12.

14

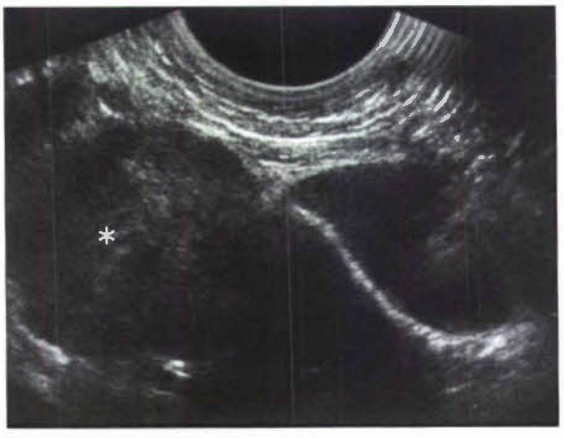

15

Fig. 8.14 Large subserous fundal myoma with central malacic foci (→). Longitudinal scan.

Fig. 8.15 Large subserous fundal myoma (9.2 × 8.2 × 8.5 cm) that has undergone sarcomatous degeneration (*). Longitudinal scan.

Fig. 8.**16** Pedunculated subserous posterior-wall myoma (1) (pedicle —). The longitudinal scan also cuts a smaller pedunculated subserous myoma of the uterine fundus (2).

16

Fig. 8.**17** Surgical specimen corresponding to Fig. 8.**16**.

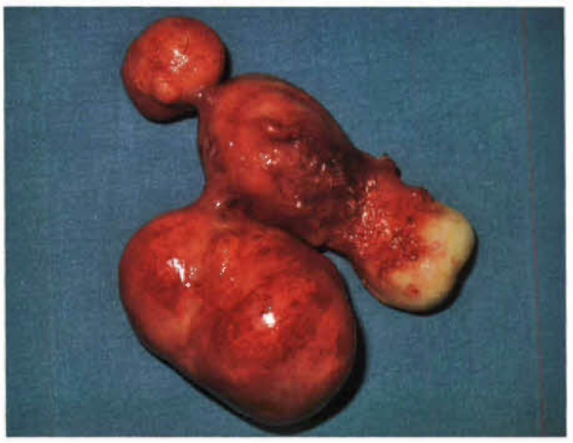

17

Fig. 8.**18** Hypoechoic, pedunculated subserous posterior wall myoma 5.8 × 4.6 cm in size (*). This appearance mimics an ovarian tumor.

18

Fig. 8.**19** Intraligamentous myoma on the right side, 4 cm in diameter. Transverse scan.
1 Uterus
2 Myoma

19

Fig. 8.**20** Large, pedunculated submucous myoma causing marked expansion of the cervical region (—). Longitudinal scan. The depth of the uterine corpus is 7.3 cm.

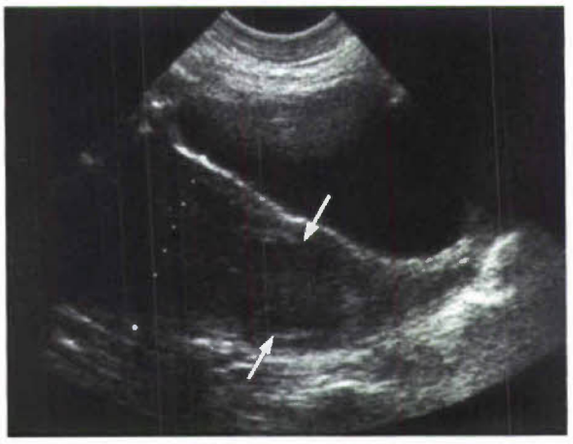

20

Fig. 8.**21** Surgical specimen corresponding to Fig. 8.**20**.

21

Fig. 8.**22** Pedunculated submucous myoma protruding through the external os (*). Longitudinal scan.

22

Fig. 8.**23** Speculum view of the tumor in Fig. 8.**22**.

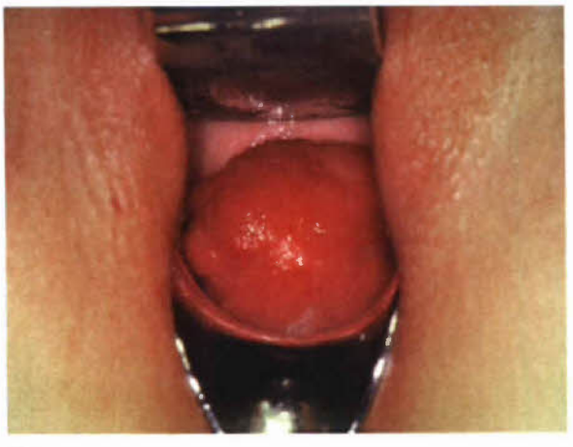

23

24

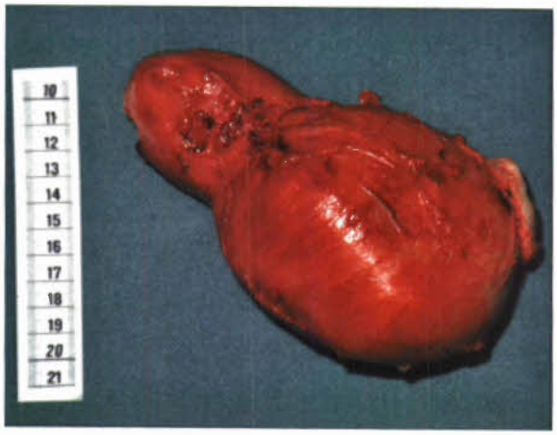

25

Fig. 8.**24** A large myoma of the posterior cervical wall (*) appearing below a normal-sized uterine corpus (→). Longitudinal scan.

Fig. 8.**25** Surgical specimen corresponding to Fig. 8.**24** (measured in cm).

26

27

Fig. 8.**26** Two large endometriotic nodules behind the cervix in the cul-de-sac (→, 3.2 cm and 1.4 cm in diameter). Longitudinal scan.

Fig. 8.**27** A giant fibroid uterus (13.5 × 8.7 × 10.2 cm) containing multiple myomatous nodules of varying size. There is a mixed pattern of low-level echoes from degenerative malacic areas and higher-level echoes from calcifications. Transverse scan.

28

29

Endometrial Polyp/ Hyperplasia

Fig. 8.**28** An endometrial polyp in a 78-year-old woman with postmenopausal bleeding. The longitudinal scan shows marked thickening of the endometrium to 1 cm (→).

Fig. 8.**29** Transverse scan of the uterus in Fig. 8.**28**.

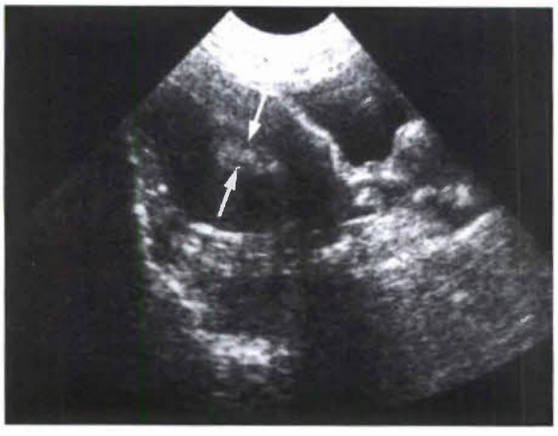

30

Fig. 8.**30** Cystic glandular hyperplasia in the presence of diffuse myomatosis. Note the hyperechoic endometrium (→), which is thickened to 1.3 cm and contains several small, peripheral cystic areas. Longitudinal scan.

Endometrial Carcinoma

31

Fig. 8.**31** Endometrial carcinoma in a 65-year-old woman. The longitudinal scan shows a conspicuous, irregular, echogenic structure (→) completely occupying the cavity of an otherwise small uterus.

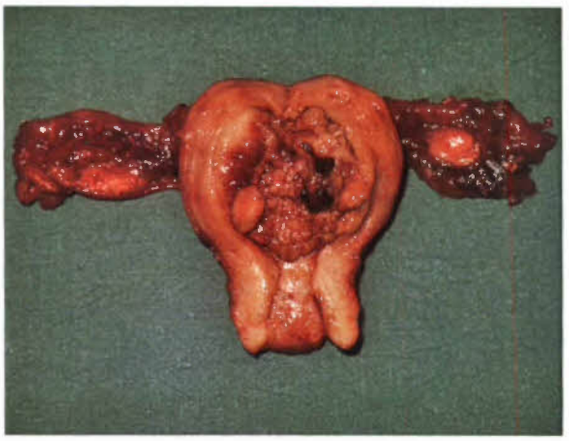

32

Fig. 8.**32** Surgical specimen corresponding to Fig. 8.**31**. The histologic examination showed carcinoma confined to the uterine corpus and invading the inner third of the myometrium.

33

Fig. 8.**33** Endometrial carcinoma in longitudinal section. The corpus is markedly distended by irregular tumor masses of mixed echogenicity.

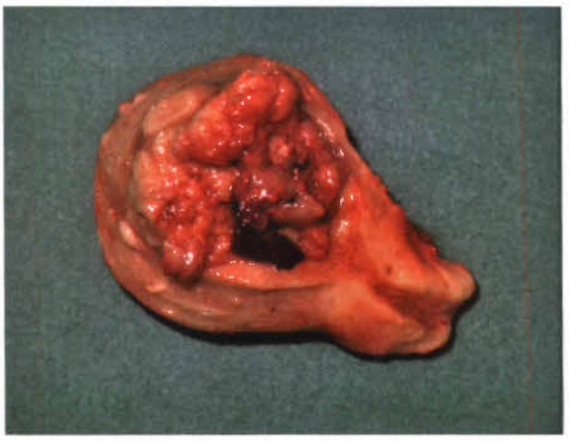

34

Fig. 8.**34** Surgical specimen corresponding to Fig. 8.**33**. Histologic examination showed carcinoma confined to the corpus and invading the inner third of the myometrium.

35

Fig. 8.**35** Transverse scan of the tumor in Figs. 8.**33** and 8.**34**. Note the irregular echo pattern within the uterine cavity.

36

Fig. 8.**36** Endometrial carcinoma in a 33-year-old woman. The tumor has invaded the myometrium as far as the posterior-wall serosa (—). Longitudinal scan.

37

Fig. 8.**37** Endometrial carcinoma of Fig. 8.**36**. Transverse scan.

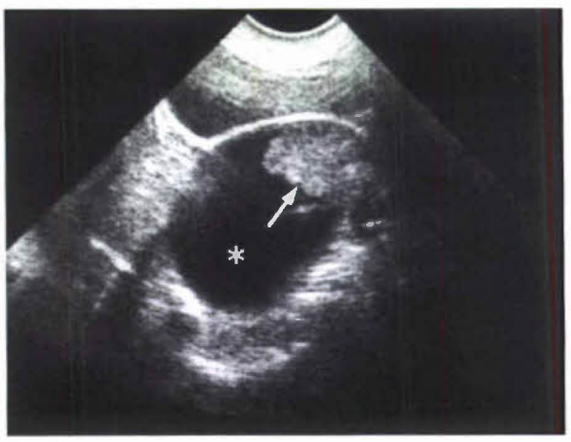

38

Fig. 8.**38** Pronounced hematometra (*) associated with endometrial carcinoma. The internal cervical os is obstructed by a polyp that has undergo carcinomatous change (→).

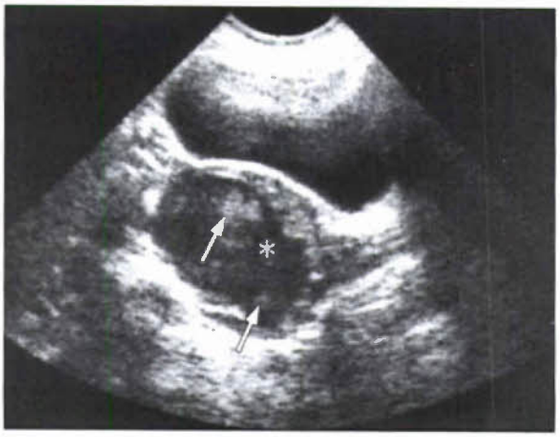

39

40

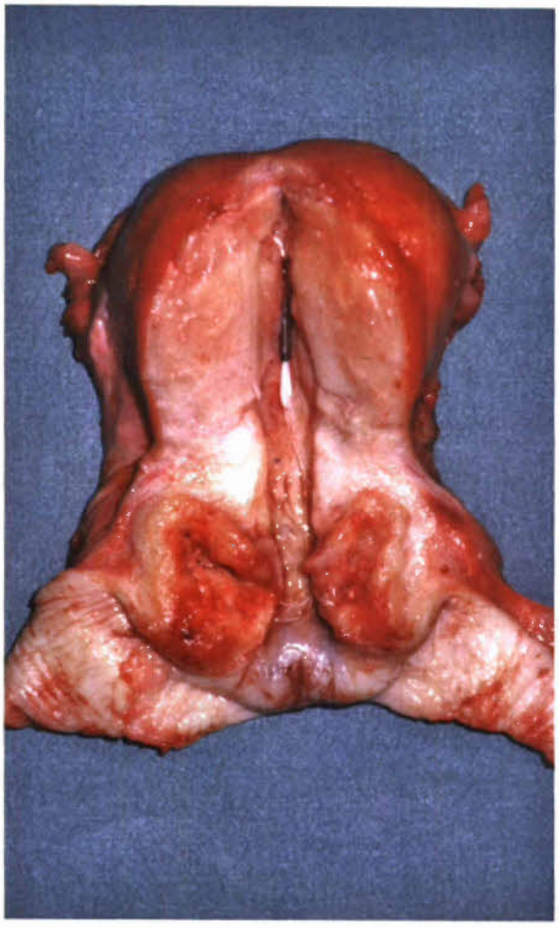

41

Cervical Carcinoma

Fig. 8.**39** Pronounced pyometra (*) associated with cervical carcinoma. The prominent echogenic areas (→) are caused by cellular debris. Longitudinal scan.

Fig. 8.**40** Carcinoma of the cervical cavity features a hyperechoic rim and a central, hypoechoic area of degenerative change (→). Longitudinal scan. An intrauterine device is visible within the uterine cavity.

Fig. 8.**41** Surgical specimen corresponding to Fig. 8.**40**.

42

43

Fig. 8.**42** Cervical carcinoma causing barrel-shaped distension of the cervix (→). Longitudinal scan.

Fig. 8.**43** Pronounced, echogenic cervical carcinoma causing barrel-shaped distension of the cervix. Longitudinal scan.

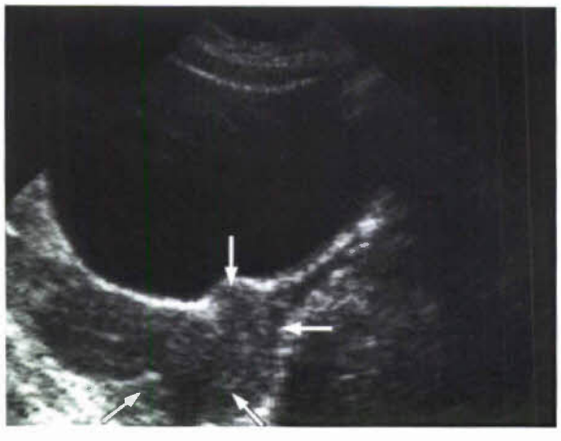

44

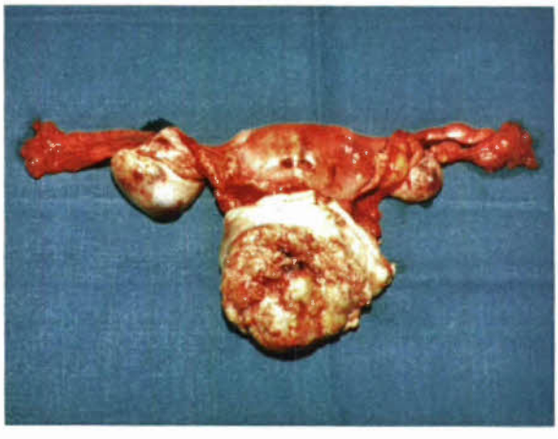

45

Fig. 8.**44** Exophytic cervical carcinoma of mixed echogenicity (→) with a normal-appearing uterine corpus. The bladder is slightly indented by the mass. Longitudinal scan.

Fig. 8.**45** Surgical specimen corresponding to Fig. 8.**44**.

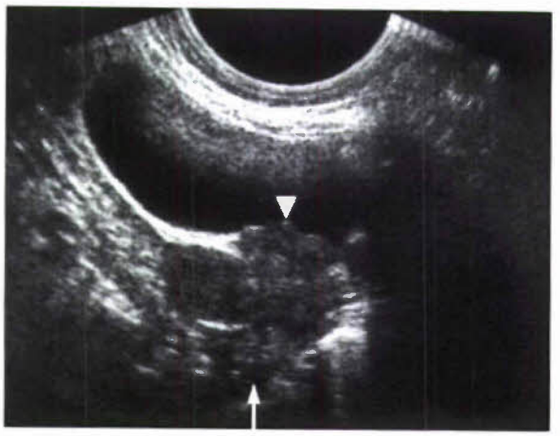

46

Fig. 8.46 Stage IV cervical carcinoma that has invaded the bladder (▶) and rectum (—). Longitudinal scan.

47

Fig. 8.47 Transverse scan of the bladder invasion seen in Fig. 8.46.

48

Fig. 8.48 Extensive area of bladder invasion (—) by a hypoechoic cervical carcinoma. Longitudinal scan.

49

Fig. 8.49 Pronounced endometriosis of the bladder (—). Longitudinal scan.

50

Fig. 8.50 Endometriosis of the bladder. Transverse scan of the case in Fig. 8.49.

51

Fig. 8.51 Transverse scan through the cervical region of a patient with stage IIb cervical carcinoma. The area of the left parametrial attachment has been invaded by hypoechoic tumor masses (→).

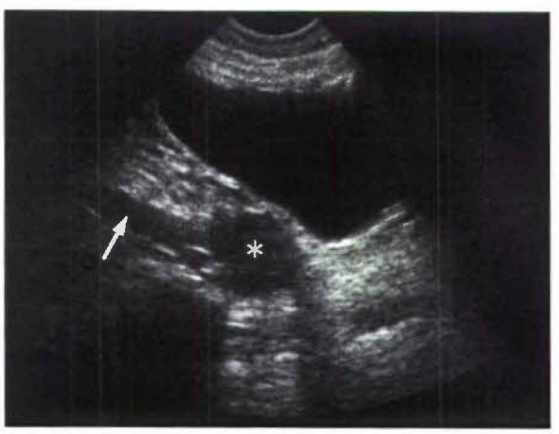

52

Fig. 8.52 Hypoechoic recurrence of an excised cervical carcinoma (*). The tumor is compressing the uterus and has caused urinary stasis (—). Longitudinal scan.

53

Fig. 8.53 An advanced cervical carcinoma has caused massive urinary stasis with ureteral compression and hydronephrosis on the left side. Longitudinal scan.
1 Obstructed and dilated renal pelvis
2 Renal parenchyma
— Obstructed ureter

9 Ovarian Masses

In the ovary as in other organs, ultrasound is not capable of distinguishing reliably between benign and malignant lesions. It can, however, assist benign–malignant differentiation by its ability to distinguish between cystic and solid masses and characterize their internal echo pattern and margins. Often these clues can supply a specific diagnosis when interpreted in the context of the history, pelvic examination, and laboratory findings.

The goals of the ultrasound examination are early detection of ovarian carcinoma and differentiation of ovarian masses with regard to their clinical significance. The overriding goal is to distinguish functional ovarian cysts from true benign and malignant neoplasms so that unnecessary surgery can be avoided.

Benign Ovarian Masses

Simple Ovarian Cysts

The most common benign lesions of the ovary are simple ovarian cysts (*follicular cysts*, *corpus luteum cysts*, and *retention cysts*). They appear sonographically as round to oval unilocular masses with a thin, smooth wall, an absence of internal echoes, and posterior acoustic enhancement [1–3] (Figs. 9.**1**–9.**4**). They are indistinguishable from small unilocular cystomas (Figs. 9.**30**, 9.**31**) or paraovarian cysts (Fig. 9.**5**).

Intracystic hemorrhage, like that sometimes seen in corpus luteum cysts (Figs. 9.**6**–9.**8**), presents with fine, high-level internal echoes that can mimic the appearance of an endometriotic cyst.

Endometriotic Cysts

Approximately 15% of women develop endometriosis during their reproductive lifetime [4]. The sonographic appearance of endometriosis is extremely variable, and all gradations from mixed to predominantly solid lesions may be found [2,5–8]. Endometriotic cysts are distinguished from simple ovarian cysts by their thicker wall and fine internal echo pattern, which may include higher-level echoes toward the periphery of the cyst [1,2,5–7] (Figs. 9.**9**–9.**16**). An organized hematoma with fibrin deposits is responsible for the dense peripheral echoes.

Endometriotic cysts may be unilateral or bilateral and are commonly found in the cul-de-sac. Often there are associated inflammatory changes, causing the cyst to adhere to the uterus and making it impossible to delineate the cyst clearly from the uterine wall. Endometriotic nodules in the cul-de-sac may appear sonographically as solid hypoechoic masses (Fig. 8.**26**). In patients with pronounced uterine adenomyosis, the myometrium is permeated by irregular echo-free areas up to 5–7 mm in size, representing blood-filled cavities [8].

With its heterogeneous appearance, endometriosis can be extremely difficult to distinguish from other lesions such as tubo-ovarian abscess, dermoid cyst, corpus luteum cyst, ectopic pregnancy, and ovarian carcinoma [2,6,8].

Often, an accurate diagnosis can be made only when the ultrasound findings are considered in relation to the history and clinical presentation (dysmenorrhea, chronic lower abdominal pain, dyspareunia), and many patients may still require an invasive procedure (laparoscopy or laparotomy) in order to establish a diagnosis.

Although endometriosis does not present consistent sonographic features, ultrasound is still an important aid to diagnosis. It can also be helpful in monitoring the response to nonoperative medical treatment.

Dermoid Cysts

A dermoid cyst of the ovary is a benign, usually cystic lesion that may contain elements derived from all three germ layers. Its sonographic features are extremely diverse and depend on the individual tissue makeup of the lesion and its degree of maturation and differentiation [9]. Dermoid cysts represent approximately 20% of ovarian cysts and 10% of ovarian masses [10]. Skin, hair, and sebaceous glands are by far the most common tissue elements found in dermoid cysts. Other constituents, in order of decreasing frequency, are fat, cartilage, nerve tissue, bone, respiratory tissue, teeth, and gastrointestinal tissue [11]. In rare cases the lesion occurs as a struma ovarii, a single germ-layer teratoma composed of thyroid tissue.

The principal complications of dermoid cysts are malignant transformation, which occurs in 1–2% of cases [11], and torsion of the tumor pedicle, occurring in 3–16% of cases [12].

Approximately 33–43% of the lesions [13,14] have a characteristic sonographic pattern [1,13,15,16], appearing a thick-walled, cystic adnexal mass containing a hyperechoic solid area of sebaceous material with epidermis, bone, cartilage, or any of the other tissue types mentioned above. A dermoid may also contain hypoechoic areas, depending on its contents (Figs. 9.**17**–9.**29**). A conspicuous sebaceous fluid level is sometimes seen [17]. The associated echogenic area may occupy either the lower portion of the cyst (Figs. 9.**17**, 9.**18**) or its upper portion (Figs. 9.**19**, 9.**20**). In place of the echogenic fluid level, it is not unusual to find a bizarrely shaped area of high echogenicity (Figs. 9.**21**, 9.**22**). The echogenic area may appear as a flat peripheral feature or as a regularly shaped structure in the interior of the cyst (Figs. 9.**23**, 9.**24**). Occasionally, a rudimentary tooth can be identified within the echogenic area (Figs. 9.**25**, 9.**26**).

Dermoids can vary markedly in appearance depending on their contents. This applies both to the echogenicity of the lesion (Fig. 9.**27**) and to the appearance of its solid and cystic elements. Thus the dermoid may appear predominantly solid (Fig. 9.**28**) or as an almost purely cystic mass (Fig. 9.**29**). Accordingly, the acoustic phenomena associated with the lesion can range from posterior acoustic enhancement (Figs. 9.**27**, 9.**29**) to posterior shadowing (Fig. 9.**28**).

Diagnostic problems invariably arise when the dermoid does not present its characteristic structure. This type of lesion can be extremely difficult to distinguish from an endometriotic cyst, a tubo-ovarian abscess, a distended bowel loop, or ovarian carcinoma. Even a corpus luteum cyst with a circumscribed, relatively hyperechoic hematoma may resemble a dermoid cyst. In the latter case, however, serial examinations show a progressive decline in the echogenicity of the corpus luteum cyst as the hematoma is reabsorbed. This helps distinguish it from a dermoid cyst, in which the internal echo pattern remains constant over time. A dermoid that consists mainly of solid, relatively hyperechoic components may be missed when surrounded by bowel loops that have a similar echo pattern [11].

Serous Cystadenomas

Most serous cystadenomas (Figs. 9.**30**, 9.**31**) are unilocular and have no internal echoes. They are therefore indistinguishable from a simple ovarian cyst by ultrasound [1]. A larger, purely cystic mass that is unilocular, has smooth margins, and contains no internal echoes would be suspicious for a serous cystadenoma (Figs. 9.**32**–9.**35**), but might also be a giant follicular cyst (Fig. 9.**36**). In rare cases, an overdistended bladder in a patient with *neurogenic bladder dysfunction* can mimic a serous cystadenoma (Figs. 9.**37**, 9.**38**), but this can be resolved by noting the absence of a bladder caudal to the "mass."

With a multilocular serous cystadenoma, very thin internal septa are observed within an otherwise smooth-walled, echo-free mass (Figs. 9.**39**, 9.**40**).

Mucinous Cystadenomas

A small mucinous cystadenoma, like a small serous cystadenoma, cannot be diagnosed with confidence on the basis of ultrasound findings. Scans show a sharply circumscribed, hypoechoic mass with fine internal echoes (Figs. 9.**41**, 9.**42**). This pattern may cause confusion with a simple retention cyst, an endometriotic cyst, or a pedunculated, degenerating myoma.

Larger mucinous cysts, which may occasionally fill the whole abdominal cavity, have a less ambiguous sonographic appearance. Both longitudinal and transverse scans demonstrate a multilocular mass containing cystic cavities of varying size and internal echoes of varying amplitude, depending on their contents [2,3,10] (Fig. 9.**43**).

The differential diagnosis of these masses should include hyperstimulated ovaries (Fig. 9.**44**) and giant renal cysts (Fig. 9.**45**).

With a large mass, ultrasound may be unable to determine whether the lesion arises from the left or right side. Similarly, in tumors with septations, it cannot always be determined whether the mass originates from one or both adnexal regions [2].

A confident benign–malignant differentiation cannot be made on the basis of ultrasound findings. Smooth margins, thin septa, the absence of irregular solid areas, and the absence of ascites are, however, suggestive of a benign lesion.

Ovarian Fibromas

Benign solid tumors of the ovary are much less common than benign cystic ovarian masses. An ovarian fibroma appears sonographically as a unilateral or bilateral, solid flat or rounded mass with smooth margins and homogeneous, low-level internal echoes (Figs. 9.**46**–9.**51**). It is not unusual for the tumor to sink due to its own weight to a dependent position in the cul-de-sac [3]. *Meigs syndrome* is a condition in which bilateral ovarian fibromas are accompanied by ascites and hydrothorax.

Ovarian fibroma mainly requires differentiation from a pedunculated subserous myoma, a predominantly solid dermoid, a distended bowel loop (Fig. 9.**52**), and the rare pelvic kidney (Fig. 9.**53**). The latter can be distinguished from an ovarian fibroma by the considerably greater echogenicity of the pyelocaliceal system at the center of the "mass."

Isolated cystic areas may be seen within a fibroma that has undergone regressive change (Fig. 9.**54**).

Potentially Malignant Ovarian Tumors

Various tumors—such as proliferating serous papillary cystadenomas, mucinous cystadenomas, granulosa-cell tumors, theca cell tumors, and Sertoli–Leydig cell tumors—differ histologically from benign tumors by virtue of their increased proliferative activity. They are classified as "potentially malignant," owing to their capacity for malignant transformation.

This type of clear histologic differentiation between tumor types cannot of course be achieved with ultrasound. Nevertheless, there are a number of sonographic features associated with these tumors that allow them to be classified as unusual or even suspicious. These signs include cystic masses that contain a peripheral, irregular solid area (Figs. 9.**55**–9.**58**) or a large solid component (Figs. 9.**59**, 9.**60**), and the presence of mixed high-level and low-level echoes within a solid tumor (Figs. 9.**61**–9.**64**).

It should be noted, however, that similar features may be seen in association with endometriosis, dermoid cyst, tubo-ovarian abscess, corpus luteum cyst, and ovarian carcinoma. For this reason, the ultrasound findings should always be interpreted in the context of the clinical findings.

Malignant Ovarian Tumors

After carcinoma of the breast, stomach, and cervix, ovarian carcinoma is the fourth most frequent cancer in women [1]. Ovarian carcinoma is bilateral in 70% of cases, as opposed to benign ovarian tumors, which are bilateral in only 5% of cases [18]. Ovarian carcinoma is still one of the most dangerous cancers, as it has often already metastasized by the time it is diagnosed [19]. The sonographic features of ovarian malignancies vary greatly depending on the cystic and solid components of the tumor [10,19–31]. All gradations can be found, ranging from a purely cystic mass to a completely solid tumor. In patients in whom ovarian carcinoma was confirmed at surgery, Requard et al. [19] found that the preoperative sonographic pattern of the tumors was solid in 19% of cases, mixed in 68%, and purely cystic in 13%.

Ultrasound should raise a suspicion of a malignant ovarian tumor whenever the lesion contains cystic areas in addition to solid irregular structures (Figs. 9.**65**–9.**74**) or when scans show a loculated, cystic mass that contains thick septa [32] and peripheral papillary growths or solid irregular areas [32] (Figs. 9.**75**–9.**78**). A predominantly solid mass with irregular margins is also suspicious for malignancy (Figs. 9.**79**, 9.**80**). With advanced ovarian carcinoma, the entire cul-de-sac may be lined by irregular tumor masses (Fig. 9.**81**).

The sonographic impression of a malignant ovarian tumor is supported by the presence of additional malignancy criteria such as ascites or hepatic metastases. Obwegeser et al. [33] documented a 76% malignancy rate when both an ovarian tumor and ascites were detected at ultrasound. It should be added, however, that almost half of ovarian carcinomas are not accompanied by ascites [19] and that ascites may also develop in association with benign ovarian masses and liver disease.

Mucinous cystadenocarcinoma may completely fill the abdomen with fluid-like echoes that may be mistaken for ascites. However, the presence of punctate, high-level internal echoes within the hypoechoic mass serves to distinguish it from ascites (Fig. 9.**82**).

An *endometrioid sarcoma* of the ovary also appears sonographically as a solid, hypoechoic mass (Figs. 9.**83**, 9.**84**). Its echo pattern is remarkable in that is consists of adjacent, irregular areas of low-level and high-level echoes.

Various groups of authors [16,33–37] have investigated the accuracy rates of transabdominal ultrasound in the diagnosis or exclusion of a malignant ovarian tumor. They found sensitivity values in the range of 62–93% and specificity values in the range of 42–95%.

In 1989, Schillinger et al. [38] presented a five-point scoring system designed to simplify the interpretation of ovarian masses (Fig. 9.**85**, Table 9.**1**). The advantage of this scheme is that it can quickly classify an ovarian mass; a disadvantage of it is that a five-point scoring system

Table 9.1 The tumor scoring system introduced by Schillinger et al. in 1989 [38]

I	Well-circumscribed solitary cysts
II	Other well-circumscribed homogeneous tumors
III	Slightly nonhomogeneous tumors, predominantly homogeneous tumors with small areas having a different consistency, or tumors with ill-defined margins
IV	Nonhomogeneous cystic/solid or solid/cystic tumors
V	Completely heterogeneous tumors with bizarre features

cannot take account of all the relevant details and risks some loss of information.

The early detection of ovarian carcinoma continues to be a major challenge (Figs. 9.**86**, 9.**87**). While subtle structural changes can be detected with a high-resolution scanner, it is still difficult to classify the lesion as definitely malignant. Transvaginal sonography can provide more accurate differentiation in these cases, owing to its superior resolution. Campbell and his group [39,40] recommend an ultrasound screening protocol for early ovarian cancer in which the structure and volumes of both ovaries are compared with each other, so that unilateral ovarian changes can be recognized at an early stage.

Whenever an ovarian malignancy is suspected, the differential diagnosis should always include a primary tumor in proximity to the ovary, such as sigmoid carcinoma (Fig. 9.**88**) or bladder carcinoma (Fig. 9.**89**). It should also be considered that an ovarian tumor may not be primary but may be metastatic to the ovary from a primary malignancy of the breast or bowel (Fig. 9.**90**). Finally, an irregularly distended bowel loop can also mimic the appearance of a malignant tumor (Fig. 9.**91**). However, unlike a true tumor, this type of mass can usually be excluded by manual examination and will tend to disappear or show a change of configuration on follow-up sonograms.

References

1 Fleischer AC, Walsh JW, Jones HW 3rd, Shaff MI, James AE Jr. Sonographic evaluation of pelvic masses: method of examination and role of sonography relative to other imaging modalities. Radiol Clin North Am 1982;20:397–412.
2 Kratochwil A. Ultraschalldiagnostik in der Gynäkologie. Gynäkologe 1976;9:166–80.
3 Schlensker KH. Atlas der Ultraschalldiagnostik in Geburtshilfe und Gynäkologie. Stuttgart: Thieme, 1984.
4 Jenkinson EL, Brown WH. Endometriosis. J Am Med Assoc 1943;122:349–54.
5 Coleman BG, Arger PH, Mulhern CB Jr. Endometriosis: clinical and ultrasonic correlation. AJR Am J Roentgenol 1979;132:747–9.
6 Lipsit ER. Inflammatory disease of the pelvis and postoperative fluid collections. In: Steel WB, Cochrane WJ, editors. Gynecologic ultrasound. Edinburgh: Churchill Livingstone, 1984: 85–104.
7 Sandler MA, Karo JJ. The spectrum of ultrasonic findings in endometriosis. Radiology 1978;127:229–31.
8 Walsh JW, Taylor JW, Rosenfield AT. Gray scale ultrasonography in the diagnosis of endometriosis and adenomyosis. AJR Am J Roentgenol 1979;132:87–90.
9 Matz MH. Benign cystic teratomas of the ovary: a review. Obstet Gynecol Surv 1961;16:591–605.
10 Hansmann M, Hackelöer BJ, Staudach A. Ultraschalldiagnostik in Geburtshilfe und Gynäkologie. Lehrbuch und Atlas. Berlin: Springer, 1985.
11 Karo JJ, Sandler MA. Benign cystic teratoma of the ovary. In: Steel WB, Cochrane WJ, editors. Gynecologic ultrasound. Edinburgh: Churchill Livingstone, 1984: 47–59.
12 Lawson TL, Albarelli JN. Diagnosis of gynecologic pelvic masses by gray-scale ultrasonography: analysis of specificity. AJR Am J Roentgenol 1977;128:1003–6.
13 Laing FC, Van Dalsem VF, Marks WM, Barton JL, Martinez DA. Dermoid cysts of the ovary: their ultrasonic appearances. Obstet Gynecol 1981;57:99–104.
14 Sandler MA, Silver TM, Karo JJ. Gray scale ultrasonic features of ovarian teratomas. Radiology 1979;131:705–9.
15 Guttman PH Jr. In search of the elusive benign cystic ovarian teratoma: application of the ultrasound "tip of the iceberg" sign. J Clin Ultrasound 1977;5:403–6.
16 Hermann UJ, Locher GW, Goldhirsch A. Sonographic patterns of ovarian tumors: prediction of malignancy. Obstet Gynecol 1987;69:777–81.
17 Hutton L, Rankin R. The fat–fluid level: another feature of dermoid tumors of the ovary. J Clin Ultrasound 1979;7:215–6.
18 Barber HR. Ovarian cancer: part I. CA Cancer J Clin 1979;29:341–51.
19 Requard CK, Mettler FA, Wicks JD. Preoperative sonography of malignant ovarian neoplasm. AJR Am J Roentgenol 1982;137:79–82.
20 Bernardino ME, Dodd GD. Imaging of the pelvic contents in the female oncologic patient. Cancer 1981;48: 504–10.
21 Birnholz JC. Ultrasonography of ovarian masses [letter]. N Engl J Med 1976; 294:906.
22 Casey MJ, Little K. Evaluation of serial grey scale ultrasound scans in a gynecologic oncology clinic. Gynecol Oncol 1981;11:213–7.
23 Coulam CM, Julian CG, Fleischer AC. Clinical efficacy of CT and US in evaluating gynecologic tumors. Appl Radiol 1982;11:79–82, 84–8.
24 Elling D, Kobs K. Erfahrungen bei der Anwendung des Ultraschall-B-Bildverfahrens zur Exploration des kleinen Beckens. Zentralbl Gynäkol 1981;103:1129–41.
25 Kabayashi M. Use of diagnostic ultrasound in trophoblastic neoplasms and ovarian tumors. Cancer 1976;38:441–52.
26 Kratochwil A. Ultrasonic diagnosis in pelvic malignancy. Clin Obstet Gynecol 1970;13:898–909.
27 Levi S, Delval R. Value of ultrasonic diagnosis of gynecologic tumors in 370 surgical cases. Acta Obstet Gynecol Scand 1976;55:261–6.
28 Paling MR, Shawker TH. Abdominal ultrasound in advanced ovarian carcinoma. J Clin Ultrasound 1981;9:435–41.
29 Samuels BI. Usefulness of ultrasound in patients with ovarian cancer. Semin Oncol 1975;2:229–33.
30 Schmidt W, Boos R, Leucht W, Kuhn W, Schmid H, Kaufmann M, et al. Zur Diagnostik von benignen und malignen Ovarialtumoren. Geburtshilfe Frauenheilkd 1985;45:840–7.
31 Wicks JD, Mettler FA Jr, Hilgers RD, Ampuero F. Correlation of ultrasound and pathologic findings in patients with epithelial carcinoma of the ovary. J Clin Ultrasound 1984;12:397–402.
32 Meire HB, Farrant P, Guha T. Distinction of benign from malignant ovarian cysts by ultrasound. Br J Obstet Gynaecol 1978;85:893–9.
33 Obwegeser R, Stumpflen I, Deutinger J, Bernaschek G. Zur echographischen Dignitätsbeurteilung von Adnextumoren. Geburtshilfe Frauenheilkd 1993;53:108–14.
34 Davies AP, Jacobs I, Woolas R, Fish A, Oram D. The adnexal mass: benign or malignant? Evaluation of a risk of malignancy index. Br J Obstet Gynaecol 1993;100: 927–31.
35 Finkler NJ, Benacerraf B, Lavin PT, Wojciechowski C, Knapp RC. Comparison of serum CA 125, clinical impression, and ultrasound in the preoperative evaluation of ovarian masses. Obstet Gynecol 1988;72:659–64.
36 Jacobs I, Oram D, Fairbanks J, Turner J, Frost C, Grudzinskas JG. A risk of malignancy index incorporating CA-125, ultrasound and menopausal status for the accurate preoperative diagnosis of ovarian cancer. Br J Obstet Gynaecol 1990;97:922–9.
37 Luxman D, Bergman A, Shi J, David MP. The postmenopausal mass: correlation between ultrasonic and pathologic findings. Obstet Gynecol 1991;77:726–8.
38 Schillinger H, Kliem M, Klosa W, Pohl J, Wilhelm C, Madjar H, et al. Dignitätsbeurteilung gynäkologischer Tumore durch einen sonographischen Tumor-Score unter besonderer Berücksichtigung des Ovarialkarzinoms. Arch Gynecol Obstet 1989;245:596–600.
39 Campbell S, Goessens L, Goswamy R, Whitehead MI. Real-time ultrasonography for determination of ovarian morphology and volume: a possible early screening test for ovarian cancer? Lancet 1982;i:425–6.
40 Goswamy RK, Campbell S, Whitehead MI. Screening for ovarian cancer. Clin Obstet Gynaecol 1983;10:621–43

Simple Ovarian Cysts

1

Fig. 9.1 Sharply circumscribed follicular cyst to the right of the uterus (*) (5 × 4 × 4 cm). The cyst is devoid of internal echoes and shows posterior acoustic enhancement. Transverse scan.

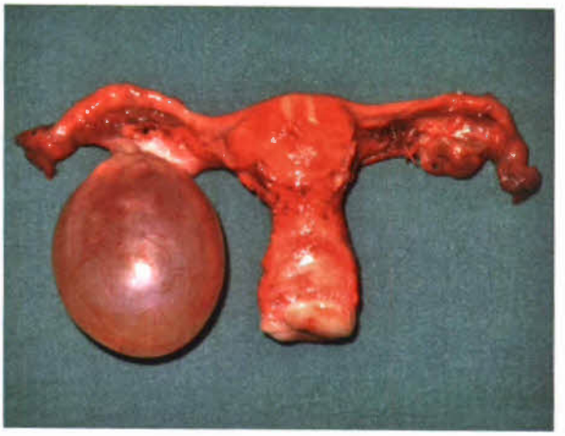

2

Fig. 9.2 Surgical specimen corresponding to Fig. 9.1.

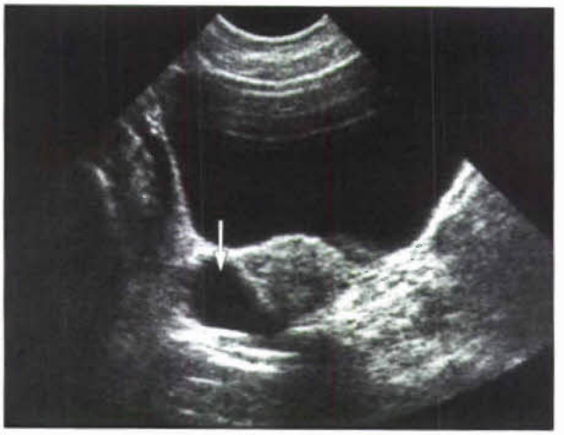

3

Fig. 9.3 Corpus luteum cyst of the right ovary (2.4 cm in diameter) with fine internal echoes (→). Transverse scan.

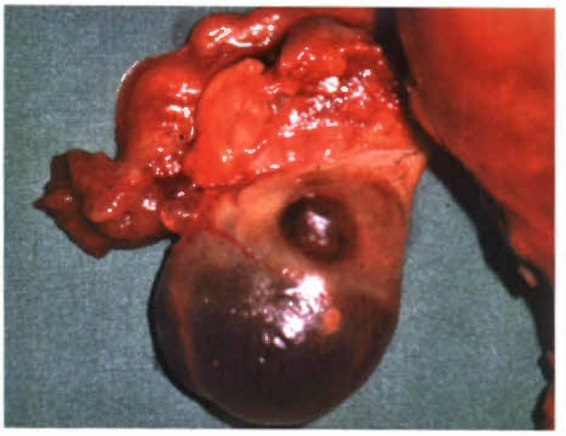

4

Fig. 9.4 Surgical specimen corresponding to Fig. 9.3.

5

Fig. 9.5 Elliptical, smooth-bordered paraovarian cyst (7.7 × 5.6 × 7.0 cm) located above the vaginal stump in a hysterectomized patient. The cyst contains fine, scattered internal echoes. Longitudinal scan.

6

Fig. 9.6 Corpus luteum cyst of the right ovary with smooth margins and irregular, high-level internal echoes (→). Transverse scan.

7

Fig. 9.7 Hemorrhagic corpus luteum cyst (1) (8.8 × 7.3 × 8.0 cm) in a patient receiving anticoagulant medication. The hematoma produces internal echoes of varying intensity. Longitudinal scan.
2 Urinary bladder.

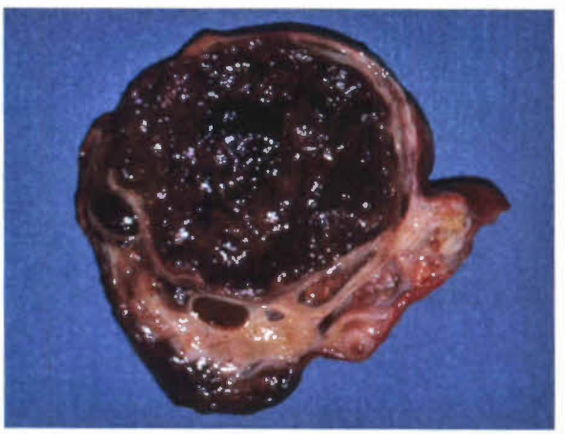

8

Fig. 9.8 Surgical specimen corresponding to Fig. 9.7.

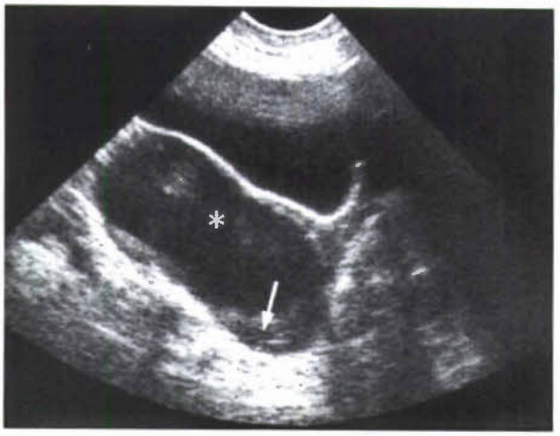

9

10

Fig. 9.**9** Oblong endometriotic cyst (11.2 × 6.4 × 8.4 cm) with diffuse internal echoes (*) and localized wall thickening (→). Longitudinal scan.

Fig. 9.**10** Surgical specimen corresponding to Fig. 9.**9**.

11

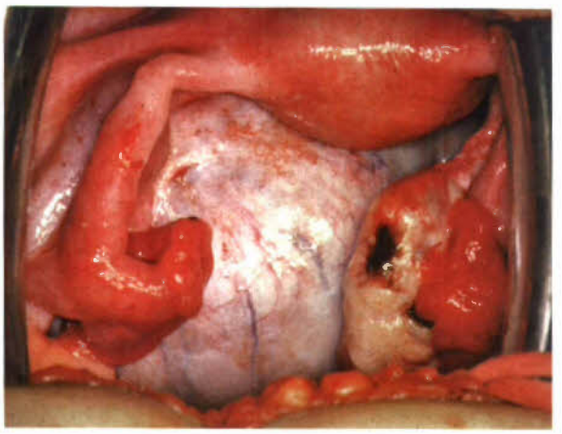

12

Fig. 9.**11** Endometriotic cyst of the left ovary (10 × 5.5 × 9.0 cm) extending into the cul-de-sac. Note the thick cyst wall and fine, diffuse internal echoes. Transverse scan.

Fig. 9.**12** The cyst in Fig. 9.**11**, viewed from the cranial aspect at operation.

13

14

Fig. 9.**13** Endometriotic cyst (6 cm in diameter) of the left ovary, with slightly irregular margins, diffuse internal echoes (*), and peripheral elements of higher echogenicity (→). Transverse scan.

Fig. 9.**14** This endometriotic cyst (7 × 5 × 6 cm) of the right ovary contains a large area of increased echogenicity (→).

15

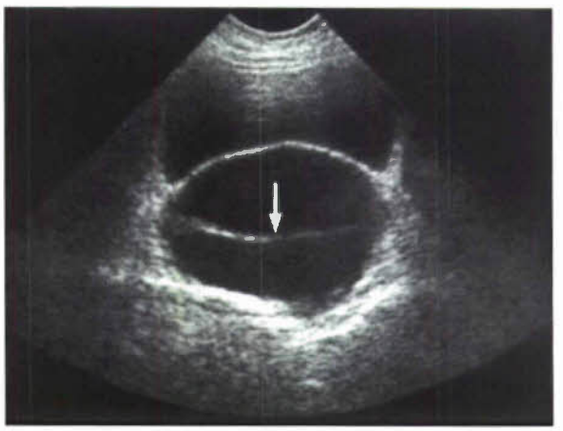

16

Fig. 9.**15** Endometriotic cyst (11.5 × 7.6 × 11.6 cm) located above the cervical stump in a hysterectomized patient. There is a conspicuous fluid level (→) with diffuse internal echoes in the posteroinferior portion of the cyst. Longitudinal scan.

Fig. 9.**16** Transverse scan of the endometriotic cyst in Fig. 9.**15**. The fluid level (→) mimics the appearance of a loculated cyst.

Dermoid Cysts

Fig. 9.**17** Dermoid cyst of the right ovary (7.0 × 3.8 × 4.0 cm), transverse scan. The sebaceous material forms a hyperechoic area in the lower part of the cystic mass, with an associated sebum–fluid level (→). An endometrial ring pattern is visible within the uterus.

17

Fig. 9.**18** Surgical specimen corresponding to Fig. 9.**17**. When cut open, the dermoid was found to contain sebum and hair.

18

Fig. 9.**19** Dermoid cyst of the right ovary (8 × 10 × 9 cm), transverse scan. In contrast to the cyst in Fig. 9.**17**, the echogenic sebaceous material is located in the upper portion of this dermoid cyst (→).

19

Fig. 9.**20** Surgical specimen corresponding to Fig. 9.**19**.

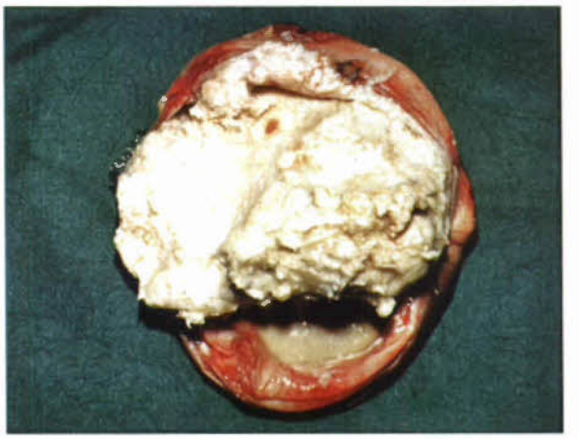

20

Fig. 9.**21** Dermoid cyst of the left ovary, containing a bizarrely shaped hyperechoic area at its center. The small uterus is displaced toward the right side (→). The echogenic area below the uterus is caused by bowel (*). Transverse scan.

21

Fig. 9.**22** Surgical specimen corresponding to Fig. 9.**21**. This dermoid contains sebum with bony plates, teeth, cartilage, and hair.

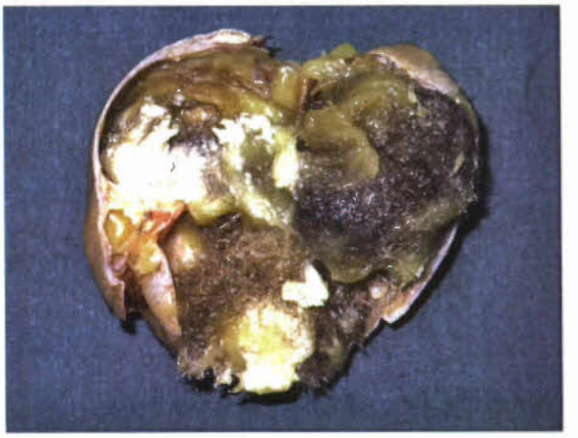

22

Fig. 9.**23** Dermoid cyst of the left ovary with an echogenic rim (↓) and a globular area of echogenic sebaceous material. Transverse scan.

23

Fig. 9.**24** Specimen corresponding to Fig. 9.**23** (measured in cm).

24

25

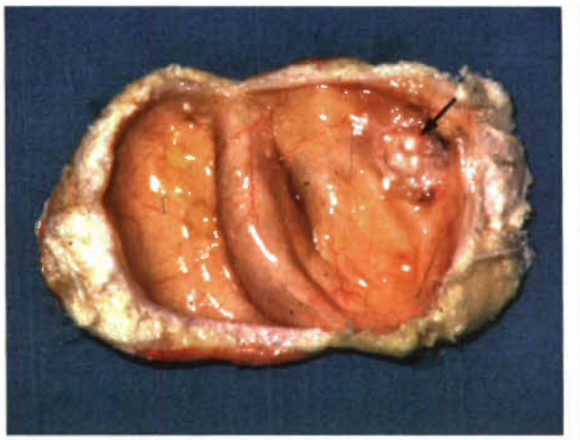

26

Fig. 9.**25** Dermoid cyst of the left ovary with a peripheral, echogenic crescent-shaped area and an echogenic rudimentary tooth (→). Transverse scan.

Fig. 9.**26** Surgical specimen corresponding to Fig. 9.**25**. Note the partially formed tooth (→).

27

28

Fig. 9.**27** This dermoid cyst of the right ovary contains a peripheral echogenic area. Transverse scan.

Fig. 9.**28** Predominantly solid-appearing dermoid of the left ovary (→) contains an echogenic area in its outer half. Transverse scan. This lesion might be mistaken for a loop of bowel (see Fig. 9.**52**).

29

Fig. 9.**29** Predominantly cystic-appearing dermoid of the left ovary (8 × 12 × 10 cm) with a small, central echogenic area. Transverse scan. The dermoid cyst completely fills the cul-de-sac.

30

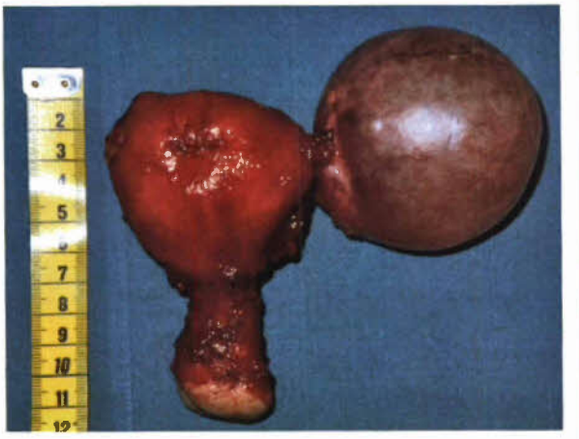

31

Serous Cystadenoma

Fig. 9.**30** Serous cystoma simplex of the left ovary (7 × 5.6 × 7 cm). Longitudinal scan. This lesion is indistinguishable on ultrasound from a simple retention cyst.

Fig. 9.**31** Surgical specimen corresponding to Fig. 9.**30**.

Fig. 9.**32** A large, unilocular serous cystoma of the left ovary extending into the upper abdomen. Longitudinal scan.
1 Urinary bladder
2 Uterus
3 Cystoma
4 Bowel

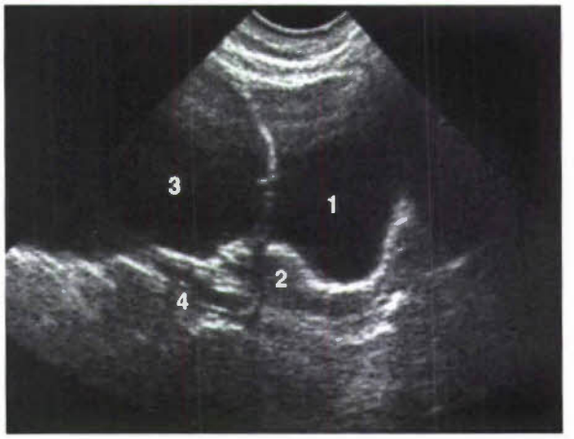

32

Fig. 9.**33** The same ovarian cystoma as in Fig. 9.**32**, displayed in a supraumbilical transverse scan.
1 Cystoma
2 Aorta
3 Vena cava
4 Spinal column

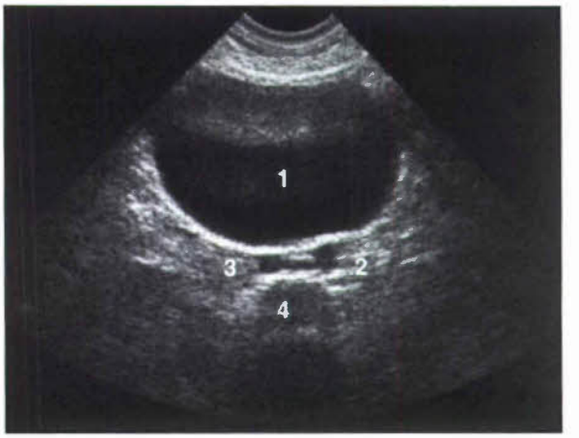

33

Fig. 9.**34** Giant serous cystoma of the right ovary (26 × 21.5 × 13.5 cm). Urinary bladder (*). Longitudinal scan with a 140° wide-angle transducer.

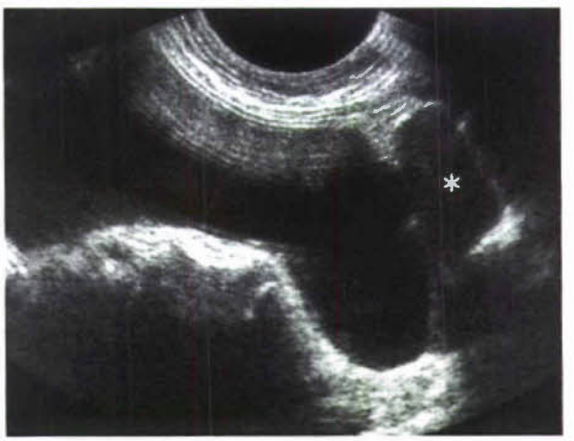

34

Fig. 9.**35** Intraoperative view of the tumor in Fig. 9.**34**.

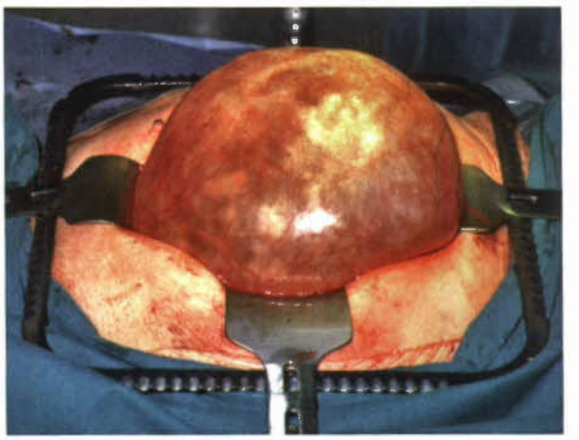

35

Fig. 9.**36** Giant follicular cyst of the right ovary (25 × 11 × 15 cm) in a 32-year-old woman. Longitudinal scan.
1 Urinary bladder
2 Uterus
3 Follicular cyst
4 Bowel

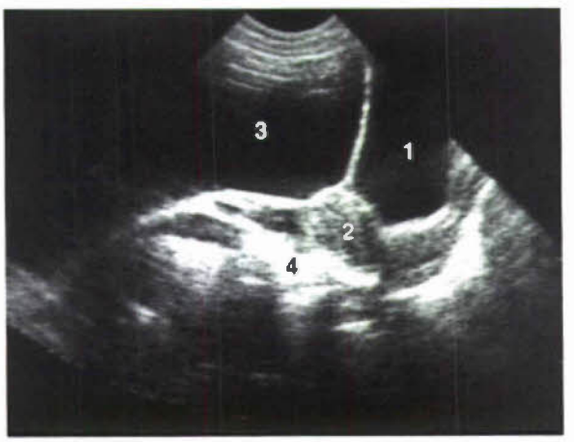

36

Fig. 9.**37** Overdistended bladder (17.6 × 13 × 15 cm) in a patient with a neurogenic bladder. Longitudinal scan. The bladder mimics the appearance of a large cystic mass in the lower abdomen. Note, however, the absence of a bladder caudal to the "mass."

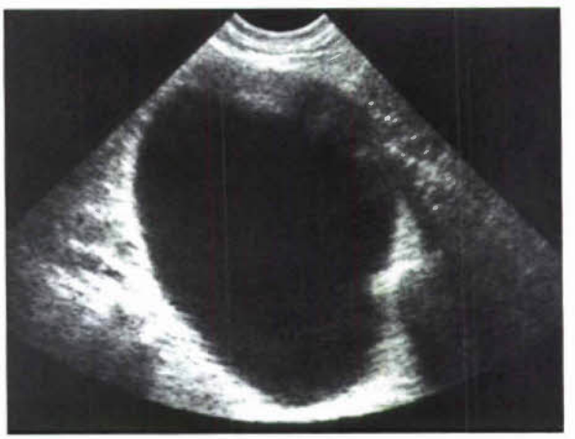

37

Fig. 9.**38** Transverse scan of the overdistended bladder in Fig. 9.**37**. Uterus (*).

38

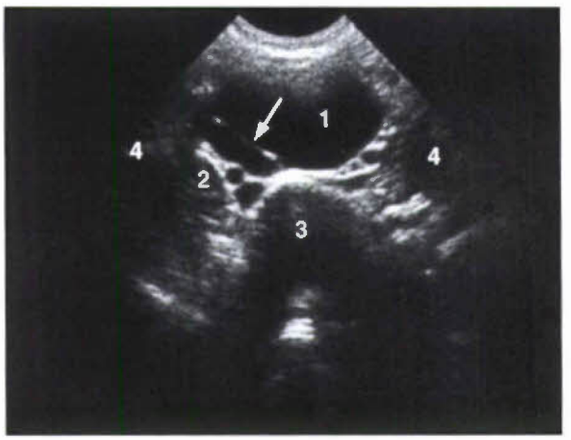

39

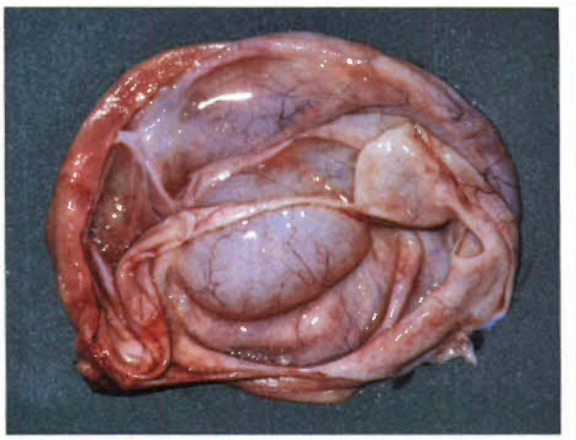

40

Fig. 9.**39** Loculated serous ovarian cystoma in the region of the lower lumbar spine. Transverse scan.
1 Cystoma with echogenic septum (→)
2 Common iliac vessels
3 Spinal column
4 Psoas muscle

Fig. 9.**40** Surgical specimen corresponding to Fig. 9.**39**.

Mucinous Cystadenoma

41

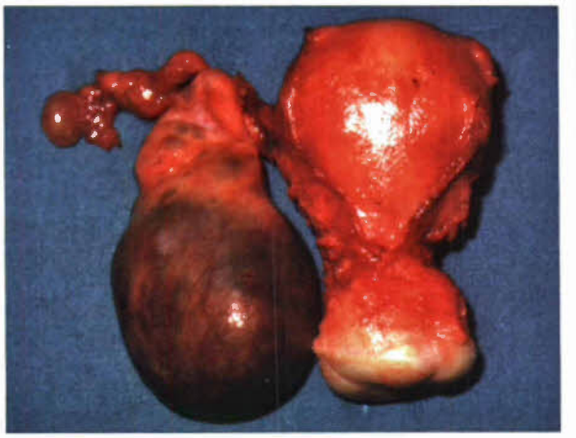

42

Fig. 9.**41** Mucinous cystadenoma (5.4 × 4.3 × 4.6 cm) in the cul-de-sac. Longitudinal scan.
1 Urinary bladder
2 Uterus
3 Cystoma

Fig. 9.**42** Surgical specimen corresponding to Fig. 9.**41**.

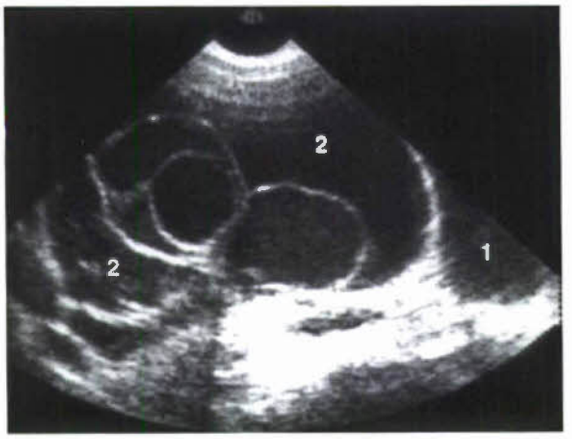

43

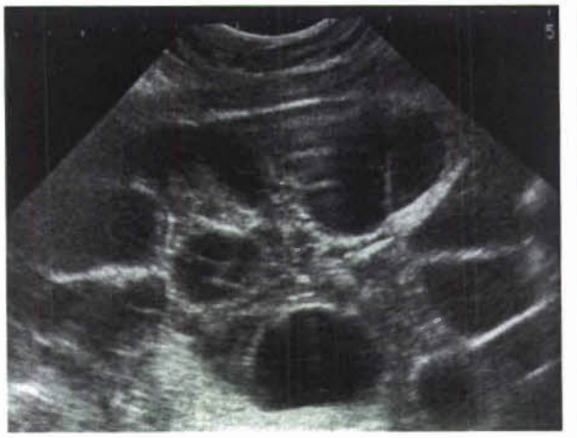

44

Fig. 9.**43** This giant, multilocular mucinous ovarian cystoma is filling the entire abdomen. Longitudinal scan. Note the varying echogenicity of the different compartments in the cystoma.
1 Urinary bladder
2 Ovarian cystoma

Fig. 9.**44** Giant, hyperstimulated right ovary (13.7 × 9.3 × 10.5 cm). Longitudinal scan.

45

Fig. 9.**45** Giant cystic right kidney extending into the true pelvis. Longitudinal scan.

Ovarian Fibroma

46

Fig. 9.**46** Left ovarian fibroma (9.0 × 5.6 × 6.5 cm). Transverse scan. The fibroma appears as a homogeneous, relatively hypoechoic solid mass displacing the small, atrophic uterus (→) toward the right side.

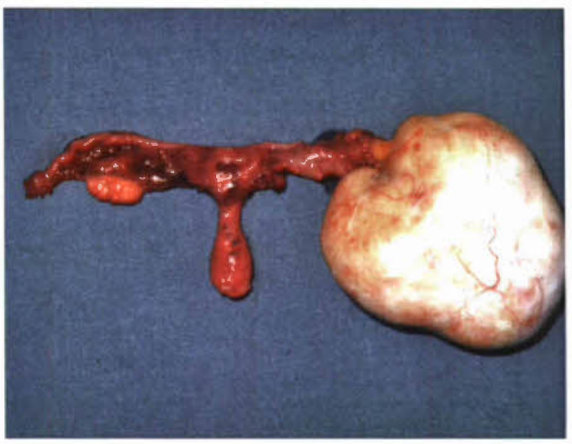

47

Fig. 9.**47** Surgical specimen corresponding to Fig. 9.**46**.

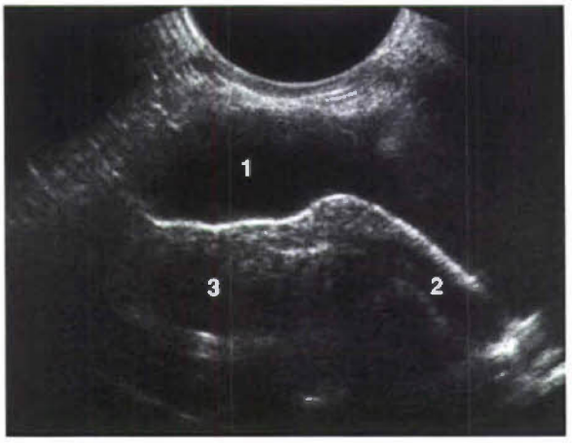

48

Fig. 9.**48** Left ovarian fibroma (22 × 13 × 11 cm). Longitudinal scan. The solid, oblong tumor is completely occupying the sacral hollow.
1 Urinary bladder
2 Uterus
3 Ovarian fibroma

49

Fig. 9.**49** Surgical specimen corresponding to Fig. 9.**48**.

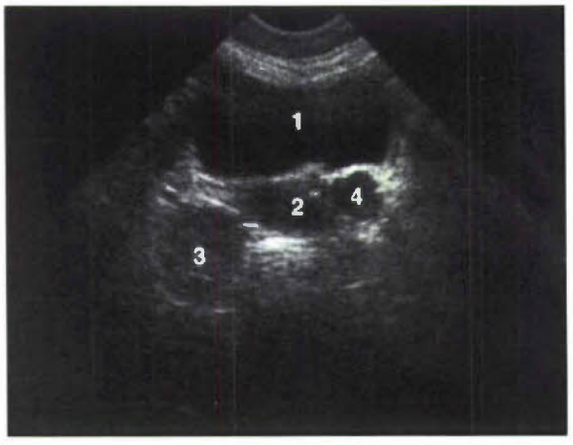

50

Fig. 9.**50** Bilateral, lobulated ovarian fibromas. Transverse scan.
1 Urinary bladder
2 Uterus
3 Right ovarian fibroma
4 Left ovarian fibroma

51

Fig. 9.**51** Surgical specimen corresponding to Fig. 9.**50**.

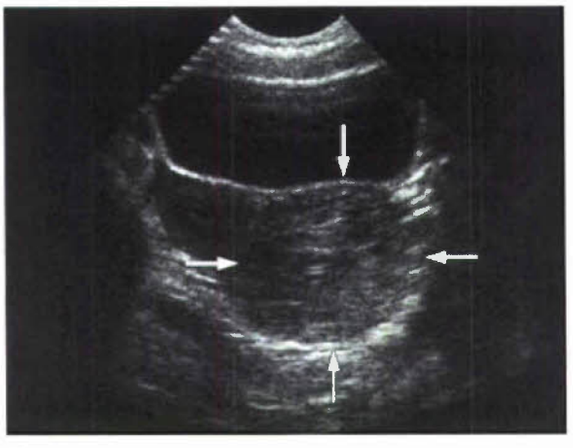

52

Fig. 9.**52** Distended bowel loop on the left side of the uterus (→). The bowel mimics an ovarian mass 7 cm in diameter. Transverse scan.

53

Fig. 9.**53** Left pelvic kidney in a patient with uterine aplasia (Rokitansky–Küster syndrome). The kidney occupies the normal uterine position, appearing as a solid, hypoechoic mass with a central echo complex (→). Longitudinal scan.

54

Fig. 9.**54** Adenofibroma with regressive changes (7.9 × 6.1 × 7.7 cm) on the right side of the uterus. Transverse scan. The tumor appears as a predominantly solid mass with isolated cystic areas.

Potentially Malignant Ovarian Tumors

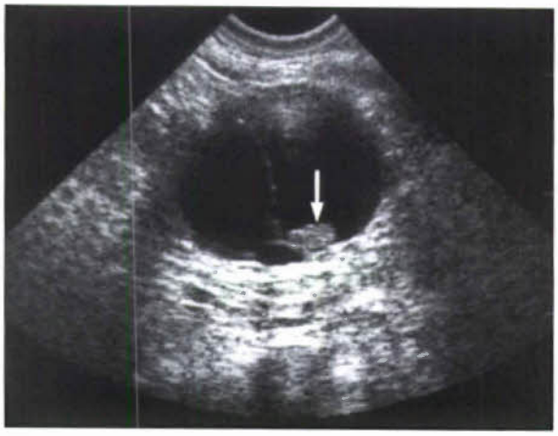

55

Fig. 9.**55** Proliferating serous papillary cystadenoma of the left ovary. A nodule composed of solid echogenic tissue (→) is visible within the loculated mass.

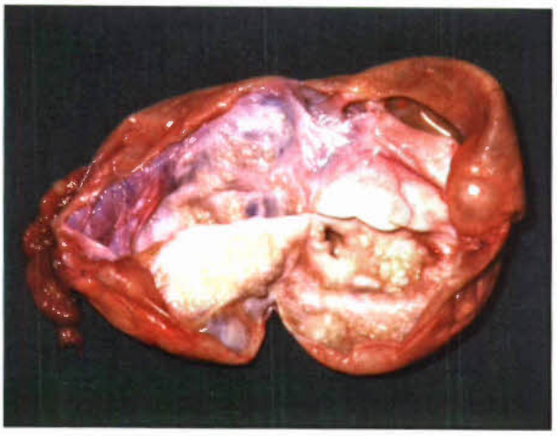

56

Fig. 9.**56** Surgical specimen corresponding to Fig. 9.**55**.

57

Fig. 9.**57** Proliferating papillary cystadenoma of the right ovary. Transverse scan. A peripheral, irregular echogenic area (→) is visible within the predominantly cystic mass.

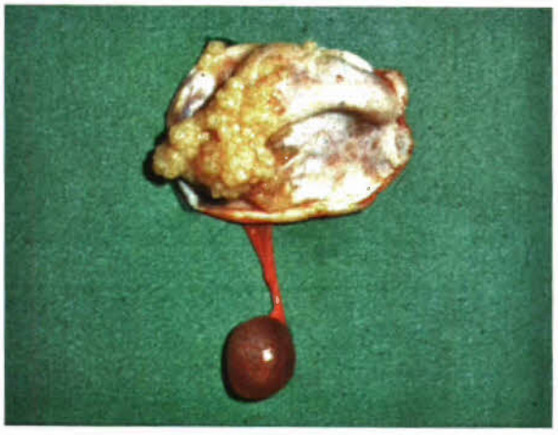

58

Fig. 9.**58** Surgical specimen corresponding to Fig. 9.**57**.

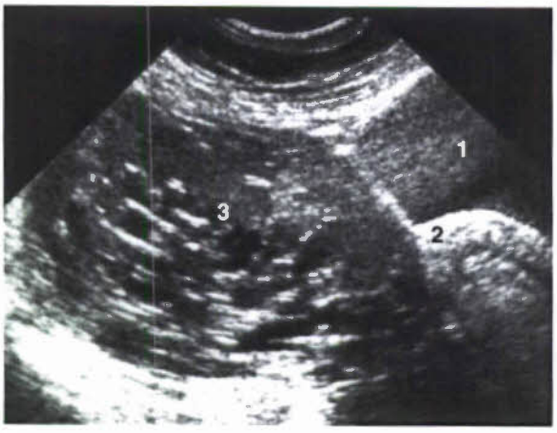

59

Fig. 9.**59** Mucinous cystoma (11.6 × 7.9 × 9.7 cm) with focal proliferation. The tumor has a generally nonhomogeneous appearance, with mixed solid and cystic areas. Longitudinal scan.
1 Urinary bladder
2 Uterus
3 Cystoma

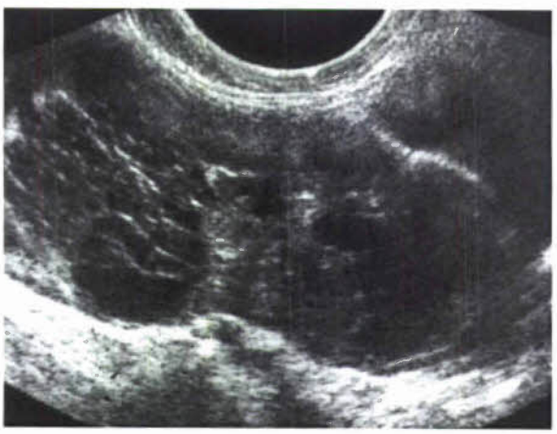

60

Fig. 9.**60** This large granulosa-cell tumor of the right ovary (22 × 18 × 12 cm) has a nonhomogeneous pattern, with a mixture of solid and cystic areas. Longitudinal scan with a 140° wide-angle transducer.

Fig. 9.**61** Theca-cell tumor of the left ovary (7 cm in diameter). Longitudinal scan in a patient who had undergone a previous hysterectomy. The tumor appears solid, with varying echogenicity.

Fig. 9.**62** Surgical specimen corresponding to Fig. 9.**61**.

61

62

Fig. 9.**63** Large (16.8 × 15 × 19.6 cm), solid, sharply demarcated Sertoli–Leydig cell tumor. Transverse scan. The tumor contains a mixture of hyperechoic and hypoechoic areas.

Fig. 9.**64** Longitudinal scan of the Sertoli–Leydig cell tumor in Fig. 9.**63**.

63

64

Malignant Ovarian Tumors

Fig. 9.**65** Serous adenopapillary ovarian carcinoma located directly above the uterus. Longitudinal scan. Solid, irregular structures are visible at the periphery of the predominantly cystic, echo-free mass.
1 Urinary bladder
2 Uterus
3 Carcinoma

Fig. 9.**66** Surgical specimen corresponding to Fig. 9.**65**.

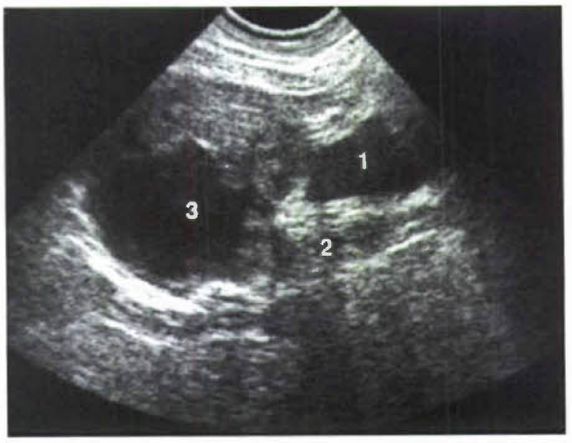

65

66

Fig. 9.**67** Adenoid ovarian carcinoma in the cul-de-sac. Longitudinal scan. Irregular echogenic structures are visible within the cystic mass.

Fig. 9.**68** Mixed cystic and solid adenocarcinoma of the right ovary (2) with irregular, echogenic proliferative foci (→). Transverse scan.
1 Uterus
2 Right ovary

67

68

69

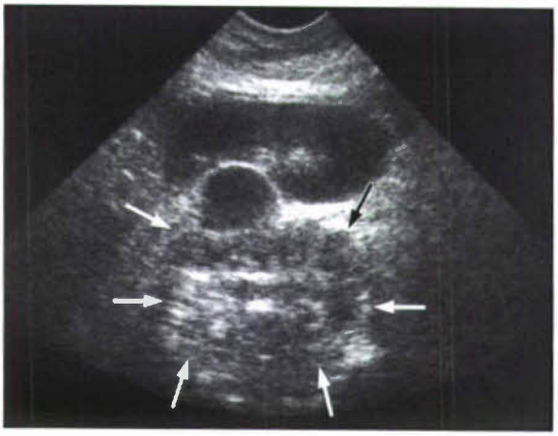

70

Fig. 9.**69** Adenopapillary carcinoma of the right ovary (6.0 × 6.6 × 4.8 cm) in a patient who had previously undergone a hysterectomy. Longitudinal scan. The bladder is indented by the tumor, which consists of mixed cystic and solid irregular components. The solid posterior part of the tumor is poorly delineated from the adjacent bowel.

Fig. 9.**70** Transverse scan of the tumor in Fig. 9.**69** defines the entire mass with its irregular internal echo pattern and indistinct margins (→).

71

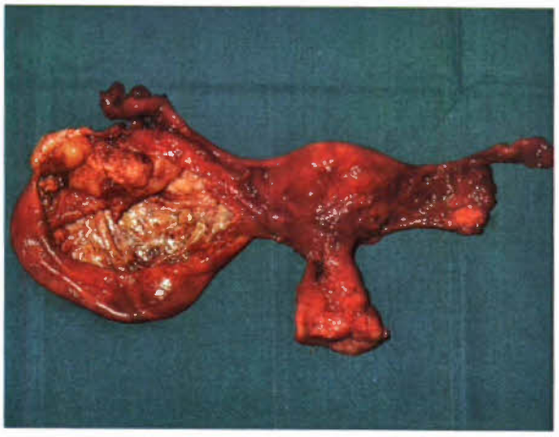

72

Fig. 9.**71** Clear-cell carcinoma of the right ovary. The longitudinal scan demonstrates irregular solid structures of high echogenicity within a cystic mass.

Fig. 9.**72** Surgical specimen corresponding to Fig. 9.**71**.

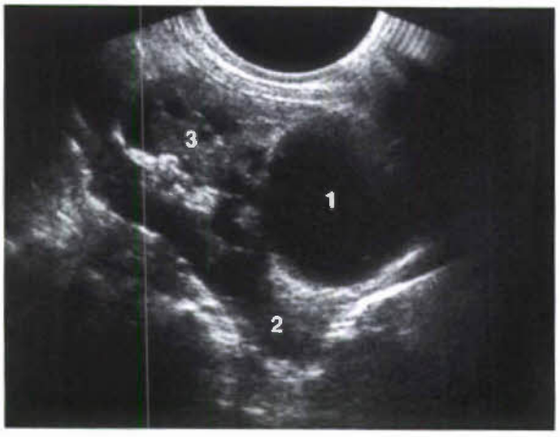

73

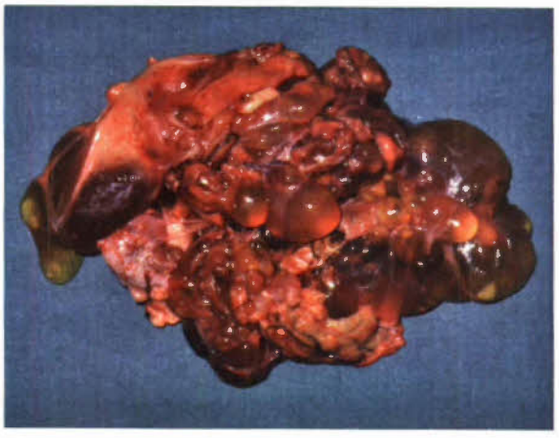

74

Fig. 9.**73** Undifferentiated ovarian carcinoma with irregular solid and cystic areas. Longitudinal scan with a 140° wide-angle transducer.
1 Urinary bladder
2 Section through uterus
3 Ovarian carcinoma

Fig. 9.**74** Surgical specimen corresponding to Fig. 9.**73**.

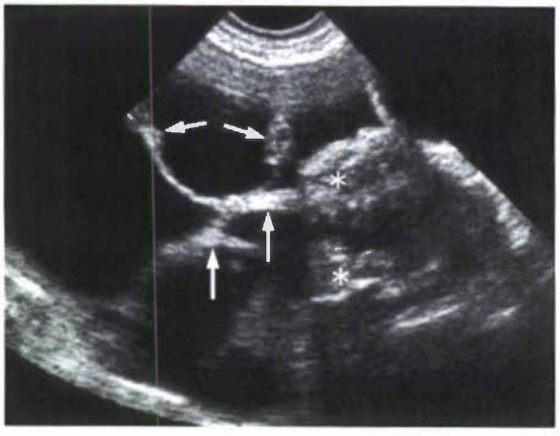

75

76

Fig. 9.**75** Large adenopapillary carcinoma of the right ovary (19 × 18 × 10 cm). Longitudinal scan. The broad septa (→) and the irregular, hyperechoic solid structures in the lower part of the tumor (*) should be noted.

Fig. 9.**76** Transverse scan of the ovarian carcinoma in Fig. 9.**75** with a 140° wide-angle transducer.

Fig. 9.**77** Intraoperative view of the tumor in Figs. 9.**75** and 9.**76**.

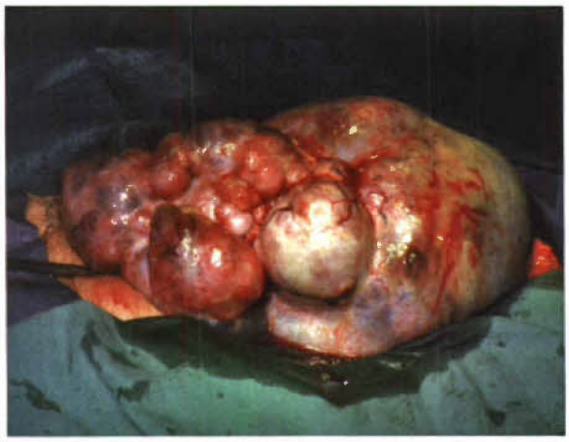

77

Fig. 9.**78** Large, cystic ovarian carcinoma. Longitudinal scan. Note the solid, irregular, hyperechoic proliferative area in the lower part of the tumor.

78

Fig. 9.**79** Papillary cystadenocarcinoma of the left ovary (7.5 × 7.0 × 4.0 cm). Transverse scan. Nodular outgrowths of low echogenicity (→) extend from the lateral border of the mass, which has a predominantly solid appearance.

79

Fig. 9.**80** Surgical specimen corresponding to Fig. 9.**79**.

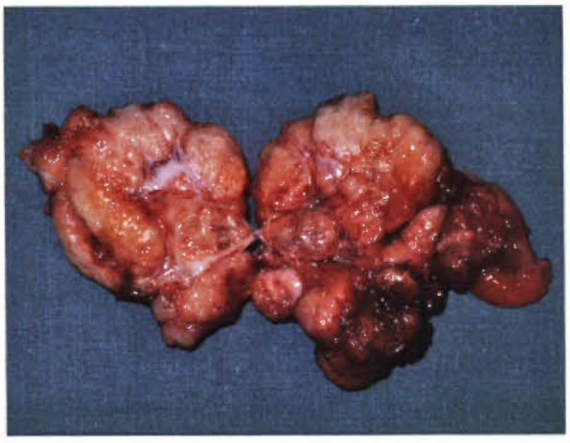

80

Fig. 9.**81** Cystadenopapillary ovarian carcinoma filling the cul-de-sac and encasing the uterus. Longitudinal scan. 1 Urinary bladder, 2 Vagina, 3 Uterus, 4 Tumor masses in the cul-de-sac, 5 Preuterine cystic tumor component, 6 Ascites

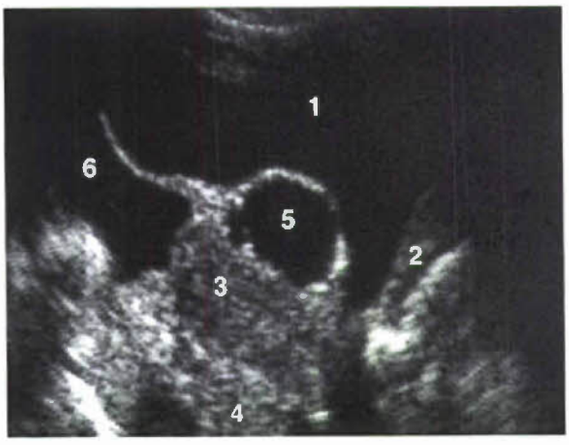

81

Fig. 9.**82** Extensive mucinous cystadenocarcinoma. Longitudinal scan. The tumor appears as a fluid-like mass filling the entire abdomen. Note the high-level punctate echoes inside the tumor. 1 Urinary bladder, 2 Carcinoma, 3 Bowel loops

82

Fig. 9.**83** Endometrioid sarcoma of the right ovary. Longitudinal scan.

83

Fig. 9.**84** Surgical specimen corresponding to Fig. 9.**83**.

84

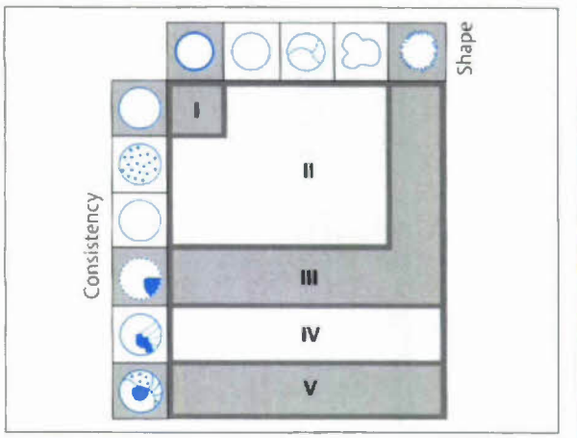

85

Fig. 9.**85** Scheme for grading ultrasound masses on the basis of their degree of homogeneity (after Schillinger et al. [38]).
I Clear, sharply circumscribed cysts
II Simple, loculated or lobulated masses, well delineated, with a uniformly cystic, doughy, or solid consistency
III Masses that have indistinct margins or include small areas with a different consistency
IV Masses that contain large areas with a different consistency
V Masses with a mixed consistency and bizarre structures

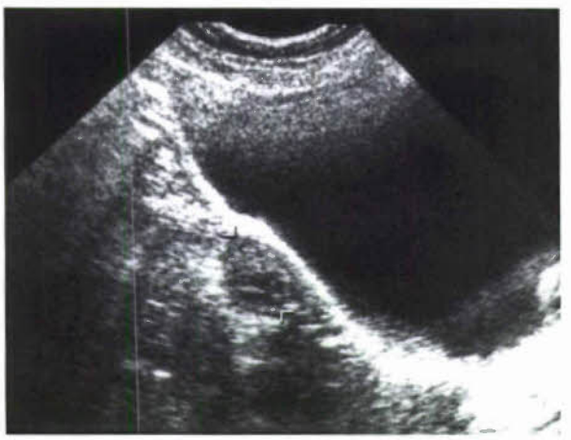

86

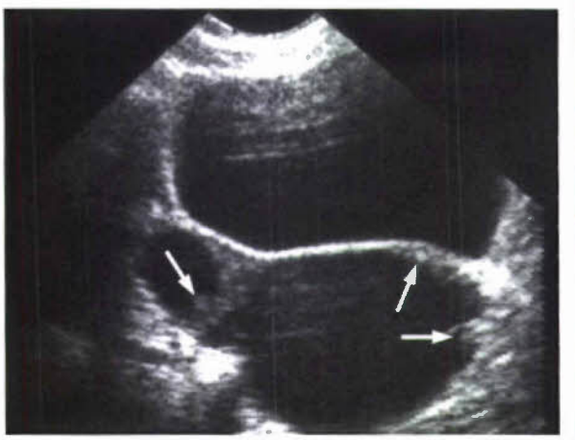

87

Fig. 9.**86** Small carcinoma of the left ovary in a 76-year-old woman (early stage). Longitudinal scan. A nonhomogeneous echo pattern is noted within the slightly enlarged ovary (3.8 × 2.8 × 1.8 cm).

Fig. 9.**87** Adenopapillary carcinomas of both ovaries, initially misinterpreted as endometriotic cysts. Transverse scan. Both tumors are predominantly cystic and contain small, solid mural projections (→).

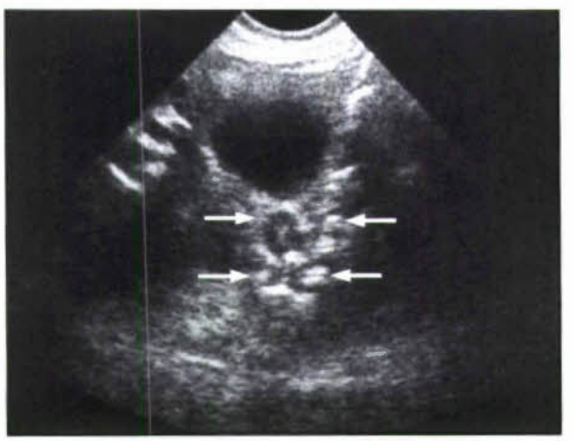

88

89

Fig. 9.**88** Sigmoid carcinoma. The transverse scan above the uterus shows an irregular, echogenic, oblong retrovesical mass (→).

Fig. 9.**89** Papillary carcinoma of the bladder. Longitudinal scan. An irregular, echogenic, nodular tumor structure is visible within the bladder.

90

91

Fig. 9.**90** Mixed cystic and solid tumor of the right ovary (10.0 × 7.4 × 7.6 cm), with predominantly smooth margins. Longitudinal scan. The tumor was metastatic to the ovary from a sigmoid carcinoma.

Fig. 9.**91** Transverse pelvic scan. A distended bowel loop (→) mimics an irregular tumor of the right ovary.

10 Tubal Masses

The normal fallopian tubes are not visualized by abdominal ultrasound, but pathologic changes that cause tubal distension [1,2] can be clearly recognized.

Benign Tubal Masses

It is extremely rare for true benign tumors such as *leiomyomas*, *hemangiomas*, *fibromas*, and *lymphangiomas* to occur in the fallopian tubes. Tubal distension is usually the result of an inflammatory or postinflammatory process (*pyosalpinx*, *hydrosalpinx*), and a small number of cases may be caused by endometriosis (*hematosalpinx*). The diagnosis of inflammatory and postinflammatory masses was reviewed in Chapter 6. The differential diagnosis should always include ectopic pregnancy in women of childbearing age.

Tubal Carcinoma

Malignant lesions of the fallopian tubes such as tubal carcinoma are rarely observed. Most tubal malignancies are unilateral and, like ovarian cancer, are diagnosed too late. A tubal carcinoma should be suspected when ultrasound demonstrates a well-defined ovary with an adjacent mass that contains irregular internal echoes.

Figure 10.**1** illustrates a carcinoma of the left fallopian tube. Note that the tube is markedly distended by echogenic tumor tissue. This lesion is difficult to distinguish sonographically from a distended loop of bowel. The suspicion of tubal carcinoma is reinforced when a repeat scan demonstrates the same lesion next to a normal-size ovary.

The late stage of tubal carcinoma is characterized by marked, irregular tubal distension accompanied by ascites in the true pelvis (Chapter 29).

References

1 Bulas DI, Ahlstrom PA, Sivit CJ, Blask ARN, O'Donell RM. Pelvic inflammatory disease in the adolescent: comparison of transabdominal and transvaginal sonographic evaluation. Radiology 1992;183:435–9.
2 Timor-Tritsch IE, Rottem S. Ultrasonographic study of the fallopian tube. Obstet Gynecol 1987;70:424–8.

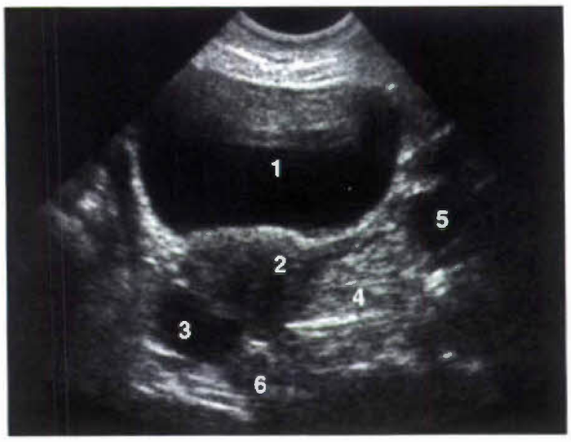

1

Fig. 10.**1** Carcinoma of the left fallopian tube with right-sided hydrosalpinx. Transverse scan. The left tube is distended by irregular, echogenic tumor masses.
1 Urinary bladder
2 Uterus
3 Hydrosalpinx in right tube
4 Carcinoma in left tube
5 Left ovary
6 Bowel

11 Secondary Changes Associated with Gynecologic Tumors

In every ultrasound evaluation of a pelvic mass, the examiner should look for secondary tumor changes such as ascites, urinary tract obstruction, lymph-node metastases, and hepatic metastases. *Ascites* appears at ultrasound as an echo-free area between the abdominal wall, bowel loops, and liver (Figs. 11.**1**–11.**4**) [1]. If there is already peritoneal carcinomatosis with adhesions on the bowel wall, ultrasound can demonstrate the standing, fixed bowel loops within the ascites (Fig. 11.**4**). A loculated form of ascites may also form, in contrast to the benign ascites of hepatic cirrhosis, which flows freely around the bowel loops [2]. Hemorrhagic ascites is distinguished by the presence of fine, diffuse echoes within the fluid collection [2].

If the greater omentum is involved by carcinoma to a sufficient degree, it may appear within the ascites as an irregular, echogenic plaque below the abdominal wall (Figs. 11.**5**, 11.**6**). *Peritoneal* and *lymph-node metastases* (Fig. 11.**7**) can be detected sonographically when they are sufficiently large [3,4], although they may be obscured by overlying bowel gas. Here, as in the detection of bowel-wall infiltration, computed tomography and radiographic contrast studies of the colon appear to be more suitable [5–7], although small peritoneal and lymph-node metastases may be missed even on CT scans [8]. *Abdominal wall metastases* (Fig. 11.**8**) can usually be detected only when the abdomen is scanned through a water path.

In patients with advanced ovarian or uterine carcinoma, it is not unusual to find *hepatic metastasis* at the time of diagnosis. These lesions may show high or low echogenicity when scanned. *Hypoechoic metastases* are most often seen in association with ovarian or uterine malignancies or breast cancer (Fig. 11.**9**), whereas *hyperechoic metastases* are more common with cancers of the gastrointestinal tract or breast (Fig. 11.**10**) [9]. Occasionally, cystic hepatic metastases are found in association with ovarian carcinoma, as well as carcinoma of the uterine cervix or corpus [10].

Urinary tract obstruction by a gynecologic malignancy can occur when the tumor encases the ureters. This may involve the parametrial region, as with a cervical carcinoma, or may occur at a higher level in the retroperitoneum (Figs. 11.**11**, 11.**12**)

References

1 Elling D, Kobs K. Erfahrungen bei der Anwendung des Ultraschall-B-Bildverfahrens zur Exploration des kleinen Beckens. Zentralbl Gynäkol 1981;103:1129–41.
2 Kratochwil A. Ultraschalldiagnostik in der Gynäkologie. Gynäkologe 1976;9:166–80.
3 Requard CK, Mettler FA, Wicks JD. Preoperative sonography of malignant ovarian neoplasm. AJR Am J Roentgenol 1982;137:79–82.
4 Wicks JD, Mettler FA Jr, Hilgers RD, Ampuero F. Correlation of ultrasound and pathologic findings in patients with epithelial carcinoma of the ovary. J Clin Ultrasound 1984;12:397–402.
5 Johnson RJ, Blackledge G, Eddleston B, Crowther D. Abdominopelvic computed tomography in the management of ovarian carcinoma. Radiology 1983;146:447–52.
6 Walsh JW, Rosenfield AT, Jaffe CC. Prospective comparison of ultrasound and CT in the evaluation of gynecologic pelvic masses. AJR Am J Roentgenol 1978;131:955–60.
7 Walsh JW, Amendola MA, Konerding KF, Tisando J, Hazra TA. Computed tomographic detection of pelvic and inguinal lymph node metastases from primary and recurrent pelvic malignant disease. Radiology 1980;137:157–66.
8 Sanders RC, McNeil BJ, Finberg HJ, Hessel SJ, Siegelmann SS, Adams DF, et al. A prospective study of computed tomography and ultrasound in the detection and staging of pelvic masses. Radiology 1983;146:439–42.
9 Fleischer AC, Walsh JW, Jones HW, Shaff MI, James AE. Sonographic evaluation of pelvic masses. Radiol Clin North Am 1982;20:397–412.
10 Scheible W, Gosink BB, Leopold GR. Gray scale echographic patterns of hepatic metastatic disease. AJR Am J Roentgenol 1977;129:983–7.

1

Fig. 11.1 Massive ascites secondary to ovarian carcinoma. Longitudinal scan. * Uterus.

2

Fig. 11.2 Massive ascites associated with a carcinoma of the left ovary. Transverse scan.
1 Uterine corpus
2 Right round ligament

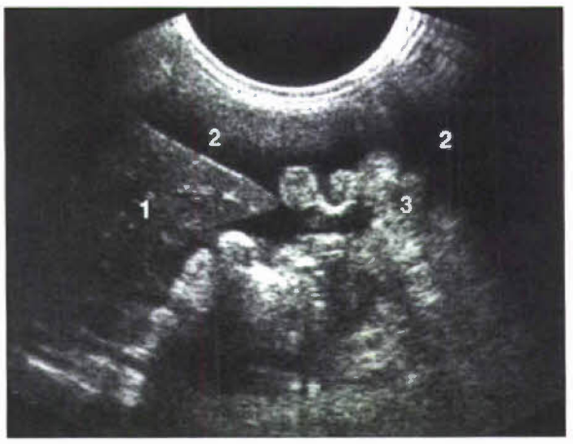

3

Fig. 11.3 Ascites in a patient with metastatic ovarian carcinoma. Longitudinal scan with a 140° wide-angle transducer.
1 Liver
2 Ascites
3 Bowel loops

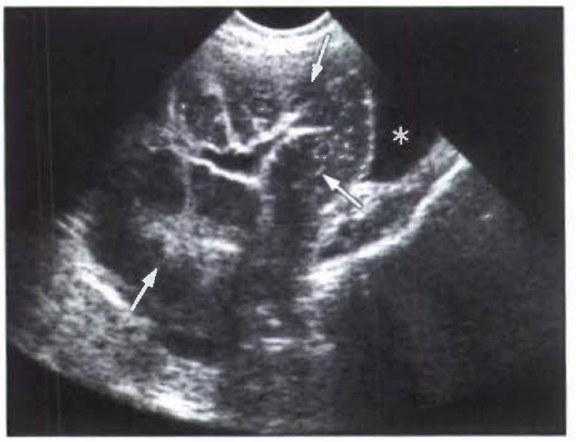

4

Fig. 11.4 Peritoneal carcinomatosis with standing bowel loops (→) within the ascites (*). Longitudinal scan.

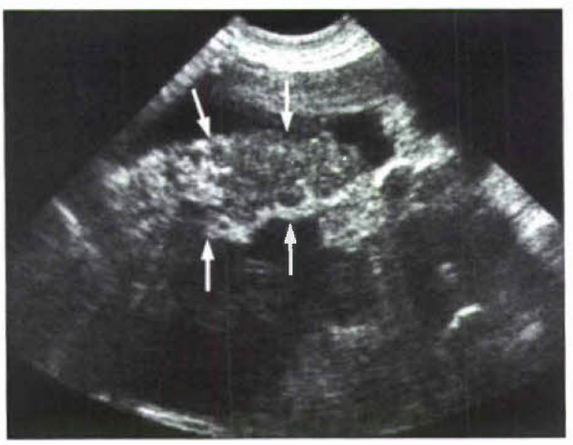

5

Fig. 11.5 Involvement of the greater omentum by ovarian carcinoma. Transverse scan. The greater omentum appears within the ascites as a partly echogenic, partly hypoechoic plaque with an irregular echo pattern (→).

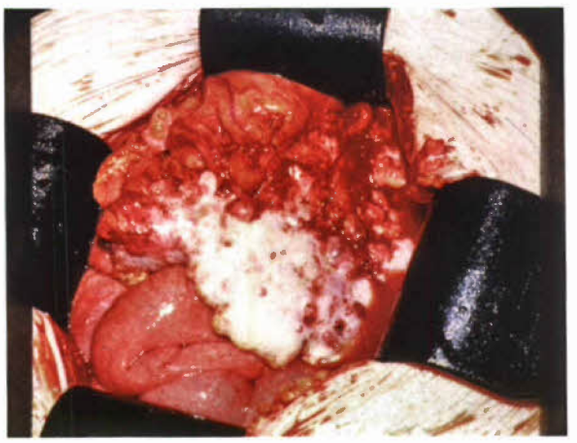

6

Fig. 11.6 Intraoperative view of the omentum in Fig. 11.5.

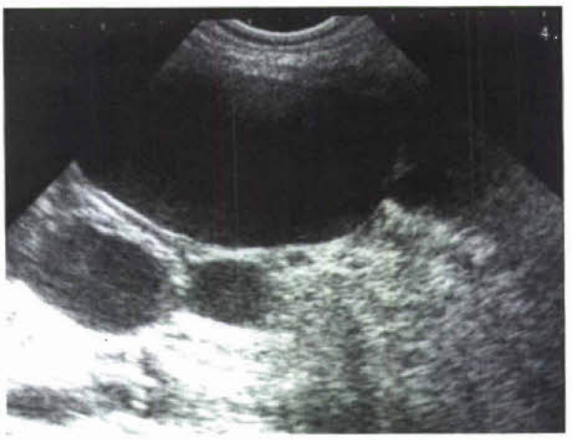

7

Fig. 11.7 Markedly enlarged retroperitoneal lymph nodes (4.5 × 3.3 cm and 3.1 × 2.2 cm) involved by ovarian carcinoma. Longitudinal scan.

8

Fig. 11.8 Hypoechoic abdominal wall metastases from an ovarian carcinoma (7.1 × 3.8 × 3.7 cm). Transverse scan. Because of its subcutaneous location, the involved area was scanned through a water path.

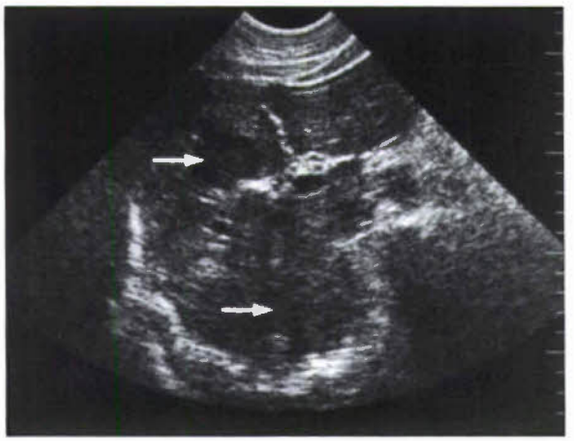

9

10

Fig. 11.9 Hypoechoic hepatic metastases (→) from breast carcinoma. Transverse scan.

Fig. 11.10 Echogenic metastasis in the right lobe of the liver (→) from breast carcinoma, 3 cm in diameter. Transverse scan.

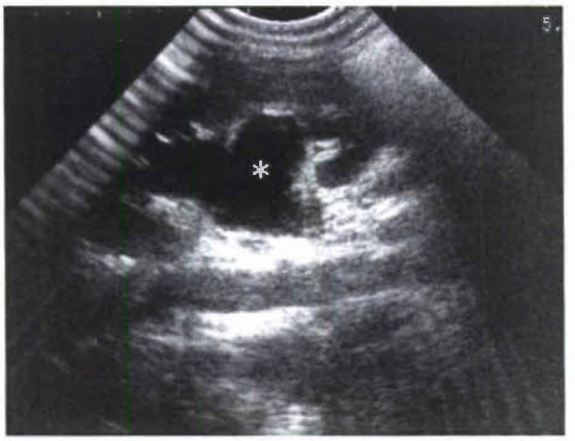

11

12

Fig. 11.11 Dilation of the right renal pelvis (*) due to a retroperitoneal urinary tract obstruction caused by a pelvic-wall recurrence of cervical carcinoma. Longitudinal scan.

Fig. 11.12 Dilation of the renal pelvis (*) and ureter (> <) due to a distal obstruction in the left parametrial region caused by cervical carcinoma invading the left parametrium.

12 Ultrasound Abnormalities in the Mid- and Upper Abdomen

Although ultrasound evaluation of the mid- and upper abdomen is outside the scope of gynecology, there may well be a rationale for the gynecologist to scan these regions after excluding a gynecologic cause for the patient's symptoms. If a mid- or upper abdominal cause is detected, the patient can then be referred for further evaluation by an internist or urologist.

Especially in the follow-up of primary gynecologic tumors, the gynecologist should be able to detect secondary changes—such as ascites, urinary stasis, and hepatic metastases—that will be instrumental in directing further management. The gynecologist investigating abdominal pain may also encounter conditions such as nephrolithiasis, cholecystolithiasis, and inflammatory bowel changes, and ileus may well be encountered in the postoperative patient. Also, it is relatively common for uterine anomalies to coexist with urinary tract anomalies such as renal agenesis and pelvic kidney. Thus, there will always be a borderline area in which the diagnostic services of different disciplines overlap.

The goal of this chapter is to review the abnormalities that the gynecologist is most likely to encounter in ultrasound scans of the abdomen.

Urinary Tract

Examination Technique

No special preparations are necessary for ultrasound scanning of the kidneys. The examination is usually performed in the supine patient, although lateral decubitus may be more favorable in an obese patient. Examination in full inspiration is helpful, as it moves the kidneys to a lower position that is more easily accessible to scanning.

Multiple longitudinal and transverse flank scans should be obtained through the kidney in order to detect any renal abnormalities (Figs. 12.**1**, 12.**2**).

The normal kidneys in an adult woman measure an average of 12 cm in length by 6 cm in width [1]. In an anatomically normal kidney (Fig. 12.**3**), the hypoechoic parenchyma at the periphery of the organ will contrast with a bright central echo complex produced by the pyelocaliceal system and hilar fatty tissue [2–4] (Fig. 12.**4**). The medullary pyramids appear as hypoechoic zones.

A nonampullary type of renal pelvis usually appears as a closed structure at ultrasound. If there is separation of the central echo complex, the renal pelvis is still considered normal up to an overall width of 1.5 cm [5].

Hydronephrosis

Hydronephrosis is diagnosed when the central collecting system of the kidney is dilated to more than 1.5 cm (Fig. 12.**5**). Three grades of severity are distinguished, depending on the degree of dilation (Table 12.**1**).

Urinary tract obstructions are referred to relative to their location, as prevesical (supravesical), vesical, or subvesical. Most *acquired urinary tract obstructions* in women are *supravesical* (stone, stricture, tumor); *vesical obstructions* (neurogenic bladder, radiogenic small bladder) and *subvesical obstructions* (radiogenic or posttraumatic urethral stricture) are much less common.

Table 12.**1** Grading of hydronephrosis (adapted from Swobodnik [5])

Severity	Sonographically detectable changes
Grade I	Central dilation of the renal pelvis to more than 1.5 cm
Grade II	Central dilation of the renal pelvis and calices to more than 1.5 cm
Grade III	Central dilation of the renal pelvis and calices to more than 1.5 cm plus thinning of the renal parenchyma (to < 1 cm)

Table 12.**2** Differential diagnosis of unilateral and bilateral hydronephrosis

Unilateral hydronephrosis	Bilateral hydronephrosis
• Ureteral stone	• Carcinoma of the uterine cervix or corpus with parametrial involvement
• Ureteral stricture (radiogenic, postoperative adhesion)	• Ovarian carcinoma
• Postoperative hematoma or postoperative lymph cyst	• Ormond disease (retroperitoneal fibrosis)
• Pelvic wall recurrence of a gynecologic tumor	

Various causes of the obstruction should be considered in the differential diagnosis, depending on whether the hydronephrosis is *unilateral* or *bilateral* (Table 12.**2**).

If ureteral dilation is present (Fig. 12.**5**), the cause of the obstruction must lie distal to the ureteropelvic junction.

Nephrolithiasis, Ureteral Stones

Kidney stones are a common incidental finding in ultrasound examinations of the upper abdomen [6,7]. At the same time, ultrasound is used selectively in patients with renal colic to locate the causative stone [2]. While stones in the renal pelvis and calices can be detected by their high echogenicity and their associated acoustic shadow (Fig. 12.**6**), it is virtually impossible to define a ureteral stone with ultrasound, although the presence of the stone may be suspected on the basis of urinary stasis.

Renal Masses

Many circumscribed renal masses that are detected sonographically are *simple renal cysts* (Figs. 12.**7**, 12.**8**). They appear as round, echo-free masses with smooth margins, thin walls, and posterior acoustic enhancement. Simple renal cysts may be solitary or multiple, unilateral or bilateral [8]. They are classified by their location as *pararenal*, *cortical*, or *parapelvic*. Cortical cysts are the most common "incidental" renal finding at ultrasound [4]. Approximately 36% of sonographically detectable renal cysts are not identified on urography [8], as they do not distort the renal pelvis or cause caliceal elongation. As a general rule, simple cortical renal cysts are harmless. *Polycystic kidneys* is an autosomal-recessive disease that affects both kidneys [9] (Fig. 12.**9**). In more severe cases, the cystic transformation causes the kidneys to become greatly enlarged and extend into the pelvis, where they may be mistaken for a cystic ovarian mass when imaged by transvaginal ultra-

Table 12.3 Benign and malignant renal tumors (after Schwerk [4])

Benign renal tumors	Malignant renal tumors
• Adenoma, lipoma, fibroma, leiomyoma, hemangioma, hamartoma	• Renal-cell carcinoma (hypernephroma, adenocarcinoma)
• Mixed tumors: angiomyolipoma	• Sarcoma, lymphoma
• Xanthogranulomatous pyelonephritis	• Metastases
	• Carcinoma of the renal pelvis

sound. *Solid renal masses* may represent benign or malignant tumors (Table 12.3).

Unlike cystic renal masses, solid tumors have conspicuous internal echoes, smooth or scalloped margins, and show little or no posterior acoustic enhancement [4]. The most common renal malignancy is renal-cell carcinoma (Fig. 12.**10**). A tumor with infiltrating margins can be difficult to delineate from its surroundings. The incidence of bilateral involvement is estimated at 1.5–4.7% [10,11]. The most common source of *secondary renal malignancies (metastases)* is *breast cancer*, which accounts for 24.5% of cases. Other renal metastases may be caused by primary tumors of the lung (24%), intestinal tract (10.5%), contralateral kidney (7.6%), stomach (6.6%), ovaries (3%), or other organs (22.8%).

Shrunken Kidneys, Renal Hypoplasia, Renal Agenesis

A *shrunken kidney* is a small kidney with a longitudinal diameter of <10 cm and a transverse diameter of <5 cm. The loss of renal parenchyma may have a vascular etiology (atherosclerosis, renal infarction) or a postinflammatory etiology (pyelonephritis, glomerulonephritis) [2].

Differentiation is required from *congenital renal hypoplasia*. *Unilateral renal aplasia* or *agenesis* presents sonographically with an empty renal fossa and has a high association with genital anomalies such as those seen in Rokitansky–Küster syndrome (Chapter 24).

Liver and Gallbladder

Examination Technique

The liver, like the kidneys, can be scanned without special preparation, but optimum evaluation of the gallbladder and extrahepatic bile ducts requires a fasted patient [12].

The liver is examined with the patient in the supine position or a slight left lateral decubitus position. Deep inspiration moves the liver to a lower position and facilitates the examination. The liver is scanned:

- In longitudinal planes
- Through the intercostal spaces
- In subcostal planes using various respiratory positions and transducer angles
- At special scanning angles based on specific findings [13] (Figs. 12.**11**–12.**13**)

Ultrasound Abnormalities of the Liver and Gallbladder

Ultrasound examination of the liver is particularly important in the follow-up of oncologic patients. Many tumors metastasize to the liver. From a gynecologic standpoint, the most important of these tumors are breast carcinoma and ovarian carcinoma.

The sonographic detection of circumscribed hepatic metastases depends on their size, their location, and their echogenicity in relation to the liver parenchyma. *Focal metastases* appear as architectural defects that may be hypoechoic, hyperechoic, or isoechoic to the surrounding liver tissue. They may have a homogeneous or nonhomogeneous echo pattern, and they may exhibit central necrosis (bull's-eye pattern) or a hypoechoic rim (target pattern, Fig. 12.**14**) [13–15]. In addition to direct visualization of metastases, there may be indirect sonographic liver changes that suggest the presence of hepatic metastases. These include the displacement or compression of vessels or bile ducts and changes in the surface contours of the liver. Markedly enlarged lymph nodes about the porta hepatis can also be a sign of hepatogenic metastasis (Fig. 12.**15**).

The sonographic appearance of hepatic metastases is not a reliable criterion for identifying the primary tumor [16]. Both breast carcinoma and ovarian carcinoma may give rise to hyperechoic or hypoechoic hepatic metastases, or even cyst-like lesions [13,16,17]. With metastatic ovarian carcinoma, concomitant ascites can usually be detected within the abdominal cavity (Fig. 12.**16**).

In contrast to focal metastases, *diffuse hepatic metastasis* is characterized by a patchy, nonhomogeneous, mottled appearance of the hepatic parenchyma [13] (Fig. 12.**16**).

Simple, smooth-walled hepatic cysts are harmless lesions that are easy to distinguish from metastases. Irregular benign cystic changes may complicate the differential diagnosis, however (Figs. 12.**17**, 12.**18**). They cannot always be definitively interpreted and may warrant further investigation by CT or fine-needle aspiration biopsy [18].

In patients with unexplained abdominal complaints, it is necessary to exclude *cholecystolithiasis* in addition to gynecologic and urologic disease. In most cases, a solitary gallstone of sufficient size can be clearly visualized within the gallbladder (Fig. 12.**19**). It produces a bright "stone echo" within the normally echo-free bile and may cast a distal acoustic shadow, depending on the degree of reflectivity and absorption [12]. Small stones may not cast an acoustic shadow. Ductal stones are much more difficult to define with ultrasound, and some cannot be visualized.

Ultrasound in *chronic cholecystitis* shows definite thickening of the gallbladder wall. Generalized calcification of the gallbladder wall results in a *porcelain gallbladder* (Fig. 12.**20**), which has a high potential for malignant transformation [19].

Spleen

As with the kidneys and liver, no special preparations are necessary for ultrasound examination of the spleen. The patient can be scanned in the supine or right semilateral position. Imaging conditions can be improved by having the patient extend the left arm above the head, as this stretches the flank region and opens up the intercostal spaces [20]. The normal spleen is approximately 10 cm long, 7 cm wide, and 5 cm thick [21]. The spleen is considered enlarged if it measures more than 11 cm in length and 5 cm in thickness [20] (Fig. 12.**21**). *Splenomegaly* is most commonly found in association with hematologic systemic diseases and infectious diseases.

Intestinal Tract

A gynecologist investigating the cause of mid- or lower abdominal pain occasionally encounters inflammatory bowel changes. Such changes in the small bowel may result from Crohn's disease or from acute ileitis in the context of yersiniosis. The differential diagnosis of these cases should include peritonitis arising from the adnexal region, acute appendicitis, and ulcerative colitis.

The advantage of ultrasonography over static imaging modalities in bowel examinations is that it can not only define structural changes but can also detect peristaltic motion. It should be noted, however, that the wall layers defined by ultrasound correspond only in part to the anatomical layers of the bowel wall [19,22,23]. Moreover, the ability to evaluate bowel loops depends on the gas content of the imaged bowel segments. The greater the amount of gas in the bowel loops, the more the gas will obscure the underlying bowel on ultrasound.

With *inflammations of the small bowel*, scans may demonstrate conspicuous wall edema (Fig. 12.**22**) or a general thickening of the bowel wall. Increased peritoneal fluid may also be found in association with an acute inflammation. Pronounced thickening of the bowel wall is particularly characteristic of chronic intestinal diseases such as *Crohn's disease*. The affected segment may also show an almost complete absence of peristalsis. With an inflammatory reaction that transcends the bowel wall, an echogenic rim or *halo* can be seen surrounding the thickened wall [23,24] (Fig. 12.**23**).

Inflammations of the colon also present sonographically with thickening of the bowel wall. The wall thickening may be focal, segmental, or generalized [23]. In some cases, the affected bowel region can be evaluated in better detail by instilling fluid into the colon [23,25].

Abdominal ultrasound can also provide a high degree of accuracy in evaluating the appendix of patients with right lower abdominal pain [26,27]. While the normal appendix is not visible sonographically under ordinary conditions, ultrasound in *acute appendicitis* will show marked thickening of the appendix wall in longitudinal section (Fig. 12.**24**) and a characteristic target pattern in transverse section [23,26,27] (Fig. 12.**25**, Table 12.**4**).

In patients with a *bowel obstruction*, ultrasound can demonstrate an abnormal intraluminal fluid collection and luminal distension affecting the small bowel (see Fig. 15.**9**). These sonographic signs of bowel obstruction can be seen even before plain abdominal radiographs show distended bowel loops and fluid levels [23].

The clinical pictures discussed here represent only a few of the medical and urological conditions capable of being diagnosed with ultrasound. For specific issues, reference should be made to textbooks on ultrasound applications in internal medicine [28,29] and urology [30].

Table 12.**4** Characteristic target sign in acute appendicitis (adapted from Schwerk et al. [27])

Hypoechoic center	Inflammatory exudate with possible mucosal involvement
Hyperechoic inner wall layer	Submucosa
Hypoechoic outer wall layer	Muscularis
Hyperechoic outer boundary	Interfacial echo at the serosa

References

1 Moell H. Size of normal kidneys. Acta Radiol 1956;46:640–5.
2 Becht E, Hutschenreiter G, Walz P, Klose K. Niere. In: Becht E, Hutschenreiter G Klose K, editors. Urologische Diagnostik mit bildgebenden Verfahren. Stuttgart: Thieme, 1988: 16–100.
3 Cook JH, Rosenfield AT, Taylor KJ. Ultrasonic demonstration of intrarenal anatomy. AJR Am J Roentgenol 1977;129:831–5.
4 Schwerk WB. Nieren. In: Braun B, Günther R, Schwerk WB, editors. Ultraschalldiagnostik. Lehrbuch und Atlas. Landsberg, Germany: Ecomed, 1985: Suppl 3, III-1.8.
5 Swobodnik W. Diagnostik von Nieren und Oberbauch in Gynäkologie und Geburtshilfe. In: Sohn C, Holzgreve W, editors. Ultraschall in Gynäkologie und Geburtshilfe. Stuttgart: Thieme, 1995: 545–559.
6 Braun B, Pernice H, Dormeyer HH, Gebauer C, Herzog P, Kujat C. Sonographische Diagnostik bei Nephrolithiasis. Dtsch Med Wochenschr 1981;106:1030–34.
7 Roters M, Scherer K. Ultraschalldiagnostik von Nierensteinen. RöFo 1979;131:379–85.
8 Schwerk WB, Braun B, Eberle F. Ultraschalltomographie zystischer Fehlbildungen der Nieren. Ein Vergleich zum Infusionsurogramm. RöFo 1979;131:29–35.
9 Weitzel D, Bahlman J, Otto P. Die Wertigkeit der Sonographie für die Diagnostik von Zystennieren. Dtsch Med Wochenschr 1974;99:1587–90.
10 Schmiedt E, Rattenhuber U, Wieland W. Parenchymatöse Nierentumoren. In: Hohenfellner R, Zingg EJ, editors. Urologie in Klinik und Praxis, vol. 1. Stuttgart: Thieme, 1982:490–504.
11 Grimaldi G, Reuter V, Russo P. Bilateral non-familiar renal cell carcinoma. Ann Surg Oncol. 1998;5:548–552.
12 Braun B. Biläres System. In: Braun B, Günther R, Schwerk WB, editors. Ultraschalldiagnostik. Lehrbuch und Atlas. Landsberg: Ecomed, 1993: Suppl 12, III-1.1.
13 Börner N, Schwerk B, Braun B. Leber. In: Braun B, Günther R, Schwerk WB, editors. Ultraschalldiagnostik. Lehrbuch und Atlas. Landsberg, Germany: Ecomed, 1987: Suppl 5, III-1.2.
14 Marchal GJ, Pylyser K, Tshibwabwa-Tumba EA, Verbeken EK, Oyen RH, Baert AL, et al. Anechoic halo in solid liver tumors: sonographic, microangiographic, and histologic correlation. Radiology 1985;156:479–83.
15 Schwerk WB. Ultraschalldiagnostik in der Gastroenterologie. Internist 1982;23:36–46.
16 Koischwitz D. Die Sonomorphologie primärer und sekundärer Leberneoplasien. RöFo 1980;133:372–8.
17 Beyer D, Friedmann G, Madder U. Leberdiagnostik mit bildgebenden Verfahren. Internist 1982;23:66–74.
18 Schwerk WB, Maroske D, Roth ST, Arnold R. Ultraschallgeführte Feinnadelpunktion in der Diagnostik und Therapie von Leber- und Milzabszessen. Dtsch Med Wochenschr 1986;111:847–53.
19 Strunk H, Jungbluth A, Frank K, Schreiber U. Wandaufbau des Gastrointestinaltraktes: eine sonographisch morphologische Vergleichsstudie. RöFo 1988;149:197–200.
20 Schwerk WB. Milz. In: Braun B, Günther R, Schwerk WB, editors. Ultraschalldiagnostik. Lehrbuch und Atlas. Landsberg, Germany: Ecomed, 1986: Suppl 4, III-1.4.
21 Korsik C, Frank K, Schmidt H. Sonographische Milzgrössenbestimmung: Normalwerte bei klinisch Gesunden. In: Judmeier G, Frommhold H, Kratochwil A. Ultraschalldiagnostik. Stuttgart: Thieme, 1985: 93–4.
22 Limberg B, Osswald B, Hapker W. Sonographische Untersuchungen der Dickdarmwand – eine in-vitro-Studie. Ultraschall Klin Prax 1987; (Suppl 1): 50.
23 Schwerk WB. Gastrointestinaltrakt. In: Braun B, Gunther R, Schwerk WB, editors. Ultraschalldiagnostik. Lehrbuch und Atlas. Landsberg: Ecomed, 1989: Suppl 7, III-1.7.
24 Worlicek H, Lutz H, Thoma B. Sonographie chronisch-entzündlicher Darmerkrankungen – eine prospektive Studie. Ultraschall 1986;7:275–80.
25 Rubin C, Kurtz A, Gildberg B. Water enema: a new ultrasonic technique in defining pelvic anatomy. J Clin Ultrasound 1978;6:28–31.
26 Jeffrey RB Jr, Laing FC, Lewis FR. Acute appendicitis: high-resolution real-time ultrasound findings. Radiology 1987;163:11–4.
27 Schwerk WB, Wichtrup B, Maroske D, Ruschoff J. Sonographie bei akuter Appendizitis. Dtsch Med Wochenschr 1988;113:493–9.
28 Kremkau FW. Diagnostic ultrasound: principles and instruments, 6th ed. Philadelphia:Saunders, 2002
29 Rettenmaier G, Seitz K. Sonographische Differentialdiagnostik. Weinheim, Germany: VCH, 1990.
30 Resnick MI, Rifkin MD. Ultrasonography of the urinary tract, 3rd ed. Baltimore: Williams & Wilkins, 1991

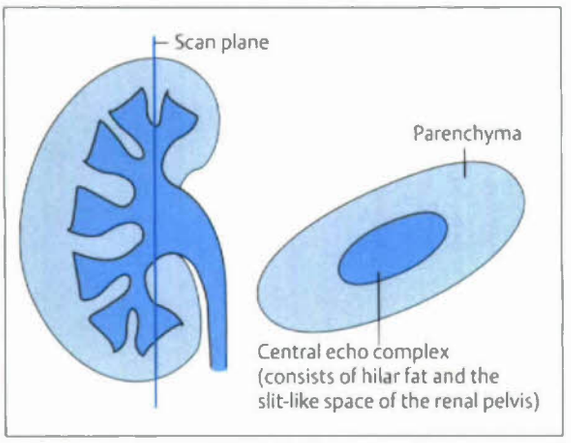

1

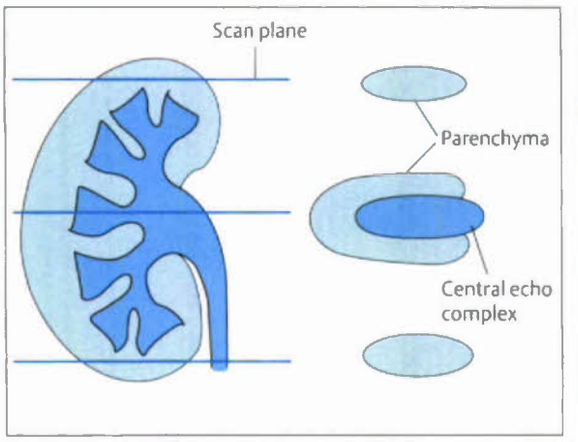

2

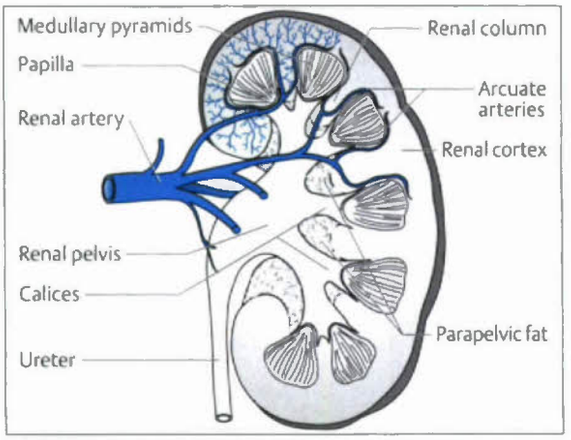

3

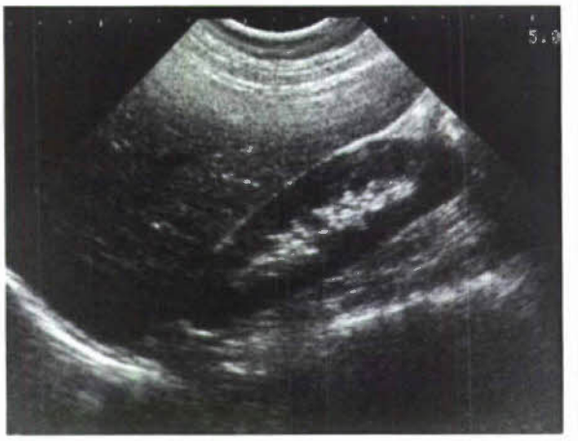

4

5

6

Examination Technique

Fig. 12.1 Renal ultrasound examination. Schematic longitudinal scan through the kidney. Normally, the renal pelvis cannot be demonstrated as a capillary space (adapted from Becht et al. [2]).

Fig. 12.2 Renal ultrasound examination. Schematic transverse scan through the kidney. The typical horseshoe-shaped figure is seen only at the center of the kidney (adapted from Becht et al. [2]).

Fig. 12.3 Schematic longitudinal section of the kidney (adapted from Schwerk [4]).

Fig. 12.4 Longitudinal scan of a normal right kidney.

Hydronephrosis

Fig. 12.5 Dilated left renal pelvis (grade II hydronephrosis) with dilation of the ureter (→). Longitudinal scan.

Fig. 12.6 Dilated renal pelvis with a solitary, hyperechoic stone (→).

Renal Masses

Fig. 12.7 Small cyst (→) in the upper portion of the right kidney (2.8 cm in diameter). Longitudinal scan.

7

Fig. 12.8 Large renal cyst (*) on the upper pole of the left kidney (5 cm in diameter).

8

Fig. 12.9 Multiple right renal cysts in a patient with bilateral polycystic kidneys.

9

Fig. 12.10 Hypernephroma on the upper pole of the kidney (*). Also a small renal cyst (→).

10

Examination Technique

Fig. 12.11 Scanning planes used for examining the liver (adapted from Börner et al. [13]).
1 Flank scan
2 Subcostal scan
3 Upper abdominal midline scan

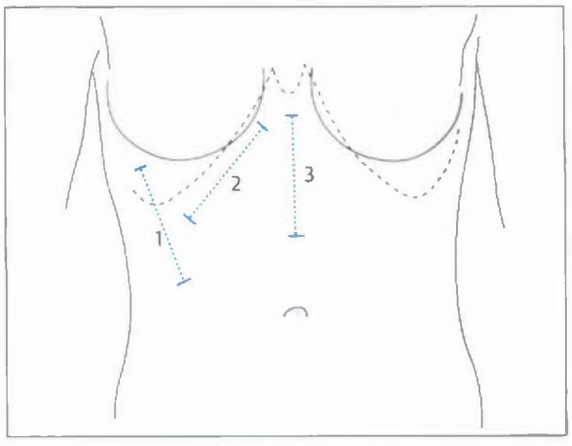

11

Fig. 12.13 Normal liver structure with the hepatic vein. Subcostal oblique scan.

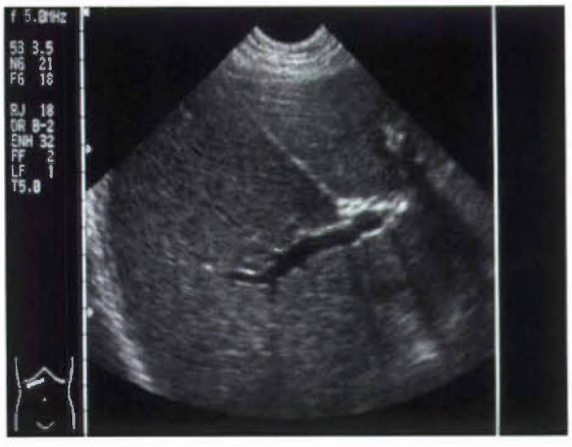

13

Fig. 12.12 The liver from the anterior aspect.

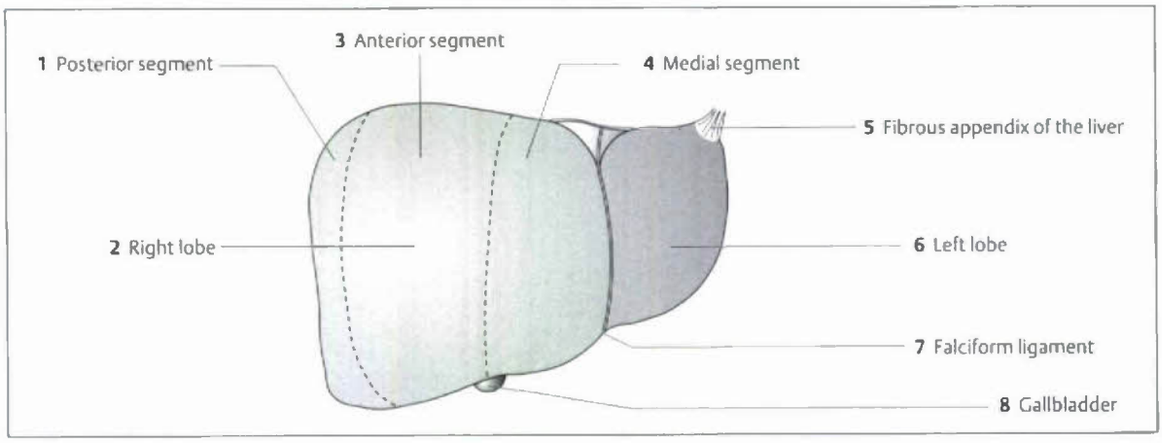

12

14

15

16

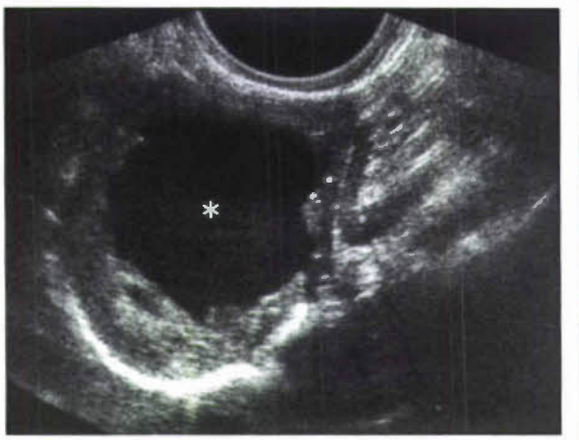

17

18

19

20

21

Abnormalities of the Liver and Gallbladder

Fig. 12.**14** Hepatic metastasis (><) from a primary breast carcinoma (target pattern), 2 cm in diameter. A marked collection of ascitic fluid is seen lateral to the right lobe of the liver (*). Subcostal oblique scan.

Fig. 12.**15** Large lymphoma at the porta hepatis (4.5 cm in diameter). Upper abdominal transverse scan.

Fig. 12.**16** Nonhomogeneous liver structure caused by diffuse hepatic metastasis from ovarian carcinoma. Ascitic fluid is completely surrounding the liver. Longitudinal scan of the right upper abdomen.

Fig. 12.**17** Abscess (*) in the right lobe of the liver (10 cm in diameter). Longitudinal scan.

Fig. 12.**18** Intrahepatic cystic mass 7 cm in diameter (*). The honeycomb internal echo pattern of the mass is consistent with a hydatid cyst. Longitudinal scan.

Fig. 12.**19** A solitary, hyperechoic gallstone with a conspicuous posterior acoustic shadow.

Fig. 12.**20** Porcelain gallbladder, with a markedly thickened wall.

Spleen

Fig. 12.**21** Marked enlargement of the spleen (20 × 10 cm) in a patient with chronic myeloid leukemia.

Intestinal Tract

Fig. 12.**22** An inflammatory bowel process in the mid-abdomen, with two thickened loops of small bowel. Transverse scan.

22

Fig. 12.**23** Thickened, fixed bowel loop with an echogenic halo (—) in a patient with Crohn's disease.

23

Fig. 12.**24** Appendix with a thickened wall in acute appendicitis (—). Longitudinal scan.

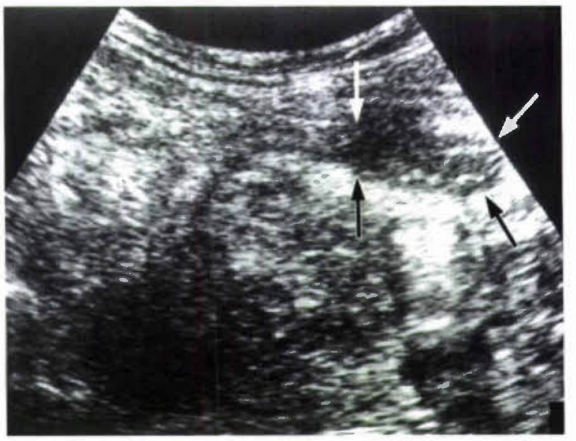

24

Fig. 12.**25** Appendix with a thickened wall in acute appendicitis (→, target pattern). Transverse scan.

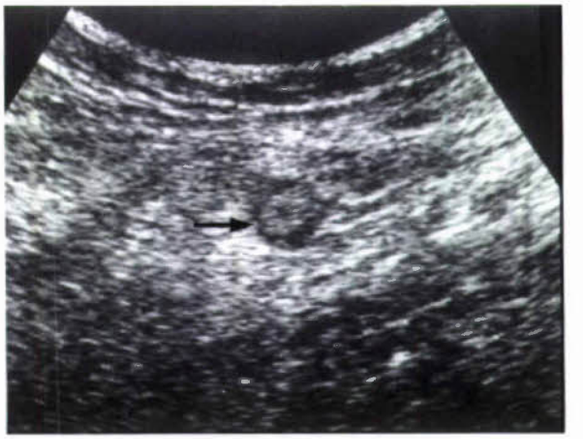

25

13 Localization of Intrauterine Contraceptive Devices

Correct Position

The intrauterine device (IUD) is the second most effective noninvasive method of pregnancy prevention after oral contraceptives. The IUDs most widely used at present include the Copper T, Copper 7, Lippes Loop, Multiload, and Progestasert. The failure rate for IUDs in general is estimated to be from two to five pregnancies per 100 woman-years [1].

The contraceptive efficacy of this method depends on the type of IUD used, the specific anatomy of the user, and correct positioning of the device within the uterus [2–4]. Bernaschek et al. [5] and Meyenburg [3] found in their studies that the device was positioned too low in approximately 80% of women who became pregnant while wearing an IUD.

Without ultrasound, the position of an IUD can be checked only by confirming that the thread is still in the cervical canal; there is no way of determining its exact intrauterine location. With ultrasound, however, the correct placement of an IUD can be confirmed easily, quickly, and noninvasively [1,2,4,6–10].

The appearance of a correctly position IUD on a longitudinal midline scan through the lower abdomen depends on the configuration of the device. For example, the Copper T appears as a bright, sharply defined linear echo (Fig. 13.**1**) while the Lippes Loop appears as a series of five bright, punctate echoes within the uterine corpus (Fig. 13.**2**).

A transverse scan through the center of the uterine corpus demonstrates the Copper T as a central, high-level echo (Fig. 13.**3**). A scan through the fundus can define the side arms of the device, which produce a transverse linear echo when they are properly extended (Fig. 13.**4**). With the Multiload device, the position of the side arms can be checked by starting with a longitudinal midline scan and moving the scan plane laterally by about 1 cm. In this view, the five spurs on each side arm can be identified as a string of bright, punctate echoes (Fig. 13.**5**). The device appears in transverse section as a series of three echoes (Fig. 13.**6**).

Abdominal ultrasound provides the best overall view of an IUD when the uterus is perpendicular to the abdominal wall. With an anteflexed uterus, this position is achieved when the urinary bladder is approximately half full. A transverse scan through the abdomen will provide a longitudinal coronal view of the uterus. In this view, the entire IUD is defined, and its type can be identified (Fig. 13.**7**).

In most cases, the IUD can be visualized without difficulty on transabdominal scans. However, factors such as obesity, inadequate bladder distension, or a retroflexed uterus can make localization far more difficult. Occasionally, a thickened secretory endometrium of high echogenicity can mimic the presence of an IUD.

In all equivocal or problematic cases, it is good practice to scan the uterus by transvaginal sonography, as this can provide better image resolution (Chapter 32).

The position of an IUD can be assessed sonographically by measuring the distance between the fundus of the uterus and the fundal end of the device. The basic rule of thumb is that this distance should not exceed 2 cm [6] (Fig. 13.**1**). However, this measurement does not take into account individual differences in the thickness of the uterine wall. This led Bernaschek et al. [2] to develop a formula for determining the fundal–IUD distance (FID), which takes the uterine wall thickness into account:

$$FID_{max} = \frac{(\text{anterior wall} + \text{posterior wall})}{2} \times 4/3$$

According to this formula, the IUD is correctly positioned only when the distance between the uterine fundus and the upper end of the IUD is equal to no more than 4/3 of the mean thickness of the uterine wall.

Applying the criteria described above, Meyenburg et al. [7] and Bernaschek et al. [2,5] discovered that 16.3% and 10%, respectively, of all IUD wearers have an incorrectly positioned IUD. If the device is positioned too low (Fig. 13.**8**), it should be removed, as an IUD in the lower uterine segment increases the risk of pregnancy and may also cause lower abdominal pain or bleeding [1,6]. *Eccentric positioning* of the IUD may be observed in a fibroid uterus or when a uterine anomaly is present.

The position of the IUD should be checked sonographically immediately after insertion and again at 4 weeks and 12 weeks, because displacement or expulsion is most likely to occur during the initial months after insertion [4]. If the position of the uterus cannot be accurately assessed by palpation in a very obese or tense patient before IUD insertion, we recommend a careful sonographic analysis of the uterine position and size before the device is inserted.

Lost IUD

All intrauterine devices have a thread at the lower end that protrudes from the cervical canal and can be felt by the patient herself or seen by a physician using a speculum. *"Lost IUD"* is a clinical term meaning that the thread of the device can no longer be felt or seen. There can be various reasons for this (Table 13.**1**).

If the IUD is still within the uterus, in most cases it can be easily detected with ultrasound. If a perforation has occurred, Kratochwil [11] states that the IUD can be located sonographically only if at least part of the device is still inside the uterus (Fig. 13.**9**). If the entire IUD has perforated into the peritoneal cavity, it is extremely difficult to locate it sonographically (Figs. 13.**10**, 13.**11**), as it may become encapsulated at various sites in the abdominal cavity.

In equivocal cases in which the uterus appears empty on ultrasound, it should be possible to locate the IUD on a plain abdominal radiograph. If the device has actually perforated into the abdominal cavity, the IUD will be visible on the radiograph and can be retrieved by means of video laparoscopy (Fig. 13.**12**).

Table 13.1 Causes of a lost intrauterine device (IUD)

• Spontaneous expulsion of the IUD, unnoticed by the patient
• Migration of the thread into the cervical canal
• Extrauterine IUD that has perforated the uterine wall

IUD Localization

1

Fig. 13.1 An intrauterine device (Copper T) correctly positioned within the uterus. Longitudinal scan. The fundal–IUD distance is 2.2 cm.

2

Fig. 13.2 A correctly positioned IUD (Lippes loop). Longitudinal scan.

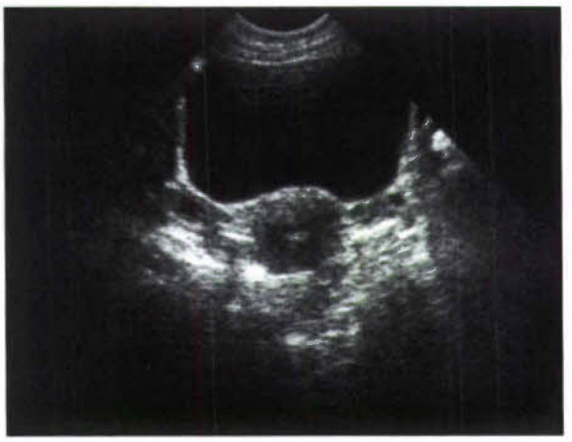

3

Fig. 13.3 A correctly positioned IUD (Copper T). Transverse scan through the center of the uterine corpus. The vertical limb of the IUD appears in cross-section as a bright central echo.

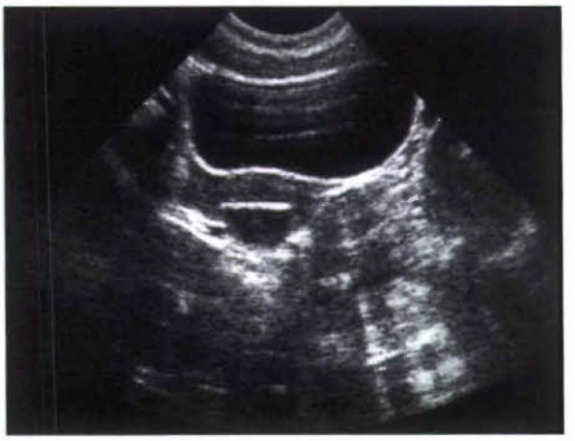

4

Fig. 13.4 A correctly positioned IUD (Copper T). Transverse scan through the upper part of the uterine corpus. The arms of the device are properly extended.

5

Fig. 13.5 Parasagittal longitudinal scan of a Multiload IUD. The five spurs on the side arm of the device form a string of punctate echoes.

6

Fig. 13.6 A correctly positioned IUD (Multiload). Transverse scan through the upper part of the uterine corpus.

7

Fig. 13.7 A coronal scan of the uterus defines the complete outline of a Lippes Loop.

8

Fig. 13.8 An incorrectly positioned IUD (Copper T). Longitudinal scan. Most of the device has been expelled into the cervical canal.

Complications Associated with IUDs

IUD wearers are at greater risk for ectopic pregnancy than oral contraceptive users [1,6,12]. Ectopic pregnancy should therefore be considered in IUD wearers who experience irregular bleeding, and follow-up scans should be taken that include detailed views of the adnexal region.

It has also been shown that IUD wearers have a two to three times greater risk of pelvic inflammatory disease in comparison with women without IUDs [13,14]. Ultrasound in patients with advanced pelvic inflammatory disease can detect inflammatory changes such as sactosalpinx and tubo-ovarian abscess.

References

1 Cochrane WJ. Ultrasonography and the intrauterine device. In: Steel WB, Cochrane WJ, editors. Gynecologic ultrasound. Edinburgh: Churchill Livingstone, 1984: 15–26.
2 Bernaschek G, Endler M, Beck A. Zur Lagekontrolle von Intrauterinpessaren. Geburtshilfe Frauenheilkd 1981;41:566–9.
3 Meyenburg H. Anwendung der Ultraschall-Schnittbildtechnik zur Darstellung von Intrauterinspiralen. Geburtshilfe Frauenheilkd 1978;38:950–7.
4 Schmidt EH, Wagner H, Quakernack K, Beller FK. Ergebnisse der Lageüberwachung von Intrauterinpessaren durch Ultraschall. Geburtshilfe Frauenheilkd 1979;39:138–43.
5 Bernaschek G, Spernol R, Beck A. IUD-Lage bei intrauterinen Schwangerschaften. Geburtshilfe Frauenheilkd 1981;41:645–9.
6 Hansmann M, Hackelöer BJ, Staudach A. Ultraschalldiagnostik in Geburtshilfe und Gynäkologie. Berlin: Springer, 1985.
7 Meyenburg M, Höbich D, Hein HW. Sonographische Darstellung von Cu-T-Intrauterinpessaren. Ultraschall 1981;2:153.
8 Nelson LH, Miller JB. Real-time ultrasound in locating intrauterine contraceptive devices. Obstet Gynecol 1979;54:711–4.
9 Nemes G, Kerenyi TD. Ultrasonic localization of the IUCD: a new technique. Am J Obstet Gynecol 1971;109:1219–20.
10 Wittmann BK, Chow TS. Diagnostic ultrasound in the management of patients using intrauterine contraceptive devices. Br J Obstet Gynaecol 1976;83:802–8.
11 Kratochwil A. Ultraschalldiagnostik in der Gynäkologie. Gynäkologe 1976;9:166–80.
12 Ory HW. Ectopic pregnancy and intrauterine devices: new perspectives. Obstet Gynecol 1981;57:137–44.
13 Golditch IM, Huston JE. Serious pelvic infections associated with the intrauterine device. Int J Fertil 1973;18:15–60.
14 Luukkainen T, Nielsen NC, Nygren KG, Pyörälä T. Nulliparous women, IUD and pelvic infection. Ann Clin Res 1979;11:121–4.

9

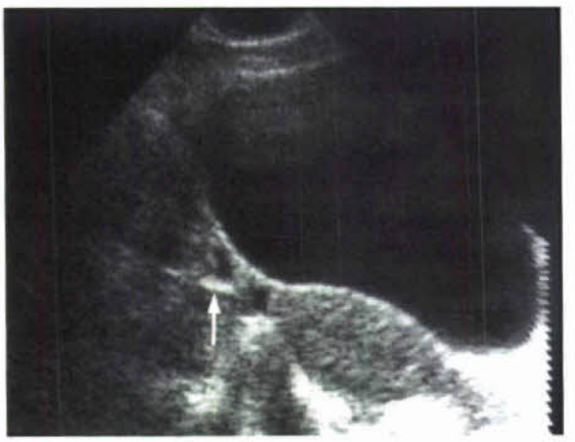

10

Lost IUD

Fig. 13.**9** Partial perforation of an IUD (Copper T) through the uterine wall (→). Longitudinal scan.

Fig. 13.**10** Complete perforation of the IUD (→). Longitudinal scan.

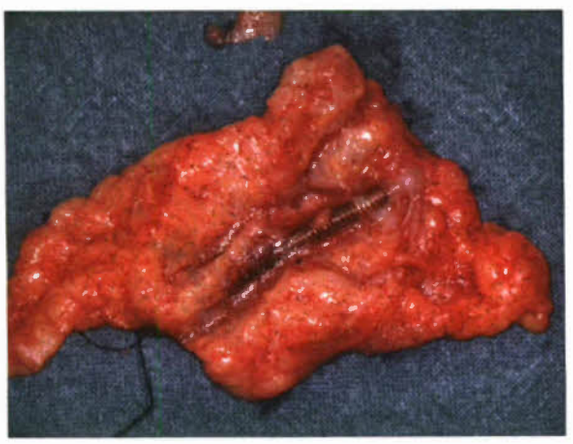

11

12

Fig. 13.**11** Surgical specimen corresponding to Fig. 13.**10**. The IUD is embedded in the greater omentum.

Fig. 13.**12** Pelvic radiograph of an IUD (Copper T) that has perforated through the uterine wall into the abdominal cavity (→).

14 Needle Procedures Guided by Abdominal Ultrasound

Various intra-abdominal lesions can be punctured through the abdominal wall under sonographic guidance for diagnostic or therapeutic purposes.

Transabdominal puncture can be performed freehand or with a needle guide (Fig. 14.**1**). Most manufacturers offer a needle guide that can direct the needle to the target at a specified angle. The angle of needle insertion can be programmed into the system to obtain a display of the desired needle path superimposed on the monitor image. In this way, the transducer can be positioned in such a way that the electronic sightline aligns precisely with the targeted mass (Fig. 14.**2**). This technique can be used on cystic masses as well as solid tumors and parenchymatous organs within the abdomen [1,2] (Table 14.**1**).

Local anesthesia can be used for the needle insertion but is not essential. The area around the puncture site is aseptically prepared, and the procedure is carried out in sterile conditions. This includes placing the transducer in a sterile wrapper along with some ultrasound gel. For a simple puncture, it is sufficient to disinfect the transducer with antiseptic solution. Antiseptic is also used as the coupling medium between the transducer and the abdominal skin.

It is important to use a needle that has favorable acoustic properties for ultrasound imaging [3,4].

There are situations in which a transabdominal puncture can eliminate the need for a more invasive surgical procedure. This particularly applies to young patients with a functional cyst [5]. This type of lesion can be aspirated percutaneously with ultrasound guidance (Figs. 14.**2**–14.**5**) for rapid relief of symptoms, and the aspirated material can be sent for cytological, microbiological, and hormonal analysis (e.g., for estradiol or progesterone). Other candidates are patients with a high medical or anesthesiological risk who require further diagnostic evaluation but should not undergo surgical procedures.

Ultrasound-guided percutaneous aspiration using a needle guide or freehand technique is also an option for the treatment of postoperative lymph cysts or the investigation of ascites (Fig. 14.**6**). The aspiration of ascites can be preceded by an ultrasound examination to locate a favorable puncture site. This is particularly important in women with suspected peritoneal carcinomatosis, who are likely to have adhesions between bowel loops and the abdominal wall.

Ultrasound can also be used to direct the placement of a drainage tube in an abscess cavity [6], hematometra [7], or lymph cyst (Figs. 14.**7**, 14.**8**).

Table 14.**1** Indications for transabdominal ultrasound-guided needle aspiration or biopsy

- Functional ovarian cyst
- Lymph cyst
- Ascites
- Abscess
- Hematometra
- Pelvic wall recurrence

References

1 Otto RC. Indikation zur ultraschallgezielten Feinnadelpunktion unter permanenter Sicht. 1: Diagnostische Punktionen. Ultraschall 1983;4:72–6.
2 Saitoh M, Watanabe H, Ohe H, Tanaka S, Itakura Y, Date S. Ultrasonic real-time guidance for percutaneous puncture. J Clin Ultrasound 1979;7:269–72.
3 Heckemann R, Seidel KJ. The sonographic appearance and contrast enhancement of puncture needles. JCU 1983;11:265–68
4 Heckemann R, Seidel KJ. The sonographic appearance and contrast enhancement of puncture needles. J Clin Ultrasound 1983;11:265–8.
5 Granberg S, Crona N, Enk L, Hammarberg K, Wikland M. Ultrasound-guided puncture of cystic tumors in the lower pelvis of young women. J Clin Ultrasound 1989;17:107–11.
6 Otto RC. Indikation für ultraschallgezielte Eingriffe unter permanenter Sicht, 2: Therapeutische Punktionen. Ultraschall 1983;4:77–80.
7 Langer D, Bordt J, Schneider HPG. Ultraschallgeleitete Punktion und Drainage einer Hämatometra bei Vaginal- und Cervixaplasie. Ultraschall Klin Prax 1989;4:39–41.

1

2

Fig. 14.1 Transabdominal aspiration of a cyst using a freehand technique.

Fig. 14.2 Transabdominal transvesical aspiration of a retrovesical cyst using an ultrasound needle guide. The superimposed dotted line indicates the path of needle insertion. Transverse scan.

3

4

Fig. 14.3 Transabdominal cyst aspiration. The needle has been advanced into the lesion, and the needle tip is visible at the center of the cyst (→). Transverse scan.

Fig. 14.4 Transabdominal cyst aspiration. All of the cystic fluid has been aspirated, and the needle is still in place within the collapsed cyst (→). Transverse scan.

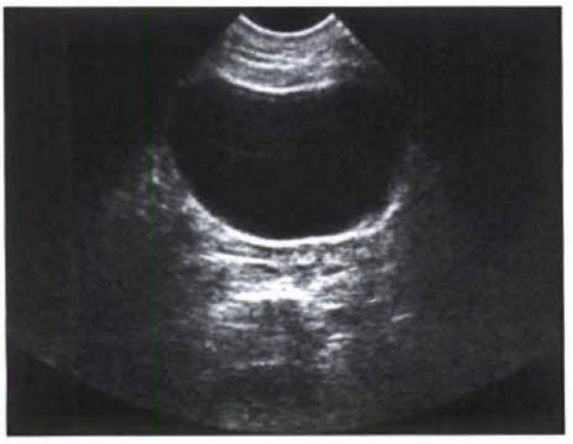

5

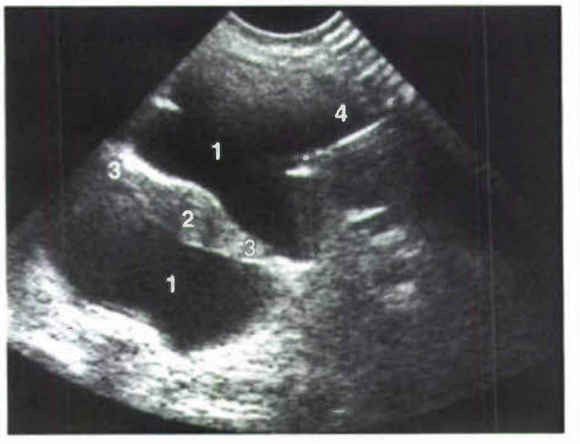

6

Fig. 14.5 Transabdominal cyst aspiration. The appearance after the needle has been withdrawn. Transverse scan.

Fig. 14.6 Percutaneous aspiration of ascites from the left side of the abdomen. Transverse scan.
1 Ascites
2 Uterus
3 Round ligament
4 Needle

7

8

Fig. 14.7 Percutaneous aspiration of a lymph cyst on the left side. A drainage tube is being introduced through the hollow needle (→). Transverse scan.

Fig. 14.8 The drainage tube has been placed within the lymph cyst (→).

15 Postoperative Abdominal Ultrasound

Investigation of Postoperative Complications

Postoperative ultrasound examinations are usually carried out with smaller units that can be wheeled to the intensive-care unit or patient's room for bedside imaging. It is convenient to use a sector transducer, which has a small footprint and can image the entire abdomen, including the true pelvis and the retroperitoneum. A transducer with a larger contact area (linear transducer, curved-array) is better for examining the abdominal wall to detect a more superficial lesion such as an abdominal wall hematoma (Fig. 15.**1**).

Abdominal ultrasound is particularly useful for detecting postoperative complications in patients who are confined to bed or have very limited mobility, as it often eliminates the need to transport or reposition the patient.

Hematomas – whether abdominal wall hematomas following pregnancy termination (Fig. 15.**2**) or retrovesical hematomas following an abdominal or vaginal hysterectomy (Figs. 15.**3**, 15.**4**) – can be quickly located with ultrasound, and their extent can be accurately determined.

Ultrasound can also be useful in patients with suspected postoperative intra-abdominal hemorrhage, to assess the quantity of free intra-abdominal fluid (Fig. 15.**5**). This makes the ultrasound examination an important decision-making tool for further clinical management.

Like hematomas and intra-abdominal fluid collections, lymph cysts that develop after extensive cancer surgery are easily detectable with ultrasound. The postoperative lymph cyst appears as a hypoechoic cystic mass, sometimes with internal septa, located in proximity to the pelvic wall (Figs. 15.**6**, 15.**7**). Large lymph cysts may cause ureteral obstruction, leading to urinary stasis and renal pelvic dilation (Fig. 15.**7**).

With its ability to define the renal pelvis, abdominal ultrasound can exclude a urinary tract obstruction quickly and safely in patients evaluated for postoperative flank pain (Fig. 15.**8**). Especially after operations that involve ureteral dissection, it is good practice to examine both kidneys with ultrasound prior to hospital release. This is recommended even in patients who do not have flank pain.

Ultrasound is also a valuable study in patients in whom there is a clinical suspicion of postoperative *ileus*. The sonographic hallmarks of ileus are an abnormal intraluminal fluid collection and luminal distension in the small bowel (Fig. 15.**9**). These signs can be detected with ultrasound even before dilated bowel loops and fluid levels can be seen in plain abdominal radiographs [1].

Residual Urine Determination

Transabdominal ultrasound provides a noninvasive alternative to bladder catheterization for determining postoperative residual urine volumes [2–6]. This is done by measuring the maximum longitudinal and transverse dimensions of the echo-free space above the still-visible urinary bladder immediately after the patient has voided (Figs. 15.**10**, 15.**11**). The residual urine volume (V) is calculated from the measured length, width, and height of the space using the formula for an ellipsoid of rotation:

$$V = \text{length} \times \text{width} \times \text{height} \times 0.524$$

The residual urine volume calculated from this formula is sufficiently precise for routine clinical evaluations [5].

For residual urine monitoring in outpatients, a special miniature ultrasound scanner has been developed that is about the size of a book and can be operated by the patient herself [6].

References

1 Schwerk WB. Gastrointestinaltrakt. In: Braun B, Günther R, Schwerk WB, editors. Ultraschalldiagnostik. Lehrbuch und Atlas. Landsberg, Germany: Ecomed, 1989: Suppl 7, III-1.7.

2 Brunn J, Ruf G. Sonographische Zystometrie. Dtsch Med Wochenschr 1980;105:1501–3.

3 McLean GK, Edell SL. Determination of bladder volumes by gray scale ultrasonography. Radiology 1978;128:181–2.

4 Pedersen JE, Bartrum RJ, Grytter C. Residual urine determination by ultrasonic scanning. AJR Am J Roentgenol 1975;125:474–8.

5 Walz P. Spezielle urologische Diagnostik: Restharnbestimmung. In: Braun B, Günther R, Schwerk WB, editors. Ultraschalldiagnostik. Landsberg, Germany: Ecomed, 1984: Suppl 1, III-1.9.1.

6 Widder B, Kornhuber HH, Renner A. Restharnmessung in der ambulanten Versorgung mit einem Klein-Ultraschall-Gerät. Dtsch Med Wochenschr 1983;108:1552–5.

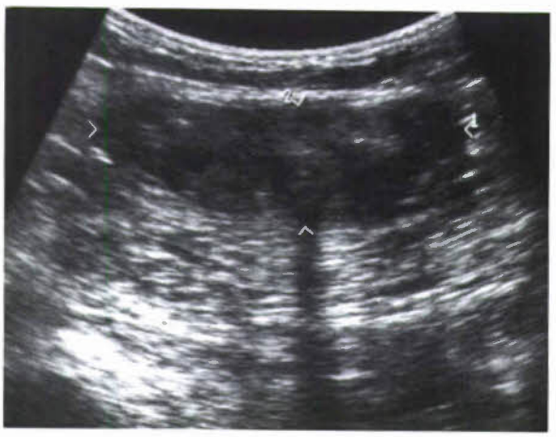

1

2

Fig. 15.1 A subfascial abdominal wall hematoma (6.4 × 1.9 × 6.0 cm) following an abdominal hysterectomy.

Fig. 15.2 An enlarged uterus with an intrauterine hematoma (*) following pregnancy termination. The bladder is only slightly distended (→). Longitudinal scan.

3

4

Fig. 15.3 A fresh retrovesical hematoma following an abdominal hysterectomy (anteroposterior diameter 5.4 cm). Longitudinal scan.

Fig. 15.4 An organized retrovesical hematoma (→) following a vaginal hysterectomy. Unlike a fresh hematoma, this lesion contains diffuse internal echoes. Longitudinal scan.

5

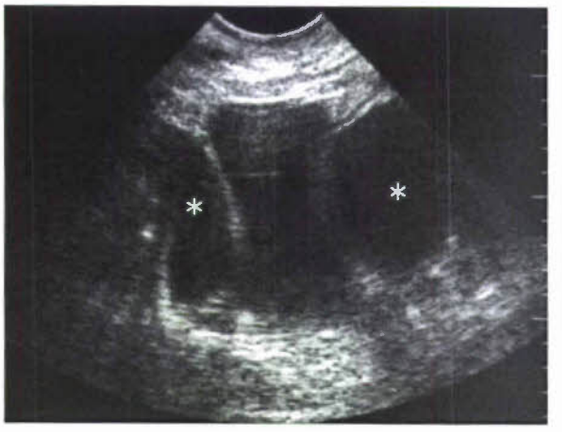

6

Fig. 15.5 Massive postoperative hemorrhage into the peritoneal cavity. Longitudinal scan.
1 Liver
2 Kidney
3 Blood

Fig. 15.6 Hypoechoic lymph cysts on both pelvic walls (*) following a Wertheim–Meigs radical hysterectomy. Lower abdominal transverse scan.

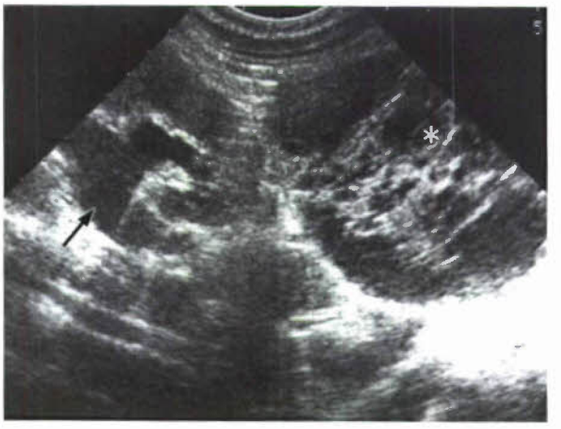

7

Fig. 15.7 A large, septate lymph cyst below the left kidney (*) is compressing the ureter and causing urinary obstruction with renal pelvic dilation (→). Longitudinal scan.

Fig. 15.8 Sonogram for postoperative exclusion of urinary tract obstruction. Longitudinal scan shows a normal-appearing right kidney.

8

Fig. 15.9 Postoperative ileus of the small bowel, with markedly dilated bowel loops. Transverse scan through the mid-abdomen.

9

Residual Urine Determination

Fig. 15.10 Sonographic determination of residual urine volume following hysterectomy. Longitudinal scan. The still-visible portion of the bladder is measured in its maximum longitudinal, transverse, and anteroposterior dimensions (→).

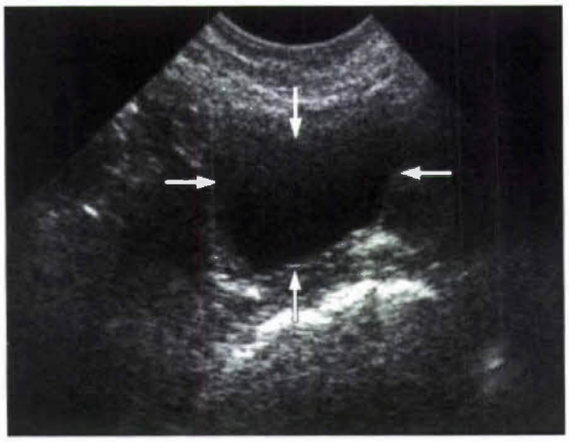

10

Fig. 15.11 Residual urine determination. The maximum transverse diameter of the bladder is shown (→). The residual urine volume is 133 mL.

11

16 Ultrasound in the Monitoring of Treatment Response

Serial ultrasound examinations are used to monitor the response to treatment for a variety of conditions (Table 16.**1**). Ultrasound is superior to manual examination, in that it can accurately define the extent of a mass, making it possible to determine the exact post-therapeutic volume reduction of the mass by taking measurements in all three planes.

Ultrasound is particularly useful in evaluating the response of *endometriosis* to medical treatment with danazol [1] (Figs. 16.**1**, 16.**2**) or gonadotropin-releasing hormone (GnRH) analogs [2], the conservative treatment of uterine *leiomyomas* with GnRH analogs [3–5], and the treatment of *polycystic ovaries* with GnRH analogs [6]. The same applies to the medical treatment of *endometrial carcinoma* and the radiotherapy of *cervical carcinoma* (Figs. 16.**3**, 16.**4**). Ultrasound can also be helpful in the expectant surveillance of a *hemorrhagic corpus luteum cyst* (Figs. 16.**5**–16.**7**), in which the impression of a functional cyst is confirmed by the rapid alteration of findings in serial examinations.

Abdominal ultrasound can also be used for *intraoperative treatment monitoring* in selected cases. The basic goal of ultrasound monitoring during a surgical operation is to lower the complication rate. In patients with postmenopausal bleeding and a cervical canal that is difficult to probe, there is a substantial risk of false passage if further attempts to explore the canal are made. Abdominal ultrasound provides an effective tool for monitoring catheter insertion in these cases. When the location and length of the uterine cavity are known, the uterine catheter can be accurately positioned in its depth and direction while eliminating the risk of *perforation* (Fig. 16.**8**). If catheterization has already been attempted without ultrasound guidance and it is suspected that a perforation has occurred, the site of the perforation can be accurately determined with ultrasound (Fig. 16.**9**).

Another *postoperative application* of ultrasound is for evaluating the result of an operation, such as the surgical construction of a neovagina (Figs. 16.**10**, 16.**11**).

It may be mentioned here once again that ultrasonography is also valuable for *oncologic follow-up* examinations [7].

Table 16.**1** Applications of ultrasound in monitoring treatment response

- Medical treatment of endometriosis
- Medical treatment of uterine leiomyomas
- Medical treatment of polycystic ovaries
- Conservative surveillance of hemorrhagic corpus luteum cyst
- Medical cancer treatment (endometrial carcinoma)
- Radiotherapy of cervical carcinoma
- Intraoperative treatment monitoring (e. g., dilation and curettage)
- Assessing the result of operative treatment (e. g., neovagina construction)
- Oncologic follow-up

References

1 Dmowski WP, Kapetanakis E, Scommegna A. Variable effects of danazol on endometriosis at four low-dose levels. Obstet Gynecol 1981;59:408–15.
2 Schenken RS. Gonadotropin-releasing hormone analogs in the treatment of endometriomas. Am J Obstet Gynecol 1990;162:579–81.
3 Filicori M, Hall DA, Loughlin JS, Rivier J, Vale W, Crowley WF. A conservative approach to the management of uterine leiomyomata: pituitary desensitization by a luteinizing hormone-releasing hormone analog. Am J Obstet Gynecol 1983;147:726–7.
4 Matta WH, Shaw RW, Nye M. Long-term follow-up of patients with uterine fibroids after treatment with the LHRH agonist buserelin. Br J Obstet Gynaecol 1989;96:200–6.
5 West CP, Lumsden MA, Lawson S, Williamson J, Baird DT. Shrinkage of uterine fibroids during therapy with goserelin (Zoladex): a luteinizing hormone-releasing hormone agonist administered as a monthly subcutaneous depot. Fertil Steril 1987;48:45–51.
6 Jaffe R, Abramowicz J, Eckstein N, Vagman I, Gejgin M, Ayalon D. Sonographic monitoring of ovarian volume during LHRH analogue therapy in women with polycystic ovarian syndrome. J Ultrasound Med 1988;7:203–6.
7 Zanetta G, Trio D, Lissoni A, Pittelli M, Di Lelio A. Ultrasound in the follow-up of young patients with malignant ovarian tumors after conservative surgery. Ultrasound Obstet Gynecol 1994;4:60–4.

1

Fig. 16.1 Extensive, bilateral endometriotic cysts prior to medical treatment with danazol. Transverse scan.

2

Fig. 16.2 The same patient as in Fig. 16.1. Ultrasound shows marked shrinkage of the endometriotic cysts after 8 months' treatment with danazol. Transverse scan.

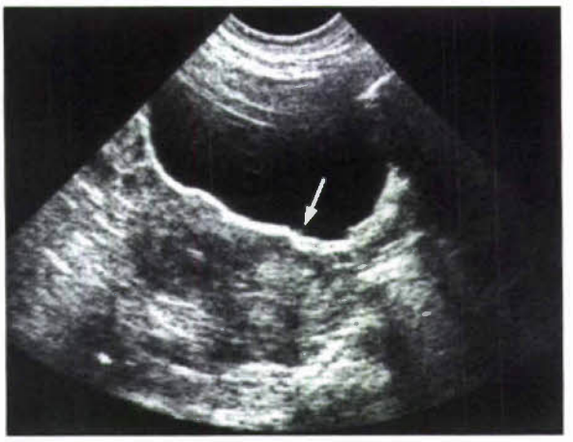

3

Fig. 16.3 Stage III cervical carcinoma prior to radium therapy. Longitudinal scan. Note the barrel-shaped distension of the cervix by echogenic tumor masses (→).

4

Fig. 16.4 The same patient as in Fig. 16.3, 4 months after a course of radium therapy. Longitudinal scan. The normal-sized cervix (→) indicates a positive response.

5

Fig. 16.5 Hemorrhagic corpus luteum cyst in a 24-year-old woman. Transverse scan. The hematoma appears as an echogenic structure completely filling the cyst (→).

6

Fig. 16.6 The same patient as in Fig. 16.5, 5 days later. The amount of solid-appearing echogenic material has decreased through resorption (→), confirming the cystic nature of the mass. Transverse scan.

7

Fig. 16.7 The same patient as in Figs. 16.5 and 16.6, 15 days later. In place of the former corpus luteum cyst, there is an almost normal-sized ovary that still contains small cystic areas. Transverse scan.

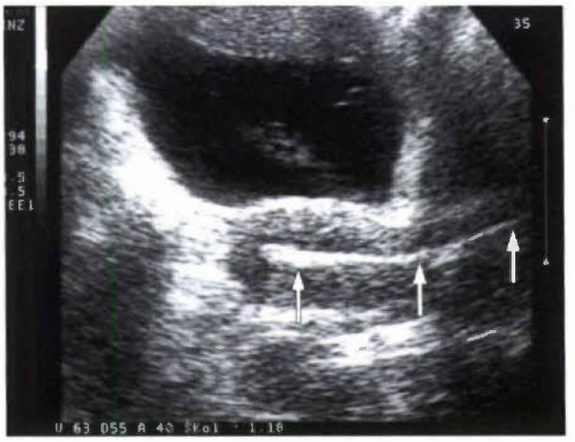

8

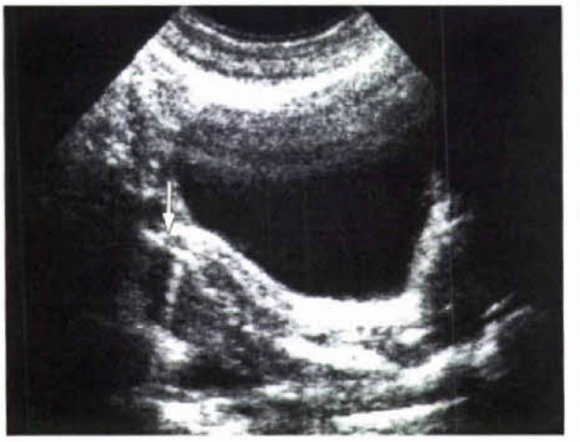

9

Fig. 16.8 Dilation and curettage with ultrasound guidance in a postmenopausal uterus with cervical synechia. The echogenic curet can be selectively advanced into the uterine cavity (→).

Fig. 16.9 Postmenopausal uterus perforated by a curet (→).

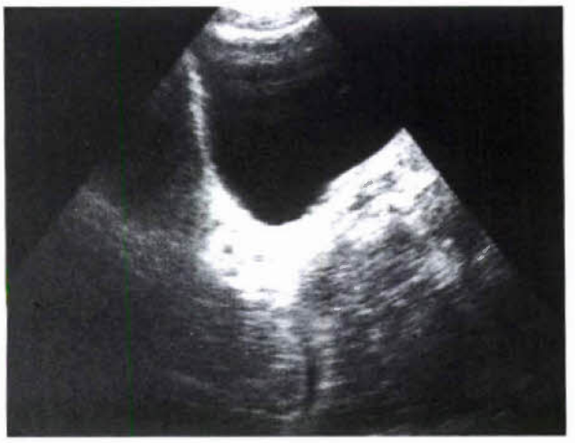

10

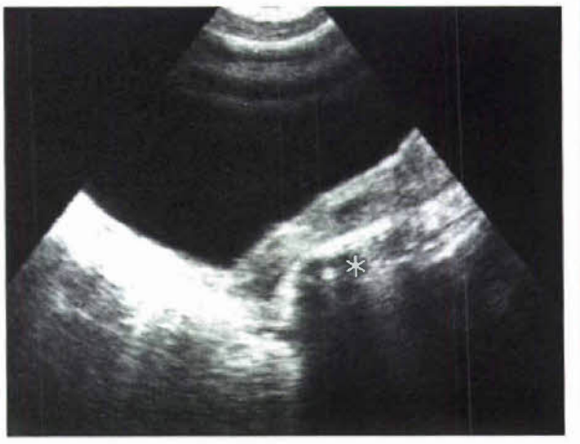

11

Fig. 16.10 Mayer–Rokitansky–Küster syndrome before the creation of a neovagina. Longitudinal scan.

Fig. 16.11 Examination after the creation of a neovagina, with a phantom inserted (*). Longitudinal scan.

Intraoperative Ultrasound

17 Technical Aspects and Applications of Intraoperative Ultrasound

The earliest applications of intraoperative ultrasound date from the 1960s. At that time, A-mode ultrasound was used for the intraoperative localization of kidney stones [1], gallstones [2,3] and even brain tumors [4]. However, as the technology at that time was still relatively primitive and few specialists were sufficiently skilled to interpret intraoperative A-mode images, the technique was not widely practiced. With the advent of easy-to-handle, high-frequency B-mode scanners in the late 1970s, intraoperative ultrasound again became an area of interest. The technique was used mainly in upper abdominal surgery for the detection of solitary, nonpalpable hepatic metastases and occult endocrine pancreatic tumors [5–7]. Intraoperative ultrasound was applied urologically in the diagnosis of kidney stones [8]. In recent years, various other applications of intraoperative ultrasound have emerged in the fields of abdominal and thoracic surgery, neurosurgery, urologic surgery, endocrine surgery [9–12], and also in gynecology [10,13,14].

Technical Aspects

Ultrasound Probes

Intraoperative ultrasound in the open abdomen has been mainly practiced using small linear or miniature convex probes operating at frequencies of 5–10 MHz. The advantage of these probes over sector transducers is that they provide a broad field of vision even in the near field.

Ultrasound probes with various scanning angles are available for intraoperative use, depending on the specific application:

- End-firing linear probes
- Angled linear probes (45° or 90°)
- End-firing mini convex probes
- Side-firing mini convex probes (90°)

Angled and side-firing probes are used chiefly in pancreatic, biliary and hepatic surgery [7]. Both angled and end-firing probes are used for examining organs in the true pelvis and for vascular investigations, depending on where the structure of interest is located (Fig. 17.**1**).

Several companies now also supply an intraoperative probe for laparoscopic applications (Fig. 17.**2**). After the probe has been introduced through its guide tube, a control handle can be used to angle the flexible transducer tip in such a way that the anterolateral window of the convex array is aimed directly at the tissue of interest. This probe can be operated at variable frequencies to ensure optimum near-field and far-field image quality.

Preparing the Probe, Positioning the Ultrasound Unit, and Placing the Probe

Ultrasound scanning in the open abdomen requires a sterile probe. Sterility can be ensured either by gas sterilization of the probe, cable, and plug (the usual method in laparoscopic procedures) or by inserting the probe into sterile plastic tubing with some coupling gel at the front (Figs. 17.**3**, 17.**4**).

The ultrasound machine is not explosion-proof, and for safety reasons it should be placed at the foot of the operating table, as that is the area with the least explosion hazard.

To carry out intraoperative ultrasound in an open field, the surgeon places the sterile or sterile-sheathed probe in contact with the organ to be examined. If the structure of interest is too close to the probe, a water standoff (e.g., a sterile glove finger filled with sterile water) should be interposed. Because the intra-abdominal organs are well moistened, there should be no difficulty in coupling the probe to the target organ. However, if the fluid film is not adequate for good acoustic coupling, the organ can be moistened with a sterile saline solution.

The operation of the ultrasound unit (B-mode optimization, image capture, color Doppler activation) and the documentation of findings (video or paper images) are usually handled by a nonsterile technician in response to the surgeon's instructions. Alternatively, the surgeon can control the unit personally using an infrared remote control paddle encased in sterile plastic.

In contrast to traditional abdominal ultrasonography, all of the scanning planes in intraoperative sonography refer directly to the imaged organ. Due to the relatively small contact area of the probe (4 or 5 cm), larger organs such as the uterus cannot be fully imaged in longitudinal section and have to be scanned in segments (Fig. 17.**5**). The probe footprint is usually adequate for obtaining complete transverse scans of the pelvic organ.

Applications in Gynecology

The gynecologic applications of intraoperative ultrasound are mainly in the areas of tumor surgery and reconstructive plastic surgery.

In tumor surgery, intraoperative ultrasound provides the surgeon with an ideal supplement to the visual and manual evaluation of a suspicious area.

In tumor surgery, as well as in plastic surgery procedures involving the abdomen (such as a transverse rectus abdominis muscle flap), intraoperative color Doppler can quickly and accurately define vascular segments that are relevant to the procedure.

The main goal with benign reproductive-tract tumors (Fig. 17.**6**) is organ preservation. Particularly in young women wanting to have children, it is important to preserve as much healthy tissue as possible by selective excision of abnormal tissue so that organ reconstruction (e.g., following a dermoid excision) can be carried out successfully.

In the case of malignant tumors, it is important to determine the extent of the primary tumor (Fig. 17.**7**) and its metastases. Intraoperative ultrasound can be used to detect metastatic deposits in the pelvic wall (Figs. 17.**8**, 17.**9**) and along the major vessels (Fig. 17.**10**). At the same time, enlarged lymph nodes along the aorta and vena cava can be excluded with a high degree of confidence (Figs. 17.**11**–17.**15**). The upper part of the retroperitoneum (Fig. 17.**16**) and the upper abdomen (Figs. 17.**17**, 17.**18**) can also be explored with intraoperative probes.

References

1 Schlegel JU, Diggdon P, Cuellar J. The use of ultrasound for localizing renal calculi. J Urol 1961;86:367–9.

2 Hayashi S, Wagai T, Miyazawa R, Ito K, Ishikawa S, Uematsu K, et al. Ultrasonic diagnosis of breast tumor and cholelithiasis. West J Surg 1962;70:34–40.

3 Knight RP, Newell JA. Operative use of ultrasonics in cholelithiasis. Lancet 1963;i:1023–5.

4 Tanaka K, Ito K, Wagai T. The localization of brain tumors by ultrasonic techniques: a clinical review of 111 cases. Neurosurgery 1965;23:135–47.

5 Castaing D, Emond J, Kunstlinger E, Bismuth H. Utility of operative ultrasound in the surgical management of liver tumors. Ann Surg 1986;204:600–5.
6 Klotter HJ, Kuhn EP, Rückert K, Neher M, Hinkel E, Kümmerle E. Intraoperative Ultraschalluntersuchungen bei Pankreaseingriffen. Dtsch Med Wochenschr 1983;108:1463–8.
7 Klotter HJ, Rückert K, Kümmerle E. Intraoperative Ultraschalldiagnostik. Munich: Urban & Schwarzenberg, 1985.
8 Cook JH, Lytton B. Introperative localization of renal calculi during nephrolithotomy by ultrasound scanning. J Urol 1977;117:543–6.
9 Machi J, Sigel B. Overview of benefits of operative ultrasonography during a ten year period. J Ultrasound Med 1989;8:647–52.
10 McGahan JP, Gerscovich E. Intraoperative and interventional ultrasound. Curr Opin Radiol 1990;2:213–22.
11 Sigel B, Spigos DG, Donahue PE, Pearl R, Popky GL, Nyhus LM. Intraoperative ultrasonic visualization of biliary calculi. Curr Surg 1979;36:158–9.
12 Sigel B, Coelho JCU, Machi J, Flannigan DP, Donahue PE, Schuler JJ, et al. The application of real-time ultrasound imaging during surgical procedures. Surg Gynecol Obstet 1983;157:33–7.
13 Jakimowicz JJ. Intraoperative ultrasonography in open and laparoscopic abdominal surgery: an overview. Surg Endosc. 2006;20 Suppl 2:S425–35.
14 Tamura RK, Sabbagha RE. Intraoperative ultrasound for gynecologic procedures. Obstet Gynecol 1985;66:440–1.

1

Fig. 17.1 End-firing and side-firing miniature convex probes suitable for intraoperative use (B-K Medical, Herlev, Denmark).

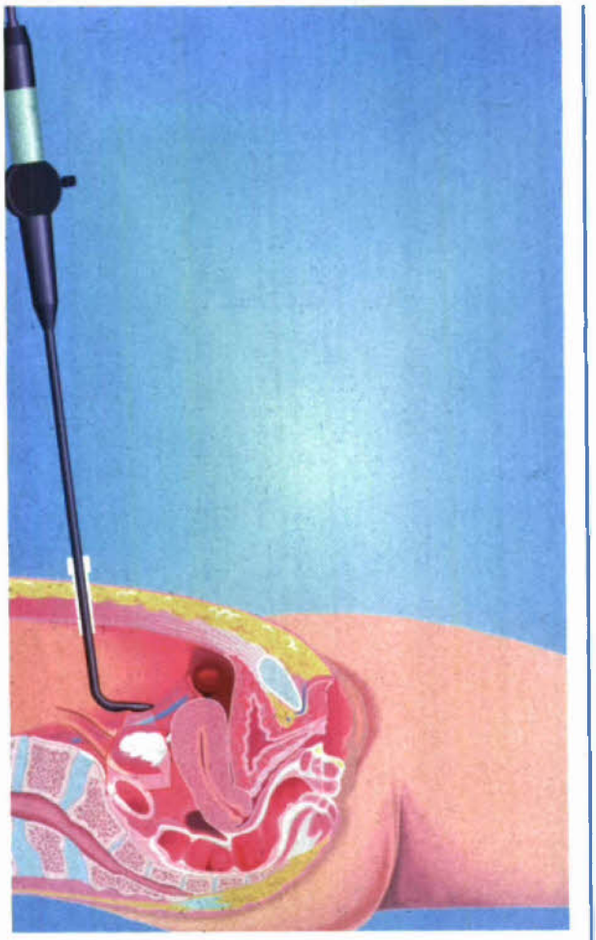

2

Fig. 17.2 Flexible intraoperative ultrasound probe for laparoscopic use (B-K Medical, Herlev, Denmark).

3

Fig. 17.3 A probe encased in a sterile plastic sheath for intraoperative use.

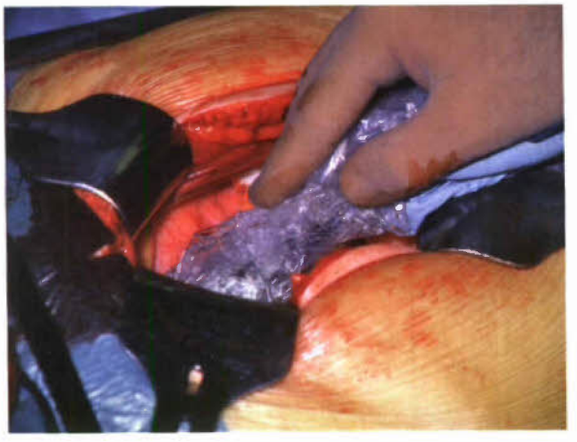

4

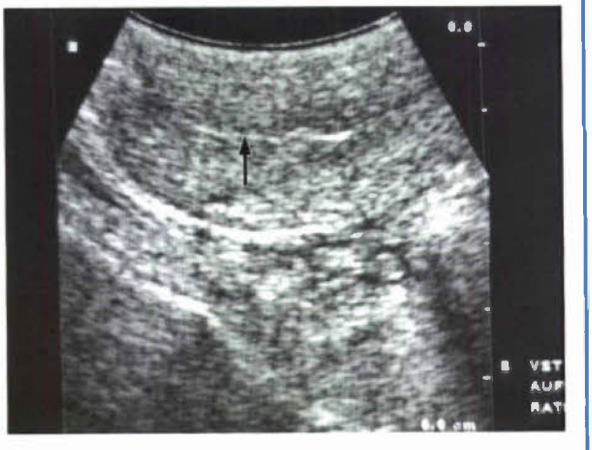

5

Applications in Gynecology

Fig. 17.4 Intraoperative use of the probe.

Fig. 17.5 Normal uterine corpus in longitudinal section. Endometrium (→).

Fig. 17.6 Echogenic dermoid in the right ovary (+ +), imaged with a 6.5-MHz laparoscopic probe.

6

Fig. 17.7 A nonkeratinizing, poorly differentiated squamous-cell carcinoma of the cervix (*), 6 × 5 cm in size, occupying the entire cervix. Endometrium (—).

7

Fig. 17.8 Recurrent melanoma on the right pelvic wall (*) (4.5 × 3.3 cm in diameter). Transverse scan.

8

Fig. 17.9 Two metastatic melanomas in the left sacral hollow, measuring 2.4 cm (+ +) and 1.6 cm (+ +) in diameter. Longitudinal scan.

9

Fig. 17.10 A metastatic lymph node (1) adjacent to the left iliac vessels (2).

10

Fig. 17.11 A normal aorta in longitudinal section. There is no abnormal enlargement of the para-aortic lymph nodes (—).

11

Fig. 17.12 Color Doppler image of the aorta. Longitudinal scan.

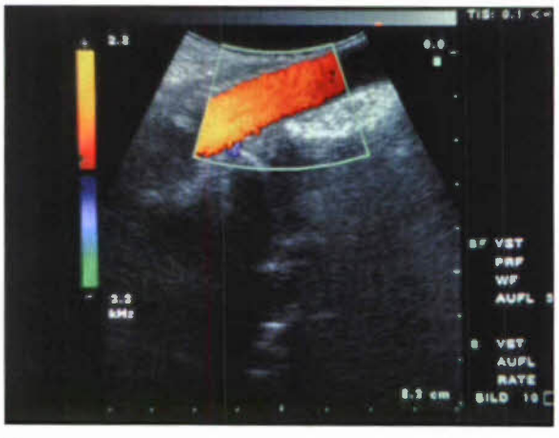

12

Fig. 17.13 Color Doppler image of the vena cava. Longitudinal scan.

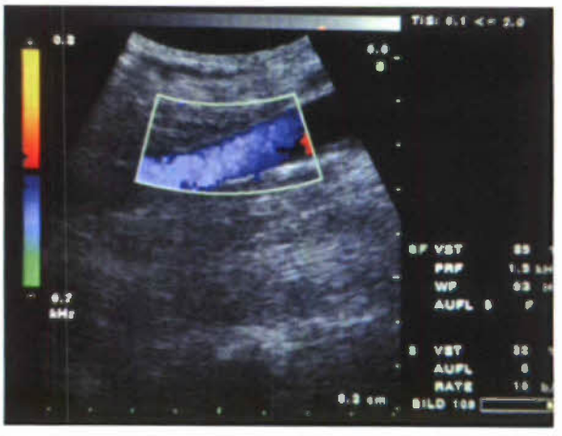

13

14

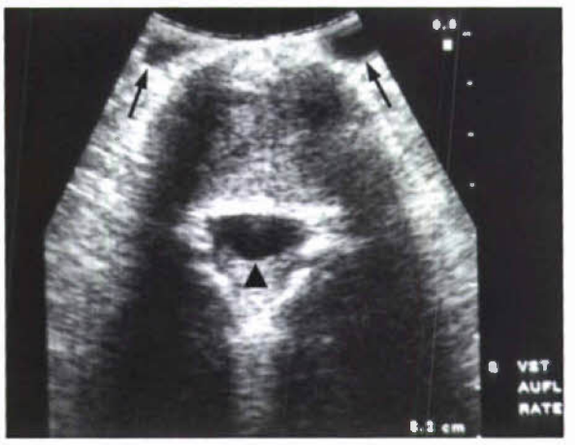

15

Fig. 17.14 Aorta (1), vena cava (2), and spinal column (3) in the lumbar region. Transverse scan.

Fig. 17.15 Transverse scan below the aortic bifurcation demonstrates the iliac vessels (→) and the spinal column with the spinal canal (>).

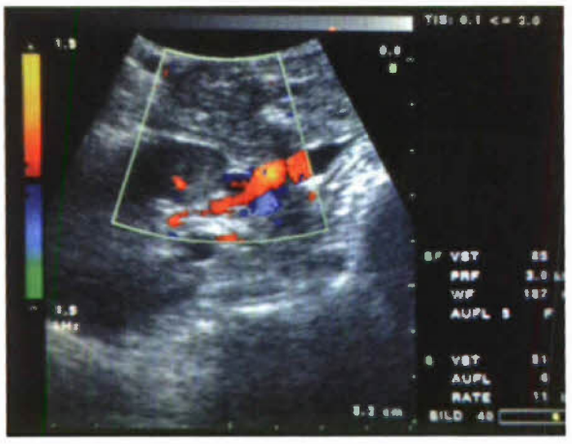

16

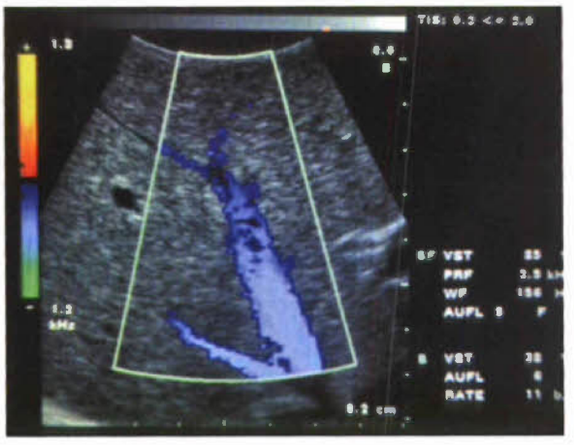

17

Fig. 17.16 Color Doppler image of the right renal vessels. Transverse scan.

Fig. 17.17 Normal liver structure with hepatic veins (color Doppler).

18

Fig. 17.18 Gallbladder with a solitary gallstone, which is casting an acoustic shadow (—).

Perineal and Introital Ultrasound

18 Evaluation of the Lower Urinary Tract with Perineal and Introital Ultrasound

The diagnostic evaluation of urinary incontinence in women is based on a detailed history and urodynamic measurements to assess the function of the bladder and urethral closure mechanism. The workup should also include an imaging study to evaluate the position of the bladder neck and urethra. Topographic evaluation of the urethrovesical unit was introduced by Thomsen in 1930 [1] and relied entirely on radiographic methods initially and for several decades thereafter. The goal is to assess the positional changes that occur in the bladder and urethra in association with urinary stress incontinence and organ descent. The standard traditional procedure for making this assessment was *lateral chain cystourethrography* [2,3]. The pelvic floor and its organs can be radiographically evaluated as a complete unit only by using expanded techniques such as colpocystorectography, with special practical emphasis on the *wick method* described by Abet and Richter [4,5]. Although these methods are technically demanding and, like all radiographic studies, expose the patient to ionizing radiation, they have been widely practiced owing to a lack of sonographic alternatives.

Sonographic Methods for Evaluating the Lower Urinary Tract

While ultrasound has long been used as an adjunct to radiography in evaluations of the upper urinary tract, studies of the lower urinary tract have relied almost exclusively on radiographic methods, and the role of ultrasound has traditionally been limited to residual urine determination. The main problem with ultrasound in that region was poor accessibility. In principle, the following anatomical approaches are available for ultrasound scanning of the lower urinary tract: transabdominal [6], transvaginal [7,8], transrectal [9], and transperineal [10–13].

Introital ultrasound is a variant of perineal ultrasound and is discussed below. Among the approaches listed above, transabdominal scanning was the first sonographic method used in an attempt to evaluate the vesicourethral angle [6]. One problem with this method was the difficulty of evaluating a deeply descended bladder floor, since the pubic symphysis prevented accurate measurement. Another problem was obesity, which made it difficult to evaluate relevant structures. These were the main reasons why abdominal ultrasound failed to provide an acceptable alternative to radiographic methods.

In 1985, Debus-Thiede et al. [7] described their initial experience with the endosonographic evaluation of incontinence in the form of transvaginal sonography of the urethra and bladder. This study employed linear scanners, generally operating at 5 MHz, using a standard endovaginal ultrasound technique. While the bladder neck region and symphysis can be demonstrated with this method, a major drawback is that the endovaginal transducer displaces the anatomical structures that are being studied. As a result, structures that have to be evaluated for a change in their position, such as a descended uterus or cystourethrocele in patients with descent of the anterior vaginal wall, may be partially reduced by the endovaginal probe, resulting in a false-negative study.

Introital ultrasound is a combination of perineal and vaginal sonography in which transperineal scanning is performed with a vaginal transducer.

Transrectal ultrasound can also be used to define and evaluate the urethrovesical junction—i.e., the bladder neck region and the pubic symphysis, which provides a bony landmark. However, the endorectal probe can alter the topography of the posterior vaginal wall. In addition, the bowel preparation required before the study makes it a more difficult procedure for both the examiner and patient than the perineal method described below.

Perineal Ultrasound

Practical Application and Diagnostic Capabilities

Perineal ultrasound employs a transperineal approach in which the probe is placed loosely between the labia majora to acquire a sagittal scan through the true pelvis. The key advantage of this method is that it demonstrates all of the bladder neck region and urethra and also displays the symphysis as a fixed reference point. The sagittal scan further demonstrates the vagina and rectum, which are also important in the evaluation of pelvic descent and urinary incontinence.

Perineal ultrasound was first described in 1976 by Lewin et al. [14], who scanned through the perineum to evaluate the cervix. The clinical application for this was in the evaluation and surveillance of women who presented with cervical insufficiency and preterm labor symptoms. Given the relatively poor image quality available at that time, however, the method did not become widely accepted. Perineal scanning started to be used again about 10 years later [10,15]. While the method was initially mainly used to evaluate cervical insufficiency during pregnancy and for placental localization, it was increasingly also used in its real field of relevance — the investigation of urinary incontinence. Kohorn et al. [15] described the method at that time as *ultrasound cystourethrography*.

Technique of Perineal Ultrasound

The best transducers for perineal ultrasound are curved-array probes operating at a frequency of 3.5–5.0 MHz. Linear probes are also generally acceptable, but sector probes are less suitable. The advantage of curved-array and convex sector probes is their approximately linear image display, combined with optimum guidance of the probe, which conforms well to the anatomy of the labia and perineum. The urethra can be easily visualized without catheterization. Care should be taken to apply an adequate amount of ultrasound coupling gel. A recommended technique is to apply copious gel to the probe, then cover the probe with a latex glove and smear the outside of the glove with more gel.

The patient is generally positioned supine on the examination couch, with the legs drawn up. The examination can also be done in the standing position, but this is somewhat more cumbersome than when the patient is supine. In some cases, imaging may be compromised by increased contractility of the pelvic floor or by overlying bowel gas in patients with a substantial rectocele.

The image obtained with perineal scanning is a sagittal section through the true pelvis that displays the bladder, urethra, vagina, rectum, and the pubic symphysis, which serves as a bony reference point (Figs. 18.**1**, 18.**2**).

Ultrasound images in urogynecology should be displayed in such a way that the top of the image is cranial and the right side of the image is anterior (Fig. 18.**3**). This is also the standard orientation used in gynecologic transvaginal ultrasound.

The first part of the examination consists of a static evaluation in resting conditions. The patient is then asked to perform a Valsalva maneuver for a dynamic evaluation.

A descriptive evaluation analogous to the Green classification [2,3] is made with regard to *vertical* and *rotational bladder neck descent* and *cystocele formation*. In addition, certain reproducible parameters are determined so that an objective classification can be made. Three key parameters based on the Green classification are defined below, with normal ranges of values given. By applying classic radiographic principles and also drawing on the Green classification, we can not only make a descriptive evaluation of the findings in terms of rotational and vertical descent and cystocele formation, but also document the findings based on pathologic values.

The three key parameters are as follows:

- The degree of *bladder neck descent* (BND), as a measure of how far the bladder neck has descended in relation to the inferior border of the symphysis.
- The change in the *posterior urethrovesical angle* (PUV) formed by the proximal ureteral segment and a line tangent to the bladder floor.
- The degree of ureteral tilt from the vertical in the sagittal image plane, defined as the angle between the proximal ureteral segment and the vertical. The change in this angle is evaluated between the resting state and a Valsalva maneuver. The *rotational angle r* is defined as the difference between the inclination angle during straining and the inclination angle at rest.

Because these sonographic parameters are acquired from a sagittal section, they cannot be compared directly with the radiographic parameters that are determined in the lateral projection. In order to establish perineal ultrasound as a separate technique, normal ranges of values were defined for the sonographic parameters (Table 18.**1**), and their diagnostic accuracy was compared with lateral cystourethrography based on the Green classification. A 96% rate of agreement was found between the sonographic and radiographic methods [12]. To test the accuracy of the classification in the diagnosis of stress incontinence, a total of 200 incontinent and 130 continent women of comparable age and body weight were examined. It was found that 61% of the clinically continent patients had normal findings on perineal ultrasound, while only 16% of the clinically incontinent patients (with all grades of incontinence) had normal perineal scans. Thirty-three percent of the incontinent patients had vertical bladder neck descent, 41% showed rotational bladder neck descent, and 10% had a cystocele. Statistical analysis showed that a true-normal result was significantly more frequent in the group of clinically continent women than in the clinically incontinent patients. Comparable data are obtained when radiographic methods are used, particularly lateral cystourethrography. These results indicate that the accuracy of perineal ultrasound is equivalent to that of conventional cystourethrography in evaluating stress urinary incontinence in women [16,17]. A certain percentage of clinically continent women will also be found to have an abnormal lateral cystourethrogram based on the Green classification.

On the basis of years of personal experience in using perineal ultrasound in urodynamic incontinence studies, we have found that more than 2 cm of bladder neck descent is the most important indicator of pelvic floor insufficiency. Other parameters, such as the posterior urethrovesical angle, are helpful in differentiating between a simple cystocele and vertical or rotational bladder neck descent. In clinical application, even an inexperienced examiner can consistently determine both of these parameters without difficulty. The third parameter, which describes the degree of urethral tilt from the vertical (the rotational angle), is used mainly to differentiate between vertical and rotational bladder neck descent. There are cases, then, in which abnormal bladder neck descent can be diagnosed without accurately determining this parameter. A distinct advantage of perineal ultrasound is the dynamic aspect of the study, which makes it possible to evaluate the mobility of the bladder neck with good reproducibility and without radiation exposure (Fig. 18.**4**). Other authors [17] have confirmed this advantage. Some methods of evaluation use additional quantitative parameters [18] to describe the pelvic floor anatomy on the basis of a coordinate system (Fig. 18.**5**).

Table 18.1 Perineal ultrasound: evaluation of the bladder neck as a function of measured values

	Normal values (threshold)	Cystocele	Vertical bladder neck descent (Green I)	Rotational bladder neck descent (Green II)
BND with straining	≤2 cm	>2 cm	>2 cm	>2 cm
PUV with straining	0	<140°	>140°	>140°
r	0	<50°	<50°	<50°

BND, bladder neck descent; PUV, posterior urethrovesical angle.

Another advantage of perineal ultrasound is that the urethra can always be visualized over its entire length without catheterization. It should be noted that the urethra always appears as a hypoechoic structure that contrasts sharply with the high echogenicity of the surrounding periurethral tissue. The rectovaginal septum generally appears as a thin, echogenic line defining the boundary of the vagina. Typical bladder neck changes, especially bladder neck funneling, can also be detected without difficulty.

Since the vagina and rectum are included in the sagittal scan, perineal ultrasound makes it possible to evaluate the pelvic floor as a structural unit. The vagina also generally appears as a hypoechoic structure, usually with echogenic borders.

The rectum can be identified as a separate air-filled and fluid-filled structure delineated by the rectovaginal septum. Particularly in the dynamic phase of the examination, portions of the small bowel are interposed in the field, making it possible to diagnose enteroceles in addition to rectoceles.

Introital Ultrasound

The technique of introital ultrasound, described by Kölbl and Bernaschek [19] in 1990, uses a vaginal scanner (generally a sector probe) operating at a frequency of 5–7 MHz. The probe is positioned at the introitus below the urethra. Particularly with small vaginal probes, care should be taken that the probe is not inserted into the vagina as in endovaginal ultrasound. Although introital ultrasound provides a smaller field of view than perineal ultrasound, it can still supply valuable information on the position of the urethra and bladder neck in relation to the pubic symphysis. Because introital ultrasound usually cannot define the entire symphysis, the inferior border of the symphysis is used as the reference point in this technique (Fig. 18.**6**). The image is evaluated by drawing a horizontal line from the inferior border of the symphysis. The *level of the internal urethral meatus* is measured as the vertical distance from the horizontal line. Strict care is taken to maintain a constant probe position when comparing the measurements between rest, straining, and pelvic floor contraction. The relative positions of the vagina and rectum cannot be evaluated concurrently with this technique.

One advantage of introital ultrasound over the perineal approach is the smaller footprint of the ultrasound probe. This makes it possible to carry out a simultaneous urodynamic evaluation without difficulty. An-

other advantage is the ability to use a 7-MHz transducer, which provides better resolution. This explains why some examiners [19,20] prefer introital ultrasound. It should be noted, however, that 7-MHz probes can also be used for perineal scanning and that the geometry of the perineal transducer can be modified (e.g., by using a curved array or water standoff) to permit a simultaneous urodynamic measurement ("ultrasound profilometry"). It should be added that a key advantage of perineal ultrasound is its ability to provide an overall impression of the organs of the pelvic floor and its stability. Examples of introital sonograms are shown in Figs. 18.**7** and 18.**8**.

Clinical Uses of Perineal and Introital Ultrasound

Both perineal and introital ultrasound provide an alternative to radiographic methods, especially in the primary evaluation of female urinary incontinence. For this indication, the examination can be performed concurrently with a urodynamic measurement or as a separate adjunct to profilometry. A particular advantage in these cases is the ability to dispense with urethral catheterization, making it possible to perform the examination noninvasively and without radiation exposure in any gynecologic office or department. Besides determining the above parameters, which allow objective and reproducible findings, the examiner can observe and evaluate dynamic changes in the bladder neck region, vagina, and rectum. Perineal ultrasound is particularly useful in the assessment of pelvic floor stability. Information such as the level of the bladder neck in relation to the inferior border of the symphysis can be an important aid in selecting a surgical procedure in patients diagnosed with stress urinary incontinence (Figs. 18.**9**–18.**12**).

Use in the Follow-Up of Incontinence Surgery

Perineal ultrasound can be used to evaluate the position and stability of the bladder neck region in patients who have undergone incontinence surgery. The same applies to other pelvic floor areas, especially the rectum. Perineal scanning can detect scar formation in the periurethral connective tissue and can demonstrate the material that has been implanted in a supportive sling procedure. It can also detect the retrosymphyseal tissue reaction and scar formation that may occur following a colposuspension procedure (Figs. 18.**13**, 18.**14**).

A complete urodynamic workup is generally not performed in women who are free of symptoms following incontinence surgery. Perineal ultrasound provides a tool for the pathoanatomic evaluation of these patients and can be added to the routine gynecologic follow-up. A urodynamic function study should be performed, however, in patients who have complaints or have undergone surgery for recurrent incontinence.

Use in Evaluating Treatment Response

Particularly in the setting of pelvic floor training or "reeducation," it is important to teach the patient how to selectively contract and relax specific pelvic floor muscles. Perineal ultrasound can give the patient immediate visual feedback on her muscular function and can also objectify the therapeutic results.

References

1 Thomsen E. Roentgen examination of the female urethra, specially in cases of prolapse and incontinence. Acta Radiol 1930;9:529–536.
2 Green TH Jr. Development of a plan for diagnosis and treatment of urinary stress incontinence. Am J Obstet Gynecol 1962;83:632–48.
3 Green TH Jr. Urinary stress incontinence: differential diagnosis, pathophysiology, and management. Am J Obstet Gynecol 1975;122:368–400.
4 Abet L, Richter J. Zur Methodik der Kolpourethrozystographie. Zentralbl Gynäkol 1981;103:1373–82.
5 Richter K. Die Bedeutung der radiologischen Beckenviszerographie für eine rationelle Therapie der weiblichen Stressinkontinenz. Geburtshilfe Frauenheilkd 1987;47:509–17.
6 Bernaschek G, Spernol R, Wolf G, Kratochwil A. Vergleichende Bestimmung des Urethra-Blasenwinkels bei Inkontinenzfällen mittels Ultraschall und lateralem Urethrozystogramm. Geburtshilfe Frauenheilkd 1981;41:339–42.
7 Debus-Thiede G, Wagner U, Schürmann R, Christ F. Erste Erfahrungen mit der transvaginalen Sonographie von Urethra und Blase im Rahmen der Inkontinenzdiagnostik. Geburtshilfe Frauenheilkd 1985;45:891–4.
8 Johnson JD, Lamensdorf H, Hollander IN, Thurman AE. Use of transvaginal endosonography in the evaluation of women with stress urinary incontinence. J Urol 1992;147:421–5.
9 Bergman A, McKenzie CJ, Richmond J, Ballard CA, Platt LD. Transrectal ultrasound versus cystography in the evaluation of anatomical stress urinary incontinence. Br J Urol 1988;62:228–34.
10 Grischke EM, Dietz HP, Jeanty P, Schmidt W. Eine neue Untersuchungsmethode: Perinealscan in der Geburtshilfe und Gynäkologie. Ultraschall 1986;7:154–61.
11 Grischke EM. Perinealsonographie. Objektive Erfolgskontrolle nach Inkontinenzoperationen. Gynäkol Prax 1989;13:473–80.
12 Grischke EM, Anton HW, Dietz P, Schmidt W. Perinealsonographie und röntgenologische Verfahren im Rahmen der weiblichen Harninkontinenzdiagnostik. Geburtshilfe Frauenheilkd 1989;49:733–6.
13 Grischke EM, Stolz W, Kaufmann M, Bastert G. Klinischer Einsatz der Perinealsonographie. Gynäkol Prax 1991;15:693–8.
14 Lewin D, Sadoul G, Sylvian-Leroy B. L'échotomographie périnéale. Une nouvelle méthode de mesure objective du col. J Gynécol Obstét Biol Réprod 1976;5:651–5.
15 Kohorn EL, Scioscia AL, Jeanty P, Hobbins C. Ultrasound cystourethrography by perineal scanning for the assessment of female stress incontinence. Obstet Gynecol 1986;68:269–72.
16 Kölbl H, Bernaschek G, Wolf G. A comparative study of perineal ultrasound scanning and urethrocystography in patients with genuine stress incontinence. Arch Gynecol Obstet 1988;244:39–45.
17 Schär G, Köchli OR, Hutzli C, Fink D, Hall U. Aussagekraft des lateralen Urethrozystogrammes und der Perinealsonographie – Gibt es Unterschiede? Geburtshilfe Frauenheilkd 1994;54:75–9.
18 Schär G, Kölbl H, Voigt R, Merz E, Anthuber C, Niemeyer R, et al. [Recommendations by the Urogynecology Working Group for sonography of the lower urinary tract in the context of urogynecologic functional diagnosis; in German.] Ultraschall Med 1996;17:38–41.
19 Kölbl H, Bernaschek G. Introitussonographie – eine neue Methode in der Blasenfunktionssonographie. Geburtshilfe Frauenheilkd 1990;50:295–8.
20 Schwenke A, Fischer W. Urogenitalsonographie bei weiblicher Harninkontinenz. 1: Stressinkontinenz. Gynäkol Prax 1994;18:683–94.

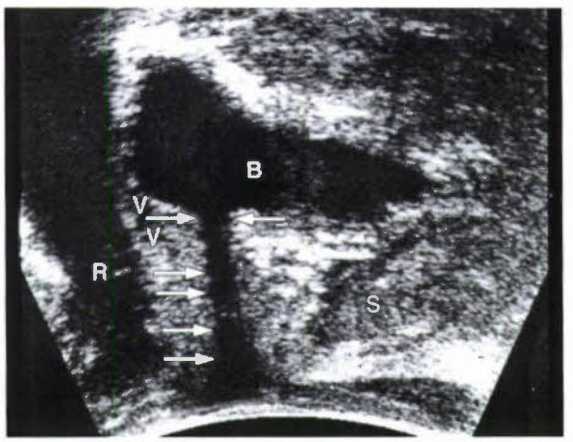

1

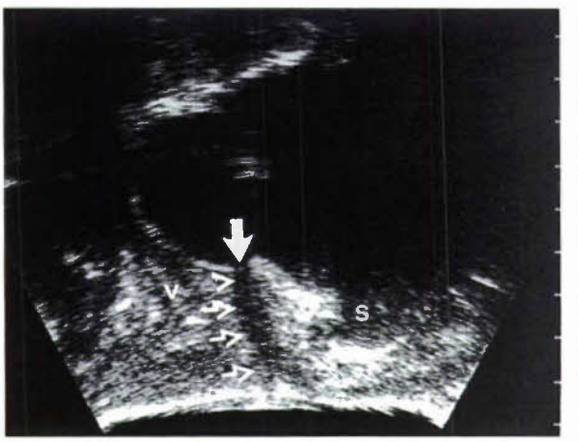

2

Fig. 18.1 The normal perineal sonogram demonstrates the symphysis (S), bladder (B), full length of the urethra (←), rectum (R), and vagina (V), which appears as a streak-like density. The internal urethral orifice (> <) is visible at the bladder neck, occupying a level well above the inferior border of the symphysis.

Fig. 18.2 A normal perineal sonogram, with greater bladder distension than in Fig. 18.1. The symphysis (S) is casting a small acoustic shadow toward the bladder. The urethra (←) appears generally hypoechoic, and its course is well defined. The posterior urethrovesical angle is clearly defined and has a maximum value of 90°.

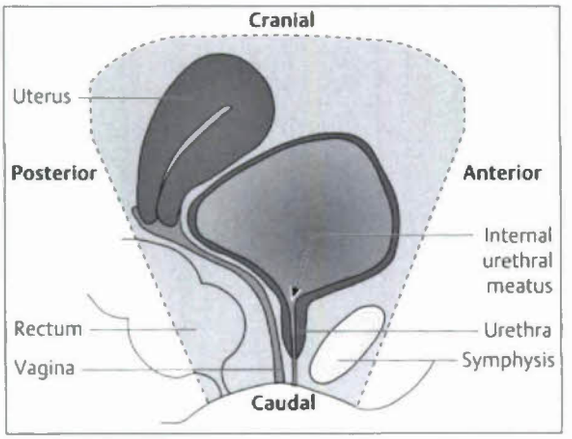

3

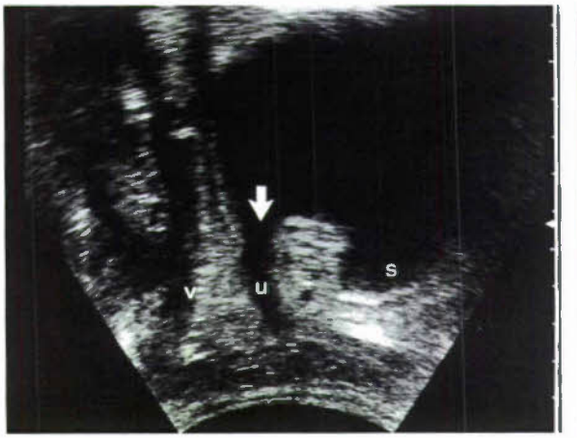

4

Fig. 18.3 The recommended display mode for urogynecologic sonograms is cranial at the top and anterior at the right (from Schär et al. [18]).

Fig. 18.4 The perineal sonogram shows effacement of the posterior urethrovesical angle at rest, although the bladder neck is still sufficiently high in relation to the inferior border of the symphysis. The urethra, displayed over its full length, is markedly broad and hypoechoic (←). S: symphysis; V: vagina; U: urethra.

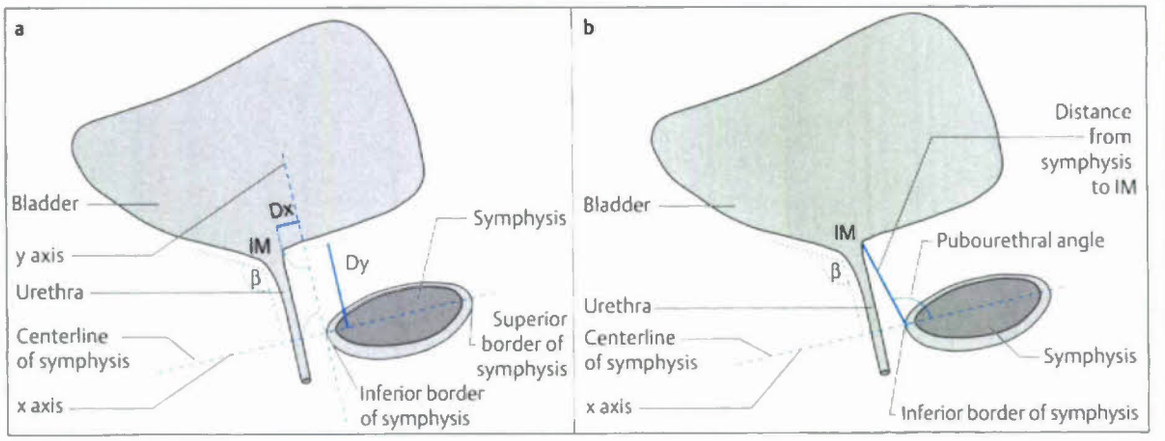

5

Fig. 18.5a, b Methods of evaluation that document urethrovesical anatomy using a coordinate system. A line through the center line of the symphysis defines the x axis, and a line perpendicular to the x axis and tangential to the inferior border of the symphysis defines the y axis. This provides a coordinate system for measuring the location of the internal urethral meatus (IM). Dx: horizontal distance of the anterosuperior urethrovesical junction from the y axis; Dy: vertical distance of the anterosuperior urethrovesical junction from the x axis or the symphyseal centerline (from Schär et al. [18]).

Introital Ultrasound

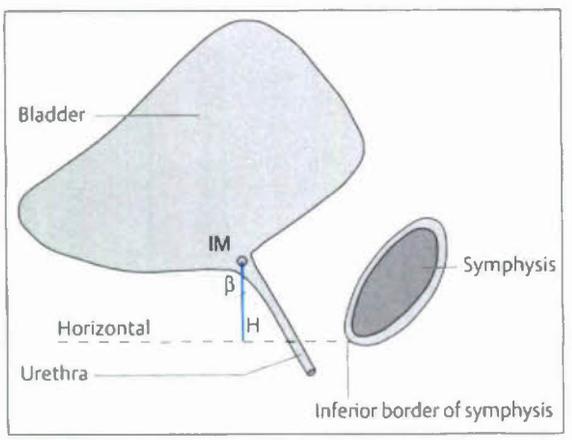

6

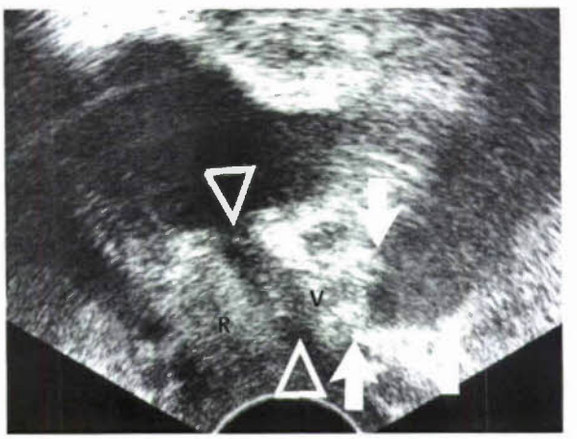

7

Fig. 18.6 Since the entire symphysis usually cannot be visualized by introital scanning, a horizontal line (H) is drawn from the inferior border of the symphysis. The level of the internal urethral meatus is measured as the vertical distance from the horizontal line (from Schär et al. [18]).

Fig. 18.7 Introital sonogram of a normal bladder neck. The vagina (V) and rectum (R) are also shown. The arrows indicate the internal urethral orifice and the course of the urethra. The symphysis is not clearly visualized in this scan. Overall, however, the posterior urethrovesical angle appears to be intact.

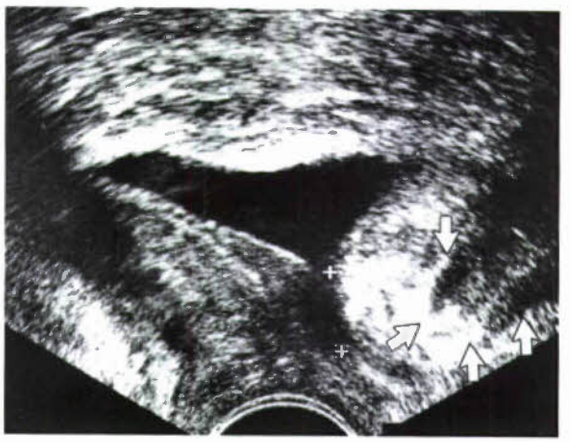

8

Fig. 18.8 Bladder neck funneling demonstrated by introital ultrasound. The relatively low bladder neck position at rest in relation to the inferior border of the symphysis (S, marked with arrows) indicates significant bladder neck funneling, with loss of the posterior urethrovesical angle.

Fig. 18.9 This perineal sonogram during a Valsalva maneuver shows a 1 cm descent of the bladder neck distal to the inferior border of the symphysis and tilting of the urethra consistent with rotational bladder neck descent. The course of the urethra (white arrows) and the inferior border of the symphysis (black arrows) should be noted. I Postoperative infiltrate around the vaginal stump, R Rectum, V Vagina, B Bladder, S Symphysis

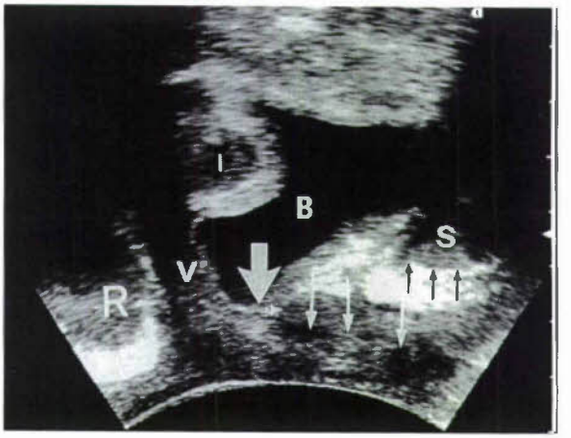

9

Fig. 18.10 The perineal sonogram shows significant vertical bladder neck descent. The bladder neck region or internal urethral orifice (arrows) is located well below the inferior border of the symphysis (S). Slight funneling of the bladder neck is also evident.

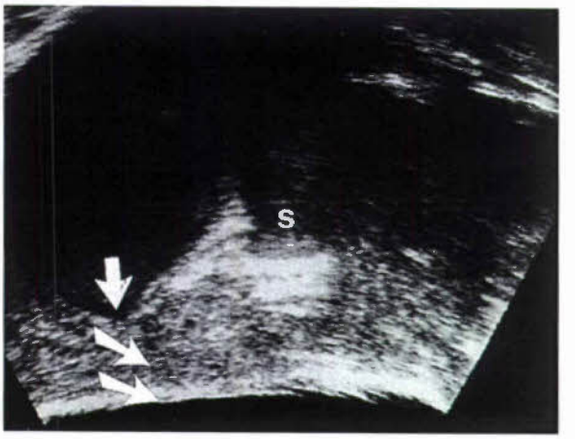

10

Fig. 18.11 The perineal sonogram demonstrates slight bladder neck funneling at rest. The symphysis (S), vagina (V), and rectum (R) are displayed. The arrows indicate the course of the urethra.

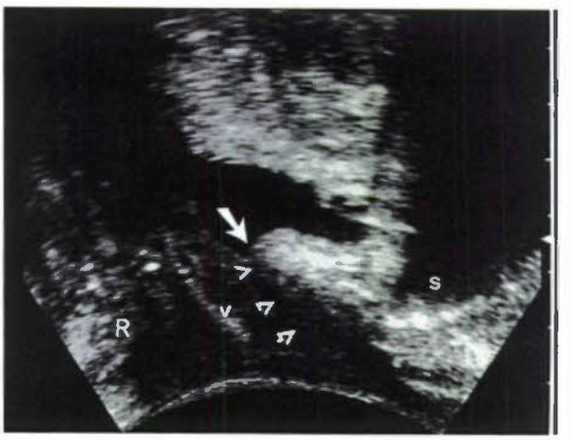

11

Fig. 18.12 Perineal sonogram of a pronounced cystocele. The scan demonstrates the symphysis (S), the internal urethral orifice (arrows), and the entire course of the urethra. The posterior urethrovesical angle is intact, and a cystocele is visible well below the inferior border of the symphysis.

12

Fig. 18.13 A perineal sonogram following surgical correction of bladder neck descent by colposuspension. The scan demonstrates the symphysis (S), vagina (V), and proximal part of the urethra (arrows). The posterior urethrovesical angle is intact, and the bladder neck is high enough to indicate a normal finding. The conspicuous echofree periurethral area cranial to the symphysis represents scarring after the colposuspension procedure.

13

Fig. 18.14 A perineal sonogram two weeks after a vaginal hysterectomy displays the symphysis (S), bladder (B), vagina (V), and rectum (R) and shows a postoperative infiltrate around the vaginal stump (I). The arrows indicate the course of the urethra and the inferior border of the symphysis. The scan indicates normal conditions at rest.

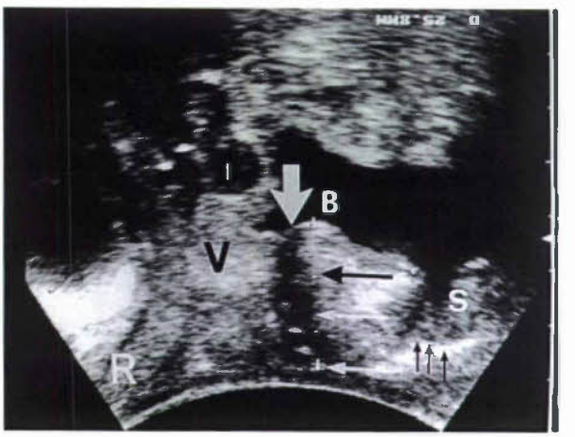

14

Transvaginal Ultrasound

Transvaginal ultrasound, like transrectal ultrasound and hysterosonography, falls under the heading of *endosonography*, a method in which the ultrasound probe is introduced into a body cavity.

19 Development and Current Role of Transvaginal Ultrasound

Historical Development

Since the resolution of an ultrasound transducer can be significantly improved only by increasing its frequency, which also shortens the penetration depth of the beam, it became clear that higher-frequency probes could be used effectively only when placed as close as possible to the organ of interest. As a result, the transvaginal approach was already being used in gynecologic and obstetric ultrasound by the mid-1960s as a way of scanning the pelvic organs at close range. The earliest attempts involved introducing a rod-shaped A-mode probe into the vagina. Orientation was often a very difficult problem with an endovaginal rod, however, and this prompted the idea of incorporating ultrasound into the bimanual pelvic examination [1]. This was accomplished by using a thimble-shaped ultrasound probe [1–3] that was placed over the tip of the palpating finger [1] (Fig. 19.**1**). A-mode probes with a thimble design were successfully used to detect IUDs within the uterine cavity [2] (Fig. 19.**2**). On the whole, however, this one-dimensional A-mode examination was found to be rather laborious. Real progress came with the development of a probe capable of generating a two-dimensional ultrasound image. It was Alfred Kratochwil, the father of endovaginal ultrasound, who chiefly promoted the development and clinical application of this probe. As early as 1969, Kratochwil reported on his experience with this new endovaginal sectional imaging technique [4]. The ultrasound probe was mounted on a colposcope stand (Figs. 19.**3**, 19.**4**) and was linked to a mechanism that allowed the probe to be advanced and retracted on its longitudinal axis and also rotated 360° [1]. The transducer element was placed at the tip of the rod-shaped probe, and the beam was emitted at right angles to the long axis of the rod [1]. An image was generated by circular tracking of the lateral beam. By combining this method with the time-motion (M-mode) technique, Kratochwil was able to detect embryonic heart activity at an early stage of pregnancy [1]. Because the probe had to be manually rotated to generate the compound scan, the apparatus was somewhat cumbersome to use. Also, the laterally directed beam was not ideal for pelvic examinations, and for these reasons the method was soon forgotten. Endovaginal ultrasound was rediscovered during the 1980s by Popp [5,6] following the development of improved endovaginal probes. The first of these probes were sector scanners that had a relatively small field of view, creating problems of orientation in the true pelvis and making it difficult to localize findings to specific organs. Linear probes were also used [7,8]. A breakthrough came in 1985 when the Austrian firm Kretztechnik introduced a wide-angle end-firing vaginal probe with a 240° sector display, providing examiners with a panoramic view of the internal genitalia.

Popp hosted a workshop on gynecologic endosonography in Hamburg in April, 1985 [9]. Despite the initial skepticism of many gynecologists, transvaginal ultrasound soon became widely practiced, first at various German-speaking centers [10–22] and then throughout the world [23–33]. Owing to its numerous advantages in examinations of the true pelvis, transvaginal scanning has now become an indispensable part of diagnostic ultrasound, and the endovaginal probe has become a standard tool in the imaging armamentarium of gynecologists and obstetricians.

Current Role

Unlike traditional transabdominal ultrasound, transvaginal ultrasound makes it possible to scan the organs of the true pelvis even when the patient does not have a full bladder [10,17,32]. This alone offers several advantages [10,12,17–19,21,34,35].

The examination can be carried out at any time, eliminating waiting periods for both the patient and physician. The patient can be scanned immediately after the manual pelvic examination, offering an ideal opportunity to compare the palpation and sonographic findings. Also, the length of the examination is not limited by painful bladder distension. This makes the examination suitable for patients who are unable to retain the urine long enough for transabdominal scanning and for those who cannot achieve normal bladder filling, such as dialysis patients.

Another major advantage of transvaginal over transabdominal ultrasound is that it provides significantly better resolution, particularly of structures situated low in the true pelvis. This is made possible by the fact that the endovaginal probe can be placed relatively close to the organ of interest. Because of this proximity, higher ultrasound frequencies can be used for imaging, and the organ under study can be positioned within the focal zone of the transducer. Owing to these advantages, a retroflexed uterus can be imaged with the same clarity and precision as an anteflexed uterus.

Moreover, while the quality of transabdominal images may occasionally be compromised by a thick or scarred abdominal wall and by gas-filled loops of bowel, this is not a problem when scans are acquired with an endovaginal probe.

When a panoramic probe is used, it provides a comprehensive, wide-angle view of the true pelvis in which the entire uterus can be evaluated, both ovaries can be seen and directly compared for size, and both pelvic walls can be simultaneously visualized.

In addition, needle aspiration of a cyst or ovarian follicle guided by transvaginal ultrasound is advantageous in comparison with transabdominal guidance, in that the needle has to travel a much shorter distance. Needle aspirations can also be performed transvaginally in cases in which adhesions would obstruct transabdominal percutaneous access.

Transvaginal ultrasound has some disadvantages as well. The beginner in particular has to become accustomed to viewing the organs from an unfamiliar perspective. Also, the penetration depth is limited by anatomical constraints and by the physical limitations of the probe. As a result, the mid- and upper abdomen are not accessible to transvaginal imaging. This limitation also makes the method poorly suited for the investigation of high-sited ovarian masses and for the monitoring of advanced fetal growth.

Another limitation of transvaginal ultrasound is that it cannot be used in all patients. For example, elderly women with a very narrow vagina or vaginal synechiae are not good candidates for endovaginal scanning. However, this problem has been reduced by the availability of very thin vaginal probes, which often make it possible to carry out a satisfactory examination. Thin probes may also be an option in young patients with an intact hymen. In cases in which a probe cannot be inserted into the vagina, the probe can be positioned at the introitus for *introital ultrasound*, which may be satisfactory in some cases.

Some women might conceivably find endovaginal scanning objectionable. However, experience in recent years shows that patient find

the method very acceptable and that this is a negligible concern. In a 1987 study by Merz, comparing transabdominal and transvaginal sonography [17], the patient acceptance rate was 100%, with 38% of the women stating that transvaginal scanning was more comfortable than transabdominal scanning, owing to the lack of bladder pressure. Only 9% of the patients, most of whom had a narrow vagina, stated a preference for abdominal scanning; 53% reported no difference between the two methods (Table 19.**1**).

For the examiner, transvaginal ultrasound provides a significant gain in diagnostic information (Figs. 19.**5**–19.**10**). In the study cited above [17], 52% of the cases were diagnosed more quickly and accurately with transvaginal ultrasound than with abdominal ultrasound. The vaginal scan was judged to be inferior to the abdominal scan in only 2% of the cases, because the structures of interest were located at a relatively high level. In the remaining 46% of cases, the transvaginal and transabdominal scans were considered to provide identical information (Table 19.**2**).

Table 19.**3** provides an overview of the advantages and disadvantages of transvaginal ultrasonography.

Table 19.**1** Patient ratings of transvaginal versus transabdominal ultrasound (n = 184) [17]

No preference	53%
Prefer transvaginal	38%
Prefer transabdominal	9%

Table 19.**2** Examiner ratings of transvaginal versus transabdominal ultrasound (n = 184) [17]

Better information with transvaginal ultrasound	52%
Same information with transvaginal and transabdominal ultrasound	46%
Better information with transabdominal ultrasound	2%

Table 19.**3** Advantages and disadvantages of transvaginal ultrasound in comparison with transabdominal ultrasound

Advantages	Disadvantages
• The examination is performed with an empty bladder. Therefore: – The patient can be examined at any time – There are no waiting periods – The images can be promptly and optimally compared with palpable findings – Patients who cannot adequately fill their bladder can still be scanned	• The examiner has to adjust to the unfamiliar orientation of transvaginal images
• Better image resolution owing to the use of higher-frequency, short-focus probes (pelvic organs are always within the focal zone of the probe)	• The mid- and upper abdomen cannot be scanned (hence the method cannot detect high ovarian tumors or monitor fetal growth)
• Image quality is not degraded by obese or scarred abdominal wall or by gas-filled bowel loops	• The method cannot be used in some women (e.g., patients with an intact hymen, very narrow vagina, or vaginal synechiae)
• Provides a panoramic view of the true pelvis	• The method may be objectionable to some patients
• The needle has to travel a much shorter distance for oocyte retrieval or cyst aspiration	

References

1 Kratochwil A. Anfänge der Vaginosonographie. In: Merz E, editor. Vaginosonographie. Stuttgart: Enke, 1992: 1–5.
2 Mizuno S, Takeuchi H, Nakano K. Diagnostic application of ultrasound in obstetrics and gynecology. In: Grossmann CC, Holmes JH, Joyner C, Purnell EW, editors. Diagnostic ultrasound: proceedings of the First International Conference in Pittsburgh, 1965. New York: Plenum Press, 1966: 452–64.
3 Winters HS. Ultrasound detection of intrauterine contraceptive devices. Am J Obstet Gynecol 1966;95:880–1.
4 Kratochwil A. Ein neues vaginales Schnittbildverfahren. Geburtshilfe Frauenheilkd 1969;29:379–85.
5 Popp LW, Lueken RP, Müller-Holve W, Lindemann HJ. Gynäkologische Endosonographie: erste Erfahrungen. Ultraschall 1983;4:92–7.
6 Popp LW. Gynäkologische Endosonographie. In: Otto RC, Jann FX, editors. Ultraschalldiagnostik 82. Stuttgart: Thieme, 1983: 466–9.
7 Debus-Thiede G, Wagner U, Schürmann R, Christ F. Erste Erfahrungen mit der transvaginalen Sonographie von Urethra und Blase im Rahmen der Inkontinenz-Diagnostik. Geburtshilfe Frauenheilkd 1985;45:891–4.
8 Haid C, Zech H, Martin J. Verbesserte Frühdiagnose der intrauterinen Schwangerschaft durch Ultraschall-Vaginalsonde. Geburtshilfe Frauenheilkd 1985;45:371–4.
9 Popp LW. Gynäkologische Endosonographie. Quickborn, Germany: Klemke, 1986.
10 Bernaschek G. Vorteile der endosonographischen Diagnostik in Gynäkologie und Geburtshilfe. Geburtshilfe Frauenheilkd 1987;47:471–6.
11 Bernaschek G. Empfehlungen für eine einheitliche endosonographische Dokumentation in Geburtshilfe und Gynäkologie. Ultraschall Klin Prax 1989;4:45–8.
12 Degenhardt F. Atlas der vaginalen Ultraschalldiagnostik. Stuttgart: Wissenschaftliche Verlagsgesellschaft, 1988.
13 Deutinger J, Bernaschek G. Die vaginosonographische Pelvimetrie als neue Methode zur sonographischen Bestimmung der inneren Beckenmasse. Geburtshilfe Frauenheilkd 1986;46:345–7.
14 Deutinger J, Reinthaller A, Riss P, Bernaschek G, Csaicsich P, Fischl F, et al. Comparison of the results of vaginal and abdominal follicle scans. Arch Gynecol Obstet 1987;241:171–6.
15 Duda V, Thein C, Rode G. Vaginalsonographie. Extr Gynaecol 1987;11:264–72.
16 Kemeter P, Feichtinger W. Transvaginal oocyte retrieval using a trans-vaginal sector scan probe combined with an automated puncture device. Hum Reprod 1986; 1:21–4.
17 Merz E. Transvaginale oder transabdominale Ultraschalldiagnostik? Ein Vergleich zweier Methoden in Gynäkologie und Geburtshilfe. Ultraschall Klin Prax 1987;2: 87–94.
18 Merz E. Sonographische Diagnostik in Gynäkologie und Geburtshilfe. Stuttgart: Thieme, 1988.
19 Merz E. Transvaginale Sonographie in der Gynäkologie. In: Friedberg V, Thomsen K, editors. Gynäkologie und Geburtshilfe, vol. III/2. Stuttgart: Thieme, 1988: 24–8.
20 Rempen A. Vaginale Sonographie der intakten Gravidität im ersten Trimenon. Geburtshilfe Frauenheilkd 1987;47:477–82.
21 Sautter T. Transvaginale Sonographie. Lehrbuch und Lehratlas. Stuttgart: Enke, 1990.
22 Schurz B, Eppel W, Egarter C, Wenzel R, Reinold E. Vaginosonographie in der Gynäkologie. Ultraschall 1989;10:90–7.
23 Baber RJ, McSweeney MB, Gill RW, Porter RN, Picker RH, Warren PS, et al. Transvaginal pulsed Doppler ultrasound assessment of blood flow to the corpus luteum in IVF patients following embryo transfer. Br J Obstet Gynaecol 1988;95:1226–30.
24 Bonilla-Musoles F, Pardo G, Perez-Gil M, Serra V, Pellicer A. Abdominal ultrasonography versus transvaginal scanning: accuracy in follicular development evaluation and prediction for oocyte retrieval in stimulated cycles. J Clin Ultrasound 1989;17: 469–73.
25 Cacciatore B, Lehtovirta P, Wahlstrom T, Ylanen K, Ylostalo P. Contribution of vaginal scanning to sonographic evaluation of endometrial cancer invasion. Acta Oncol 1989;28:585–8.
26 Granberg S, Crona N, Enk L, Hammarberg K, Wikland M. Ultrasound-guided puncture of cystic tumors in the lower pelvis of young women. J Clin Ultrasound 1989; 17:107–11.
27 Kurjak A, Zalud I. Transvaginaler Farbdoppler für die Beurteilung von gynäkologischen Pathologien im kleinen Becken. Ultraschall Med 1990;11:164–8.
28 Leroy B, Jeny R. Vaginosonographie mit Multiarray- und Rotationsscannern. In: Popp LW, editor. Gynäkologische Endosonographie, 1. Quickborn, Germany: Klemke, 1986: 67–77.
29 Levi S, Lyons EA, Lindsay DJ. Early diagnosis of nonviable pregnancy with endovaginal ultrasound. Radiology 1988;167:383–5.
30 Mendelson EB, Bohm-Velez M, Joseph N, Neiman HL. Gynecologic imaging: transabdominal and transvaginal sonography. Radiology 1988;166:321–4.
31 Rodriguez MH, Platt LD, Medearis AL, Lacarra M, Lobo RA. The use of transvaginal sonography for evaluation of postmenopausal ovarian size and morphology. Am J Obstet Gynecol 1988;159:810–4.
32 Timor-Tritsch IE, Bar-Yam Y, Elgali S, Rottem S. The technique of transvaginal sonography with the use of a 6.5 MHz probe. Am J Obstet Gynecol 1988;158:1019–24.
33 Wikland M, Enk L, Hammarberg K, Nilsson L. Use of vaginal transducer for oocyte retrieval in an IVF/ET program. J Clin Ultrasound 1987;15:245–51.
34 Bernaschek G, Deutinger J, Kratochwil A. Endosonography in obstetrics and gynecology. Berlin: Springer, 1990.
35 Merz E, editor. Vaginosonographie. Stuttgart: Enke, 1992.

Historical Development

Fig. 19.1 A thimble-shaped ultrasound probe for endovaginal use (from Kratochwil [1]).

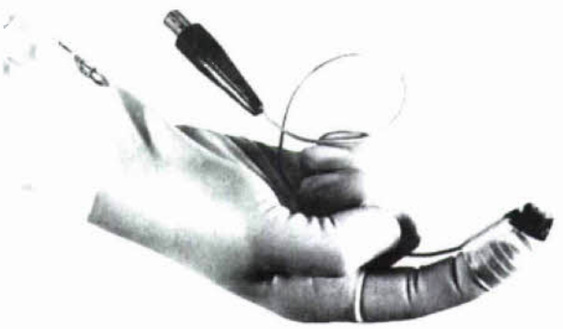

1

Fig. 19.2 Ultrasound incorporated into the bimanual examination (from Kratochwil [1]).

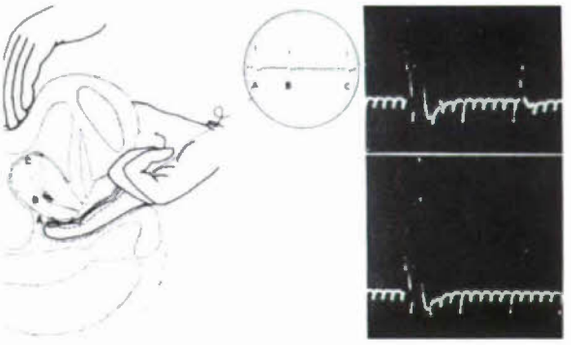

2

Fig. 19.3 First endovaginal probe, mounted on a colposcope stand (from Kratochwil [1]).

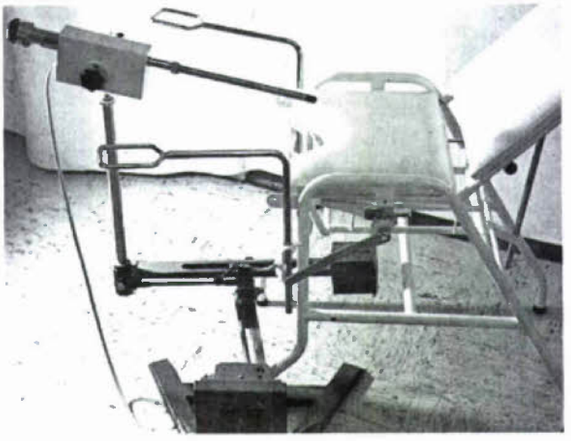

3

Fig. 19.4 The first endovaginal probe.

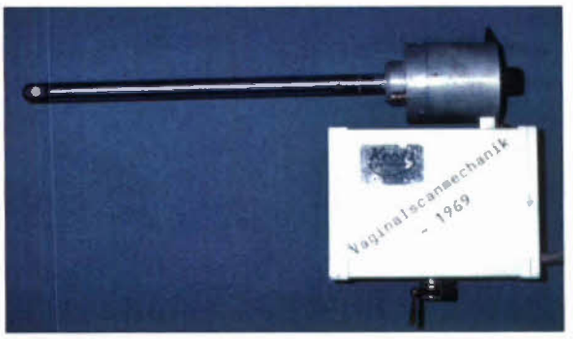

4

5

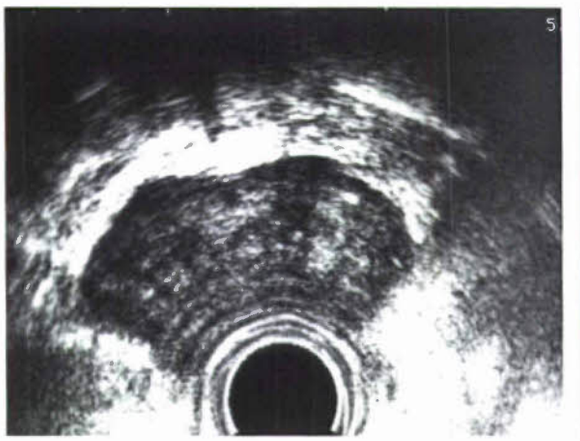

6

Comparison of Transabdominal and Transvaginal Ultrasound

Fig. 19.5 Myomas of the posterior uterine wall demonstrated by transabdominal ultrasound (transverse scan).

Fig. 19.6 The same myomas demonstrated by transvaginal ultrasound (coronal scan). The transvaginal scan defines the internal structure of the myomas with greater clarity.

7

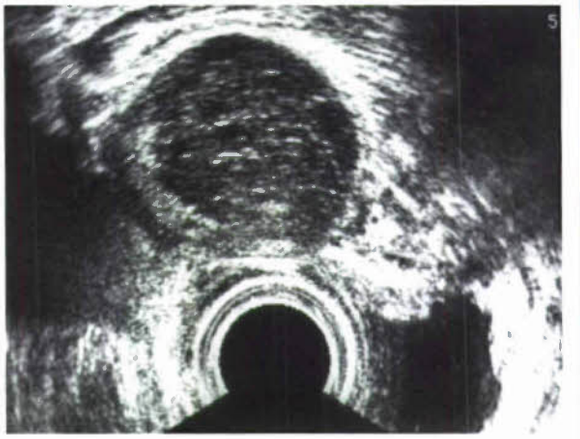

8

Fig. 19.7 Transabdominal sonogram of a hemorrhagic corpus luteum cyst (longitudinal scan).

Fig. 19.8 Transvaginal sonogram of the same hemorrhagic corpus luteum cyst (coronal scan). The internal echoes are defined more clearly.

9

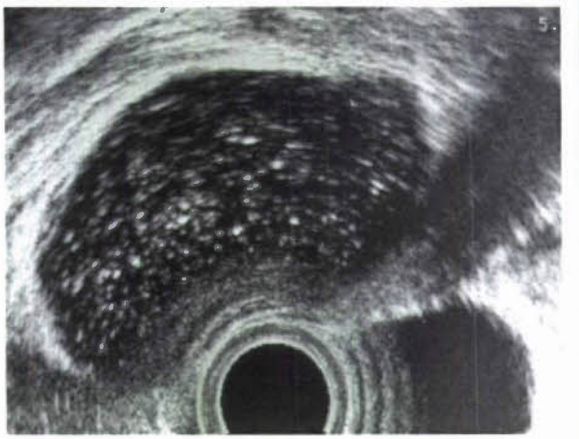

10

Fig. 19.9 Transabdominal sonogram of a mucinous cystoma located behind the vaginal stump (longitudinal scan).

Fig. 19.10 Transvaginal sonogram of the lesion in Fig. 19.9 defines the internal echoes more clearly (coronal scan).

20 Ultrasound Probes, Image Orientation, and Examination Technique

Ultrasound Probes

All manufacturers of ultrasound equipment now supply one or more endovaginal probes for transvaginal ultrasound imaging. All of these probes are of the end-firing type, meaning that their scanning direction is essentially in line with the longitudinal axis of the probe. The differences between the probes supplied by different manufacturers affect the design (Fig. 20.**1**), the scanning principle (mechanical or electronic), the field of view (Fig. 20.**2**), the scanning angle (symmetrical or asymmetrical, Fig. 20.**3**), the sound frequency, the Doppler and color Doppler capabilities, and compatibility with needle guides [1] (Table 20.**1**).

The broader the *field of view* that can be achieved with the vaginal probe, the easier it is for the examiner to establish orientation in the true pelvis and the less the probe has to be manipulated within the vagina to display all necessary organs. The best view of the pelvis is obtained with a panoramic probe, which provides a 240° field of view. This probe can display the entire uterus in sagittal section while providing a simultaneous coronal view of both ovaries, which is ideal for comparing them with each other.

At present, *mechanical probes* are the only type of vaginal probe that can provide a full 240° field of view. The panoramic probe is a rotary-type scanner in which the transducer elements are mechanically rotated around a fixed axis. Other mechanical probes use a "wobbler" principle, in which one or more transducer elements move rapidly back and forth in an oscillating fashion. This type of probe can provide up to a 200° field of view.

Electronic probes may have a phased-array or curved-array design, the curved array being the more common. At present, electronic probes are limited by technical constraints to a maximum field of 160°, but the majority have a 120° viewing angle. The disadvantage of electronic probes in comparison with mechanical probes is that their smaller field of view makes orientation in the true pelvis somewhat more difficult. The main advantages of electronic probes are their excellent near-field resolution and their compatibility with color Doppler, whereas mechanical probes have only a gray-scale Doppler capability (Table 20.**2**). Phased-array probes with a viewing angle of 90° or less can display only a small portion of the true pelvis at any one time. Making a survey comparable to a panoramic scan requires considerably greater probe manipulation within the vagina, which is uncomfortable for many patients [1].

To reduce the need for endovaginal manipulations with a 90° probe and still obtain a wide field of view, some manufacturers have developed probes that allow lateral deflection of the beam. By continually shifting the scan laterally, the probe can extend the field of view in the true pelvis up to a range of 220° without having to be physically moved within the vagina. One drawback of this technique is that the laterally angled beam can deviate markedly from the longitudinal axis of the probe, depending on the field-of-view setting; this may create more confusion for some examiners than it aids orientation.

The same is true of probes with an *asymmetrical scanning angle* (Fig. 20.**3**), in which the beam is not directly in line with the probe axis, but is angled to the side by 15–45°. An angled scan can be advantageous for evaluating an anteflexed or retroflexed uterus in the sagittal plane, but tends to be confusing in the coronal plane because when the probe shaft is held straight, the examiner cannot obtain a symmetrical, straight-ahead view into the true pelvis.

The general rule for *probe frequency* is that the higher the transmission frequency, the sharper the resolution and the better the image quality in the near field. However, higher frequencies are associated with a reduction in the depth of penetration (Table 20.**3**). While a 5 MHz probe can provide good resolution to a depth of approximately 8 cm, a 7.5 MHz probe has a useful range of only about 5 cm, with the result that structures in the area of the pelvic wall or pelvic inlet may not be visualized.

Some vaginal probes can be used with a *needle guide* that allows precise needle insertion in the true pelvis.

Table 20.**1** Criteria that distinguish commercially available end-firing vaginal probes

- Design
- Scanning principle (mechanical or electronic)
- Angle of beam divergence
- Scan angle (symmetrical or asymmetrical)
- Transducer frequency
- Doppler and color Doppler compatibility
- Compatibility with a needle guide

Table 20.**2** Differences between mechanical and electronic vaginal probes

	Mechanical probes	Electronic probes
Probe types	Rotary scanner Wobbler	Phased-array and curved-array probes
Maximum beam divergence	240°	160°, usually 90–120°
Immediate near-field resolution	Reasonably good	Very good
Gray-scale Doppler compatibility	Yes	Yes
Color Doppler compatibility	No	Yes

Table 20.**3** Depth of beam penetration (≈ 40/MHz) as a function of probe frequency

Frequency	Approximate penetration depth
3.5 MHz	12 cm
5.0 MHz	8 cm
7.0 MHz	6 cm
7.5 MHz	5 cm
10.0 MHz	4 cm

Scan Planes and Image Orientation

Scan Planes

In contrast to traditional abdominal ultrasound, in which the pelvis can be scanned in *sagittal* and *transverse* planes but not in the coronal plane, transvaginal scans can be acquired in the *sagittal* and *coronal* planes, but not in the transverse plane (Figs. 20.**4**–20.**13**).

Image Orientation

While a fairly standard image orientation format has been established for abdominal ultrasound (*sagittal scans:* top of image = anterior, bottom of image = posterior, right side of image = caudal, left side of image = cranial; *transverse scans:* top of image = anterior, bottom of image = posterior, right side of image = patient's left side, left side of image = patient's right side; see Table 2.**3**, p. 7), various different conventions are still followed in articles and even recent textbooks on transvaginal ultrasound, especially in the sagittal plane [2–10]. This lack of consistency can be particularly confusing for less experienced examiners. For example, the probe itself may be displayed at either the top or bottom of sagittal scans, and anterior and posterior are frequently interchanged (Fig. 20.**4**). Perhaps the most confusing method is to orient transvaginal images in the same way as transabdominal scans, with the tip of the probe displayed at the top of the image. This is particularly common in the United States, in contrast to Europe, where 59% of transvaginal sonograms are displayed the opposite way [11,12] – i.e., with the probe at the bottom of the image. Because the probe is introduced from the caudal aspect, it is more logical to display the image with the probe at the bottom. The advantage of this display mode is that the viewer can tell at once that the image is a transvaginal scan.

Anterior–posterior is another area of confusion. Although standard guidelines have repeatedly been issued in Germany, for example, for displaying transvaginal sonograms [1,6,7,13–17] (Table 20.**4**), there are still textbooks [3,9] in which the left side of the image is anterior (i.e., with the bladder appearing on the left side).

The guidelines recommended by the Ultrasound Division of the German Society of Gynecology and Obstetrics [17] are perhaps the easiest to understand, as they are derived from transabdominal imaging. If we imagine that a patient lying supine for a transabdominal scan is brought to an upright position (Fig. 20.**5**), then the orientation in a sagittal scan (Figs. 20.**6**–20.**9**) will be cranial at the top of the image, caudal at the bottom of the image, anterior on the right side of the image, and posterior on the left side of the image. In a coronal scan (Figs. 20.**10**–20.**13**), the right side of the image corresponds to the patient's left side, while the left side of the image corresponds to the patient's right side, just as in an abdominal sonogram (Table 20.**4**).

Table 20.**4** Image orientation in transvaginal ultrasound

Sagittal scans	
Top of image	Cranial
Bottom of image	Caudal
Right side of image	Anterior
Left side of image	Posterior
Coronal scans	
Top of image	Cranial
Bottom of image	Caudal
Right side of image	Left
Left side of image	Right

Examination Technique

Transvaginal scanning can be carried out with the patient in a gynecologic examination chair or on an ordinary examination table. The chair is advantageous in that it allows scanning to be carried out immediately after the bimanual examination. Also, it is easier to angle the vaginal probe to its lowest position, acquiring an angled coronal scan that is excellent for showing retrosymphysial lesions and lesions close to the abdominal wall. This can be done on a table only by placing a cushion under the patient's buttocks. On the other hand, patients often find the table more comfortable than the chair [1], as they can assume a more relaxed position. According to an international survey by Bernaschek et al. [11,12], an examination table is most commonly used in the German-speaking countries (67%), while a gynecologic chair is preferred in other countries (55%).

Regardless of whether a table (Fig. 20.**14**) or gynecologic chair is used, it is advantageous to have a second, separate monitor available for the patient so that she can watch the progress of the examination comfortably without having to crane her neck.

The endovaginal probe is sheathed with an ordinary non-reservoir condom that has been filled at the tip with ultrasound coupling gel (Fig. 20.**15**). The outside of the condom is also lubricated with some ultrasound gel or saline solution.

The examiner should wear rubber gloves, at least when introducing the probe.

After spreading the labia apart with one hand, the examiner carefully inserts the probe into the vagina with the other hand and slowly advances it to the cervix (Fig. 20.**16**). The entire true pelvis can be surveyed in various planes by raising and lowering the probe and by angling it from side to side.

As in abdominal ultrasound, it is helpful to begin transvaginal imaging with a midsagittal scan through the true pelvis to establish orientation before proceeding with a series of coronal sections.

When the examination is completed, the probe is withdrawn as carefully as it was inserted. If the condom has been damaged during the examination, the probe should be thoroughly cleaned with water and treated with a disinfectant solution before it is used again.

Applications of Transvaginal Ultrasound in Gynecology

The universal use of this dynamic examination technique led to a dramatic increase in the areas of its application and the frequency of its use in the space of only a few years. In the field of gynecology, transvaginal ultrasound has almost completely superseded traditional abdominal ultrasound. An overview of the gynecologic applications of transvaginal ultrasound is given in Table 20.5.

Table 20.5 Applications of transvaginal ultrasound in gynecology

- Folliculometry
- Evaluation of the endometrium
- Detection of polycystic ovaries
- Investigation of genital anomalies
- Investigation of unexplained abdominal pain
- Evaluation of pelvic masses
- Tumor follow-up
- IUD localization
- Follicular aspiration (for IVF)
- Aspiration of cysts
- Selective tissue biopsy
- Investigation of postoperative complications
- Doppler examinations
- Investigation of the tubal factor using contrast material
- Three-dimensional imaging

IUD, intrauterine device; IVF, in-vitro fertilization.

References

1 Merz E. Aktueller Stand der Vaginosonographie. Teil 1: Grundlagen und gynäkologische Diagnostik. Ultraschall Med 1994;15:2–10.
2 Bernaschek G, Deutinger J, Kratochwil A. Endosonography in obstetrics and gynecology. Berlin: Springer, 1990.
3 Degenhardt F. Endosonographie in Gynäkologie und Geburtshilfe. Stuttgart: Wissenschaftliche Verlagsgesellschaft, 1994.
4 Fleischer AC, Jones HW 3rd. Early detection of ovarian carcinoma with transvaginal sonography: potentials and limitations. Raven Press, New York 1993.
5 Kurjak A. Ultrasound and the ovary. New York: Parthenon, 1994.
6 Merz E. Ultrasound in gynecology and obstetrics: textbook and atlas. Stuttgart: Thieme, 1991.
7 Merz E. Vaginosonographie. Stuttgart: Enke, 1992.
8 Sautter T. Transvaginale Sonographie. Lehrbuch und Lehratlas. Stuttgart: Enke, 1990.
9 Sohn C, Holzgreve W. Ultraschall in Gynäkologie und Geburtshilfe. Stuttgart: Thieme, 1995.
10 Timor-Tritsch IE, Rottem S. Transvaginal sonography, 2nd ed. New York: Elsevier, 1991.
11 Bernaschek G, Deutinger J, Endler M. Derzeitiger Stand der Vaginosonographie – eine weltweite Umfrage. Geburtshilfe Frauenheilkd 1991;51:729–33.
12 Bernaschek G, Deutinger J. Current status of vaginosonography: a world-wide inquiry. Ultrasound Obstet Gynecol 1992;2:352–6.
13 Bernaschek G. Empfehlungen für eine einheitliche endosonographische Dokumentation in Geburtshilfe und Gynäkologie. Ultraschall Klin Prax 1989;4:45–8.
14 Bernaschek G, Deutinger J. Endosonography in obstetrics and gynecology: the importance of standardized image display. Obstet Gynecol 1989;74:817–20.
15 Bernaschek G. [Basic principles of vaginal ultrasound; in German.] Gynäkologe 1995;28:220–4.
16 Merz E. Sonographische Diagnostik in Gynäkologie und Geburtshilfe. Stuttgart: Thieme, 1988.
17 Merz E. Standardisierung der Bilddarstellung bei der transvaginalen Sonographie. Gynäkol Geburtshilfe 1991;1:37–8.

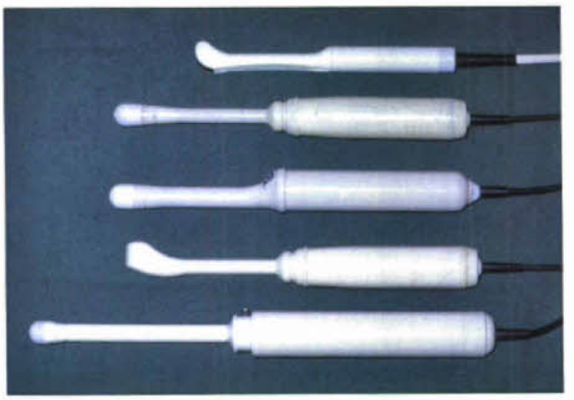

1

Fig. 20.1 Transvaginal ultrasound probes of varying design.

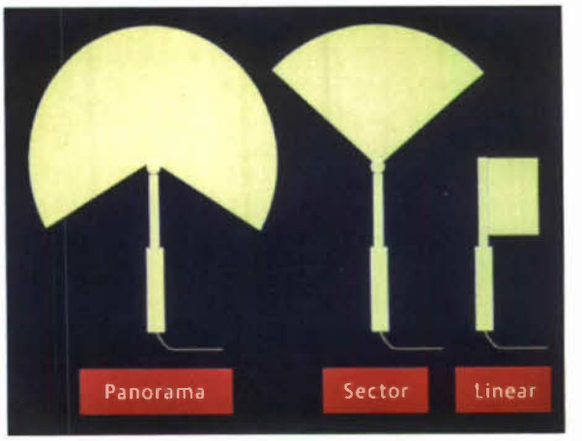

2

Fig. 20.2 Scanning directions and fields of view of different endovaginal probes.

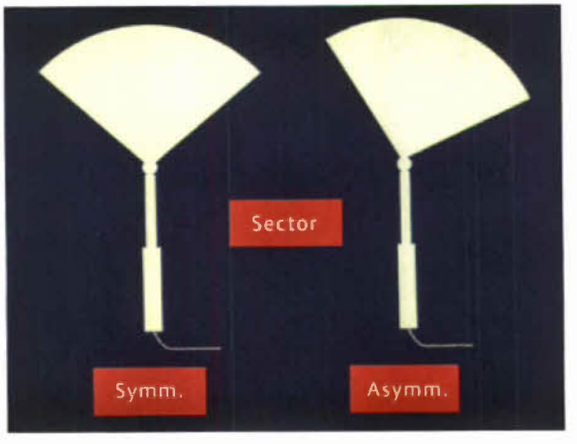

3

Fig. 20.3 End-firing endovaginal probes with symmetrical and asymmetrical scan angles.

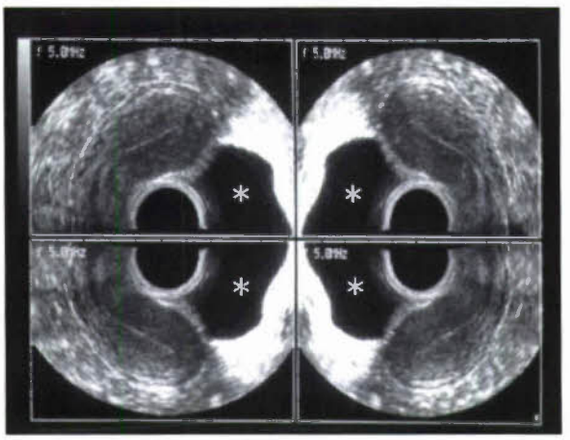

4

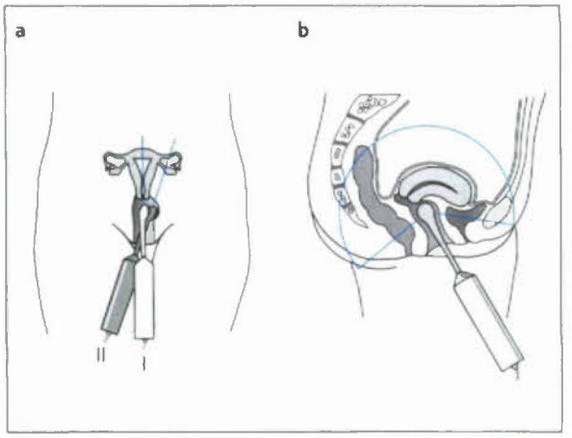

6

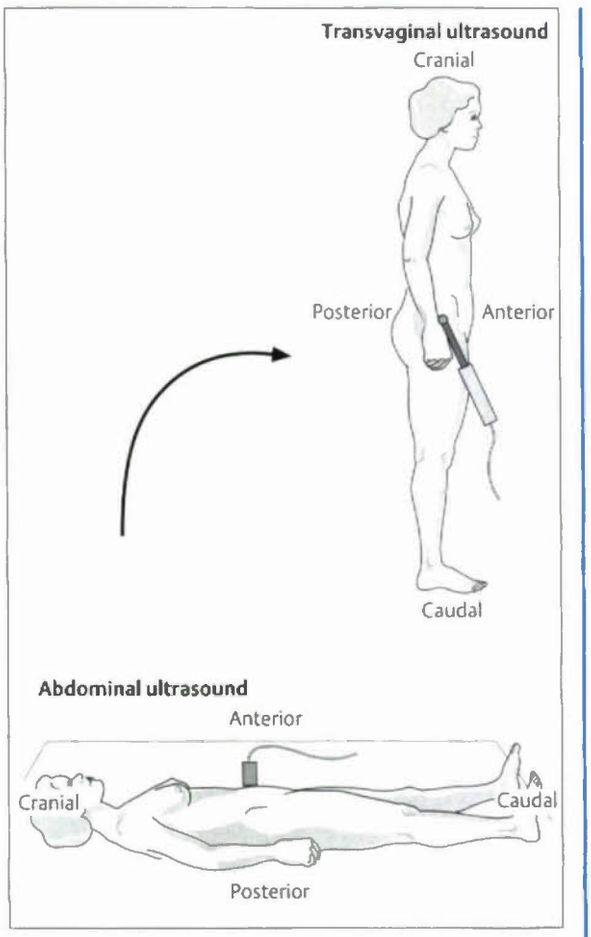

5

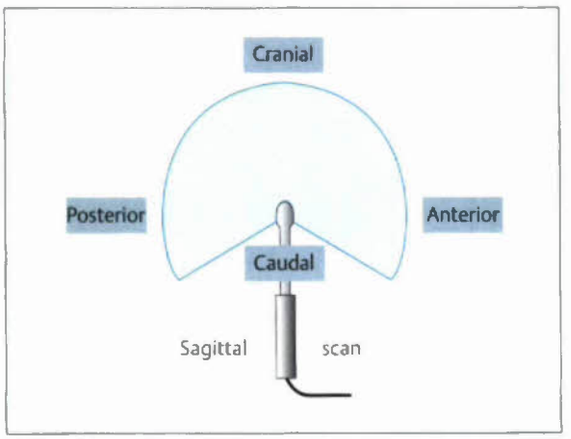

7

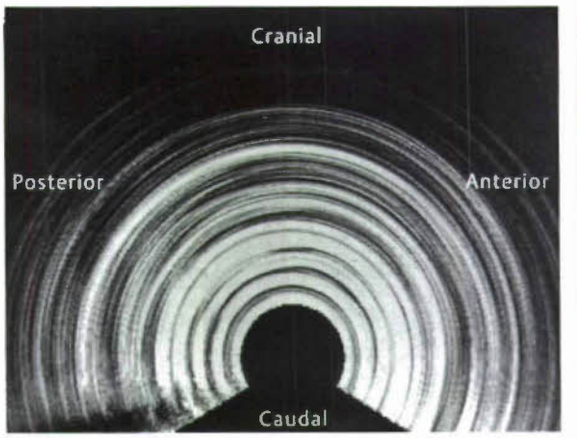

8

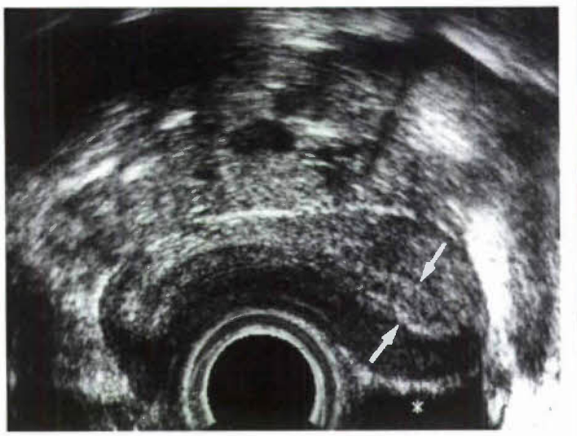

9

Fig. 20.4 Different modes for displaying the image of an anteflexed uterus. * Moderately distended bladder. The recommended display mode is shown on the upper left.

Fig. 20.5 Display modes used in transabdominal and transvaginal ultrasound.

Fig. 20.6 Schematic representation of longitudinal scan planes in transvaginal ultrasound with a 240° end-firing probe.
a Anterior aspect (I = midsagittal scan, II = oblique longitudinal scan).
b Lateral aspect.

Fig. 20.7 Display mode for sagittal images.

Fig. 20.8 Image orientation in a longitudinal scan acquired with an end-firing panoramic endovaginal probe (240°).

Fig. 20.9 Longitudinal scan of a normal-sized anteflexed uterus with a prominent, streak-like endometrial echo (→). The bladder (*) is almost empty.

Fig. 20.**10** Schematic diagram of the coronal planes that can be imaged with an end-firing 240° endovaginal probe.
a Anterior aspect. For clarity, the uterus is shown in a straightened position.
b Lateral aspect (III = transverse scan through the cervix, IV = transverse scan through the uterine corpus).

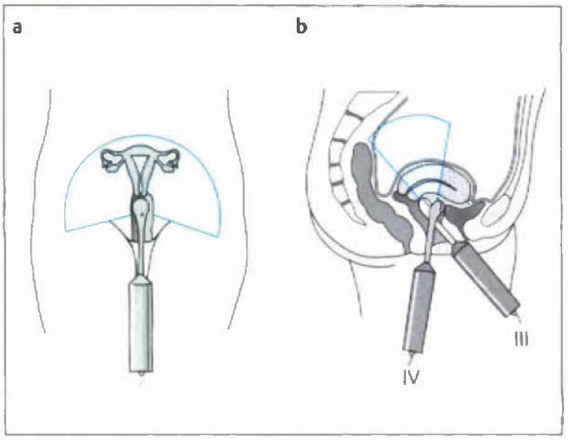

10

Fig. 20.**11** Image orientation in transvaginal coronal scans.

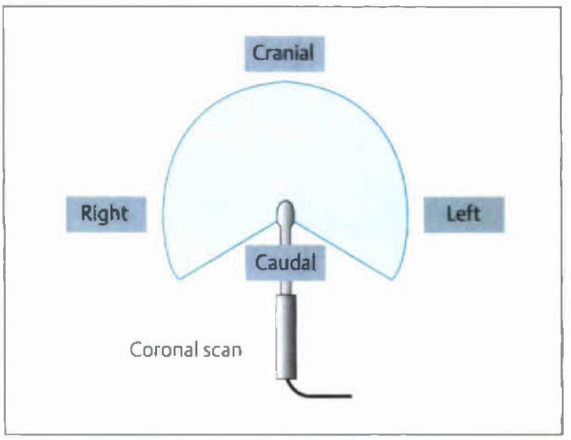

11

Fig. 20.**12** Image orientation with an end-firing panoramic endovaginal probe (240°) in the coronal plane.

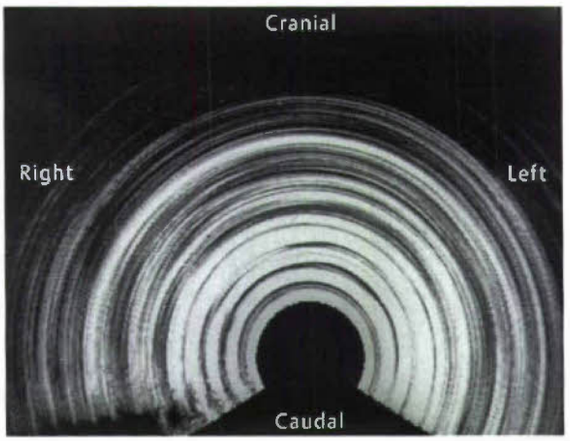

12

Fig. 20.**13** Coronal scan of the true pelvis showing the anteflexed uterus in a transverse section. Hyperechoic secretory endometrium. The relatively hypoechoic ovaries are displayed on either side of the uterine corpus.

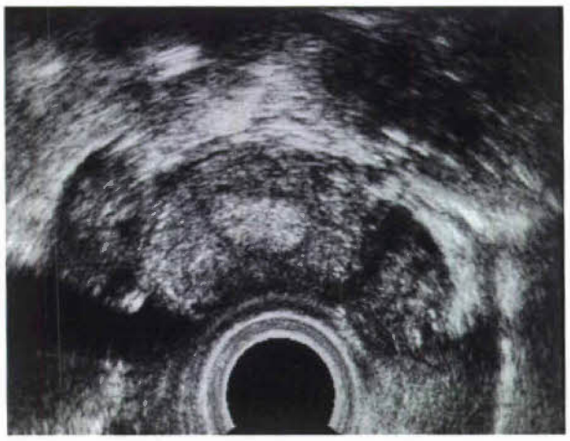

13

Fig. 20.**14** Set-up for a transvaginal ultrasound examination on a table. The examiner sits on the left side of the patient. The examiner and patient each have their own monitor.
1 Midsagittal scan
2 Oblique sagittal scan through the right adnexal region
3 Oblique sagittal scan through the left adnexal region

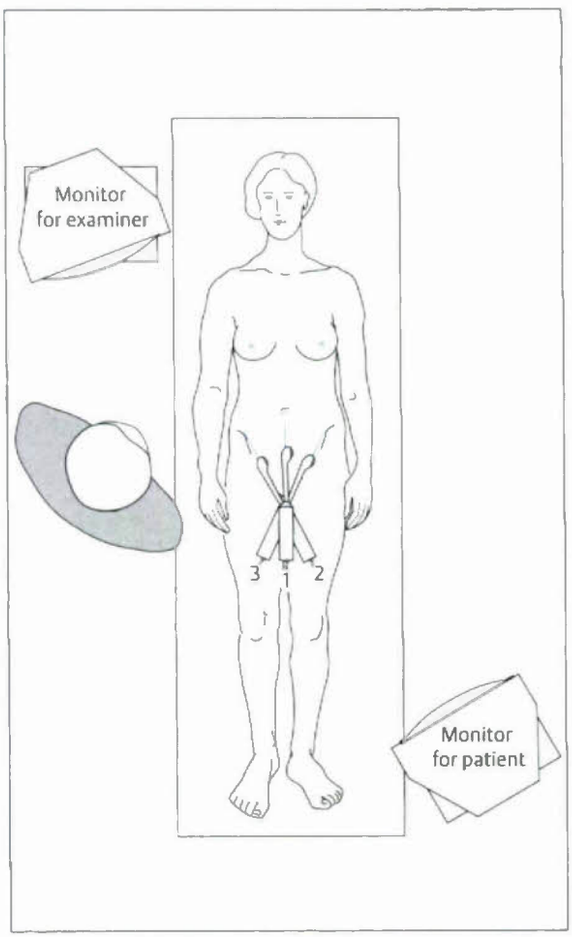

14

Fig. 20.**15** An endovaginal probe sheathed in a condom. Ultrasound coupling gel has been applied to the front end of the condom.

15

Fig. 20.**16** The endovaginal probe inserted.

16

21 Anatomy of the Female Pelvis in Transvaginal Ultrasound

Unlike abdominal ultrasound, in which the full urinary bladder displaces the uterus and adnexa into an artificial position, transvaginal ultrasound can demonstrate these organs in their natural anatomical position [1–12] (Figs. 3.**1**, 21.**1**–21.**3**).

Vagina

When the ultrasound probe is inserted only a short distance into the vagina, a longitudinal sagittal scan will display the vagina as a relatively hypoechoic tubular structure with a wall thickness of 2–3 mm, located posterior to the bladder (Figs. 21.**3**, 21.**4**). As the probe is slowly advanced toward the cervix, the vaginal lumen will be seen to expand. Abnormalities in the vaginal wall are easily missed if they are in direct proximity to the probe tip and therefore outside the focal zone of the transducer. To scrutinize a particular area of the vagina, the examiner should withdraw the vaginal probe by about 2–3 cm.

Uterus

The uterus is a pear-shaped organ situated midway between the bladder and rectum and held loosely in place by its suspensory apparatus (the uterine round ligaments, cardinal ligaments, and sacrouterine ligaments). Its position depends on various factors: body posture, the degree of distension of surrounding organs, and the condition of its suspensory apparatus. When the bladder is empty, the uterus will usually be found in an anteverted and anteflexed position, but occasionally it may be retroflexed or straight (Fig. 21.**5**). A retroflexed uterus is most commonly found in multiparous women with stretched uterine ligaments.

When a panoramic (240°) probe is used, both the position and overall size of the uterus can be evaluated in the midsagittal scan (Fig. 21.**6**). Probes with a smaller sector angle may provide only partial views, depending on the size of the uterus. With an *anteflexed uterus*, the probe tip will usually enter the anterior vaginal fornix, so that the cervix appears posterior to the probe, the uterine fundus cranial or anterior, and the slightly distended bladder anterior to the probe in the transvaginal scan (Fig. 21.**7**). With a *retroflexed uterus*, on the other hand, the probe tip usually enters the posterior fornix, so that the uterine fundus appears caudal to the probe, the cervix cranial or anterior, and the bladder anterior (Fig. 21.**8**). In patients with a *straight uterus*, the tip of the vaginal probe will lie just anterior to the cervix, and the uterine corpus will lie in direct continuity with the cervical os. While the uterine corpus and cervix can be defined equally well in the anteflexed and retroflexed uterus by transvaginal scanning, the corpus is often difficult to evaluate in a straight uterus (Fig. 21.**9**). The examiner can aid visualization in some of these cases by placing the left hand above the pubic symphysis and pressing inward against the vaginal probe, which will sometimes provide a better view of the uterine corpus. In other cases, the best solution is to reexamine the patient with a different degree of bladder distension.

As a rule, the uterine corpus and cervix have a relatively homogeneous internal echo pattern of moderate echogenicity. Occasionally, the cervix is found to contain rounded, echo-free zones that represent individual nabothian cysts and are not abnormal (Chapter 27). In a midsagittal scan through the uterus, the uterine vessels appear as separate echo-spared areas in the outer third of the myometrium (Fig. 21.**10**). At the center of the uterus, the endometrium contrasts sharply with the less echogenic myometrium (Fig. 21.**10**). The changing endometrial patterns familiar in abdominal ultrasound can be appreciated transvaginally at different points during the menstrual cycle (Chapter 22) [13–18].

The hypoechoic rim surrounding the endometrium is produced by the relatively well-visualized, compact zone of the inner third of the myometrium (Fig. 21.**10**) [19].

Uterine Biometry

The uterus of a sexually mature nullipara has average sonographic dimensions of 7.3 cm (uterine length) × 4.0 cm (corpus width) × 3.2 cm (corpus height) [20]. Generally, these dimensions are increased in women who have delivered one or more children (Table 21.**1**). The uterus decreases markedly in size after menopause (≤ 5 years), measuring an average of approximately 6.7 × 3.6 × 3.1 cm (Fig. 21.**11**). Uterine dimensions continue to decrease with increasing postmenopausal age (≥ 5 years) (Table 21.**1**) [20].

Because the uterine corpus and cervix do not lie on a straight line when the bladder is empty or only slightly distended, the best way to determine total uterine length is to measure the corpus and cervix separately and add the values together (Fig. 21.**12**). The corpus height and cervix height are measured in the same sagittal plane perpendicular to the long axis of the uterus. When these dimensions are measured in a coronal scan, they are taken in an oblique plane that distorts the measurements, causing them to appear larger than they really are.

The corpus width and cervical width are determined in angled coronal scans through the true pelvis, the exact angle of the scans depending on the uterine position. With an anteflexed uterus, the uterine corpus is displayed in transverse section with an anteriorly angled coronal scan (Figs. 21.**13**, 21.**14**), and the cervix is displayed in transverse section with a posteriorly angled coronal scan (Figs. 21.**13**, 21.**15**).

Table 21.1 Uterine dimensions in women of reproductive age and in postmenopausal women as a function of parity and years after menopause (adapted from Merz et al. [20])

Parity or menopausal status	0-para x (SD) cm	1-para x (SD) cm	≥ 2-para x (SD) cm	MP ≤ 5 years x (SD) cm	MP > 5 years x (SD) cm
Uterine length	7.3 (0.8)	8.3 (0.8)	9.2 (0.8)	6.7 (0.7)	5.6 (0.9)
Corpus length	4.4 (0.6)	4.9 (0.6)	5.6 (0.9)	3.8 (0.5)	3.3 (0.6)
Corpus width	4.0 (0.6)	4.6 (0.5)	5.1 (0.5)	3.6 (0.5)	3.1 (0.5)
Corpus height	3.7 (0.5)	3.9 (0.5)	4.3 (0.6)	3.1 (0.4)	2.5 (0.4)
Cervical length	2.9 (0.5)	3.4 (0.5)	3.7 (0.6)	2.9 (0.4)	2.4 (0 5)
Cervical width	2.9 (0.5)	3.3 (0.5)	3.4 (0.5)	2.7 (0.5)	2.3 (0.4)
Cervical height	2.6 (0.4)	2.7 (0.4)	3.0 (0.6)	2.4 (0.4)	2.1 (0.4)
Corpus–cervix ratio	1.6 (03)	1.6 (0.4)	1.5 (0.3)	1.4 (0.2)	1.4 (0.2)

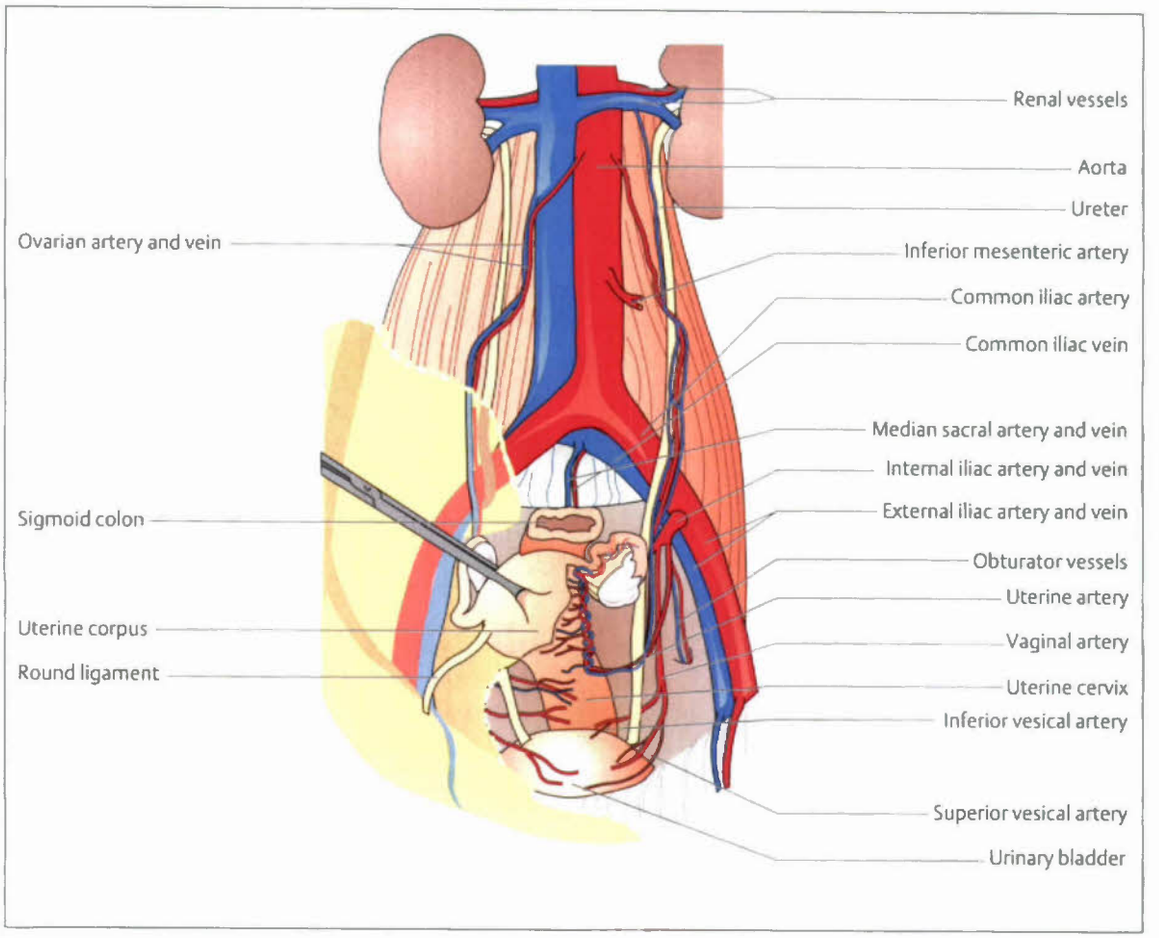

1

Fig. 21.1 Anatomical diagram of the true pelvis viewed from the anterior aspect (adapted from Netter [30]).

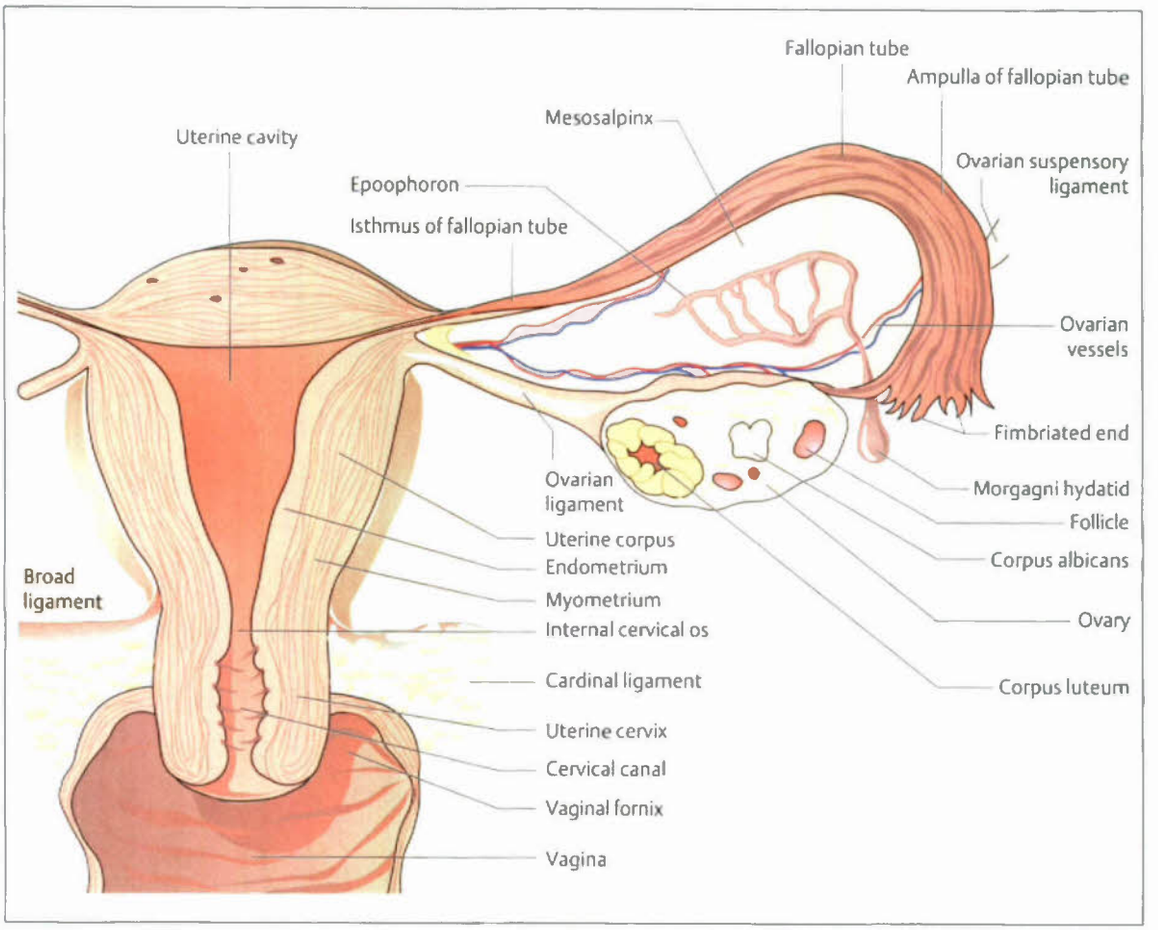

2

Fig. 21.2 Anatomical diagram of the uterus and left adnexal region in coronal section (adapted from Netter [30]).

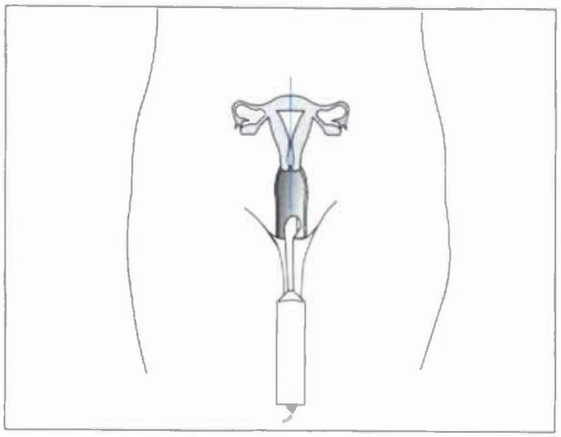

3

4

Vagina

Fig. 21.3 Diagram of a midsagittal scan with the probe at the vaginal introitus.

Fig. 21.4 Vagina (1) with the probe inserted only a few millimeters. Midsagittal scan.

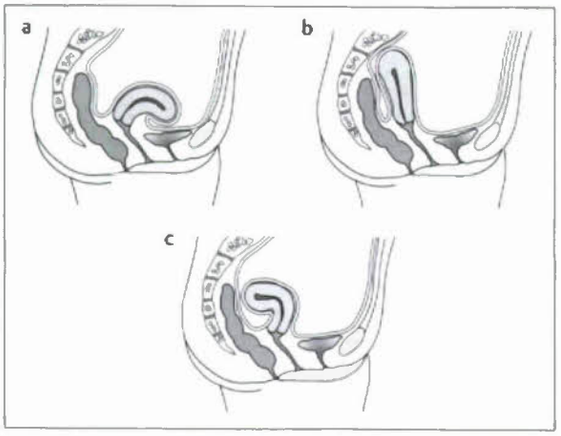

5

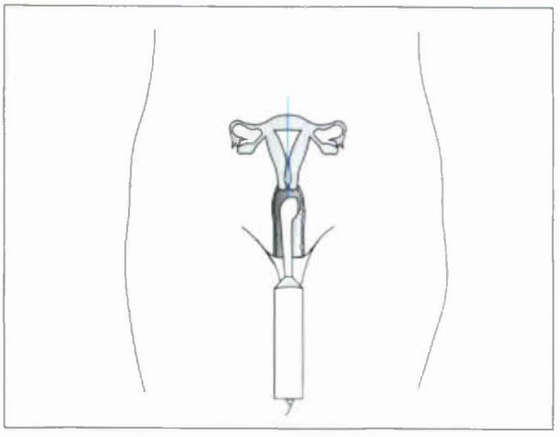

6

Uterus

Fig. 21.5 Position of the uterus in the true pelvis with varying degrees of uterine flexion.
a Normal anteflexed uterus.
b Straight (axial) uterus.
c Retroflexed uterus.

Fig. 21.6 Diagram of a midsagittal scan with the probe at the level of the cervix.

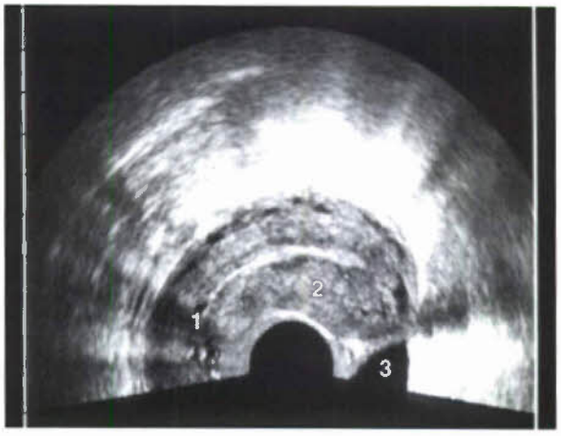

7

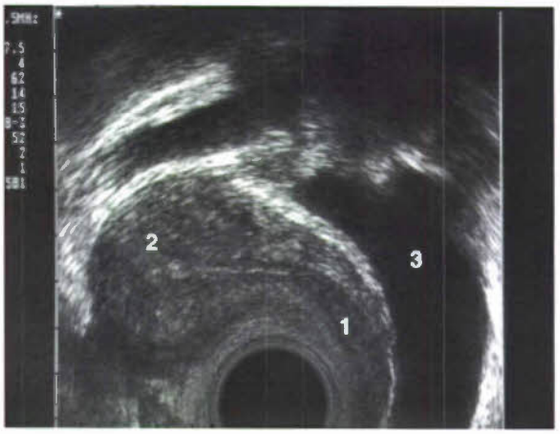

8

Fig. 21.7 Anteflexed uterus in a nullipara. Median longitudinal scan. The tip of the vaginal probe is in the anterior fornix.
1 Cervix
2 Corpus
3 Bladder

Fig. 21.8 Retroflexed uterus in a multipara. Median longitudinal scan. The tip of the vaginal probe is in the posterior fornix.
1 Cervix
2 Corpus
3 Bladder

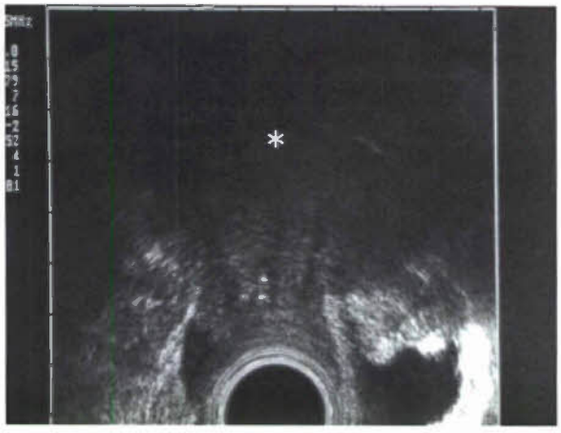

9

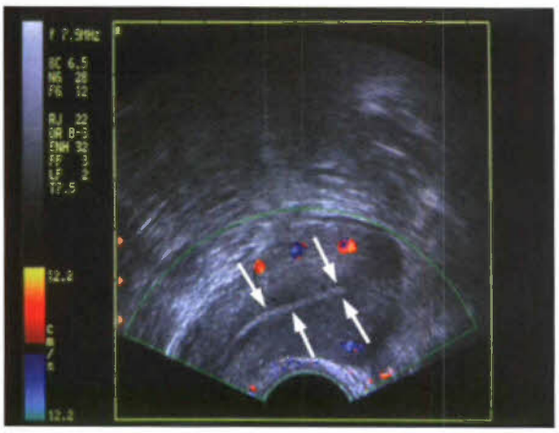

10

Fig. 21.9 Straight uterus. Median longitudinal scan. This image is unfavorable for evaluating the uterine corpus (*).

Fig. 21.10 Anteflexed uterus. The inner third of the myometrium appears as a hypoechoic zone (1). With color Doppler activated, multiple vessels can be seen in the outer third of the myometrium.

Fig. 21.**11** Small, anteflexed uterus in a postmenopausal patient (5.0 × 2.1 × 2.8 cm).

11

Fig. 21.**12** Uterine biometry in a normal anteflexed uterus. Corpus length = 4.1 cm (1), cervical length = 3.2 cm (2), corpus height = 3.2 cm (3), cervical height = 2.0 cm (4).

12

Fig. 21.**13** Scan planes through the uterine corpus (II) and cervix (I) for measuring the width of the corpus and cervix.

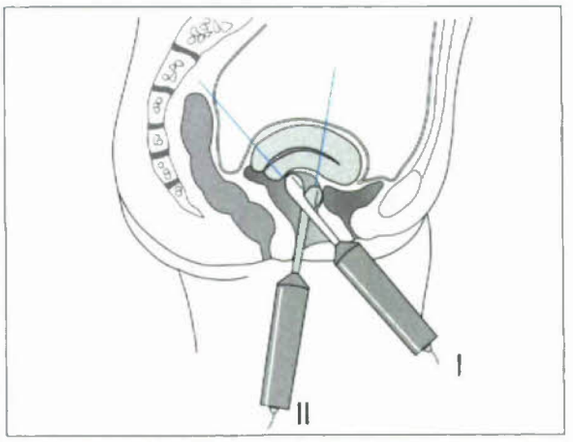

13

Fig. 21.**14** A coronal scan through the true pelvis demonstrates the uterine corpus and endometrium in transverse section. The corpus width is 3.7 cm.

14

Fig. 21.**15** A coronal scan through the true pelvis demonstrates the uterine cervix in transverse section. Cervical width is 2.6 cm.

15

Fig. 21.**16** Endometrial biometry. The endometrial thickness is determined by measuring the total thickness of the anterior and posterior endometrial layers (> <) in a longitudinal sagittal scan.

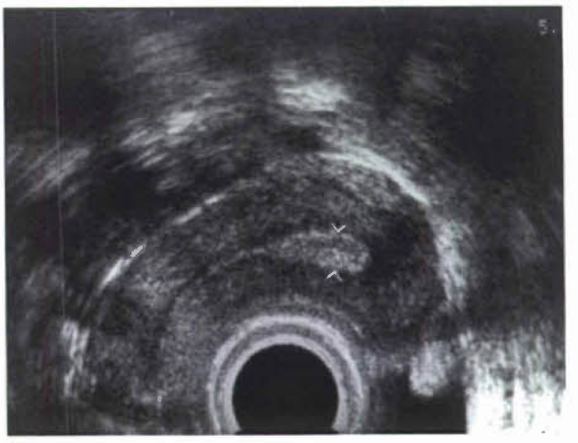

16

Fig. 21.**17** Retroflexed uterus in a 58-year-old postmenopausal woman. Longitudinal scan. The endometrial thickness is 3 mm (> <).

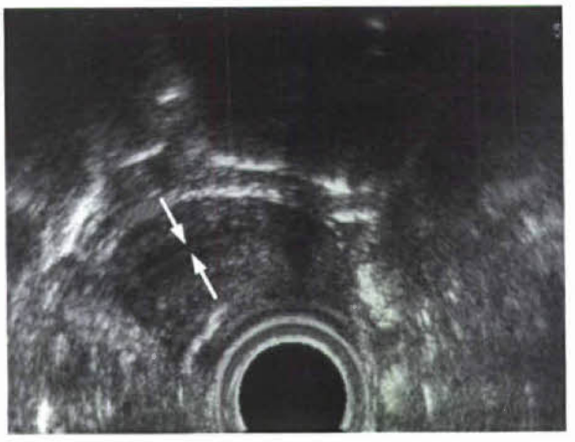

17

Fig. 21.**18** A small intrauterine fluid collection in a 71-year-old woman. Longitudinal scan.

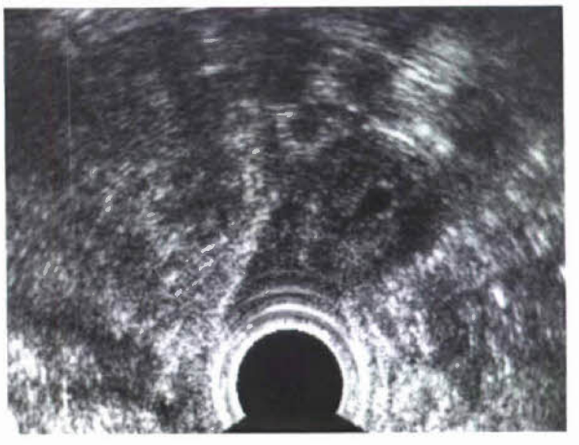

18

Endometrial thickness is measured as the anteroposterior dimension in a longitudinal sagittal scan. The measurement itself is made from the myometrial–endometrial boundary to the opposite endometrial–myometrial boundary. This yields the total (double) thickness of the anterior and posterior endometrial layers together (Fig. 21.**16**). The maximum premenopausal thickness (without hormone replacement) is 1.5 cm. In the postmenopausal atrophic uterus, the endometrium usually appears only as a thin, echogenic line [10,20,21]; normally it is no more than 5 mm thick, unless hormone replacement therapy (HRT) has been administered [20] (Fig. 21.**17**).

If the patient is receiving HRT, the endometrial thickness may exceed 1 cm in the absence of malignancy, depending on age and response rate [15,22].

Dilation of the uterine cavity by an echo-free area is occasionally seen in elderly and postmenopausal women (Fig. 21.**18**) [23]. This is caused by mild *fluid retention* secondary to atrophic occlusion of the cervix. When this type of intrauterine fluid collection is found, the height of the fluid space should be subtracted from the total endometrial measurement to determine the actual endometrial thickness.

Ovaries

A longitudinal sagittal scan directed lateral to the pelvic wall demonstrates the ovaries as ellipsoidal structures of relatively low echogenicity, often located in close proximity to the iliac vessels (Figs. 21.**19**, 21.**20**). If both ovaries lie at approximately the same level, they can be displayed simultaneously in a coronal scan using a transducer with a sufficiently wide field of view (Figs. 21.**21**, 21.**22**). If the probe has a smaller sector angle, the monitor image can be split to display the right ovary on the left side of the screen and the left ovary on the right side, corresponding to their anatomical positions. This also allows the right and left ovaries to be compared for size and echo pattern.

Usually, the ovaries in a woman of childbearing age can be demonstrated without difficulty by transvaginal scanning owing to their relatively large size. A follicle or corpus luteum can often be identified on one of the ovaries in women who are not taking oral contraceptives. Problems in identifying the ovaries are likely to arise only if one ovary is very high or is encased by adhesions.

Unlike the premenopausal ovaries (Figs. 21.**20**, 21.**22**, 21.**23**), which can be defined in 96% of cases when both are present [20], visualization of the postmenopausal ovaries (Fig. 21.**24**) is successful in only 64% of cases, due to their smaller size [20]. Sladkevicius et al. [24] reported a sonographic detection rate of 65% for the right ovary and 62% for the left ovary in postmenopausal women.

Ovarian Biometry

The average ovary before the menopause measures approximately 3.5 × 2.5 × 1.5 cm (length × width × height) and approximately 2.0 × 1.5 × 1.0 cm after the menopause. Ovarian size is assessed by imaging the ovaries first in an oblique sagittal scan and then in a coronal scan through the pelvis. This allows the ovaries to be measured in all three planes (Figs. 21.**23**, 21.**24**). The volume of the ovary can be calculated using the standard formula for an ellipsoid ($V = 4/3 \times 3.14 \times (d_1/2 \times d_2/2 \times d_3/2)$ [20,25] or by using the simplified formula for an ellipsoid [26]:

$$V = \tfrac{1}{2} \times \text{length} \times \text{height} \times \text{width}$$

Ovarian volume is not altered by parity in premenopausal women. It decreases markedly after menopause (Table 21.**2**).

Table 21.**2** Ovarian volume in women of reproductive age and in postmenopausal women as a function of parity and years after menopause (adapted from Merz et al. [20])

Parity or menopausal status	0-para x (SD) cm³	1-para x (SD) cm³	≥2-para x (SD) cm³	MP ≤5 years x (SD) cm³	MP >5 years x (SD) cm³
Right ovarian volume	7.8 (2.6)	7.8 (2.3)	7.8 (2.6)	3.4 (1.3)	2.5 (1.3)
Left ovarian volume	7.4 (2.4)	7.7 (2.3)	7.5 (2.3)	3.8 (1.6)	2.5 (1.1)

Fallopian Tubes

While transabdominal scans can demonstrate the fallopian tubes only if they are abnormal, transvaginal ultrasound can define even healthy tubes, provided there is some free fluid present in the true pelvis [27]. A coronal scan through the uterine fundus portrays the fallopian tubes as hypoechoic band-like structures (Fig. 21.**25**) with the ovaries at their distal ends. If there is a relatively large amount of exudate in the cul-de-sac, the unfolded fimbriated end of the tube can also be identified (Fig. 21.**26**). The tubal lumen can be evaluated with ultrasound only when a contrast agent (Echovist) has been instilled (Chapter 33).

Bladder

Transvaginal ultrasound is an ideal method for evaluating the urinary bladder. Besides its ability to define the layers of the bladder wall, it is a dynamic modality that can be used to monitor physiologic processes such as bladder filling and emptying without exposure to ionizing radiation (for investigation of urinary incontinence, see Chapter 18).

The bladder appears anterior to the uterus and vagina and posterior to the symphysis in the midsagittal scan. When only slightly distended, the bladder has the shape of a rounded triangle with a relatively thick wall (approximately 8 mm) (Fig. 21.**27**). With increasing distension, the bladder roof moves cephalad and forward, while the bladder wall becomes thinner (Fig. 21.**28**). When the bladder is maximally distended by approximately 500 mL of fluid, its wall is stretched to a thickness of only about 2 mm and its inner surface displays a smooth contour. Folds are visible in the mucosal lining only when the bladder is almost empty. The moderately distended bladder appears as a symmetrical organ in coronal section. When the probe is inserted only a short distance into the vagina and aimed at the bladder floor, the two ureteral orifices can be identified as small prominences (Fig. 21.**29**). When these sites are observed for a prolonged period of time, jets of urine can be seen entering the bladder lumen intermittently (the *ureteral jet phenomenon*) (Fig. 21.**30**) [28,29]. When the bladder is well distended, these jets are associated with a swirling intraluminal echo pattern.

When the bladder is empty or only slightly full, the *retropubic space* (Retzius cavity) can be seen in a sagittal scan between the hypoechoic symphysis and the bladder (Fig. 21.**27**). This space, which is filled with extraperitoneal fat, is compressed to a slit when the bladder is full.

When the vaginal probe is retracted to the introitus, the urethra and the internal urethral orifice can be visualized in both sagittal and coronal sections (Figs. 21.**31**, 21.**32**).

Ovaries

Fig. 21.**19** An oblique longitudinal scan through the left ovary.

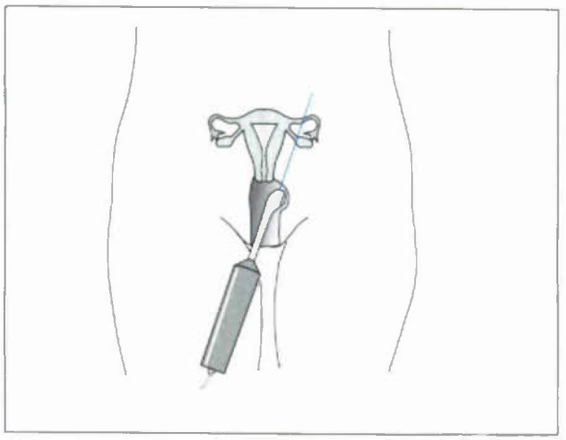

19

Fig. 21.**20** The ovary in a woman of childbearing age. Longitudinal scan. The ovarian dimensions are 3.6 × 2.2 × 3.5 cm.

20

Fig. 21.**21** Coronal scan through the true pelvis. Both ovaries are demonstrated in this plane. Side views.

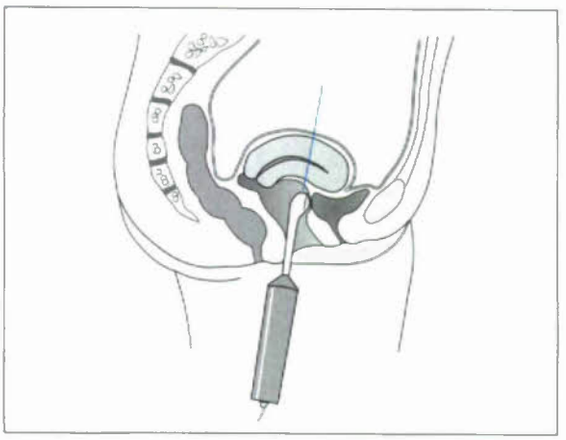

21

Fig. 21.**22** Coronal scan through the true pelvis. The uterine corpus in transverse section, flanked by the ovaries is shown.
1 Uterine corpus in transverse section
2 Left ovary
3 Right ovary

22

Fig. 21.**23** Ovarian biometry in three planes. The premenopausal ovary measures 3.8 × 1.8 × 2.7 cm. Oblique longitudinal scan (left) and coronal scan (right).

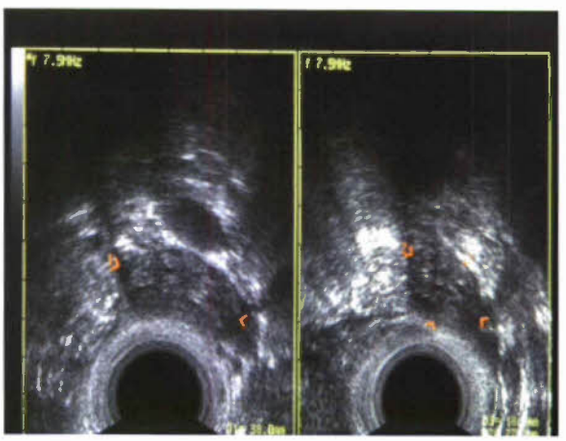

23

Fig. 21.**24** Postmenopausal ovary (<<). Oblique longitudinal scan. The ovarian dimensions are 2.1 × 1.4 × 1.9 cm.

24

Fallopian Tubes

Fig. 21.**25** Right fallopian tube in coronal section (—).

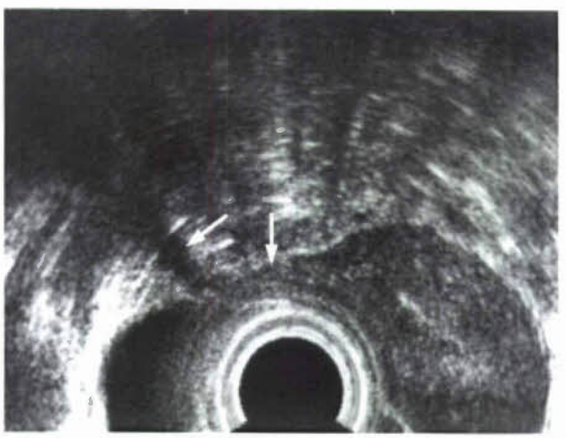

25

Fig. 21.**26** The fimbriated end of the fallopian tube (—), imaged through serous fluid present in the cul-de-sac. Superimposed over the tube is the ovary, on which two follicles (*) can be seen.

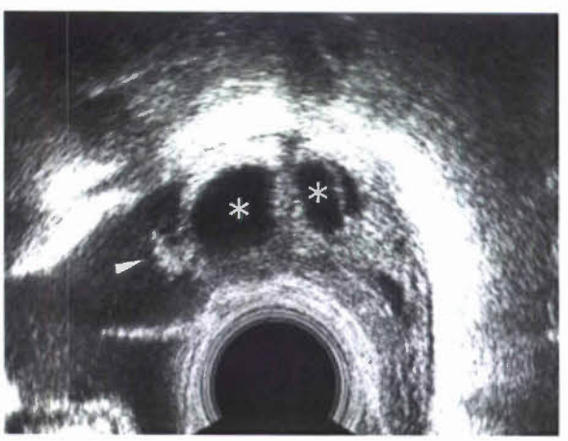

26

27

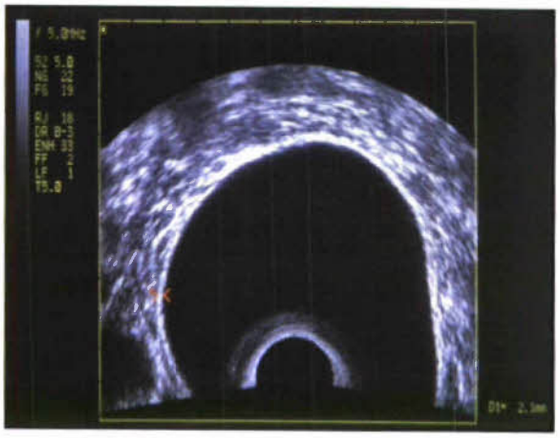

28

Bladder

Fig. 21.**27** View of the partially distended bladder. Midsagittal scan. * Retropubic space.

Fig. 21.**28** The bladder is maximally distended, showing a wall thickness of only 2 mm. Midsagittal scan.

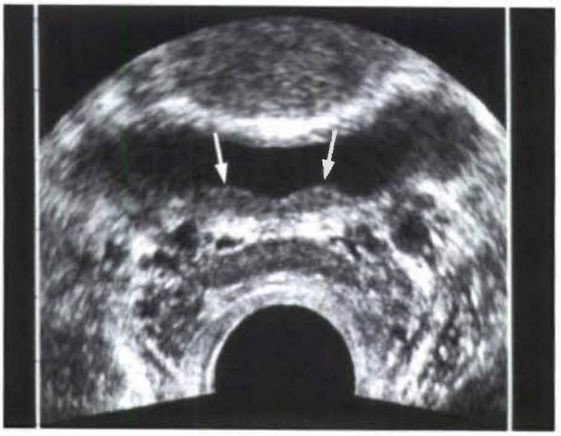

29

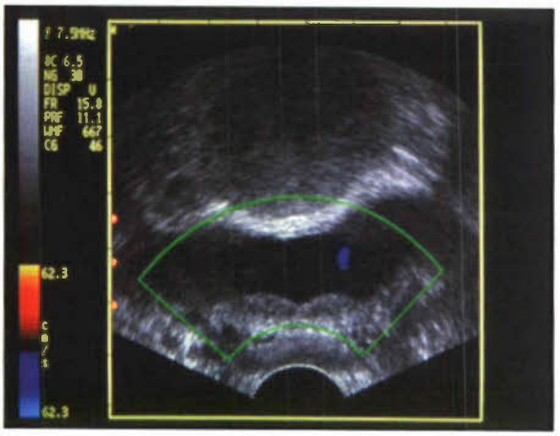

30

Fig. 21.**29** View of the partially distended bladder, showing the bladder trigone and both ureteral orifices (|). Coronal scan.

Fig. 21.**30** Color Doppler image of a urine stream entering the bladder (jet phenomenon).

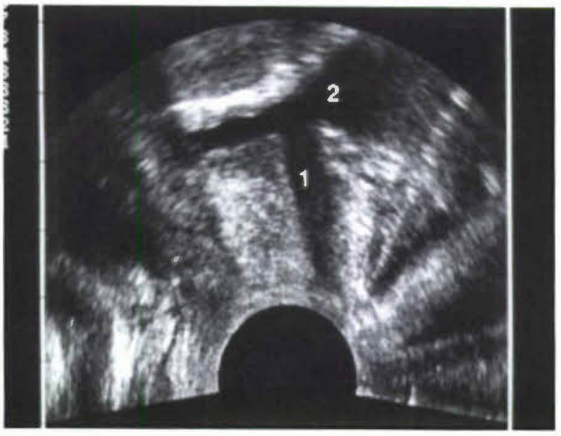

31

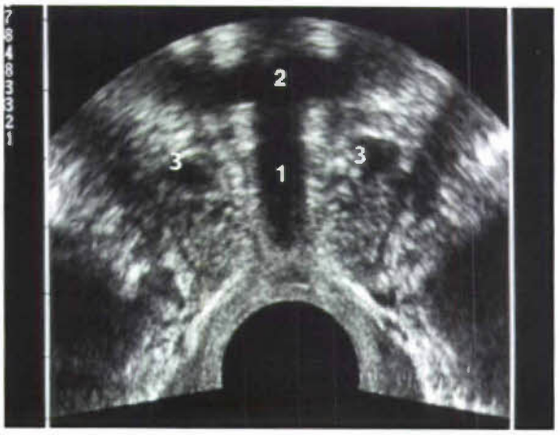

32

Fig. 21.**31** To define the urethra in a midsagittal scan, the tip of the probe has to be withdrawn to the vaginal introitus.
1 Urethra
2 Bladder

Fig. 21.**32** The urethra and internal urethral orifice in coronal section.
1 Urethra
2 Bladder
3 Ureters

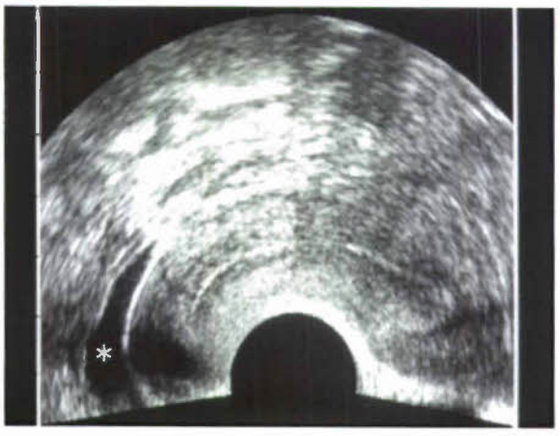

33

Cul-de-Sac

Fig. 21.**33** This midsagittal scan demonstrates a small amount of fluid in the cul-de-sac (*).

Ureters

As the ureter enters the true pelvis, it crosses over the common iliac artery and runs along the lateral pelvic wall to the floor of the pelvis. At the level of the ischial spine, it turns forward and medially, crosses under the uterine vessels in the parametrial area approximately 2 cm from the cervix, and then curves upward to the bladder floor, entering the bladder at the lateral angle of the bladder trigone. In an unobstructed state, the ureters are poorly delineated from the surrounding tissues by transvaginal ultrasound (Fig. 21.**32**). When the ureters are obstructed, they appear more clearly as hypoechoic vessel-like structures in the region of the bladder floor.

Cul-de-Sac

The cul-de-sac appears directly behind the cervix and posterior fornix in a midsagittal scan. The normal cul-de-sac often contains a small amount of fluid (approximately 5–10 mL), making it easy to visualize with ultrasound (Fig. 21.**33**).

Bowel

The *rectum* appears in a longitudinal sagittal scan as an elongated band of varying thickness (hypoechoic outside, echogenic inside) located behind the uterus and vagina (Fig. 21.**34**). When a coronal scan through the true pelvis is angled sharply upward and posteriorly with the probe inserted only a short distance into the vagina, the rectum can be identified as a hypoechoic, ring-shaped structure with an echogenic center (Fig. 21.**35**). Hypoechoic loops of small bowel may also be seen lateral or posterior to the uterus, depending on the uterine position (Fig. 21.**36**). Their conspicuous motility serves to distinguish them from colon.

Pelvic Walls

The true pelvis is lined by various muscles (Fig. 21.**37**). Below the sacral promontory on each side is the piriformis muscle, and below that is the coccygeus. The piriformis extends laterally from the sacrum to the greater sciatic foramen, and the coccygeus extends laterally from the ischial spine to insert on the sacrum. The pelvic floor is formed by the levator ani. The pelvic walls are bounded laterally by the obturator internus, which arises partly from the circumference of the obturator groove and partly from the obturator membrane and passes through the true sciatic foramen to the inner surface of the greater trochanter. The psoas muscle is located farther anteriorly, at the boundary of the greater and true pelvis. Arising from the T12 vertebra and the upper four lumbar vertebrae, it runs downward with the iliacus muscle and inserts by a common tendon on the true trochanter.

In transvaginal ultrasound, a laterally directed coronal scan can demonstrate the obturator internus muscle as a hypoechoic area near the lateral pelvic wall on each side (Fig. 21.**38**). Somewhat farther anteriorly is the hypoechoic psoas muscle, upon which course the iliac vessels. The muscles that line the true pelvis posteriorly, such as the piriformis (Fig. 21.**39**), are frequently obscured by loops of bowel.

Vessels

In an oblique coronal scan through the true pelvis, the pulsating external iliac artery and external iliac vein appear as adjacent, hypoechoic bands on the anterolateral pelvic wall. They run medial to the psoas major to the inferior border of the inguinal ligament (Figs. 21.**40**, 21.**41**). A lateral sagittal scan demonstrates the *internal iliac artery* (Figs. 21.**40**, 21.**42**), which arises from the common iliac artery, runs posteriorly to the greater sciatic notch, and then divides into an anterior and posterior trunk. The *uterine artery* arises from the internal iliac artery and runs in the connective tissue of the broad ligament to the isthmus of the uterus (Fig. 21.**43**). There it divides into a lower branch that is distributed to the vagina (vaginal artery) and a main branch that runs up along the side of the uterus to the uterine fundus. The uterine vessels that course along the lateral border of the uterus show considerable tortuosity. On vaginal ultrasound, a longitudinal coronal scan is best for defining the uterine vessels lateral to the cervix, where they appear as a more or less pronounced, hypoechoic mass of tortuous vessels (Fig. 21.**44**).

The uterine vessels—the *ovarian artery* and *ovarian vein*—course within the ovarian suspensory ligament to the mesovarium, where they are distributed to the ovary and fallopian tube (Fig. 21.**43**). Some branches supply the ovary while others (lateral, middle and median branches) are distributed to the fallopian tube, and another branch communicates with the ovarian branch of the uterine vessels. The ovarian vessels appear sonographically as narrow, hypoechoic elliptical or round structures in the ovarian or periovarian region, depending on which branch of the ovarian vessels is scanned and which vessels are cut by the longitudinal or transverse scan plane. It is much easier to locate and identify the ovarian vessels with color Doppler than with traditional ultrasound (Fig. 21.**45**).

Lymph Nodes

The pelvic lymph nodes are generally located in very close proximity to large blood vessels (Fig. 21.**46**). The lymph nodes that are relevant in transvaginal ultrasound pelvic examinations are the common iliac nodes, the external and internal iliac nodes, and the lateral sacral nodes.

As a rule, the pelvic lymph nodes are difficult to define sonographically in an unenlarged condition, as they are usually smaller than 1 cm in diameter. They typically have an elliptical shape and a relatively hypoechoic, homogeneous internal echo pattern (Fig. 21.**47**). They are considerably easier to detect when enlarged due to reactive lymphadenopathy.

Bowel

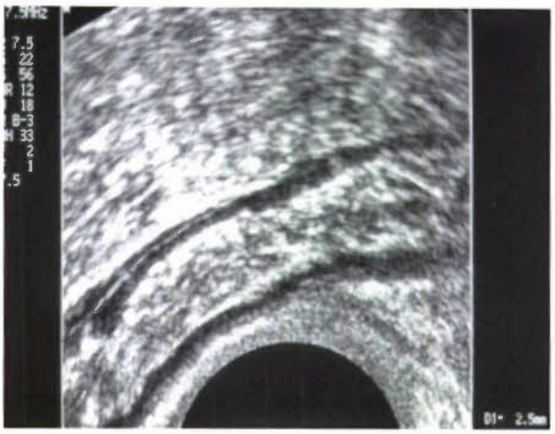

34

Fig. 21.**34** Longitudinal scan of the rectum.

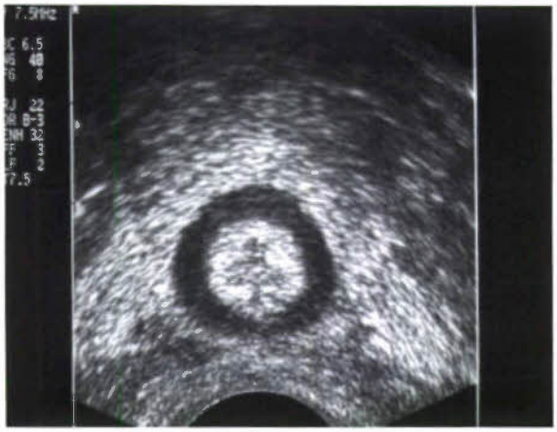

35

Fig. 21.**35** Transverse scan of the rectum.

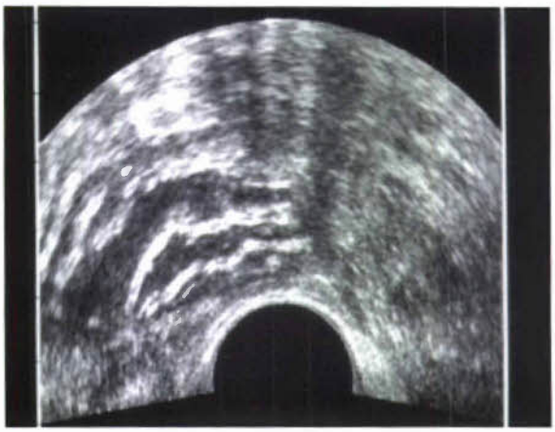

36

Fig. 21.**36** A loop of small bowel is seen cranial to the uterus. Coronal scan.

Pelvic Walls

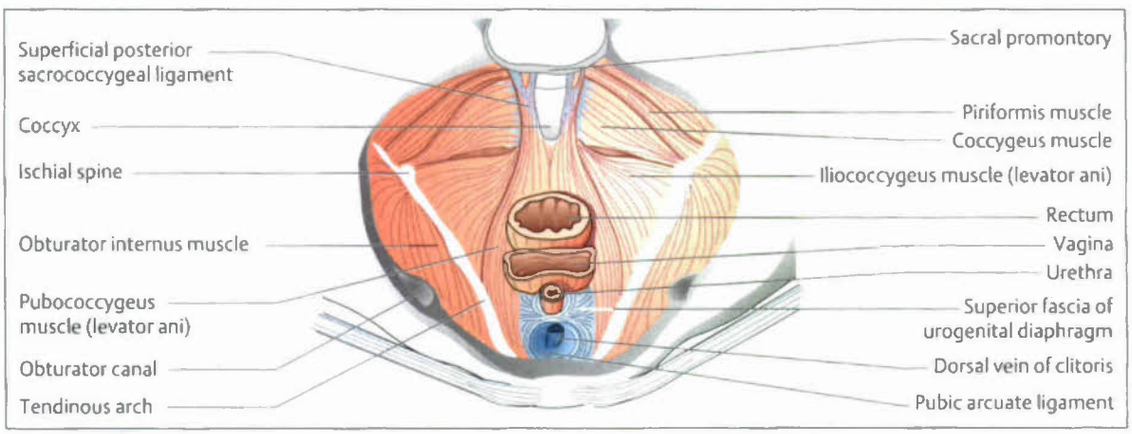

37

Fig. 21.**37** The anatomical structure of the pelvic floor. Internal aspect (adapted from Netter [30]).

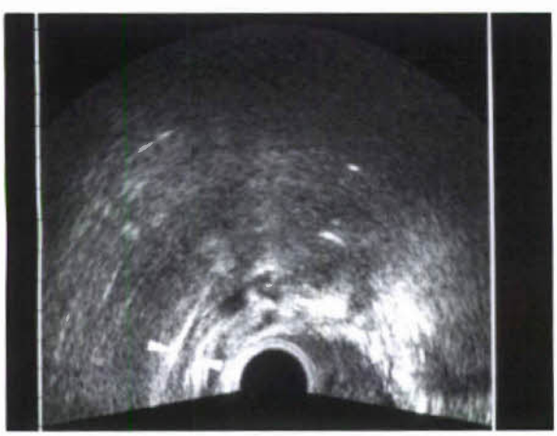

38

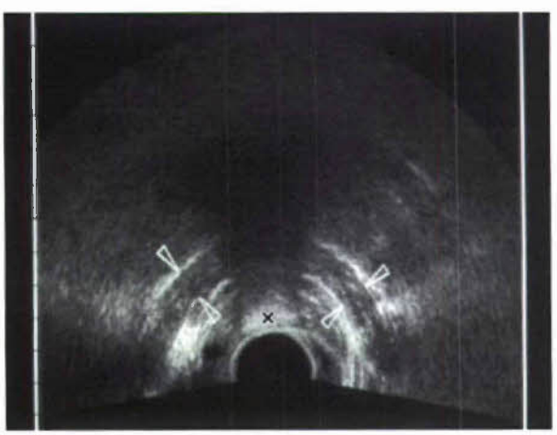

39

Fig. 21.**38** The right pelvic wall, with the obturator internus muscle (→ ←). Lateral coronal scan.

Fig. 21.**39** The posterior pelvic wall, with the piriformis muscle on each side. X = Sigmoid colon. Coronal scan.

Vessels

Fig. 21.40 The anatomical structure of the left lateral pelvic wall. Internal aspect (adapted from Netter [30]).

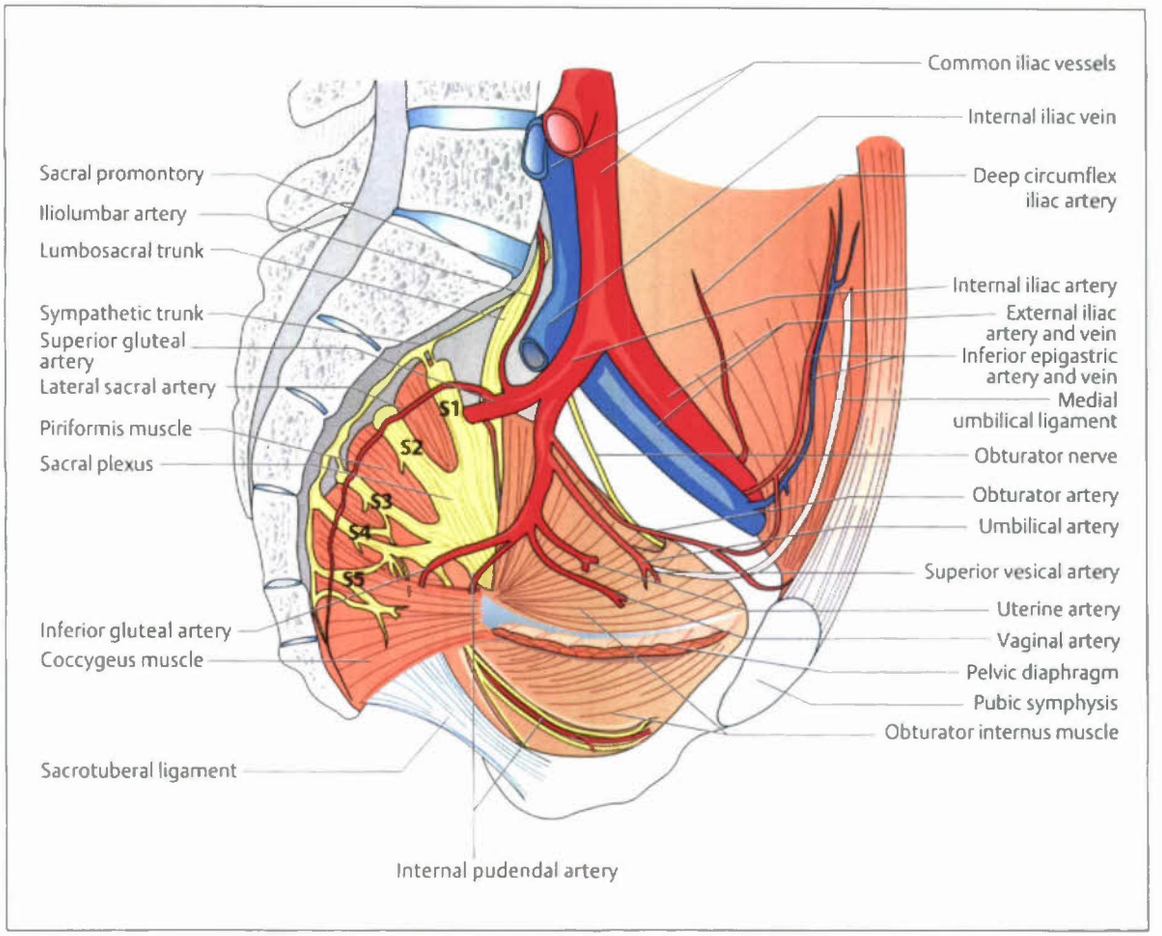

40

Fig. 21.41 The external iliac artery and vein in the region of the left pelvic wall. Oblique coronal scan.

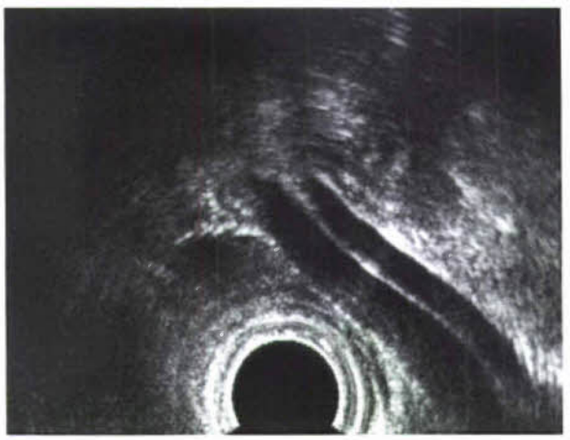

41

Fig. 21.42 Color Doppler view of the left internal iliac vessels. Lateral longitudinal scan.

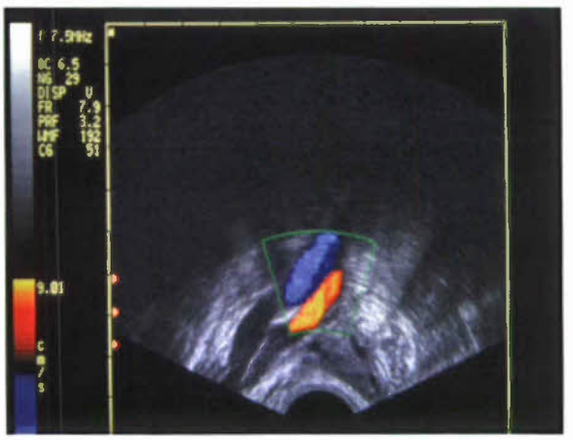

42

References

1 Bernaschek G. Vorteile der endosonographischen Diagnostik in Gynäkologie und Geburtshilfe. Geburtshilfe Frauenheilkd 1987;47:471–6.
2 Bernaschek G. Grundlagen der Vaginosonographie. Gynäkologe 1995;28:220–4.
3 Degenhardt F. Endosonographie in Gynäkologie und Geburtshilfe. Stuttgart: Wissenschaftliche Verlagsgesellschaft, 1994.
4 Duda V, Thein C, Rode G. Vaginalsonographie. Extr Gynaecol 1987;11:264–72.
5 Mendelson EB, Bohm-Velez M, Joseph N, Neiman HL. Gynecologic imaging: transabdominal and transvaginal sonography. Radiology 1988;166:321–4.
6 Merz E. Transvaginale oder transabdominale Ultraschalldiagnostik? Ein Vergleich zweier Methoden in Gynäkologie und Geburtshilfe. Ultraschall Klin Prax 1987;2:87–94.
7 Merz E. Vaginosonographie. Stuttgart: Enke, 1992.
8 Merz E. Aktueller Stand der Vaginosonographie. Teil 1: Grundlagen und gynäkologische Diagnostik. Ultraschall Med 1994;15:2–10.
9 Sautter T. Transvaginale Sonographie. Lehrbuch und Lehratlas. Stuttgart: Enke, 1990.
10 Schurz B, Eppel W, Egarter C, Wenzel R, Reinold E. Vaginosonographie in der Gynäkologie. Ultraschall 1989;10:90–7.
11 Timor-Tritsch IE, Bar-Yam Y, Elgali S, Rottem S. The technique of transvaginal sonography with the use of a 6.5 MHz probe. Am J Obstet Gynecol 1988;158:1019–24.
12 Timor-Tritsch I, Rottem S. Transvaginal sonography. Amsterdam: Elsevier, 1991.
13 Bald R, Hackelöer BJ. Ultraschalldarstellung verschiedener Endometriumformen. In: Otto RC, Jann FX, editors. Ultraschalldiagnostik 82. Stuttgart: Thieme, 1983: 187–92.
14 Fleischer AC, Kalemeris GC, Entman SS. Sonographic depiction of the endometrium during normal cycles. Ultrasound Med Biol 1986;12:271–7.
15 Merz E. Ultrasound in gynecology and obstetrics: textbook and atlas. Stuttgart: Thieme, 1991.
16 Sakamoto C, Nakano H. The echogenic endometrium and alterations during menstrual cycle. Int J Gynaecol Obstet 1982;20:255–9.
17 Yloestalo PR. Ultrasonography of endometrium. Ann Med 1990;22:105–6.

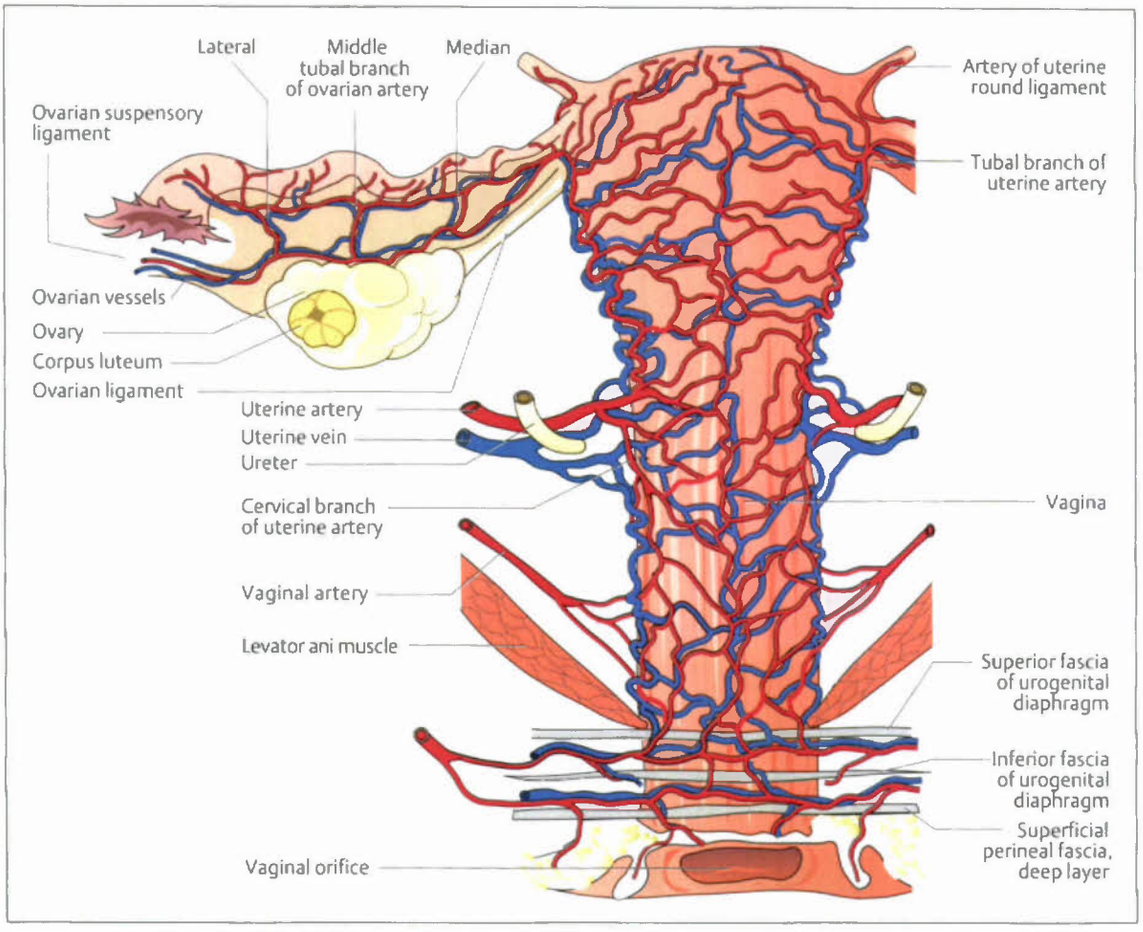

43

Fig. 21.**43** Vascular supply of the uterus and ovaries (adapted from Netter [30]).

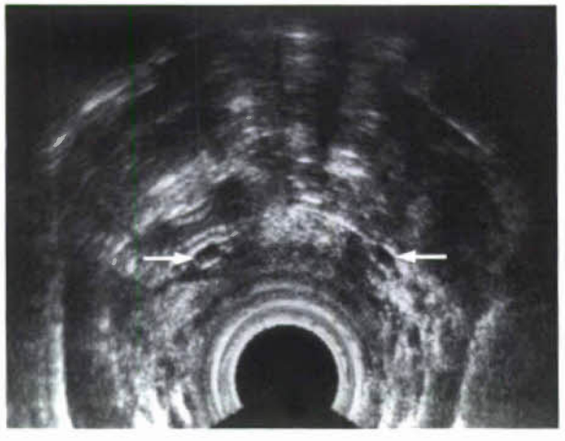

44

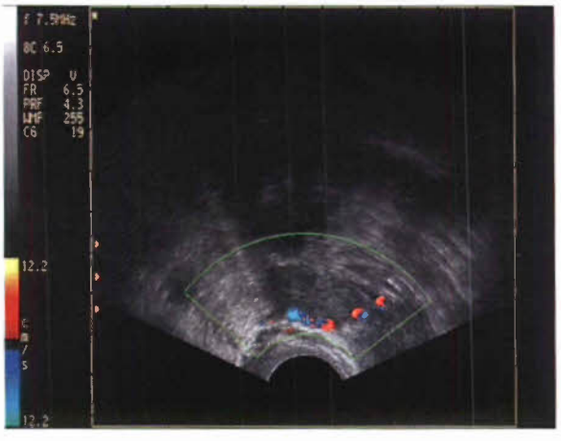

45

Fig. 21.**44** Transverse scan through the cervix. The uterine vessels appear lateral to the cervix (→).

Fig. 21.**45** Color Doppler view of the ovarian artery and vein in the ovarian region.

18 Yoshimitsu K, Nakamura G, Nakano H. Dating sonographic endometrial images in the normal ovulatory cycle. Int J Gynaecol Obstet 1989;28:33–9.
19 Fleischer AC, Kalemeris GC, Machin JE, Entman SS, James AE Jr. Sonographic depiction of normal and abnormal endometrium with histopathologic correlation. J Ultrasound Med 1986;5:445–52.
20 Merz E, Miric-Tesanic D, Weber G, Bahlmann F. Sonographic size of the uterus and ovaries in pre- and postmenopausal women. Ultrasound Gynecol Obstet 1996;7:1–5.
21 Schurz B, Eppel W, Huber JC, Reinold E. Vaginosonographische Darstellung des Endometriums postklimakterischer Frauen. Ultraschall 1988;9:37–40.
22 Schurz B, Metka M, Heytmanek G, Wimmer-Greinecker G, Reinold E. Sonographic changes in the endometrium of climacteric women during hormonal treatment. Maturitas 1988;9:367–74.
23 McCarthy KA, Hall DA, Kopans DB, Swann CA. Postmenopausal endometrial fluid collections: always an indicator of malignancy? J Ultrasound Med 1986;5:647–9.
24 Sladkevicius P, Valentin L, Marsal K. Transvaginal gray-scale and Doppler ultrasound examinations of the uterus and ovaries in healthy postmenopausal women. Ultrasound Obstet Gynecol 1995;6:81–90.
25 Campbell S, Goessens L, Goswamy R, Whitehead M. Real-time ultrasonography for determination of ovarian morphology and volume: a possible early screening test for ovarian cancer? Lancet 1982;i:425–6.
26 Sample WF, Lippe BM, Gyepes MT. Gray-scale ultrasonography of the normal female pelvis. Radiology 1977;125:477–83.
27 Timor-Tritsch IE, Rottem S. Transvaginal ultrasonographic study of the fallopian tube. Obstet Gynecol 1987;70:424–8.
28 Hanbury DC, Coulden RA, Framan P, Sherwood T. Ultrasound cystography in the diagnosis of vesicoureteric reflux. Br J Urol 1990;65:250–3.
29 Kremer H, Dobrinski W, Mikyska M, Baumgärtner M, Köhler C, Zöllner N. Sonographischer Nachweis dynamischer Einstromphänomene in der Harnblase. Ultraschall 1981;2:183–4.
30 Netter FH. Farbatlanten der Medizin, vol. 3. Genitalorgane. Stuttgart: Thieme, 1978.

Lymph Nodes

Fig. 21.**46** Lymphatic vessels and lymph nodes in the pelvis (adapted from Netter [30]).

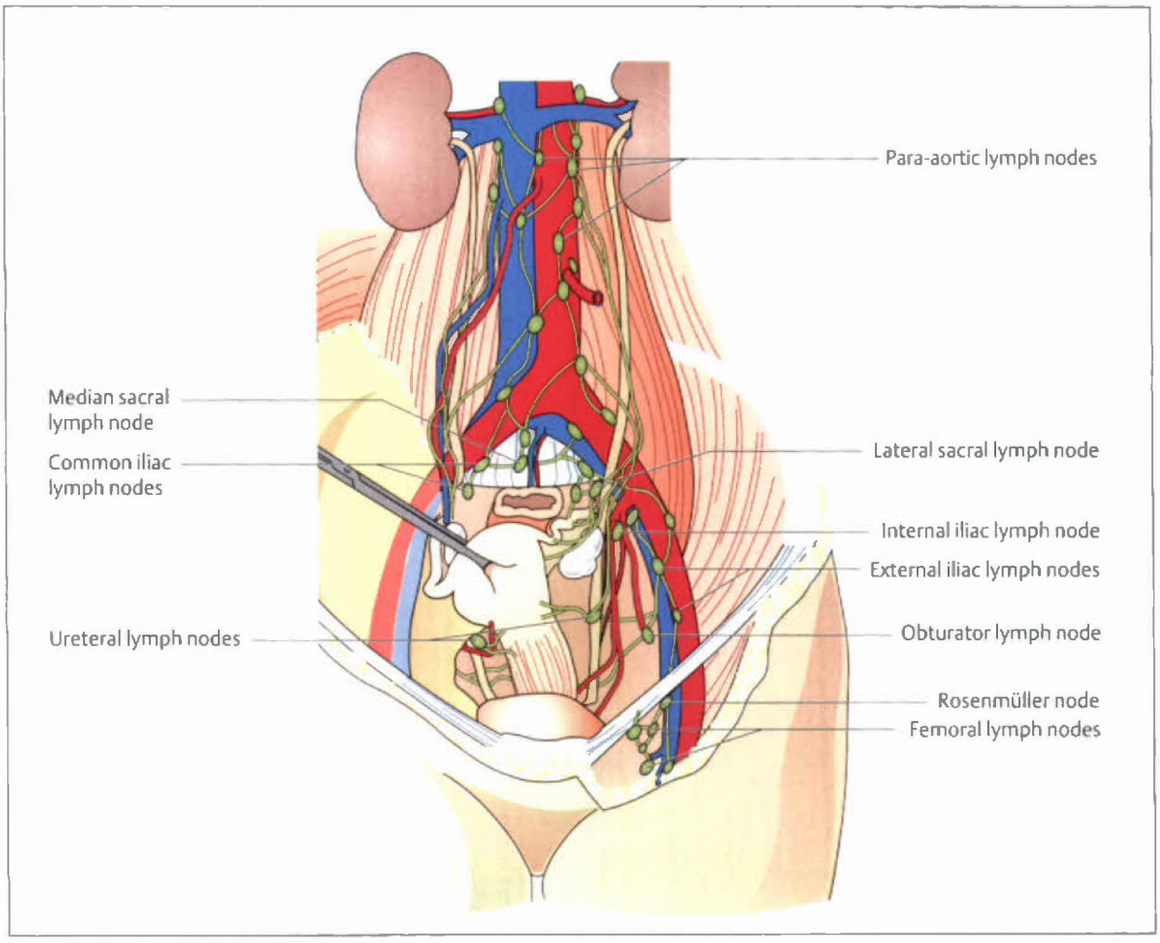

46

Fig. 21.**47** Lymph nodes in the region of the left iliac vessels (1.2 × 0.7 cm).

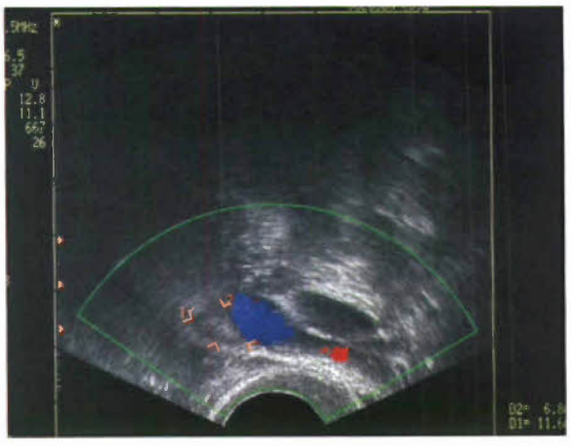

47

22 Uterine and Ovarian Changes during the Menstrual Cycle

Uterine Changes during the Menstrual Cycle

Physiologic Endometrial Changes in the Ovulatory Cycle

Under the influence of the ovarian hormones estradiol and progesterone, cyclic changes occur in the endometrium during the menstrual cycle of the sexually mature woman. These changes can be subdivided into three characteristic phases: desquamation, proliferation, and secretion (Fig. 22.**1**).

During the desquamation phase (known also as menses or the menstrual period), the functional layer of the endometrium is sloughed. The functional layer is regenerated during the proliferative phase, and in the secretory phase the functional layer undergoes secretory transformation.

Sonographic Changes

As we know from transabdominal ultrasound studies [1,2], the cyclic changes in the endometrium can be clearly visualized sonographically (see Figs. 4.**12** and 4.**13**).

Transvaginal ultrasound can display these changes more easily and accurately than abdominal ultrasound [3]. The close proximity of the endometrium to the vaginal probe and the markedly better image resolution obtained with the higher scanning frequency allow for accurate evaluation of the endometrium even in a retroflexed uterus.

To obtain an adequate evaluation of the entire uterus, it is recommended that the uterus be scanned not only in a longitudinal survey section but also in multiple transverse planes across the corpus. This is necessary in order to detect any local variations in endometrial thickness. The formal measurement is made strictly in a longitudinal uterine scan perpendicular to the long axis of the body; this is done to avoid oblique scans that would distort the true endometrial thickness.

Endometrium during the First Half of the Cycle

During menstruation, the endometrial thickness initially decreases markedly and may reach values less than 1 mm. As a result, ultrasound in the early proliferative phase shows only a streak-like endometrial echo (*type 1 endometrium*, Figs. 22.**2**, 22.**3**). As the proliferative phase continues, the thickness of the endometrium constantly increases [4]. In a stable 28-day cycle, a *type 2 endometrium* can be observed, starting on about the eighth day of the cycle (Figs. 22.**4**, 22.**5**). A *type 3 endometrium* is seen approximately 2–3 days later (Figs. 22.**6**, 22.**7**). Due to edema of the superficial cells, the previously dense and echogenic endometrium acquires a looser texture and becomes a sonographic *type 4 endometrium*, characterized by a narrow hyperechoic border and a thin, high-level central echo separated by a hypoechoic zone (Figs. 22.**8**, 22.**9**). About 1 day before ovulation, there may be further dissolution of the central and peripheral echoes, with the result that little if any endometrial structure can be discerned at this stage (*type 5*, Figs. 22.**10**, 22.**11**). The endometrium reaches a thickness of 1.0–1.2 cm before ovulation. After ovulation, the *endometrial ring sign* can be seen; this is a subtle ring-like feature (*type 6*, Figs. 22.**12**, 22.**13**) that coincides with the rise in progesterone (Table 22.**1**).

Table 22.1 Sonographic endometrial patterns during the first half of the menstrual cycle (adapted from Bald and Hackelöer [1]).

Type 1	Thin, streak-like endometrium ≤ 2 mm
Type 2	Endometrium 3–5 mm
Type 3	Endometrium > 5 mm
Type 4	Endometrium with a hyperechoic border and bright central echo, with an otherwise hypoechoic functional layer
Type 5	Similar to type 4, but with fading of the hyperechoic border and central echo
Type 6	Prominent ring structure of high echogenicity

Endometrium during the Second Half of the Cycle

In the *early luteal phase* (days 15–19 of the cycle), the endometrial thickness shows a further slight decrease due to the regression of stromal edema. In the *midluteal phase* (days 20–25 of the cycle), the endometrium reaches its maximum thickness of 1.0–1.5 cm as a result of secretory transformation, becoming increasingly dense and echogenic on ultrasound imaging (Figs. 22.**14**, 22.**15**). Comparative sonographic and morphologic studies have shown that the echogenicity of the endometrium increases in proportion to its luteal transformation [5]. In the *late secretory phase* (days 26–28 of the cycle) shortly before menstruation, endometrial thickness again shows a marked decline. With the onset of the menstrual period, hypoechoic zones are noted in the uterine cavity as evidence of desquamation.

If pregnancy should occur during the observed cycle, both the thickness and echogenicity of the endometrium increase toward the end of the cycle, signifying the decidual reaction of pregnancy [6].

On the basis of transvaginal ultrasound observations, Deichert and Michaels [7] distinguished only four endometrial patterns:

- *Proliferative type (P or type 1):* a hypoechoic endometrium, basically showing the same echogenicity as the surrounding myometrium. This type is found after menstruation, during the early to mid-proliferative phase. A faint central echo is sometimes observed.
- *Midcycle or periovulatory type (M or type 2).* A distinct echogenic boundary with the adjacent myometrium and a continuous central echo delineating the endometrium from the anterior and posterior uterine wall are observed during the late proliferative phase and are a general characteristic feature of the endometrium at midcycle. The ultrasound findings vary in degree both before and after ovulation.
- *Secretory type I (S1 or type 3).* The start of the late luteal phase is characterized by increasing echogenicity of the endometrium and a gradual fading of the central echo. This echogenicity increase is centripetal, proceeding from the periphery of the uterine cavity toward its center, with a markedly less echogenic area persisting at the center—i.e., in the portion of the endometrium facing the cavity.
- *Secretory type II (S_2 or type 4).* The S_1 pattern in some cycles persists through the midluteal phase, with no change in echo texture but with occasional breakup of the central echo. There may be further

characteristic changes as the rising echogenicity of the endometrium increases toward the uterine cavity, resulting in a completely echogenic endometrial pattern classified as secretory type II.

With the second and fourth types, and especially with the S_2 pattern, posterior acoustic enhancement is observed on transvaginal ultrasound.

Subendometrial Contractions

When the uterus is observed sonographically for an extended period of time during the late proliferative phase and periovulatory phase in a woman of reproductive age, the observer notes wave-like subendometrial contractions that travel from the cervix toward the uterine fundus [8–10]. The contractions occur at a frequency of approximately three per minute around the time of ovulation. These contractions are believed to play an important role in intrauterine sperm transport.

Cervical Changes during the Menstrual Cycle

Ultrasound can also detect cervical changes during the course of the menstrual cycle. The cervical canal during the early and mid-follicular phase appears only as a thin, echogenic streak between the anterior and posterior half of the cervix (Fig. 22.**6**). Increasing dilation of the cervical canal is observed in the late follicular phase, and the presence of cervical mucus causes the entire canal to appear hypoechoic. Dilation of the canal is maximal on the day of ovulation (Figs. 22.**16**, 22.**17**). The quantity of mucus decreases swiftly after ovulation, and the cervical canal is closed again by the second day after ovulation [7].

Deichert and Michaels [7] devised a three-part classification for the cervical patterns that can be observed during the course of the menstrual cycle (Table 22.**2**).

Ovarian Changes during the Menstrual Cycle

Structural and Physiologic Changes during the Ovulatory Cycle

The ovaries contain a total of 400,000 primordial follicles when puberty begins. Only about 400 of these follicles will mature and ovulate during the woman's reproductive lifetime, while the great majority of follicles become atretic [11,12].

The normal ovarian cycle in a woman of reproductive age has an average duration of 28 days and is regulated by the interaction of the hypothalamus, anterior pituitary, and ovary (Fig. 22.**1**). It can be divided into various phases on the basis of functional and hormonal criteria: *menses* (days 1–5), the *early follicular phase* (days 6–8), the *late follicular phase* (days 9–13), the *ovulatory phase* (day 14), the *early luteal phase* (days 15–19), the *midluteal phase* (days 20–25), and the *late luteal phase* (days 26–28).

Table 22.**2** Classification of cervical changes during the menstrual cycle (adapted from Deichert and Michaels [7]).

Z type	Closed cervical canal that appears sonographically as a continuous echogenic streak
O type II	Initial opening of the cervical canal, appearing sonographically as echogenic double lines
W type	The cervical canal is widely open around the time of ovulation, appearing sonographically as a broad, uninterrupted hypoechoic to echo-free band with echogenic borders

Normal follicular growth is a continuous, irreversible process that ends with either ovulation or atresia [11] and already starts approximately 90 days before ovulation [13]. During this period, the primordial follicle develops into a primary follicle, which in turn matures into the antral and preovulatory graafian follicle [12] (Fig. 22.**18**).

During the follicular phase, which spans the last 14 days of follicular maturation, stimulation by the gonadotropins follicle-stimulating hormone (FSH) and luteinizing hormone (LH) induces the selection of a lead follicle, which suppresses the simultaneous growth of other follicles and grows into a mature follicle. The maturation of this dominant follicle is associated with a marked rise in serum estradiol levels. Approximately 12–24 hours after the serum LH level reaches its peak, ovulation occurs [14,15]. After ovulation, vascularization of the granulosa lutein cells takes place during the early luteal phase of the cycle, and the corpus luteum is formed. Corpus luteum formation is associated with a marked increase in the synthesis and secretion of progesterone. By the advanced luteal phase, the corpus luteum is fully developed and attains its greatest endocrine activity on the seventh or eighth day after the LH peak. If pregnancy does not occur, the corpus luteum becomes functionally inactive between days 23 and 25 of the cycle. The serum progesterone level falls, and menstruation begins.

Sonographically Detectable Ovarian Changes

Follicular Growth in the Normal Cycle

The ovaries, like the uterus, can be defined much more clearly by transvaginal ultrasound than abdominal ultrasound, owing to the proximity of the endovaginal probe. This also makes it easier to observe follicular maturation [16]. Not only can the follicles be seen earlier and with greater clarity, but the internal structure of the follicles can be evaluated with better accuracy. Transvaginal scanning also facilitates follicular monitoring in obese patients, in whom follicular imaging is often difficult and tedious when done with an abdominal transducer.

Besides the fact that more accurate follicular imaging allows more accurate interpretation of hormonal findings, the ability to scan the ovaries on an empty bladder is a major reason why transvaginal ultrasound was quickly accepted by patients being evaluated and treated for infertility.

The Maturing Follicle

In most cases, an ovarian follicle cannot be observed by transvaginal ultrasound during the first 5 days of an unstimulated cycle (Fig. 22.**19**). Between days 5 and 7 of the cycle, one or more small follicles can be identified as round, echo-free zones within the ovary, measuring 2–3 mm in diameter. After 5–7 days, a follicle on one of the ovaries becomes the *dominant follicle* (Fig. 22.**20**) while the other follicles become atretic. This lead follicle grows at a linear rate that averages 2–3 mm per day (Figs. 22.**21**, 22.**22**), reaching a size of approximately 21 mm (24–26 mm) just before ovulation (Fig. 22.**23**). Two dominant follicles can be detected sonographically in approximately 10% of spontaneous cycles [17].

Folliculometry

The follicle is measured from inner border to inner border. Because some follicles have an oval shape, the most accurate results in follicu-

lometry are obtained by measuring all three diameters and calculating the mean follicular diameter (FD):

$$FD = (D1 + D2 + D3)/3$$

Signs of Impending Ovulation

Various sonographic changes can be interpreted as signs that ovulation is about to take place (Table 22.**3**). They include follicle size, the detection of a cumulus oophorus, and a change in the echo pattern of the follicle wall (crenation pattern on the inner wall) [17,18]. A thin hypoechoic zone surrounding the follicle is also considered a sign of imminent ovulation [18]. This zone is believed to be caused by edema of the theca-cell layer.

It may be that color Doppler ultrasound can provide additional information that will aid in determining the time of ovulation. For example, Bourne et al. [19] observed that initial color Doppler signals appeared in the peripheral part of the follicle at the time of the LH peak.

On the whole, however, all of these signs are subject to considerable variation. Thus, even when sonographic criteria are applied, predicting the time of ovulation still involves a significant uncertainty factor.

After ovulation has taken place, the follicle can no longer be visualized with ultrasound. In some cases the collapsed follicle still contains a small amount of residual fluid that shows scattered internal echoes. Meanwhile the discharged follicular fluid can be recognized as a hypoechoic zone in the cul-de-sac. Baber et al. [20] reported the detection of marked vascularity at the periphery of the corpus luteum (Table 22.**4**).

Corpus Hemorrhagicum, Corpus Luteum

Initial bleeding in the ruptured follicle produces a *corpus hemorrhagicum*, which contains fine internal echoes (Fig. 22.**24**).

The *corpus luteum* is formed by vascular invasion of the ruptured follicle and the formation of granulosa cells. The corpus luteum may present various sonographic features [21]. Usually it appears either as a predominantly cystic, hypoechoic body with an echogenic border (Figs. 22.**25**, 22.**26**) or a predominantly solid, echogenic corpus luteum. Several mixed forms may also be encountered. The size of the corpus luteum is also subject to marked variation.

A persistent *corpus luteum cyst* is a possible early sign of implantation.

The *corpus albicans* appears sonographically as an echogenic, lobulated structure within the ovary (Fig. 22.**27**).

Table 22.**3** Sonographic signs of impending ovulation

Ovary	• Follicle size > 20 mm • Detection of a cumulus oophorus within the follicle • Crenation pattern within the follicle • Presence of a narrow hypoechoic zone outside the follicle wall • Color Doppler signals at the follicle periphery
Uterus	• Type 4/5 endometrium • Marked dilation of the cervical canal

Table 22.**4** Sonographic signs that ovulation has occurred

Ovary	• A follicle is no longer visualized • Collapsed follicle; cystic area smaller than the previous mature follicle • Visualization of the corpus luteum • Color Doppler shows marked peripheral vascularization of the corpus luteum
Uterus	• Endometrial ring sign
Cul-de-sac	• Fluid detected in the cul-de-sac

References

1 Bald R, Hackelöer BJ. Ultraschalldarstellung verschiedener Endometriumformen. In: Otto RC, Jann FX, editors. Ultraschalldiagnostik 82. Stuttgart: Thieme, 1983: 187–92.
2 Merz E. Sonographische Diagnostik in Gynäkologie und Geburtshilfe. Stuttgart: Thieme, 1988.
3 Yoshimitsu K, Nakamura G, Nakano H. Dating sonographic endometrial images in the normal ovulatory cycle. Int J Gynaecol Obstet 1989;28:33–9.
4 Yloestalo PR. Ultrasonography of endometrium. Ann Med 1990;22:105–6.
5 Doherty CM, Silver B, Binor Z, Molo MW, Radwanska E. Transvaginal ultrasonography and the assessment of luteal phase endometrium. Am J Obstet Gynecol 1993;168:1702–9.
6 Imoedemhe DAG, Shaw RW, Kirkland A, Chan R. Ultrasound measurement of endometrial thickness on different ovarian stimulation regimens during in-vitro fertilization. Hum Reprod 1987;2:545–7.
7 Deichert U, Michaels W. Zyklische Veränderungen am Uterus. In: Deichert U, Duda V, Schlief R, editors. Funktionelle Sonographie in Gynäkologie und Reproduktionsmedizin. Berlin: Springer, 1993: 43–69.
8 Abramowicz JS, Archer DF. Uterine endometrial peristalsis: a transvaginal ultrasound study. Fertil Steril 1990;54:451–4.
9 Chalubinski K, Deutinger J, Bernaschek G. Vaginosonography for recording of cycle-related myometrial contractions. Fertil Steril 1993;59:225–8.
10 Lyons EA, Taylor PJ, Zheng HX, Ballard G, Levi CS, Kredentser JV. Characterization of subendometrial myometrial contractions throughout the menstrual cycle in normal fertile women. Fertil Steril 1991;54:771–4.
11 Peters H, Byskow AG, Himmelstein-Braw R, Faber M. Follicular growth: the basic event in the mouse and human ovary. J Reprod Fertil 1976;45:559–66.
12 Wildt L, Neuwinger J. Regulation der Funktion des Ovars. In: Schneider HPG, Bohnet HG, editors. Klinik der Frauenheilkunde und Geburtshilfe, vol. 1: Endokrinologie und Reproduktionsmedizin. 1. Grundlagen der gynäkologischen Endokrinologie, Klinik der endokrinen Störungen, 3rd. ed. Munich: Urban & Fischer, 1995: 25–50.
13 Gougeon A. Dynamics of follicular growth in the human: a model from preliminary results. Hum Reprod 1986;1:81–7.
14 Pauerstein CJ, Eddy CA, Croxatto HD, Hess R, Siler-Khodr TM, Croxatto HB. Temporal relationships of estrogen, progesterone and luteinizing hormone levels to ovulation in women and infrahuman primates. Am J Obstet Gynecol 1978;130:876–86.
15 Testart J, Frydman R. Minimum time lapse between luteinizing hormone surge or human chorionic gonadotropin administration and follicular rupture. Fertil Steril 1982;37:50–3.
16 Andreotti RF, Thompson GH, Janowitz W, Shapiro AG, Zusmer NR. Endovaginal and transabdominal sonography of ovarian follicles. J Ultrasound Med 1989;8:555–60.
17 Picker RH, Smith DH, Tucker MH, Saunders DM. Ultrasonic signs of imminent ovulation. J Clin Ultrasound 1983;11:1–2.
18 Ritchie WGM. Ultrasound in the evaluation of normal and induced ovulation. Fertil Steril 1985;43:167–81.
19 Bourne TH, Jurkovic D, Waterstone J, Campbell S, Collins WP. Intrafollicular blood flow during human ovulation. Ultrasound Obstet Gynecol 1991;1:53–9.
20 Baber RJ, McSweeney MB, Gill RW, Porter RN, Picker RH, Warren PS, et al. Transvaginal pulsed Doppler ultrasound assessment of blood flow to the corpus luteum in IVF patients following embryo transfer. Br J Obstet Gynaecol 1988;95:1226–30.
21 Deichert U, Daume E. Zyklische Veränderungen am Ovar. In: Deichert U, Duda V, Schlief R, editors. Funktionelle Sonographie in Gynäkologie und Reproduktionsmedizin. Berlin: Springer, 1993: 71–132.
22 Netter FH. Farbatlanten der Medizin, vol. 3: Genitalorgane. Stuttgart: Thieme, 1978.

Fig. 22.1 Functional relationships between the pituitary, ovary, and endometrium during the menstrual cycle (adapted from Netter [22]).

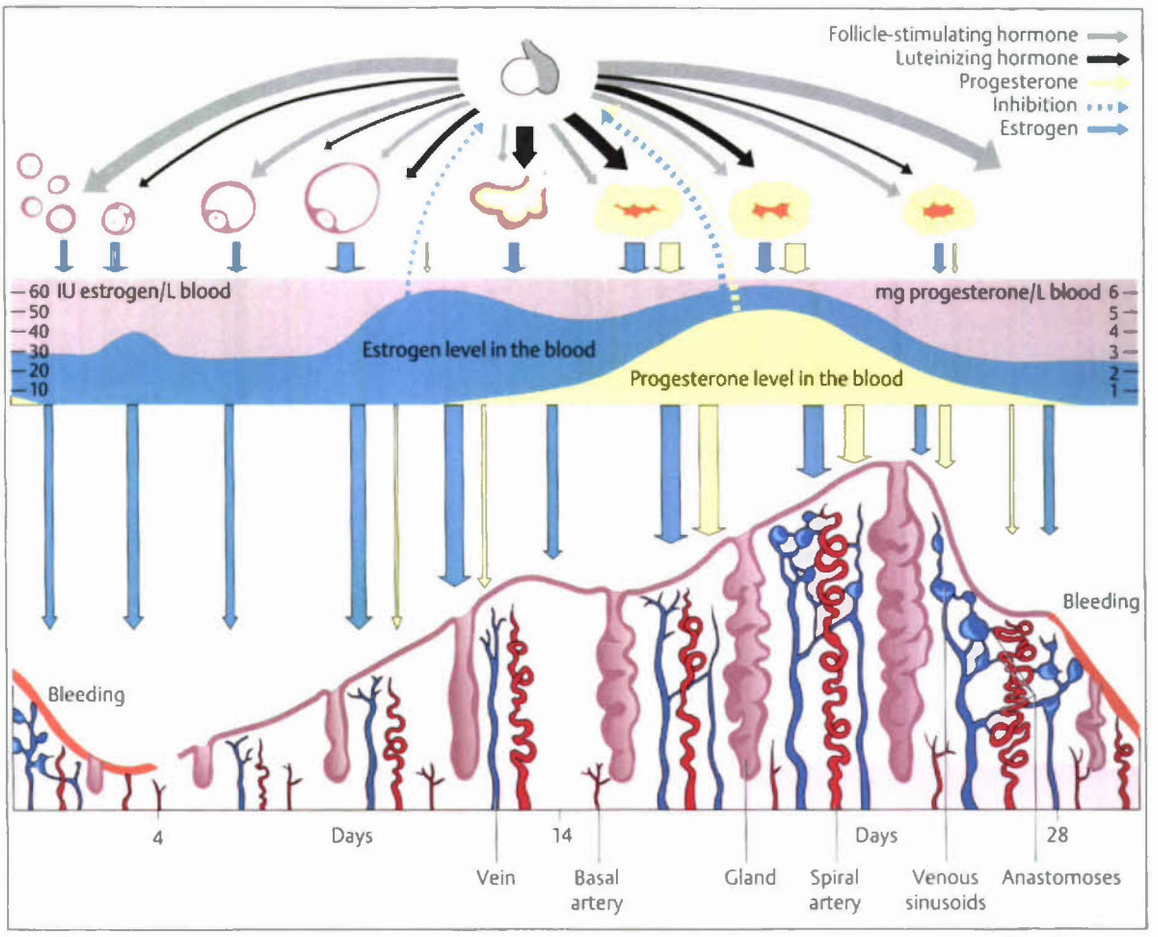

1

Endometrium in the First Half of the Cycle

Fig. 22.2 Endometrium in the early proliferative phase, day 5 of the menstrual cycle (type I endometrium). Endometrial thickness is 2 mm. Longitudinal scan.

Fig. 22.3 Type 1 endometrium. Transverse scan of the uterus.

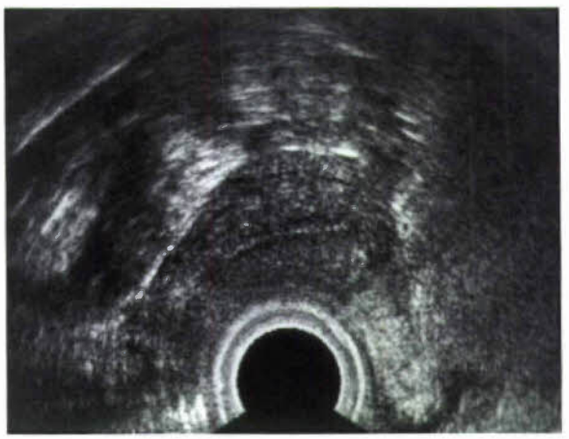

2

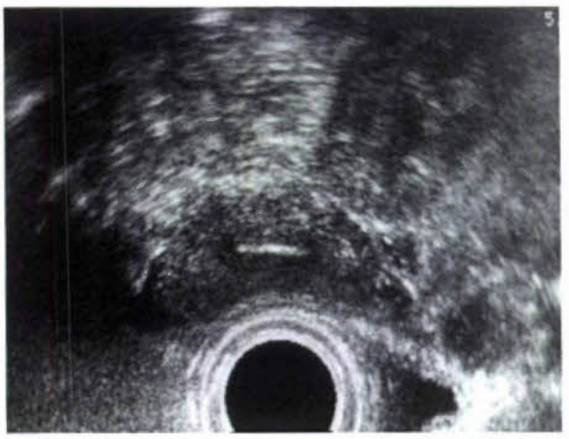

3

Fig. 22.4 Endometrium in the mid-proliferative phase, day 8 of the menstrual cycle (type 2 endometrium). The endometrial thickness is 4 mm. Longitudinal scan.

Fig. 22.5 Type 2 endometrium. Transverse scan of the uterus.

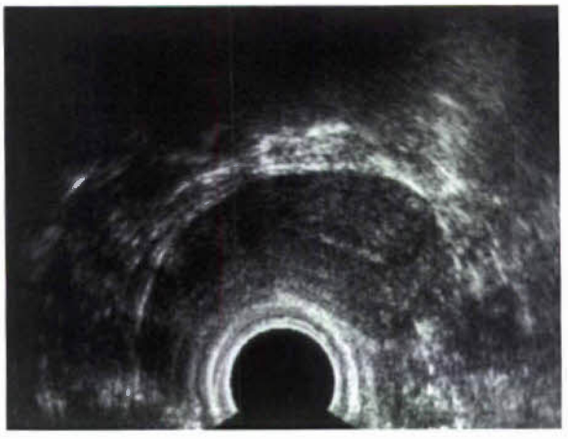

4

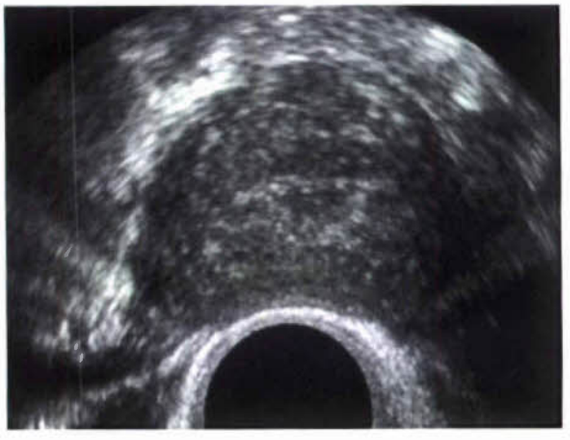

5

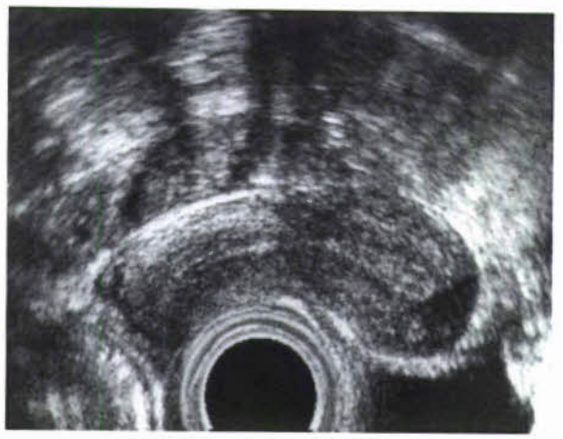

6

7

Fig. 22.6 Endometrium in the late proliferative phase, day 11 of the menstrual cycle (type 3 endometrium). Longitudinal scan.

Fig. 22.7 Type 3 endometrium. Transverse scan of the uterus.

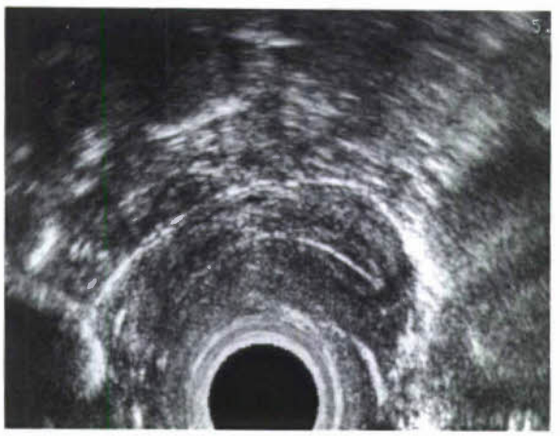

8

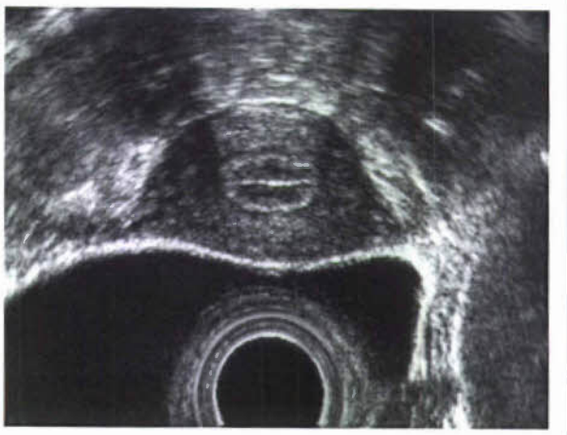

9

Fig. 22.8 Type 4 endometrium, day 13 of the menstrual cycle. Longitudinal scan.

Fig. 22.9 Type 4 endometrium. Transverse scan of the uterine corpus.

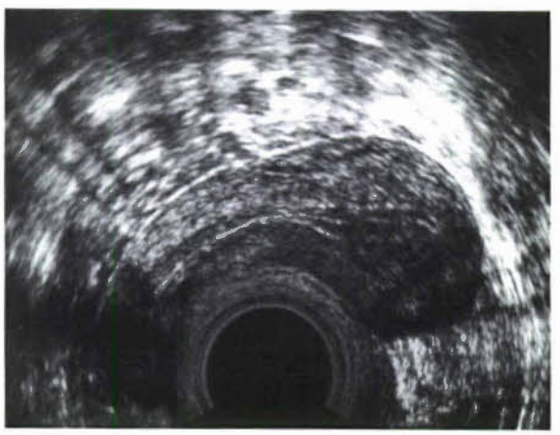

10

11

Fig. 22.10 Preovulatory endometrium (type 5). Longitudinal scan.

Fig. 22.11 Preovulatory endometrium (type 5). Transverse scan of the uterus.

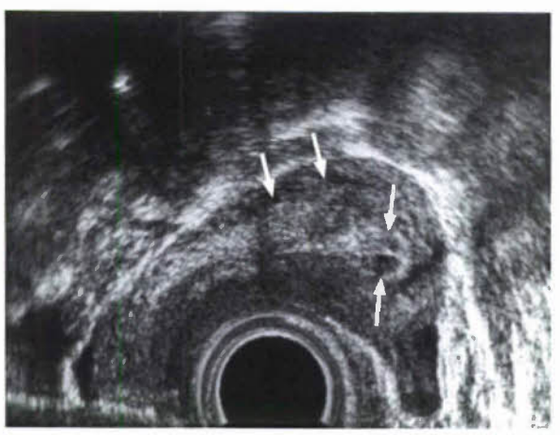

12

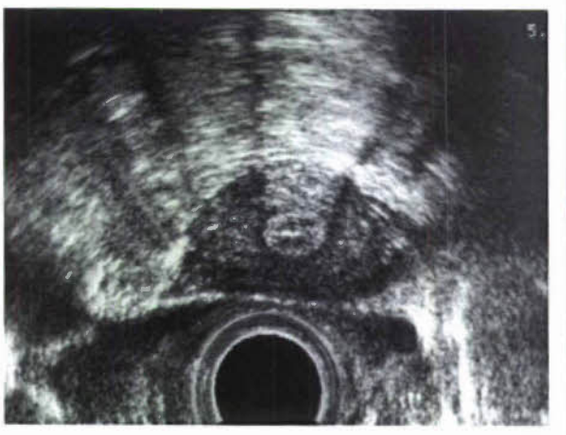

13

Fig. 22.12 The longitudinal scan displays the ring structure of the postovulatory endometrium (> <). The endometrial thickness is 1.1 cm. The uterine vessels appear as distinct hypoechoic areas in the outer third of the myometrium (→).

Fig. 22.13 Postovulatory endometrium. Transverse scan of the uterine corpus.

Endometrium in the Second Half of the Cycle

Fig. 22.**14** Endometrium in the luteal phase, day 24 of the menstrual cycle. The endometrial thickness is 1.0 cm. Longitudinal scan.

Fig. 22.**15** Endometrium in the luteal phase, day 24 of the menstrual cycle. Transverse scan of the uterine corpus.

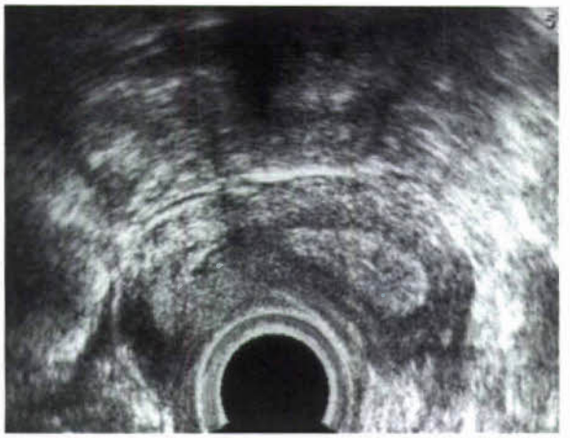

14

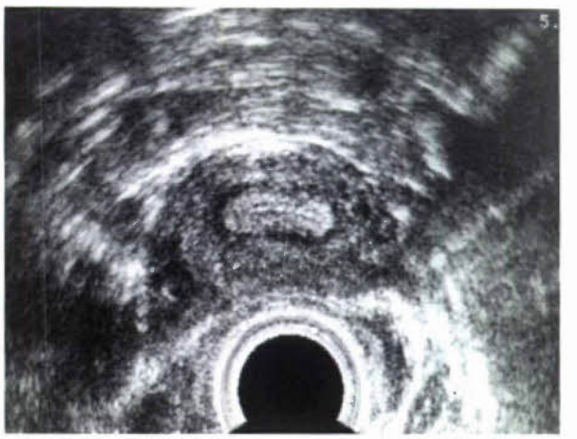

15

Cervical Changes during the Menstrual Cycle

Fig. 22.**16** Preovulatory expansion of the cervical canal by hypoechoic mucus. Longitudinal scan of the uterus.

Fig. 22.**17** Preovulatory expansion of the cervical canal by hypoechoic mucus. Transverse scan of the cervix (same case as in Fig. 22.**16**).

16

17

Ovarian Changes during the Menstrual Cycle

Fig. 22.**18** The ovulatory cycle (adapted from Netter [22]).

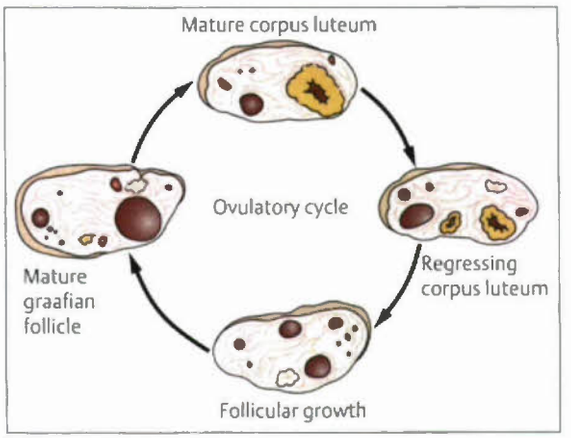

18

Fig. 22.**19** Ovary without a follicle in the early proliferative phase.

Fig. 22.**20** Ovary with a small follicle on day 7 of the menstrual cycle. The follicular diameter is 0.6 cm.

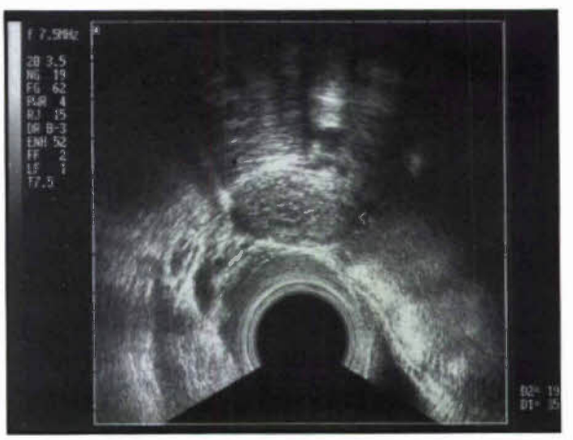

19

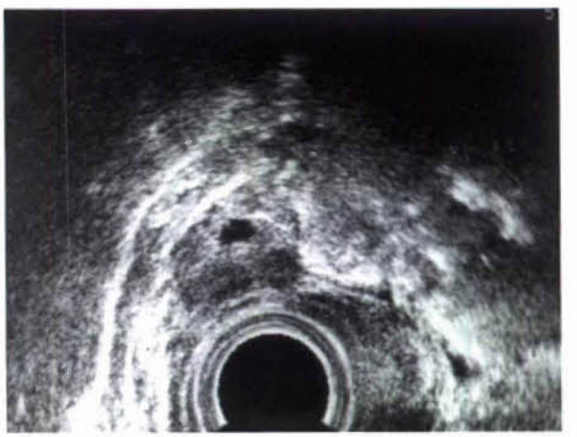

20

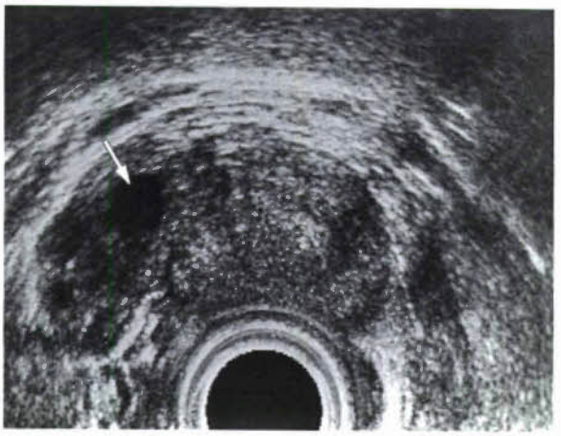

21

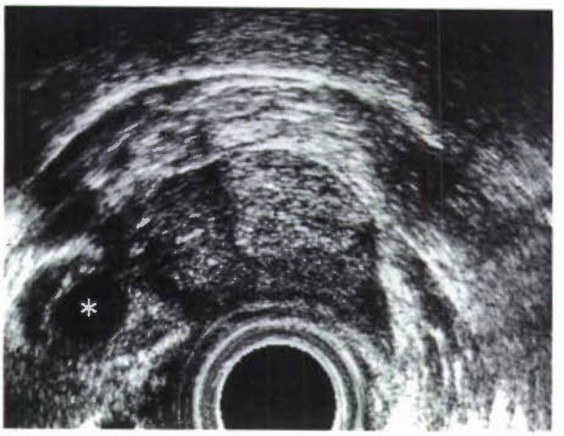

22

Fig. 22.**21** Follicular maturation, day 11 of the menstrual cycle. The follicular diameter in the right ovary is 1.2 cm (→). Coronal scan.

Fig. 22.**22** Coronal scan through the uterus and adjacent right ovary, which contains a follicle 1.6 cm in diameter.

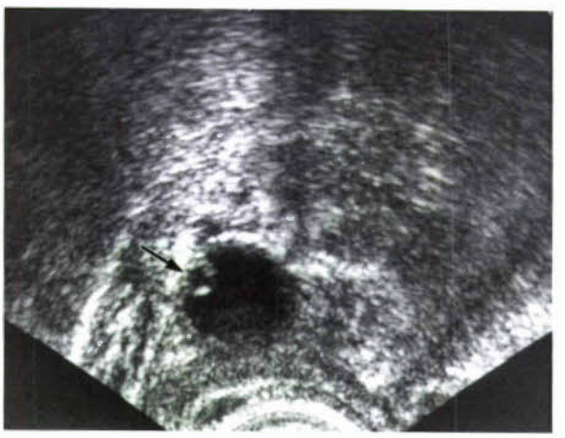

23

Fig. 22.**23** Follicular maturation, day 15 of the menstrual cycle. The coronal scan shows the cumulus oophorus (→) in a preovulatory follicle.

24

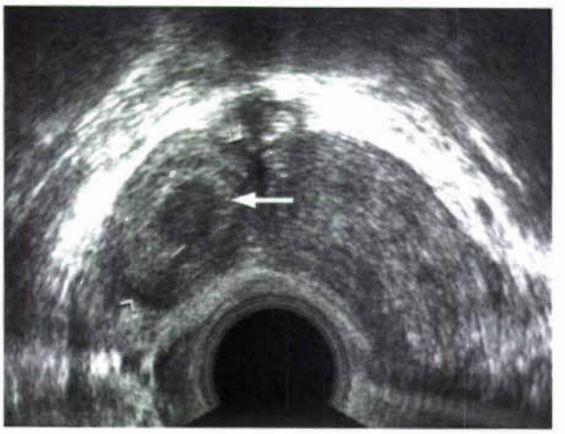

25

Corpus Hemorrhagicum, Corpus Luteum

Fig. 22.**24** Corpus hemorrhagicum with fresh bleeding in the follicular cavity. Coronal scan.

Fig. 22.**25** Corpus luteum in the right ovary shows a distinct, echogenic ring structure (→). Coronal scan.

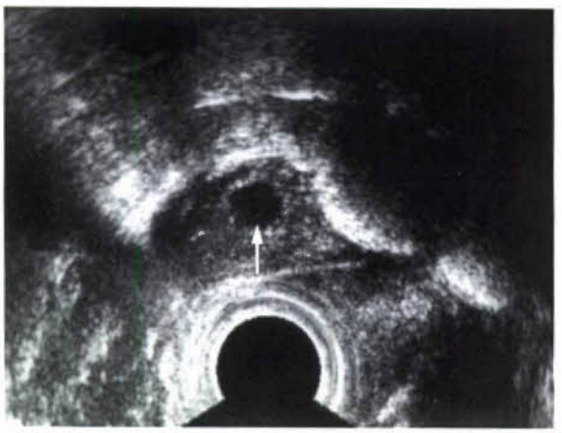

26

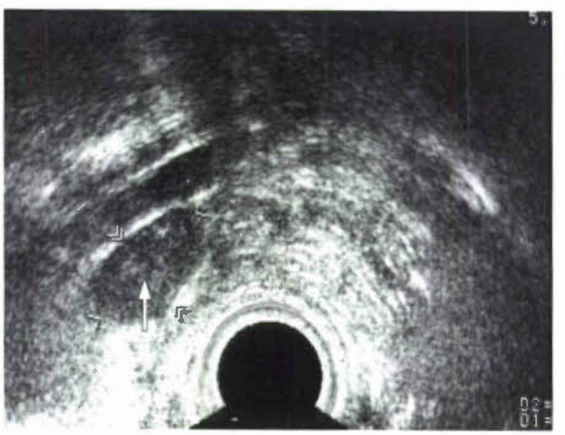

27

Fig. 22.**26** Corpus luteum in the right ovary (→), 1.1 cm in diameter, day 26 of the cycle. Longitudinal scan.

Fig. 22.**27** Corpus albicans (→).

23 Sonographic Changes in the Stimulated Cycle and the Detection of Menstrual Disorders

Sonographic monitoring of the internal genitalia is an absolutely essential adjunct to hormone studies in all forms of stimulation therapy. The sonographer can quickly detect or exclude abnormalities of the internal genitalia [1,1a,1b] and can also evaluate the position and size of the individual organs and changes in them during the stimulated cycle (Table 23.**1**).

Serial observations of the uterus and ovaries are particularly important in stimulated cycles, because the dynamics of organ changes can be appreciated only by conducting close-interval follow-ups. It also needs to be taken into account that a patient may have different reactions to the same medication in different cycles.

Table 23.1 Advantages of ultrasound monitoring in the stimulated cycle

Uterus	• Evaluate position • Exclude myomas and uterine anomalies • Evaluate the endometrium • Determine probe length
Ovary	• Evaluate size • Exclude ovarian cysts • Monitor ovarian response to therapy • Identify the side of follicular development • Detect multifollicular development • Determine timing of ovulation induction with HCG • Confirm that ovulation has occurred • Evaluate corpus luteum formation • Detect LUF syndrome • Detect hyperstimulation
Cul-de-sac	• Detect fluid in the cul-de-sac

HCG, human chorionic gonadotropin; LUF, luteinized unruptured follicle syndrome.

The Endometrium in the Stimulated Cycle

There is no significant difference between the progression of endometrial thickness in the stimulated cycle and that in the unstimulated cycle, despite marked differences in the serum levels of estradiol and progesterone [2–5].

Various groups of researchers [6,7] have shown that the sonographically determined endometrial thickness in the *follicular phase* is not a reliable predictor of successful implantation during that particular cycle.

For the *luteal phase*, however, Rabinowitz et al. [7] found that the prospects for conception were favorable when an endometrial thickness of at least 13 mm was measured on day 9 after follicular aspiration.

When a normal implantation has occurred, a high-resolution endovaginal probe can detect a small gestational sac in the endometrium only about 14 days after follicular aspiration.

When pituitary down-regulation is administered with gonadotropin-releasing hormone (GnRH) analogs before stimulation therapy, a low endometrial thickness provides good evidence that hormonal suppression has been achieved [7a] (Fig. 23.**1**).

Follicular Growth in the Stimulated Cycle

In the stimulated cycle, two or more follicles develop to maturity, depending on the type of therapy applied (Figs. 23.**2**–23.**5**). Stimulation with human menopausal gonadotropin (HMG) is associated with a considerably higher risk of multifollicular development than clomiphene stimulation [8].

To allow early detection of multifollicular development, ultrasound monitoring in the stimulated cycle should usually begin on day 8 of the cycle, depending on the known cycle length. If the cycle is very short, the first examination should be scheduled for day 6. In all cases, stimulation therapy should be preceded by a baseline ultrasound examination to exclude cystic changes in the ovary.

If more than three equal-sized "lead follicles" are identified on further monitoring, stimulation therapy and HCG use should be discontinued and contraceptive measures instituted to avoid the risk of a higher-order multiple pregnancy.

The issue of whether the maturing follicle is on the right or left side is of interest in patients with a unilateral tubal occlusion, or when one ovary is encased by heavy adhesions. In patients selected for homologous or heterologous insemination, stimulation therapy can be reasonably continued only if it is known that the follicles are developing on the unaffected side.

In addition to lateralization issues and knowing the number of maturing follicles, it is also important to assess how the individual follicles are progressing in size, so that the correct timing for ovulation induction can be determined. This is of interest because a high serum estradiol level in the stimulated cycle does not tell the therapist whether multiple smaller follicles or one or two large follicles are present.

Transvaginal ultrasound is superior to abdominal ultrasound [9,10] for defining and delineating the individual follicles from one another. Two closely adjacent follicles can be positively identified as such, eliminating the risk of premature ovulation induction based on the false assumption that there is one large follicle.

As soon as the largest follicle(s) have reached a size of 15 mm, the patient is monitored daily until ovulation occurs.

In comparison with follicular development in a spontaneous cycle, stimulated follicles grow an average of 2–3 mm larger than unstimulated follicles just before ovulation [11,12] and may reach up to 25 mm in size.

Once the lead follicle has reached a size of 18–20 mm by ultrasound, ovulation is induced with 10,000 IU of HCG. Ovulation should then occur approximately 36 hours later. If insemination is planned, it is carried out on the day after the HCG is administered.

Ultrasound monitoring of the luteal phase is advised after treatment with HCG, especially in the stimulated cycle, so that a hyperstimulation syndrome can be promptly detected. The basic monitoring protocol is outlined in Table 23.**2**.

Monitoring Oocyte Maturation in an IVF Cycle

Multifollicular growth is acceptable in the stimulated in-vitro fertilization (IVF) cycle in order to improve the chance of successful fertilization. Since the goal is to retrieve several mature oocytes if possible, the sonographic detection of optimum follicular size is of key importance. When several follicles have reached a size of 18–21 mm, 10,000 IU of

Table 23.2 General protocol for ultrasound monitoring of the menstrual cycle (should be adjusted for individual cycle length)

Days of menstrual cycle	Goal of examination
Premenstrual (before start of cycle)	Exclude ovarian cysts
8	Make initial assessment of ovarian response
10–14 (ovulation)	Evaluate daily: • Follicular growth • Endometrium • Cervical change
15–16	Detect ovulation
20–22	Evaluate corpus luteum and endometrium, exclude hyperstimulation
28–35	Detect intrauterine pregnancy

HCG is administered to induce ovulation. Transvaginal follicular aspiration is then carried out 32–34 hours later [13].

The IVF cycle differs from an ordinary stimulated cycle in that it is important to consider not just the number and size of the maturing follicles, but also the accessibility of the ovaries. If one of the ovaries is fixed at a relatively high level due to adhesions, it is likely that it will be too far away for transvaginal follicular aspiration, or that an attempted aspiration will injure the bowel.

Abnormalities of Follicular Development

Anovulatory Cycles

An anovulatory cycle can be definitely confirmed only by a combination of endocrinologic and sonographic monitoring. Transvaginal imaging demonstrates little or no follicular growth despite rising hormone levels.

PCO Syndrome

Polycystic ovary (PCO) syndrome [14,15,15a] is characterized by hirsutism, obesity, oligomenorrhea, an elevated testosterone level, a high luteinizing hormone–follicle-stimulating hormone (LH/FSH) ratio, and polycystic ovaries with a thick tunica albuginea.

Ultrasound demonstrates enlarged ovaries with a relatively echogenic stroma and small peripheral cysts 6–10 mm in diameter arranged in a string-of-beads pattern (Figs. 23.**6**, 23.**7**) [15b].

The superior resolution of transvaginal ultrasound allows significantly more accurate assessment of ovarian structure in PCO syndrome than is possible with traditional abdominal ultrasound. The string-of-beads ovarian cysts can be defined with much greater clarity.

If the hormonal profile is suspicious for PCO syndrome but ultrasound reveals normal-sized ovaries with no evidence of small peripheral cysts, the case should be diagnosed simply as *hyperandrogenemia* rather than PCO syndrome.

When a patient with a known PCO syndrome is receiving stimulation therapy, ovulation induction should be followed by close-interval ultrasound follow-ups, since the risk of hyperstimulation is significantly increased in the setting of PCO syndrome.

LUF Syndrome

In luteinized unruptured follicle (LUF) syndrome [16–18], ovulation fails to occur after normal follicular maturation, and the unruptured follicle becomes luteinized.

The etiology of this syndrome is not yet fully understood, but it may be related to stress or stress-induced hyperprolactinemia [19]. Its estimated incidence is approximately 5% [20].

Daily periovulatory ultrasound scans and progesterone assays are necessary in order to establish a diagnosis of LUF syndrome. The syndrome should be suspected if an ultrasound examination 36 hours after the LH peak shows that the mature follicle has not changed in size but contains internal echoes and there is a concomitant rise in serum progesterone. The absence of increased fluid in the cul-de-sac also supports the diagnosis.

It can be difficult to distinguish sonographically between LUF syndrome and a cystic corpus luteum unless continuous periovulatory monitoring has been maintained.

According to Deichert and Daume [21], the differential diagnosis is aided by noting that the cystic area in the postovulatory corpus luteum is always found to be smaller at ultrasound than the follicular diameter measured before ovulation.

Hyperstimulation Syndrome

Hyperstimulation syndrome develops as a result of massive follicular luteinization. It most commonly occurs in the stimulated cycle (HMG, clomiphene) following the administration of HCG. Although there is a close relationship between preovulatory estrogen levels and the incidence of hyperstimulation syndrome [22], the syndrome is less common in patients in whom HCG is not administered [23].

A critical factor in the development of the syndrome is the response rate of the ovaries to the administered hormone, although the exact pathogenesis of ovarian hyperstimulation syndrome is not yet fully understood. Because luteinization is necessary in order for the syndrome to develop, it is reasonable to assume that substances originating in the ovary or corpus luteum are of pathogenic significance [24].

The risk for developing hyperstimulation syndrome is increased in patients with hyperandrogenemia, PCO syndrome, or hyperprolactinemia. The hyperstimulation typically occurs between 3 and 7 days after the administration of HCG. The clinical manifestations vary with the grade of severity (Table 23.**3**).

With *mild hyperstimulation*, the ovaries are enlarged to up to 5 cm in diameter as a result of cyst formation. With *severe hyperstimulation*, which occurs in 1.2% [25] of treated cycles, the ovaries may become massively enlarged (Figs. 23.**8**, 23.**9**), in some cases extending to the umbilicus and causing very severe pain (with muscular guarding). Ascites is found in the cul-de-sac (Figs. 23.**9**, 23.**10**). In most cases, the greatly enlarged ovaries can be imaged in their entirely only by transabdominal scanning (Chapter 4).

Cases of mild to moderate hyperstimulation can be managed with sonographic and laboratory follow-up on an outpatient basis.

Severe hyperstimulation definitely requires in-patient monitoring, due to the potential for serious complications: ascites, pleural effusion, liver dysfunction, diarrhea, oliguria, elevated hematocrit, and arterial thromboembolism [26–28].

Table 23.3 Classification of hyperstimulation syndrome (adapted from Schenker and Weinstein [29])

Grade of severity	Clinical features
Mild hyperstimulation	
• **Grade 1**	Hyperstimulation with serum estradiol values >1500 pg/mL
• **Grade 2**	Hyperstimulation with ovaries enlarged to 5 cm
Moderate hyperstimulation	
• **Grade 3**	Hyperstimulation with tense abdominal wall
• **Grade 4**	Same as grade 3, plus nausea and vomiting
Severe hyperstimulation	
• **Grade 5**	Ovaries >5 cm in diameter, ascites, hydrothorax
• **Grade 6**	Hemoconcentration, coagulopathy

References

1 Homer HA, Li TC, Cooke ID. The septate uterus: a review of management and reproductive outcome. Fertil Steril. 2000;73:1–14.
1a Hart R, Khalaf Y, Yeong CT, Seed P, Taylor A, Braude P. A prospective controlled study of the effect of intramural uterine fibroids on the outcome of assisted conception. Hum Reprod. 2001;16:2411–7.
1b Strandell A, Lindhard A. Hydrosalpinx and ART. Salpingectomy prior to IVF can be recommended to a well-defined subgroup of patients. Hum Reprod. 2000;15:2072–4.
2 Giorlandino C, Gleicher N, Nanni C, Vizzone A, Gentili P, Taramanni C. The sonographic picture of endometrium in spontaneous and induced cycles. Fertil Steril 1987;7:508–11.
3 Imoedemhe DAG, Shaw RW, Kirkland A, Chan R. Ultrasound measurement of endometrial thickness on different ovarian stimulation regimens during in-vitro fertilization. Hum Reprod 1987;2:545–7.
4 Randall JM, Fisk NM, Mctavish A, Templeton AA. Transvaginal ultrasonic assessment of endometrial growth in spontaneous and hyperstimulated menstrual cycles. Br J Obstet Gynaecol 1989;96:954–9.
5 Sakamoto C, Yoshimitsu K, Nakamura G, Ootsuka H, Yoshida K. Sonographic study of the endometrial responses to ovarian hormones in patients receiving ovarian stimulation. Int J Gynaecol Obstet 1988;27:407–14.
6 Glissant A, de Mouzon J, Frydman R. Ultrasound study of the endometrium during in vitro fertilization cycles. Fertil Steril 1985;44:786–90.
7 Rabinowitz R, Laufer N, Lewin A, Navot D, Bar L, Margalioth E, et al. The value of ultrasonographic endometrial measurement in the prediction of pregnancy. Fertil Steril 1986;45:824–8.
7a Child TJ, Sylvestre C, Tan SL. Endometrial volume and thickness measurements predict pituitary suppression and non-suppression during IVF. Hum Reprod. 2002;17:3110–3.
8 Ritchie WGM. Sonographic evaluation of normal and induced ovulation. Radiology 1986;161:1–10.
9 Bonilla-Musoles F, Pardo G, Perez-Gil M, Serra V, Pellicer A. Abdominal ultrasonography versus transvaginal scanning: accuracy in follicular development evaluation and prediction for oocyte-retrieval in stimulated cycles. J Clin Ultrasound 1989;17:469–73.
10 Deutinger J, Reinthaller A, Riss P, Bernaschek G, Csaicsich P, Fischl F, et al. Comparison of the results of vaginal and abdominal follicle scans. Arch Gynecol Obstet 1987;241:171–6.
11 De Cherney AH, Romero R, Polan ML. Ultrasound in reproductive endocrinology. Fertil Steril 1982;37:323–33.
12 Ylöstalo P, Siegberg R. Ovarian stimulation during gonadotropin treatment after hCG administration monitored by ultrasound and serum estradiol and progesterone. Int J Fertil 1988;33:259–64.
13 Edwards RG, Steptoe PC, Purdy JM. Establishing full-term human pregnancies using cleaving embryos grown in vitro. Br J Obstet Gynaecol 1980;87:737–57.
14 Moltz L, Sörensen R, Römmler A, Schwartz U, Hammerstein J. Polyzystische Ovarien: ein eigenständiges Krankheitsbild oder unspezifisches Symptom? Geburtshilfe Frauenheilkd 1985;45:107–14.
15 Orsini LF, Venturoli S, Lorusso R, Pluchinotta V, Paradisi R, Bovicelli L. Ultrasonic findings in polycystic ovarian disease. Fertil Steril 1985;43:709–14.
15a Lowe P, Kovacs G, Howlett D. Incidence of polycystic ovaries and polycystic ovary syndrome amongst women in Melbourne, Australia. Aust N Z J Obstet Gynaecol. 2005;45:17–9.
15b Battaglia C, Mancini F, Persico N, Zaccaria V, de Aloysio D. Ultrasound evaluation of PCO, PCOS and OHSS. Reprod Biomed Online. 2004;9:614–9
16 Coulam CB, Hill LM, Breckle R. Ultrasonic evidence for luteinization of unruptured preovulatory follicles. Fertil Steril 1982;37:524–9.
17 Jewelewicz R. Management of infertility resulting from anovulation. Am J Obstet Gynecol 1975;122:909–20.
18 Koninckx PR, DeMoor P, Brosens IA. Diagnosis of the luteinized unruptured follicle syndrome by steroid hormone says on peritoneal fluid. Br J Obstet Gynaecol 1980;87:929–34.
19 Koninckx PR, Brosens IA. Clinical significance of the luteinized unruptured follicle syndrome as a cause of infertility. Eur J Obstet Gynecol 1982;13:355–68.
20 Kerin JF, Kirby C, Morris D, McEvoy M, Ward B, Cox LW. Incidence of the luteinized unruptured follicle phenomenon in cycling women. Fertil Steril 1983;40:620–6.
21 Deichert U, Daume E. Zyklische Veränderungen am Ovar. In: Deichert U, Duda V, Schlief R, editors. Funktionelle Sonographie in Gynäkologie und Reproduktionsmedizin. Berlin: Springer, 1993: 71–132.
22 Runnebaum B, Rabe T. Gynäkologische Endokrinologie. Berlin: Springer, 1987.
23 Hancock KW, Stich SR, Oakey RE, Scott JS, Levell MJ. Response to gonadotropins. Lancet 1970;ii:482–5.
24 Bider D, Menashe Y, Oelsner G, Serr DM, Mashiach S, Ben-Rafael Z. Ovarian hyperstimulation syndrome due to exogenous gonadotropin administration. Acta Obstet Gynecol Scand 1989;68:511–4.
25 Thompson CR, Hansen LM. Pergonal (menotropins): a summary of clinical experience in the induction of ovulation and pregnancy. Fertil Steril 1970;21:844–53.
26 Balasch J, Carmona F, Llach J, Arroyo V, Jové I, Vanrell JA. Acute prerenal failure and liver dysfunction in a patient with severe ovarian hyperstimulation syndrome. Hum Reprod 1990;5:348–51.
27 Lunenfeld B, Lunenfeld E, Shenhav M. Komplikationen der Gonadotropintherapie. Aktuelle Endokrinol Stoffwechs 1989;10:1–5.
28 Rizk B, Meagher S, Fisher AM. Severe ovarian hyperstimulation syndrome and cerebrovascular accidents. Hum Reprod 1990;5:697–8.
29 Schenker JG, Weinstein D. Ovarian hyperstimulation syndrome: a current survey. Fertil Steril 1978;30:255–68.

Fig. 23.1 Streak-like endometrium (> <) after treatment with gonadotropin-releasing hormone (GnRH) analogs.

Follicular Growth in the Stimulated Cycle

Fig. 23.2 Follicular growth on day 8 of a clomiphene-stimulated cycle. This coronal scan through the right ovary demonstrates two adjacent follicles 1.5 and 1.4 cm in diameter.

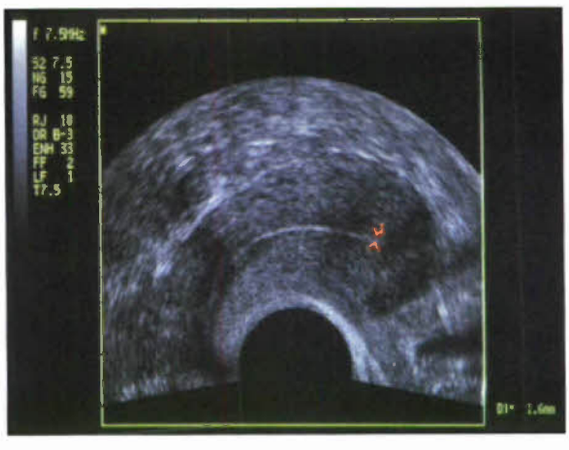

1

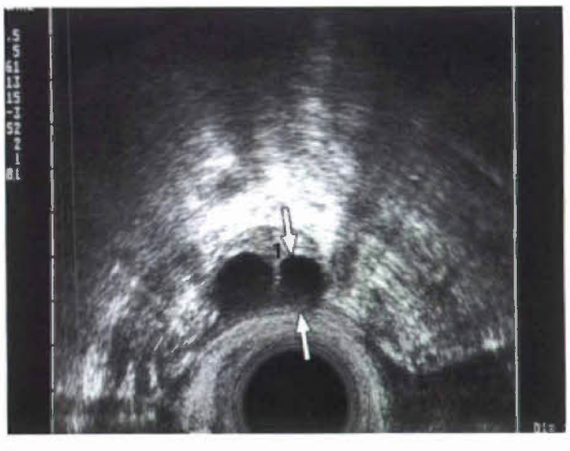

2

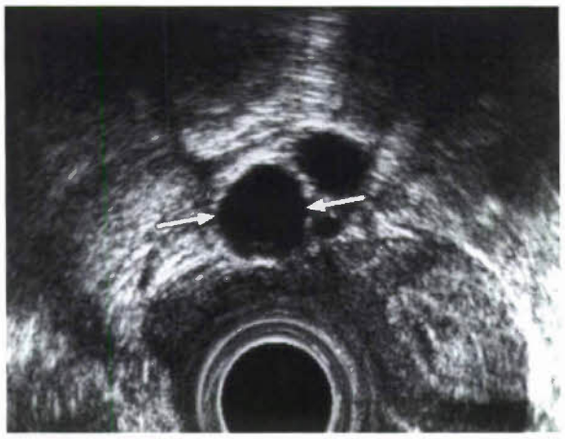

3

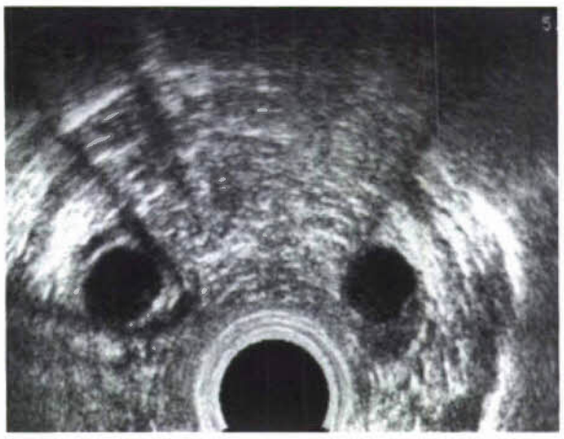

4

Fig. 23.3 Follicular maturation on day 12 of a clomiphene-stimulated cycle. The oblique longitudinal scan shows a 2.4-cm follicle (> <) and a 1.8-cm follicle in the right ovary behind the uterus.

Fig. 23.4 Bilateral follicular growth in response to clomiphene stimulation. Coronal scan through both ovaries. The follicular diameter is 1.8 cm on the right side and 1.7 cm on the left side.

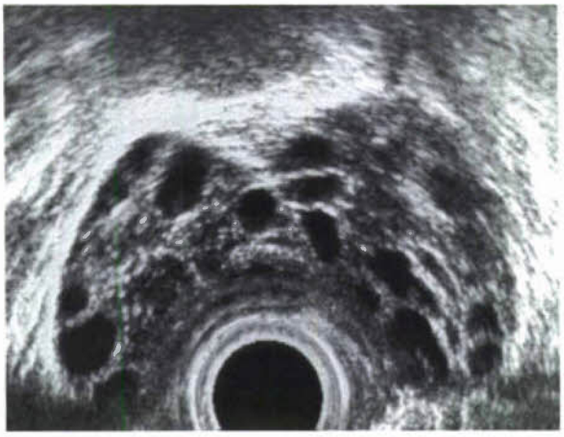

5

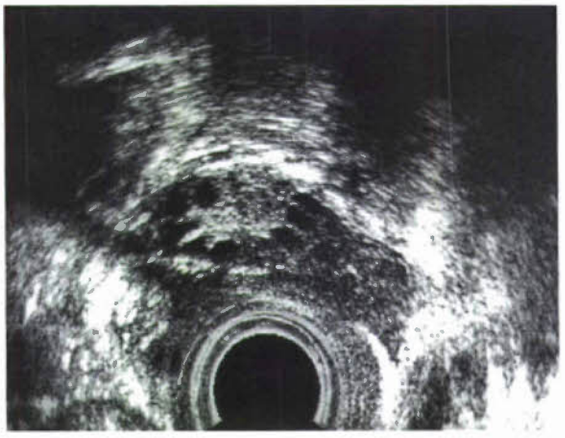

6

Fig. 23.5 Multifollicular growth in both ovaries in a patient treated with follicle-stimulating hormone/human menopausal gonadotropin (FSH/HMG) on day 10 of the menstrual cycle. Coronal scan.

Polycystic Ovary Syndrome

Fig. 23.6 Polycystic ovary in a patient with Stein–Leventhal syndrome (polycystic ovary syndrome). Coronal scan. The ovary measures 4.3 × 2.9 × 3.8 cm.

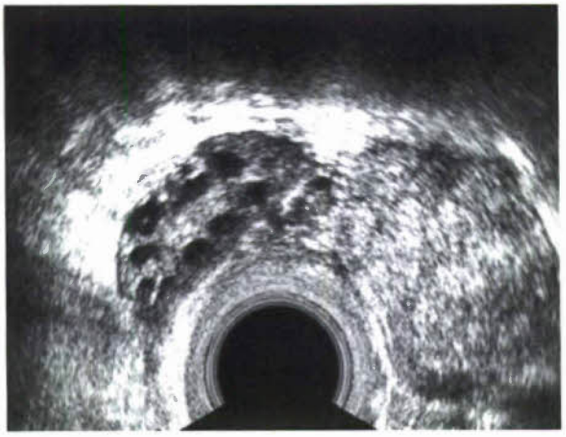

7

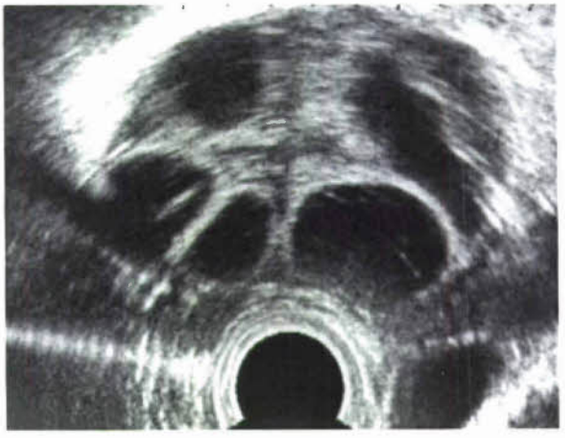

8

Fig. 23.7 An enlarged polycystic right ovary, showing a string-of-beads arrangement of peripheral follicles 6 mm in diameter. Coronal scan.

Hyperstimulation Syndrome

Fig. 23.8 Marked ovarian enlargement due to hyperstimulation with human menopausal gonadotropin (HMG). Longitudinal scan of the right ovary (10.0 × 6.5 × 7.4 cm).

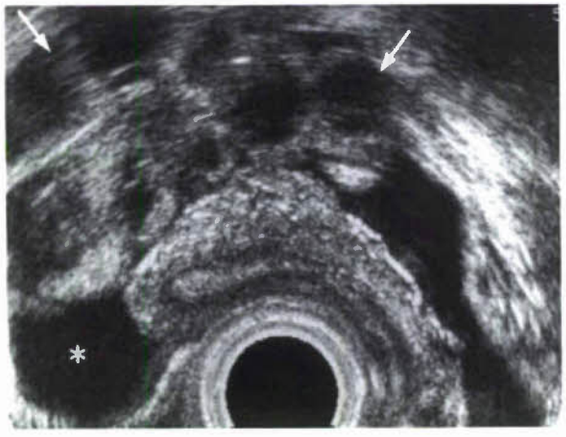

9

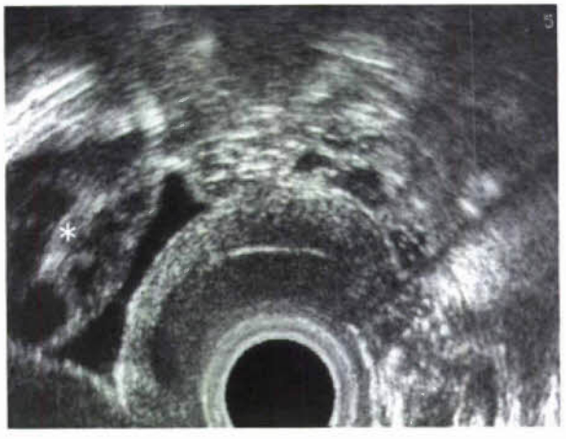

10

Fig. 23.9 Severe hyperstimulation syndrome. Markedly enlarged ovary with multiple follicles (—) and copious ascites (*). Retroflexed uterus. Longitudinal scan.

Fig. 23.10 Hyperstimulation syndrome in regression. The ovaries are still enlarged (*) and there is slight residual ascites. Longitudinal scan taken on the third day after the onset of menses.

24 Genital Tract Anomalies

Uterine Anomalies

Congenital uterine anomalies have an incidence of approximately 1% [1] to 1.9% [2] and result from incomplete union of the müllerian ducts (Fig. 24.**1**).

Three characteristic periods can be distinguished in the embryonic development of the internal genitalia [3]:

- The period between *weeks 6 and 9*, in which both müllerian ducts are formed and are arranged parallel to the urogenital sinus. The urinary passages also develop during this period.
- The period between *weeks 10 and 12*, in which the lower portions of the müllerian ducts fuse together, followed by disappearance of the intervening septum, starting from the uterine isthmus. The uterine horns also unite during this period (weeks 11–12). The uppermost portions of the müllerian ducts remain unfused to form the fallopian tubes.
- The period between *weeks 13 and 17*, in which the uterus acquires its definitive internal and external shape through absorption of the fibrous septum separating the uterine horns.

Uterine anomalies show varying degrees of severity, depending on the period of embryonic development in which the disturbance occurred (Table 24.**1**, Fig. 24.**2**). The causal factors that underlie these malformations are poorly understood. Uterine anomalies are frequently accompanied by urinary tract anomalies. Patients with a *bicornuate uterus* have associated urinary tract anomalies in approximately 30% [3] to 35% of cases [4]. By contrast, urinary tract anomalies have not been found in association with a *septate uterus* [3]. It is very likely, then, that the presence of a urinary tract anomaly precludes the existence of a septate uterus.

Women with a uterine anomaly have been found to have a markedly higher incidence of primary infertility and a higher spontaneous abortion rate [1,4].

As we know from transabdominal scanning, ultrasound is a valuable tool for detecting and differentiating uterine anomalies [5,6]. Thus, when a uterine anomaly is suspected, sonography heads the list of diagnostic options and should precede hysterosalpingography (HSG) and diagnostic laparoscopy.

When a high-resolution endovaginal probe is used, uterine anomalies can be detected clearly and quickly in a longitudinal coronal scan through the uterus, and also in transverse scans through the uterine corpus and cervix, with very little preparation. Attention is given to the overall contours of the uterus, the width of the corpus and cervix, and the structure of the endometrium (Table 24.**2**).

A markedly broad uterine corpus may be found in association with a relatively broad endometrium or two separate endometrial streaks, depending on whether the anomaly is a simple, heart-shaped *arcuate uterus* (Figs. 24.**2a**, 24.**3**, 24.**4**), a *uterus bicornis unicollis* (Figs. 24.**2b**, 24.**5**), or a *subseptate or septate uterus* (Figs. 24.**2e–g**, 24.**6**).

With a *bicornuate double uterus* (Figs. 24.**2c**, 24.**7**), the paired uterine horns are accompanied by an abnormal cervical width with two adjacent cervical cavities.

With a *uterus didelphys* (Figs. 24.**2d**, 24.**8**), ultrasound can demonstrate two completely separate uteri situated side by side. Transvaginal scanning can display both uteri in the same image only when a panoramic transducer is used. When a probe with a smaller field of 90–120° is used, it is helpful to split the monitor image and display the two uteri separately on the right and left sides of the screen.

Table 24.1 Uterine anomalies related to the timing of the causal disturbance (adapted from Kaskarelis [3])

Timing of the disturbance	Type of anomaly
Embryonic weeks 6–9	Uterine aplasia • complete aplasia • incomplete aplasia (Mayer–Rokitansky–Küster syndrome) • complete aplasia of a uterine horn; unicornuate uterus • incomplete aplasia of a uterine horn; pseudo-unicornuate uterus
Embryonic weeks 10–12	Bicornuate uterus • Uterus bicornis unicollis • Uterus bicornis bicollis • Uterus bicollis with a nonpatent cervix • Uterus bicollis opening into an occluded hemivagina • Communicating forms
Embryonic weeks 13–17	Septate uterus • arcuate • unicervical • bicervical • communicating

Table 24.2 Sonographic signs indicating a uterine anomaly

- Abnormal uterine contour
- Abnormally broad uterine corpus
- Abnormally broad cervix
- Detection of two separate endometrial streaks
- Absence of one kidney (on abdominal ultrasound)

Because genital anomalies are commonly associated with urinary tract malformations, scans will occasionally demonstrate a *pelvic kidney* lateral and cranial to the uterus, appearing as a hypoechoic "mass" with an echogenic center (Figs. 30.**2**, 30.**3**).

High-sited rudimentary uterine horns located at the pelvic inlet are demonstrated more clearly by transabdominal scanning. The renal fossae can be examined at the same time to detect or exclude unilateral renal aplasia [7].

Vaginal Aplasia

Vaginal aplasia is diagnosed with the aid of abdominal ultrasound (Chapter 5).

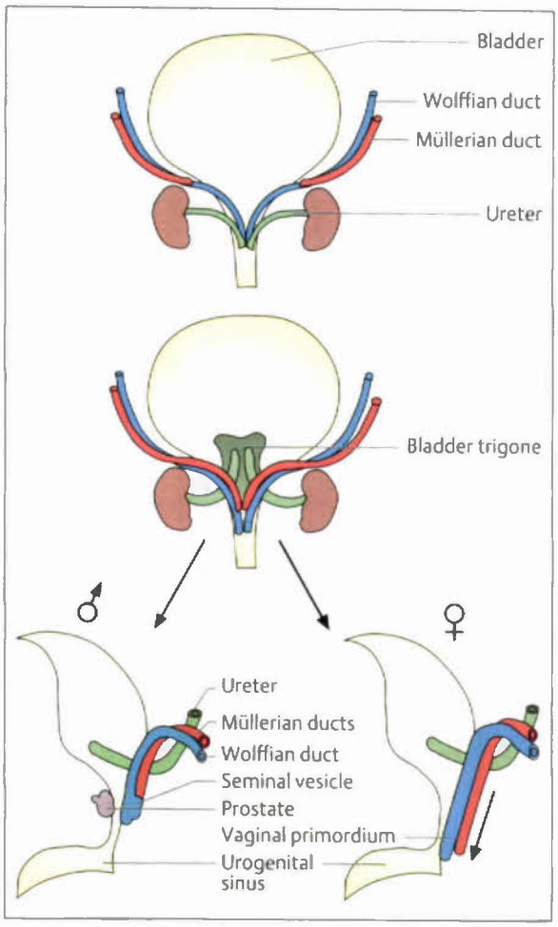

1

Fig. 24.1 Diagram showing the course of the müllerian ducts (after Drews [8]).

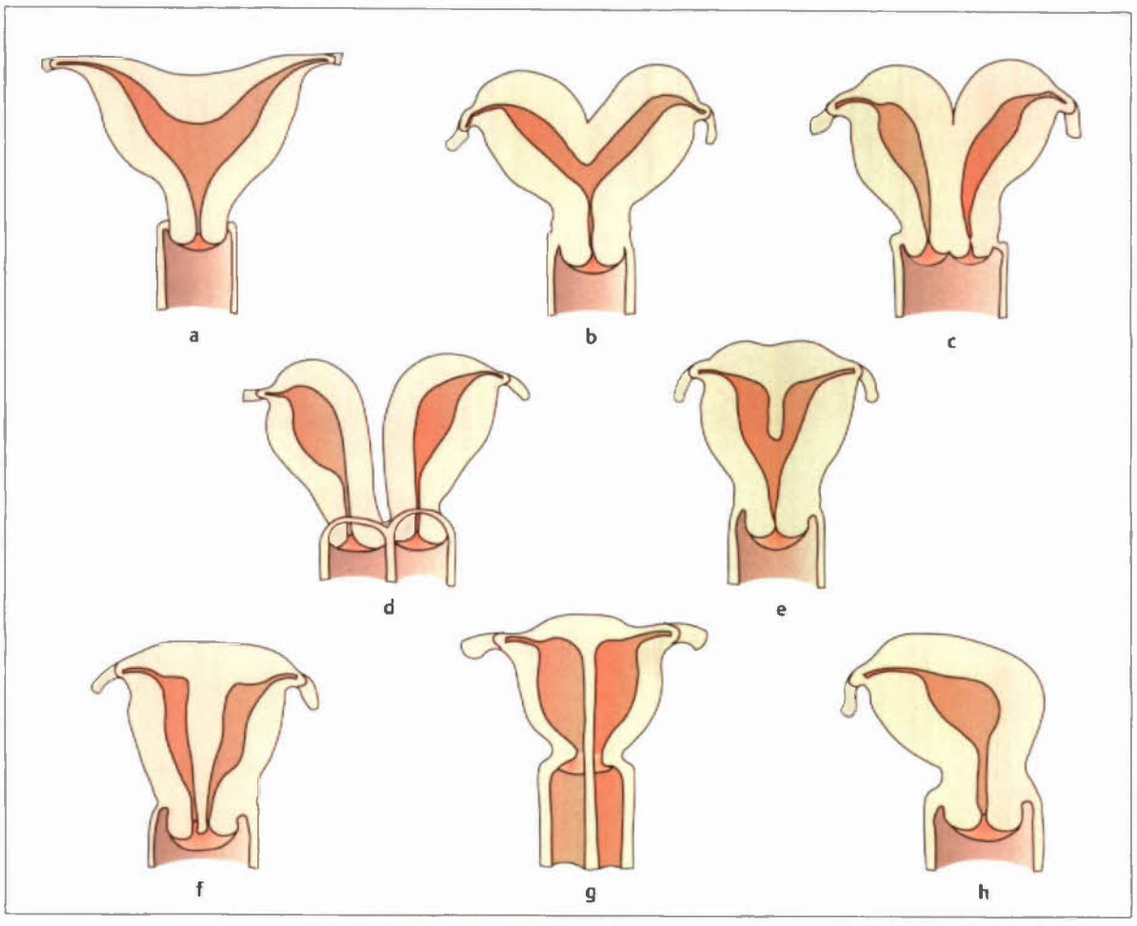

2

Fig. 24.2 Schematic representation of various uterine anomalies.
a Arcuate uterus.
b Uterus bicornis unicollis.
c Bicornuate double uterus.
d Uterus didelphys.
e Subseptate uterus.
f Septate uterus.
g Septate uterus and vagina.
h Unicornuate uterus.

Uterine Anomalies

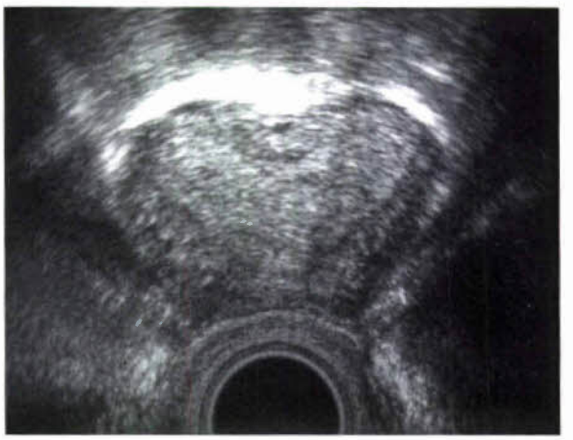

3

Fig. 24.3 Arcuate uterus in longitudinal coronal section.

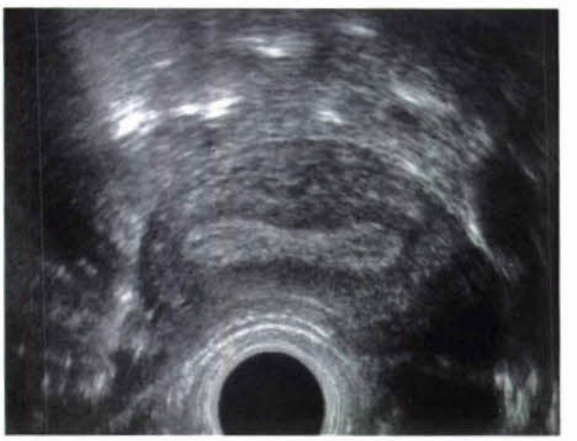

4

Fig. 24.4 Arcuate uterus. Transverse scan of the upper part of the uterine corpus.

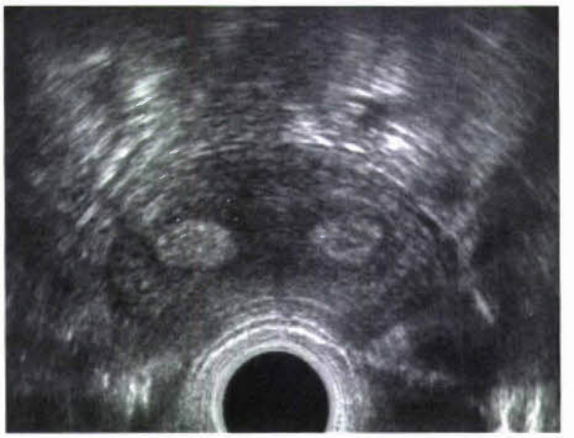

5

Fig. 24.5 Bicornuate uterus. Transverse scan of the uterus at the level of the uterine horns.

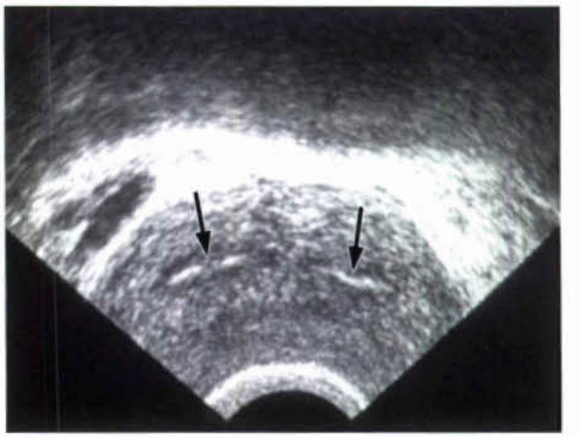

6

Fig. 24.6 Subseptate uterus. The transverse scan of the uterine corpus shows two separate endometrial streaks (↓ ↓) flanking a central septum.

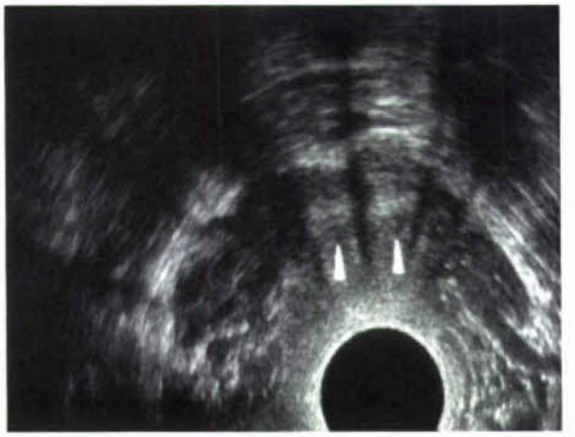

7

Fig. 24.7 Both cervical segments (∧ ∧) are displayed in a bicornuate double uterus. Coronal scan through the cervix.

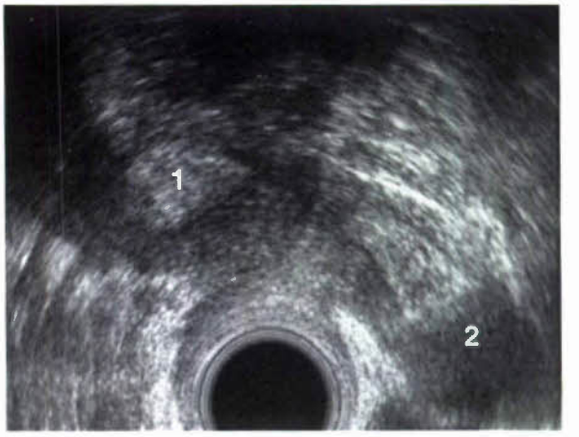

8

Fig. 24.8 This coronal scan of a double uterus demonstrates two separate uteri.
1 Right uterus
2 Left uterus

References

1 Rudigoz RC, Gaucherand P, Dargent D. [The obstetrical outlook in uterine malformations; in French.] J Gynecol Obstet Biol Reprod (Paris) 1989;18:185–91.
2 Ashton D, Amin HK, Richart RM, Neuwirth RS. The incidence of asymptomatic uterine anomalies in women undergoing transcervical tubal sterilization. Obstet Gynecol 1988;72:28–30.
3 Kaskarelis DB. Restaurative Chirurgie bei angeborenen Missbildungen des Uterus und bei Uterussynechien. Gynäkologe 1980;13:142–51.
4 Heinonen PK. Uterus didelphys: a report of 26 cases. Eur J Obstet Gynaecol 1983;17:311–6.
5 Fedele L, Ferrazzi E, Dorta M, Vercellini P, Candiani GB. Ultrasonography in the differential diagnosis of double uteri. Fertil Steril 1988;50:361–4.
6 Funk A, Fendel H. Beitrag zur sonographischen Diagnostik kongenitaler Uterusanomalien. Z Geburtshilfe Perinatol 1988;192:77–82.
7 Nakada T, Katayama T, Shimazaki J. Unilateral renal agenesis associated with bicornuate uterus. Urol Int 1988;43:352–5.
8 Drews U. Morphologische Entwicklung der Sexualorgane. Gynäkologe 1995;28:5–11.

25 Pelvic Inflammatory Disease

Pelvic inflammatory disease is the leading cause of pain, infertility, and tubal pregnancy. It is estimated that approximately 30% of infertility cases and 50% of ectopic pregnancies are caused by inflammatory changes in the lower abdomen [1].

In addition to typical clinical symptoms such as pain, vaginal discharge and fever, an acute inflammation of the internal genitalia is associated with significant laboratory abnormalities (elevated erythrocyte sedimentation rate, leukocytosis, elevated C-reactive protein). Although bimanual examination is carried out routinely in these cases to assess the location and extent of the inflammatory process, the tenderness of the uterus and adnexa often prevents adequate evaluation of the affected organs. The lower abdomen is particularly difficult to palpate when guarding is present due to peritoneal irritation. In addition, there is the risk of rupturing a tubo-ovarian abscess or pyosalpinx due to overvigorous palpation.

Ultrasound examination of the lower abdomen is less traumatizing than any manual examination in patients with pelvic inflammatory disease. Abdominal ultrasound [2–7] has long been established as a noninvasive option, although the movements of the transducer over the abdomen have been found to cause discomfort in most women.

When the patient is scanned transvaginally [8–12], especially with a panoramic probe, the true pelvis can be examined with considerably less discomfort. Once the probe has been carefully inserted into the vagina, the entire true pelvis can be adequately explored with very little need for endovaginal probe manipulations. It has also been shown that transvaginal scanning can provide considerably greater image detail than transabdominal scanning in patients with pelvic inflammatory disease [8]. As a result, transvaginal ultrasound has become an indispensable tool in the diagnostic evaluation of pain in the true pelvis, even when the pain does not have a gynecologic cause (Table 25.**1**). Vaginal scanning is of particular value when used in close-interval follow-up examinations to assess the response of inflammatory changes to therapy.

The ultrasound findings in patients with an ascending infection are extremely diverse, depending on the extent of the inflammatory process. In most cases, no sonographic changes are detected during the early stage of an ascending infection. In cases with significant endomyometritis, increased fluid can be detected within the uterine cavity (Fig. 25.**1**). Once the inflammation has spread to the fallopian tube, a fluid collection can also be observed within the tubal lumen. This is usually accompanied by marked thickening of the tubal wall (Fig. 25.**2**).

In patients with *acute adnexitis*, ultrasound will usually demonstrate an increased fluid collection in the cul-de-sac (Fig. 25.**3**). With adhesions at the fimbriated end, scans will show a definite, oblong expansion of the fallopian tube, depending on the nature and volume of the retained secretions. *Pyosalpinx* is manifested by the appearance of fine, diffuse internal echoes within the markedly thickened and expanded tube (Figs. 25.**4**, 25.**5**) caused by debris within the purulent fluid [6].

Severe forms of adnexitis may incite the formation of a pelvic abscess (tubo-ovarian abscess, cul-de-sac abscess). With a pronounced *tubo-ovarian abscess*, ultrasound reveals a unilocular or multilocular thick-walled mass with diffuse internal echoes [3,6,13] (Figs. 25.**6**, 25.**7**). As the debris settles, a layering effect can be seen within the cystic mass [7]. The outer margins of a tubo-ovarian abscess are poorly delineated from the surrounding tissues, due to the inflammatory adhesions that form between the abscess and the adjacent uterus, bowel, and pelvic wall. In rare cases, genital tuberculosis may underlie a tubo-ovarian abscess. These patients present sonographically with an adnexal mass accompanied by ascites, peritoneal thickening, and adhesions [14].

The differential diagnosis of tubo-ovarian abscess includes a number of noninflammatory conditions that can produce similar sonographic changes in the true pelvis (Table 25.**2**).

It can also be difficult to diagnose a conglomerate mass caused by matted adhesions based on ultrasound findings alone [15]. But this can usually be accomplished by interpreting the scans within the context of the history, clinical findings, and laboratory parameters. If the mass is located at a relatively high level, transvaginal scanning alone cannot provide an adequate evaluation and should be supplemented by abdominal ultrasound [5] (Chapter 6).

If a *cul-de-sac abscess* forms as a result of pelvic inflammatory disease, it can be recognized at transvaginal ultrasound by its fine internal echo pattern (Figs. 25.**8**, 25.**9**). Free blood in the cul-de-sac may have a similar appearance, but laboratory tests in this case will not show such a marked increase in inflammatory parameters. Any doubts as to the correct diagnosis can be quickly resolved by ultrasound-guided transvaginal aspiration of the fluid area [16,17].

Transvaginal ultrasound is also usually better than abdominal ultrasound for the investigation of postinflammatory changes such as *hydrosalpinx* (Figs. 25.**10**, 25.**11**) [10,11] and *postinflammatory conglomerate masses*. *Postinflammatory adhesions* in the cul-de-sac can be detected by transvaginal scanning only if they are immersed in free fluid (Figs. 25.**12**, 25.**13**). Otherwise, they are extremely difficult to detect because of their thin, web-like structure.

References

1 Todth M, Chervenak FA. Clinical and ultrasound dimensions of infections of the ovary and Fallopian tube. In: Kurjak A, editor. Ultrasound and the ovary. New York: Parthenon, 1994: 165–77.

Table 25.1 Differential diagnosis of acute lower abdominal pain

Genital causes	Extragenital causes
• Adnexitis	• Appendicitis
• Parametritis	• Diverticulitis
• Ovarian abscess	• Gastroenteritis
• Cul-de-sac abscess	• Crohn's disease
• Torsion of an ovarian mass	• Bowel obstruction
• Hemorrhagic ovarian cyst	• Acute porphyria
• Endometriosis	• Urolithiasis
• Ruptured ovarian cyst	• Cystitis
• Myoma protruding through the cervical os	• Pelvic venous thrombosis
• Hematometra	
• IUD expulsion	
• Ectopic pregnancy	
• Incipient abortion	

IUD, intrauterine device.

Table 25.2 Differential diagnosis of tubo-ovarian abscess

- Endometriotic cyst
- Dermoid cyst
- Hemorrhagic corpus luteum cyst
- Pedunculated myoma
- Torsion of an ovarian mass
- Perityphlitic abscess
- Peritubal hematoma associated with ectopic pregnancy
- Inflammatory conglomerate mass associated with terminal ileitis
- Coproma

2 Henkel B. Die ultrasonographische Diagnostik pathologischer Veränderungen der Tuba uterina. Ultraschall 1982;3:152–9.
3 Lipsit ER. Inflammatory disease of the pelvis and postoperative fluid collections. In: Steel WB, Cochrane WJ, editors. Gynecologic ultrasound. Edinburgh: Churchill Livingstone, 1984: 85–104.
4 McArdle CR, Simon L, Kiejna C. Vaginal drainage of posthysterectomy abscess under direct ultrasonic guidance. Obstet Gynecol 1984;63:905–925.
5 Spirtos NJ, Bernstine RL, Crawford WL, Fayle J. Sonography in acute pelvic inflammatory disease. J Reprod Med 1982;6:312–9.
6 Taylor KJ, Wasson JF, De Graff C, Rosenfield AT, Andriole VT. Accuracy of grey-scale ultrasound diagnosis of abdominal and pelvic abscesses in 220 patients. Lancet 1978;i:83–4.
7 Uhrich PC, Sanders RC. Ultrasonic characteristics of pelvic inflammatory masses. J Clin Ultrasound 1976;4:199–204.
8 Bulas DI, Ahlstrom PA, Sivit CJ, Blask ARN, O'Donnell RM. Pelvic inflammatory disease in the adolescent: comparison of transabdominal and transvaginal sonographic evaluation. Radiology 1992;183:435–9.
9 Patten RM, Vincent LM, Wolner-Hanssen P, Thorpe E Jr. Pelvic inflammatory disease: endovaginal sonography with laparoscopic correlation. J Ultrasound Med 1990;9:681–90.
10 Tessler EN, Perella RR, Fleischer AC, Grant EG. Endovaginal sonographic diagnosis of dilated fallopian tubes. AJR Am J Roentgenol 1989;15:523–5.
11 Timor-Tritsch IE, Bar-Yam Y, Elgali S, Rottem S. The technique of transvaginal sonography with the use of a 6.5 MHz probe. Am J Obstet Gynecol 1988;158:1019–24.
12 Molander P, Paavonen J, Sjoberg J, Savelli L, Cacciatore B. Transvaginal sonography in the diagnosis of acute appendicitis. Ultrasound Obstet Gynecol. 2002;20:496–501.
13 Lande IM, Hill MC, Cosco FE, Kator NN. Adnexal and cul-de-sac abnormalities: transvaginal sonography. Radiology 1988;166:325–32.
14 Yapar EG, Ekici E, Karashin E, Gökmen O. Sonographic features of tuberculous peritonitis with female genital tract tuberculosis. Ultrasound Obstet Gynecol 1995;6:121–5.
15 Landers DV, Sweet RL. Current trends in the diagnosis and treatment of tuboovarian abscess. Am J Obstet Gynecol 1985;151:1098–110.
16 Corsi PJ, Johnson SC, Gonik B, Hendrix SL, McNeeley SG Jr, Diamond MP. Transvaginal ultrasound-guided aspiration of pelvic abscesses. Infect Dis Obstet Gynecol. 1999;7:216–21.
17 Gjelland K, Ekerhovd E, Granberg S. Transvaginal ultrasound-guided aspiration for treatment of tubo-ovarian abscess: a study of 302 cases. Am J Obstet Gynecol. 2005;193:1323–30.

Fig. 25.1 Acute endomyometritis and adnexitis. Ultrasound shows fluid collections inside the uterus and also in the fallopian tube behind the uterus (↓).

Fig. 25.2 Acute adnexitis with a markedly thickened left tube, a fluid collection in the tubal lumen (→), and fluid in the cul-de-sac (*). Oblique coronal scan.

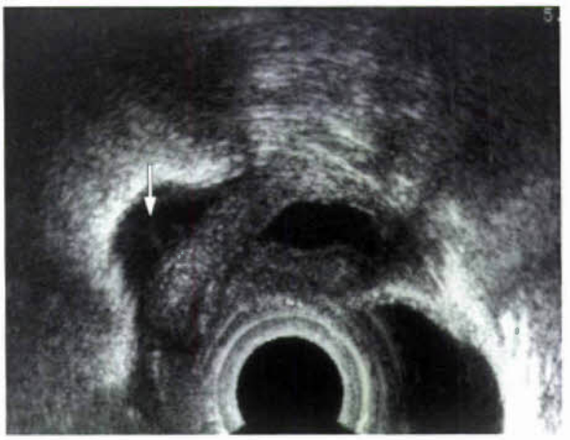

1

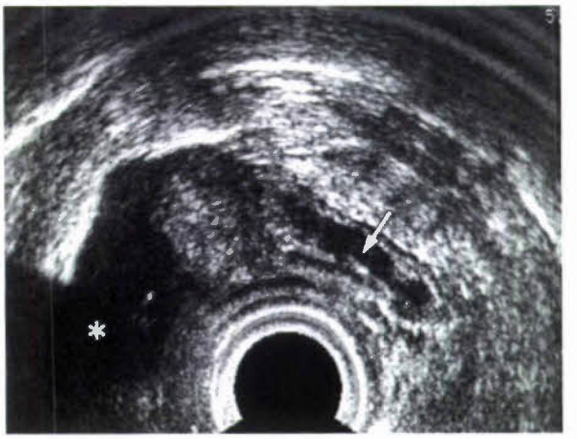

2

Fig. 25.3 Acute adnexitis with copious fluid in the cul-de-sac (*) and a retroflexed uterus. Longitudinal scan.

Fig. 25.4 Left pyosalpinx with marked thickening of the tubal wall and intraluminal debris. Coronal scan.

3

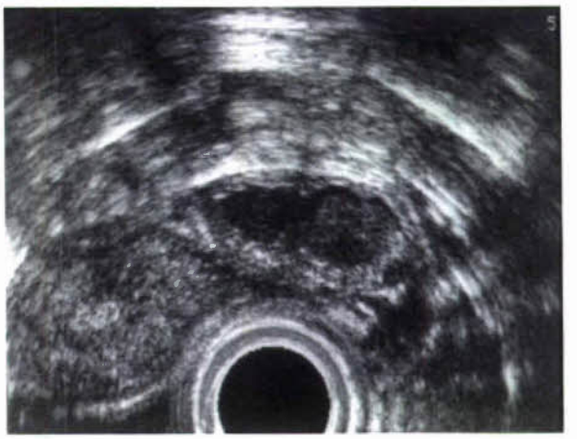

4

Fig. 25.5 Pyosalpinx containing fine, diffuse internal echoes. Longitudinal scan.
1 Uterine cervix
2 Uterine corpus
3 Cornual region
4 Ampulla of fallopian tube

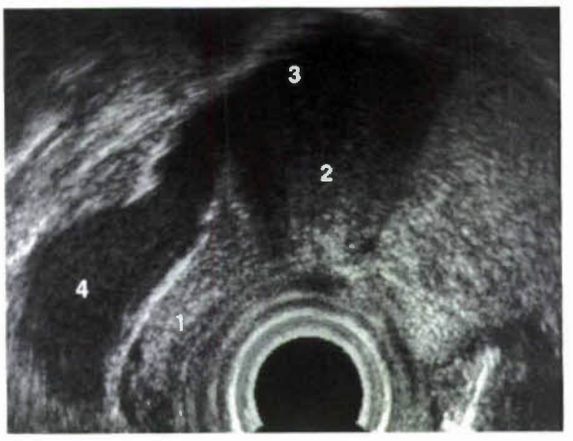

5

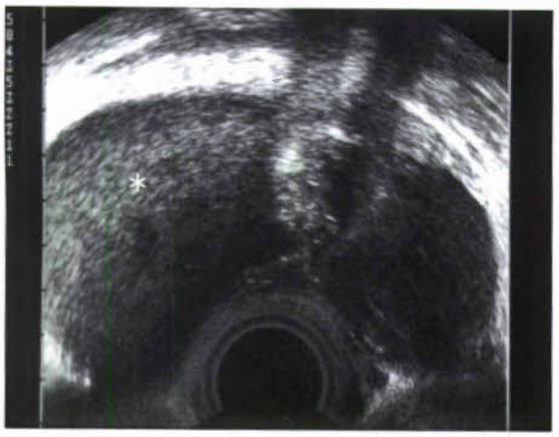

6

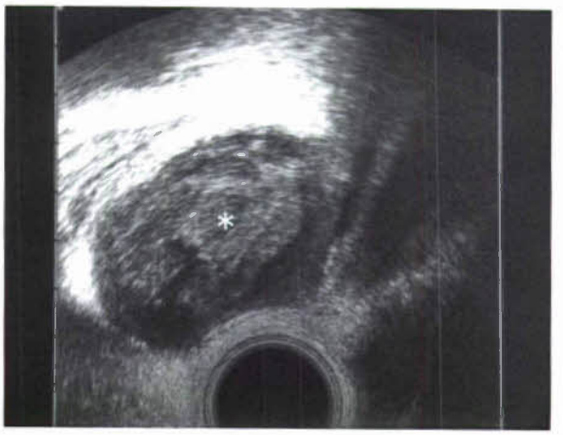

7

Fig. 25.**6** Right tubo-ovarian abscess (*) with fine, homogeneously distributed internal echoes (7.6 × 6 × 6 cm). Erythrocyte sedimentation rate = 100/135 mm Wintrobe.

Fig. 25.**7** Right ovarian abscess (*) (7.6 × 3.9 × 5.9 cm). The abscess contains dense internal echoes of moderate echogenicity. Longitudinal scan.

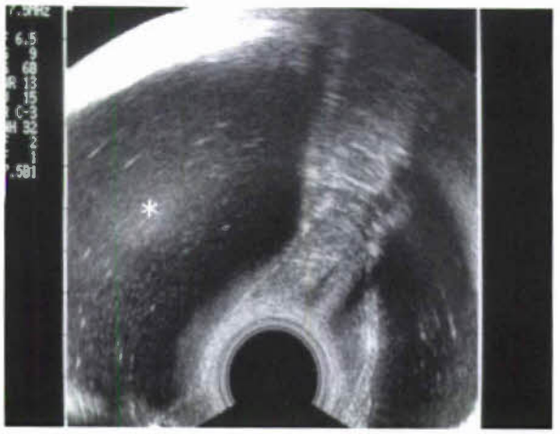

8

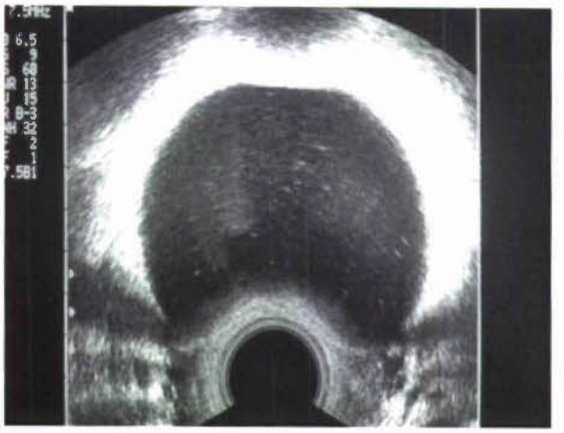

9

Fig. 25.**8** Cul-de-sac abscess (*) with fine internal echoes and marked posterior acoustic enhancement. Longitudinal scan.

Fig. 25.**9** Cul-de-sac abscess with fine internal echoes and marked posterior acoustic enhancement. Coronal scan of the lesion in Fig. 25.**8**.

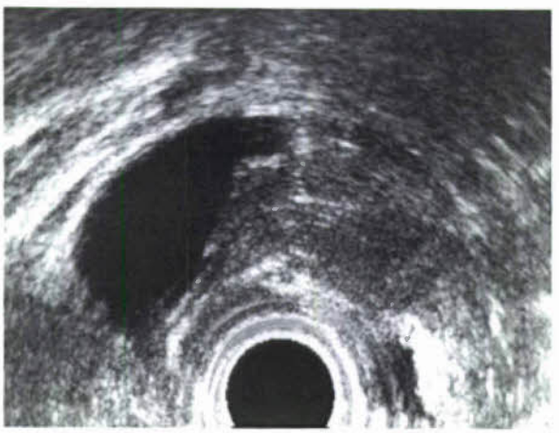

10

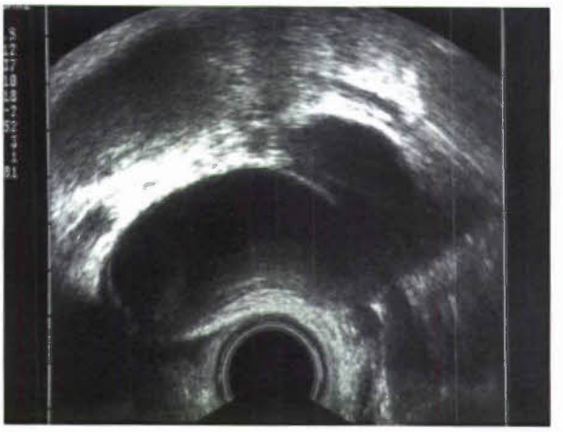

11

Fig. 25.**10** Left hydrosalpinx, devoid of internal echoes. Longitudinal scan.

Fig. 25.**11** Hydrosalpinx appearing as a prominent, curved echo-free mass. Longitudinal scan.

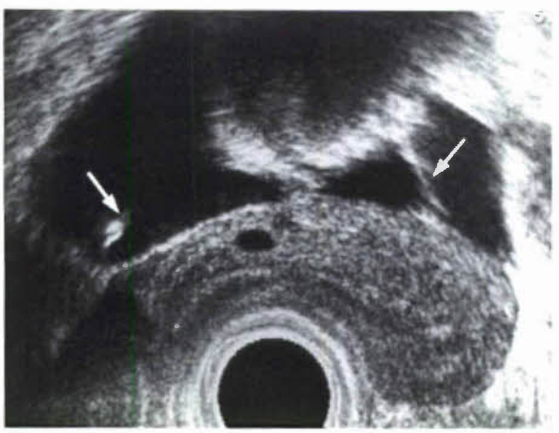

12

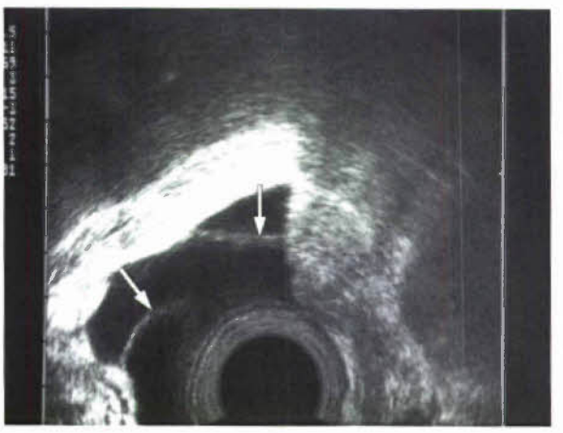

13

Fig. 25.**12** Adhesions between the uterus and bowel (↓), with copious free fluid in the cul-de-sac. Longitudinal scan.

Fig. 25.**13** Adhesions in the cul-de-sac (↓). Longitudinal scan.

26 Vaginal Masses

Masses in the vaginal region can often be successfully evaluated by inspection and palpation. It is not uncommon, however, for ultrasonography to provide important additional information. Ultrasound is particularly useful in defining the precise extent of the mass and determining its relationship to neighboring organs. As a result, transvaginal ultrasound has become an important preoperative examination. It should be emphasized, however, that a 5–7 MHz transducer should not be placed too close to the region being examined, due to the loss of resolution that occurs in the very near field. A distance of approximately 2 cm should be maintained between the tip of the endovaginal probe and the mass being examined. As an alternative, transrectal scanning is also an accurate method for investigating primary lesions and evaluating recurrent lesions in the vaginal area.

Benign Vaginal Masses

The majority of benign vaginal masses are cystic masses that result from abnormalities of genital development (müllerian epithelium, Gartner duct) [1]. Occasional cystic lesions in the vagina may also consist of endometriotic cysts or post-traumatic epithelial cysts.

Müllerian epithelial cysts, which account for approximately 75% of vaginal cysts, are caused by the persistence of müllerian epithelium. They may be located in the posterior or anterior vaginal wall (Fig. 26.**1**).

Gartner duct cysts are remnants of the mesonephric duct. They are located deep in the lateral vaginal wall and may be single or multiple. Relatively large cysts may exert mass effects on the surrounding organs. If the contents of the cyst are heavily inspissated, the lesion will appear sonographically as a solid mass. Typically, however, acoustic enhancement is observed behind the mass (Fig. 26.**2**).

Cysts of the paraurethral glands and *vestibular glands* occur exclusively on the anterior wall of the lower third of the vagina. Differentiation is required from a diverticulum of the bladder or urethra.

Traumatic epithelial cysts may occur anywhere in the vaginal region.

A *post-traumatic hematoma* in the vaginal region (Fig. 26.**3**) can mimic a vaginal cyst. Its ultrasound appearance can range from a honeycomb internal echo pattern (as in a hemorrhagic ovarian cyst) to a purely cystic echo pattern, depending on the state of the hematoma.

Benign connective-tissue tumors of the vagina are very rare and are derived from subepithelial mesenchymal tissue [1,2]. The most common of these tumors are *fibroleiomyomas* (Fig. 26.**4**) [3]; other tumors such as hemangiomas, lipomas, neurofibromas, and neuroblastomas are considerably less common. Solid benign tumors have sharply circumscribed margins and, unlike a cystic mass, do not show posterior acoustic enhancement.

Malignant Vaginal Tumors

Malignant tumors of the vagina are rare, representing only about 2% of genital tract malignancies [4]. While their peak incidence is in the sixth and seventh decades [5], these tumors may occur at almost any age [6]. Approximately 90–95% of vaginal malignancies are squamous-cell carcinomas. The rest consist of adenocarcinomas arising from preexisting structures (müllerian, wolffian and Gartner ducts, heterotopic cervical glands, paraurethral glands) or malignant tumors of nonepithelial origin (sarcomas) [6].

Vaginal carcinomas that have a superficial type of growth are virtually undetectable by transvaginal scanning, as the tumor is too close to the transducer. However, tumors that cause local thickening of the vaginal wall or spread into paravaginal tissues (Table 26.**1**) can be detected sonographically as a local, irregular, hypoechoic thickening of the vaginal wall (Fig. 26.**5**).

Secondary Vaginal Malignancies

Metastatic vaginal tumors are more common than primary vaginal carcinoma. Most result from the direct spread of cervical carcinoma, but some are lymphogenous or hematogenous metastases arising from other genital tumors, renal carcinoma, malignant melanoma (Fig. 26.**6**), or chorionic carcinoma [6].

Table 26.**1** TNM clinical classification of malignant vaginal tumors (After Sobin LH and Wittekind Ch [7]).

T-Primary tumor		
TNM categories	**FIGO stages**	**Characteristics**
TX		Primary tumor cannot be assessed
T0		No evidence of a primary tumor
Tis	0	Carcinoma in situ (preinvasive carcinoma)
T1	I	Tumor confined to vagina
T2	II	Tumor invades paravaginal tissues but does not extend to pelvic wall
T3	III	Tumor extends to pelvic wall
T4	IV A	Tumor invades *mucosa* of bladder or rectum, and/or extends beyond the true pelvis **Note:** The presence of bullous oedema is not sufficient evidence to classify a tumor as T4.
M1	IV B	Distant metastasis

N–Regional Lymph Nodes
- NX Regional lymph nodes cannot be assessed
- N0 No regional lymph node metastasis
- N1 Regional lymph node metastasis

M–Distant Metastasis
- MX Distant metastasis cannot be assessed
- M0 No distant metastasis
- M1 Distant metastasis

FIGO: International Federation of Gynecology and Obstetrics.

References

1 Dallenbach-Hellweg G. Weibliches Genitale. In: Remmele W. Pathologie, vol. 3. Berlin: Springer, 1984: 202–304.
2 Blaustein A, Sedlis A. Diseases of the vagina. In: Blaustein A, editor. Pathology of the female genital tract. Berlin: Springer, 1984: 59–98.
3 Krüger EH. Beitrag zur Kenntnis der Fibromyome in der Scheide. Zentralbl Gynäkol 1950;72:1078–84.
4 Ries J, Ludwig H. Zur Therapie des primären Karzinoms der Vagina. Strahlentherapie 1962; 118:92–110
5 Sheets JL, Dockerty MB, Decker DG, Welch JS. Primary epithelial malignancy in the vagina. Am J Obstet Gynecol 1964;89:121–9.
6 Von Fournier D, Leppien G, Junkermann H. Präneoplasien und Neoplasien der Vagina. In: Schmidt-Matthiesen H, Baltzer J, editors. Klinik der Frauenheilkunde und Geburtshilfe. 3rd ed., vol. 11: Spezielle gynäkologische Onkologie. 1. Vorsorge und Früherkennung, Tumoren der Vulva und Vagina, der Zervix und des Corpus uteri, Sarkosen und Trophoblasttumoren. Munich: Urban & Fischer, 1991: 105–127.
7 Sobin LH, Wittekind Ch. TNM Classification of Malignant Tumors. New York, Wiley-Liss, 2002.

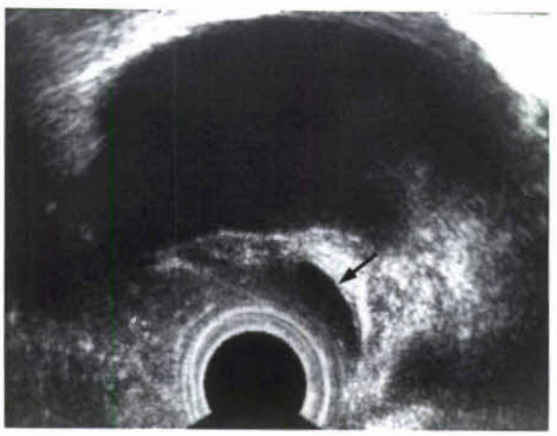

1

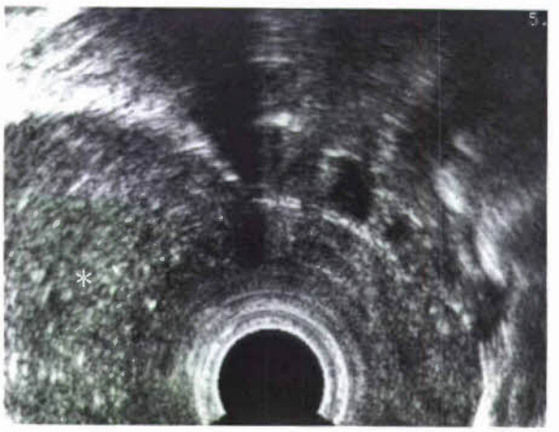

2

Benign Vaginal Masses

Fig. 26.1 A vaginal cyst (2.6 × 1.2 × 1.7 cm) between the anterior vaginal wall and the bladder (→). Longitudinal scan.

Fig. 26.2 A large Gartner duct cyst (11 cm in diameter), with inspissated secretions on the posterior vaginal wall (*). Longitudinal scan.

3

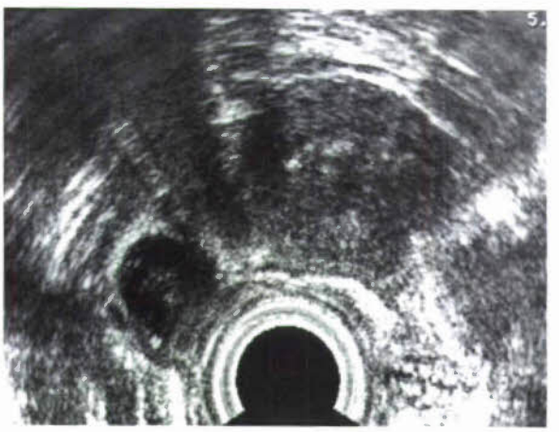

4

Fig. 26.3 A paravaginal hematoma on the right side (5.6 cm in diameter), with a honeycomb internal echo pattern.

Fig. 26.4 A small, hypoechoic vaginal fibroleiomyoma (2.3 × 2.0 cm) in the right vaginal fornix. Coronal scan.

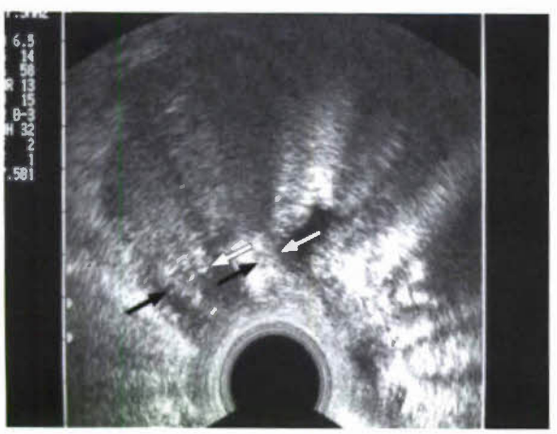

5

6

Malignant Vaginal Tumors

Fig. 26.5 Cervical carcinoma with involvement of the posterior third of the vagina. Longitudinal scan. Note the pronounced thickening and irregularity of the anterior and posterior vaginal walls (→ ←).

Fig. 26.6 A sharply circumscribed melanomatous nodule, with an irregular internal echo pattern, in the posterior right vaginal fornix (2.2 × 1.5 cm) (→). Coronal scan.

27 Uterine Masses

Benign Masses in the Uterine Corpus

Myomas (Fibroids)

Uterine myomas, also known as fibroids or leiomyomas, are the most common benign lesions of the uterus. These smooth-muscle neoplasms are also the most common gynecologic tumor [1]. Some 20–50% of women have uterine fibroids, which are three to nine times more prevalent among blacks than whites.

Approximately 90% of leiomyomas occur in the uterine corpus, the rest in the cervical region. They are usually multiple and may involve the uterus diffusely (diffuse myomatosis, fibroid uterus), or may be described by their location as intramural, subserous, submucous, or intraligamentous [2] (Fig. 27.**1**).

In patients with *diffuse myomatosis*, ultrasound shows only a general enlargement of the uterus, which maintains a relatively homogeneous myometrial structure (Fig. 27.**2**). Differentiation is required from *uterine adenomyosis* ("uterine endometriosis") (Fig. 27.**3**). Ultrasound demonstrates an enlarged uterus in which the myometrium contains irregular, echo-free zones that represent blood-filled cavities [3].

Myomas present smooth margins on ultrasound, which are sharply demarcated from the myometrium. They may contain areas of higher or lower echogenicity as a result of degenerative changes. Well-perfused or degenerating myomas appear hypoechoic in comparison with normal myometrium (Fig. 27.**4**). Calcifications, on the other hand, appear as sonodense, hyperechoic zones (Figs. 27.**5**–27.**8**). *Intramural myomas* appear as sharply circumscribed round areas within the myometrium (Figs. 27.**4**–27.**6**). Larger intramural myomas (Figs. 27.**6**, 27.**7**) may enlarge the uterine corpus to such a degree that the examiner may be unable to define the entire uterus by transvaginal scanning, even with a panoramic probe. In this case, vaginal ultrasound should be supplemented by abdominal ultrasound so that the uterus can be fully delineated and its size determined.

Subserous myomas are located in the outer third of the myometrium and distort the uterine contours to varying degrees, depending on their size (Figs. 27.**8**–27.**11**). With a pedunculated subserous myoma, the pedicle can be defined reasonably well with transvaginal imaging (Figs. 27.**12**–27.**14**). A tumor with a long pedicle may occupy a high position that places it outside the visual field of an endovaginal probe, so that it may be missed if the uterus is scanned only by that route. In doubtful cases, transvaginal ultrasound should be supplemented with transabdominal scans.

Sometimes a subserous myoma can be difficult to distinguish from an ovarian tumor. The ability to separate the tumor from the uterus can be a helpful differentiating criterion: when the tip of the endovaginal probe is advanced between the tumor and the uterus, an ovarian tumor will be pushed to one side, whereas a subserous myoma will not separate from the uterus. With further lateral pressure on the uterus, a pedunculated myoma will continue to move laterally with the uterus.

Intraligamentous myomas present at the level of the uterine isthmus, showing lateral ingrowth into the uterine broad ligament (Figs. 27.**15**, 27.**16**). Because of their location, they require differentiation from tumors of the ovaries, bowel, and cervix.

Submucous myomas of the uterine corpus appear sonographically as round masses located at the center of the corpus (Figs. 27.**17**–27.**20**). Larger lesions can cause marked expansion of the uterine cavity. Although subserous myomas are the least common type, accounting for just 5% of all fibroids, they are of major clinical importance, as they project into the uterine cavity and can cause mucosal lesions and metrorrhagia.

The incidence of leiomyomas during pregnancy is 1–3%. Ultrasound can be an important tool in these cases, both for localizing the tumors and for monitoring them for changes in size during the pregnancy [4].

Functional Disturbances of the Endometrium

A very common functional disturbance of the endometrium in perimenopausal and postmenopausal women is endometrial hyperplasia. Histologically, a cystic glandular form is distinguished from adenomatous hyperplasia.

Cystic glandular hyperplasia of the endometrium may be caused by persistent ovarian follicles, estrogen-forming ovarian tumors, or most commonly by exogenous hormone administration. A common factor in all these causes is the persistently high estrogen level, which induces the typical proliferative changes. If the estrogen level remains high after menopause, it will evoke a substantial increase in glandular proliferation, triggering a progression from cystic glandular hyperplasia to adenomatous hyperplasia. The latter condition is characterized by glandular proliferation with a small alveolar hyperplasia.

Adenomatous hyperplasia is reversible by lowering the estrogen level or discontinuing exogenous estrogen use. However, if the estrogen levels remain high, eventual progression to adenocarcinoma is inevitable [5].

The hyperplastic endometrium appears sonographically as an echogenic band more than 15 mm thick before menopause or more than 5 mm thick after menopause (double endometrial thickness) [6,7]. It is sharply demarcated with respect to the myometrium. The presence of multiple small, round, hypoechoic areas within the endometrium is suspicious for cystic glandular hyperplasia (Figs. 27.**21**, 27.**22**). The cystic glandular and adenomatous forms of endometrial hyperplasia are indistinguishable by their ultrasound features.

Tamoxifen-Associated Endometrial Changes

Tamoxifen is a nonsteroidal antiestrogen that possesses some estrogenic activity and has been used effectively in the treatment of breast cancer for 20 years. An initial report was published in 1985 on the development of endometrial carcinoma in three women treated with tamoxifen [8], and subsequent studies confirmed a causal link between long-term tamoxifen therapy and endometrial carcinoma [9,10]. According to Fornander et al. [11], the relative risk of developing endometrial carcinoma is 6.4% in women who have been taking tamoxifen for 3–4 years. According to van Leenwen et al. [10] the risk of endometrial cancer in women who had used tamoxifen for more than 2 years is 2.3 (0.9–5.9) times higher than in never users.

Transvaginal ultrasound is an easy-to-use, noninvasive study that has become important for endometrial surveillance in women receiving tamoxifen therapy [11a–11c]. Transvaginal scans usually show a thickened endometrium with numerous microcystic to macrocystic structures and, in a number of cases, polypoid lesions (Figs. 27.**23**–27.**25**). Although the tamoxifen-associated changes tend to be nonspecific, polyps

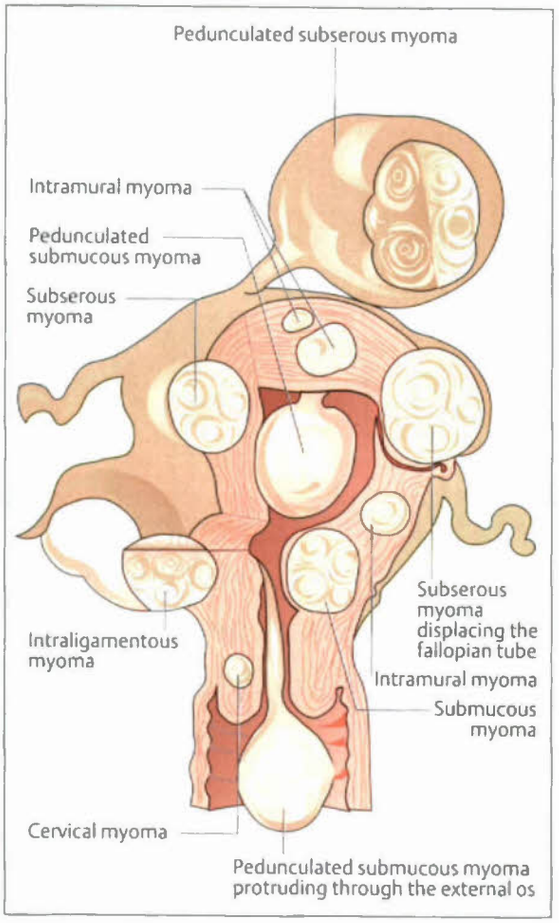

1

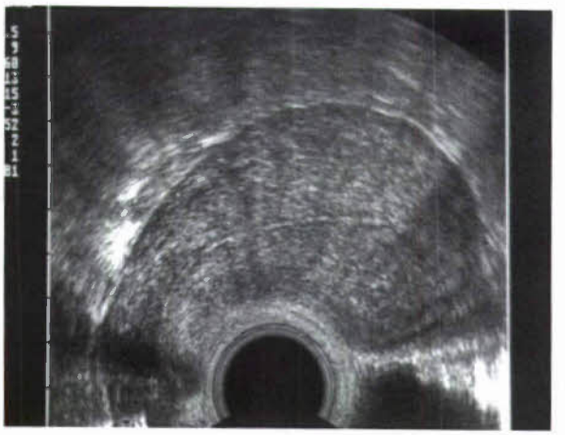

2

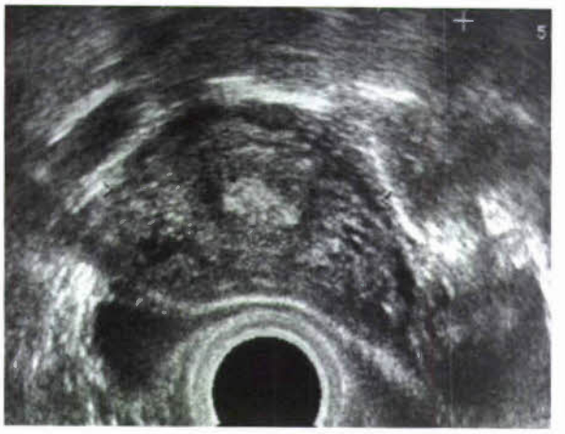

3

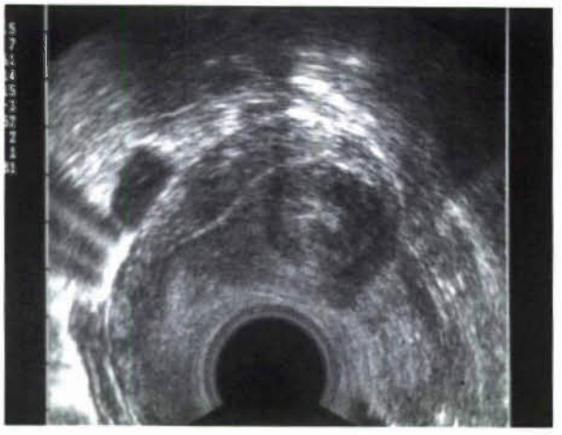

4

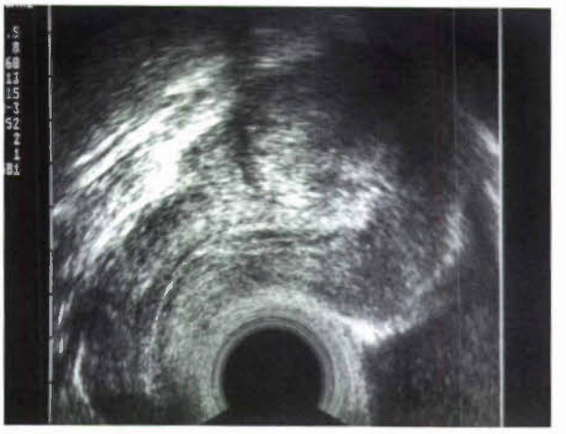

5

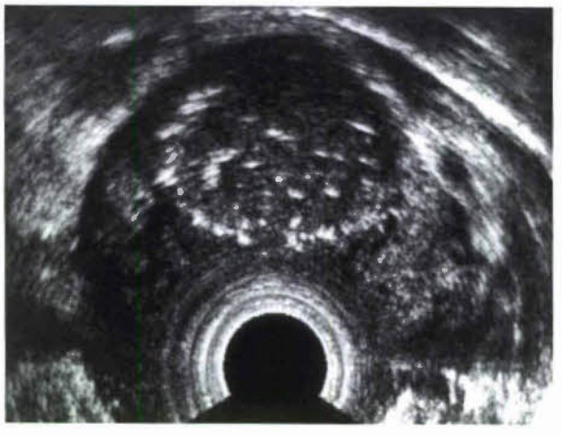

6

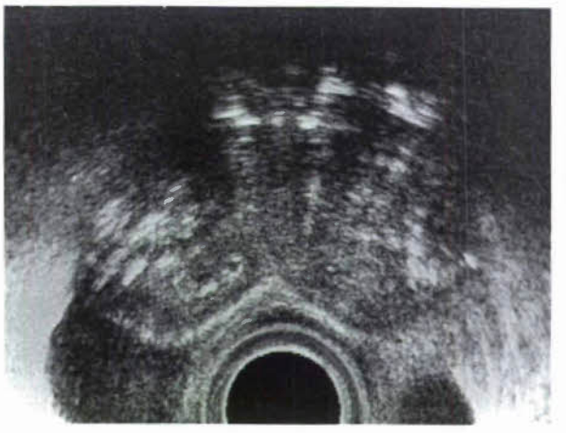

7

Myomas

Fig. 27.1 Diagram illustrating the different growth patterns of uterine myomas (after Netter [2]).

Fig. 27.2 Diffuse myomatosis with general enlargement of the uterus (11.0 × 5.1 × 6.4 cm). Longitudinal scan.

Fig. 27.3 Uterine adenomyosis with numerous hypoechoic zones within the myometrium. Transverse scan through the uterine corpus.

Fig. 27.4 Hypoechoic intramural myoma of the anterior uterine wall (2.5 cm in diameter). Longitudinal scan of the uterus.

Fig. 27.5 Echogenic intramural myoma of the posterior uterine wall (3.5 cm in diameter). Longitudinal scan of the uterus.

Fig. 27.6 Large, calcified myoma of the posterior uterine wall (8.7 × 7.7 × 5.5 cm). Coronal scan. Foci of calcification within the tumor appear as hypoechoic areas.

Fig. 27.7 Myomatous uterus with calcified myomas (4.5 and 5.7 cm in diameter) in the uterine fundus. Coronal scan.

Fig. 27.8 Anterior intramural myoma containing hyperechoic foci of calcification (2.1 cm in diameter) in an anteflexed uterus. The bladder is partially distended. Longitudinal scan.

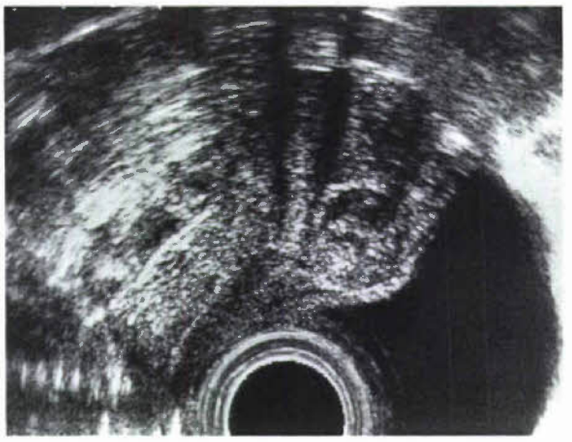

8

Fig. 27.9 Subserous myoma of the left anterior uterine wall (2.1 cm in diameter). Transverse scan of the uterine corpus.

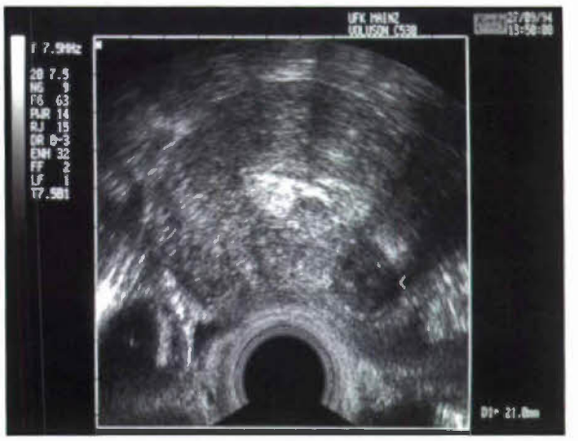

9

Fig. 27.10 Hypoechoic subserous myoma of the posterior uterine wall (*) 4.5 cm in diameter. Longitudinal scan.

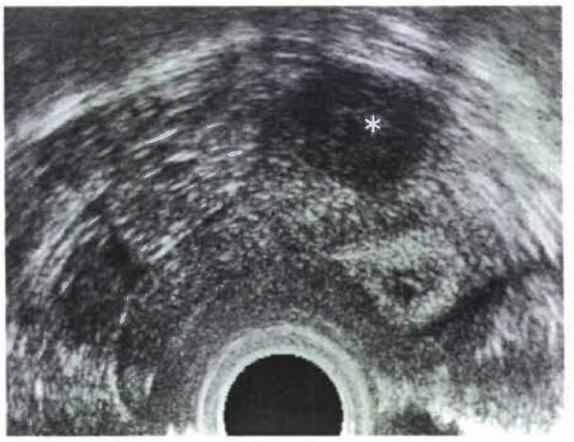

10

Fig. 27.11 Posterior subserous myoma (3.5 cm in diameter) involving the isthmic portion of an anteflexed uterus. Longitudinal scan.

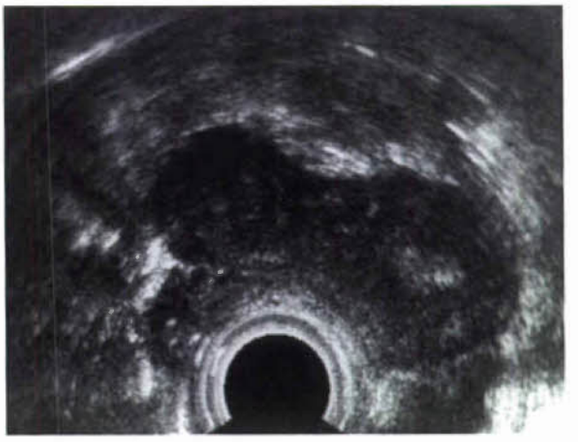

11

Fig. 27.12 Pedunculated subserous myoma (> <, 5 cm in diameter) on the posterior wall of a retroflexed uterus. Longitudinal scan. (→ Pedicle of the myoma.)

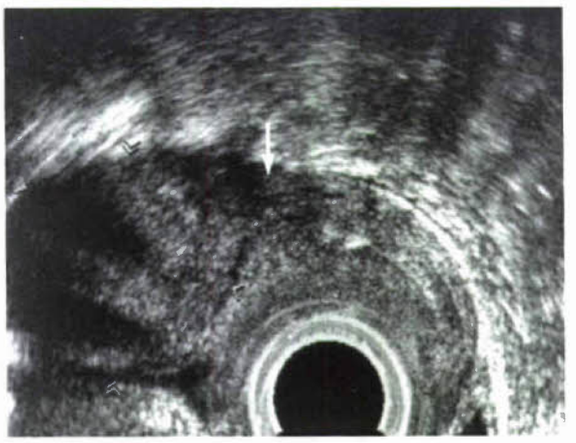

12

Fig. 27.13 Pedunculated subserous myoma of the uterine fundus (7.2 × 4.4 cm). The thickness of the tumor pedicle is 1.2 cm (> <). Longitudinal scan.

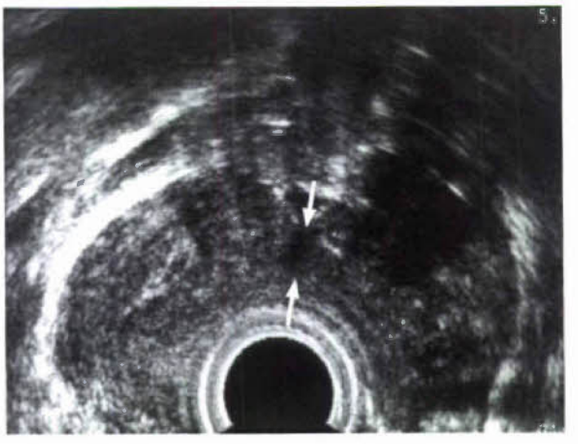

13

Fig. 27.14 Surgical specimen corresponding to Fig. 27.13.

14

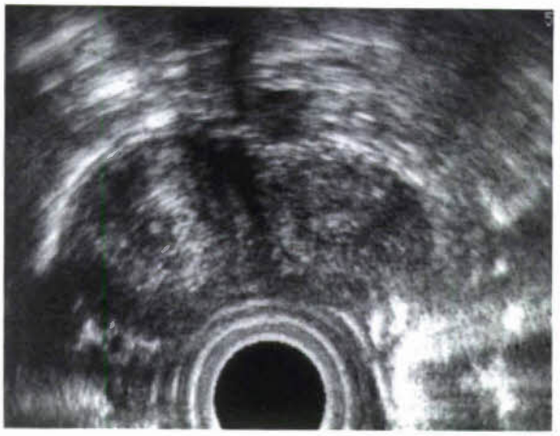

15

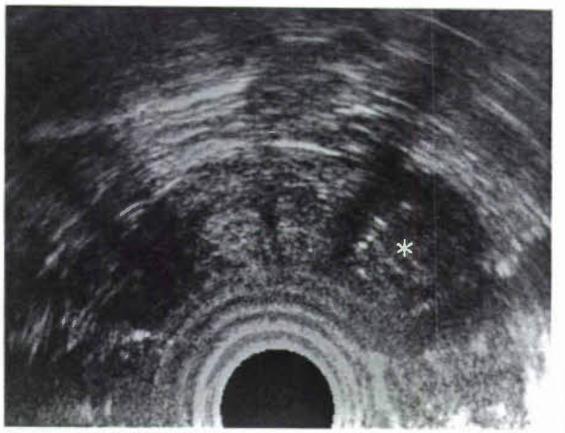

16

Fig. 27.**15** Intraligamentous myoma of the right uterine wall (4 cm in diameter). Coronal scan through the true pelvis.

Fig. 27.**16** Intraligamentous myoma of the left uterine wall with a central, hyperechoic calcified area (*). The myoma is 4 cm in diameter. Coronal scan through the true pelvis.

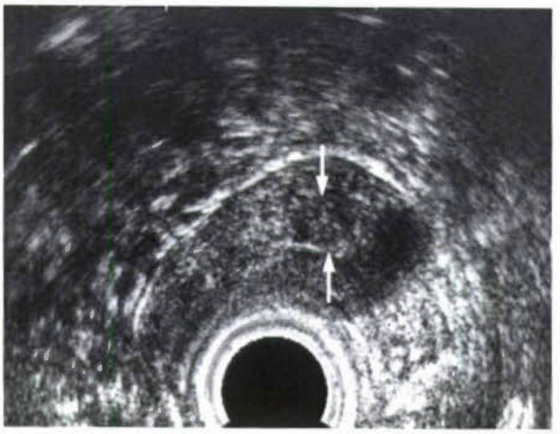

17

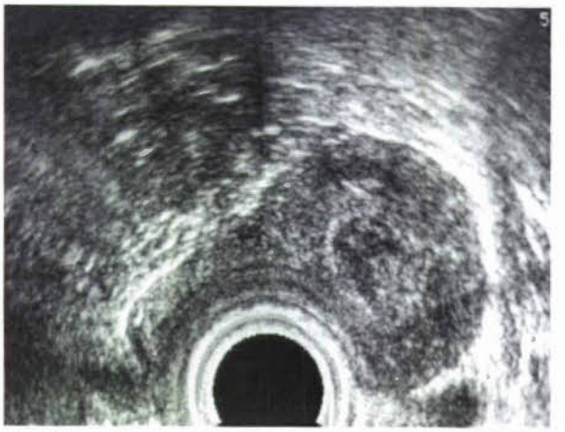

18

Fig. 27.**17** Small, submucous myoma of the uterine corpus, 1.5 cm in diameter (→).

Fig. 27.**18** Small, relatively hypoechoic submucous myoma (2.5 × 2.2 cm). Longitudinal scan of the uterus.

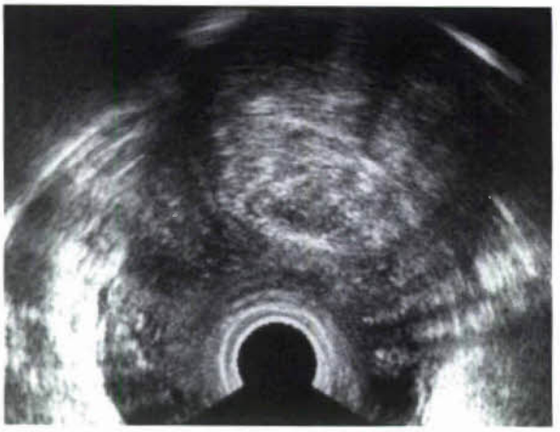

19

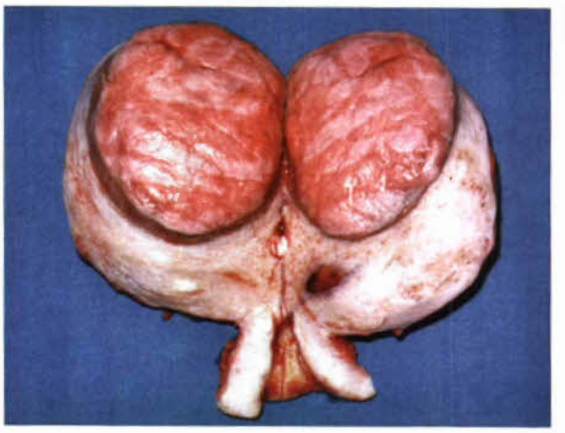

20

Fig. 27.**19** Large, predominantly echogenic submucous myoma of the posterior uterine wall (7.8 × 6.6 × 8.4 cm). Longitudinal scan of the uterus.

Fig. 27.**20** Surgical specimen corresponding to Fig. 27.**19**.

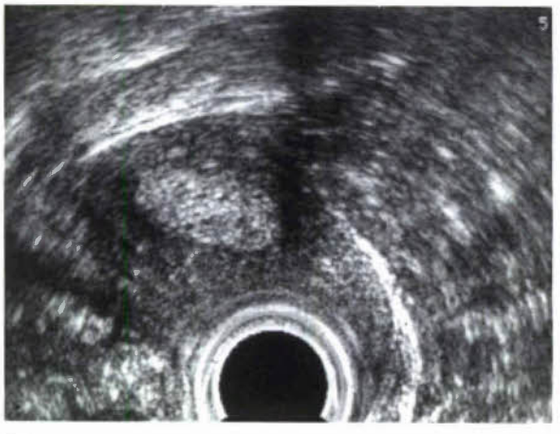

21

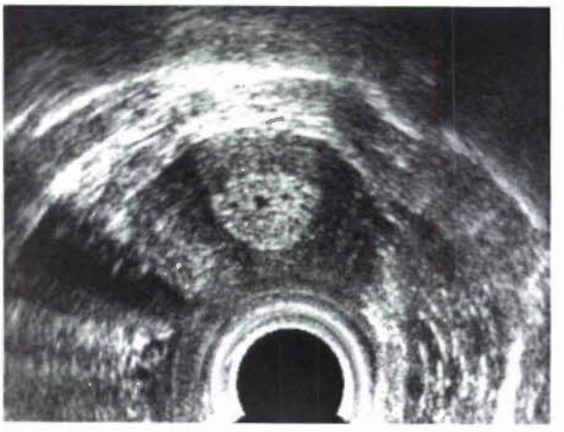

22

Functional Disturbances of the Endometrium

Fig. 27.**21** Cystic glandular hyperplasia with multiple pinhead-size hypoechoic areas. Endometrial thickness is 1.6 cm. Retroflexed uterus. Longitudinal scan.

Fig. 27.**22** Cystic glandular hyperplasia in a 54-year-old woman. Transverse scan through the uterus shows a thickened, echogenic endometrium (1.8 cm) with small, hypoechoic cystic areas.

are a common histologic finding in microcystic endometrial hyperplasia, whereas solid, nonhomogeneous endometrial hyperplasia is more commonly associated with the presence of adenocarcinoma [12]. The study by Perrot et al. [13] illustrates how difficult it can be to interpret ultrasound findings in patients on tamoxifen therapy. While transvaginal ultrasound showed a thickened, echogenic endometrium with numerous microcysts and irregular borders, the histologic examination of a hysterectomy specimen showed only cystic atrophy of the endometrium accompanied by extensive cystic foci of uterine adenomyosis. Bourne et al. [14] showed in their 1994 study that fluid instillation into the uterine cavity for transvaginal ultrasound improved diagnostic accuracy in the detection of tamoxifen-associated endometrial polyps.

At present, there are no uniform guidelines for determining the timing of ultrasound follow-ups and the need for dilation and curettage. We schedule ultrasound follow-ups at 3-month intervals for our patient who are receiving tamoxifen. We recommend evaluation by dilation and curettage if ultrasound shows either a marked increase in endometrial thickness or a definite structural change within the endometrium.

Endometrial Polyps

Endometrial polyps are circumscribed hyperplastic lesions of the endometrial mucosa that form in response to hormonal stimulation. The lesions are described according to the nature and extent of the stimulation as *glandular*, *glandular cystic*, or *adenomatous polyps*. The structure of each of these lesions corresponds to the homonymous form of hyperplasia. Clinically, endometrial polyps can often cause troublesome bleeding and therefore are a frequent indication for dilation and curettage. If the polyps remain in the uterine cavity for a prolonged period of time, they may reach a considerable size and completely fill the uterus. This can lead to secondary changes such as hemorrhagic necrosis and inflammation.

Sonographically, endometrial polyps appear as smooth-bordered or irregular, lobular, predominantly echogenic masses (Figs. 27.**26**–27.**33**) [14a] that, when large, may completely fill the uterine cavity. With their high echogenicity and poor delineation from the endometrium, they are sometimes mistaken for endometrial hyperplasia. Less echogenic lesions (Fig. 27.**32**) are apt to be confused with a submucous myoma.

If hemorrhagic necrosis occurs within these structures, their echo pattern becomes irregular and can mimic a malignant tumor.

In asymptomatic patients the detection of the feeding artery improves the ultrasound diagnosis of endometrial polyps [14b].

Intrauterine Fluid Collections

Fluid collections in the uterine cavity are of little value for benign–malignant differentiation, especially after menopause, because they may be found in association with uterine malignancies [15] as well as nonmalignant changes [16,17]. Particularly after menopause, it is not unusual to find a small fluid collection within the otherwise smooth outlines of the uterine cavity (Fig. 27.**34**). This is usually caused by an atrophic occlusion of the cervical canal.

An intrauterine fluid collection in premenopausal women may be caused by cervical occlusion secondary to inflammatory or postoperative scarring (Fig. 27.**35**). Irregular echogenic lesions in the cervical region (Fig. 27.**36**) may also represent benign postinflammatory changes, although cervical carcinoma should be excluded as a cause.

Intrauterine Calcifications

Uterine ultrasound may occasionally demonstrate regular or irregular structures of high echogenicity with associated acoustic shadows located at various sites within the uterine cavity (Fig. 27.**37**). They represent foci of calcification or ossification in the endometrium and are caused by the fibrosis or calcification of decidual residues following a previous delivery. Some configurations can even mimic the appearance of an intrauterine device [18] (Chapter 40).

Benign Masses in the Uterine Cervix

Cystic Lesions of the Cervix

Rounded, echo-free zones are occasionally observed within the relatively homogeneous structure of the cervix. Depending on their location, these lesions may represent superficial nabothian cysts (Figs. 27.**38**, 27.**39**) or inclusion cysts of deep cervical glands caused by the occlusion of their excretory ducts (Figs. 27.**40**–27.**42**).

Cervical Polyps

Polyps of the cervical mucosa are very common and occur at all ages, from puberty to old age. They are very rare before puberty, and polypoid lesions of the cervical mucosa in this age group are often malignant (botryoid sarcoma). Like endometrial polyps, cervical polyps are interpreted as circumscribed areas of hyperplasia. The presumed etiology is chronic inflammation [19].

Cervical polyps appear at ultrasound as circumscribed, sessile, echogenic or hypoechoic lesions located within the cervical canal or at the isthmocervical junction (Figs. 27.**43**, 27.**44**). They may have smooth or irregular margins. Pedunculated cervical polyps may cause expansion of the cervical canal (Fig. 27.**45**).

The malignant transformation of cervical polyps is extremely rare, occurring in less than 0.5% of cases.

Cervical Myomas

Cervical myomas comprise approximately 8% of all leiomyomas. Lesions that expand the cervix can mimic a barrel-shaped carcinoma of the cervix, and subserous lesions (Fig. 27.**46**) may be mistaken for an ovarian or cul-de-sac tumor.

Paracervical Varicosities

Multiple conspicuous, adjacent hypoechoic zones may be seen lateral to the cervix in some patients (Fig. 27.**47**). They are caused by varicose transformation of the uterine vessels, and a distinctive sonographic pattern is produced when the large-caliber varicose vessels are imaged partly in transverse section and partly in longitudinal section.

Malignant Uterine Tumors

Endometrial Carcinoma

Endometrial carcinoma is the most common malignant genital tumor in women. Approximately 38000 new cases are diagnosed in the U.S. each year, and 3000 women die of the disease [20]. The peak incidence

23

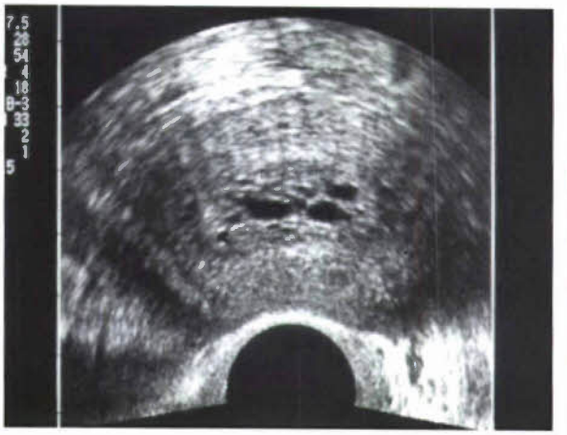

24

Tamoxifen-Associated Endometrial Change

Fig. 27.**23** Microcystic endometrial change in response to tamoxifen therapy. Longitudinal scan of the uterus. The endometrial thickness is 1.4 cm.

Fig. 27.**24** Transverse scan of the uterus in Fig. 27.**23**.

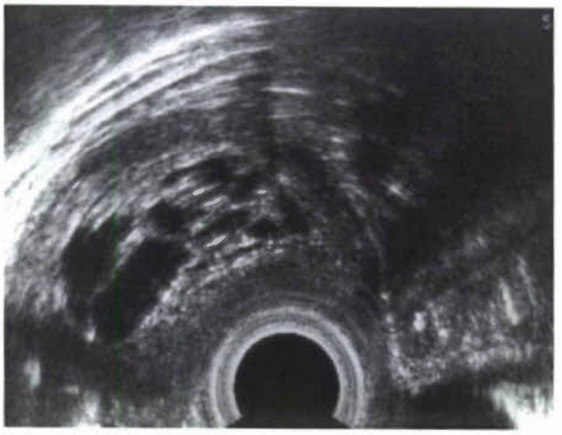

25

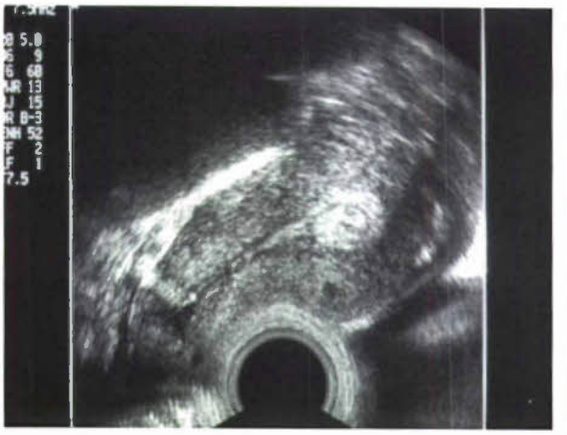

26

Fig. 27.**25** Macrocystic endometrial change in response to tamoxifen therapy (Swiss-cheese pattern) in a retroflexed uterus. Longitudinal scan.

Endometrial Polyps

Fig. 27.**26** Small, echogenic polyp on the right side of the uterine fundus (1.5 × 0.9 × 1.6 cm). Longitudinal scan.

27

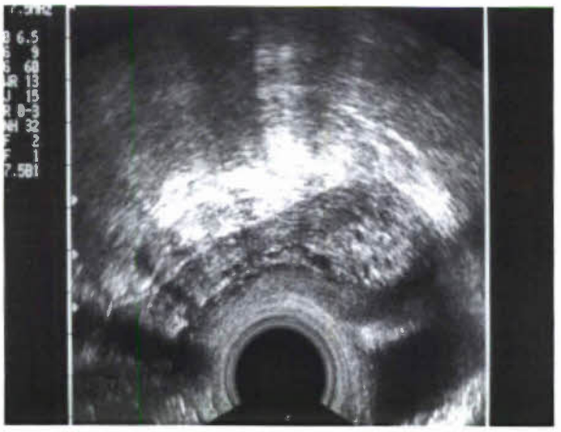

28

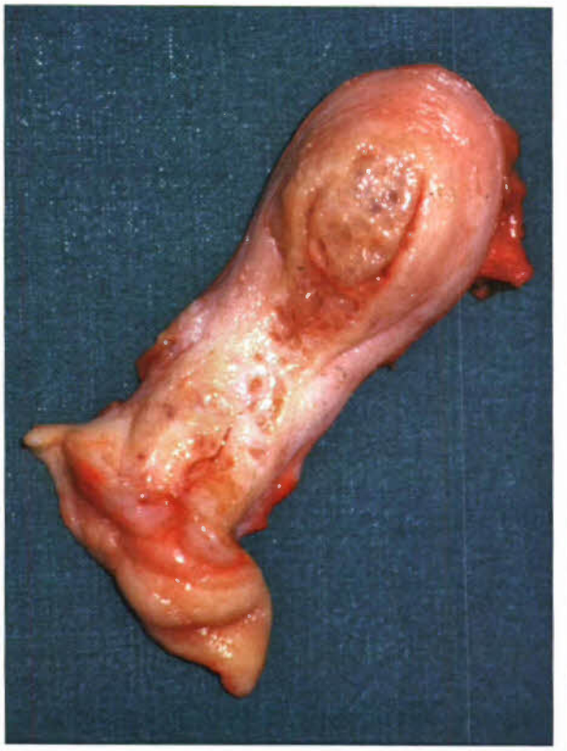

29

Fig. 27.**27** Transverse scan of the uterus in Fig. 27.**26** (→).

Fig. 27.**28** Endometrial polyp with associated cystic glandular hyperplasia. Longitudinal scan of the uterus.

Fig. 27.**29** Surgical specimen corresponding to Fig. 27.**28**.

Fig. 27.**30** Transverse scan of the uterus in Figs. 27.**28** and 27.**29**.

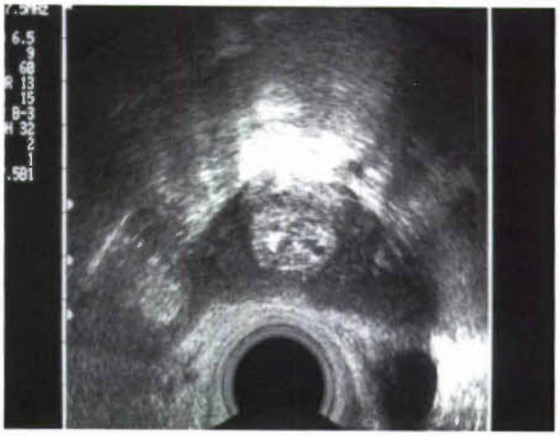

30

Fig. 27.**31** Histologic section from the lesion in Figs. 27.**28**–27.**30**.

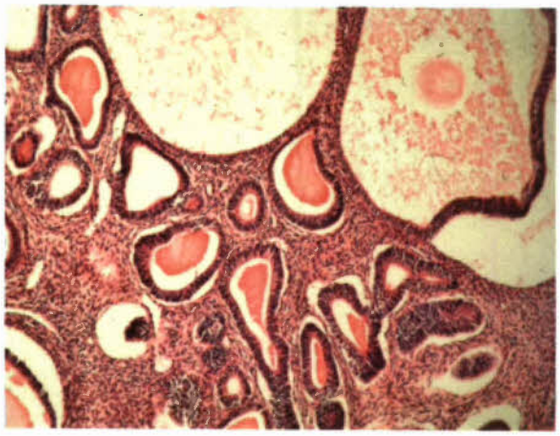

31

Fig. 27.**32** A large, more hypoechoic endometrial polyp (3.2 × 2.9 × 4.0 cm). Longitudinal scan of the uterus.

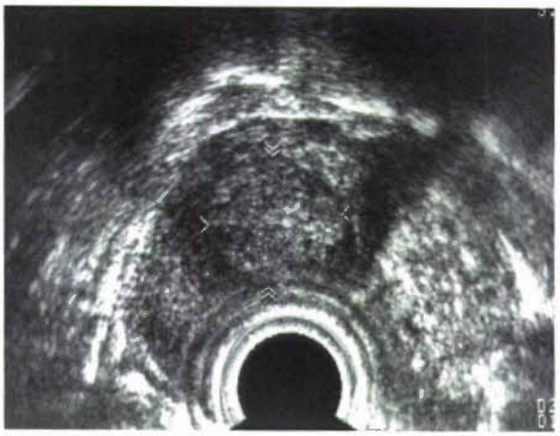

32

Fig. 27.**33** Surgical specimen corresponding to Fig. 27.**32**.

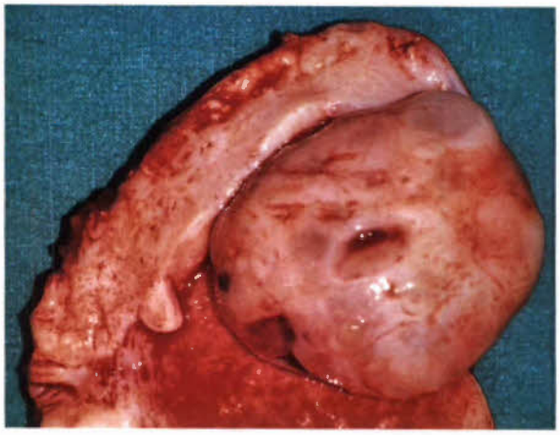

33

Intrauterine Fluid Collection

Fig. 27.**34** Small fluid collection in a postmenopausal uterus with cervical atrophy. The endometrium is extremely thin. Longitudinal scan of the uterus.

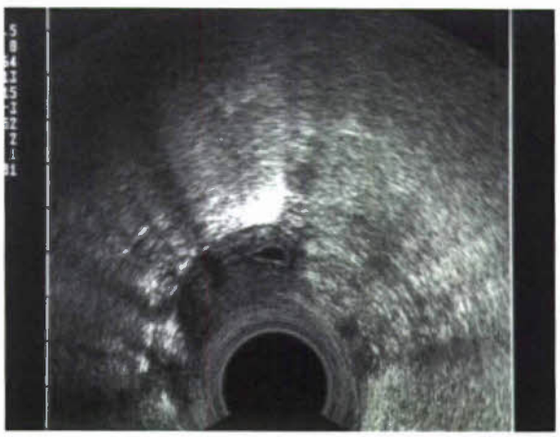

34

Fig. 27.**35** Pronounced hematometra (fine internal echoes) secondary to postinflammatory occlusion of the cervix following conization. Longitudinal scan of the uterus.

35

Fig. 27.**36** Hematometra distending the cervix secondary to postinflammatory occlusion of the external os. Longitudinal scan of the uterus.

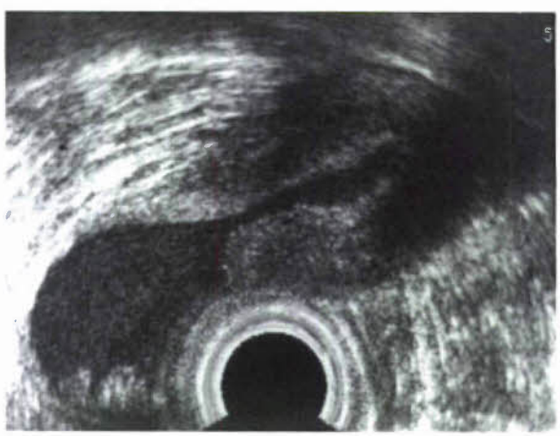

36

Fig. 27.**37** A calcified area 1.1 cm long in the isthmic portion of the uterus, with a conspicuous posterior acoustic shadow. Longitudinal scan of the uterus.

37

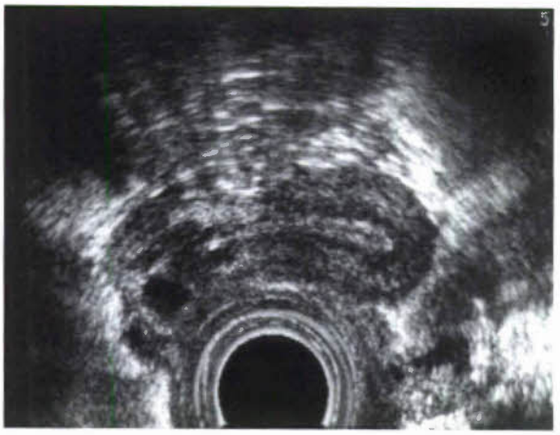

38

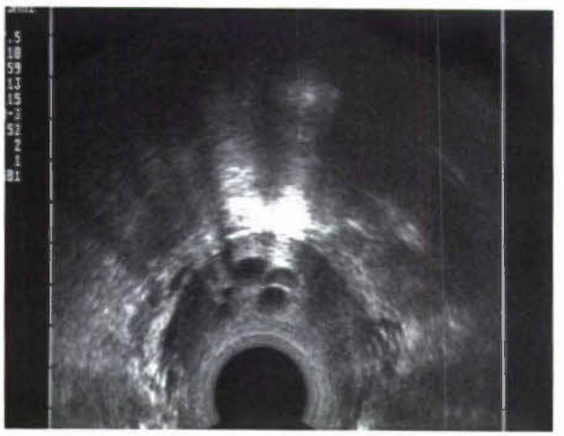

39

Cystic Lesions of the Cervix

Fig. 27.**38** Nabothian cysts in a longitudinal scan of the uterus.

Fig. 27.**39** Multiple nabothian cysts (1 cm in diameter). Transverse scan of the cervix.

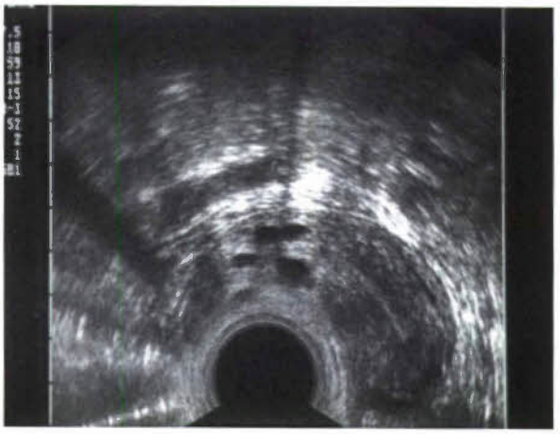

40

41

Fig. 27.**40** Multiple deep cervical inclusion cysts (0.8 cm in diameter). Longitudinal scan of the uterus.

Fig. 27.**41** Transverse scan of the cysts in Fig. 27.**40**.

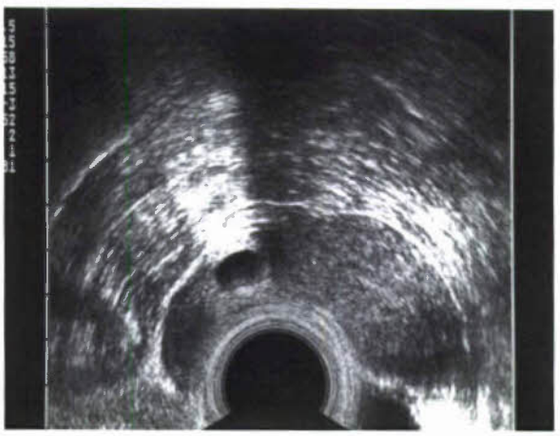

42

43

Fig. 27.**42** Relatively large, solitary inclusion cyst in the posterior cervical wall (1.5 × 1.2 cm). Longitudinal scan of the uterus.

Cervical Polyps

Fig. 27.**43** Two small, echogenic polyps in the isthmus region (—) (8 × 5 mm). Longitudinal scan of the uterus.

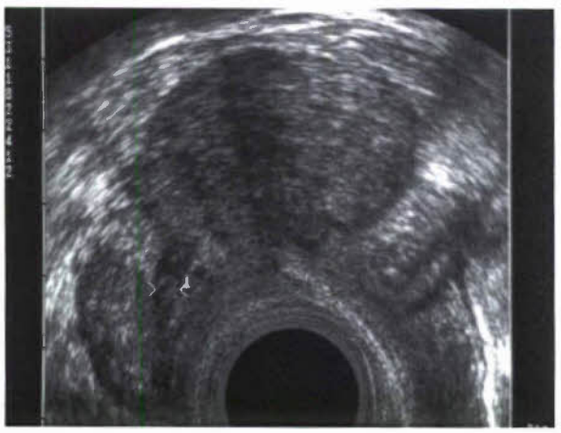

44

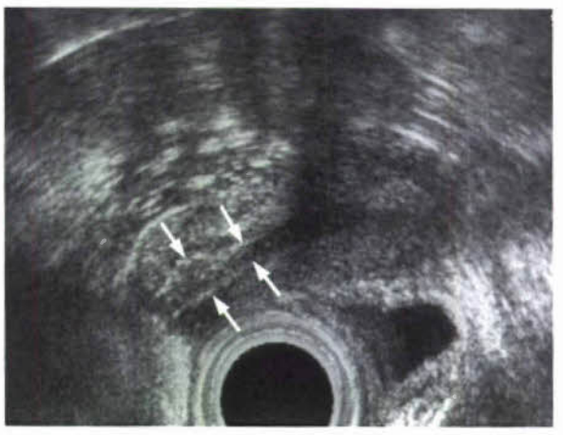

45

Fig. 27.**44** Small, more hypoechoic polyp on the anterior cervical wall (> <) (4 mm in diameter). Longitudinal scan of the uterus.

Fig. 27.**45** Pedunculated intracervical polyp (→ ←) (2 × 0.9 × 1.2 cm). Longitudinal scan of the uterus.

is between 50 and 70 years of age, and 70% of cases are diagnosed after menopause [21]. Only 5% of affected women are under 40 years of age [22]. The incidence is higher among whites than blacks [23]. The incidence rates have been increasing in both premenopausal and postmenopausal women [24].

At one time, radiotherapy was recommended as the treatment of choice for endometrial carcinoma. Today, surgery is preferred as it can be carried out even in high-risk patients and is effective in preventing local recurrences.

The following histologic types are distinguished: adenocarcinoma, adenocancroid, adenosquamous carcinoma, clear-cell carcinoma, and papillary carcinoma [5].

Due to the good accessibility of the uterus to sonographic imaging, transvaginal ultrasound has quickly become the method of choice for detecting endometrial carcinoma [9,17,25–30b]. This is particularly true after menopause, when it is easy to recognize any changes that occur in the normally streak-like endometrium. Transvaginal ultrasound is also used in the investigation of *postmenopausal bleeding*, where it can provide valuable information on the cause of the bleeding. Whereas bleeding due to sclerotic vascular changes is usually associated with an atrophic endometrium less than 5 mm thick, endometrial carcinoma is often accompanied by pronounced thickening of the endometrium to more than 8 mm [17,18,31] (Figs. 27.**48**–27.**59**). In addition to endometrial thickening, other ultrasound signs suggestive of endometrial carcinoma are a nonhomogeneous endometrial echo pattern and irregular endometrial boundaries (Table 27.**1**, Figs. 27.**49**–27.**59**). Color Doppler ultrasound additionally shows abnormal color signals within the endometrium as evidence of tumor angiogenesis (Fig. 27.**55**). Pulsed Doppler sampling reveals abnormally low resistance values within the tumor vessels (Table 27.**1**) (Chapter 39).

Defining a cut-off level for endometrial thickness (Table 27.**1**) will naturally involve a compromise between the sensitivity and specificity of a diagnostic method. The cut-off levels given in Table 27.**1** are valid only for patients who are not receiving hormone replacement therapy.

Endometrial carcinoma is known to have a number of well-defined prognostic factors that correlate with the occurrence of lymph-node metastasis and with survival [32]. For example, the depth of myometrial invasion correlates directly with the survival rate (Fig. 27.**60**) [33]. Moreover, the invasion depth and grade of tumor differentiation are known to correlate directly with the incidence of pelvic lymph-node metastasis [34].

Following the TNM scheme for the classification of endometrial carcinoma (Table 27.**2**), the sonographic evaluation distinguishes between tumors that *invade less than one-half of the myometrium* and tumors that *invade one-half or more of the myometrium*.

The depth of tumor invasion is determined by relating the anteroposterior (AP) diameter of the total measured endometrial thickness to the AP diameter of the uterine corpus [18] (Table 27.**3**, Fig. 27.**61**). If this ratio is less than 50%, it indicates that the tumor has invaded less than half of the myometrium. If the ratio is greater than 50%, this is considered evidence that the tumor has invaded the outer half of the myometrium.

Preoperative tumor staging should be as accurate as possible to provide a basis for individualized treatment planning (Table 27.**2**) [34a]. It is important, therefore, to determine both the depth of myometrial invasion and the extent of tumor spread to the cervix during the ultrasound examination. Cervical involvement is assumed to be present if ultrasound shows that the tumor has reached the isthmic region in its craniocaudal extent (Figs. 27.**56**, 27.**58**).

In a prospective study conducted by the authors [18], the *depth of myometrial invasion* determined sonographically agreed with the histologically determined depth of invasion in 68 of 80 carcinomas – i.e., in 85% of the cases studied (Fig. 27.**62**). Ultrasound overestimated the depth of invasion in nine cases and underestimated it in three cases.

With regard to *tumor staging*, ultrasound and histology yielded identical results in 70 of the 80 cases (87.5%) (Fig. 27.**63**). Ultrasound understaged the tumor in eight cases, and in two cases histology did not confirm ultrasound signs of cervical involvement. These numbers are consistent with results reported by other authors; Bidzinski and Lemieszczuk [35] found that transvaginal ultrasound was 88.7% accurate in assessing myometrial invasion and 93.5% accurate in assessing cervical invasion. The results of studies by Shipley et al. [36], Sahakian et al. [37], Karlsson et al. [27], and Cacciatore et al. [25,38] also show a better than 80% accuracy rate in assessing the depth of myometrial invasion

Table 27.**1** Sonographic signs suggestive of endometrial carcinoma

- Abnormal endometrial thickness (> 15 mm before menopause, > 5 mm after menopause)
- Nonhomogeneous endometrial echo pattern
- Irregular endometrial boundaries
- Detection of abnormal angiogenesis within the endometrium by color Doppler ultrasound
- Resistance index < 0.42 within the tumor vessels

Table 27.**2** TNM clinical classification of malignant tumors of the corpus uteri (After Sobin LH and Wittekind Ch [44]).

T– Primary tumor		
TNM categories	**FIGO stages**	**Characteristics**
TX		Primary tumor cannot be assessed.
T0		No evidence of a primary tumor
Tis	0	Carcinoma in situ (preinvasive carcinoma)
T1	I	Tumour confined to corpus uteri
T1a	IA	Tumor limited to endometrium
T1b	IB	Tumor invades less than one half of myometrium
T1c	IC	Tumor invades one half or more of myometrium
T2	II	Tumor invades cervix but does not extend beyond uterus
T2a	IIA	Endocervical glandular involvement only
T2b	IIB	Cervical stromal invasion
T3 and/or N1	III	Local and/or regional spread as specified in T3a, b, N1, and FIGO IIIA, B, C below
T3a	IIIA	Tumor involves serosa and/or adnexa (direct extension or metastasis) and/or cancer cells in ascites or peritoneal washings
T3b	IIIB	Vaginal involvement (direct extension or metastasis)
N1	IIIC	Metastasis to pelvic and/or para-aortic lymph nodes
T4	IVA	Tumor invades bladder *mucosa* and/or bowel *mucosa* **Note:** The presence of bullous edema is not sufficient evidence to classify a tumor as T4. The lesion should be confirmed by biopsy.
M1	IVB	Distant metastasis (*excluding* metastasis to vagina, pelvic serosa, or adnexa) **Note:** FIGO (2001) recommends that Stage I patients given primary radiation therapy can be clinically classified as follows: Stage I: Tumor confined to corpus uteri StageIA: Length of uterine cavity 8 cm or less Stage IB: Length of uterine cavity more than 8 cm

N–Regional lymph nodes
NX Regional lymph nodes cannot be assessed
N0 No regional lymph node metastasis
N1 Regional lymph node metastasis

M– Distant metastasis
MX Distant metastasis cannot be assessed
M0 No distant metastasis
M1 Distant metastasis

FIGO: International Federation of Gynecology and Obstetrics.

Table 27.**3** Determining the depth of invasion (I) by endometrial carcinoma

$$I = \frac{d2\ (\text{endometrial AP [mm]})}{d1\ (\text{corpus AP [mm]})} \times 100$$

I < 50% = Invasion of the inner half of the myometrium
I > 50% = Invasion of the outer half of the myometrium

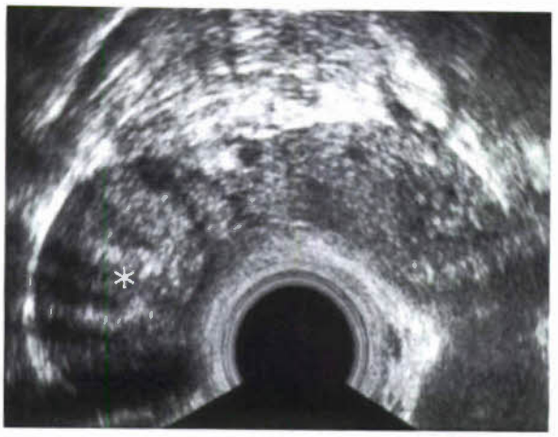

46

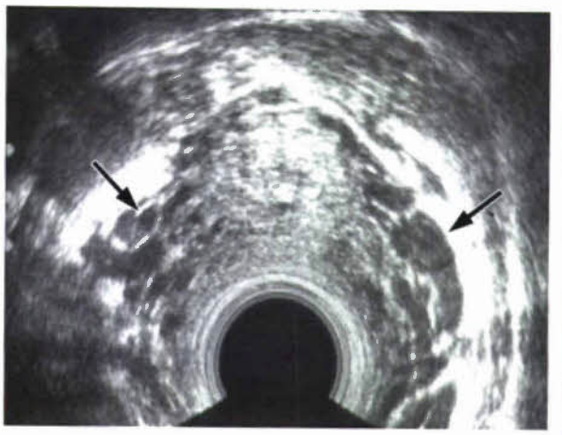

47

Fig. 27.**46** Large, pedunculated cervical myoma (*) (5.8 × 3.6 cm) arising from the posterior cervical wall. Longitudinal scan of the uterus.

Fig. 27.**47** Conspicuous varicose vessels in the paracervical region (—). Coronal scan through the true pelvis.

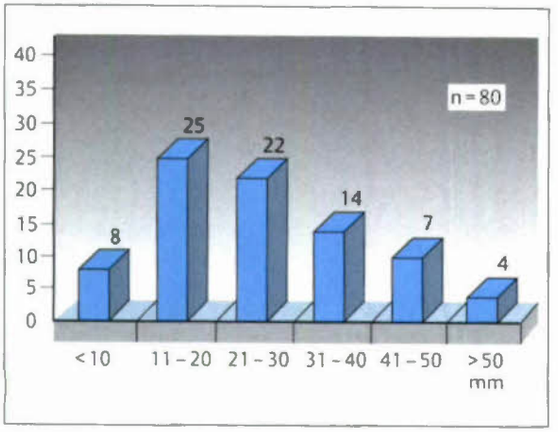

48

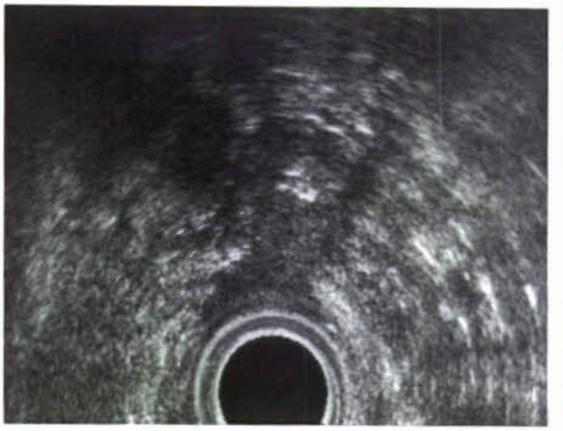

49

Endometrial Carcinoma

Fig. 27.**48** Endometrial thickness measured by transvaginal ultrasound in 80 patients with endometrial carcinoma (after Weber et al. [18]).

Fig. 27.**49** Small endometrial carcinoma in a postmenopausal patient. Longitudinal scan. Invasion is limited to the inner half of the myometrium.

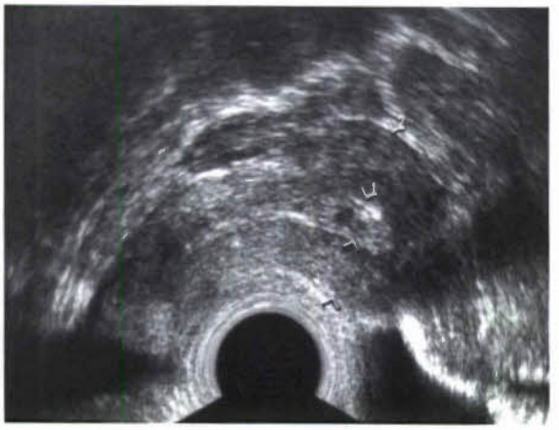

50

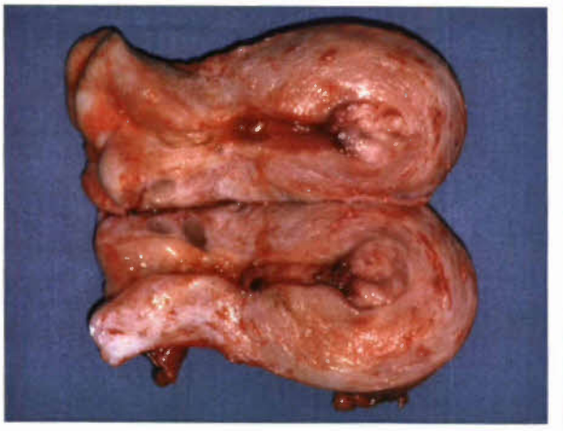

51

Fig. 27.**50** Early endometrial carcinoma in a postmenopausal patient, appearing as an irregular endometrial area in the fundal region (endometrial thickness 8 mm). Longitudinal scan.

Fig. 27.**51** Surgical specimen corresponding to Fig. 27.**50**.

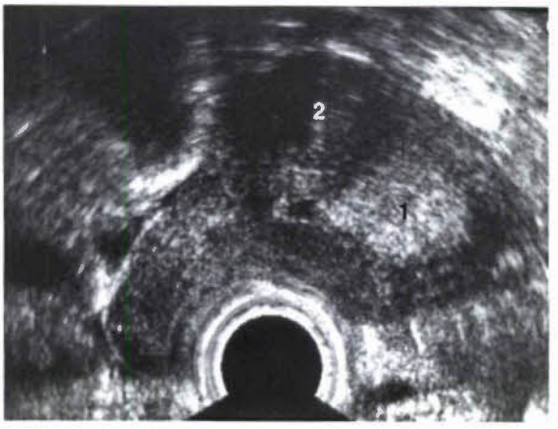

52

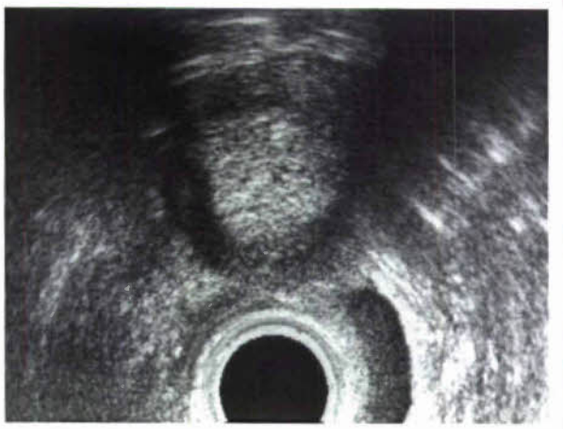

53

Fig. 27.**52** Endometrial carcinoma in a myomatous uterus. Longitudinal scan. Note the irregular borders of the endometrium and its thickness, which is much greater than it should be after menopause. Invasion is limited to the inner half of the myometrium.
1 Carcinoma
2 Posterior wall myoma

Fig. 27.**53** Endometrial carcinoma invading the inner half of the myometrium. Coronal scan.

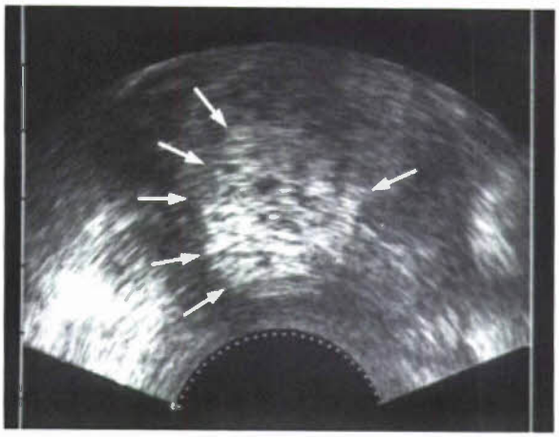

54

Fig. 27.**54** Endometrial carcinoma. The transverse scan of the uterus shows multiple sites of myometrial invasion (→).

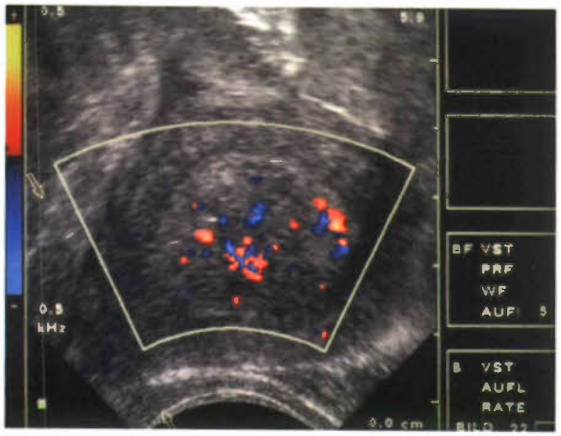

55

Fig. 27.**55** Endometrial carcinoma. Transverse scan of the uterus. Color Doppler shows numerous color signals within the tumor as a result of angiogenesis.

56

Fig. 27.**56** Extensive endometrial carcinoma that has spread to the cervix. Longitudinal scan.

57

Fig. 27.**57** Advanced endometrial carcinoma invading the outer half of the myometrium. Coronal scan.

58

Fig. 27.**58** Extensive endometrial carcinoma invading the entire posterior uterine wall, with a fluid collection in the uterine cavity. Longitudinal scan.

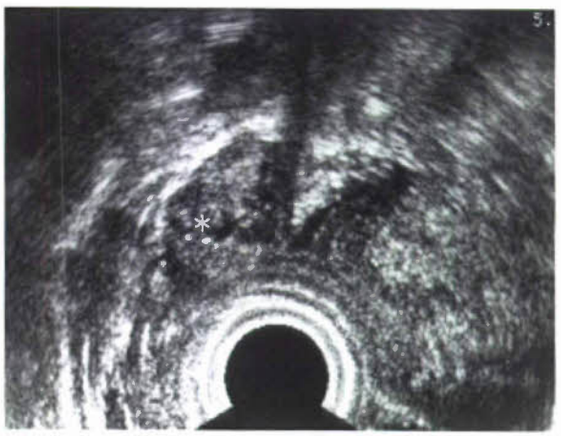

59

Fig. 27.**59** Extensive endometrial carcinoma invading the right ovary (*). Coronal scan through the true pelvis.

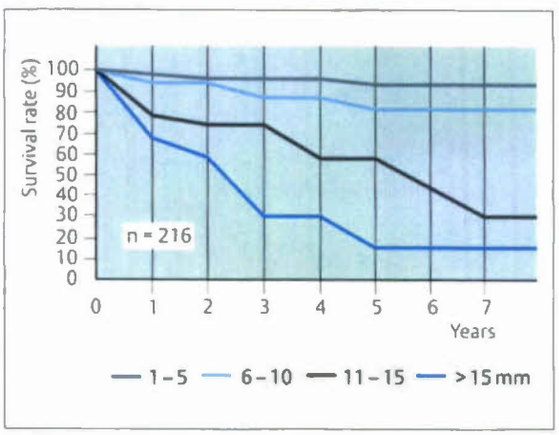

60

Fig. 27.**60** Survival rate of patients with endometrial carcinoma versus depth of tumor invasion (after Baltzer and Lohe [33]).

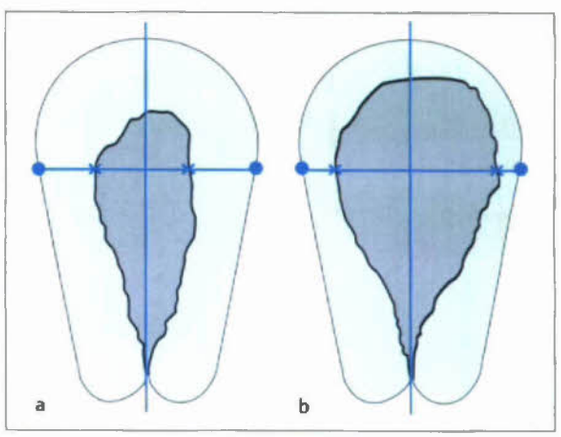

61

Fig. 27.**61** Schematic representation of the depth of myometrial invasion.
a < 50 %. I = d2/d1 × 100 = < 50 %;
•–• = d1, × – × = d2.
b > 50 %. I = d2/d1 × 100 = > 50 %;
•–• = d1, × – × = d2 (after Weber et al. [18]).

Table 27.4 Differential diagnosis of sonographic endometrial abnormalities

- Hormone replacement therapy
- Cystic glandular hyperplasia
- Adenomatous hyperplasia
- Polyp
- Carcinoma
- Submucous myoma
- Intrauterine hematoma

and preoperative staging, confirming that the sonographic diagnosis is extremely reliable. Transvaginal ultrasound may thus be regarded as an accurate, noninvasive, cost-effective procedure that is of substantial value in planning the surgical treatment of endometrial carcinoma on the basis of the individual extent of disease.

The differential diagnosis of endometrial abnormalities should include hormone replacement therapy, cystic glandular hyperplasia, adenomatous hyperplasia, submucous myoma (Fig. 27.**64**), intrauterine hematoma (Fig. 27.**65**), and an endometrial polyp (Fig. 27.**66**). With the latter lesion, it should be considered that polyps may undergo malignant transformation (Figs. 27.**67**, 27.**68**) (Table 27.**4**). If ultrasound images do not allow a confident benign–malignant differentiation, color Doppler may be a helpful adjunct (Fig. 27.**69**) [38a–38d].

Uterine Sarcoma

Sarcomas of the uterus are rare. The ratio of uterine sarcomas to carcinomas is 1:50. Leiomyosarcoma is three times more common than endometrial sarcoma. The peak incidence is at 50 years of age.

Pure sarcomas that occur in the uterus almost always involve the endometrium (primarily or secondarily) and are subdivided into three types: endometrial stromal sarcoma, malignant mesenchymal mixed tumor, and leiomyosarcoma.

Endometrial stromal sarcoma is a lobulated, polypoid intrauterine tumor that may enlarge the uterus to the size of a human head. Ultrasound demonstrates marked expansion of the uterine corpus by a hypoechoic, loculated mass; the endometrium can no longer be discerned (Figs. 27.**70**, 27.**71**).

Malignant mesenchymal mixed tumors contain two or more sarcomatous components.

Most *leiomyosarcomas* arise within a leiomyoma; very few develop in the myometrium in the absence of this precursor lesion. Unlike benign leiomyomas, leiomyosarcomas are highly variable in their macroscopic features. All gradations may be observed ranging from a leiomyoma-like appearance to diffuse invasion of the uterine wall [39]. At ultrasound, the echo pattern of this malignancy is virtually indistinguishable from that of a myoma that has undergone regressive changes (Figs. 27.**72**, 27.**73**). The most suspicious ultrasound finding is the observation of rapid growth in close-interval follow-ups.

Table 27.5 Clinical classification of malignant tumors of the cervix uteri (After Sobin LH and Wittekind Ch [44]).

T– Primary tumor		
TNM categories	**FIGO stages**	**Characteristics**
TX		Primary tumor cannot be assessed
T0		No evidence of primary tumor
Tis	0	Carcinoma in situ (preinvasive carcinoma)
T1	I	Cervical carcinoma confined to uterus (extension to corpus should be disregarded)
T1a	IA	Invasive carcinoma diagnosed only by microscopy. All macroscopically visible lesions — even with superficial invasion — are T1b/Stage IB
T1a1	IA1	Stromal invasion no greater than 3.0 mm in depth and 7.0 mm or less in horizontal spread
T1a2	IA2	Stromal invasion more than 3.0 mm and not more than 5.0 mm with a horizontal spread 7.0 mm or less
		Note: The depth of invasion should not be more than 5 mm taken from the base of the epithelium, either surface or glandular, from which it orignates. The depth of invasion is defined as the measurement of the tumor from the epithelial-stromal junction of the adjacent most superficial epithelial papilla to the deepest point of invasion. Vascular space involvement, venous or lymphatic, does not affect classification.
T1b	IB	Clinically visible lesion confined to cervix or microscopic lesion greater than T1a2/IA2
T1b1	IB1	Clinically visible lesion 4.0 cm or less in greatest dimension
T1b2	IB2	Clinically visible lesion more than 4 cm in greatest dimension
T2	II	Tumor invades beyond uterus but not to pelvic wall or to lower third of vagina
T2a	IIA	Without parametrial invasion
T2b	IIB	With parametrial invasion
T3	III	Tumor extends to pelvic wall, involves lower third of the vagina, or causes hydronephrosis or non-functioning kidney
T3a	IIIA	Tumor involves lower third of vagina, no extension to pelvic wall
T3b	IIIB	Tumor extends to pelvic wall or causes hydronephrosis or non-functioning kidney
T4	IVA	Tumor invades *mucosa* of bladder or rectum or extends beyond true pelvis
		Note: The presence of bullous oedema is not sufficient to classify a tumor as T4. The lesion should be confirmed by biopsy.
M1	IVB	Distant metastasis

N–Regional lymph nodes
NX Regional lymph nodes cannot be assessed
N0 No regional lymph node metastasis
N1 Regional lymph node metastasis

M– Distant metastasis
MX Distant metastasis cannot be assessed
M0 No distant metastasis
M1 Distant metastasis

*New FIGO classification (adapted from Creasman [45]).

Cervical Carcinoma

Approximately 16000 new cases of cervical carcinoma are diagnosed in the U.S. each year. Accounting for 20% of all genital cancers in women, cervical carcinoma ranks third in frequency behind endometrial and ovarian carcinoma. The peak incidence is 45 years of age, or age 35 for carcinoma in situ [20]. Approximately 90% of all cervical carcinomas fall within the group of squamous cell carcinomas, and most are nonkeratinizing. Less than 10% are adenocarcinomas. Grossly, an early stage of cervical carcinoma lies within the transformation zone in 98% of cases. Three main growth patterns are observed: an endophytic type, an exophytic type, and a primary ulcerating type [19].

The sonographic detection of cervical carcinoma depends on the stage of the tumor (Table 27.**5**) and its type of growth [39a]. An additional tumor characterization may be possible by transvaginal color flow Doppler ultrasound [39b,39c]. Early invasive carcinomas are not detectable by ultrasound.

Advanced endocervical carcinomas cause varying degrees of cervical expansion, depending on their extent. They present a nonhomogeneous echo pattern consisting of hypoechoic and echogenic areas (Figs. 27.**74**, 27.**75**). A necrotic cavity forming within the tumor appears as an irregular hypoechoic zone (Fig. 27.**74**). In rare cases, metastasis within the cervix can mimic a primary cervical carcinoma (Fig. 27.**76**).

Exophytic carcinomas lead to irregular expansion of the cervix, depending on the tumor size. They cause a more or less irregular, conical deformity of the ectocervix, depending on which lip of the cervix is

Fig. 27.62 Sonographically determined depth of tumor invasion compared with histologically detected invasion depth in 80 endometrial carcinomas (after Weber et al. [18]).

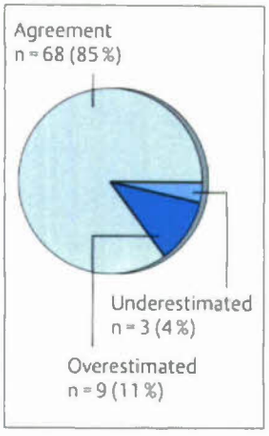

62

Fig. 27.63 Comparison of sonographic and histologic staging of 80 endometrial carcinomas (after Weber et al. [18]).

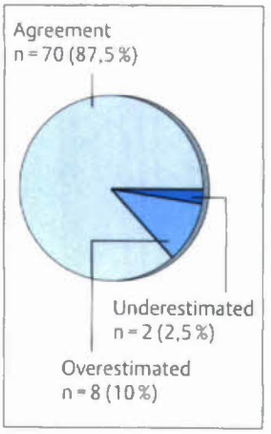

63

Fig. 27.64 An echogenic submucous myoma with an irregular echo pattern mimics the appearance of endometrial carcinoma.

64

Fig. 27.65 An extensive, nonhomogeneous intrauterine hematoma following an anticoagulant overdose mimics endometrial carcinoma.

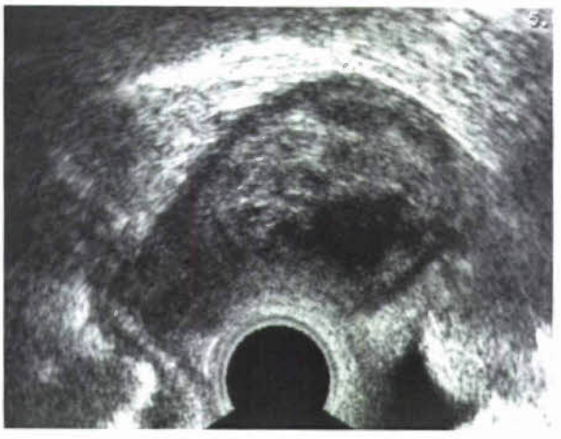

65

Fig. 27.66 A 2-cm polyp on the uterine corpus (> <) mimics an endometrial carcinoma. Retroflexed uterus. Longitudinal scan.

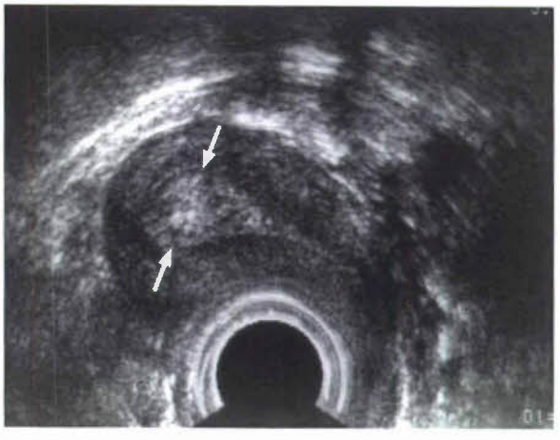

66

Fig. 27.67 Malignant transformation of a polyp on the posterior wall of the uterine cavity. There is copious intrauterine fluid. Longitudinal scan of the uterus.

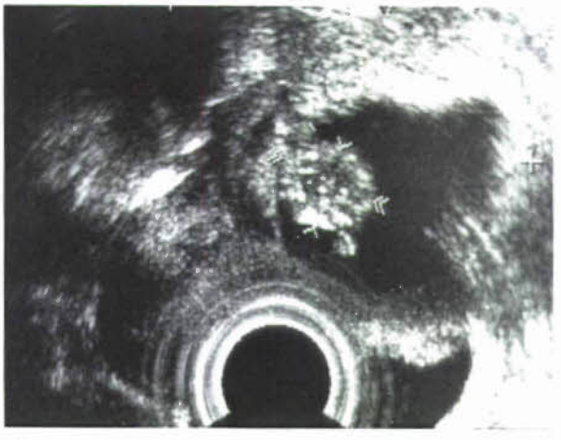

67

Fig. 27.68 Surgical specimen corresponding to Fig. 27.67.

68

Fig. 27.69 Endometrial polyp. Color Doppler shows only scant color echoes, contrasting with the color flow signals associated with endometrial carcinoma (Fig. 27.55). Transverse scan of the uterine corpus.

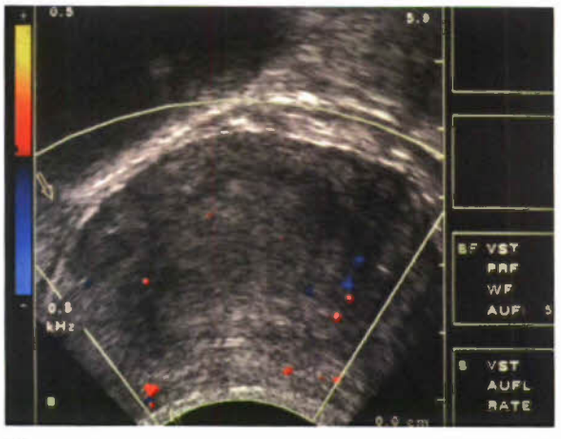

69

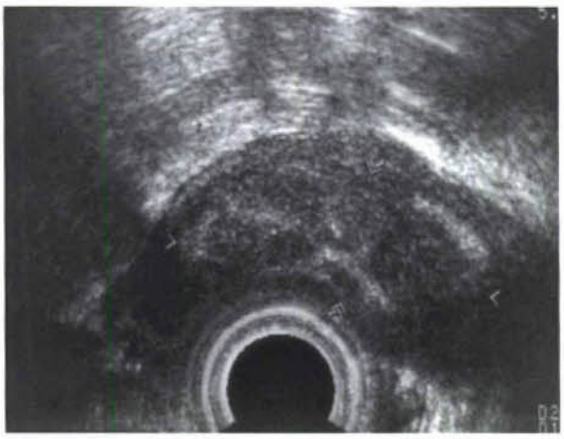

70

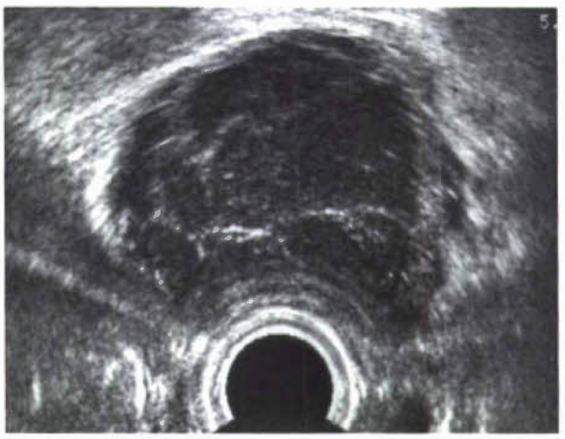

71

Uterine Sarcoma

Fig. 27.**70** Typical echogenic septations are visible in a hypoechoic endometrial stromal sarcoma (7.4 × 3.0 × 3.7 cm). Longitudinal scan of the uterus.

Fig. 27.**71** Echogenic septations in a hypoechoic endometrial stromal sarcoma (7.2 × 5.0 × 6.9 cm). Longitudinal scan of the uterus.

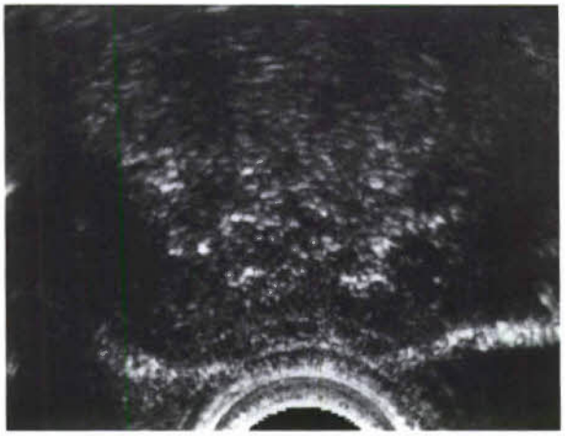

72

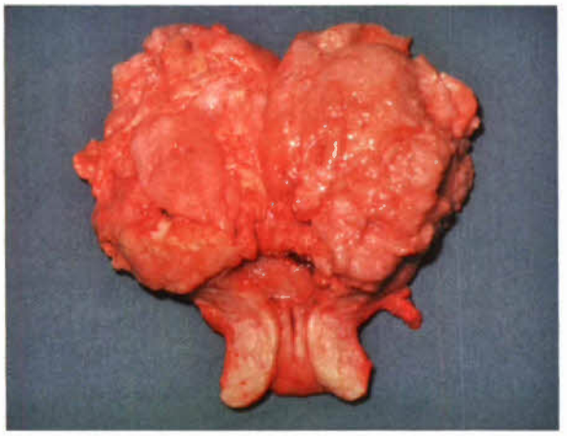

73

Fig. 27.**72** Large, rapidly growing leiomyosarcoma of the uterine corpus, exhibiting an irregular echo pattern (6.8 cm). Transverse scan of the uterus.

Fig. 27.**73** Surgical specimen corresponding to Fig. 27.**72**.

Cervical Carcinoma

74

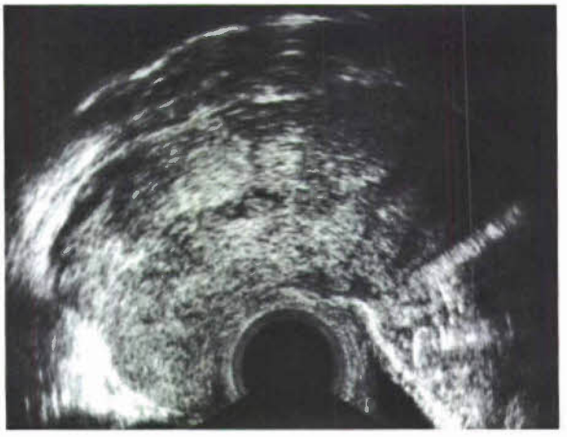

75

Fig. 27.**74** Stage 1b cervical carcinoma. A hypoechoic necrotic cavity is visible within the cervix, surrounded by echogenic irregular tumor tissue (→). There is very little cervical expansion. Longitudinal scan of the uterus.

Fig. 27.**75** Barrel-shaped carcinoma of the cervix, predominantly hyperechoic, with tumor extension into the upper part of the uterine corpus. Longitudinal scan.

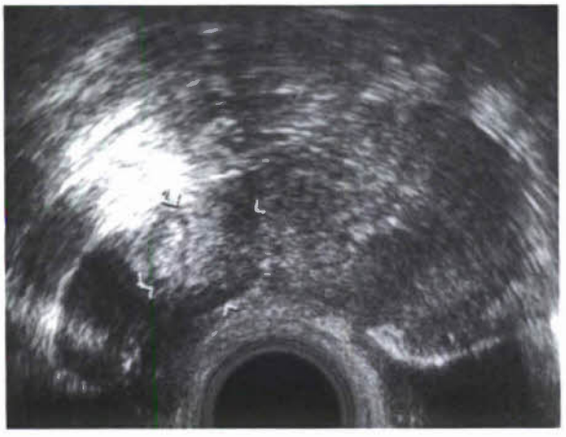

76

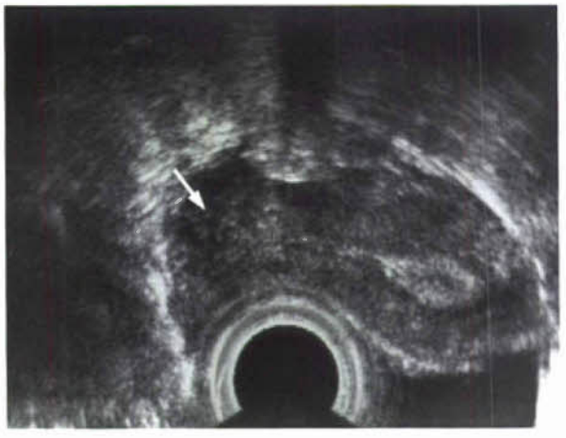

77

Fig. 27.**76** Mixed hypoechoic and hyperechoic, sharply circumscribed tumor nodule in the isthmic region (2.5 × 2.1 cm). Histology identified the lesion as metastatic breast carcinoma. Longitudinal scan.

Fig. 27.**77** Exophytic cervical carcinoma (stage 2b) causing mushroom-shaped cervical expansion to 4.4 × 5.9 cm (→). Longitudinal scan of the uterus.

Fig. 27.**78** Exophytic cervical carcinoma. It is mainly the anterior lip of the cervix that has been expanded by hypoechoic tumor masses (*). Longitudinal scan.

Fig. 27.**79** Surgical specimen corresponding to Fig. 27.**78**.

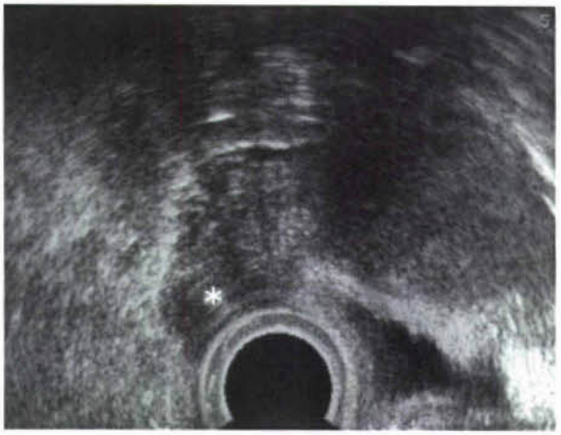

78

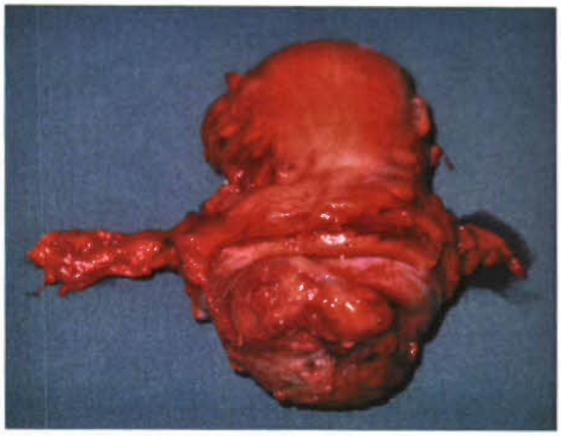

79

Fig. 27.**80** Cervical carcinoma with early, bilateral invasion of the parametrial attachments (→ ←). Coronal scan through the true pelvis.

Fig. 27.**81** Cervical carcinoma with cone-shaped areas of parametrial invasion on both sides (→). Ultrasound detection signifies grossly visible parametrial involvement: 2.6 cm on the left side, 1.4 cm on the right side. Coronal scan.

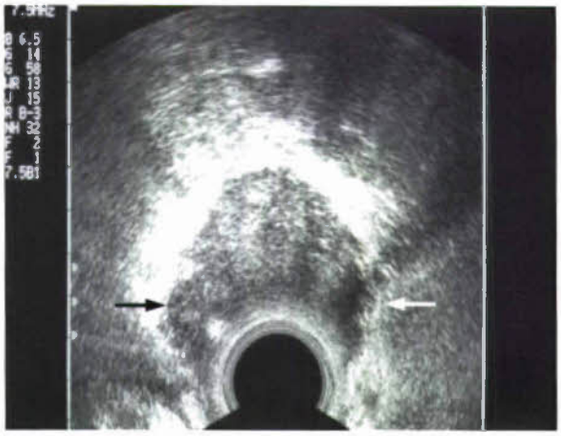

80

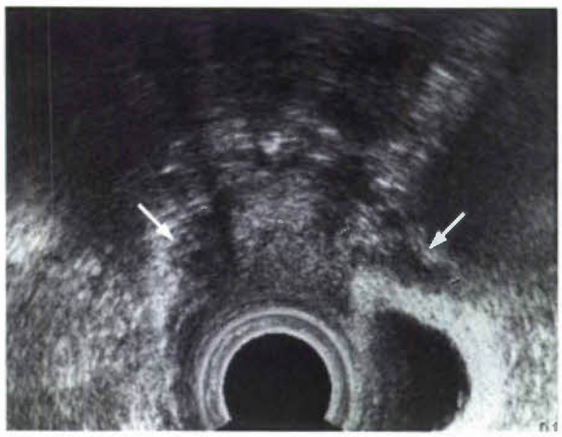

81

Fig. 27.**82** Stage 1b cervical carcinoma with a large (5.6 × 3.2 × 3.4 cm) hypoechoic lymph node on the left pelvic wall (><). Coronal scan.

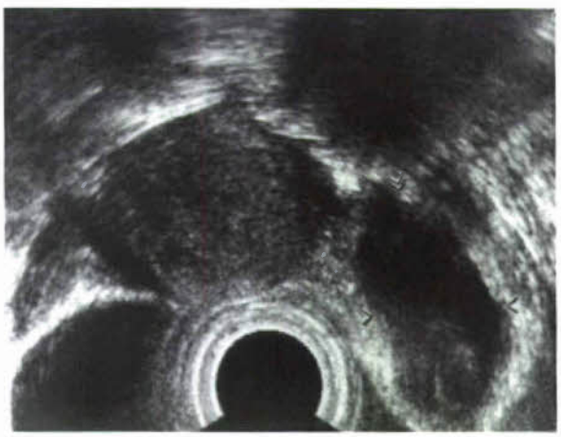

82

affected more. The tumor tissue typically appears as a relatively hypoechoic area (Figs. 27.**77**–27.**79**).

Parametrial invasion is detectable sonographically only if the tumor has grossly invaded the parametrium (Figs. 27.**80**, 27.**81**). It may be possible to improve sonographic accuracy by means of transrectal scanning [40] or by fine needle aspiration biopsy [40a]. However, many cases involve only microscopically detectable tumor spread within the lymphatics, and these cases would not be detectable by transvaginal or transrectal ultrasound imaging.

Enlarged lymph nodes can occasionally be appreciated as hypoechoic masses on the pelvic wall, depending on the stage of disease (Fig. 27.**82**).

Three-dimensional (3D) ultrasound is opening up new horizons in data acquisition and image display, particularly in the diagnosis of cervical carcinoma [40b]. The "niche mode" display in the 3D ultrasound can provide a cutaway view of the uterus, yielding important information on intrauterine tumor extension [41].

Future studies will tell us more about the accuracy of 3D ultrasound in the evaluation of parametrial tumor spread. The evaluation of parametrial invasion, considered the most important staging factor for cervical carcinoma, currently relies on magnetic resonance imaging, which has an accuracy rate of almost 90%. The diagnostic accuracy of magnetic resonance imaging (MRI) for all stages of cervical carcinoma is in the range of 80–90% [42,43].

References

1 Clarke-Pearson DL. Benign diseases of the uterus: leiomyomas, adenomyosis, hyperplasia and polyps. In: Clarke-Pearson DL, Dawood MY. Green's gynecology: essentials of clinical practice. Boston: Little, Brown, 1990.
2 Netter FH. Farbatlanten der Medizin, 2nd ed., vol. 3: Genitalorgane. Stuttgart: Thieme, 1987.
3 Walsh JW, Taylor KJ, Rosenfield AT. Grey scale ultrasonography in the diagnosis of endometriosis and adenomyosis. AJR Am J Roentgenol 1979;132:87–90.
4 Merz E. Benigne Uterusveränderungen. In: Merz E, editor. Vaginosonographie. Stuttgart: Enke, 1992: 29–32.
5 Dallenbach-Hellweg G. Endometrium. In: Remmele W, editor. Pathologie, vol. 3. Berlin: Springer, 1984: 249–69.
6 Granberg S, Wikland M, Karlsson B, Norström A, Friberg LG. Endometrial thickness as measured by endovaginal ultrasonography for identifying endometrial abnormality. Am J Obstet Gynecol 1991;164:47–52.
7 Merz E. Value of vaginosonography in the identification of normal and abnormal endometrium [paper presented at the 4th International Symposium on Gynecologic Oncology, Surgery and Urology, Mayo Clinic, Rochester, Minnesota, USA, April 16–19, 1989].
8 Killackey MA, Hakes TB, Pierce VK. Endometrial adenocarcinoma in breast cancer patients receiving antiestrogens. Cancer Treat Rep 1985;69:237–8.
9 Gusberg SB. Tamoxifen for breast cancer: associated endometrial cancer. Cancer 1990;65:1463–4.
10 van Leeuwen FE, Benraadt J, Coebergh JW, Kiemeney LA, Gimbrere CH, Otter R, Schouten LJ, Damhuis RA, Bontenbal M, Diepenhorst FW et al. Risk of endometrial cancer after tamoxifen treatment of breast cancer. Lancet 1994;343:978
11 Fornander T, Rutqvist LE, Cedermark B, Glas U, Mattsson A, Silfverswärd C, et al. Adjuvant tamoxifen in early breast cancer: occurrence of new primary cancers. Lancet 1989;i:117–20.
11a Markovitch O, Tepper R, Fishman A, Shapira J, Aviram R, Cohen I. The value of transvaginal ultrasonography in the prediction of endometrial pathologies in asymptomatic postmenopausal breast cancer tamoxifen-treated patients. Gynecol Oncol. 2004; 95:456–62.
11b Weaver J, McHugo JM, Clark TJ. Accuracy of transvaginal ultrasound in diagnosing endometrial pathology in women with post-menopausal bleeding on tamoxifen. Br J Radiol. 2005;78:394–7.
11c Fung MF, Reid A, Faught W, Le T, Chenier C, Verma S, Brydon E, Fung KF. Prospective longitudinal study of ultrasound screening for endometrial abnormalities in women with breast cancer receiving tamoxifen. Gynecol Oncol. 2003;91:154–9.
12 Hulka CA, Hall DA. Endometrial abnormalities associated with tamoxifen therapy for breast cancer: sonographic and pathologic correlation. AJR Am J Roentgenol 1993;160:809–12.
13 Perrot N, Guyot B, Antoine M, Uzan S. The effect of tamoxifen on the endometrium. Ultrasound Obstet Gynecol 1993;4:83–4.
14 Bourne TH, Lawton F, Leather A, Granberg S, Campbell S, Collins WP. The use of intracavity saline instillation and transvaginal ultrasonography to detect tamoxifen-associated endometrial polyps. Ultrasound Obstet Gynecol 1994;4:73–5.
14a Goldstein SR, Monteagudo A, Popiolek D, Mayberry P, Timor-Tritsch I. Evaluation of endometrial polyps. Am J Obstet Gynecol. 2002;186:669–74.
14b Jakab A, Ovari L, Juhasz B, Birinyi L, Bacsko G, Toth Z. Detection of feeding artery improves the ultrasound diagnosis of endometrialpolyps in asymptomatic patients. Eur J Obstet Gynecol Reprod Biol. 2005;119:103–7.
15 Breckenridge JW, Kurtz AB, Ritchie WG, Macht EL Jr. Postmenopausal uterine fluid collection: indicator of carcinoma. AJR Am J Roentgenol 1982;139:529–34.
16 McCarthy KA, Hall DA, Kopans DB, Swann CA. Postmenopausal endometrial fluid collections: always an indicator of malignancy? J Ultrasound Med 1986;5:647–9.
17 Merz E, Macchiella D, Mitze M. Die Vaginosonographie als nichtinvasives Hilfsmittel bei der Abklärung von Blutungen in der Postmenopause. Ultraschall Klin Prax 1990;5:1–7.
18 Dallenbach-Hellweg, G. Portio und cervix. In: Remmele W, editor. Pathologie, vol. 3. Berlin: Springer, 1984: 228–49.
19 Benrubi GL. Carcinoma of the cervix. In: Stovall TG, Summitt RL Jr, Beckmann CRB, Ling FW, editors. Clinical manual of gynecology. New York: McGraw-Hill, 1992: 486–502.
20 Glassburn JR, Brady LW, Grigsby PW. Endometrium. In: Perez CA, Brody LW, editors. Principles and practice of radiation oncology, 2nd ed. Philadelphia: Lippincott, 1992.
21 Cowan BD, Morrison JC. Management of abdominal genital bleeding in girls and women. N Engl J Med 1991;324:1710–5.
22 [No authors listed.] Third national cancer survey: incidence data. Natl Cancer Inst Monogr 1975;41:i–x, 1–454.
23 Kaiser R, Schulz KD. Gegenwärtige Gesichtspunkte zur Epidemiologie und Ätiologie des Endometriumkarzinomes. Gynäkologe 1983;16:82–6.
24 Cacciatore B, Lehtovira P, Wahlström T, Ylänen K, Ylöstalo P. Contribution of vaginal scanning to sonographic evaluation of endometrial cancer invasion. Acta Oncol 1989;28:585–8.
25 Cruickshank DJ, Randall JM, Miller LD. Vaginal endosonography in endometrial cancer. Lancet 1989;i:445–6.
26 Karlsson B, Norström A, Granberg S, Wikland M. The use of endovaginal ultrasound to diagnose invasion of endometrial cancer. Ultrasound Obstet Gynecol 1992;2: 35–9.
27 Osmers R, Völksen M, Schauer A. Vaginosonography for early detection of endometrial carcinoma. Lancet 1990;335:1569–71.
28 Osmers R, Völksen M, Rath W, Kuhn W. Vaginosonographic detection of endometrial cancer in postmenopausal women. Int J Gynecol Obstet 1990;32:35–7.
29 Schurz B, Eppel W, Egarter C, Wenzel R, Reinold E. Vaginosonographie in der Gynäkologie. Ultraschall Med 1989;10:90–7.
30 Osmers R, Völksen M, Kuhn W. Vaginosonographisch gemessene Endometriumdicke und deren histologisches Korrelat bei Postmenopausenblutungen. Ultraschall Klin Prax 1990;5:8–11.
30a Patai K, Szentmariay IF, Jakab Z, Szilagyi G. Early detection of endometrial cancer by combined use of vaginal ultrasound and endometrial vacuum sampling. Int J Gynecol Cancer. 2002;12:261–4.
30b Sawicki W, Spiewankiewicz B, Stelmachow J, Cendrowski K. The value of ultrasonography in preoperative assessment of selected prognostic factors in endometrial cancer. Eur J Gynaecol Oncol. 2003;24:293–8.
31 Weber G, Merz E, Bahlmann F, Mitze M, Weikel W, Knapstein PG. Assessment of myometrial infiltration and preoperative staging in patients with endometrial carcinoma by transvaginal ultrasound. Ultrasound Obstet Gynecol 1995;6:362–7.
32 Pfleiderer A. Die Therapie des Endometriumkarzinomes. Geburtshilfe Frauenheilkd 1991;51:787–97.
33 Baltzer J, Lohe KJ. Pathologie, Diagnostik und Behandlung des Endometriumkarzinoms und seiner Vorstufen. In: Käser O, Friedberg V, Ober KG, Thomsen K, Zander J, editors. Gynäkologie und Geburtshilfe, vol. III, part 2. Stuttgart: Thieme, 1988:14.161–14.208.
34 Creasman WT, Morrow CP, Bundy BN, Homesley HD, Graham JE, Heller PB. Surgical pathological spread patterns of endometrial cancer: a Gynecologic Oncology Group Study. Cancer 1987;60(8 Suppl):2035–41.
34a Kose G, Aka N, Api M. Preoperative assessment of myometrial invasion and cervical involvement of endometrial cancer by transvaginal ultrasonography. Gynecol Obstet Invest. 2003;56:70–6.
35 Bidzinski M, Lemieszczuk B. The value of transvaginal ultrasonography (TVS) in the assessment of myometrial and cervical invasion in corpus uteri neoplasma. Eur J Gynaecol Oncol 1993;14 Suppl:86–91.
36 Shipley CF, Smith ST, Dennis EJ, Nelson GH. Evaluation of pretreatment transvaginal sonography in the management of patients with endometrial carcinoma. Am J Obstet Gynecol 1992;167:406–11.
37 Sahakian V, Syrop C, Turner D. Endometrial carcinoma: transvaginal ultrasonography prediction of depth of myometrial invasion. Gynecol Oncol 1991;43:217–9.
38 Cacciatore B, Lehtovira P, Wahlström T, Ylöstalo P. Preoperative sonographic evaluation of endometrial cancer. Am J Obstet Gynecol 1989;160:133–7.
38a Emoto M, Tamura R, Shirota K, Hachisuga T, Kawarabayashi T. Clinical usefulness of color Doppler ultrasound in patients with endometrial hyperplasia and carcinoma. Cancer. 2002;94:700–6.
38b Testa AC, Ciampelli M, Mastromarino C, Lopez R, Zannoni GF, Mancuso S, Scambia G. Detection of central pelvic recurrent disease with transvaginal color Doppler ultrasound in women treated for gynecological malignancy. Ultrasound Obstet Gynecol. 2002;19:490–5.
38c Arslan M, Erdem A, Erdem M, Yazici G, Himmetoglu O, Gursoy R. Transvaginal color Doppler ultrasonography for prediction of pre-cancerous endometrial lesions. Int J Gynaecol Obstet. 2003;80:299–306.
38d Alcazar JL, Castillo G, Minguez JA, Galan MJ. Endometrial blood flow mapping using transvaginal power Doppler sonography in women with postmenopausal bleeding and thickened endometrium. Ultrasound Obstet Gynecol. 2003;21:583–8.
39 Dallenbach-Hellweg G. Myometrium. In: Remmele W, editor. Pathologie, vol. 3. Berlin: Springer, 1984: 269–74.
39a Follen M, Levenback CF, Iyer RB, Grigsby PW, Boss EA, Delpassand ES, Fornage BD, Fishman EK. Imaging in cervical cancer. Cancer. 2003;98(9 Suppl):2028–38.
39b Carter JR. Cervical tumor characterization by transvaginal color flow Doppler ultrasound. Int J Gynecol Cancer. 1999;9:279–284.
39c Alcazar JL, Castillo G, Jurado M, Lopez-Garcia G. Intratumoral blood flow in cervical cancer as assessed by transvaginal color doppler ultrasonography: Correlation with tumor characteristics. Int J Gynecol Cancer. 2003;13:510–4.
40 Aoki S, Hata T, Senoh D, Makihara K, Takumiya O, Kitao M. Parametrial invasion of uterine cervical cancer assessed by transrectal ultrasonography: preliminary report. Gynecol Oncol 1990;36:82–9.
40a Cendrowski K, Sawicki W, Spiewankiewiez B, Stelmachow J. The importance of fine needle aspiration biopsy and sonographic evaluation of parametria in cervical cancer. Eur J Gynaecol Oncol. 2003;24:413–6.
40b Testa AC, Ferrandina G, Distefano M, Fruscella E, Mansueto D, Basso D, Salutari V, Scambia G. Color Doppler velocimetry and three-dimensional color power angiography of cervical carcinoma. Ultrasound Obstet Gynecol. 2004;24:445–52.
41 Merz E, Weber G, Bahlmann F, Macchiella D. Transvaginale 3D-Sonographie in der Gynäkologie. Gynäkologe 1995;28:270–5.
42 Cobby M, Brawing J, Jones A. Magnetic resonance imaging, computed tomography and endosonography in the local staging of carcinoma of the cervix. Br J Radiol 1990;63:673–9.
43 Sironi S, Belloni C, Taccagni GL, DelMaschio A. Carcinoma of the cervix: value of MR imaging in detecting parametrial involvement. AJR Am J Roentgenol 1991;156: 753–6.
44 Sobin LH, Wittekind Ch. TNM Classification of Malignant Tumors. New York, Wiley-Liss, 2002.
45 Creasman WT. New gynecologic cancer staging. Gynecol Oncol 1995;58:157–8.

28 Ovarian Masses

Owing to its higher resolution, transvaginal ultrasound is clearly superior to abdominal ultrasound in the evaluation of ovarian masses [1,2]. Vaginal ultrasound also has several disadvantages, however:

- Large ovarian masses can be only partially visualized with a vaginal probe.
- Very high-sited ovarian masses are not visualized, due to the limited penetration depth of the vaginal probe.
- Some lesions, such as hemorrhagic corpus luteum cysts, present such remarkable and diverse patterns that they are apt to be overinterpreted, especially by inexperienced examiners.

Every ultrasound assessment of an ovarian mass should include an evaluation of the criteria listed in Table 28.**1**.

Not all ovarian masses can be assigned directly and unambiguously to the ovary on the basis of ultrasound findings. There are cases, for example, in which a solid ovarian tumor abutting the uterus is indistinguishable from a uterine myoma by ultrasound. Conversely, a subserous myoma of the lateral uterine wall may mimic an ovarian tumor. It can also be very difficult to localize a very large ovarian mass to the right or left side, as these lesions often lie close to the midline. Comparative studies have shown that the sonographic assessment of ovarian tumor size is far more accurate than size assessment by palpation alone [3]. Shape can be a helpful criterion in determining whether a cystic mass should be localized to the ovary or to the fallopian tube (sactosalpinx).

The echo pattern is a critical parameter in terms of classifying an ovarian mass as benign or malignant. Ovarian masses can be classified into three main groups on the basis of their internal echo pattern: purely cystic, purely solid, and mixed cystic and solid. The latter group can be further subdivided on the basis of the relative extent of the cystic or solid component: cystic-solid (cystic component > 50%) or solid-cystic (solid component > 50%) (Table 28.**2**).

With *cystic ovarian masses*, transvaginal ultrasound is superior to abdominal ultrasound for determining the number of compartments in loculated masses, measuring septal and wall thicknesses, and particularly for evaluating internal features such as internal echoes and solid mural echo complexes (e.g., papillary growths). This is particularly true when a suspicious mural structure is located in the lower or posterior part of the mass. The criteria used in evaluating the ultrasound morphology of cystic ovarian masses are listed in Table 28.**3**.

With *solid ovarian tumors*, the high resolution of endovaginal probes allows considerably more detailed evaluation of the overall tissue structure (Table 28.**3**). It can discriminate between a homogeneous or nonhomogeneous structure and between a uniform or nonuniform echo pattern.

With cystic masses, as well as purely solid tumors or mixed cystic and solid lesions, it is reasonable to assume that the more heterogeneous the echo pattern of the lesion, the greater the likelihood that the lesion is histologically malignant. Another important criterion is the nature of the tumor margins. Smooth margins are suggestive of a benign tumor, although they cannot positively exclude an early invasive stage of cancer. Conversely, markedly irregular margins are suggestive of a malignant tumor that has already crossed organ boundaries. This is also suggested in cases in which the lesion cannot be clearly delineated from adjacent tissues, although inflammatory conglomerate masses may also be poorly delineated from their surroundings.

Posterior acoustic effects (enhancement with cystic masses, attenuation or shadowing with solid tumors and tumors with solid components), as well as compressibility, can help in determining whether the lesion is more likely to be a cystic mass that mimics a solid tumor due to the presence of dense internal echoes, or a solid tumor that appears hypoechoic due to a rich blood supply and may thus be mistaken for a cystic lesion. It should be noted that internal echoes can be accurately evaluated only if the gain setting has been properly adjusted on the ultrasound scanner.

Finally, color Doppler ultrasound can be used to detect tumor-induced angiogenesis [4–7]. Tumor vessels can be selectively visualized and their hemodynamics evaluated by sampling pulsed Doppler spectra and determining the resistance index or pulsatility index.

Although transvaginal ultrasound is far more accurate than abdominal ultrasound for evaluating ovarian tumors, it can still detect only gross abnormalities; microscopic changes are not accessible to imaging. While color Doppler adds the important capability of vascular diagnosis, definitive identification of an indeterminate tumor still has to rely on histologic examination.

The key issue in terms of management is not that ultrasound can accurately predict the histologic diagnosis, but that it can distinguish between lesions that can safely be followed from lesions that require an immediate surgical diagnosis.

Important factors in addition to the overall echo structure of an ovarian mass are the age of the patient and her premenopausal or postmenopausal status. For example, a 4-cm purely cystic mass with no internal

Table 28.**1** Criteria for the ultrasound evaluation of ovarian masses

- Can the mass be localized to a specific organ? To the right or left side?
- Dimensions of the mass (length × height × width, in millimeters or centimeters)
- Shape of the mass (round, elliptical, oblong)
- Structure of the mass (homogeneous or nonhomogeneous)
- Echogenicity (hypoechoic, moderately echogenic, hyperechoic)
- Margins (regular or irregular)
- Delineation from adjacent structures
- Posterior acoustic shadowing or enhancement
- Compressibility
- Vascular findings by Doppler or color Doppler

Table 28.**2** Classification of ovarian masses by their ultrasound morphology

- Purely cystic ovarian masses
- Purely solid ovarian masses
- Mixed cystic and solid ovarian masses
  - Cystic-solid (cystic component > 50%)
  - Solid-cystic (solid component > 50%)

Table 28.**3** Criteria for the structural evaluation of cystic and solid masses

Cystic ovarian masses
• Number of compartments
• Wall thickness
• Septal thickness
• Internal echoes (distribution, echogenicity)
• Detection of one or more solid echo complexes
Solid ovarian masses
• Internal echoes (structural pattern, echogenicity)

Table 28.4 Sonomorphologic features that are suggestive of a benign or malignant ovarian tumor

Benign ovarian tumor	Malignant ovarian tumor
• Smooth margins	• Irregular margins
• Thin wall (<3 mm)	• Thick wall (>3 mm)
• Thin septa (≤3 mm)	• Thick septa (≥3 mm)
• Homogeneous echo pattern	• Nonhomogeneous echo pattern
• Uniform echogenicity	• Nonuniform echogenicity

echoes should be interpreted differently in an 18-year-old patient than in a 68-year-old woman.

Table 28.4 lists the morphologic parameters that are suggestive of benign status or malignancy in an ultrasound lesion.

Benign Adnexal Tumors

Simple Ovarian Cysts

Sonographically "simple" ovarian cysts are among the most common benign ovarian lesions. They include functional cysts that develop during the reproductive years, such as follicular and corpus luteum cysts, as well as inclusion cysts of the superficial ovarian epithelium, which are most common after menopause.

Follicular cysts result from the persistence of an unruptured graafian follicle. They appear sonographically as unilateral, round to oval, unilocular cysts with a thin, smooth wall, an absence of internal echoes, and posterior acoustic enhancement (Fig. 28.**1**). On average, they range from 3 to 6 cm in diameter. Increased estrogen synthesis continues as long as the follicular cyst has an intact layer of granulosa cells. Follicular cysts generally resolve in two to three cycles. Treatment with an ovulation inhibitor may be beneficial.

The differential diagnosis of a simple ovarian cyst with no internal echoes includes a paraovarian cyst (Fig. 28.**2**) and unilocular cystoma (Fig. 28.**28**; Table 28.**5**).

Corpus luteum cysts resemble follicular cysts in their size and shape (Figs. 28.**3**–28.**10**) but develop only after ovulation has occurred when there is a delay in corpus luteum regression. The wall of the cyst contains scant numbers of luteinized granulosa and theca cells. Because progesterone synthesis continues unabated, the patient may experience temporary amenorrhea or persistent spotting. A corpus luteum cyst can be distinguished sonographically from a follicular cyst only if the cycle has been closely monitored and ovulation has been confirmed. It is relatively common to find a hematoma within the lumen of a corpus luteum cyst. The cyst can present a range of sonographic features, depending on the age of the hematoma and its stage of evolution (Figs. 28.**4**–28.**10**) [8]. Applying pressure to the cyst with the endovaginal probe will elicit an indentation of the cyst wall, with deformation of the hematoma (Fig. 28.**5**). Color Doppler can also be helpful by showing an absence of color flow signals within the hematoma (Fig. 28.**6**). If the cyst has been present for several weeks, residues from the hematoma can produce a fine internal echo pattern that may be mistaken for endometriosis (Fig. 28.**10**). The presence of two or more adjacent corpus luteum cysts may be noted following stimulation therapy (Figs. 28.**11**, 28.**12**). A trial of progestin therapy may be beneficial for persistent corpus luteum cysts.

Table 28.5 Differential diagnosis of sonographically simple cysts (without internal echoes) in the lower abdomen

- Follicular cyst
- Corpus luteum cyst
- Retention cyst
- Hydrosalpinx
- Peritoneal cyst
- Paraovarian cyst
- Serous cystoma
- Overflow bladder

Theca lutein cysts develop from unruptured follicles in an exaggerated ovarian response to a gonadotropin excess. This may follow iatrogenic ovarian hyperstimulation, or may occur in association with a hydatidiform mole or chorionic epithelioma. The cysts are bilateral, and luteinizing theca cells are present in the cyst wall (Fig. 28.**13**). Theca lutein cysts may grow to more than 15 cm in size. Differentiation is required from a true epithelial tumor with septum formation.

Retention cysts are formed as inclusion cysts of the superficial ovarian epithelium. They occur predominantly in the postmenopausal ovary and are of variable size (Figs. 28.**14**, 28.**15**). Because retention cysts may progress directly to cystadenoma or cystadenofibroma (Fig. 28.**16**) and occasionally undergo malignant transformation [9], there should be little hesitation in recommending surgery.

A loculated *peritoneal cyst* is indistinguishable from a retention cyst by ultrasound (Fig. 28.**17**), unless it is found to be clearly separate from the ovary. Larger peritoneal cysts may even encompass the ovary (Fig. 28.**18**).

The risk of ovarian carcinoma underlying an ovarian cyst with "simple" ultrasound features is extremely low in a premenopausal patient (Table 28.**6**) [10–16]. The risk appears to be somewhat higher in postmenopausal women, although the incidence rates reported by different authors vary considerably. While Osmers [15] reported a remarkably high malignancy rate of 9.6% in sonographically simple cysts detected after menopause, we were unable to find a single case of histologic malignancy in the cases that we examined [13] (Table 28.**6**).

The sonographer examining a simple cyst should closely scrutinize the entire cyst wall for any evidence of a solid mural echo complex. This should be done regardless of the patient's age, but is particularly important in older patients.

Endometriotic Cysts

The etiology of endometriosis is still poorly understood. Of the various transplantation theories that have been advanced (review in [17]), the Sampson theory [18] is the most widely accepted. This theory holds that viable endometrial tissue passes through the fallopian tubes into the lesser pelvis by retrograde menstruation and becomes implanted into the peritoneum. Endometriosis is most prevalent between 20 and 40 years of age, but its actual incidence is unknown. It is estimated that approximately 2–3% of the female population have endometriosis dur-

Table 28.6 Incidence of benign and malignant findings in patients with a sonographically simple, echo-free ovarian cyst

First author	Year	n	Benign	Malignant
Premenopausal and postmenopausal patients				
Granberg [11]	1989	296	295 (99.7%)	1 (0.3%)
Obwegeser [14]*	1993	144	141 (98%)	3 (2%)
Premenopausal patients				
Osmers [15]	1995	641	636 (98.2%)	5 (0.8%)
Prömpeler [16]	1996	230	228 (99.1%)	2 (0.9%)
Merz [13]	1997	152	152 (100%)	0 (0%)
Postmenopausal patients				
Andolf [10]	1989	152	149 (98%)	3 (2%)
Luxman [12]	1991	33	31 (94%)	2 (6%)
Osmers [15]	1995	135	122 (90.4%)	13 (9.6%)
Prömpeler [16]	1996	151	147 (97.4%)	4 (2.6%)
Merz [13]	1997	38	38 (100%)	0 (0%)

*Abdominal ultrasound.

Simple Ovarian Cysts

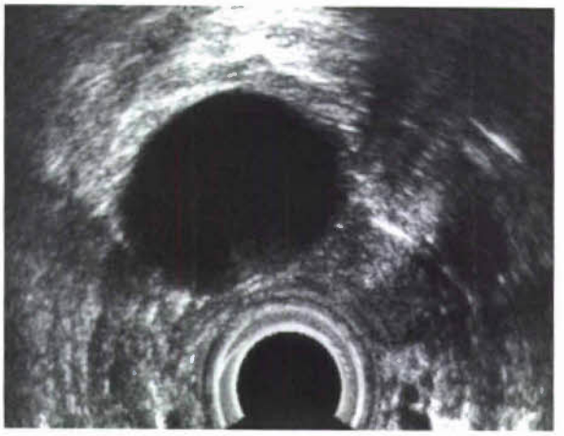

1

Fig. 28.1 Simple cyst (follicular cyst, 4.5 × 3 × 3 cm) of the right ovary. Oblique longitudinal scan.

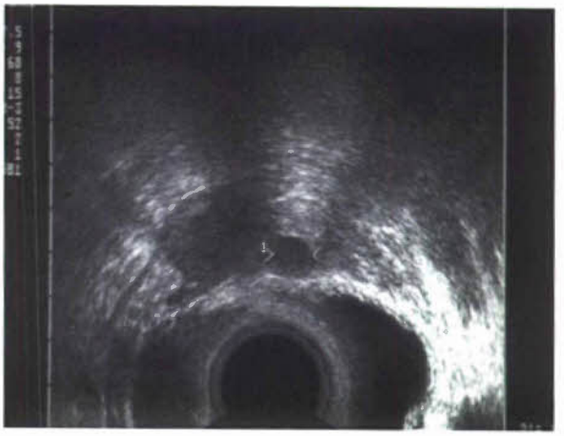

2

Fig. 28.2 Small paraovarian cyst (1 cm in diameter) on the left side. Coronal scan.

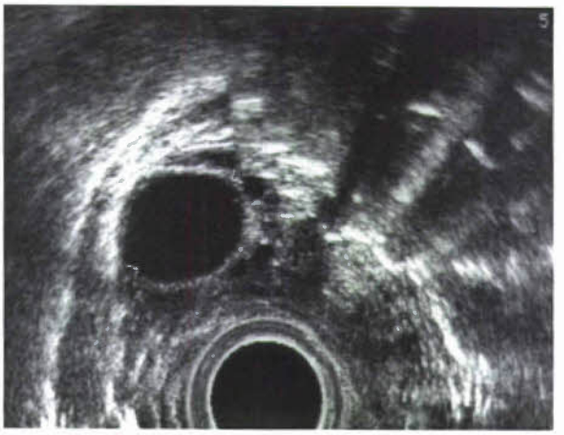

3

Fig. 28.3 Corpus luteum cyst of the right ovary (3.0 × 2.6 cm).

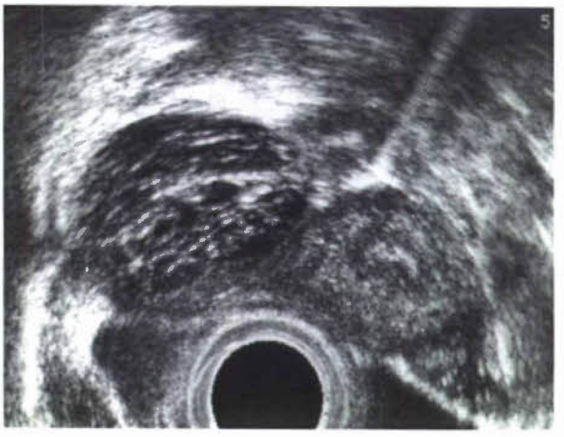

4

Fig. 28.4 Hemorrhagic corpus luteum cyst of the right ovary (5.1 × 4.0 × 5.0 cm) with a reticular hematoma pattern. Coronal scan.

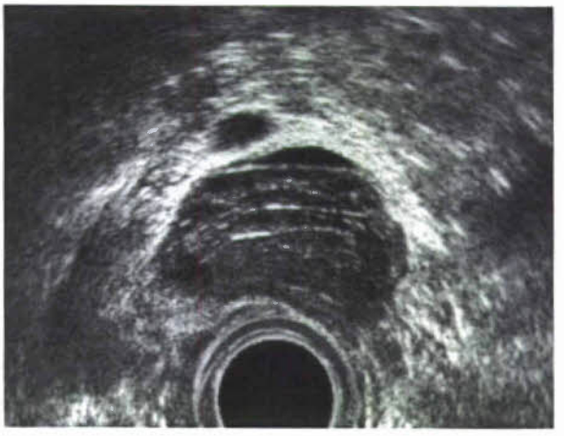

5

Fig. 28.5 Corpus luteum cyst of the right ovary (5.0 × 4.3 × 4.8 cm). Intracystic hematoma shows a streak-like echo pattern. Compression of the cyst with the endovaginal probe indents the cyst wall and deforms the hematoma. Coronal scan.

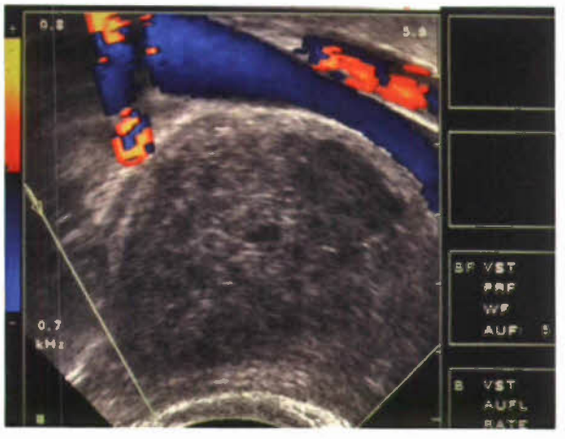

6

Fig. 28.6 Hemorrhagic corpus luteum cyst (4.1 × 3.6 × 3.2 cm) of the left ovary adjacent to the iliac vessels. Color Doppler shows no color flow signals within the mass.

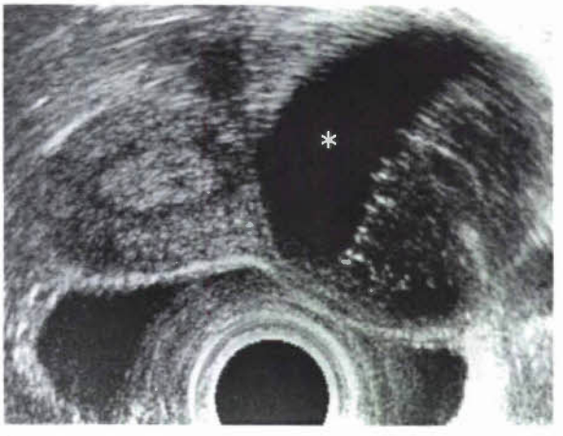

7

Fig. 28.7 Hemorrhagic corpus luteum cyst 6.2 cm in diameter. Coronal scan. The hematoma has been partially reabsorbed (*), leaving a hypoechoic fluid collection in the medial part of the cyst.

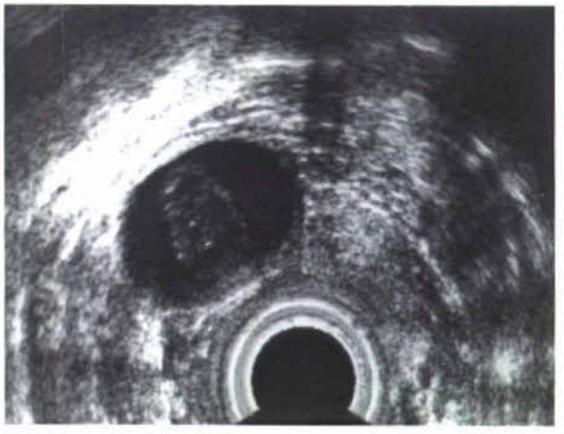

8

Fig. 28.8 Hemorrhagic corpus luteum cyst of the right ovary (4.5 × 3.4 cm) in coronal section. A residual hematoma appears as a hypoechoic nodular structure at the center of the cyst.

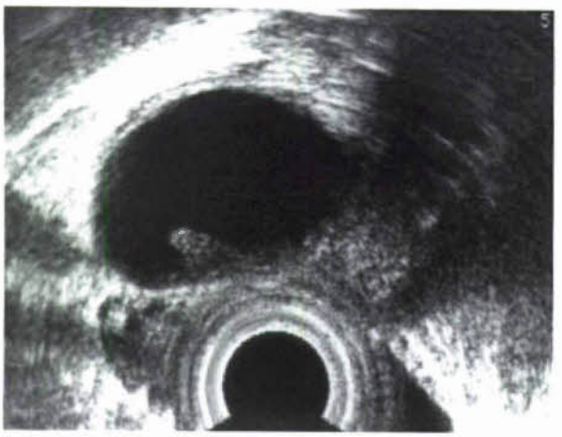

9

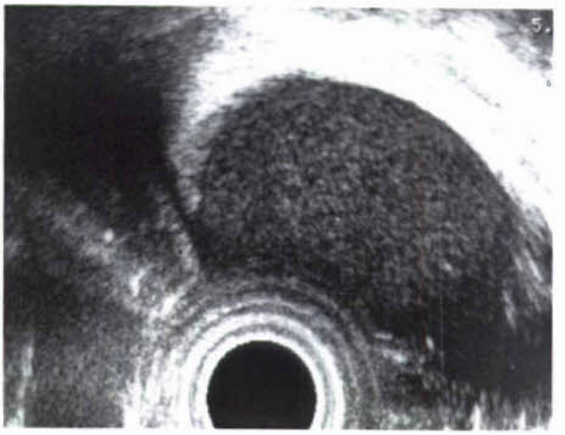

10

Fig. 28.9 The same corpus luteum cyst as in Fig. 28.8, 1 week later. Coronal scan.

Fig. 28.10 An older corpus luteum cyst shows a homogeneous pattern of fine internal echoes. Longitudinal scan.

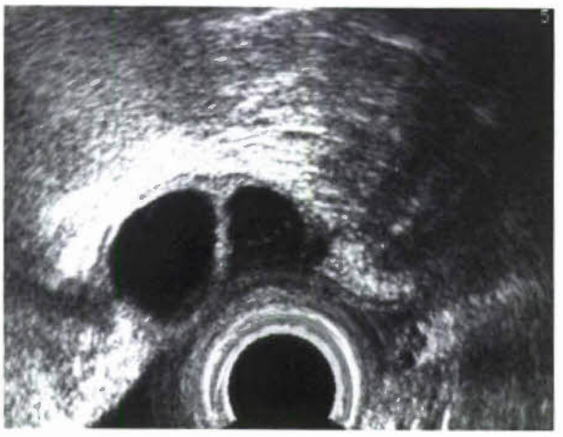

11

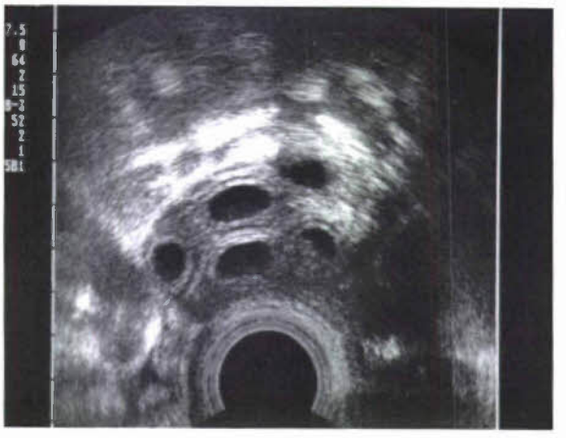

12

Fig. 28.11 Two adjacent corpus luteum cysts, following stimulation therapy. Coronal scan.

Fig. 28.12 Multiple corpus luteum cysts following gonadotropin therapy and transvaginal follicular aspiration. Longitudinal scan.

13

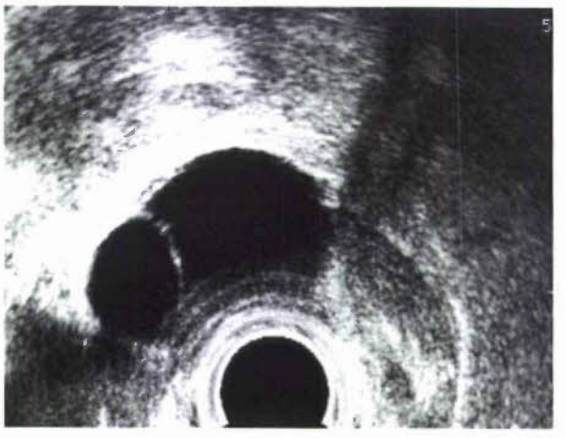

14

Fig. 28.13 Lutein cysts following gonadotropin therapy. Coronal scan.

Fig. 28.14 A cystic right ovary, with two retention cysts of different sizes in a postmenopausal patient. Coronal scan.

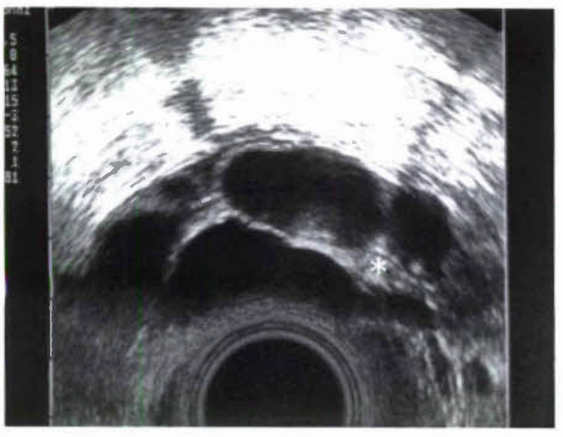

15

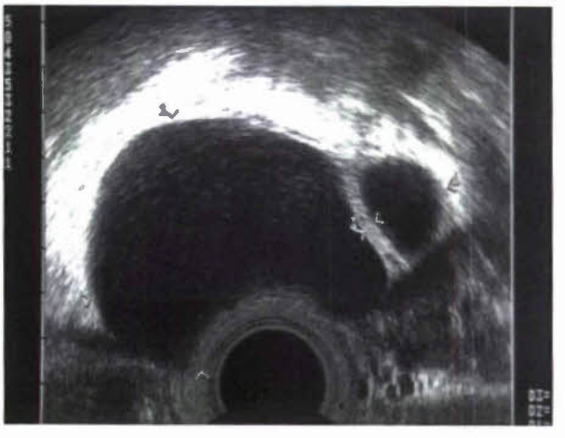

16

Fig. 28.15 A cystic right ovary, with multiple retention cysts of different sizes and residual ovarian tissue (*). Longitudinal scan.

Fig. 28.16 Loculated cystoma (8.8×5.8 cm) with a thick septum (4 mm). Coronal scan.

ing their reproductive years. Endometriotic foci have been found in 70–80% of women with unexplained infertility, and approximately half of these patients have ovarian involvement [17].

The sonographic features of endometriosis are extremely diverse. All gradations may be found, from purely cystic and mixed lesions to predominantly solid tumors [19–22]. Endometriotic cysts on the ovary may be small (Fig. 28.**19**) or large, unilocular or multilocular, and unilateral or bilateral. They differ from simple ovarian cysts in their thicker wall, the presence of fine internal echoes, and possible echogenic components at the periphery of the cyst (Figs. 28.**20**, 28.**21**). The internal echoes are caused by an inspissated, chocolate-colored fluid that results from repeated intracystic hemorrhages with fibrin deposition.

Endometriotic cysts are often fixed to their surroundings by inflammatory adhesions, making it difficult or impossible to separate them visually from adjacent organs. With its protean features, endometriosis can be extremely difficult to differentiate from other adnexal lesions such as corpus luteum cyst, tubo-ovarian abscess, dermoid cyst, and other lesions (Table 28.**7**).

Some endometriotic cysts may even have features that resemble ovarian carcinoma.

Often, an accurate diagnosis can be made only by relating the ultrasound findings to the patient's history and clinical symptoms (dysmenorrhea, chronic lower abdominal pain, dyspareunia), and definitive diagnosis has to rely on laparoscopy or laparotomy. Unlike a hemorrhagic corpus luteum cyst, which usually regresses on serial scans, an endometriotic cyst is more likely to increase in size. Elevated serum CA-125 levels may also be found in association with an endometriotic cyst [23].

Transvaginal ultrasound is not only an important aid in the diagnostic investigation of endometriosis, but can also be used successfully in monitoring the response of endometriotic lesions to conservative medical therapy [21,24].

Dermoid Cysts

Dermoid cysts of the ovary (cystic teratomas) are classified as germ-cell tumors (Table 28.**8**). They represent approximately 10–20% of benign ovarian cysts [9] and contain derivatives of all three germ layers. From 8% to 15% of dermoids are bilateral [9]. With their varying tissue composition and different grades of maturation and differentiation, dermoid cysts have an extremely variable sonographic appearance [25], making them the ultrasound "chameleon" of ovarian tumors. Dermoid cysts most commonly contain skin, hairs, and sebaceous glands. They may also contain fat, cartilage, nerve tissue, bone, respiratory tissue, teeth, and gastrointestinal tissue [26]. There are also rare instances of teratomas containing a single germ layer consisting of thyroid tissue (*struma ovarii*).

Table 28.7 Differential diagnosis of a lower abdominal cystic mass with internal echoes

- Corpus luteum cyst
- Endometriotic cyst
- Tubo-ovarian abscess
- Ovarian torsion with intraovarian hemorrhage
- Dermoid
- Pyosalpinx
- Serous cystadenoma
- Mucinous cystadenoma
- Ovarian carcinoma
- Degenerative myoma
- Ectopic pregnancy
- Distended bowel loop
- Bowel obstruction
- Postoperative hematoma

The echogenicity and solid/cystic composition of dermoid cysts are subject to wide variation, depending on the cyst contents (Figs. 28.**22**–28.**27**). Thus, a dermoid may appear as a predominantly solid tumor (Figs. 28.**22**, 28.**23**) or as a predominantly cystic mass (Figs. 28.**24**–28.**26**) with an irregular solid component. As a result, varying degrees of acoustic shadowing may be seen behind the tumor, as well as areas of marked acoustic enhancement.

The "characteristic" ultrasound appearance of a dermoid cyst, seen in approximately 33–43% of cases [27,28], is that of a thick-walled cystic adnexal mass containing a *hyperechoic solid area*. The solid area represents a collection of sebaceous material with epidermis, bone, cartilage, or other structures listed above.

Some dermoid cysts present as a sharply circumscribed mass with a conspicuous fluid level (Fig. 28.**27**) formed by a sebum–fluid interface [29]. In this case, the hyperechoic area may occupy the upper or lower portion of the cyst.

It is difficult to interpret a dermoid that does not present a characteristic sonographic pattern. This type of lesion can be extremely difficult to distinguish from an endometriotic cyst, a hemorrhagic corpus luteum cyst, a tubo-ovarian abscess, a distended bowel loop, or ovarian carcinoma.

Possible complications of dermoid cysts are malignant transformation in 1–2% of cases [26] and torsion of a pedunculated dermoid in 3–16% of cases [30].

Serous Cystadenomas

Serous cystadenomas are frequently unilocular and may contain faint internal echoes (Fig. 28.**28**). Most are indistinguishable from simple ovarian cysts by their sonographic appearance. It is helpful to note, however, that the larger the cystic mass and the older the patient, the more likely it is that the lesion will be an epithelial tumor. In an older patient with neurogenic bladder dysfunction, an overdistended bladder can create a large "cystic mass" that mimics the appearance of serous cystadenoma (Fig. 28.**29**). Two differentiating features are helpful in these cases: prolonged ultrasound observation fails to demonstrate a bladder in front of the "mass," and color Doppler may detect a urine jet entering the apparent mass (Fig. 28.**30**).

Multilocular serous cystadenomas contain predominantly thin, smooth-walled septa within a purely cystic mass.

Mucinous Cystadenomas

Mucinous cystadenomas present a more intense internal echo pattern than serous cystadenomas. They may contain fine medium-level echoes, as well as coarse echoes of relatively high amplitude (Figs. 28.**31**, 28.**32**). The internal echo pattern may vary in the different compartments of a multilocular mucinous cystadenoma. Differentiation is required from a dermoid cyst, an endometriotic cyst, or a subserous myoma that has undergone regressive changes.

Like serous cystomas, mucinous cystomas may reach a tremendous size with a volume of several liters, and may fill the entire abdomen. The full extent of very large tumors can be appreciated only with abdominal ultrasound (Chapter 9).

Ovarian Fibromas

Fibromas are a very rare type of ovarian tumor. They are benign and most often unilateral. They are most prevalent in the perimenopausal age group.

Ovarian fibroma appears sonographically as a sharply circumscribed, solid, oblong tumor with a relatively low-level, homogeneous internal

Table 28.8 Histologic classification of ovarian tumors (after Serov et al. [9])

I Epithelial tumors

A. Serous tumors
1. Benign
a) Cystadenomas and papillary cystadenomas
b) Superficial papillomas
c) Adenofibromas and cystic fibromas
2. Borderline tumors (carcinomas of low malignant potential)
a) Cystadenomas and papillary cystadenomas
b) Superficial papillomas
c) Adenofibromas and cystadenofibromas
3. Malignant
a) Adenocarcinomas, papillary adenocarcinomas
b) Superficial papillary carcinomas
c) Malignant adenofibromas and cystadenofibromas

B. Mucinous tumors
1. Benign
a) Cystadenomas
b) Adenofibromas and cystadenofibromas
2. Borderline tumors (carcinomas of low malignant potential)
a) Cystadenomas
b) Adenofibromas and cystadenofibromas
3. Malignant
a) Adenocarcinomas and cystadenocarcinomas
b) Malignant adenofibromas and cystadenofibromas

C. Endometrioid tumors
1. Benign
a) Adenomas and cystadenomas
b) Adenofibromas and cystadenofibromas
2. Borderline tumors (carcinomas of low malignant potential)
a) Adenomas and cystadenomas
b) Adenofibromas and cystadenofibromas
3. Malignant
a) Carcinomas
(I) Adenocarcinomas
(II) Adenocanthomas
(III) Malignant adenofibromas and cystadenofibromas
b) Endometrioid stromal sarcomas
c) Mesodermal (müllerian) mixed tumors, homologous and heterologous

D. Clear-cell (mesonephroid) tumors
1. Benign: adenofibromas
2. Borderline tumors (carcinomas of low malignant potential)
3. Malignant: carcinomas and adenocarcinomas

E. Brenner tumors
1. Benign
2. Proliferative
3. Malignant

F. Mixed epithelial tumors
1. Benign
2. Borderline tumors
3. Malignant

G. Undifferentiated carcinoma
H. Unclassified epithelial tumors

II Sex cord stromal tumors

A. Granulosa-stromal tumors
1. Granulosa-cell tumors
2. Tumors of thecoma–fibroma group
a) Thecomas
b) Fibromas
c) Unclassified

B. Androblastomas; Sertoli–Leydig cell tumors
1. Well-differentiated
a) Tubular adenoblastoma; Sertoli cell tumor (Pick adenoma)
b) Tubular adenoblastoma with lipid storage; Sertoli cell tumor with lipid storage (*folliculoma lipidique Lecène*)
c) Sertoli–Leydig cell tumor (tubular adenoma with Leydig cells)
d) Leydig cell tumor; hilar-cell tumor
2. Intermediate types
3. Undifferentiated (sarcomatoids)
4. With heterologous elements

C. Gynandroblastomas
D. Unclassified

III Lipid (lipoid) cell tumors

IV Germ-cell tumors

A. Dysgerminoma
B. Endodermal sinus tumor
C. Embryonal carcinoma
D. Polyembryoma
E. Choriocarcinoma
F. Teratomas
1. Immature
2. Mature
a) Solid
b) Cystic
(I) Dermoid cyst (mature cystic teratoma)
(II) Dermoid cyst with malignant transformation
3. Monodermal and highly specialized
a) Struma ovarii
b) Carcinoid
c) Struma ovarii and carcinoid
d) Others
G. Mixed teratomas

V Gonadoblastomas

A. Mature
B. Mixed with dysgerminomas or other germ-cell tumors

VI Nonspecific connective tissue tumors

VII Unclassified tumors

VIII Secondary (metastatic) tumors

echo pattern (Fig. 28.**33**). Bilateral ovarian fibromas accompanied by ascites and hydrothorax are observed in *Meigs syndrome*.

Ovarian fibroma has to be differentiated from a pedunculated subserous myoma, a predominantly solid dermoid, other solid ovarian tumors, a distended bowel loop, pelvic kidney, and other conditions (Table 28.**9**).

Table 28.9 Differential diagnosis of purely solid lower abdominal tumors

- Ovarian fibroma
- Dermoid
- Brenner tumor
- Thecoma
- Granulosa-cell tumor
- Sertoli–Leydig cell tumor
- Ovarian carcinoma
- Ovarian sarcoma
- Pedunculated subserous myoma
- Endometriotic nodule
- Distended bowel loop
- Pelvic kidney
- Ovarian metastases (from breast cancer)
- Hyperplastic lymph node
- Tubal carcinoma
- Intestinal tumor
- Bladder carcinoma
- Retroperitoneal tumor
- Recurrent tumor

Potentially Malignant Ovarian Tumors

Various ovarian tumors—such as proliferative serous papillary and mucinous cystadenomas, granulosa-cell tumors, theca-cell tumors, and Sertoli–Leydig cell tumors—have an inherent potential for malignant transformation, owing to their increased proliferative activity. Although transvaginal ultrasound generally does not allow confident differentiation between benign and malignant ovarian tumors, there are certain criteria that can be recognized more clearly than with abdominal ultra-

Fig. 28.17 Peritoneal cyst with a thin septum (5.8 × 5.2 × 5.2 cm). The patient had a prior history of abdominal hysterectomy with bilateral adnexectomy. Coronal scan.

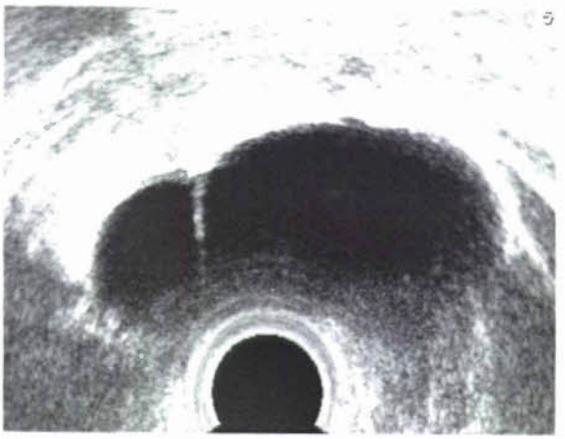

17

Fig. 28.18 Large, loculated peritoneal cyst encompassing the left ovary (←). Longitudinal scan.

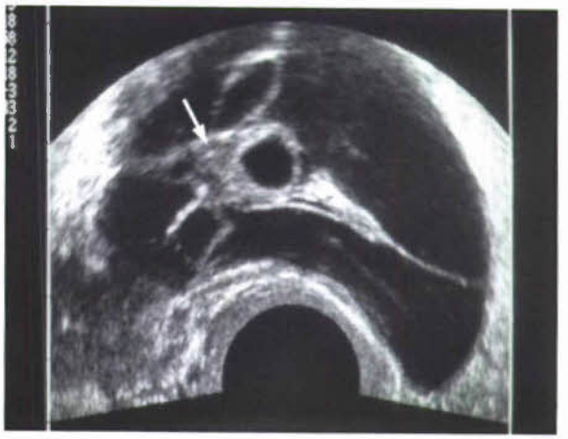

18

Endometriotic Cysts

Fig. 28.19 Small endometriotic cyst (3.5 × 2.5 × 2.8 cm) with a thick wall and fine internal echoes. Coronal scan.

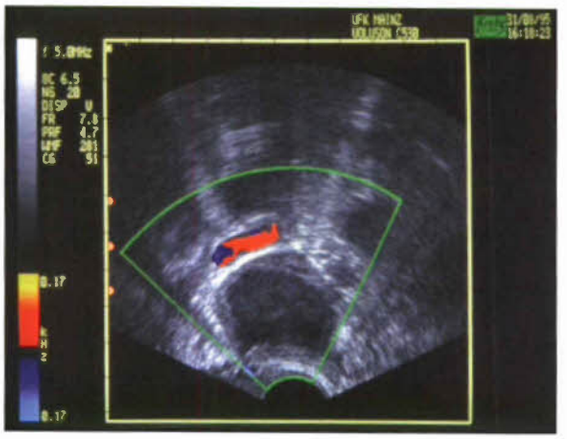

19

Fig. 28.20 Large endometriotic cyst (5.5 × 5.5 × 5.0 cm) with a thick wall and moderately coarse internal echoes. Longitudinal scan.

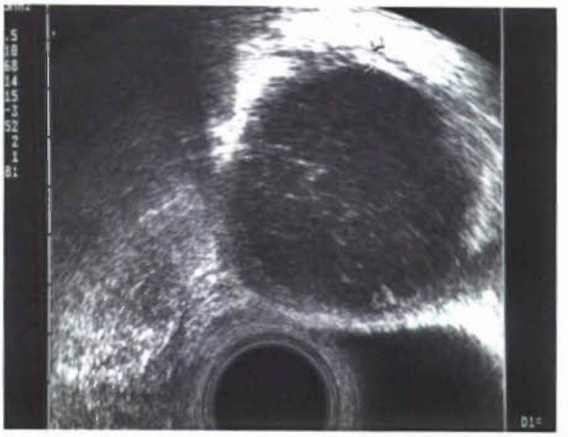

20

Fig. 28.21 Bilateral endometriotic cysts with thick walls; the wall thickness is 3 mm on the left side (> <) and 5 mm on the right side (>> <<). The cysts contain irregularly distributed internal echoes of mixed low and moderate intensity. Coronal scan.

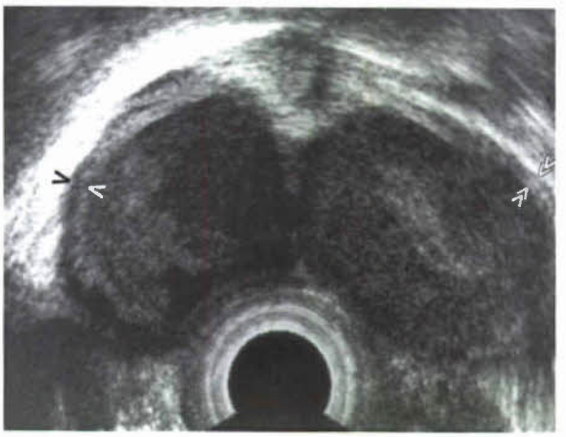

21

Dermoid Cysts

Fig. 28.22 Small, hyperechoic dermoid in the right ovary (diameter 1.8 cm). Longitudinal scan.

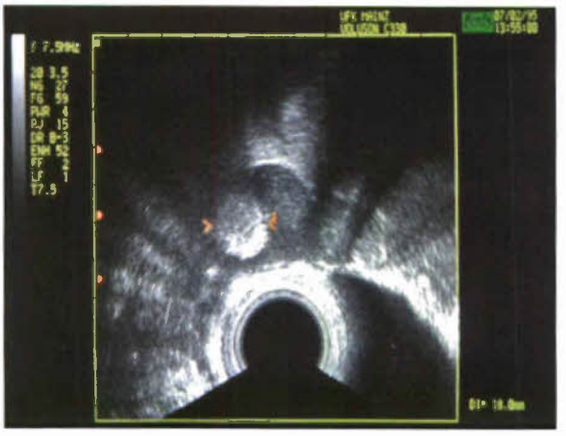

22

Fig. 28.23 Small dermoid on the right ovary. Echogenic sebaceous material is visible within the cystic mass, which measures 3.6 cm in diameter. Oblique longitudinal scan.

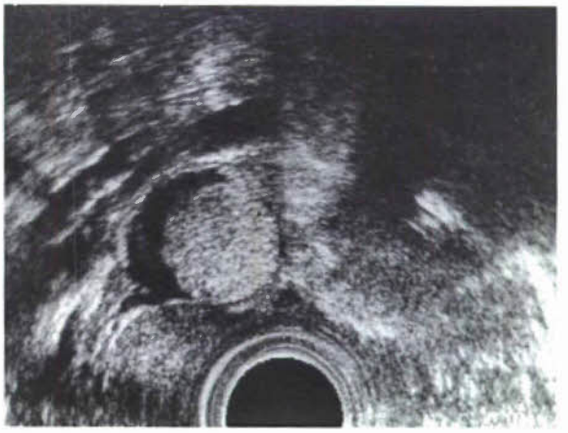

23

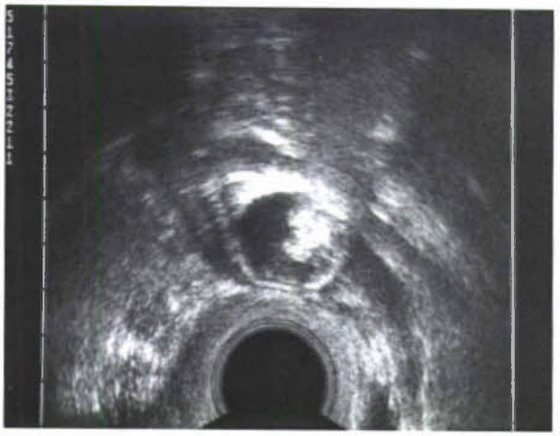

24

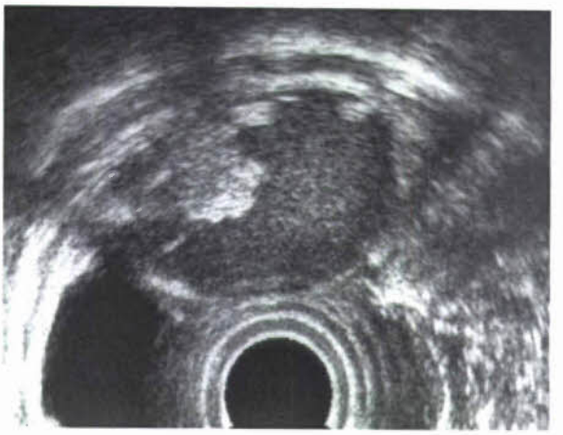

25

Fig. 28.**24** Small dermoid cyst on the left side (2.7 × 2.4 × 2.6 cm). An irregular, 1.2-cm hyperechoic structure is visible on the inner wall. Coronal scan.

Fig. 28.**25** Dermoid cyst on the right side contains an irregular, hyperechoic mass of sebaceous material and a predominantly hypoechoic fluid zone in which hairs are visible. Longitudinal scan.

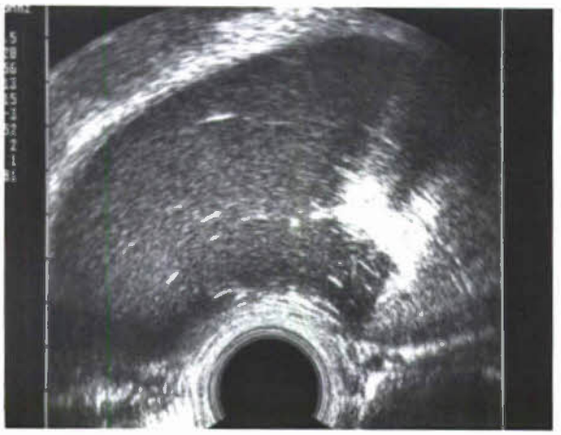

26

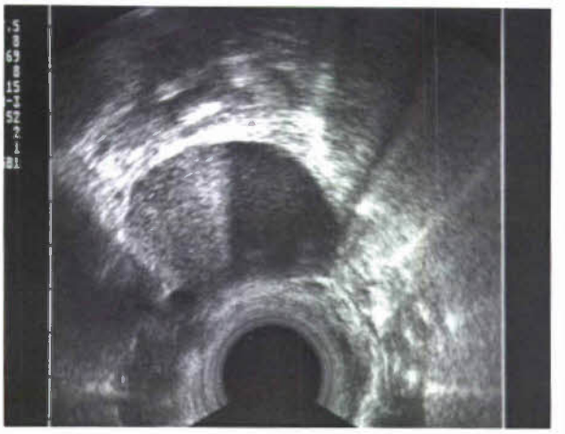

27

Fig. 28.**26** Large dermoid cyst on the left side (13 × 7.6 × 12 cm), with fine internal echoes and an irregular hyperechoic area. Longitudinal scan.

Fig. 28.**27** Dermoid cyst on the right side (4.8 × 3.6 × 4.0 cm), with a fluid level. There is no sign of the typical hyperechoic area.

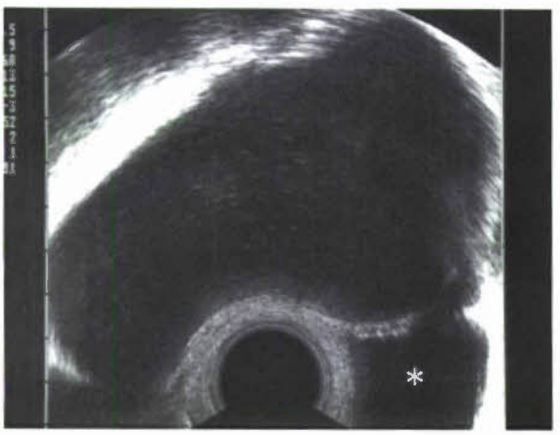

28

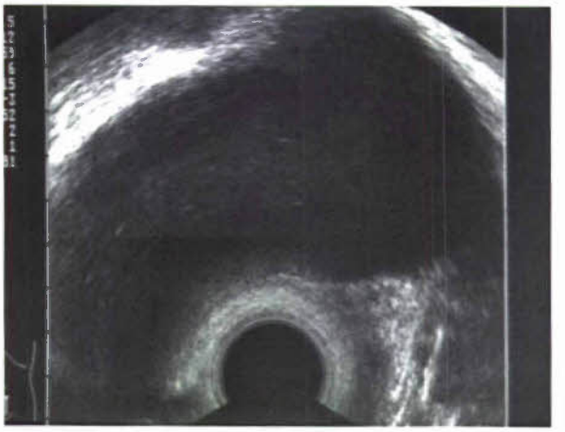

29

Serous Cystadenomas

Fig. 28.**28** Simple cystoma with scattered fine internal echoes. Longitudinal scan. * = Bladder.

Fig. 28.**29** Overdistended bladder mimics an ovarian mass. Median longitudinal scan.

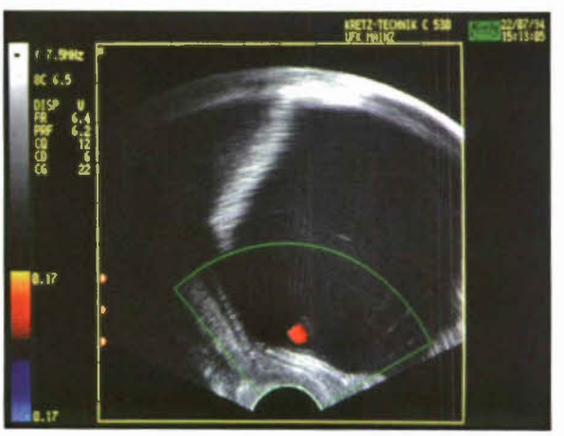

30

Fig. 28.**30** Color Doppler scan of a full bladder demonstrates a urine jet entering the bladder.

Mucinous Cystadenomas

Fig. 28.**31** Unilocular mucinous cystoma of the left ovary (6.8 × 4.5 × 5.2 cm), with dense, flocculent internal echoes. Coronal scan.

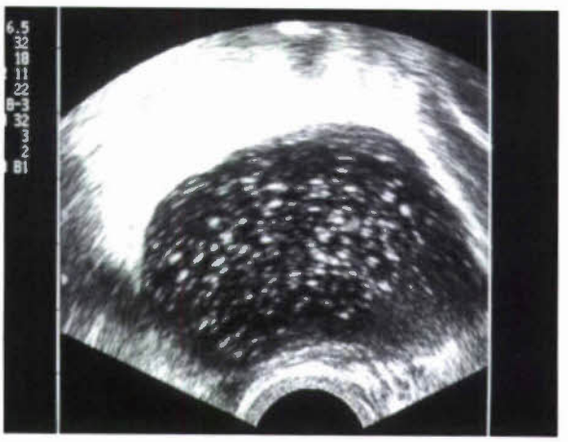

31

Fig. 28.**32** Mucinous cystoma (9.3 × 7.2 × 7.4 cm). Fine internal echoes are seen within compartments of varying size. Longitudinal scan.

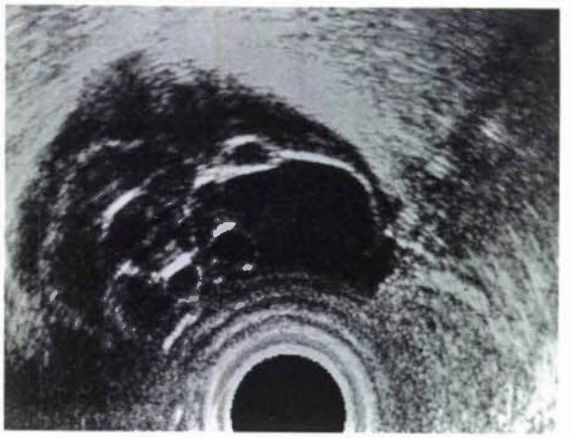

32

Ovarian Fibroma

Fig. 28.**33** Right ovarian fibroma (*) (6.5 × 4.4 × 5.4 cm) with smooth margins and a dense pattern of medium-level internal echoes. Coronal scan.

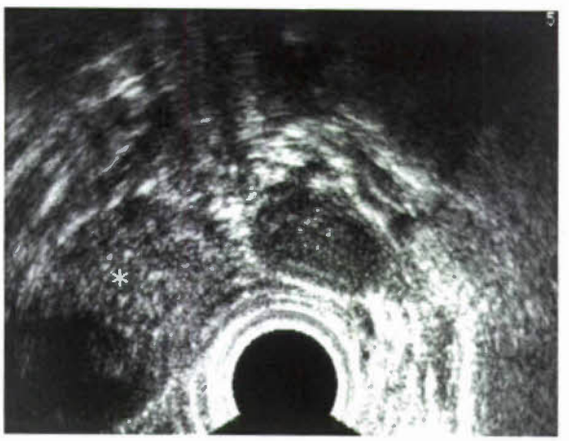

33

Potentially Malignant Ovarian Tumors

Fig. 28.**34** Serous papillary cystadenoma of the left ovary (10.8 × 8.0 × 8.1 cm). Longitudinal scan. An echogenic mural papillary growth (→) is visible within the cystic mass. * = Bladder.

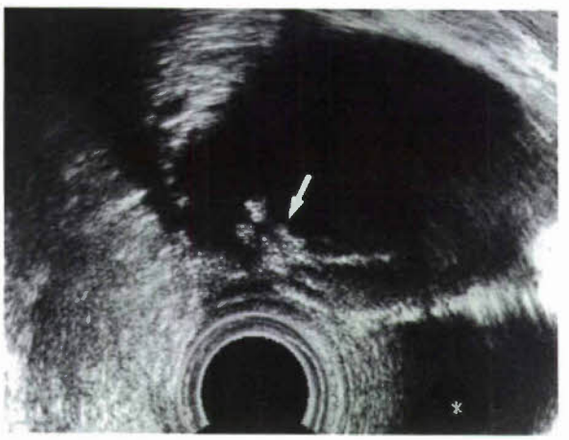

34

Fig. 28.**35** Loculated proliferative serous ovarian cystoma with multiple mural projections (→). Coronal scan.

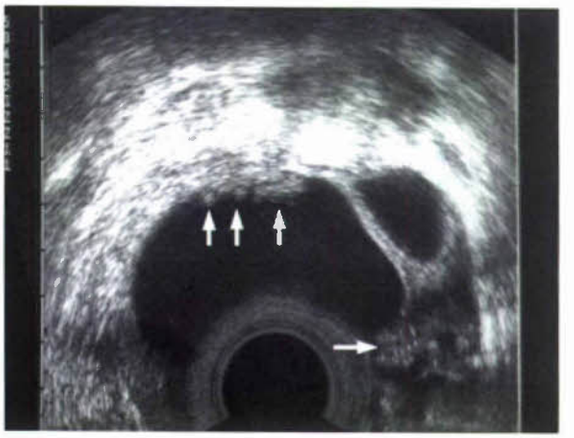

35

Fig. 28.**36** Proliferative serous ovarian cystoma with an irregular, echogenic, 2.2-cm nodule on its posterior wall. Longitudinal scan.

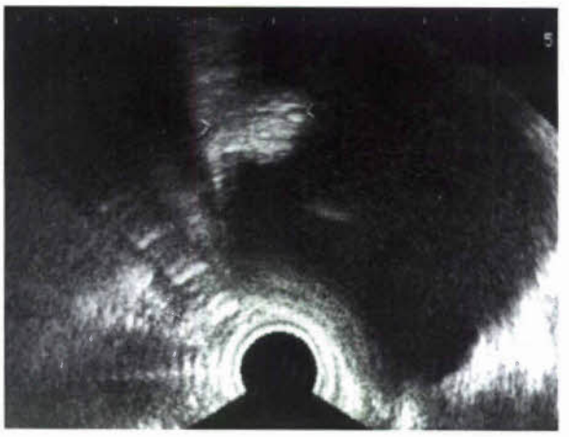

36

Fig. 28.**37** The surgical specimen corresponding to Fig. 28.**36**.

37

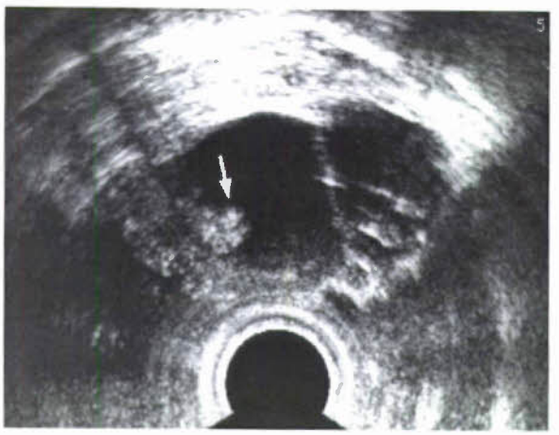

38

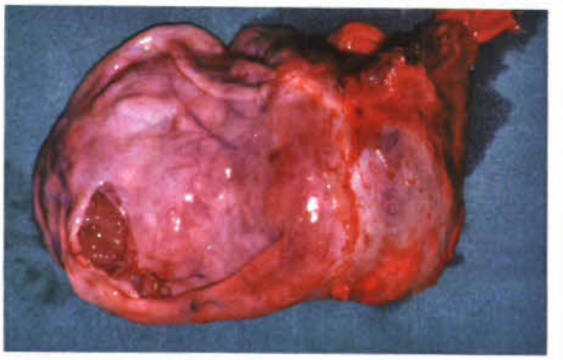

39

Fig. 28.**38** Loculated proliferative ovarian cystoma with a small, irregular, echogenic mural nodule in the largest compartment. Coronal scan.

Fig. 28.**39** The surgical specimen corresponding to Fig. 28.**38**.

40

41

Fig. 28.**40** Ovarian cystoma with papillary growths projecting from a septum. Coronal scan.

Fig. 28.**41** Multilocular papillary ovarian cystoma with a small proliferative focus (—). Color Doppler yields only a faint color signal.

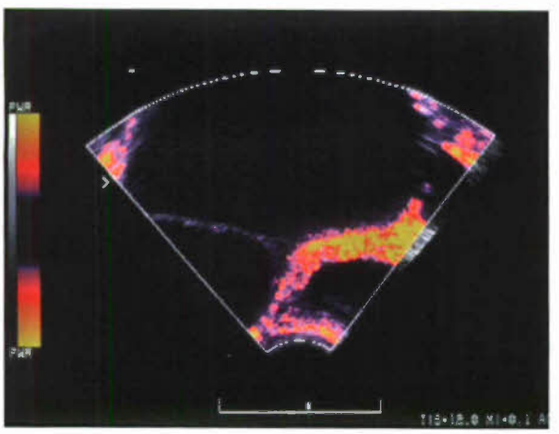

42

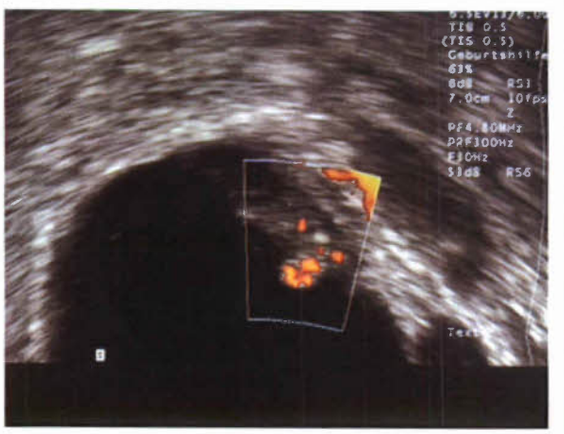

43

Fig. 28.**42** Power Doppler scan of the tumor in Fig. 28.**41**. This mode provides a much clearer depiction of blood flow in the proliferative focus and also within the septa.

Fig. 28.**43** Serous papillary cystoma of the left ovary. Power Doppler demonstrates conspicuous color signals within the mural proliferative focus. Coronal scan.

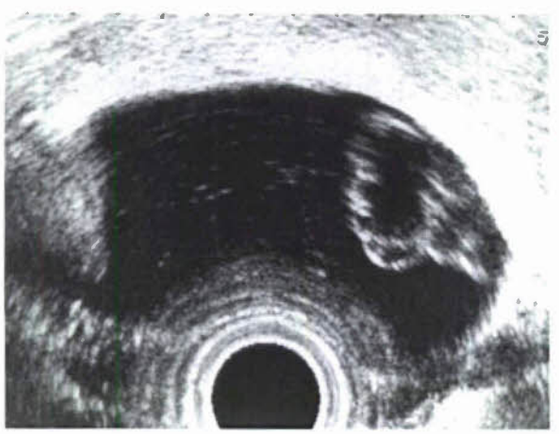

44

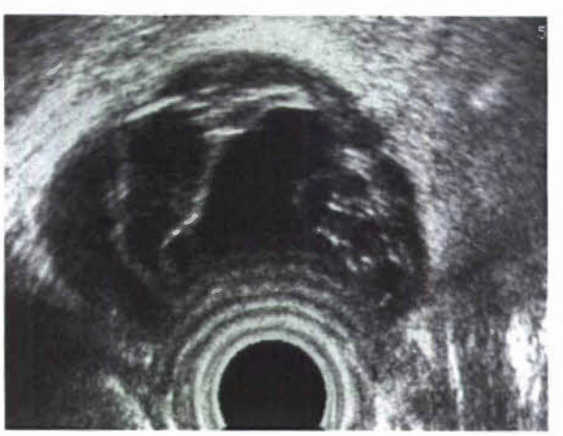

45

Fig. 28.**44** Multilocular mucinous cystoma (10.3 × 7.3 × 9.4 cm), with scattered coarse internal echoes. Coronal scan.

Fig. 28.**45** Multilocular mucinous cystoma (9.3 × 8.2 × 7.4 cm), with contrasting internal echo patterns in the different compartments. Longitudinal scan.

Table 28.10 TNM clinical classification of malignant ovarian tumors (After Sobin LH and Wittekind Ch. [49])

T– Primary Tumor

TNM categories	FIGO stages	Characteristics
TX		Primary tumor cannot be assessed
T0		No evidence of primary tumor
T1	I	Tumor limited to the ovaries
T1a	IA	Tumor limited to one ovary, capsule intact, no tumor on ovarian surface; no malignant cells in ascites or peritoneal washings
T1b	IB	Tumor limited to both ovaries, capsule intact, no tumor on ovarian surface; no malignant cells in ascites or peritoneal washings
T1c	IC	Tumor limited to one or both ovaries with any of the following: capsule ruptured, tumor on ovarian surface, malignant cells in ascites or peritoneal washings
T2	II	Tumor involves one or both ovaries with pelvic extension
T2a	IIA	Extension and/or implants on uterus and/or tube(s); no malignant cells in ascites or peritoneal washings
T2b	IIB	Extension to other pelvic tissues; no malignant cells in ascites or peritoneal washings
T2c	IIC	Pelvic extension (2a or 2b) with malignant cells in ascites or peritoneal washings
T3 and/or N1	III	Tumor involves one or both ovaries with microscopically confirmed peritoneal metastasis outside the pelvis and/or regional lymph node metastasis
T3a	IIIA	Microscopic peritoneal metastasis beyond pelvis
T3b	IIIB	Macroscopic peritoneal metastasis beyond pelvis 2 cm or less in greatest dimension
T3c and/or N1	IIIC	Peritoneal metastasis beyond pelvis more than 2 cm in greatest dimension and/or regional lymph node metastasis
M1	IV	Distant metastasis (excludes peritoneal metastasis

Note: Liver capsule metastasis is T3/stage III, liver parenchymal metastasis M1/stage IV. Pleural effusion must have positive cytology for M1/stage IV.

N– Regional lymph nodes
- NX Regional lymph nodes cannot be assessed.
- N0 No regional lymph node metastasis
- N1 Regional lymph node metastasis

M– Distant metastasis
- MX Distant metastasis cannot be assessed
- M0 No distant metastasis
- M1 Distant metastasis

Table 28.11 Differential diagnosis of mixed cystic and solid lower abdominal tumors

- Ovarian carcinoma
- Ovarian sarcoma
- Dermoid
- Hemorrhagic corpus luteum cyst
- Endometriosis
- Distended bowel loop
- Ovarian metastases
- Tubal carcinoma
- Bowel carcinoma
- Bladder carcinoma
- Retroperitoneal tumor

Table 28.12 Comparison of several scoring systems

First author (ref.)	Year	n	Sensitivity	Specificity	Positive predictive value	Negative predictive value
Finkler [62]	1988	102	62%	95%	88%	81%
Sassone [59]	1991	143	100%	83%	37%	100%
Timor-Tritsch [61]	1992	115	94%	87%	60%	99%
Lerner [58]	1994	350	97%	77%	29%	99%
Merz [13]	1997	509	99%	88%	73%	98%

Table 28.13 The scoring system used by Merz et al. [13] for the ultrasound evaluation of ovarian tumors (a total score ≥ 9 is suspicious for malignancy)

Score	0	1	2	Σ
Overall tumor structure	–	Simple	Complex	
Overall tumor margins	Smooth	Slightly irregular	Markedly irregular	
Wall thickness	≤ 3 mm	> 3 mm ≤ 5 mm	> 5 mm or cannot be assessed	
Internal echoes in cystic part of mass	None	Homogeneous	Nonhomogeneous	
Septa	None	≤ 3 mm	> 3 mm	
Shape of echo complex or of solid tumor	No solid component	Regular	Irregular	
Echogenicity of echo complex or of solid tumor	No solid component	Homogeneous	Nonhomogeneous	
Posterior acoustic effects	Acoustic enhancement	Partial shadowing	Complete shadowing	
Ascites	None	Scant	Copious	
Hepatic metastases, peritoneal involvement	Not detectable	Cannot be clearly assessed	Detectable	
			Total score	

sound and can be used to classify a tumor as potentially malignant [30a]. The most important of these criteria are the presence of solid mural nodules, thick septa with deposits, and a generally nonhomogeneous echo pattern (showing mixed sonodensity and echogenicity).

Especially with cystic tumors, most notably *proliferative serous cystadenomas*, transvaginal ultrasound can detect small papillary structures arising from the cyst wall or from an intracystic septum (Figs. 28.**34**–28.**43**). Color Doppler scans can be added in an attempt to detect any vascularity associated with intracystic proliferations. Often, the slow blood flow velocities in these vessels approach the lower limits of the Doppler technique (Fig. 28.**41**). These cases may be an indication for *power Doppler imaging*, which can detect even low flow velocities independent of the beam–vessel angle (Figs. 28.**42**, 28.**43**).

With *proliferative mucinous ovarian cystomas*, ultrasound may demonstrate ill-defined mural projections and may show different internal echo patterns in the different compartments of the tumor (Figs. 28.**44**, 28.**45**).

Predominantly solid *ovarian tumors with a potential for malignant transformation* are much more difficult to evaluate sonographically than proliferative cystic ovarian lesions. All of these tumors have well-defined margins with an irregular internal echo pattern (Figs. 28.**46**–28.**48**). Generally, they cannot be further differentiated on the basis of their ultrasound features. *Brenner tumors* represent approximately 2% of ovarian tumors, and 99% of these tumors are benign [9]. They are predominantly unilateral and have an average diameter of 5 cm. Ultrasound demonstrates a unilateral ovarian tumor with smooth margins.

A number of solid ovarian tumors are *hormonally active* and are manifested by bleeding abnormalities or virilization. Classified as sex cord stromal tumors, they are semimalignant neoplasms that are intermediate between benign and malignant ovarian tumors [9].

The most common hormonally active ovarian tumor is the *granulosa-cell tumor*, which is characterized by paraneoplastic estrogen synthesis. It is typically unilateral and may occur at any age. It appears sonographically as a well-circumscribed solid tumor with a nonhomogeneous echo pattern (Chapter 9).

Another sex cord stromal tumor, *thecoma*, is the second most common hormonally active ovarian tumor (producing estrogen and, in about 2% of cases, androgen). Malignant transformation is extremely rare. Its ultrasound appearance is that of a well-circumscribed solid tumor permeated by echogenic strands of connective tissue (Figs. 28.**46**, 28.**47**).

Sertoli–Leydig cell tumor (arrhenoblastoma) is an androgen-producing ovarian tumor that is most prevalent between 20 and 25 years of age. It may occur at any age, however [31]. Heavy androgen production by the tumor incites a rapidly progressive virilization, with hirsutism, acne, clitoral hypertrophy, deepening of the voice, and an increase in muscle mass. Serum testosterone levels are markedly elevated.

Ultrasound again shows a predominantly solid tumor with an irregular echo pattern. Cystic areas may be observed in some lesions (Fig. 28.**48**).

In women with a history of hysterectomy, loops of small bowel behind the floor of the vagina may be matted together to create the impression of a solid ovarian or pelvic tumor with an irregular internal echo pattern (Fig. 28.**49**).

Malignant Ovarian Tumors

Ovarian malignancies are the fourth most common gynecologic tumor in Germany, accounting for 9.5% of cases [32]. The worldwide incidence is approximately 10 new cases per 100000 women per year, compared with about 13 cases per 100000 women in Germany [32]. Whereas cervical and endometrial carcinoma appear to be on the decline, the incidence of ovarian carcinoma has remained constant for years [32–35]. When the incidence rates are broken down by age groups [32], it is found that the incidence is less than five per 100000 women under 40 years of age but rises sharply thereafter, increasing to more than 50 per 100000 women over the age of 70. If there is a positive family history of ovarian cancer, the risk of acquiring the disease increases from 1.6% to 5–7% [36].

Ovarian carcinoma is still considered one of the most dangerous cancers in women. Among the four most common gynecologic malignancies, it has the lowest 5-year survival rate, at 33% [32]. This is because, in approximately 70% of cases, the tumor has already reached an advanced stage (FIGO III or IV) by the time it is diagnosed [33]. The 5-year survival rates with ovarian carcinoma vary dramatically relative to the stage of the disease [37] (Fig. 28.**50**).

Ovarian carcinoma is bilateral in 70% of cases, whereas benign ovarian tumors are bilateral in only 5% of cases [38]. The most prevalent histologic types are serous (44%), mucinous (11.4%), and endometrioid carcinoma (12.2%), while other types are far less common [39].

Malignant ovarian tumors present a variety of ultrasound appearances [7,14,40–47]. All gradations may be seen, ranging from an almost entirely cystic mass to an almost completely solid tumor. In a series of preoperative abdominal ultrasound examinations of intraoperatively confirmed ovarian carcinomas, Requard et al. [48] found that 19% of the lesions were solid on ultrasound, 68% were mixed solid and cystic, and 13% were purely cystic.

Malignancy should be suspected in an ovarian mass that presents a markedly irregular sonographic structure with varying echogenicity (Figs. 28.**51**–28.**56**, Table 28.**4**). The highest incidence of malignancy is found in the group of mixed solid and cystic ovarian tumors: 17% [15] or 15.5% [13] in premenopausal women and up to 66% in postmenopausal women [13,15]. Particular attention should be given to mural papillary growths and irregular solid areas. If irregular tumor margins are noted, it should be assumed that the tumor has already crossed the organ boundaries (Table 28.**10**) [49]. The ultrasound impression of a malignant ovarian tumor is supported by the presence of associated malignancy criteria such as ascites or hepatic metastases. Although nearly half of ovarian carcinomas are not accompanied by ascites [3], and ascites occurs in association with benign ovarian tumors as well as hepatic diseases, Obwegeser et al. [14] found a high malignancy rate of 76% for ovarian tumors and accompanying ascites in their (abdominal) ultrasound study.

The differential diagnosis of a mixed cystic and solid mass with an irregular echo pattern should always include benign ovarian tumors (especially dermoids), semimalignant ovarian tumors, primary tumors of nearby structures (tubal carcinoma, sigmoid carcinoma, bladder carcinoma), and even an irregularly distended loop of bowel (Table 28.**11**). Differentiation is also required from *sarcoma* (Fig. 21.**57**) and an *ovarian metastasis* from a primary carcinoma of the breast or bowel (Figs. 28.**58**–28.**60**).

The goal of ultrasonography is not to detect carcinomas that have reached the symptomatic stages III or IV, but rather to achieve early detection of ovarian carcinomas that are still at stage I. This has prompted various groups of authors to develop ultrasound screening programs [4,41,50–53]. It is true in abdominal ultrasound [54], as well as in vaginal ultrasound, that ovarian changes are most clearly appreciated by making a side-to-side comparison of the volume and echo pattern of the two ovaries. Often both ovaries can be compared in the same image when a panoramic transducer is used. If this is not possible because the ovaries are positioned asymmetrically, another option is to store the two ovaries as separate images and display them side by side for comparison (Fig. 28.**61**). An ovary should be considered suspicious if it appears twice as large as the contralateral ovary, especially after the menopause [55]. One difficulty in the sonographic diagnosis of ovarian carcinoma is that the affected ovary is not always enlarged [56] (Fig. 28.**62**). Moreover, intraperitoneal spread may already have occurred at an early stage. The changes that are detectable with ultrasound in early cystic ovarian carcinoma consist of small, irregular mural projections (Fig. 28.**63**).

One disadvantage of transvaginal ultrasound is that while it is able to detect subtle structural changes, it is difficult to classify the lesion as malignant with a high degree of confidence.

Various investigators have devised an ultrasound scoring system for evaluating ovarian tumors (Table 28.**12**, 28.**13**) [13,57–62]. This allows even less experienced examiners to find evidence of ovarian carcinoma.

Several reports [4,42,57,63] have shown that color Doppler ultrasound can detect tumor angiogenesis in early ovarian cancers (Chapter 39). Tumor vessels, unlike normal vessels, have a tunica media that is devoid of muscle fibers [5]. This leads to an increase in diastolic flow, causing a low pulsatility index in the Doppler spectrum. Fleischer et al. [42] found PI values of 0.7±0.2 (SD) in malignant ovarian tumors, in contrast with 1.9±0.7 (SD) in benign tumors. Decreased values were also found in three relatively benign tumors, however, and therefore Doppler analysis was unable to discriminate between benign and malignant tumors in all cases.

On the basis of their experience with 624 benign and 56 malignant ovarian tumors, Kurjak and Zalud [7] recommend a resistance index of 0.4 as the cut-off level for differentiating between benign and malignant tumors. According to their findings, tumors with an RI of less than 0.4 are considered suspicious for malignancy. Further research is needed to determine the value of this criterion in accurately discriminating between benign and malignant ovarian tumors.

In contrast to color Doppler ultrasound, which can detect only larger tumor vessels and blood flows, *power Doppler imaging* (power color Doppler, color perfusion imaging) is able to detect even very small vessels and flows within a tumor (Fig. 28.**64**). The use of a power Doppler vascularity index has shown a high diagnostic value in discriminating between benign and malignant tumors [63a].

Fig. 28.**46** Thecoma of the left ovary (5.9 × 4.3 × 6.8 cm). The tumor is moderately echogenic and contains streak-like zones of high echogenicity. Longitudinal scan.

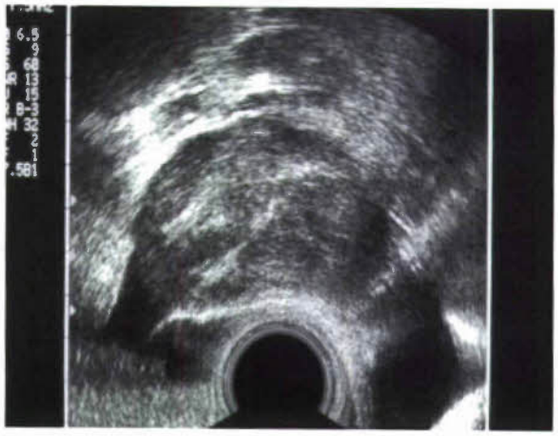

46

Fig. 28.**47** The surgical specimen corresponding to Fig. 28.**46**.

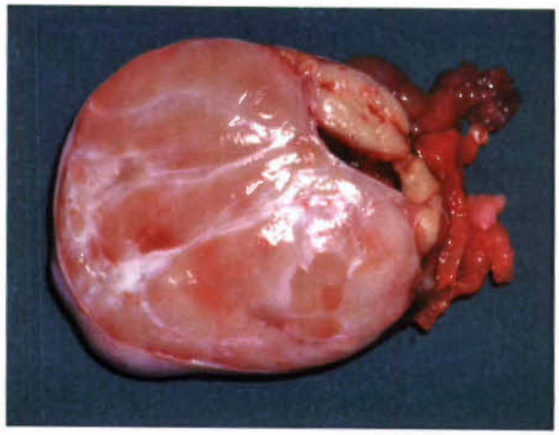

47

Fig. 28.**48** A Sertoli–Leydig cell tumor of the left ovary appears as a well-circumscribed solid mass, with a nonhomogeneous internal echo pattern (5.7 × 3.5 × 4.6 cm). Oblique coronal scan.

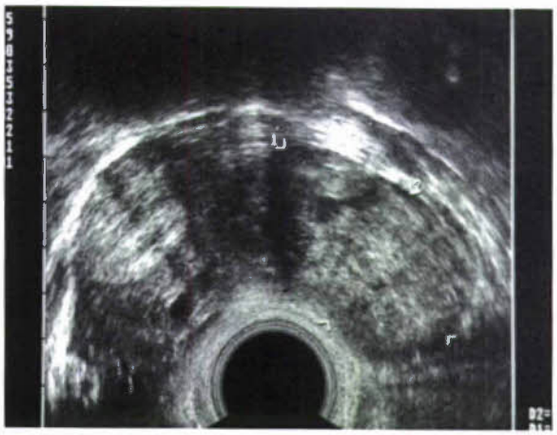

48

Fig. 28.**49** A conglomerate mass composed of matted small-bowel loops behind the floor of the vagina mimics a pelvic tumor. The patient had previously undergone an abdominal hysterectomy and bilateral adnexectomy.

49

Malignant Ovarian Tumors

Fig. 28.**50** Survival rates for ovarian carcinoma as a function of tumor stage (after Malkasian et al. [37]).

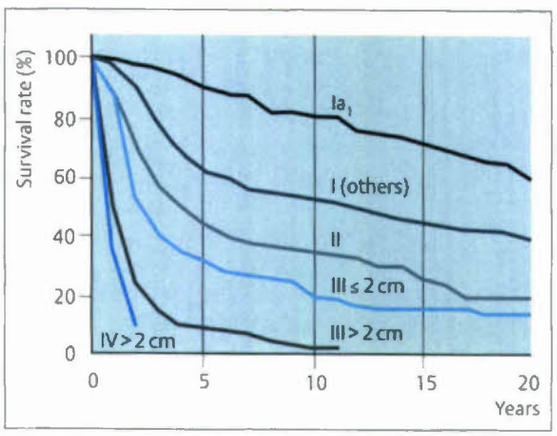

50

Fig. 28.**51** Mixed cystic and solid ovarian carcinoma, with irregular, echogenic tumor tissue on the inner wall. Longitudinal scan.

51

Fig. 28.**52** Predominantly cystic carcinoma of the right ovary (9.1 × 4.1 × 7.1 cm). Longitudinal scan. Septal thickness is 6 mm.

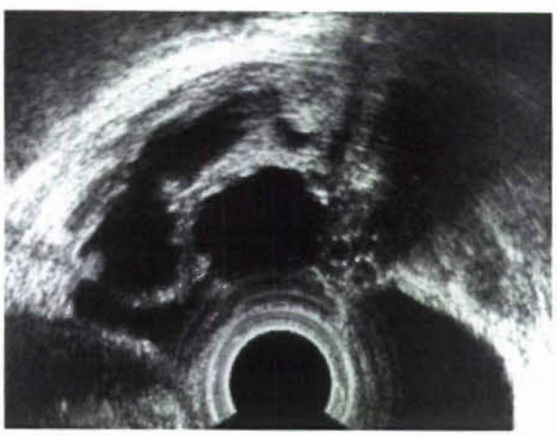

52

Fig. 28.**53** Mixed cystic and solid carcinoma of the left ovary (9.3 × 7.1 × 8.7 cm), with irregular papillary structures and a thick septum. Coronal scan.

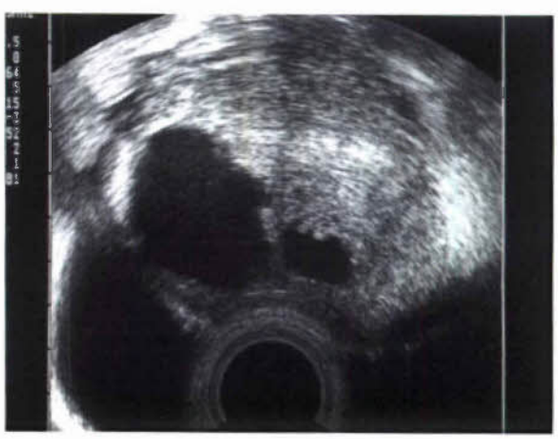

53

54

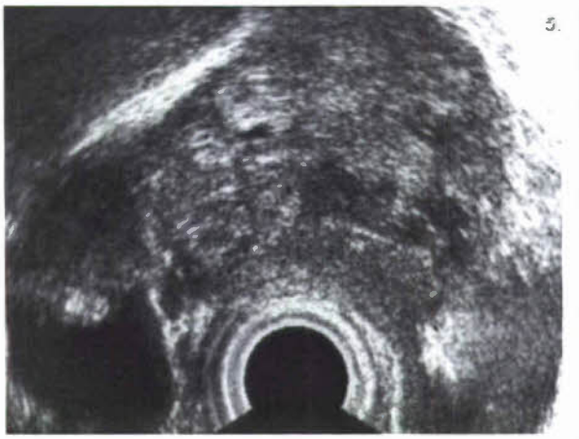

55

Fig. 28.**54** Predominantly cystic, papillary carcinoma of the left ovary. Longitudinal scan shows multiple small papillary projections on the septum and cyst wall.

Fig. 28.**55** Endometrioid carcinoma of the right ovary, stage pT1c, with a predominantly solid, irregular structure (6.5 × 6.6 × 8.9 cm). Longitudinal scan.

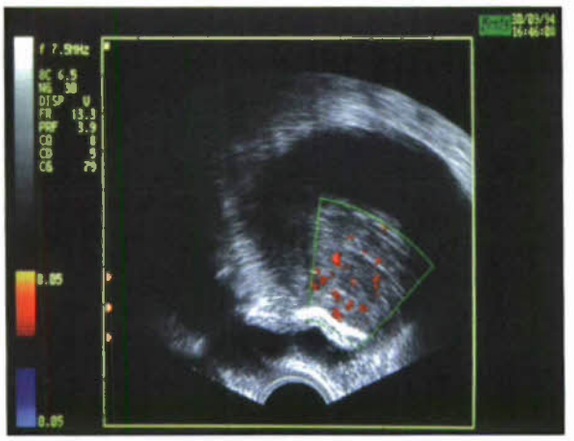

56

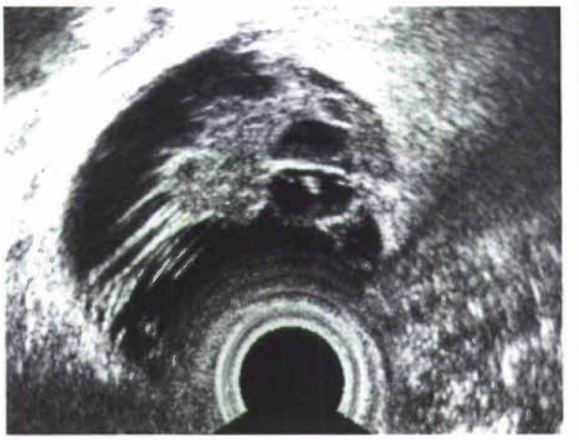

57

Fig. 28.**56** Predominantly cystic ovarian carcinoma, with a solid, irregular tumor area. Color Doppler sampling of that area yields multiple color flow signals, consistent with marked tumor angiogenesis. Coronal scan.

Fig. 28.**57** Sarcoma of the right ovary (8.6 × 6.3 × 8.8 cm). The longitudinal scan shows conspicuous, hyperechoic striate markings in an otherwise hypoechoic tumor.

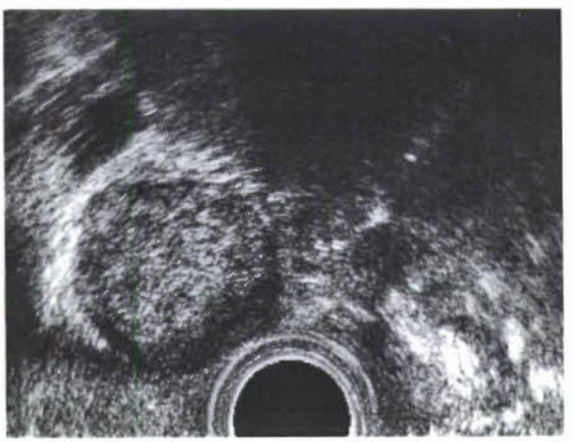

58

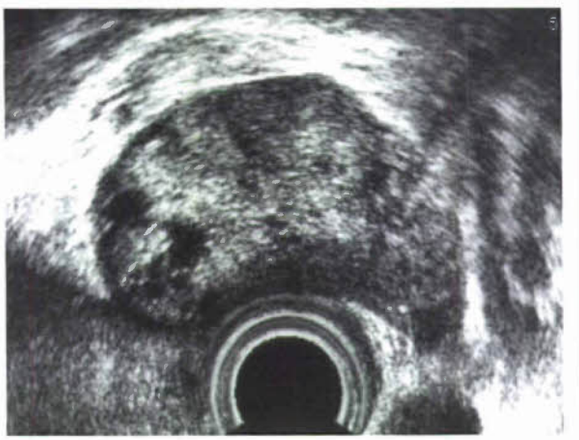

59

Fig. 28.**58** Solid right-sided ovarian tumor, with a nonhomogeneous internal echo pattern (3.4 × 3.5 × 5.2 cm). Coronal scan. The histological findings indicated metastatic breast carcinoma.

Fig. 28.**59** Predominantly solid tumor of the left ovary, with a smooth outer wall but a nonhomogeneous internal echo pattern. Coronal scan. The histological findings indicated metastatic breast carcinoma.

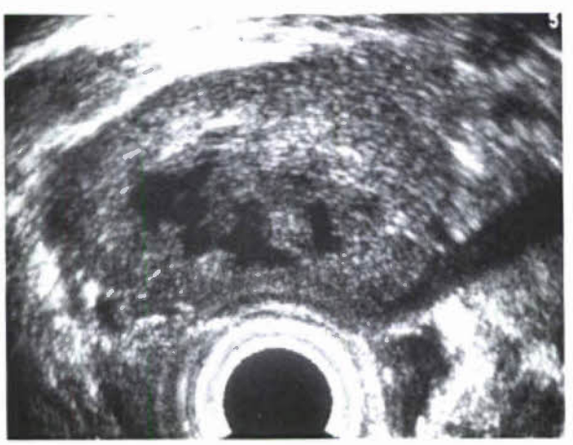

60

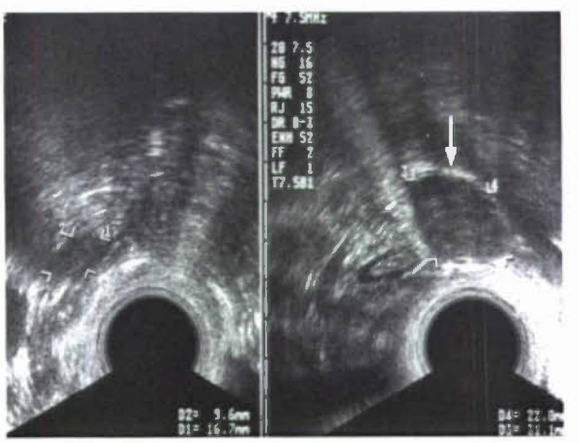

61

Fig. 28.**60** Circumscribed, predominantly solid tumor of the right ovary, with central, irregular, hypoechoic degenerative foci. Longitudinal scan. The histological findings indicated metastatic intestinal carcinoma.

Fig. 28.**61** Markedly enlarged left ovary (—) in a postmenopausal patient. The side-by-side display of both ovaries clearly demonstrates the marked size discrepancy. Longitudinal scans. The right ovary measures 1.7 × 1.0 × 1.9 cm, the left ovary 3.1 × 2.2 × 3.4 cm.

Fig. 28.62 Small carcinoma of the right ovary (4.6 × 2.5 × 4.0 cm) (> <). Longitudinal scan. The ovary is conspicuous by its markedly irregular internal echo pattern and echogenicity.

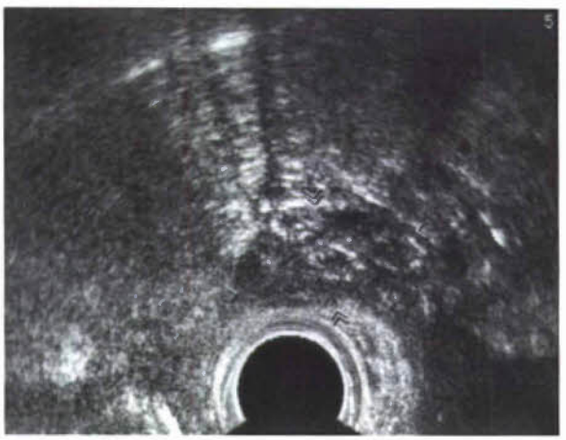

62

Fig. 28.63 Early cystic ovarian carcinoma (stage pT1a) with a 5-mm mural nodule (I).

63

Fig. 28.64 Simple ovarian cystoma. Power Doppler scanning clearly demonstrates the vascularity in the cyst wall.

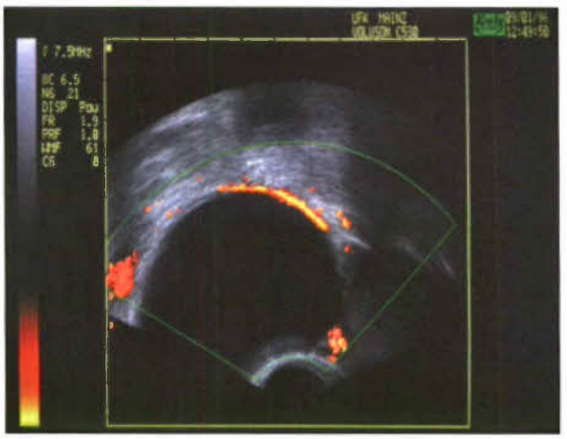

64

Fig. 28.65 Ultrasound screening strategy for the detection of malignant ovarian tumors.

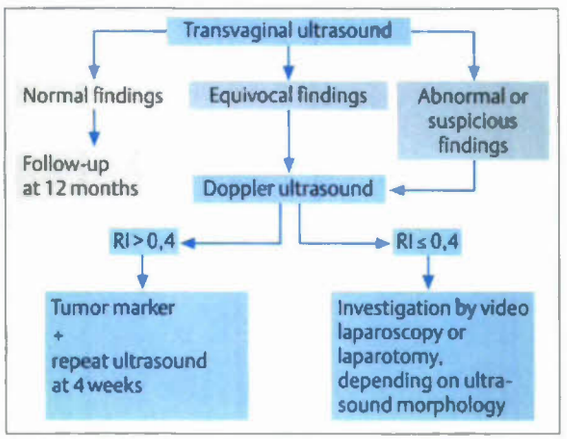

65

Ultrasound Screening for Ovarian Carcinoma

Recognizing that ultrasound is clearly superior to palpation for detecting, excluding, and differentiating between ovarian masses, various investigators [50,51,64] had already used abdominal scanning in an effort to determine the feasibility of ultrasound screening for ovarian cancer. Campbell and his group [51,64] conducted the first large abdominal ultrasound screening study in a series of 5479 self-selected asymptomatic women over 44 years of age. They detected five primary ovarian carcinomas (four at stage Ia and one at stage Ib) and four ovarian metastases. In another abdominal study [50], however, six of 100 ovarian carcinomas were not detected by preoperative ultrasound.

After comparative studies [65,66] had shown that transvaginal ultrasound had definite advantages over abdominal ultrasound in gynecologic diagnosis, considerable hopes were placed on transvaginal ovarian cancer screening. Van Nagell et al. [53] reported in 1990 on 1000 asymptomatic women over the age of 40 who had been examined by transvaginal ultrasound. Only one malignancy (an ovarian metastasis) was detected in this series. Duda et al. [41] screened 221 women over the age of 45 with no palpable abnormalities and similarly detected only one ovarian metastasis.

In other screening studies using transvaginal ultrasound, three stage I ovarian carcinomas were detected in 3220 postmenopausal women [52], and three stage I tumors were found in 776 women who had a positive family history of ovarian cancer [4].

In ultrasound screening programs conducted to date, it has been demonstrated that stage I ovarian carcinoma can be detected by a competent examiner (Table 28.**14**) [4,41,51,52]. However, if the extremely high costs of such screening programs are taken into account, it appears that ultrasound screening is not cost-effective, given the relatively low incidence of ovarian cancer in women who are not in a high-risk category [67]. In addition, in view of the potential costs entailed by unnecessary surgery for sonographically suspicious functional cysts in young women, it is extremely difficult to justify a universal screening program. On the other hand, a screening program for postmenopausal women is a more promising concept, since these women have a significantly higher incidence of ovarian cancer and are unlikely to present with other functional changes. Ultrasound screening may also be worthwhile in high-risk patients selected on the basis of their medical history [67b] have demonstrated. Further multicenter studies are needed to determine whether adjunctive techniques such as color Doppler [68], power Doppler [68a], three-dimensional ultrasound [69,69a], or the use of tumor markers such as CA-125 [70] can ultimately increase the detection rate of early ovarian cancer.

The algorithm presented in Fig. 28.**65** can be used as a screening strategy in a high-risk population.

Table 28.**14** Number of stage I ovarian carcinomas detected by abdominal or transvaginal ultrasound

First author	Year	Abdominal/ transvaginal	Women examined (n)	Ovarian carcinomas detected at stage I	
				n	%
Bhan [51]	1989	Abdominal	5479	4	0.07%
Duda [41]	1990	Transvaginal	221	0	0.00%
Bourne [4]	1991	Transvaginal	776	3	0.39%
DePriest [52]	1993	Transvaginal	3220	3	0.09%
Total			9696	10	0.10%

References

1 Granberg S, Norstrom A, Wikland M. Tumors in the lower pelvis as imaged by vaginal sonography. Gynecol Oncol 1990;37:224–9.
2 Lande IM, Hill MC, Cosco FE, Kator NN. Adnexal and cul-de-sac abnormalities: transvaginal sonography. Radiology 1988;166:325–32.
3 Granberg S, Wikland M. A comparison between ultrasound and gynecologic examination for detection of enlarged ovaries in a group of women at risk for ovarian carcinoma. J Ultrasound Med 1988;7:59–64.
4 Sawicki W, Spiewankiewicz B, Cendrowski K, Stelmachow J. Preoperative discrimination between malignant and benign adnexal masses with transvaginal ultrasonography and colour blood flow imaging. Eur J Gynaecol Oncol. 2001;22:137–42.
5 Folkman J, Watson K, Ingber D, Hanahan D. Induction of angiogenesis during the transition from hyperplasia to neoplasia. Nature 1989;339:58–61.
6 Alcazar JL, Galan MJ, Ceamanos C, Garcia-Manero M. Transvaginal gray scale and color Doppler sonography in primary ovarian cancer and metastatic tumors to the ovary. J Ultrasound Med. 2003;22:243–7.
7 Kurjak A, Zalud I. The characterization of uterine tumors by transvaginal color Doppler. Ultrasound Obstet Gynecol 1991;1:50–2.
8 Yoffe N, Bronshtein M, Brandes J. Hemorrhagic ovarian cyst detection by transvaginal sonography: the great imitator. Gynecol Endocrinol 1991;5:123–9.
9 Serov SS, Scully RE, Sobin LH. Histological classification of ovarian tumors. International Histological Classification of Tumors, vol. 9. Geneva: WHO, 1973.
10 Andolf E, Jörgensen C. Cystic lesions in elderly women, diagnosed by ultrasound. Br J Obstet Gynaecol 1989;96:1076–9.
11 Granberg S, Wikland M, Jansson I. Macroscopic characterization of ovarian tumors and relation to the histological diagnosis: criteria to be used for ultrasound evaluation. Gynecol Oncol 1989;35:139–44.
12 Luxman D, Bergman A, Shi J, David MP. The postmenopausal mass: correlation between ultrasonic and pathologic findings. Obstet Gynecol 1991;77:726–8.
13 Merz E, Weber G, Bahlmann F, Kiesslich R. A new sonomorphologic scoring system (Mainz Score) for the assessment of ovarian tumors using transvaginal ultrasonography, 1: a comparison between the scoring-system and the assessment by an experienced sonographer. Ultraschall Med 1998;19:99–107.
14 Obwegeser R, Stümpflen I, Deutinger J, Bernaschek G. Zur echographischen Dignitätsbeurteilung von Adnextumoren. Geburtshilfe Frauenheilkd 1993;53:108–14.
15 Osmers R. Transvaginale Adnexdiagnostik. Gynäkologe 1995;28:233–9.
16 Prömpeler HJ. Transvaginalsonographie und Farbdopplersonographie zur Differenzierung von Ovarial- und Adnextumoren [postdoctoral dissertation]. Freiburg, Germany: University of Freiburg, 1996.
17 Stegner HE. Geschwülste der Adnexe. In: Käser O, Friedberg V, Ober KG, Thomsen K, Zander J, editors. Gynäkologie und Geburtshilfe, vol. 3, part 1. Stuttgart: Thieme, 1985: 10.1–10.77.
18 Sampson JA. Perforating hemorrhagic (chocolate) cysts of the ovary, their importance and especially their relation to pelvic adenomas of the endometrial type. Arch Surg 1921;3:245–323.
19 Athey PA, Diment DD. The spectrum of sonographic findings in endometriomas. J Ultrasound Med 1989;8:487–91.
20 Kupfer M, Schwimer S, Lebovic J. Transvaginal sonographic appearance of endometriomata: spectrum of findings. J Ultrasound Med 1992;11:129–33.
21 Sandler MA, Karo JJ. The spectrum of ultrasonic findings in endometriosis. Radiology 1978;127:229–31.
22 Walsh JW, Taylor JW, Rosenfield AT. Gray scale ultrasonography in the diagnosis of endometriosis and adenomyosis. AJR Am J Roentgenol 1979;132:87–90.
23 Dawood MY, Khan-Dawood FS, Ramos J. Plasma and peritoneal levels of CA 125 in women with endometriosis. Am J Obstet Gynecol 1988;159:1526–31.
24 Reichel RP, Schweppe KW, Zoladex Endometriosis Study Group. Goserelin (Zoladex) depot in the treatment of endometriosis. Fertil Steril 1992;57:1197–1202.
25 Matz MH. Benign cystic teratomas of the ovary: a review. Obstet Gynecol Surv 1961;16:591–605.
26 Karo JJ, Sandler MA. Benign cystic teratoma of the ovary. In: Steel WB, Cochrane WJ, editors. Gynecologic ultrasound. Edinburgh: Churchill Livingstone, 1984: 47–59.
27 Laing FC, Van Dalsem VF, Marks WM, Barton JL, Martinez DA. Dermoid cysts of the ovary: their ultrasonic appearances. Obstet Gynecol 1981;57:99–104.
28 Sandler MA, Silver TM, Karo JJ. Gray scale ultrasonic features of ovarian teratomas. Radiology 1979;131:705–9.
29 Hutton L, Rankin R. The fat–fluid level: another feature of dermoid tumors of the ovary. J Clin Ultrasound 1979;7:215–6.
30 Lawson TL, Albarelli JN. Diagnosis of gynecologic pelvic masses by gray-scale ultrasonography: analysis of specificity and accuracy. AJR Am J Roentgenol 1977;128: 1003–6.
31 Novak ER, Long JH. Arrhenoblastoma of the ovary: a review of the ovarian tumor registry. Am J Obstet Gynecol 1965;92:1082–93.
32 Kolles H, Stegmaier C, Seebach HB, Ziegler H. Deskriptive Epidemiologie und Prognose maligner gynäkologischer Tumoren. Geburtshilfe Frauenheilkd 1989;49:573–8.
33 Buser K, Hänggi W, Greiner R, Schatzmann E. Das Ovarialkarzinom: neue therapeutische Aspekte. Schweiz Med Wochenschr 1990;120:1617–32.
34 Pfleiderer A. Tumoren des Eierstocks. In: Bender HG, editor. Gynäkologische Onkologie für die Praxis. Stuttgart: Thieme, 1984: 172–219.
35 Pfleiderer A. Malignome des Ovars. In: Schmidt-Matthiesen H, Bastert G, editors. Klinik der Frauenheilkunde und Geburtshilfe, vol. 12: Spezielle gynäkologische Onkologie. 2. Trophoblasttumoren, Tumoren der Adnexe und der Mamma, besondere Behandlungsaspekte. 2nd ed. Munich Urban & Fischer, 1989: 45–129.
36 Nguyen HN, Averette HE, Janicek M. Ovarian carcinoma: a review of the significance of familial risk factors and the role of prophylactic oophorectomy in cancer prevention. Cancer 1994;74:545–55.
37 Malkasian GD Jr, Melton LJ 3rd, O'Brien PC, Greene MH. Prognostic significance of histologic classification and grading of epithelial malignancies of the ovary. Am J Obstet Gynecol 1984;149:274–82.
38 Barber HRK. Ovarian cancer. Part I. Cancer 1979;29:341–51.
39 Kolstad P. Malignant tumours of the ovary: Norwegian experience and protocols for management. In: Copleson M, editor Gynecologic oncology. Edinburgh: Churchill Livingstone, 1981: 721–30.
40 Timmerman D, Valentin L, Bourne TH, Collins WP, Verrelst H, Vergote I: International Ovarian Tumor Analysis (IOTA) Group. Terms, definitions and measurements to describe the sonographic features of adnexal tumors: a consensus opinion from the International Ovarian Tumor Analysis (IOTA) Group. Ultrasound Obstet Gynecol. 2000;16:500–5.
41 Duda V, Rode G, Them C, Schulz KD. Vaginalsonographie: Pilotstudie für den Einsatz als Ovarial-Screening-Verfahren. Geburtshilfe Frauenheilkd 1990;50:388–93.
42 Fleischer AC, Rogers WH, Rao BK, Kepple DM, Jones HW. Transvaginal color Doppler sonography of ovarian masses with pathological correlation. Ultrasound Obstet Gynecol 1991;1:275–8.
43 Valentin L, Hagen B, Tingulstad S, Eik-Nes S. Comparison of ‚pattern recognition' and logistic regression models for discrimination between benign and malignant pelvic masses: a prospective cross validation. Ultrasound Obstet Gynecol. 2001;18:357–65.
44 Merz E. Ultrasound in gynecology and obstetrics: textbook and atlas. Stuttgart: Thieme, 1991.
45 Valentin L. Use of morphology to characterize and manage common adnexal masses. Best Pract Res Clin Obstet Gynaecol. 2004;18:71–89.
46 Valentin L, Ameye L, Testa A, Lecuru F, Bernard JP, Paladini D, Van Huffel S, Timmerman D. Ultrasound characteristics of different types of adnexal malignancies. Gynecol Oncol. 2006;102:41–8.
47 Wicks JD, Mettler FA Jr, Nilgers RD, Ampuero F. Correlation of ultrasound and pathologic findings in patients with epithelial carcinoma of the ovary. J Clin Ultrasound 1984;12:397–402.
48 Requard CK, Mettler FA, Wicks JD. Preoperative sonography of malignant ovarian neoplasm. AJR Am J Roentgenol 1982;137:79–82.
49 Sobin LH, Wittekind Ch. TNM Classification of Malignant Tumors. New York, Wiley-Liss, 2002.
50 Benacerraf BR, Finkler NJ, Wojciechowski C, Knapp RC. Sonographic accuracy in the diagnosis of ovarian masses. J Reprod Med 1990;35:491–5.
51 Bhan V, Amso N, Whitehead MI, Campbell S, Royston P, Collins WP. Characteristics of persistent ovarian masses in asymptomatic women. Br J Obstet Gynaecol 1989;96:1384–91.
52 DePriest PD, van Nagell JR Jr, Gallion HH, Shenson D, Kunter JE, Andrews SJ, et al. Ovarian cancer screening in asymptomatic postmenopausal women. Gynecol Oncol 1993;51:205–9.
53 Van Nagell JR Jr, Higgins RV, Donaldson ES, Gallion HH, Powell DE, Pavlik EJ, et al. Transvaginal sonography as a screening method for ovarian cancer. Cancer 1990;65:573–7.
54 Campbell S, Goessens L, Goswamy R, Whitehead MI. Real-time sonography for determination of ovarian morphology and volume: a possible early screening test for ovarian cancer. Lancet 1982;i:425–6.
55 Campbell S, Royston P, Bhan V, Whitehead MI, Collins WP. Novel screening strategies for early ovarian cancer by transabdominal ultrasonography. Br J Obstet Gynaecol 1990;97:304–11.
56 Feuer GA, Shevchuck M, Calanog A. Normal-sized ovary carcinoma syndrome. Obstet Gynecol 1989;73:786–92.
57 Fleischer AC, Jones HW 3rd. Early detection of ovarian carcinoma with transvaginal sonography: potentials and limitations. New York: Raven Press, 1993.
58 Lerner JP, Timor-Tritsch IE, Federman A, Abramovich G. Transvaginal ultrasonographic characterization of ovarian masses with an improved, weighted scoring system. Am J Obstet Gynecol 1994;170:81–5.
59 Sassone MA, Timor-Tritsch IE, Artner A, Westhoff C, Warren WB. Transvaginal sonographic characterization of ovarian disease: evaluation of a new scoring system to predict ovarian malignancy. Obstet Gynecol 1991;78:70–6.
60 Schillinger H, Kliem M, Klosa W, Pohl J, Wilhelm C, Madjar H, et al. Dignitätsbeurteilung gynäkologischer Tumore durch einen sonographischen Tumor-Score unter besonderer Berücksichtigung des Ovarialkarzinoms. Arch Gynecol Obstet 1989;245:596–600.
61 Timor-Tritsch IE, Lerner JP, Monteagudo A, Santos R. Transvaginal ultrasonographic characterization of ovarian masses by means of color flow-directed Doppler measurements and morphologic scoring system. Am J Obstet Gynecol 1993;168:909–13.
62 Finkler NJ, Benacerraf B, Lavin PT, Wojciechowski C, Knapp RC. Comparison of serum CA 125, clinical impression and ultrasound in the preoperative evaluation of ovarian masses. Obstet Gynecol 1988;72:659–64.
63 Kurjak A, Zalud I. Early detection of ovarian cancer by transvaginal color Doppler. J Ultrasound Med 1991;10:S57.
64 Campbell S, Bhan V, Royston P, Whitehead MI, Collins WP. Transabdominal ultrasound screening for early ovarian cancer. Br Med J 1989;2991363–7.
65 Mendelson EB, Bohm-Velez M, Joseph N, Neiman HL. Gynecologic imaging: comparison of transabdominal and transvaginal sonography. Radiology 1988;166:321–4.
66 Merz E. Transvaginale oder transabdominale Ultraschalldiagnostik? Ein Vergleich zweier Methoden in Gynäkologie und Geburtshilfe. Ultraschall Klin Prax 1987;2: 87–94.
67 Droegemueller W. Screening for ovarian carcinoma: hopeful and wishful thinking. Am J Obstet Gynecol 1994;170:1095–8.
68 Kurjak A, Predanic M. New scoring system for prediction of ovarian malignancy based on transvaginal color Doppler sonography. J Ultrasound Med 1992;11:631–8.
68a Alcazar JL, Merce LT, Garcia Manero M. Three-dimensional power Doppler vascular sampling: a new method for Predicting ovarian cancer in vascularized complex adnexal masses. J Ultrasound Med. 2005;24:689–96.
69 Merz E, Weber G, Bahlmann F, Macchiella D. Transvaginale 3D-Sonographie in der Gynäkologie. Gynäkologe 1995;28:270–5.
70 Jacobs I, Cram D, Fairbanks J, Turner J, Frost C, Grudzinskas JG. A risk of malignancy index corporating CA 125, ultrasound and menopausal status for the accurate preoperative diagnosis of ovarian cancer. Br J Obstet Gynaecol 1990;97:922–9.

29 Tubal Masses

Benign Tubal Masses

A fallopian tube affected by pathologic changes is much easier to define with ultrasound than a normal tube [1–4]. Even with transvaginal ultrasound, a normal fallopian tube can be clearly visualized only if there is an increased fluid collection in the cul-de-sac [5].

Postinflammatory *hydrosalpinx* is the most common benign tubal abnormality that is detected with ultrasound, appearing as a tortuous, tube-like structure with a thin wall and no internal echoes (Fig. 29.**1**). In typical cases the ampullary tubal segment is much more dilated than the isthmic segment. Occasionally, the ampulla may be distended into a globular shape that mimics an ovarian cyst (Table 29.**1**).

Hematosalpinx has a similar ultrasound appearance, but contains fine internal echoes. Potential causes are intraluminal tubal endometriosis, inflammatory hemorrhage, and tubal torsion. It should be added that *tubal* or *adnexal torsion* is usually associated with acute lower abdominal pain. The twisted tubal segments are edematous and undergo hemorrhagic infarction, appearing sonographically as adjacent cystic areas whose number depends on the degree of torsion (Figs. 29.**2**, 29.**3**).

True benign tumors, such as *leiomyomas*, *hemangiomas*, *fibromas*, and *lymphangiomas*, are extremely rare in the fallopian tubes. They may be suspected on ultrasound only if they present as a mass that is clearly separate from the ovary (Figs. 29.**4**, 29.**5**).

Tubal Carcinoma

Primary tubal carcinoma is a rare entity that most commonly affects only one fallopian tube. Like ovarian cancer, it is usually diagnosed much too late. The detection of tubal carcinoma by transvaginal ultrasound [2,3,6] is definitely among the challenges of ultrasound tumor diagnosis. We were able to detect a stage I tubal carcinoma by transvaginal scanning [3]. The patient presented clinically with an amber-colored vaginal discharge, and transvaginal scans revealed an irregular, unilateral distention of the fallopian tube (Fig. 29.**6**).

A lower abdominal mass can be confidently localized to the fallopian tube only if ultrasound scans clearly demonstrate that the mass is separate from the ovary. The differential diagnosis should also include various other benign and malignant lesions in addition to a coproma (Table 29.**2**).

In the late stage of tubal carcinoma, irregular dilation of the fallopian tube is accompanied by ascites in the true pelvis (Fig. 29.**7**).

Table 29.**3** Gives an overview of the TNM classification of malignant tumors of the fallopian tube.

References

1 Bulas DI, Ahlstrom PA, Sivit CJ, Blask ARN, O'Donell RM. Pelvic inflammatory disease in the adolescent: comparison of transabdominal and transvaginal sonographic evaluation. Radiology 1992;183:435–9.
2 Kol S, Gal D, Friedman M, Paldi E. Preoperative diagnosis of fallopian tube carcinoma by transvaginal sonography and CA-125. Gynecol Oncol 1990;37:129–31.
3 Merz E. Ultrasound in gynecology and obstetrics: textbook and atlas. Stuttgart: Thieme, 1991.
4 Timor-Tritsch IE, Rottem S. Ultrasonographic study of the fallopian tube. Obstet Gynecol 1987;70:424–8.
5 Steinkampf MP, Blackwell RE, Younger JB. Visualization of free peritoneal fluid with transvaginal sonography: a preliminary study. J Reprod Med 1991;36:729–30.
6 Haratz-Rubinstein N, Russell B, Gal D. Sonographic diagnosis of Fallopian tube carcinoma. Ultrasound Obstet Gynecol. 2004;24:86–8.
7 Sobin LH, Wittekind Ch. TNM Classification of Malignant Tumors. New York, Wiley-Liss, 2002

Table 29.**1** Differential diagnosis of cystic dilatation of the fallopian tube

- Hydrosalpinx
- Hematosalpinx
- Pyosalpinx
- Elliptical ovarian cyst
- Torsion (of fallopian tube or adnexa)
- Fluid-filled bowel segment

Table 29.**2** Differential diagnosis of solid expansion of the fallopian tube

- Tubal carcinoma
- Tubal endometriosis
- Benign tubal mass (myoma)
- Enlarged lymph node
- Ovarian carcinoma
- Intestinal carcinoma
- Coproma

Table 29.**3** TNM clinical classification of malignant tumors of the fallopian tube (After Sobin LH and Wittekind Ch [7]).

T– Primary Tumor

TNM categories	FIGO stages	Characteristics
TX		Primary tumor cannot be assessed
T0		No evidence of primary tumor
Tis	0	Carcinoma in situ (preinvasive carcinoma)
T1	I	Tumour confined to fallopian tube(s)
T1a	IA	Tumor limited to one tube, without penetrating the serosal surface
T1b	IB	Tumor limited to both tubes,without penetraiting the serosal surface
T1c	IC	Tumor limited to one or both tube(s) with extension onto or through the tubal serosa, or with malignant cells in ascites or peritoneal washings
T2	II	Tumor involves one or both fallopian tube(s) with pelvic extension
T2a	IIA	Extension and/or metastasis to uterus and/or ovaries
T2b	IIB	Extension to other pelvic structures
T2c	IIC	Pelvic extension (2a or 2b) with malignant cells in ascites or peritoneal washings
T3 and/ or N1	III	Tumor involves one or both fallopian tube(s) with peritoneal implants outside the pelvis and/ or positive regional lymph nodes
T3a	IIIA	Microscopic peritoneal metastasis outside the pelvis
T3b	IIIB	Macroscopic peritoneal metastasis outside the pelvis 2 cm or less in greatest dimension
T3c and/ or N1	IIIC	Peritoneal metastasis more than 2 cm in greatest dimension and/or positive regional lymph nodes
M1	IV	Distant metastasis (excludes peritoneal metastasis)

Note: Liver capsule metastasis is T3/stage III, liver parenchymal metastasis M1/stage IV. Pleural effusion must have positive cytology for M1/stage IV.

N– Regional lymph nodes
NX Regional lymph nodes cannot be assessed.
N0 No regional lymph node metastasis
N1 Regional lymph node metastasis

M– Distant metastasis
MX Distant metastasis cannot be assessed
M0 No distant metastasis
M1 Distant metastasis

Benign Tubal Masses

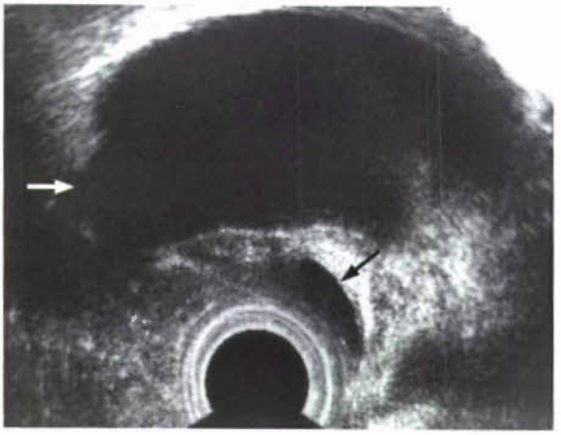

1

Fig. 29.1 Hydrosalpinx, with occlusion of the fimbriated end (→).

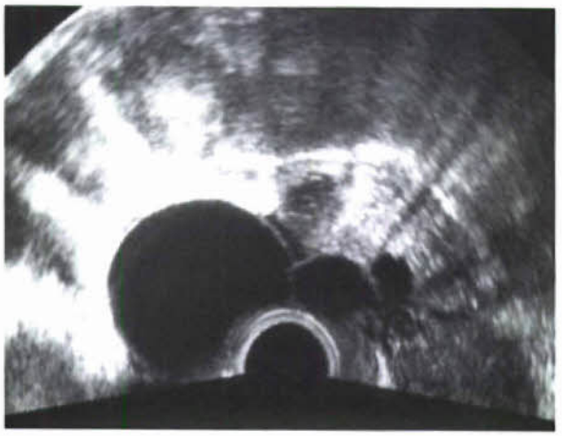

2

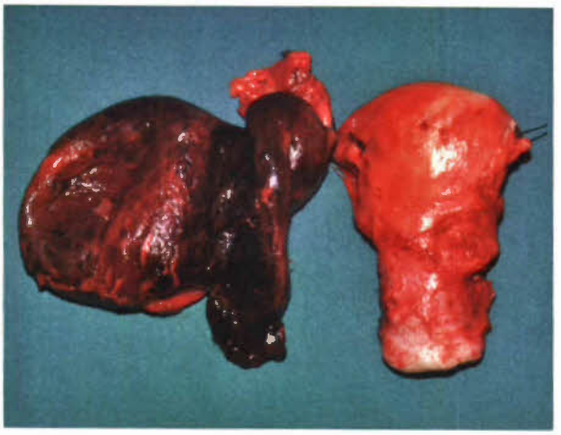

3

Fig. 29.2 Acute torsion of the right adnexa, with marked cystic expansion of the individual tubal segments.

Fig. 29.3 The surgical specimen corresponding to Fig. 29.2.

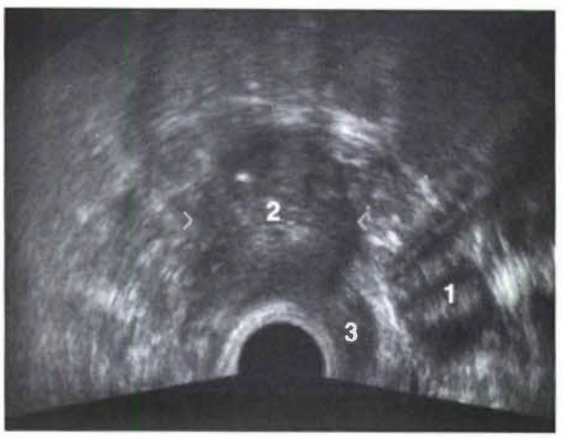

4

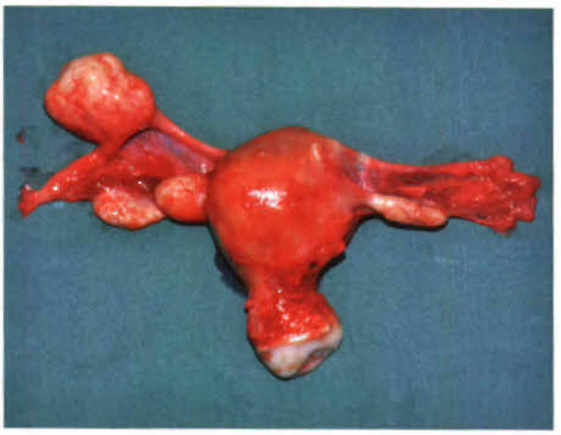

5

Fig. 29.4 Sharply circumscribed, hypoechoic subserous myoma of the right uterine side wall (1) and a well-circumscribed hypoechoic myoma of the right fallopian tube (4.8 cm in diameter) (2). Between the two lesions, there is a normal-appearing postmenopausal ovary (3).

Fig. 29.5 The surgical specimen corresponding to Fig. 29.4.

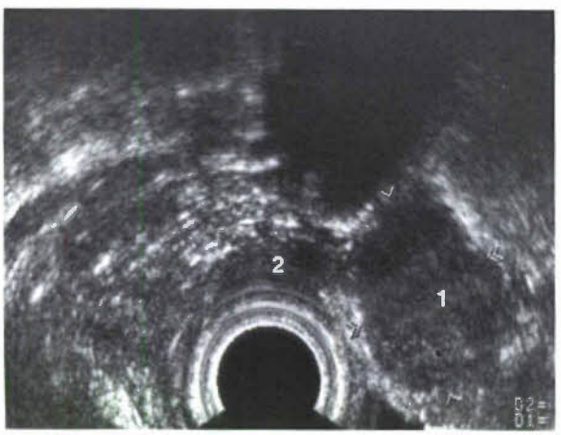

6

7

Fig. 29.6 Carcinoma of the left fallopian tube (T1N0M0) (1). Oblique longitudinal scan. The tubal diameter is enlarged to 3.5 cm by irregular, sonodense tissue of moderate echogenicity. The left ovary (2) appears normal.

Fig. 29.7 This advanced carcinoma of the right fallopian tube in coronal section contains markedly irregular solid components and multiple cystic areas. Tubal cross-section (→). * = Ascites.

30 Extragenital Masses

In addition to gynecologic masses in the true pelvis, transvaginal ultrasound may occasionally reveal masses that do not originate from the internal genitalia. These include tumors of the urinary tract, intestinal tract, and retroperitoneum.

Ultrasound can exclude a gynecologic mass only if the uterus and both adnexa are seen to be distinctly separate from the mass and exhibit normal features. A range of diagnoses may be considered for extragenital masses, depending on whether the lesion is predominantly cystic or solid (Table 30.**1**).

In principle, any of these nongynecologic changes in the true pelvis can mimic a gynecologic disease or a gynecologic mass.

In the urinary tract [1,2], a pronounced *cystic kidney* (Fig. 30.**1**), a *pelvic kidney*, or a low-lying *renal allograft* can mimic a solid ovarian tumor in the true pelvis (Figs. 30.**2**, 30.**3**). *Endometriosis of the bl*adder (Figs. 30.**4**, 30.**5**) and primary *bladder carcinoma* (Figs. 30.**6**–30.**9**) [3] can be difficult to distinguish from cervical carcinoma.

Various diseases of the intestinal tract [4] can raise problems of differential diagnosis. A *mucocele of the appendix* may be mistaken for an ovarian tumor (Figs. 30.**10**, 30.**11**), and a *perityphlitic abscess* can mimic an ovarian abscess. If the uterus is absent, adjacent and *low-lying small-bowel loops* may create the impression of a postinflammatory adnexal conglomerate mass (Fig. 30.**12**). A markedly *fluid-filled* and *distended bowel loop* may be mistaken for a *sactosalpinx*, while an incipient *small-bowel obstruction* with greatly enlarged, fluid-filled bowel loops may be misinterpreted as torsion of an adnexal mass (Figs. 30.**13**, 30.**14**). In the colon region, a rectal carcinoma, intestinal endometriosis [5], or a cross-sectional scan of the bowel may be misinterpreted as an ovarian mass (Fig. 30.**15**). The latter can be correctly identified by rotating the scan plane 90° to image the colon in longitudinal section (Figs. 30.**16**). An elongated colon segment, especially with chronic inflammatory thickening of the bowel wall [6], is apt to be mistaken for a hematosalpinx or pyosalpinx.

Table 30.**1** Extragenital masses in the true pelvis

Predominantly cystic masses	Predominantly solid masses
• Cystic kidney	• Pelvic kidney
• Peritoneal cyst	• Endometriosis of bladder or bowel
• Dilated ureter	• Perityphlitic abscess
• Fluid-filled bowel loop	• Bladder carcinoma
• Crohn's disease	• Rectal carcinoma
• Bowel obstruction	• Metastasis from a nongynecologic tumor (e.g., melanoma)
• Retroperitoneal tumor (neurinoma)	• Distended bowel loop (pseudotumor)
• Appendiceal mucocele	• Retroperitoneal tumor (neurinoma, schwannoma, lymphoma)

Retroperitoneal tumors (*neurinoma*, *schwannoma*) can pose major problems of differential diagnosis (Figs. 30.**17**, 30.**18**). They can be distinguished from an ovarian tumor only by determining their precise location and also confirming that the ovaries are normal and unenlarged. Retroperitoneal spread of the tumor can be detected sonographically in some cases (Fig. 30.**18**).

Finally, other nongynecologic primary tumors such as melanoma may metastasize to the true pelvis, causing them to be mistaken for a primary ovarian tumor.

References

1 Becht E, Hutschenreiter G, Klose K. Urologische Diagnostik mit bildgebenden Verfahren. Stuttgart: Thieme, 1988: 16–100.
2 Schwerk WB. Nieren. In: Braun B, Günther R, Schwerk WB, editors. Ultraschalldiagnostik. Lehrbuch und Atlas. Landsberg, Germany: Ecomed, 1985: III-1.8.
3 Tsyb AF, Slesarev VL, Komarevtsev VN. Transvaginal longitudinal ultrasonography in diagnosis of carcinoma of the urinary bladder. J Ultrasound Med 1988;7:179–82.
4 Schwerk WB. Gastrointestinaltrakt. In: Braun B, Günther R, Schwerk WB, editors. Ultraschalldiagnostik. Lehrbuch und Atlas. Landsberg, Germany: Ecomed, 1989: I 7. Erg.Lfg. III-1.7.
5 Gorell HA, Cyr DR, Wang KY, Greer BE. Rectosigmoid endometriosis: diagnosis using endovaginal sonography. J Ultrasound Med 1989;8:459–61.
6 Worlicek H, Lutz H, Thoma B. Sonographie chronisch-entzündlicher Darmerkrankungen – eine prospektive Studie. Ultraschall 1986;7:275–80.

Fig. 30.**1** Giant cystic right kidney next to the distended urinary bladder. Coronal scan.

Fig. 30.**2** Left pelvic kidney viewed in oblique longitudinal section (7.3 × 4.6 × 6.8 cm).

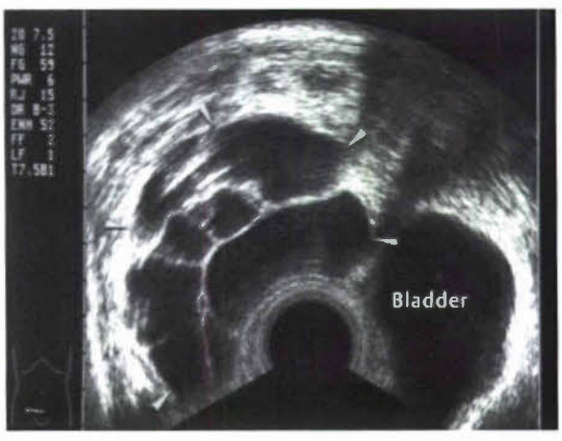

1

2

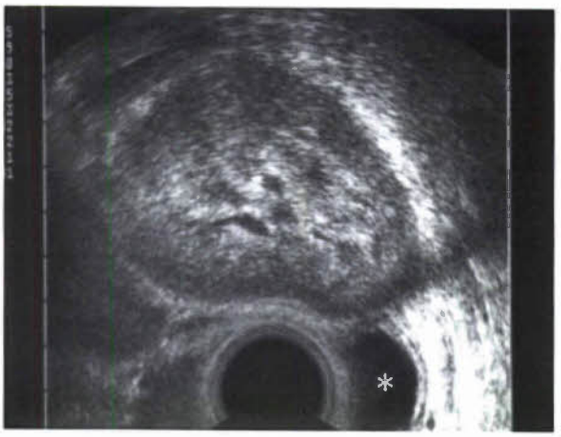

3

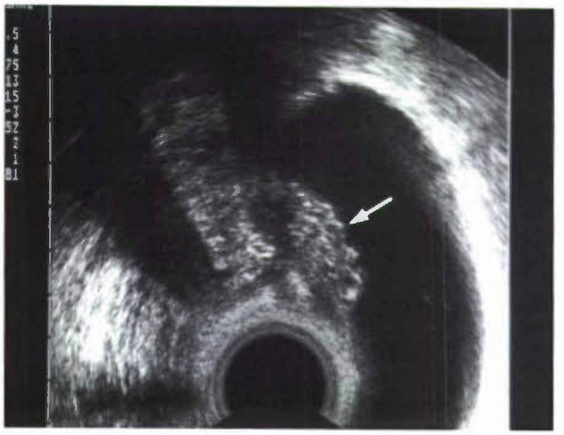

4

Fig. 30.3 Renal allograft on the left side of the true pelvis. * = Bladder. Longitudinal scan.

Fig. 30.4 Bladder endometriosis in longitudinal section (←) (3.7 × 2.5 × 3.1 cm).

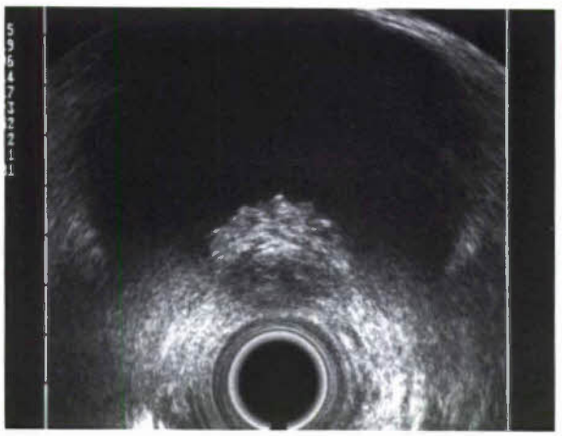

5

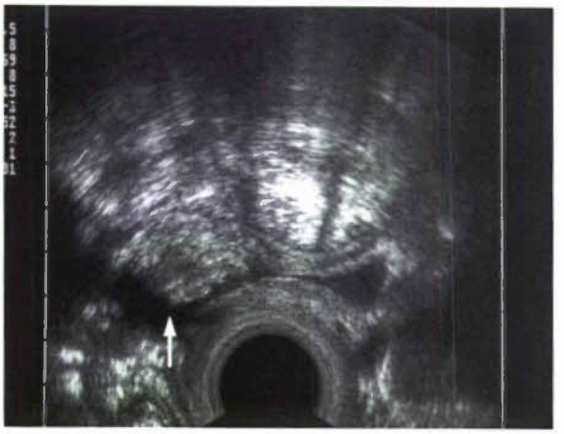

6

Fig. 30.5 Coronal scan of the case in Fig. 30.4.

Fig. 30.6 Bladder carcinoma in the right vesicourethral angle (|) (3.1 × 2.2 × 2.9 cm). Coronal scan.

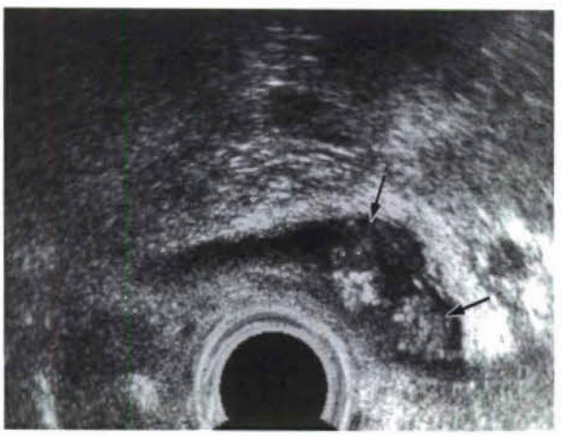

7

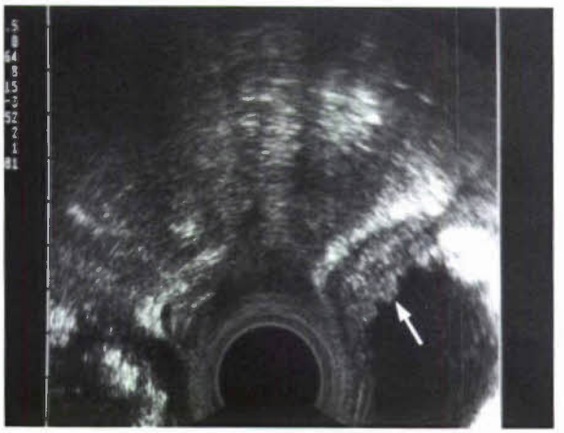

8

Fig. 30.7 Bladder carcinoma in a 74-year-old woman. The coronal scan demonstrates echogenic, polypoid tumor masses occupying the left half of the bladder (→).

Fig. 30.8 Bladder carcinoma, with marked thickening of the bladder wall adjacent to the uterus (→). Longitudinal scan.

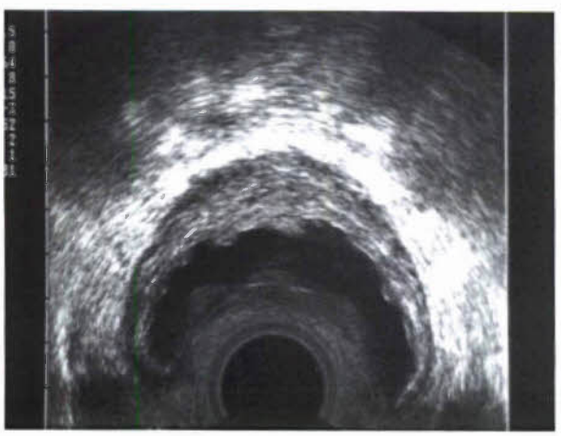

9

10

Fig. 30.9 Coronal scan of the bladder carcinoma in Fig. 30.8.

Fig. 30.10 Mucocele of the appendix. Coronal scan.

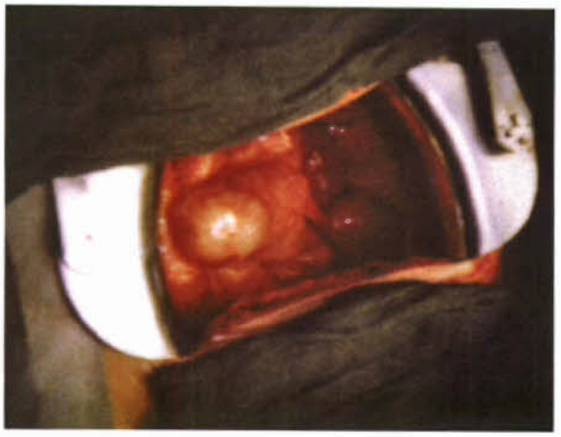

11

Fig. 30.**11** Intraoperative view of the lesion in Fig. 30.**10**.

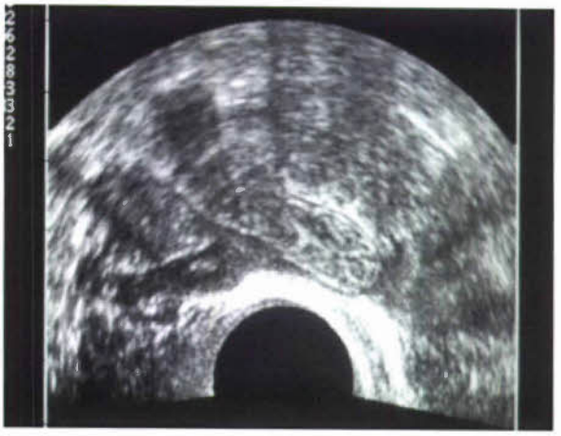

12

Fig. 30.**12** Low-lying, adjacent loops of normal small bowel in a patient who had previously undergone a vaginal hysterectomy. Coronal scan.

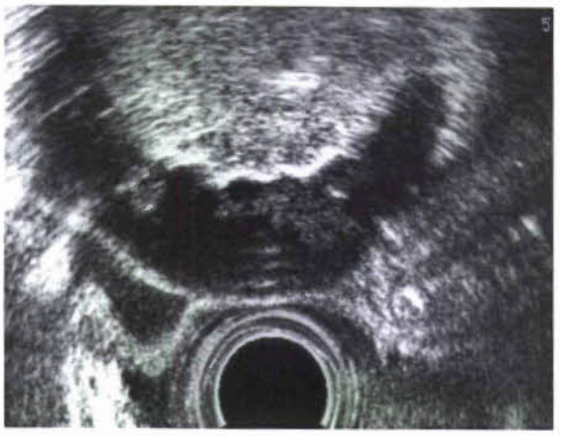

13

Fig. 30.**13** A bowel loop markedly distended by fluid. Coronal scan. Not an abnormal finding.

14

Fig. 30.**14** Small-bowel obstruction with massive dilation of bowel loops. Coronal scan.

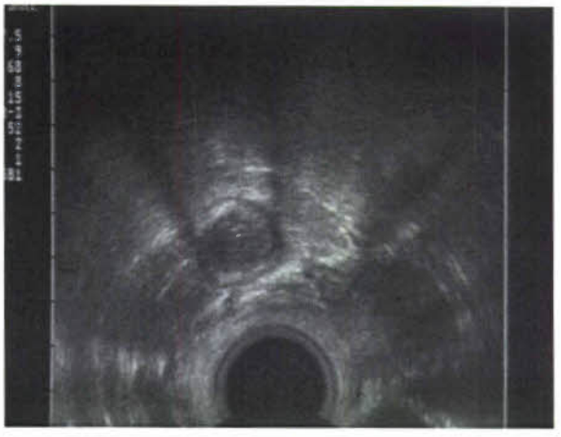

15

Fig. 30.**15** A distended colon segment scanned in cross-section can mimic an ovarian tumor.

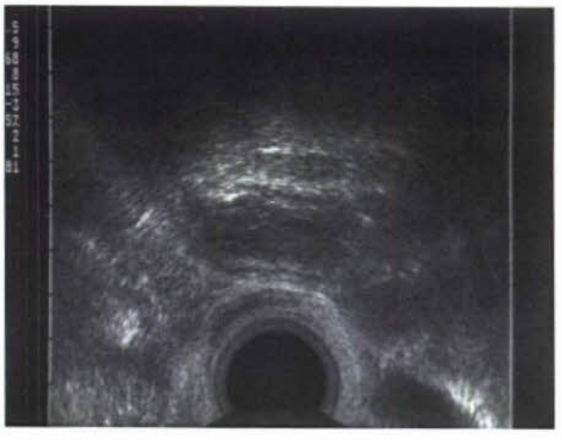

16

Fig. 30.**16** The same case as in Fig. 30.**15**. When the transducer is rotated to a longitudinal scan, the distended bowel segment is easily distinguished from an ovarian tumor.

17

Fig. 30.**17** A neurinoma appears as a mixed cystic and solid mass in the sacral hollow. Coronal scan.

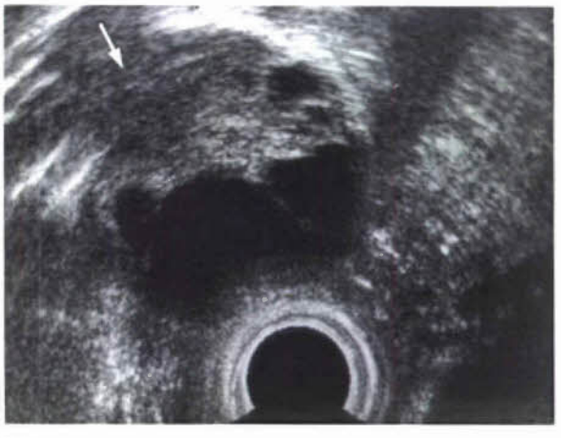

18

Fig. 30.**18** A mixed cystic and solid retroperitoneal mass located in the sacral hollow (a schwannoma, measuring 9.2 × 5.8 × 7.1 cm). Longitudinal scan. Posteriorly, the solid portion of the tumor cannot be delineated from the surrounding retroperitoneal tissues (→).

31 Ultrasound in the Follow-Up of Gynecologic Cancers

With the exception of ovarian carcinoma, the majority of women survive their gynecologic cancer for at least 5years. In the case of uterine carcinoma, a permanent cure is achieved in half of the patients. In the case of breast cancer, the most common cancer in women, approximately 70% of patients die from the disease within 20years [1], although 75% of patients with negative lymph nodes survive for 5years and almost 65% survive for 10years [2].

Goals of Cancer Follow-Up Care

Because every newly diagnosed and untreated cancer in women—even early-stage disease that does not result in severe somatic changes—still causes psychological distress relating to the cancer diagnosis, there is need for a comprehensive program of cancer follow-up care after the primary treatment. The main goals of this follow-up care are to counter the negative or fatalistic attitude of many patients by confirming the success of the treatment, and also to detect any recurrence of the cancer at the earliest possible stage.

The specific goals of cancer follow-up care, defined as periodic re-examinations and counseling after clinical treatment, are as follows:

- Providing access to human and medical resources, support, and counseling
- Instituting rehabilitative measures
- Diagnosing and treating any side effects relating to cancer treatment, and determining the most successful treatment modality
- Detection and treatment of recurrences and metastases
- Screening for other cancer illness
- Providing adjunctive measures to support the treatment result

Decades of experience in cancer follow-up care have led to standard recommendations for the scheduling of follow-up visits, which depends essentially on the likelihood of a recurrence and on associated side effects. Eighty percent of recurrences take place during the first 2years after primary treatment; the risk of recurrence declines considerably thereafter. With the exception of breast cancer, recurrences and metastases are extremely unlikely to occur more than 5years after the primary treatment [3].

Gynecologic Ultrasound Examination

The search for local recurrences always starts with a physical examination, but imaging procedures are essential for making a specific evaluation. Both abdominal and transvaginal ultrasound are reliable, noninvasive, and cost-effective studies that can be used firstly to confirm that an equivocal palpable finding is not a recurrence and secondly to detect a local recurrence or metastasis at the earliest possible stage.

Local recurrences of gynecologic tumors following surgery and/or radiotherapy pose a major diagnostic and therapeutic challenge. The scar tissue that forms after surgery or radiotherapy can hamper the physical examination, making it difficult or impossible to distinguish post-therapeutic scarring from a local recurrence on the basis of palpable findings alone. Transvaginal and transrectal sonography are more suitable for distinguishing between a local recurrence and a scar.

A direct sonographic sign of a recurrence is a hypoechoic, nonhomogeneous area on the vaginal floor (Figs. 31.**1**–31.**3**) or pelvic wall. A scar has a more homogeneous appearance (Fig. 31.**4**) and is usually indistinguishable from normal tissue by ultrasound [4].

Recurrent tumors in the true pelvis require differentiation from endometriotic foci on the vaginal stump. The latter appear as hypoechoic areas with a thickened rim and fine internal echoes and may contain more echogenic peripheral components (Fig. 31.**5**).

Indirect signs of a recurrence in the true pelvis are urinary stasis and hydronephrosis [5].

The ultrasound follow-up of gynecologic tumors should always include transabdominal scans to screen for secondary changes such as urinary tract obstruction, ascites, lymph node metastases, and hepatic metastases. With *ascites*, a fluid collection as small as 50mL will form a conspicuous echo-free area in the cul-de-sac. In cases with *peritoneal carcinomatosis*, ultrasound may demonstrate standing, fixed bowel loops within the ascites as a result of bowel adhesions [6] (Fig. 31.**6**). In some cases, papillary deposits on the peritoneum can be directly visualized as small, nonhomogeneous hypoechoic structures (Fig. 31.**7**). *Lymph-node metastases* in the true pelvis are not often detectable with ultrasound, due to overlying bowel gas [3]. Computed tomography and magnetic resonance imaging appear to be more rewarding for this application [7].

Abdominal wall metastases, on the other hand, can be clearly defined with ultrasound (Chapter 11). This requires the use of a higher-frequency transducer with near-field focusing or a standoff pad.

The liver is a frequent site of metastasis for cancers of the breast, uterus, ovaries, and gastrointestinal tract. *Hepatic metastases* can be classified sonographically as hypoechoic or hyperechoic. *Hypoechoic metastases* are more characteristic of ovarian and uterine malignancies, while *hyperechoic metastases* are more typical of gastrointestinal cancer and breast cancer [8] (Chapters 11, 12). Cystic hepatic metastases are occasionally found in association with ovarian, cervical and endometrial carcinoma [9].

Approximately 6% of ovarian carcinomas are metastatic [10]. The primary tumors most commonly originate in the gastrointestinal tract, breast, or other organs of the true pelvis. The metastases are bilateral in 75% of cases. *Krukenberg tumors*, a special metastatic form arising from signet-ring cell–forming gastric carcinoma, appear as large, solid, bilateral ovarian lesions with a nonhomogeneous echo pattern caused by extensive necrosis and intratumoral hemorrhage.

References

1 Haagensen CD. Diseases of the breast, 2nd ed. Philadelphia: Saunders, 1971.
2 Hindle WH, Ling FW. Diseases of the breast. In: Stovall TG, Summitt RL, Beckmann CRB, Ling FW, editors. Clinical manual of gynecology, 2nd. ed. New York: McGraw-Hill, 1992: 49–65.
3 Wicks JD, Mettler FA Jr, Hilgers RD, Ampuero F. Correlation of ultrasound and pathologic findings in patients with epithelial carcinoma of the ovary. J Clin Ultrasound 1984;12:397–402.
4 Hötzinger H, Tuthoff J, Beyer KH. Local recurrences of gynecologic malignancies: diagnosis by vaginosonography and rectosonography. J Ultrasound Med 1988;7: 83.
5 Sanders RC. Ultrasound in pelvic malignancy. In: Steel WB, Cochrane WJ, editors. Gynecologic ultrasonography. Edinburgh: Churchill Livingstone, 1984: 139–156.
6 Merz E. Sonographische Diagnostik in Gynäkologie und Geburtshilfe. Lehrbuch und Atlas. Stuttgart: Thieme, 1988: 68.
7 Dooms GC, Hricak H, Crooks LE, Higgins CB. Magnetic resonance imaging of the lymph nodes: comparison with CT. Radiology 1984;153:719–28.
8 Fleischer AC, Walsh JW, Jones HW, Schaff MI, James AE. Sonographic evaluation of pelvic masses. Radiol Clin N Am 1982;20:397–412.
9 Scheible W, Gosink BB, Leopold GR. Gray scale sonographic pattern of hepatic metastatic disease. AJR Am J Roentgenol 1977;129:983–7.
10 Young RH, Scally RE. Metastatic tumors of the ovary. In: Kurman RJ, editor. Blaustein's pathology of the female genital tract, 3rd ed. Berlin: Springer, 1987: 742–68.

Gynecologic Ultrasound Examination

Fig. 31.1 Spinal recurrence on the right side (—) (2.6 × 1.9 × 2.3 cm) following a radical Wertheim–Meigs operation for cervical carcinoma. Oblique longitudinal scan.

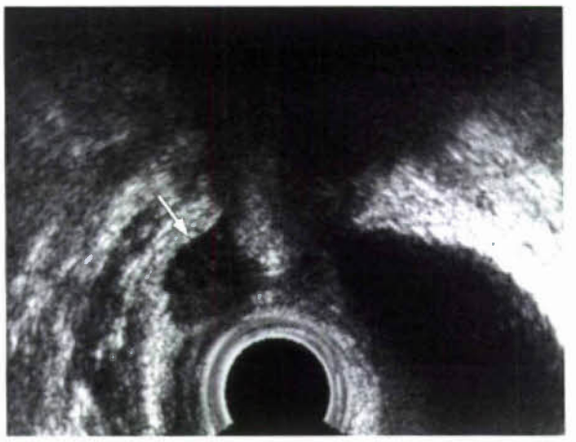

1

Fig. 31.2 Recurrence of sarcoma on the vaginal floor (3.9 × 2.6 cm). Longitudinal scan.

2

Fig. 31.3 Recurrent ovarian carcinoma on the vaginal floor (2.5 × 2.0 × 2.1 cm) with invasion of the urinary bladder (—). Longitudinal scan.

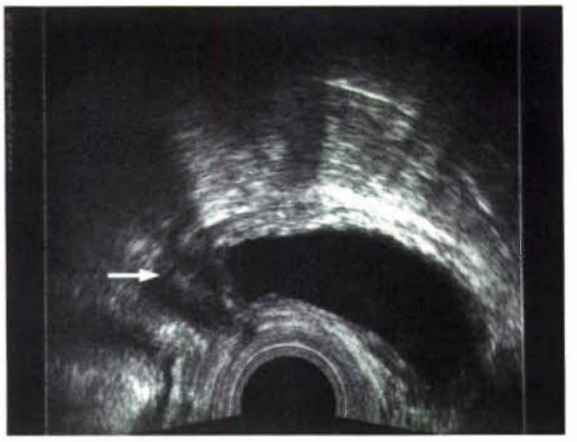

3

Fig. 31.4 Small nodular scar (1.0 × 0.8 cm) on the vaginal floor following a prior vaginal hysterectomy. Longitudinal scan.

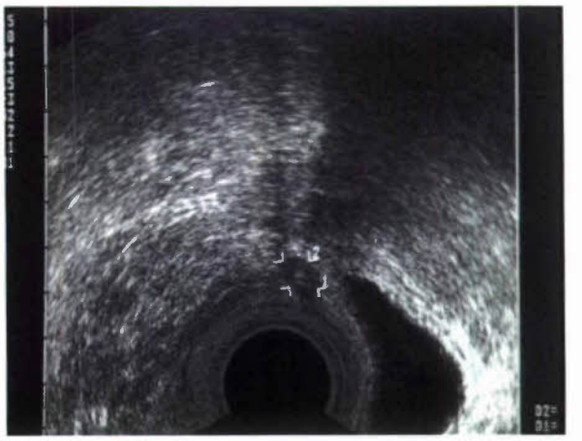

4

Fig. 31.5 Cul-de-sac endometriosis (1.8 × 2.6 × 1.8 cm) following a prior abdominal hysterectomy. Coronal scan.

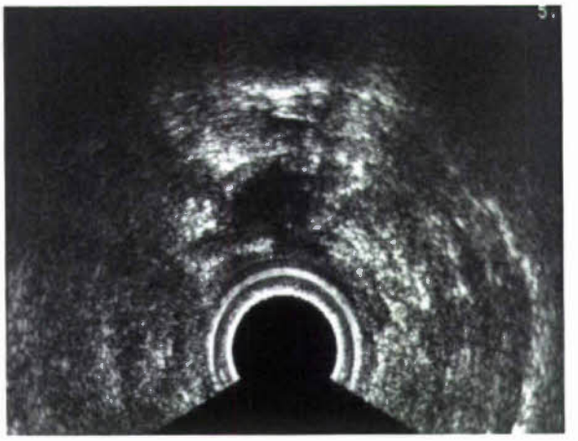

5

Fig. 31.6 Copious ascites (*) and neoplastic thickening of a bowel loop (—) in a patient with ovarian carcinoma and a retroflexed uterus.

6

Fig. 31.7 Peritoneal carcinomatosis in a patient with ovarian carcinoma. Besides the thickened peritoneum, ultrasound reveals several bulky proliferative excrescences (—) in the cul-de-sac (*). Retroflexed uterus. Longitudinal scan.

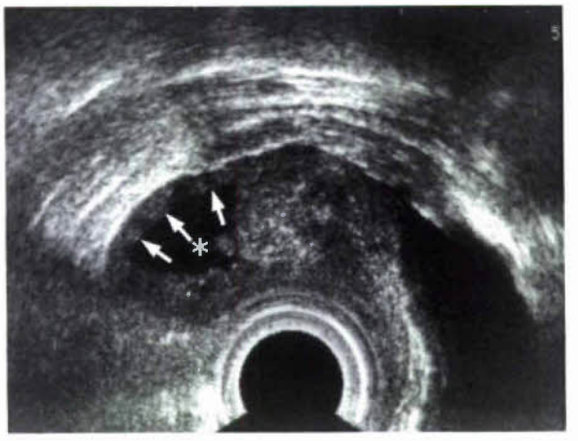

7

32 Localization of Intrauterine Devices

The intrauterine device (IUD) is currently the second most widely practiced method of birth control. On a worldwide scale, it is estimated that 156 million women wear an IUD. Just over two-thirds, or 104 million, are in China, where IUDs are used by 45% of married woman [1].

The most commonly used IUDs at present are copper-based devices: the Nova T (Schering), Copper T, Gravigard Copper 7 (Searle), and Multiload Cu 250 (Nourypharma). An all-plastic IUD, the Lippes Loop (Cilag), is also occasionally used (Fig. 32.**1**). The Lippes Loop is unique in that it can maintain contraceptive efficacy for an indefinite period of time, whereas IUDs that release copper ions have to be replaced at specified intervals.

The Pearl Index [2] ranges from 0.7 to 2.7, depending on the type of IUD [3]. The contraceptive efficacy of an IUD depends not only on the design and lifespan of the device, but also on its correct positioning within the uterus. When an IUD becomes displaced, its contraceptive efficacy is significantly compromised [4,5].

Of all the methods available for checking the position of an IUD, the current method of choice is transvaginal ultrasound. Since patients can be examined on an empty bladder, transvaginal scans can be acquired immediately after insertion of the IUD to confirm that it has been correctly placed. Moreover, while obesity or a retroflexed uterus can interfere with transabdominal scanning, they are not a problem in transvaginal scanning.

Transvaginal ultrasound offers a number of advantages in patients selected for IUD insertion (Table 32.**1**). It can be performed before IUD placement to check for anomalies of uterine position (retroflexion) and also detect uterine abnormalities (malformations, fibroids) that might contraindicate an IUD. Sonographic measurement of the "probe length" is also helpful in selecting an IUD of the correct size.

An IUD with a rod-shaped stem appears as a bright linear echo in a sagittal scan of the uterus (Fig. 32.**2**), while a transverse scan displays it as a punctate echo at the center of the uterine cavity (Fig. 32.**3**). If the IUD is wrapped with a coiled copper wire, it is even possible to define the wire with a high-resolution probe. An acoustic shadow can be seen distal to the IUD (Fig. 32.**2**).

In an exact midsagittal scan through the uterus, the retrieval thread of the IUD can be identified as an echogenic line within the cervix (Fig. 32.**2**).

With a T-shaped IUD, a coronal scan through the uterine fundus can confirm that the side arms of the device are properly extended (Fig. 32.**4**).

Table 32.**1** Advantages of localizing intrauterine devices (IUDs) with transvaginal ultrasound

Before IUD insertion	• Detection of an anomalous uterine position (retroflexion) • Detection of a submucous myoma • Detection of a uterine malformation (bicornuate or subseptate uterus) • Measurement of the probe length
Immediately after IUD insertion and in subsequent follow-ups	• Checking correct positioning of the IUD • Confirming proper side-arm extension of a Copper T • Detection of potential complications (e.g., uterine perforation)

Correct Position of the IUD

Various criteria are used to evaluate the correct position of an IUD. According to Meyenburg [6], the sonographically measured distance between the uterine fundus and the fundal end of the IUD should not exceed 2 cm. One drawback of this method is that it does not take into account individual differences in the thickness of the uterine wall or the possible presence of fundal myomas.

Bernaschek et al. [4] included uterine wall thickness in their formula for calculating the fundal-IUD distance (FID). According to this method, the IUD is correctly positioned when the distance between the uterine fundus and the upper end of the IUD is less than four-thirds of the mean thickness of the uterine wall:

$$\text{FID} = \frac{(\text{anterior wall} + \text{posterior wall})}{2} \times 4/3$$

Both methods are derived from abdominal ultrasound. However, with the higher image resolution of transvaginal ultrasound, we use the endometrial distance that can be measured above the IUD as our criterion. When the IUD is correctly positioned, we can measure no more than about 0.8 cm of endometrial distance above the device. We also check to make sure the lower end of the IUD is above the internal cervical os.

The position of the IUD should be checked sonographically immediately after insertion. It should be checked again at 4 and 12 weeks, since the risk of displacement or expulsion is highest during the initial months [5]. Annual follow-ups should also be observed to confirm acceptable placement. Special examinations should be scheduled if the patient complains of bleeding abnormalities or lower abdominal pain, if the IUD thread is no longer visible ("lost IUD"), or if pregnancy occurs (Table 32.**2**).

IUD Mimics

Occasionally, a thickened, echogenic endometrium can mimic an IUD during the secretory phase of the menstrual cycle. Also, calcifications caused by regressive changes in retained placental tissue following a delivery or miscarriage can produce an echo pattern that is remarkably similar to that of an IUD [7] (Fig. 32.**5**; see also Chapter 40).

Table 32.**2** Timing of ultrasound examinations for intrauterine devices (IUDs)

First examination	Before IUD insertion
Second examination	Immediately after IUD insertion
Third examination	4 weeks later
Fourth examination	12 weeks later
Further examinations	Every 12 months
Additional examinations	• For pain or abnormal bleeding • IUD thread not visible • Early pregnancy

Lost IUD

A "lost IUD" is one in which the retrieval thread cannot be located by speculum examination of the cervix. These patients should be referred at once for ultrasound evaluation to locate the missing device. Ultrasound can quickly determine whether the thread of a normally positioned IUD has simply retracted into the cervical canal or whether the device has become displaced, expelled, or has perforated through the uterus.

If the IUD is displaced but is still within the uterus, ultrasound may show that it has migrated too low in the corpus or cervix (Fig. 32.**6**) or has shifted to an oblique position.

If the thread cannot be found and the IUD is displaced from its normal position, a "blind" instrument extraction of the IUD may prove difficult and even hazardous due to the risk of uterine perforation. IUD removal under sonographic guidance is a good alternative in these cases. With the bladder partially filled, the displaced IUD is grasped and extracted with a forceps under transabdominal ultrasound guidance. The same technique is used to retrieve a side arm that has broken off the device (Fig. 32.**7**). The fragment can first be located by transvaginal scanning and then removed under transabdominal ultrasound guidance.

A perforated IUD can be visualized with ultrasound only if part of the device is still in the uterus (Figs. 32.**8**, 32.**9**) [8]. A reverberation artifact can occasionally mimic a partially perforated IUD (Fig. 32.**10**). If the entire IUD has perforated into the peritoneal cavity, it is extremely difficult to locate with ultrasound. In equivocal cases in which the uterus appears empty on ultrasound, a plain abdominal radiograph can be obtained for definitive localization (Chapter 13).

Other Complications Associated with IUDs

The risk of *pelvic inflammatory disease* is two to three times higher in IUD wearers than in women without an IUD [9,10]. Ultrasound can be used in women with unexplained lower abdominal pain to detect or exclude inflammatory or postinflammatory changes, such as tubo-ovarian abscess or sactosalpinx.

When *irregular bleeding* occurs in an IUD wearer, it is important to consider not just the possibility of IUD displacement but also ectopic pregnancy, which is more prevalent among IUD wearers than in oral contraceptive users [11,12]. These cases therefore require a meticulous examination of both adnexal regions in addition to a β-HCG test.

References

1 China to upgrade its IUD technology. Progress WHO, Geneva 2002; 60:4
2 Pearl R. Contraception and fertility in 2000 women. Hum Biol 1932;4:363–407.
3 Moyer DL, Shaw ST, Fu JU. Clinical aspects of inert and medicated intrauterine devices. In: Hafez ESE, editor. Human reproduction: conception and contraception, 2nd ed. Hagerstown, MD: Harper & Row, 1980.
4 Bernaschek G, Spernol R, Beck A. IUD-Lage bei intrauterinen Schwangerschaften. Geburtshilfe Frauenheilkd 1981;41:645–7.
5 Schmidt EH, Wagner H, Quakernack K, Beller FK. Ergebnisse der Lageüberwachung von Intrauterinpessaren durch Ultraschall. Geburtshilfe Frauenheilkd 1979;39: 138–43.
6 Meyenburg M. Anwendung der Ultraschall-Schnittbildtechnik zur Darstellung von Intrauterinpessaren. Geburtshilfe Frauenheilkd 1978;38:950–7.
7 Merz E, Weber G, Macchiella D, Bahlmann F. 3D-Volumensonographie in der transvaginalen Diagnostik. Gynäkologe 1995;28:270–5.
8 Kratochwil A. Ultraschalldiagnostik in der Gynäkologie. Gynäkologe 1976;9:166.
9 Golditch IM, Huston JE. Serious pelvic infections associated with intrauterine contraceptive device. Int J Fertil 1973;18:156–60.
10 Luukkainen T, Nielsen NC, Nygren KG, Pyörälä T. Nulliparous women, IUD and pelvic infection. Ann Clin Res 1979;11:121–4.
11 Cry HW. Ectopic pregnancy and intrauterine contraceptive devices: new perspectives. The Women's Health Study. Obstet Gynecol 1981;57:137–44.
12 Zielske F, Becker K, Knauf P. Schwangerschaften bei Intrauterinpessaren in situ. Geburtshilfe Frauenheilkd 1977;37:473–84.

Fig. 32.1 Intrauterine devices in common use.
a Copper T.
b Copper 7.
c Multiload.
d Nova T.
e Lippes Loop.

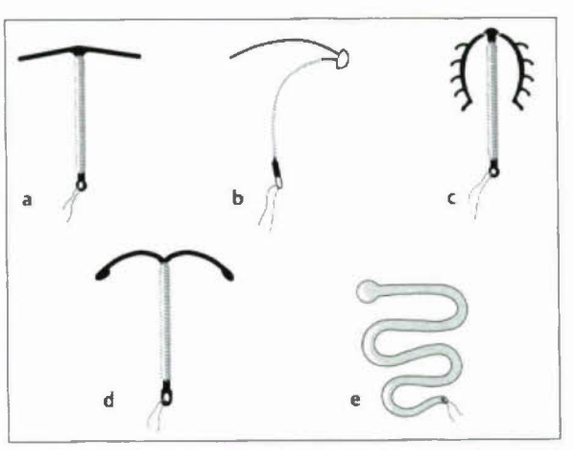

1

Fig. 32.2 Correctly positioned intrauterine device (→). Longitudinal scan. The thread of the device appears as a bright linear echo within the cervical canal.

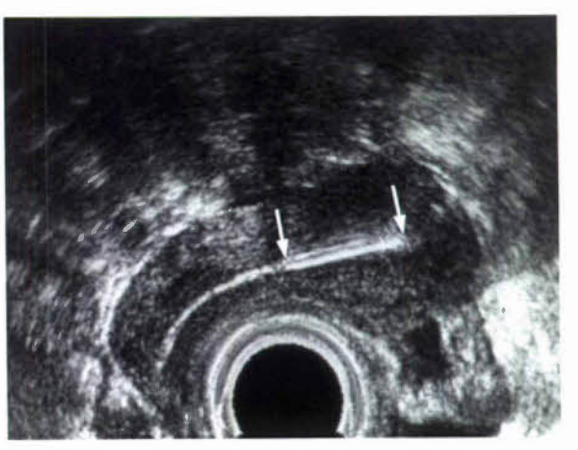

2

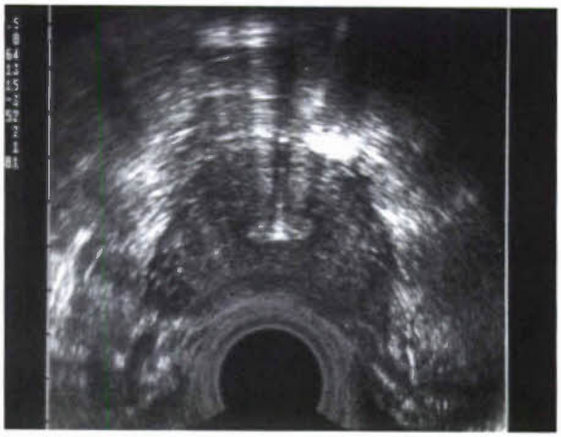

3

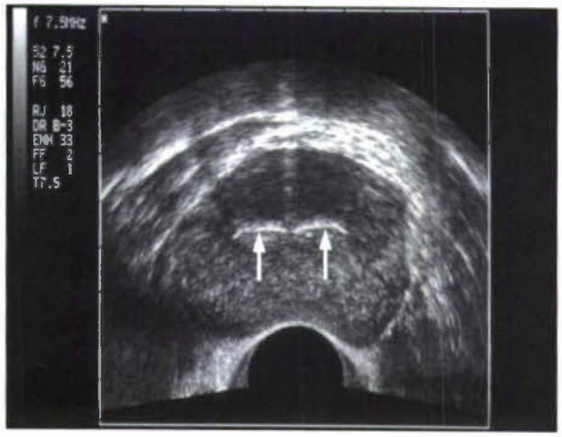

4

Fig. 32.3 Normal central positioning of the intrauterine device. Transverse section of the center of the uterine corpus.

Fig. 32.4 A correctly positioned Copper T intrauterine device in transverse section. Both arms of the device are properly extended (—).

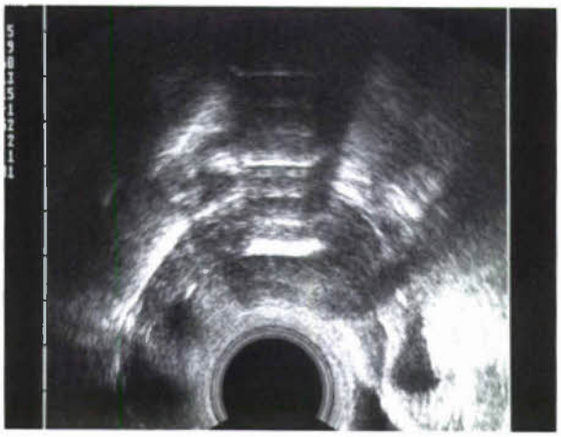

5

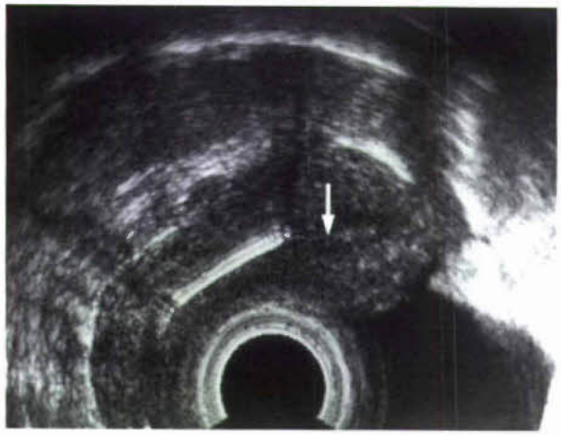

6

Fig. 32.5 An elongated calcified area in the uterine cavity mimics the appearance of an intrauterine device. Longitudinal scan.

Fig. 32.6 Displaced intrauterine device. Longitudinal scan. The corpus endometrium can be clearly recognized above the intrauterine device (—).

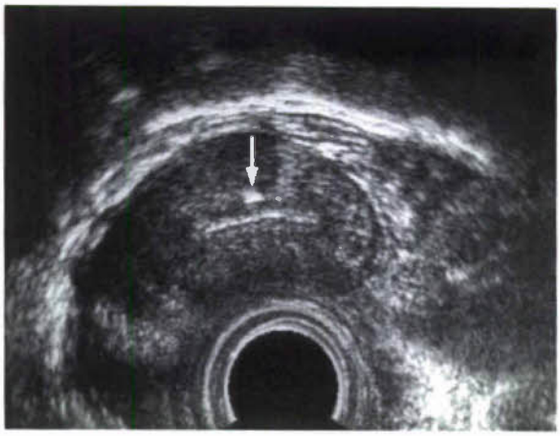

7

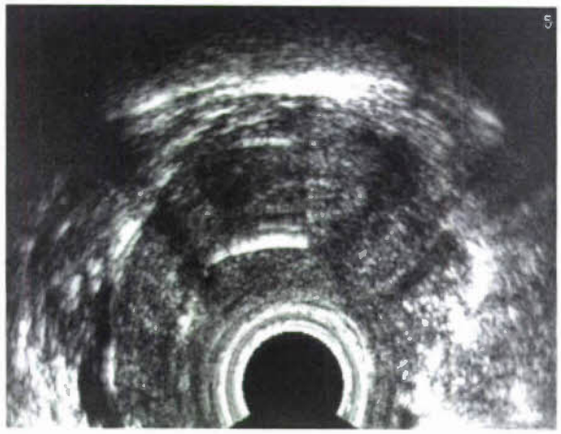

8

Fig. 32.7 Transvaginal scan of a detached intrauterine device side arm that has grown into the myometrium (—). Longitudinal scan.

Fig. 32.8 A displaced intrauterine device that has penetrated into the myometrium. Longitudinal scan.

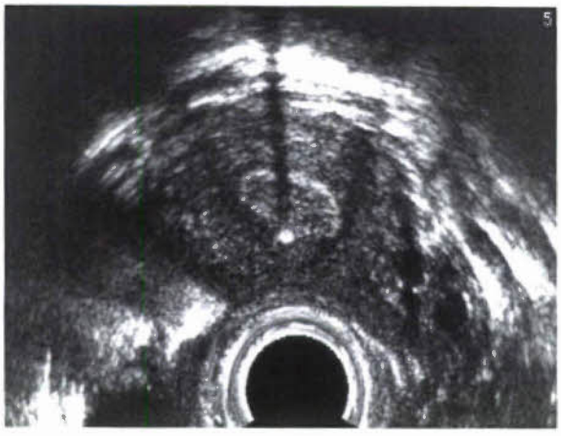

9

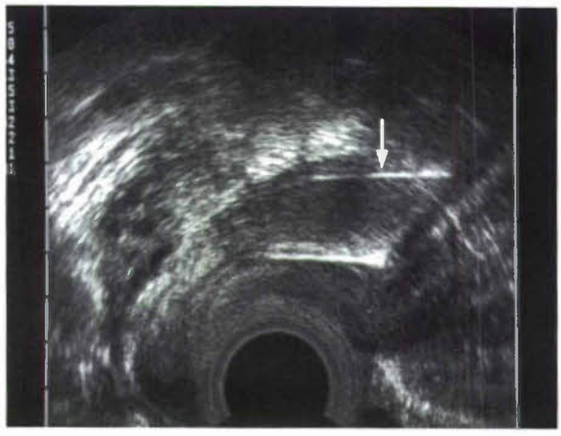

10

Fig. 32.9 Transverse scan of the intrauterine device in Fig. 32.8.

Fig. 32.10 A correctly positioned intrauterine device (IUD). The reverberation artifact behind the IUD (—) mimics a second IUD that is partly inside and partly outside the posterior myometrium.

33 Hysterosalpingo-Contrast Sonography

An important part of infertility testing is to assess the condition of the fallopian tubes. The causes of infertility are diverse and range from long-term intrauterine device (IUD) use and pelvic inflammatory disease to uterine and adnexal surgery and poor sperm quality in the male partner.

Traditional methods of assessing tubal patency include CO_2 pertubation, hysterosalpingography, and chromolaparoscopy combined with hysteroscopy [1–4].

A procedure for testing tubal patency under sonographic vision is ultrasound contrast hysterosalpingography (known also as hysterosalpingo-contrast sonography, or HyCoSy) [5–8,8a,8b].

The technique of *CO_2 pertubation* is used with a pressure manometer or stethoscope to detect abnormalities of tubal patency. The uterine cavity cannot be assessed with this technique, and the exact site of a tubal obstruction cannot be located. It is also extremely difficult to determine whether one or both fallopian tubes are patent or occluded. Because of these limitations, CO_2 pertubation can no longer be recommended as a test of tubal patency.

In conventional *hysterosalpingography*, the movement of contrast medium through the uterine cavity and fallopian tubes is assessed by continuous radiographic monitoring (Fig. 33.**1**). The myometrium and ovaries cannot be visualized. In many cases, the procedure is carried out with the patient under brief general anesthesia or sedation. Disadvantages are radiation exposure, discomfort, and the need for brief hospitalization [9,10].

The only conventional procedure that can reliably evaluate tubal patency and function is *chromolaparoscopy*. This procedure can assess tubal patency as well as the condition of the tubes, the tubal wall and surrounding tissues, and even the entire abdomen if need be (Fig. 33.**2**). The uterine cavity is not visualized, however, and so the procedure should be supplemented by hysteroscopy. Changes in the myometrium are not detected. The combination of both procedures requires general anesthesia and a brief hospital stay. Another disadvantage is that the patient cannot witness the procedure unless it is recorded on a video medium for later viewing.

Hysterosalpingo-contrast sonography using an endovaginal transducer and the ultrasound contrast medium Echovist (Schering, Berlin) makes it possible to examine the uterine cavity and evaluate tubal patency. The endometrium, myometrium, adnexa, and true pelvis can also be assessed. Examining the fallopian tubes with ultrasound is advantageous over other methods, as the test can be done in an outpatient setting without special preparations and without general anesthesia [11,12]. Also, the patient can watch the examination on the monitor as it is being performed, which can have psychological benefits in terms of further infertility treatment.

Prerequisites and Preparations

Ordinarily, infertility testing should be initiated only after the patient has been trying to achieve pregnancy for longer than 12 months. Primary tests include BBT charting, hormone status, postcoital testing, semen analysis, and evaluation of the fallopian tubes [13,14]. Once all of these parameters have been evaluated and the necessary conclusions drawn, tubal patency should be tested before the patient is referred for any infertility treatment that may be indicated. At least one of the tubes must be patent so that the sperm can encounter and fertilize a secondary oocyte.

Table 33.1 Criteria for outpatient hysterosalpingo-contrast sonography

- No galactose intolerance
- White blood count less than 10000/μL
- First half of menstrual cycle
- No uterine bleeding
- No genital tract inflammation

Hysterosalpingo-contrast sonography (HyCoSy) for assessing the uterine cavity and tubal patency should always be scheduled before the predicted time of ovulation (i.e., before day 14 of the cycle) so that early pregnancy can be excluded. The period between days 8 and 13 of the cycle is ideal, since normally the cervical canal is slightly dilated at that time and it is easier to insert the balloon catheter for instilling contrast medium into the uterine cavity. Tubal patency may be tested during the second half of the cycle only if the patient signs a statement attesting that she has not engaged in unprotected sexual intercourse during the current cycle.

Because the contrast solution has a galactose base, it should be confirmed that the patient is not galactose-intolerant. Galactose intolerance has an incidence of approximately one in 30000 and is a contraindication to HyCoSy. This does not apply to patients with known diabetes mellitus [7].

A white blood count (WBC) should be obtained 24–48 hours before the examination to exclude infectious disease. If the count is higher than 10000/μL, the examination should be postponed until the WBC returns to a normal range. The examination should also be deferred in patients with uterine bleeding, due to the risk of inciting an ascending infection (Table 33.**1**). This precaution has proven effective, and to date there have been only rare instances of lower abdominal inflammation. The WBC should again be checked 1–2 days after HyCoSy to exclude incipient pelvic inflammatory disease (PID) or allow for prompt, effective treatment of suspected PID.

The patient who presents for HyCoSy should receive appropriate written and verbal information about the procedure and provide her written informed consent. Because most women who desire pregnancy are over 18 years of age, it is rarely necessary to obtain a third-party signature.

The patient should also be told that her partner may be present during the examination. This is beneficial for many women, the presence of a trusted person helping them to feel less threatened by unfamiliar examination personnel.

Indications for Ultrasound Tubal Assessment

Although transvaginal ultrasound examination of the fallopian tubes is considered a low-risk procedure, it is still important to apply strict patient selection criteria. Necessary preliminary tests should have already been completed. Primary ultrasound evaluation of the fallopian tubes is not indicated in nulliparae over 33–35 years of age. These women have relatively little time left to achieve pregnancy, and a comprehensive evaluation by chromolaparoscopy and hysteroscopy would be more appropriate. In younger women, however, HyCoSy can be recom-

Table 33.2 Indications for hysterosalpingo-contrast sonography

- Tubal assessment in patients unable to achieve pregnancy
- Insemination for various indications
- Previous surgery on the uterus or adnexa
- Previous microsurgical procedure
- Before intratubal transfer in in-vitro fertilization and embryo transfer
- Previous incomplete tubal sterilization

mended without hesitation for the assessment of tubal patency.

It is important to evaluate tubal patency prior to insemination, especially when intratubal insemination is proposed. The latter method is suitable only if ovulation occurs in the ovary on the side known to have a patent tube. A preliminary assessment of tubal patency should be done in cases where intratubal embryo transfer is planned in the setting of an IVF program.

The assessment of tubal patency is also indicated in women who have had previous surgery on the organs of the true pelvis such as a myoma enucleation, ovarian cyst removal, or the laparoscopic treatment of ectopic pregnancy. It may also be indicated after microsurgical procedures not followed by open exposure in order to assess the result of the surgery. On the other hand, the preliminary assessment of tubal patency is not recommended as a prelude to a microsurgical procedure, because the information can be obtained more reliably by chromolaparoscopy [15,16].

HyCoSy has a limited indication for assessing tubal patency after an elective tubal coagulation. This is of particular interest when the surgeon is uncertain for technical reasons whether a complete tubal occlusion has been achieved. In this case the ultrasound tubal study should not be done within the first 6–8 weeks after the initial operation.

A primary assessment of tubal patency is particularly important before a planned insemination, on the basis of an abnormal postcoital test for sperm–mucus compatibility (the Sims–Huhner test) or abnormal sperm quality (Table 33.**2**).

When the fallopian tubes are assessed with ultrasound, the uterine cavity can also be inspected to exclude abnormalities. If changes are detected in the uterine cavity, they can subsequently be addressed by hysteroscopy or laparotomy.

Examination Technique

There is no need for routine premedication, general anesthesia, or paracervical blockade, because HyCoSy is relatively painless. In rare cases, a sedative may be appropriate in very nervous patients.

After emptying the bladder, the patient is placed in the lithotomy position on a gynecologic chair. Before the fallopian tubes are assessed, the organs of the true pelvis should be examined by transvaginal scanning to check for abnormalities. Next, the vulva and vagina are aseptically prepared, and a self-retaining speculum is introduced to expose the vagina and cervix. This frees both of the examiner's hands for the rest of the procedure.

Aided by a forceps and guided by direct vision, the examiner takes a soft, double-lumen balloon catheter (5 or 6 Fr, previously tested for function), advances it through the external cervical os into the uterine cavity, and inflates the balloon to secure the catheter position. Room air should be used for this purpose, as it is less painful than water. Next, the catheter is carefully withdrawn until the balloon occludes the internal cervical os (felt as resistance to further traction). Placing the balloon at the internal os is advantageous, because positioning the balloon too high will allow unnecessary outflow of echogenic contrast medium through the cervix and might obscure intrauterine changes located below the balloon (Fig. 33.**3**). In rare cases, it may be necessary first to pass a Hegar dilator through the cervical canal or use a tenaculum to steady the uterus for catheter insertion. This may prove necessary in patients who have had a previous cervical operation such as conization. The balloon should not be inflated while still in the cervical canal, as this would cause pain that might hamper the rest of the examination.

At this point, the self-retaining speculum is removed, and the endovaginal ultrasound probe is introduced into the upper third of the vagina for assessment of tubal patency. The soft balloon catheter will not interfere with defining the ultrasound planes that are necessary in this procedure.

The contrast medium is prepared by instilling the galactose solution into the granulate bottle through the supplied mini-spike, shaking the mixture for about 10 seconds, and drawing it into a disposable syringe. This white, echogenic fluid is a total reflector of ultrasound that will remain stable in suspension for approximately 10–15 minutes (Fig. 33.**4**), allowing ample time for tubal evaluation. To save costs, it is best to mix the Echovist 200 after the balloon catheter has been inserted; otherwise, the mixture may have to be discarded if the insertion proves difficult.

An assistant slowly instills the fluid in portions through the balloon catheter into the uterine cavity. Only about 2–3 mL of contrast medium is needed to define the uterine cavity, which is scanned in longitudinal and transverse planes (Fig. 33.**5**). The examiner can systematically survey and evaluate the uterus by rotating and angling the endovaginal probe. Abnormalities are detected by looking for changes in the echogenic fluid layer lining the uterine cavity. If one or both intramural tubal segments are patent, the white fluid will enter the tubal ostium relatively quickly. This is seen most clearly in transverse section (Fig. 33.**6**). The flow of contrast medium can then be traced through the different portions of the tube, although this is subject to limitations. In many cases, the full length of the tube can be visualized only in multiple, separate segments. Spillage of contrast medium from the ampullary end of the tube into the peritoneal cavity confirms patency even in tubal segments that cannot be optimally visualized. Factors that are important in diagnosing *unrestricted tubal patency* are contrast spillage from the ampullary end and the distribution of contrast medium over the ovarian surface. This will not be seen if the ampulla is occluded.

On completion of the ultrasound examination, which the patient can watch on the monitor screen, the balloon catheter is deflated and removed, and the uterine cavity is reexamined. At this point the sonographer can scrutinize even the small portion of the uterine cavity that was initially obscured by the narrow acoustic shadow from the balloon catheter.

At the end of the examination, the vagina is reinspected through the speculum, and any contrast material that has refluxed from the cervix is blotted away. The patient is told that she may experience vaginal discharge or lower abdominal discomfort similar to menstrual cramps for the next 1–2 hours. The possibility of transient nausea or vomiting should also be noted. The patient is instructed to call her doctor if she experiences any unexplained complaints. She is also reassured that contrast medium that entered the abdominal cavity from the fallopian tube will be reabsorbed by the body in 6–8 hours and that, if her tube is patent, she can try to achieve pregnancy during the current cycle. Finally, the WBC is checked a second time before the patient leaves the examination suite (Table 33.**3**).

The findings of the examination are documented with representative sonograms. The assessment of tubal patency takes from 5 to 15 minutes (average 9 minutes) to complete, depending on the findings.

Table 33.3 Possible complications of hysterosalpingo-contrast sonography

- Nausea
- Vomiting
- Pelvic inflammatory disease
- Lower abdominal complaints

Evaluating the Uterus and Uterine Cavity

Evaluation of the uterus and uterine cavity is not necessarily a primary goal of HyCoSy, but it is valuable in that it can detect changes within the uterine cavity as well as changes affecting the uterine wall. Myomas, polyps, and uterine anomalies are among the lesions that may be detected as incidental findings. Changes that do not involve the uterine cavity can be detected with HyCoSy only to the extent that they are reached by the contrast medium, and so this study cannot provide additional information on changes located outside the uterine cavity.

A normal uterine cavity appears in longitudinal section as an elongated fluid column that widens at the fundal end and is convex superiorly. The uterine cavity presents smooth borders when viewed in transverse sections. From the internal os upward, it displays an increasingly broad, transverse oval shape that is drawn out into three peaks at the cornual level (Fig. 33.**7**). The intramural tubal segment appears as a short, narrow, white band with sharply defined borders.

Surface irregularities in the endometrium appear as contrast voids in the smooth outline of the echogenic fluid within the uterine cavity (Fig. 33.**8**). They rarely signify pathology.

Polyps appear as narrow-based structures of varying size projecting into the uterine cavity (Fig. 33.**9**). They should be reexamined with ultrasound after the next menstrual bleed. They display the same central echo pattern as the endometrium itself.

Myomas, on the other hand, appear as round masses that are attached to the myometrium by a sessile base of varying width. The detection of myomas located at the uterotubal junction is important in the treatment of infertility. When unfavorably positioned, these tumors may obstruct the tubal ostium. If a myoma is pedunculated, its pedicle can usually be visualized in additional planes of section, appearing as a hypoechoic filling defect within the contrast medium (Fig. 33.**10**). Detection and measurement of the tumor pedicle is important for proposed operative intervention, and the ultrasound findings can help determine whether the mass should be approached by hysteroscopy or laparotomy [15,17].

At the reflection of the bladder peritoneum, a tridentate area of high-level echoes extending into the myometrium is generally seen in patients who have had a caesarean section. Representing the scar left by the hysterotomy (Fig. 33.**11**), this feature is important only if it is broad and raises suspicion of an incompletely healed incision (Fig. 33.**12**). Often it is not detectable until after the catheter is removed, since the balloon may have obstructed the internal os and kept echogenic fluid from reaching that part of the uterus. This finding always warrants further investigation by hysteroscopy.

Uterine malformations are usually detected at routine vaginal ultrasound (Fig. 33.**13**). They can be investigated further by HyCoSy. An arcuate uterus, for example, appears as a concave feature in the fundal region that is most clearly appreciated in coronal sections of the uterus (Fig. 33.**14**). A uterine septum appears as a more or less broad and long contrast filling defect extending along the midline of the uterine cavity (Fig. 33.**15**), seen most clearly in transverse scans through the fundus. The examiner can define the extent of the septum by making slow angling movements with the endovaginal probe. Difficulties can arise in patients with a *uterus didelphys* or a *double uterus and vagina*. In these cases, a separate balloon catheter should be placed in each half of the uterus for hysterosonographic imaging (Fig. 33.**16**), and initially both parts of the uterus should be evaluated separately. At the end of the examination, Echovist 200 should be instilled simultaneously, so that both uterine cavities can be evaluated at the same time. These patients should be investigated further by laparoscopy with hysteroscopy and, if necessary, with subsequent surgical exposure. A *double uterus* does not necessarily require surgical treatment.

A condition encountered rarely in infertility patients is *Asherman syndrome*, which usually occurs after a technically flawed dilation and curettage or uterine inflammation. When this condition is present, it can be difficult to place the balloon catheter in the uterine cavity because of intrauterine adhesions. The only alternative in these cases is the somewhat more painful placement of the balloon catheter in the cervical canal. When the contrast medium is instilled, ultrasound will immediately show a nonuniform distribution of the fluid within the uterine cavity. Smoothly outlined portions of the uterus alternate with nonhomogeneous areas (Fig. 33.**17**). It is quite possible that little or no fluid can be instilled into the uterine cavity. Operative hysteroscopy should be performed if pregnancy is desired, as spontaneous pregnancy is very rarely achieved in this syndrome.

Approximately 2–3 mL of contrast medium is required to define a normal uterine cavity. A larger amount of Echovist 200 is needed to detect polyps or myomas.

Initial visualization and evaluation of the uterine cavity can also be accomplished with approximately 20 mL of physiologic saline solution. This option may be preferable for cost reasons if the examination is confined to the uterine cavity. Saline solution is not suitable for the assessment of tubal patency, however.

Evaluating the Fallopian Tube and Ovary

Evaluation of the fallopian tube should begin by assessing the intramural tubal segment, which is defined by filling the uterine cavity with Echovist 200 and allowing the fluid to enter the tube. It appears sonographically as a narrow echogenic area with smooth margins. After passing through the intramural tube, the contrast medium enters the isthmic segment and then is slowly distributed along the further course of the tube. This process can be followed in the real-time display as the narrow white band of contrast medium progressively fills the more distal tubal segments (Fig. 33.**18**). Since the full length of the tube cannot always be defined in one image, it is often necessary to scan the tubal segments in succession in order to track the fluid. If a relatively long portion of the tube can be visualized in one plane, the movement of the fluid column, approximately 1 mm wide, can be demonstrated along the tube (Fig. 33.**19**). If only small portions of the tube can be defined at one time, the bright punctate echo of intraluminal contrast medium can be tracked laterally to the ampulla by continually adjusting the scanning plane [18–21].

In patients with an *intramural tubal occlusion*, the instilled contrast medium slowly fills and distends the uterine cavity, and some material may reflux into the vagina, as the balloon catheter cannot adequately occlude the internal os due to the expanding intrauterine fluid collection (Fig. 33.**20**). The great majority of women in this situation report increasing pain, which can be alleviated by reaspirating some of the instilled fluid. Contrast medium can then be reinstilled in an attempt to flush out any mucosal polyps or endometrial tissue that may be obstructing the tubal ostium. This maneuver should not be tried too often and should be continued only depending on pain tolerance. If the maneuver has not succeeded after about 5 minutes, the examination should be terminated. If the intramural occlusion is unilateral, the contrast fluid will be able to escape through the patent side and will not cause uterine distension.

If the Echovist 200 does not enter the tested fallopian tube right away, it is advisable to evaluate the contralateral tube in order to gain time. It is known that a *physiologic tubal spasm* may occur, often resulting in a delay of up to 5 minutes before contrast medium can be detected in the intramural tubal segment. So far, there have been no reports of this delay exceeding 5 minutes. If the examination were to be stopped too soon, it would result in a false-positive diagnosis of intramural tubal occlusion.

With a *patent ampullary tubal segment*, the fluid will gradually drain from the fimbriated end and can be demonstrated as a funnel-shaped

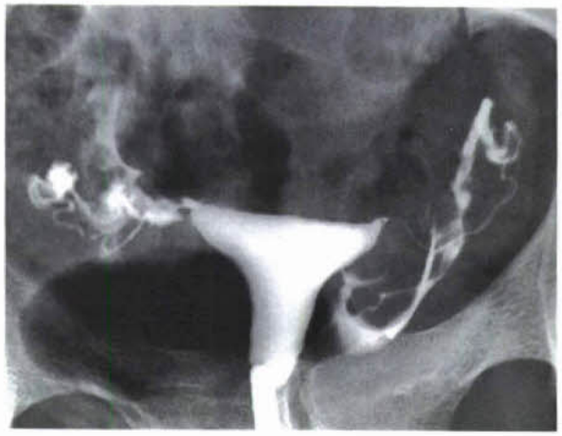

1

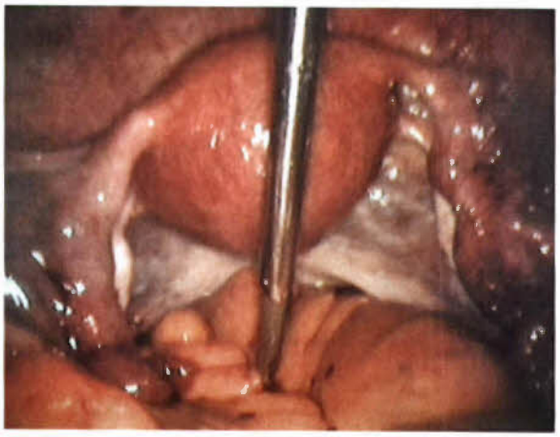

2

Fig. 33.1 Visualization of the uterus and adnexa by hysterosalpingo-contrast sonography.

Fig. 33.2 Laparoscopic evaluation of the uterus and adnexa.

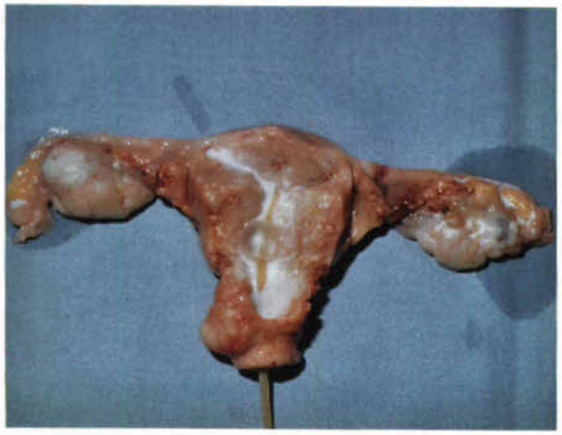

3

4

Examination Technique

Fig. 33.3 Position of the balloon catheter and contrast medium illustrated in a surgical specimen.

Fig. 33.4 Echovist 200 with mini-spike and disposable syringe. The galactose solution is on the right, the galactose granulate on the left.

5

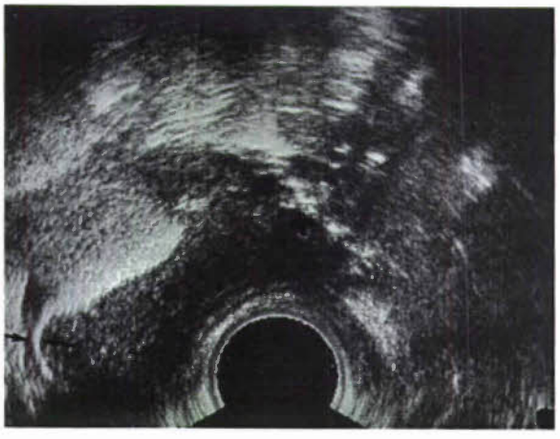

6

Evaluating the Uterus and Uterine Cavity

Fig. 33.5 Longitudinal scan of the uterus with the balloon catheter in place and Echovist 200 in the uterine cavity.

Fig. 33.6 Transverse scan through the fundal region, showing a patent intramural tubal segment (—).

7

8

Fig. 33.7 Oblique scan through the uterine corpus, illustrating the three-peaked configuration of the uterine cavity.

Fig. 33.8 Longitudinal scan of the uterus, showing a nonhomogeneous mucosal structure (—).

Fig. 33.9 Sessile endometrial polyp (P).

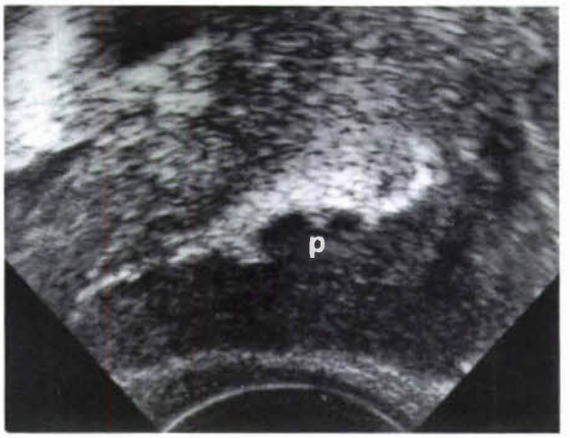

9

Fig. 33.10 A large intracavitary myoma (M) adjacent to the intramural, patent right uterotubal junction (⟩).

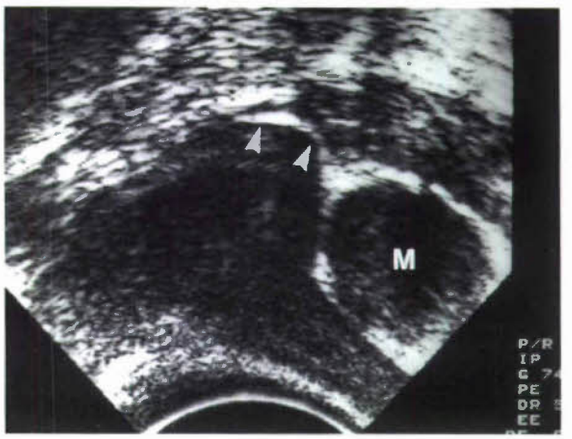

10

Fig. 33.11 A normal-appearing scar from a cesarean section (⟩).

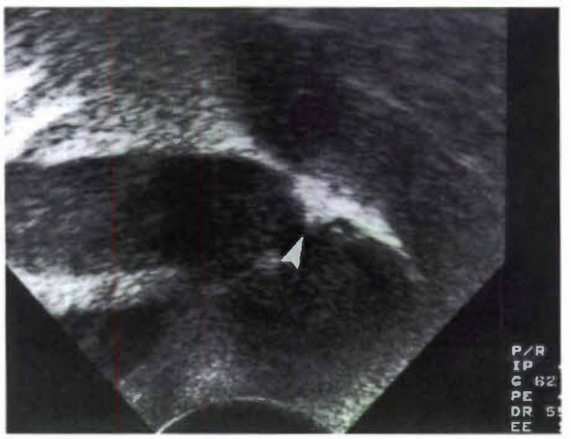

11

Fig. 33.12 An abnormally broad caesarean section scar, consistent with incomplete healing (⟩).

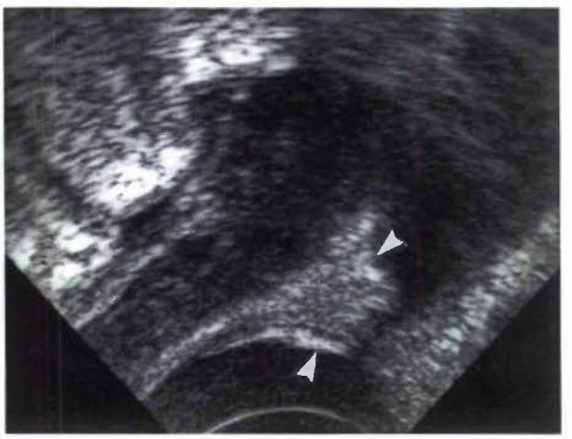

12

Fig. 33.13 Transvaginal scan of a septate uterus with double mucosal echoes (1 and 2).

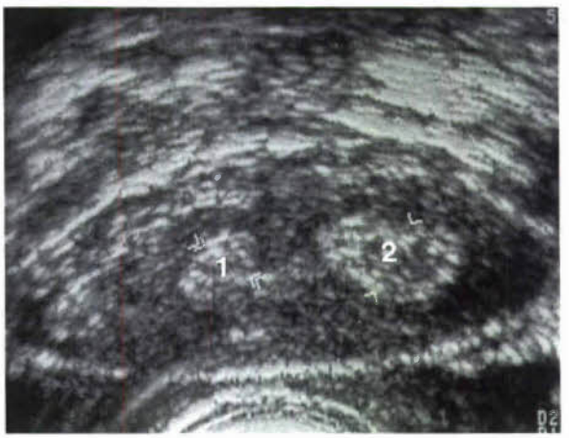

13

Fig. 33.14 Arcuate uterus, with patent intramural and isthmic tubal segments on both sides (—).

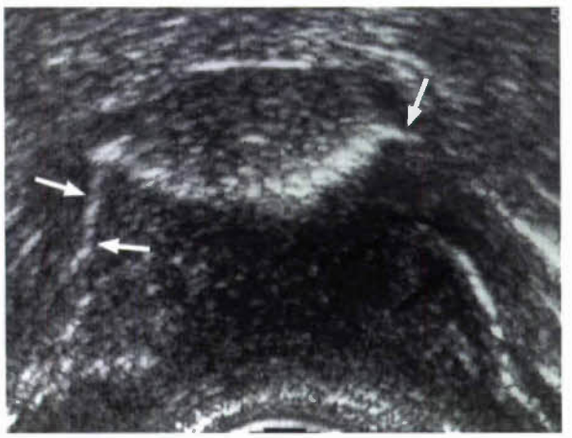

14

Fig. 33.15 Uterine septum (S) in longitudinal section.

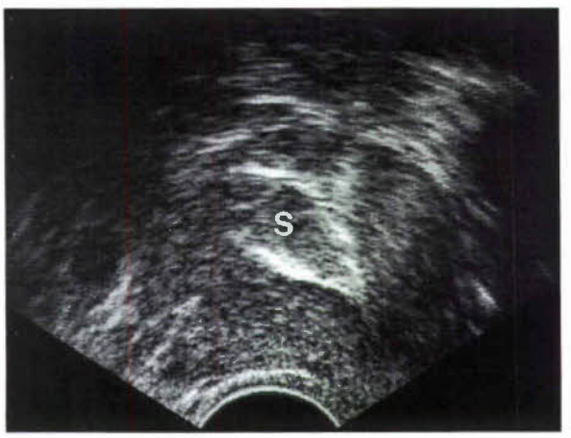

15

Fig. 33.16 Double uterus, with Echovist echoes in each uterine cavity (1 and 2).

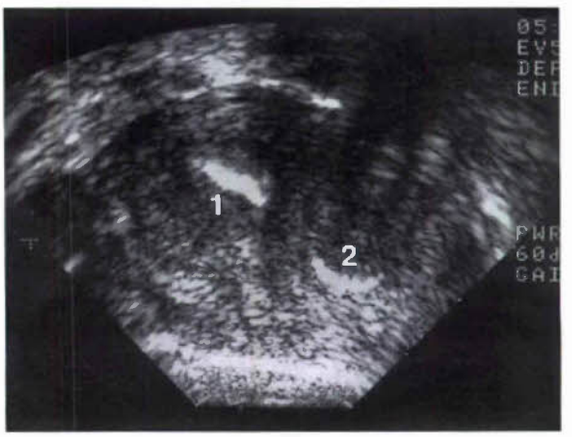

16

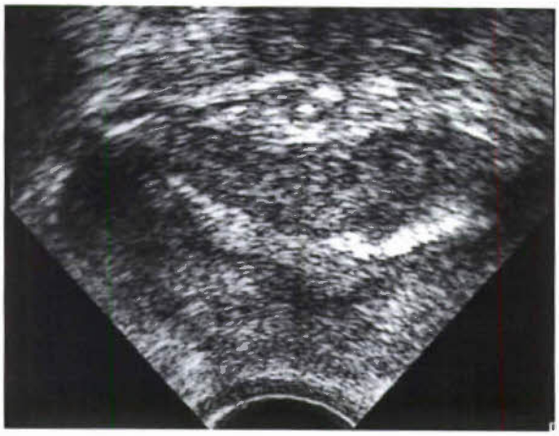

17a

17b

Fig. 33.17 Asherman syndrome.
a Transvaginal sonogram.
b Appearance after contrast instillation. The nonhomogeneous echo on the right side (A) should be noted.

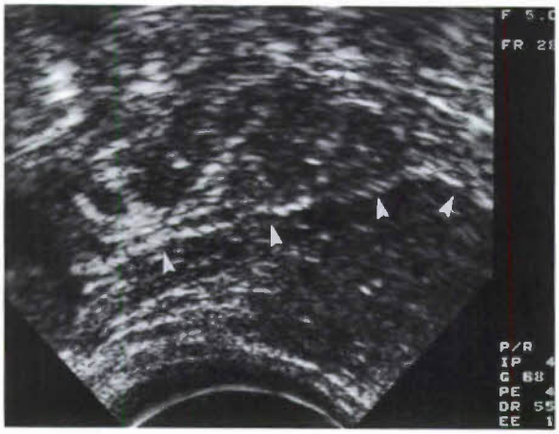

18

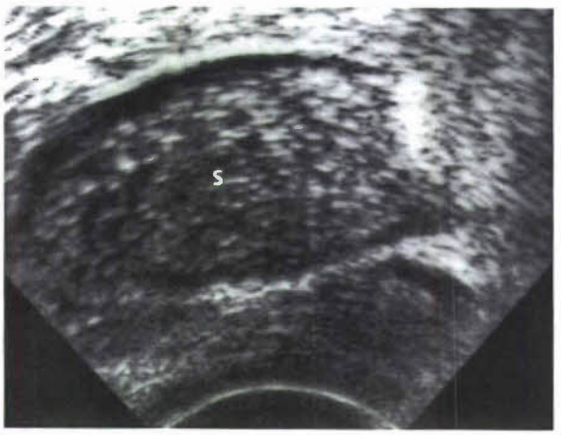

19

Evaluating the Fallopian Tube and Ovary

Fig. 33.18 Scan defining all portions of the fallopian tube (→).

Fig. 33.19 Sactosalpinx (S) partially filled with ultrasound contrast medium.

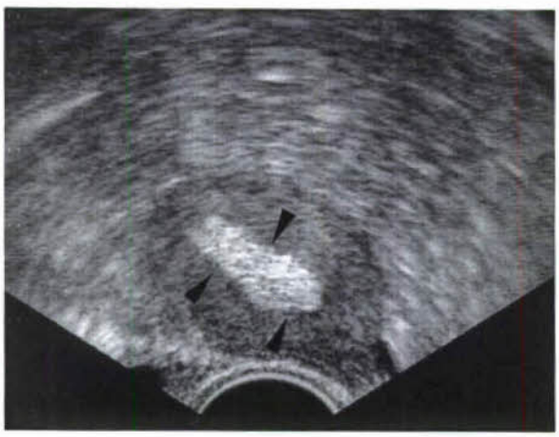

20

21

Fig. 33.20 Dilation of the uterine cavity (↑) due to bilateral intramural tubal occlusion.

Fig. 33.21 Ampullary end of the fallopian tube (black arrow), with contrast medium distributed around the ovary (→).

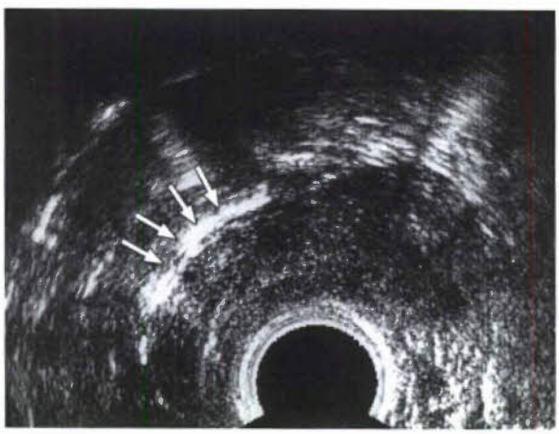

22

23

Fig. 33.22 Contrast medium in the cul-de-sac (↕).

Fig. 33.23 Sactosalpinx (S) with distension of the ampullary tubal segment (↑). Contrast medium and free fluid are visible in the ampulla.

echogenic area surrounding the ovary (Fig. 33.**21**). If this is not observed, it should be assumed that there are adhesions in the ampullary segment that restrict tubal mobility. A peripheral tubal occlusion should also be considered. Finally, the contrast medium can be identified as a hyperechoic deposit in the cul-de-sac (Fig. 33.**22**). If Echovist 200 is found in the cul-de-sac but has not been detected in the various tubal segments, its presence in the cul-de-sac does not constitute proof of tubal patency, since a fistula in an occluded tube can produce the same result.

In cases with *ampullary phimosis* of the tube, the ampulla is expanded allowing whole drops of the instilled contrast medium to spill into the peritoneal cavity.

With *sactosalpinx*, ultrasound shows a globular expansion of the tubal ampulla with no drainage of contrast medium into the cul-de-sac (Fig. 33.**23**). If free fluid was present in the tube before the examination, the echogenic contrast medium entering the tube will gradually mix with the fluid already present. The additional fluid volume entering the tube can no longer be reaspirated and may cause stretch pain and local irritation. Experience has shown that it is worthwhile to prescribe an analgesic and/or antibiotic in this situation.

The volume of contrast medium needed to evaluate both fallopian tubes is approximately 2–5 mL. Combined with the amount needed to define the uterine cavity, the contents of a 15 mL bottle of Echovist 200 are sufficient for a complete examination without Doppler flow sampling. The agreement between the results of HyCoSy and those of conventional hysterosalpingography or chromolaparoscopy is in the range of 91.3–94.4%, which is better than that between hysterosalpingography and chromolaparoscopy (75–85%).

There are factors that can limit the quality of fallopian tube assessment by ultrasound contrast hysterosalpingography. The main limiting factors, encountered in 2.9% of cases, are obesity, significant adhesions, or fallopian tubes that are fixed high in the true pelvis. Stenosis of the cervical canal following an operation on the cervix can completely prevent an ambulatory tubal assessment.

Adjunctive Techniques

Adjunctive but not essential techniques for the assessment of tubal patency are Doppler and color Doppler scanning and three-dimensional (3D) ultrasound. Doppler flow sampling provides additional information on tubal patency, while 3D ultrasound permits only an enhanced evaluation of various organ structures.

Doppler ultrasound can be used to resolve any doubts that the examiner may have about unrestricted tubal patency. The use of color Doppler affords few if any advantages over gray-scale Doppler. If the sample volume is not optimally positioned or if the flow velocity setting on the ultrasound scanner has been set too high, the color signals will be more troublesome than useful during the examination [22–24].

To assess tubal patency with Doppler, the sample volume is positioned over a tubal segment close to the uterus and spectra are recorded during the continuous instillation of contrast medium. If the fallopian tube is patent at that location, the Doppler spectral waveform will rise quickly to a plateau and will not return to baseline until the intrauterine fluid instillation is stopped (Fig. 33.**24**). If the sampled tube is occluded, the waveform will fall off rapidly after an initial rise [17,25,26]. When the sample volume is placed over a far lateral tubal segment in a hypoplastic tube, an undulating spectrum is recorded. This waveform is caused by tubal segments with normal wall musculature alternating with segments that have little or no musculature (Fig. 33.**25**).

Doppler ultrasound is of little value in cases with a suspected ampullary tubal occlusion. Normal waveforms may be recorded despite the peripheral occlusion of both tubes, and the flow signal disappears only after the rising pressure resistance in the lateral portion of the tube prevents additional fluid inflow [15,26]. Because a sactosalpinx can easily hold 10 mL or more of fluid, the attainable information gain of 1.5–2.3% does not justify the costs incurred by the extra bottle of Echovist 200 that is usually required. Based on experience to date, no more than two bottles of the solution should be used for one examination.

3D ultrasound is a technique in which images are rendered based on the acquisition and storage of volume data (Figs. 33.**26**, 33.**27**). Every image that is acquired can be postprocessed to generate an enhanced view of abnormalities. This technique is of particular interest for investigating intrauterine lesions such as polyps and myomas. Small pedicles and other changes previously difficult to evaluate can be brought out in greater detail. 3D ultrasound can also supply additional information on changes in the ampullary tubal segment. With 4D ultrasound the filling of the uterine cavity and of the tubes can be observed in real time in all three dimensions.

Advantages of Hysterosalpingo-contrast Sonography in Routine Applications

Ultrasound contrast hysterosalpingography offers several advantages over conventional hysterosalpingography and chromolaparoscopy. The examination causes little discomfort. More than 90% of women examined claim that the pain associated with the tubal contrast examination is less than their menstrual pain. The placement and inflation of the balloon catheter is described as somewhat more painful than the contrast examination itself. Adnexal inflammation or a higher-than-normal WBC 48 hours after HyCoSy has been reported in just 0.5% of cases. Nausea, vomiting, and uterine bleeding are rare after examination with Echovist 200.

The ability to watch the examination on the monitor can be a significant factor in the patient's desire to have a child. The very act of seeing her own internal genital organs, which generally are viewed only in the form of an anatomical diagram, can be of psychological benefit, especially if the patient learns that one or both of her tubes are patent and do not pose an anatomical barrier to conception. Witnessing a normal result can positively affect the somewhat obsessive wish for a child that some patients may have. It may be that the unconscious desire to have a child is transformed over time into a desire to be able to become pregnant. It is known that many women with a history of "idiopathic" infertility become pregnant only after they have given up their desire to achieve pregnancy.

The number of spontaneous pregnancies that occur after ultrasound contrast hysterosalpingography underscores the impression of a psychological benefit from HyCoSy. A total of 37.3% of surveyed women with at least one patent tube became pregnant within the first 12 months after their tubal examination. The pregnancy rate during the first three months after HyCoSy was relatively high, at 22.9%. Another 45.9% became pregnant within 7–12 months after HyCoSy, and 31.2% within 4–6 months. The spontaneous abortion rate of 13.4% during the first 12 weeks of gestation is within normal limits (Table 33.**4**).

There are no reported cases of pregnancy occurring after the sonographic diagnosis of bilateral tubal occlusion or the unilateral occlusion of a single tube. Different authors have described a wide range of pregnancy rates following conventional hysterosalpingography or chromo-

Table 33.**4** Pregnancy rates within 12 months after outpatient hysterosalpingo-contrast sonography and spontaneous abortion rates during the first 12 gestational weeks

• Pregnancies in months 1–3	22.9%
• Pregnancies in months 4–6	31.2%
• Pregnancies in months 7–12	45.9%
• Abortion rate up to 12th week	13.4%

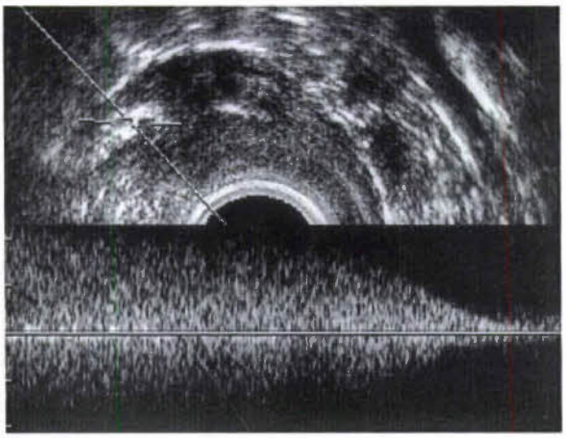

24

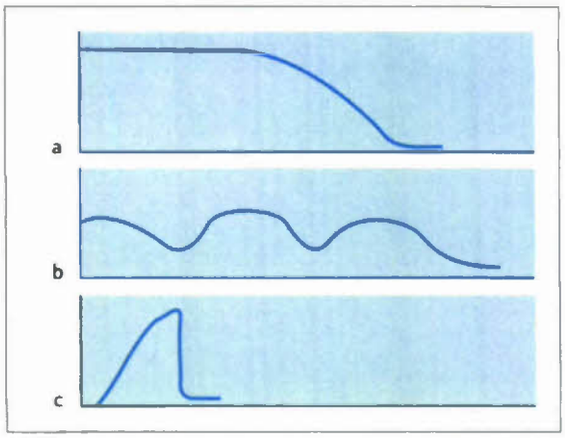

25

Adjunctive Techniques

Fig. 33.**24** Doppler spectrum characteristic of tubal patency.

Fig. 33.**25** Doppler spectral waveforms characteristic of tubal patency (**a**), tubal hypoplasia (**b**), and tubal occlusion (**c**).

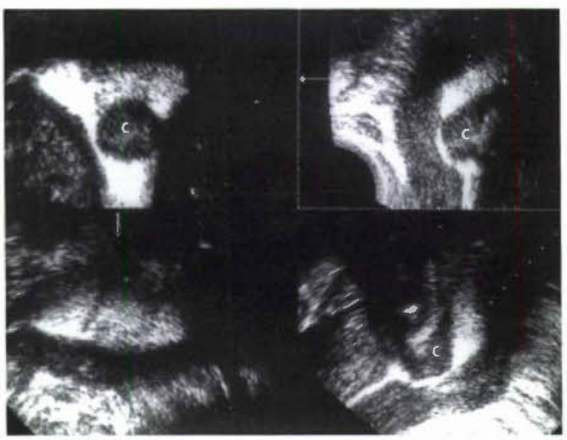

26

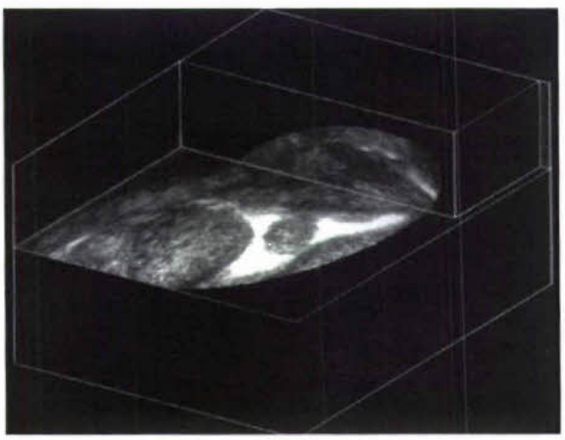

27

Fig. 33.**26** 3D image of a uterine cavity in the coronal, sagittal, and transverse planes, showing the balloon catheter (C) in place.

Fig. 33.**27** 3D display of the balloon catheter within the uterine cavity.

laparoscopy [7,14,27, 28], with reports ranging from "rare" to approximately 50%. The data from our own cases indicate a pregnancy rate of 26.1% after conventional hysterosalpingography and 27.3% after chromolaparoscopy, which are well below the rates following HyCoSy.

Hysterosalpingo-contrast sonography is an outpatient examination that is an important addition to conventional methods for assessing tubal patency. In patients being treated for infertility, it can be used to determine whether the tubes are patent before the patient is referred for intensive hormonal therapy in the form of tablets or injections. If HyCoSy confirms tubal patency but pregnancy does not occur within 12–18 months, the condition of the tubes should then be evaluated by chromolaparoscopy. On grounds of radiation exposure alone, conventional hysterosalpingography should no longer be recommended for the assessment of tubal patency [15].

HyCoSy will continue to rank behind chromolaparoscopy for tubal assessment, however, mainly because abnormalities in the true pelvis, such as changes in the tubal wall, the tubal collection mechanism, tubal motility, and existing adhesions can be visualized and evaluated better with chromolaparoscopy than with ultrasound. The advantage of HyCoSy is that it is well tolerated and can be used at frequent intervals during a protracted course of infertility therapy. It should not, however, be applied less critically than any other method.

References

1 Lüning M, Felix R. Komplexe bildgebende Diagnostik: Becken. Stuttgart: Thieme, 1994.
2 Mitri FF, Andronikou AD, Perpinyal S. A clinical comparison of sonographic hydropertubation and hysterosalpingography. Br J Obstet Gynaecol 1991;98:1031–6.
3 Naether OGJ. Different methods to diagnose tubal patency. Gynaecol Snapshot 1994;2:12–4.
4 Randolph JF Jr, Ying YK, Maier DB, Schmidt CL, Riddick DH. Comparison of real-time ultrasonography, hysterosalpingography and laparoscopy/hysteroscopy in the evaluation of uterine abnormalities and tubal patency. Fertil Steril 1986;46:828–32.
5 Balen FG, Allen CM, Lees WR. Ultrasound contrast agents. Clin Radiol 1994;49: 77–82.
6 Degenhardt F, Jibril S, Eisenhauer B, Schlösser HW. Die ambulante Hystero-Salpingo-Kontrastsonographie (HKSG) als Möglichkeit zur Kontrolle der Tubendurchgängigkeit. Geburtshilfe Frauenheilkd 1995;55:143–149.
7 Schlief R. Physikalisch-pharmakologische Eigenschaften, Ergebnisse klinischer Prüfungen und Anwendungspotentiale eines neuartigen Ultraschall-Kontrastmittels. In: Gockel HP, editor. Jahrbuch der Radiologie. Münster, Germany: Wissenschaftliche Verlagsgesellschaft Regensberg & Biermann, 1988: 163–170.
8 Schlief R. First steps in ultrasound contrast media. In: Felix R, editor. Contrast media from the past to the future: symposium Berlin, 27–28th March, 1987. Stuttgart: Thieme, 1989.
8a Boudghene FP, Bazot M, Robert Y, Perrot N, Rocourt N, Antoine JM, Morris H, Leroy JL, Uzan S, Bigot JM. Assessment of Fallopian tube patency by HyCoSy: comparison of a positive contrast agent with saline solution. Ultrasound Obstet Gynecol. 2001;18:525–30.
8b Exacoustos C, Zupi E, Carusotti C, Lanzi G, Marconi D, Arduini D. Hysterosalpingo-contrast sonography compared with hysterosalpingography and laparoscopic dye pertubation to evaluate tubal patency. J Am Assoc Gynecol Laparosc. 2003;10:367–72.
9 Bonilla-Musoles F. An assessment of hysterosalpingography (HSG) as a diagnostic tool for uterine cavity defects and tubal patency. J Clin Ultrasound 1992;20:175–81.
10 Fayez JA, Mutie G, Schneider PJ. The diagnostic value of hysterosalpingography and hysteroscopy in infertility investigation. Am J Obstet Gynecol 1987;156:558–60.
11 Böhmes S, Degenhardt F, Gohde M, Schneider J. Ambulante vaginosonographische Durchgängigkeitsprüfung der Eileiter mit der Hysterosalpingo-Kontrastsonographie (HKSG). Fertilität 1992;8:62–5.
12 Degenhardt F. Die Hystero-Kontrast-Sonographie (HKSG) – eine neue Alternative zur Kontrolle der Tubendurchgängigkeit? Zentralbl Gynäkol 1991;113:799–801.
13 Grünberges V, Ulm R. Diagnostische Methoden in Geburtshilfe, Gynäkologie sowie gynäkologischer Endokrinologie. Stuttgart: Thieme, 1986.

14 Riedo R, Cavin C, Samartzis S, Enz O, Hauser GA. Abklärung der Therapieergebnisse bei tubarer Sterilität. Ther Umsch 1987;44:383–90.
15 Degenhardt F. Vaginal hysterosalpingo-contrast-sonography (HyCoSy) in sterility investigations: an outpatient procedure. Gynaecol Snapshot 1994;2:15–7.
16 Degenhardt F, Jibril S, Eisenhauer B, Gohde M, Schlösser HW. Vaginal hysterosalpingo-contrast sonography. Br Med Ultrasound Soc Bull 1993;1:36–7.
17 Degenhardt F. Endosonographie in Gynäkologie und Geburtshilfe. Atlas und Handbuch für Praxis und Klinik. Stuttgart: Wissenschaftliche Verlagsgesellschaft, 1994.
18 Deichert U, Schlief R. Die Abklärung der Tubendurchgängigkeit mittels Kontrastsonographie. Fortschr Diagn 1990;3:15–17.
19 Deichert U, van de Sandt M. Transvaginal hysterosalpingo-contrast-sonography (HyCoSy): the assessment of tubal patency and uterine abnormality by contrast enhanced sonography. Adv Echo-Contrast 1993;55–8.
20 Schlief R, Deichert U. Hysterosalpingo-contrast sonography of the uterus and fallopian tubes: results of a clinical trial of a new contrast medium in 120 patients. Radiology 1991;178:213–5.
21 Venezia R, Zangara C. Echohysterosalpingography: new diagnostic possibilities with S HU 454 Echovist. Acta Eur Fertil 1991;22:279–82.
22 Deichert U, Schlief R, van de Sandt M, Göbel R, Daume E. Transvaginale Hysterosalpingo-Kontrastsonographie (HKSG) im B-Bild-Verfahren und in der farbcodierten Duplexsonographie zur Abklärung der Tubenpassage. Geburtshilfe Frauenheilkd 1990; 50:717–21.
23 Stern J, Peters A, Coulam CB. Colour Doppler ultrasonography assessment of tubal patency: a comparison study with traditional techniques. Fertil Steril 1992;58: 897–900.
24 Yarali H, Gurgan T, Erden A, Kisnisci HA. Colour Doppler hysterosalpingography: a simple and potentially useful method to evaluate Fallopian tube patency. Hum Reprod 1994;9:64–6.
25 Deichert U, Schlief R, van de Sandt M, Daume E. Transvaginal hysterosalpingo-contrast sonography for the assessment of tubal patency with gray scale imaging and additional use of pulsed wave Doppler. Fertil Steril 1992;57:62–7.
26 Hüneke B, Lindner C, Brändle W. Untersuchung der Tubenpassage mit der vaginalen gepulsten Kontrastmittel-Doppler-Sonographie. Ultraschall Klin Prax 1989;4:192–8.
27 Krysiewicz S. Infertility in women: diagnostic evaluation with hysterosalpingography and other imaging techniques. AJR Am J Roentgenol 1992;159:253–61.
28 Schürmann R, Schlief R. Transvaginale Hysterosalpingo-Kontrastsonographie mit Echovist®: Ein neues Verfahren zur Diagnostik von Tubendurchgängigkeit und Uterusanomalien. In: Ertan AK u. Schmidt W, eds. Jahrbuch der Gynäkologie und Geburtshilfe. Zülpich, Germany: Biermann, 1993: 211–216.

34 Use of Transvaginal Ultrasound to Guide Needle Procedures in the True Pelvis

Puncture Technique

The transvaginal ultrasound-guided puncture of structures in the true pelvis has several advantages over ultrasound-guided transabdominal puncture (Table 34.**1**). The main advantage is the short needle path from the vaginal floor to the targeted structure (approximately 2–4 cm), which is considerably shorter than the distance from the abdominal wall. The risk of infection is also lower, because the needle does not have to traverse the full bladder, as in a transabdominal puncture. Bacterial colpitis must be excluded, however, before a transvaginal puncture is performed.

A transabdominal puncture carries a high risk of bowel injury when intra-abdominal adhesions are present. However, a transvaginal puncture can usually be performed without difficulty in these cases, since the bowel is located above the targeted structure.

Two main techniques are available for carrying out a transvaginal puncture under sonographic guidance; the procedure can be performed manually or with the aid of an automated puncture device.

In a *manual puncture*, the needle is advanced by hand through a needle guide attached to the transducer (Fig. 34.**1**). The puncture is carried out with the patient under intravenous sedation or local anesthesia, due to the pain caused by the manual needle movements.

When an *automated puncture device* is used (Figs. 34.**2**, 34.**3**), there is no need for premedication or analgesics [1] (Table 34.**2**). At the touch of a button, the spring-loaded needle is advanced along the electronic sight-line to the designated depth at such a high velocity that the patient feels a brief pressure sensation, but no pain. The desired penetration depth is read from the monitor in the form of markings along the superimposed sight-line (Fig. 34.**4**); it is then set on the puncture device itself in millimeter increments (Fig. 34.**5**). This ensures that the needle will advance precisely to the desired depth with minimal tissue trauma.

In preparation for the puncture, the transducer probe is sheathed in a sterile condom, and the sterile automated puncture device is mounted on the probe. With the device attached and secured, the examiner spreads the labia apart and carefully inserts the probe into the vagina, positioning the tip in the left or right fornix (Fig. 34.**6**).

The main disadvantages of automated puncture are that the cost of the equipment is relatively high and some experience is needed in handling the device (Table 34.**2**).

Table 34.**1** Advantages of transvaginal puncture over transabdominal puncture

- Shorter path to the target (only 2–4 cm)
- Less pain
- Less risk of infection
- Less risk of bowel injury

Table 34.**2** Advantages and disadvantages of manual and automated transvaginal puncture

	Manual puncture	Automated puncture
Advantages	• Greater freedom of movement • Multiple successive targets can be reached with one puncture	• Precision • Little or no pain, eliminating the need for premedication or sedation • Minimal tissue trauma
Disadvantages	• Less precise • Painful, requiring intravenous sedation	• Relatively high purchase costs • Learning curve for operating the automated puncture device

Transvaginal Follicular Aspiration

Owing to the general advantages of transvaginal punctures (with the outpatient setting and a shorter path from the vaginal fornix to the ovaries), ultrasound-guided transvaginal follicular aspiration [2–8] has largely superseded other techniques of oocyte collection such as laparoscopic follicular aspiration [9], ultrasound-guided transabdominal-transvesical aspiration [10–13], and transurethral–transvesical aspiration [13,14].

Transvaginal follicular aspiration is usually conducted with the patient in a gynecologic chair. The vagina is initially irrigated with NaCl. The ultrasound probe, sheathed in a sterile condom and with the needle guide attached, is then introduced into the vagina (Fig. 34.**6**). The follicles are targeted using the sight-line superimposed on the monitor and are successively aspirated (Fig. 34.**7**). If an ovary is located so high that the follicles cannot be reached transvaginally, it is necessary either to limit the aspiration to follicles on the accessible ovary or to switch to a transabdominal puncture. If the ovary is fixed behind the uterus by adhesions and is not accessible from the lateral fornix via the transvaginal route, it may still be possible to retrieve oocytes using a transvaginal–transuterine approach.

Transvaginal ultrasound-guided follicular aspiration is comparable to conventional laparoscopic or transvesical follicular aspiration in terms of retrieval rates as well as fertilization and pregnancy rates (Table 34.**3**).

The potential complications of transvaginal follicular aspiration [7,8, 8a,15,15a,16,16a] include pelvic inflammatory disease and intra-abdominal bleeding caused by vascular injury in the true pelvis. It is important to avoid the puncture of a large vessel, which may be mistaken for a follicle in cross-section, as this can cause profuse intra-abdominal bleeding that would necessitate an emergency laparotomy.

Table 34.**3** Rates of oocyte retrieval by various routes (adapted from Feldberg et al. [21])

	Laparoscopic oocyte retrieval	Transvesical oocyte retrieval	Transvaginal oocyte retrieval
Oocytes retrieved per patient	6.4 ± 0.9 (SD)	6.2 ± 0.3(SD)	5.7 ± 0.6(SD)
Retrieval rate per follicle	93%	86%	82%
Fertilization rate	73.6%	72.3%	70.9%
Pregnancy rate per transfer	26.6%	26.7%	25.9%

Transvaginal Aspiration of Cysts

Although it is a low-risk procedure, the transvaginal aspiration of cysts still requires strict patient selection criteria and a preliminary assessment of laboratory parameters (blood count, coagulation).

Transvaginal aspiration is mainly indicated for simple, unilocular ovarian cysts that show no sonographic signs of malignancy. Equivocal lesions – particularly multilocular ovarian masses of indeterminate nature and tumors strongly suspicious for carcinoma – are a contraindication to transvaginal puncture [17].

There are three main types of candidate for this procedure:

- Young women with persistent or very painful functional ovarian cysts
- Patients with multiple previous operations
- Older women with a high medical risk

Because the risk of a malignant tumor in women under 40 years of age is only 1.8 per 100000 women per year [18], transvaginal cyst aspiration [1,18,19,19a] is a good option for young women as an initial invasive therapeutic procedure before pelviscopic removal or laparotomy is performed. Women who have already had multiple previous abdominal operations will often decline another operation to remove a cyst. Transvaginal cyst aspiration can be offered to these women as a means of avoiding another operation in at least a certain percentage of cases. Transvaginal aspiration also provides a minimally invasive option in older women with a poor medical risk for diagnostic surgery under general anesthesia. When used with an automated puncture device, the procedure is painless and can be done without premedication or analgesia [1].

The puncture procedure can be carried out on an ordinary examination table or in a gynecologic chair. First the vagina is prepared with a povidone–iodine solution. The ultrasound probe is sheathed in a sterile condom, the automated puncture device is mounted on the probe, and the assembly is inserted into the vagina. The necessary puncture depth is measured on the monitor, the needle is fired precisely to the center of the cyst (Figs. 34.**8**–34.**19**), and the cyst contents are aspirated with a suction tube. The cyst fluid is then evaluated for quantity, color, and consistency (Figs. 34.**13**, 34.**15**, 34.**17**, 34.**19**) and, depending on the clinical question, is sent for cytologic and/or bacteriologic testing and hormonal analysis.

The recurrence rate of cysts following transvaginal cyst aspiration is approximately 33% [1].

A transvaginal ultrasound-guided aspiration can also be performed in endometriomas [19b,19c]. However the risk of recurrence is high.

Transvaginal Aspiration of Ascites

In women with a history of multiple abdominal operations or known intra-abdominal adhesions, the transabdominal aspiration of ascites for tumor cell detection may be associated with a high risk of bowel injury. In such cases the ascites can be safely aspirated from the cul-de-sac under sonographic guidance using a transvaginal needle [19] (Fig. 34.**20**). Transvaginal aspiration is particularly suitable for smaller volumes of ascites.

Transvaginal Tissue Biopsy

Just as an ovarian cyst can be aspirated without difficulty under transvaginal ultrasound guidance, a biopsy punch or special biopsy needles can be directed by transvaginal ultrasound to take tissue samples from solid masses in the true pelvis [19,20,22] (Fig. 34.**21**). This technique is used to detect solid recurrent tumors on the pelvic wall (recurrence of cervical carcinoma) or evaluate suspicious nodules behind the vaginal stump.

As in cyst aspiration, the distance to the suspicious tissue area is first measured by vaginal ultrasound, and the biopsy needle is then fired to the center of the mass under sonographic vision (Fig. 34.**22**). As the procedure can be carried out with intravenous sedation using an automated biopsy punch, it is particularly suitable for older patients who would be poor candidates for general anesthesia. The tissue cores obtained with the biopsy needle provide adequate material for histologic examination.

References

1 Merz E, Macchiella D, Bahlmann, F Weber, G. Transvaginale Punktion von Ovarialzysten ohne Narkose. Ultraschall Klin Prax 1992;7:195
2 Argiriou C, Popp LW, Abd-El-Maeboud K, Mettler L, Semm K. Ultrasound-guided follicular puncture: results and experience [abstract]. In: Abstracts from the 4th Annual Meeting of the European Society of Human Reproduction and Embryology, Barcelona, Spain, July 1988. Hum Reprod 1988;3(Suppl 1):41.
3 Baber R, Porter R, Picker R, Robertson R, Dawson E, Saunders D. Transvaginal ultrasound directed oocyte collection for in vitro fertilization: success and complications. J Ultrasound Med 1988;7:377–9.
4 Feichtinger W, Kemeter P. Transvaginal sector scan sonography for needle guided transvaginal follicle aspiration and other applications in gynecologic routine and research. Fertil Steril 1986;45:722–5.
5 Kemeter P, Feichtinger W. Trans-vaginal oocyte retrieval using a trans-vaginal sector scan probe combined with an automated puncture device. Hum Reprod 1986;1:21–4.
6 Merz E, Bartzke G, Kunz K, Schommer M. Transvaginal oocyte retrieval using an automatic puncturing device: initial results [abstract]. In: Abstracts from the 4th Annual Meeting of the European Society of Human Reproduction and Embryology, Barcelona, Spain, July 1988. Hum Reprod 1988;3(Suppl 1):41.
7 Michelmann HW, Tinneberg HR, Weisner D, Mettler L. Die transvaginale ultraschallkontrollierte Follikelpunktion im Rahmen der menschlichen In-vitro-Fertilisation. Geburtshilfe Frauenheilkd 1987;47:619–22.
8 Wikland M, Enk L, Hammarberg K, Nilsson L. Use of a vaginal transducer for oocyte retrieval in an IVF/ET program. J Clin Ultrasound 1987;15:245–51.
8a Bennett SJ, Waterstone JJ, Cheng WC, Parsons J. Complications of transvaginal ultrasound-directed follicle aspiration: a review of 2670 consecutive procedures. J Assist Reprod Genet. 1993;10:72–7.
9 Steptoe PC, Edwards RG. Laparoscopic recovery of preovulatory human oocytes after priming of ovaries with gonadotrophins. Lancet 1970;i:683–9.
10 Habermann PG, Hünlich T, Siebzehnrübl E, Trotnow S. Die ultraschallkontrollierte Follikelpunktion in der "Zwei-Instrumente-Technik." Ultraschall 1986;7:179–82.
11 Lenz S. Ultrasonically guided aspiration of human oocytes. Ultrasound Med 1984; 10:625–8.
12 Wikland M, Nilsson L, Hannson R, Hamberger L, Janson PO. Collection of human oocytes by the use of sonography. Fertil Steril 1983;39:603–8.
13 Wikland M, Hamberger L, Enk L, Nilsson L. Sonographic techniques in human in-vitro fertilization programmes. Hum Reprod 1988;3(Suppl 2):65–8.
14 Parsons J, Riddle A, Brooker M, Sharma V, Goswamy R, Wilson L, et al. Oocyte retrieval for in-vitro fertilization by ultrasonically guided needle aspiration via the urethra. Lancet 1985;i:1076–7.
15 Evers JL, Larsen JF, Gnany GG, Sieck UV. Complications and problems in transvaginal sector scan-guided follicle aspiration. Fertil Steril 1988;49:278–82.
15a Almog B, Rimon E, Yovel I, Bar-Am A, Amit A, Azem F. Vertebral osteomyelitis: a rare complication of transvaginal ultrasound-guided oocyte retrieval. Fertil Steril. 2000; 73:1250–2.
16 Howe RS, Wheeler C, Mastroianni L, Blasco L, Tureck R. Pelvic infection after transvaginal ultrasound guided ovum retrieval. Fertil Steril 1988;49:726–8.
16a El-Shawarby S, Margara R, Trew G, Lavery S. A review of complications following transvaginal oocyte retrieval for in-vitro fertilization. Hum Fertil. 2004;7:127–33.
17 De Crespigny LC, Robinson HP, Davoren RAM, Fortune D. The "simple" ovarian cyst. Br J Obstet Gynaecol 1989;96:1035–9.
18 Granberg S, Crona N, Enk L, Hammarberg K, Wikland M. Ultrasound-guided puncture of cystic tumors in the lower pelvis of young women. J Clin Ultrasound 1989;17: 107–11.
19 Merz E. Vaginosonographisch gesteuerte Punktionen im kleinen Becken. In: Merz E, editor. Vaginosonographie. Stuttgart: Enke, 1992.
19a Zanetta G, Lissoni A, Torri V, Dalla Valle C, Trio D, Rangoni G, Mangioni C. Role of puncture and aspiration in expectant management of simple ovarian cysts: a randomised study. BMJ. 1996;313:1110–3.

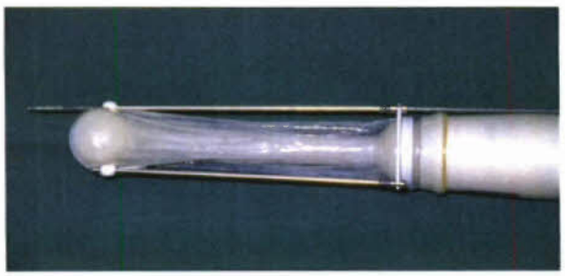

1

2

3

4

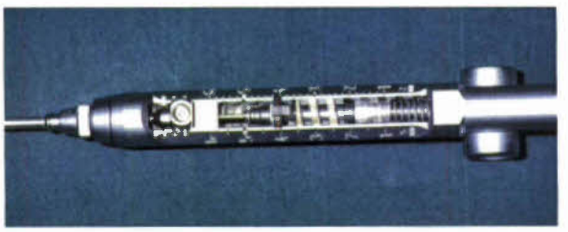

5

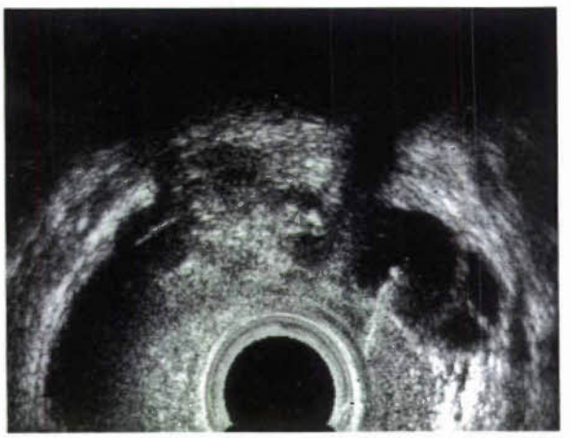

Puncture Technique

Fig. 34.1 Transvaginal ultrasound probe with a manual needle guide.

Fig. 34.2 The automated puncture device for transvaginal aspirations and biopsies (Labotect, Germany).

Fig. 34.3 The automated puncture device mounted on a transvaginal probe.

Fig. 34.4 The electronic sight-line is superimposed on the monitor. The depth markings are spaced at intervals of 1 cm.

Fig. 34.5 The automatic puncture mechanism allows precise adjustment of the desired depth of puncture.

Transvaginal Follicular Aspiration

Fig. 34.6 The ultrasound probe with an automated puncture device inserted into the vagina.

Fig. 34.7 Transvaginal follicular aspiration in the left ovary following stimulation treatment with human menopausal gonadotropin/human chorionic gonadotropin. Coronal scan.

19b Zanetta G, Lissoni A, Dalla Valle C, Trio D, Pittelli M, Rangoni G. Ultrasound-guided aspiration of endometriomas: possible applications and limitations. Fertil Steril. 1995;64:709-13.
19c Kafali H. Rapid recurrence of endometrioma after transvaginal ultrasound-guided aspiration. Eur J Obstet Gynecol Reprod Biol. 2004;113:114.
20 Nash JD, Burke TW, Woodward JE, Hall KL, Weiser EB, Heller PB. Diagnosis of recurrent gynecologic malignancy with fine needle aspiration cytology. Obstet Gynecol 1988;71:333–7.
21 Feldberg D, Goldman JA, Ashkenazi J, Shelef M, Dicker D, Samuel N. Transvaginal oocyte retrieval controlled by vaginal probe for in vitro fertilization: a comparative study. J Ultrasound Med 1988;7:339–43.
22 Zanetta G, Brenna A, Pittelli M, Lissoni A, Trio D, Riotta S. Transvaginal ultrasound-guided fine needle sampling of deep cancer recurrences in the pelvis: usefulness and limitations. Gynecol Oncol. 1994;54:59-63.

Transvaginal Cyst Aspiration

Fig. 34.**8** Transvaginal cyst aspiration (I). The needle has not yet been inserted. Scan demonstrates a sharply circumscribed 5-cm cyst with fine internal echoes behind the vaginal floor. Coronal scan.

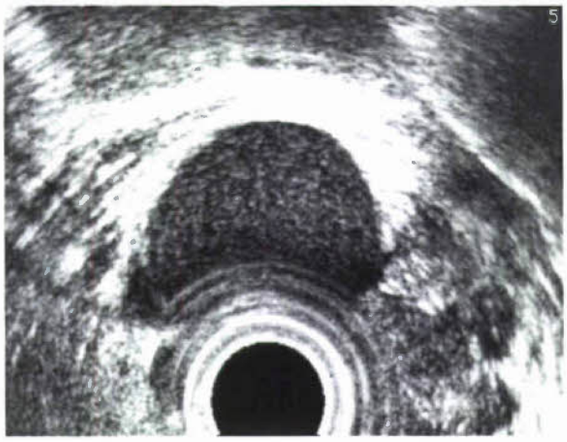

8

Fig. 34.**9** Transvaginal cyst aspiration (II). The tip of the aspirating needle has been advanced to the center of the cyst.

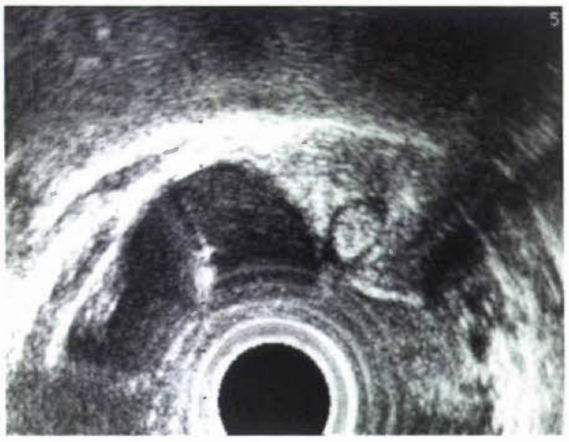

9

Fig. 34.**10** Transvaginal cyst aspiration (III). Most of the cyst fluid has been aspirated.

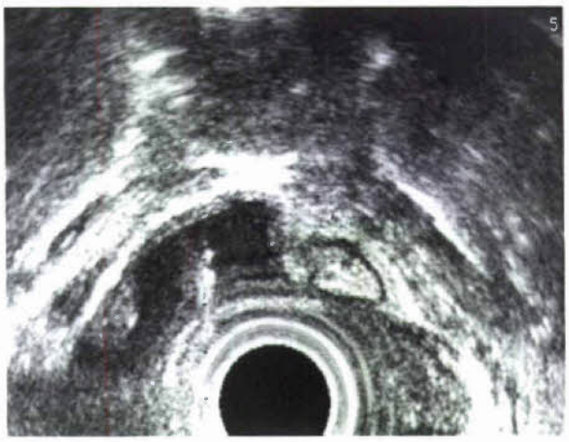

10

Fig. 34.**11** Transvaginal cyst aspiration (IV). All of the cyst fluid has been aspirated, and the needle is still in place.

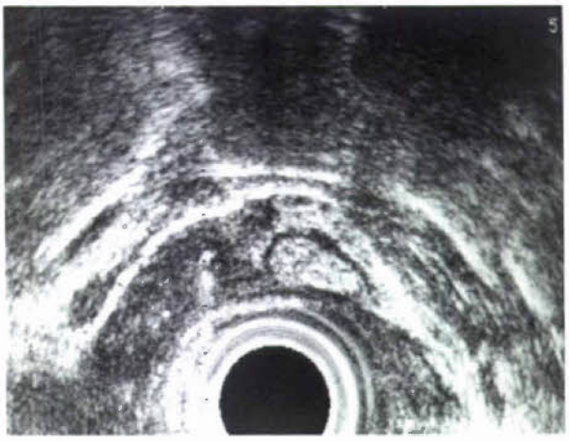

11

Fig. 34.**12** Transvaginal aspiration of a simple cyst without internal echoes. The needle is in place.

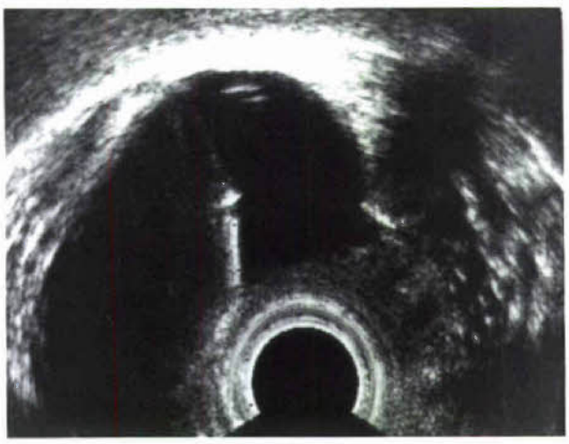

12

Fig. 34.**13** Clear, pale yellow fluid aspirated from the cyst in Fig. 34.**12**.

13

Fig. 34.**14** Transvaginal aspiration of a sharply circumscribed right ovarian cyst with diffuse, medium-level internal echoes (serosanguineous fluid). Coronal scan.

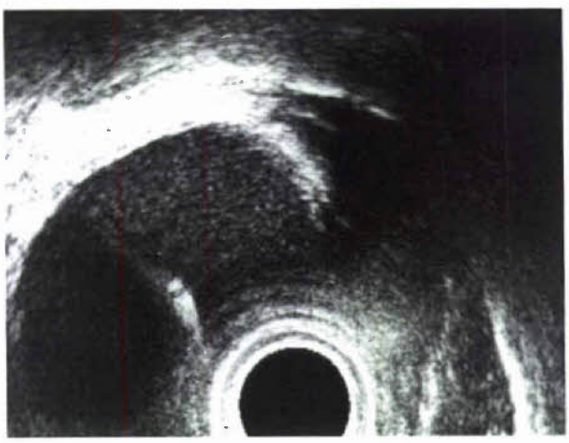

14

Fig. 34.**15** Dark red serosanguineous fluid aspirated from the hemorrhagic corpus luteum cyst in Fig. 34.**14**.

15

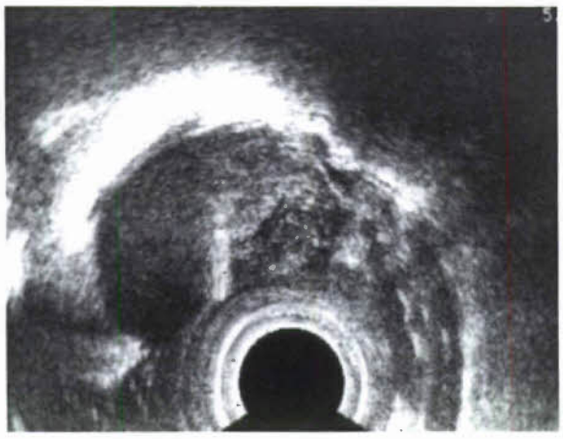

16

17

Fig. 34.16 Aspiration of an endometriotic cyst with mixed fine and coarse internal echoes.

Fig. 34.17 Dark brown to black fluid aspirated from the cyst in Fig. 34.16.

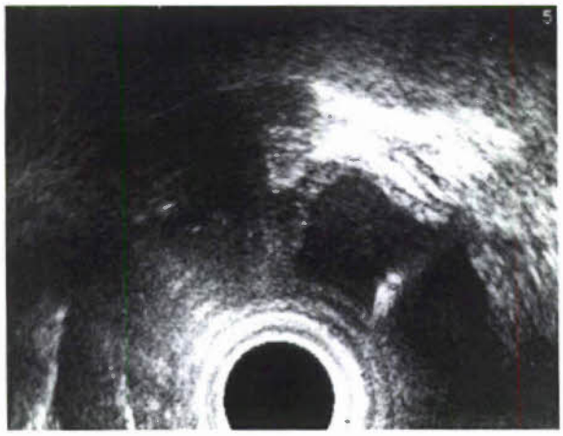

18

19

Fig. 34.18 Transvaginal aspiration of a left ovarian abscess. Coronal scan.

Fig. 34.19 Copious putrid fluid aspirated from the abscess in Fig. 34.18.

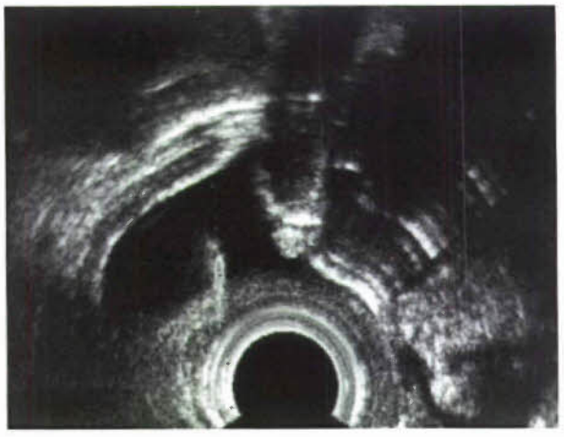

20

Fig. 34.20 Transvaginal aspiration of ascites on the right side, with a relatively scant volume of ascites and abdominal wall adhesions. Longitudinal scan.

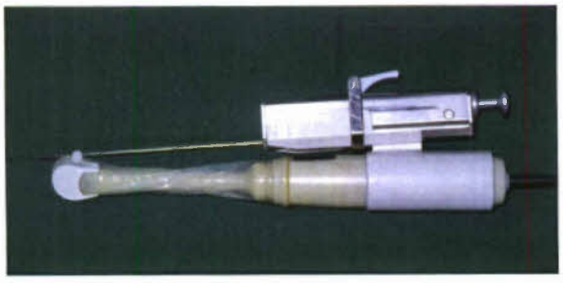

21

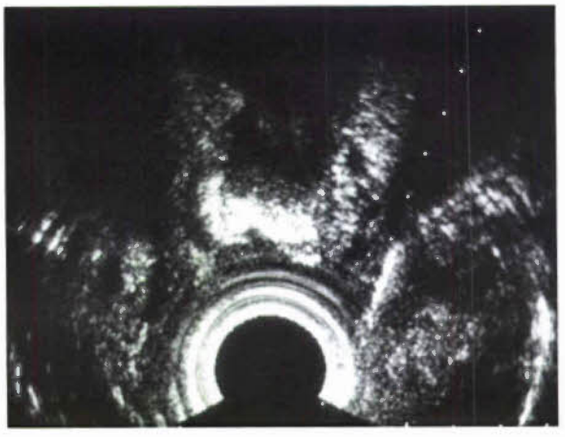

22

Fig. 34.21 Biopsy punch mounted on a transvaginal probe for automated puncture.

Fig. 34.22 Transvaginal tissue biopsy from a suspicious nodule behind the vaginal stump on the left side. The lesion proved to be a recurrence of cervical carcinoma following a radical Wertheim–Meigs operation.

35 Transvaginal Ultrasound in the Investigation of Postoperative Complications

It is critically important for postoperative complications to be detected at an early stage and treated appropriately in order to reduce patient morbidity, shorten the duration of illness, and reduce costs.

Normally, the circumscribed space of the true pelvis and its anatomical relationships are easily accessible to clinical examination by vaginal and rectal palpation. Vaginal and abdominal wounds are also accessible to direct inspection. When these findings are combined with clinical laboratory values, it is usually possible to assess the nature and severity of a complication.

Patients with clinically obscure or occult pathology should be investigated by imaging procedures. Transvaginal ultrasound provides an effective, noninvasive diagnostic tool that is a valuable adjunct for diagnosing complications in the true pelvis. In addition to the evaluation of hemorrhagic and lymphatic effusions and the localization and characterization of infections and abscesses, the detection of morphologic changes in operated organs and adjacent organs is an important part of the transvaginal ultrasound examination. The ultrasound-guided aspiration of postoperative fluid collections also has therapeutic value in addition to its diagnostic capabilities. When applied in conjunction with clinical and simple technical parameters, transvaginal ultrasound has gained an established role in the diagnosis and treatment of postoperative gynecologic complications.

According to statistics compiled by the Association of Swiss Departments of Gynecology from 1983 to 1989, medium and larger gynecologic operations (e.g., all operations not involving curettage, conization, radium implants, laparoscopy, laser therapy, excisional biopsy, marsupialization, or breast surgery) were associated with a general complication rate of 8.99% [1]. These complications included postoperative bleeding and infectious complications as well as thrombosis and embolism.

The *complication rate* of a procedure depends not only on technical factors but also on patient selection and postoperative care. Various risk factors, such as the presence of underlying disease and the age of the patient, influence the frequency of postoperative complications. The complication rate of gynecologic procedures is generally higher in older patients. The nature and extent of the operation also affect the complication rate. The procedures with the highest complication rates are operations for malignant disease.

Ultrasound Diagnosis

Because almost all surgical procedures in obstetrics and gynecology are performed in the true pelvis, a clinical examination that includes inspection plus vaginal and rectal palpation can yield considerable information on a postoperative disorder. Imaging procedures are necessary, however, for the further differentiation of lesions such as effusions, abscesses, hemorrhages, and hollow viscus pathology. With transvaginal ultrasound, it is possible to detect and characterize the location and nature of the complication. At the same time, general "complication screening" with transvaginal ultrasound after gynecologic and obstetric procedures cannot be recommended. In a study by Klug [2], sonographic abnormalities were detected in 12% of patients who had undergone 355 surgical procedures, but only one-tenth of the cases were classified as clinical complications.

Table 35.1 Outline of the four main groups of postoperative complications

Bleeding	• Intraperitoneal bleeding • Retrovaginal hematoma • Pelvic wall hematoma • Subvesical and paravesical hematomas
Lymph collections	• Lymph cysts
Infections	• Parametrial abscess • Intraperitoneal abscess • Parametrial cellulitis
Organ pathology	• Ileus • Fistula • Ureteral lesions

Four main types of postoperative complication are accessible to ultrasound diagnosis: bleeding, lymph cysts, infection, and organ pathology (Table 35.**1**).

The ultrasound diagnosis of complications centers mainly on bleeding and infection, which present as free or encapsulated fluid. Organ pathology may involve the operated organ as well as adjacent organs and may require further imaging studies or function tests.

Bleeding (Usually Early Complications)

A large percentage of gynecologic operations are performed in the vesicouterine space and cul-de-sac, and therefore bleeding complications are most commonly detected in those regions. While a *fresh hematoma* (Fig. 35.**1**) typically appears echo-free, the hematoma tends to acquire fine septations or an echogenic honeycomb structure as it becomes more organized (Figs. 35.**2**–35.**6**).

An *intraperitoneal hemorrhage* can generally be distinguished sonographically from an *extraperitoneal hemorrhage*, providing a specific indication for laparotomy.

Blood collections after hysterectomy are most common after high peritonealization, regardless of whether drainage is directed through the open vagina or flank drains [3]. They are less common when the pelvic peritoneum has not been closed [4]. With a large intra-abdominal blood collection, a pronounced hematoma is usually found in the cul-de-sac, provided that area was not obliterated during the operation (Fig. 35.**3**).

Small fluid collections between paralytic bowel loops are difficult to detect by transvaginal scanning. It may necessary to add transabdominal scans, giving attention to the regions next to and below the liver.

Retrovaginal hematomas are occasionally found after an abdominal or vaginal hysterectomy. They appear as a hypoechoic mass located just behind the vaginal floor (Fig. 35.**4**).

Pelvic wall hematomas present a similar structure, but have a considerably more lateral location (Fig. 35.**5**).

Subvesical and paravesical hematomas are most common following a "diaphragm repair" or colposuspension [5]. Bleeding-related bladder wall suffusions or hematomas may be the source of unexplained gross hematuria. Prospective studies are needed to determine how these changes might inhibit the resumption of bladder function or worsen the long-term prognosis.

Retrovesical hematoma following myoma removal or cesarean section appears as a swelling of variable echogenicity at the hysterotomy site or on the posterior bladder wall (Fig. 35.**6**).

Lymph Collections (Early and Late Complications)

Lymph effusions occur in up to 50% of patients who have undergone pelvic lymphadenectomy [6]. Their incidence appears to depend on the technique of peritonealization [7] and the mode of heparin administration [8]. They are most commonly located on the pelvic wall. Effusions that extend as far as the internal femoral canal or abdominal wall can also be diagnosed by transabdominal ultrasound. In contrast to hematomas, lymph cysts usually appear weeks or even months after the operation. Lymphoceles are generally echo-free initially but soon develop fine internal septations (Fig. 35.**7**). Abscess formation may also occur. Abscesses differ from hematomas by retaining their hypoechoic septations for a longer time [3], and this can be used as a differentiating criterion.

Infections and Abscesses (Late Complications)

Whereas fresh clots appear almost echo-free or contain fine septa and seromas have sharp margins and are completely echo-free, *abscesses* have a thicker, sonodense capsule and their contents have a flocculent, hypoechoic appearance [5] (Chapters 6, 25). With a subcutaneous abscess, the clinical diagnosis is usually clear-cut. In cases in which an abscess has infiltrated the abdominal wall or urinary tract, abdominal ultrasound is the method of choice for diagnosis, observation, and ultrasound-guided intervention. *Subfascial seromas* and *abscesses* may go clinically undetected, however, and may be misinterpreted as "wound pain" or "cystitis." Abscesses involving the *parametria* and *ovarian suspensory ligament* are particularly likely to mimic a urinary tract infection. Imaging procedures with universal applications such as transvaginal ultrasound, supplemented if necessary by transabdominal scanning, can be of crucial help in the investigation of these cases. Particularly in patients who have undergone a vaginal hysterectomy with or without incontinence repair and develop clinical manifestations of infection such as fever, a foul-smelling wound discharge, and parametrial infiltration, transvaginal ultrasound can detect a suppurative inflammation involving the parametrial stumps as a relatively well-defined, complex cloudy structure, thus distinguishing it from a phlegmonous inflammation. This diagnosis can be followed if necessary by ultrasound-guided aspiration and drainage of the abscess [9].

Sites of predilection for complications following a cesarean section or myoma enucleation are the hysterotomy site or the myoma bed. Infiltrates or abscesses in these areas are not detectable by palpation, as they are located below the abdominal wound and behind the bladder. Transvaginal ultrasound can provide a detailed view of these zones so that any complications can be detected early and treated appropriately.

Organ Pathology (Early and Late Complications)

Organ pathology may involve the operated organ as well as neighboring organs. For example, if a postoperative infiltration or abscess is not promptly diagnosed, it may spread by seepage to involve adjacent organs in the true pelvis such as the bladder or bowel.

In patients with postoperative *ileus*, both abdominal and transvaginal ultrasound can detect an abnormal intraluminal fluid collection and luminal distension in the small bowel (Chapter 30). *Fistulas* are generally difficult to diagnose with ultrasound and require radiographic contrast imaging or colored dye injection [10]. The same applies to *ureteral complications*, although transvaginal ultrasound can detect an intra-abdominal urinoma or a low ureteral obstruction with dilation of the ureter.

References

1 Hochuli E. Standardmorbidität bei gynäkologischen Eingriffen. In: Hochuli E. Perioperative Gynäkologie. Berlin: Springer, 1993: 25–35.
2 Klug PW. Vaginosonographische Abklärung gynäkologischer Operationskomplikationen. Gynäkologe 1995;28:262–9.
3 Klug PW. Vaginosonographie gynäkologischer Operationskomplikationen. Ultraschall Klin Prax 1990;5:57–61.
4 Naegele F, Kurz C, Nusslein P. Abdominale Hysterektomie ohne innere Peritonealisierung. Gynäkol Rundsch 1993;33(Suppl 1):271–3.
5 Takeuchi H, Kobori H, Kikuchi I, Sato Y, Mitsuhashi N. A prospective randomized study comparing endocrinological and clinical effects of two types of GnRH agonists in cases of uterine leiomyomas or endometriosis. J Obstet Gynaecol Res. 2000;26:325–31.
6 Bozzini N, Messina ML, Borsari R, Hilario SG, Pinotti JA. Comparative study of different dosages of goserelin in size reduction of myomatous uteri. J Am Assoc Gynecol Laparosc. 2004;11:462–3.
7 Dimpfl T, Stumpfe M, Baasen V, Genz T. Lymphocelen und Komplikationen nach pelviner und paraaortaler Lymphadenektomie in Abhängigkeit vom Verschluss des Peritoneums. Geburtshilfe Frauenheilkd 1994;54:233–6.
8 Breddin HK, Brocks JO. Lymphocelen nach pelvinen und paraaortalen Lymphonodektomien aus der Sicht des Angiologen. Gynäkologe 1992;25:52–4.
9 Van Sonnenberg E, D'Agostino HB, Casola G, Goodacre BW, Sachez RB, Taylor B. Ultrasound-guided transvaginal drainage of pelvic abscesses and fluid collections. Radiology 1991;181:53–6.
10 Alvarez RD. Gastrointestinal complications in gynecologic surgery: a review. Obstet Gynecol 1988;72:533–40.
11 Fedele L, Bianchi S, Zanconato G, Tozzi L, Raffaelli R. Gonadotropin-releasing hormone agonist treatment for endometriosis of the rectovaginal septum. Am J Obstet Gynecol. 2000;183:1462–7.
12 Franke HR, van de Weijer PH, Pennings TM, van der Mooren MJ. Gonadotropin-releasing hormone agonist plus „add-back" hormone replacement therapy for treatment of endometriosis: a prospective, randomized, placebo-controlled, double-blind trial. Fertil Steril. 2000;74:534–9.
13 Acien P, Perez-Albert G, Quereda FJ, Sanchez-Ferrer M, Garcia-Almela A, Velasco I. Treatment of endometriosis with transvaginal ultrasound-guided drainage under GnRH analogues and recombinant interleukin-2 left in the cysts. Gynecol Obstet Invest. 2005;60:224–31.w

Bleeding (Usually Early Complications)

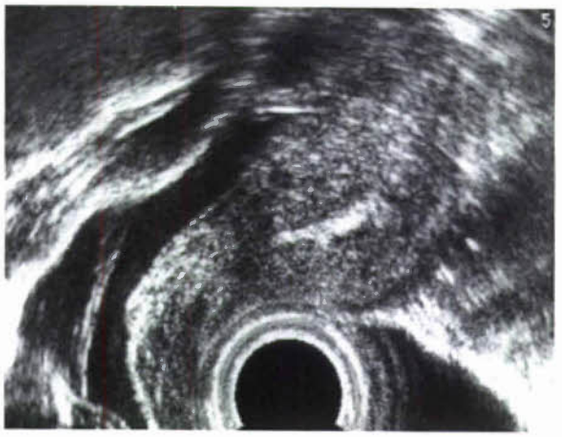

1

Fig. 35.1 Fresh intra-abdominal postoperative hemorrhage, with detection of blood in the cul-de-sac. Longitudinal scan.

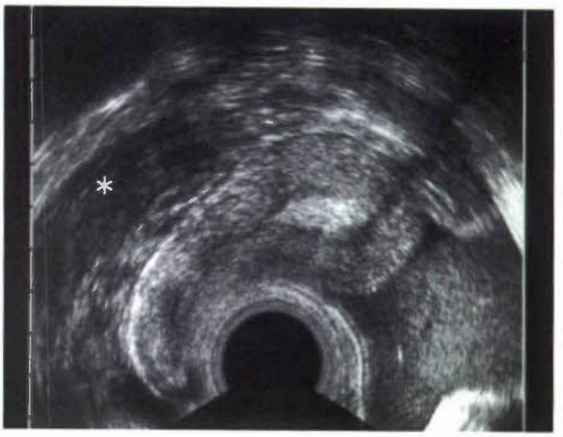

2

Fig. 35.2 Partly organized hematoma in the cul-de-sac (*). Longitudinal scan.

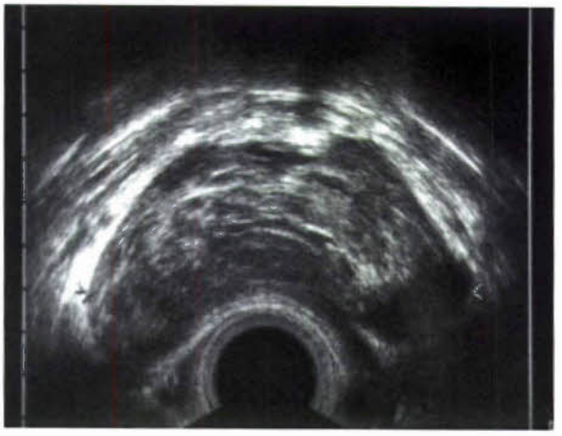

3

Fig. 35.3 Large, organized, mixed hypoechoic and hyperechoic hematoma in the cul-de-sac. Coronal scan.

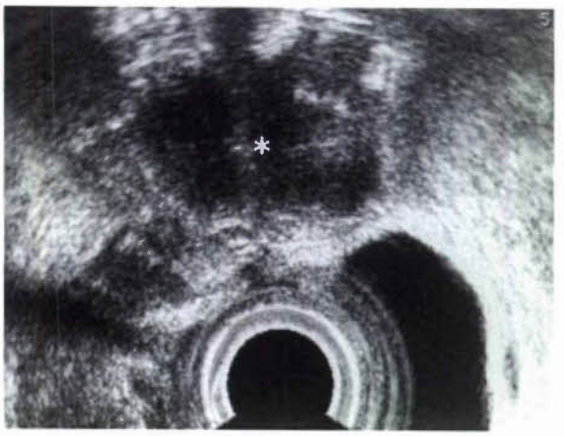

4

Fig. 35.4 Large, hypoechoic hematoma (5.8 × 5.0 × 3.8 cm) behind the vaginal floor (*) following abdominal hysterectomy and bilateral adnexectomy. Longitudinal scan.

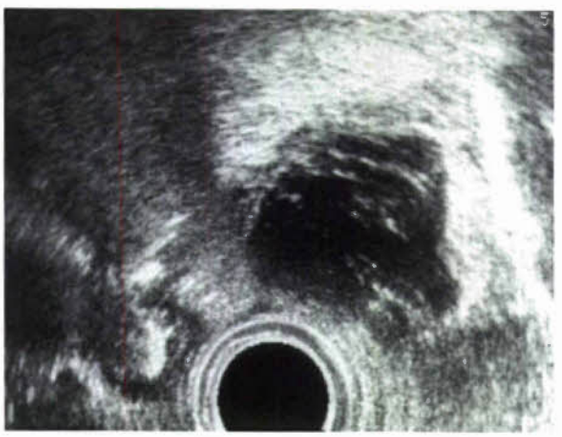

5

Fig. 35.5 Large, hypoechoic hematoma (6.2 × 3.5 × 4.7 cm) on the left pelvic wall, following a radical Wertheim–Meigs operation. Coronal scan.

6

Fig. 35.6 Retrovesical hematoma (*) arising from the hysterotomy following a cesarean section. Transabdominal oblique longitudinal scan.

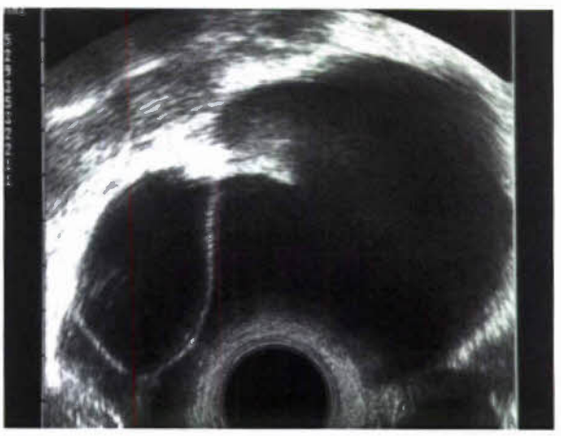

7

Fig. 35.7 Large, loculated lymph cyst (9.8 × 9.0 × 5.5 cm) on the left pelvic wall following a radical Wertheim–Meigs operation. Longitudinal scan.

36 Transvaginal Ultrasound in the Assessment of Treatment Response

As a noninvasive study that can be performed at any time, transvaginal ultrasound is ideal for conducting serial examinations to evaluate the response to certain pharmacologic therapies. These mainly involve the medical reduction of myomas or endometriotic lesions with agents such as gonadotropin-releasing hormone (GnRH) agonists. The regular sonographic measurement of myomas or endometriotic foci/cysts in all three planes can determine relatively quickly whether or not the lesions are responding to the initiated treatment. If shrinkage of the lesions is observed, the degree of change can be taken as a measure of the treatment response.

Myoma Reduction

As early as 1983, Filicori et al. [1] reported on successful reduction of the size of a uterine myoma using treatment with a GnRH agonist. Since then, various ultrasound studies have been published documenting a significant volume reduction of uterine myomas during the first 3–4 months of this form of treatment [2–6] (Figs. 36.**1**, 36.**2**). Considerably less response is achieved after that period. As growth of the myomas resumes after the suppression therapy is discontinued, the main goal of the therapy is to debulk the tumors as a prelude to conservative myoma surgery.

In some cases, myomas are unresponsive to GnRH agonists. Ultrasound can clearly demonstrate both the presence and absence of size changes in response to the therapy.

Endometriosis

The inhibitory effect of GnRH agonists on endogenous gonadotropin secretion and the resulting suppression of ovarian function can lead to a partial or complete regression of endometriotic lesions [5,7–9] (Figs. 36.**3**, 36.**4**). In these cases as well, transvaginal ultrasound can quickly determine whether the treatment that has been instituted can reduce the sonographically detected endometriotic nodule, or whether the nodule is unresponsive to the transient induction of a postmenopausal state.

The role of transvaginal ultrasound in radiotherapy for gynecologic tumors is discussed in Chapter 37.

Myoma Reduction

Fig. 36.**1** Fibroid uterus before conservative therapy.

Fig. 36.**2** Fibroid uterus after 3 months' treatment with a gonadotropin-releasing hormone analog. There is a marked reduction in the diameter of the myoma.

Endometriosis Therapy

Fig. 36.**3** Endometriosis of the left ovary before conservative therapy. Coronal scan.

Fig. 36.**4** Endometriosis after 3 months' treatment with a gonadotropin-releasing hormone analog. Ultrasound documents moderate regression of the endometriotic cyst.

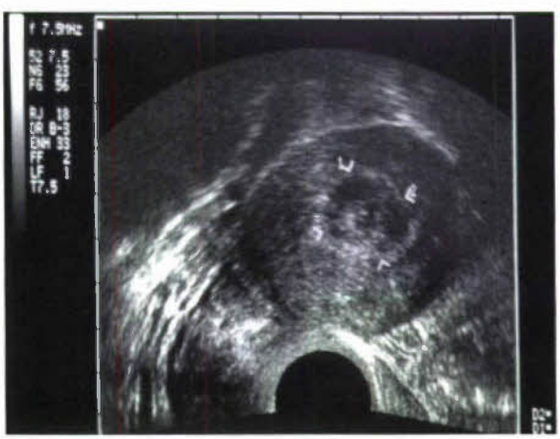

1

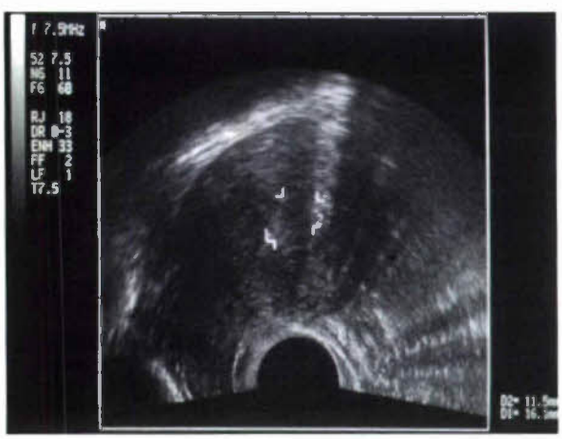

2

3

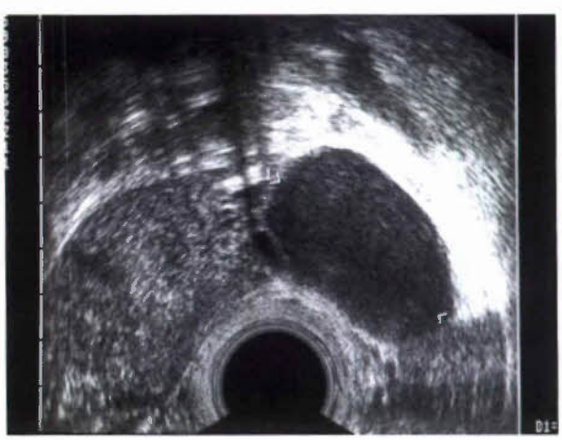

4

References

1 Filicori M, Hall DA, Loughlin JS, Rivier J, Vale W, Crowley WF. A conservative approach to the management of uterine leiomyomata: pituitary desensitization by a luteinizing hormone-releasing hormone analog. Am J Obstet Gynecol 1983;147:726–7.

2 De Aloysio D, Altieri P, Pretolani G, Romeo A, Paltrinieri F. The combined effect of a GnRH analog in premenopause plus postmenopausal estrogen deficiency for the treatment of uterine leiomyomas in perimenopausal women. Gynecol Obstet Invest 1995;39:115–9.

3 Matta WH, Shaw RW, Nye M. Long-term follow-up of patients with uterine fibroids after treatment with the LHRH agonist buserelin. Br J Obstet Gynaecol 1989;96: 200–6.

4 West CP, Lumsden MA, Lawson S, Williamson J, Baird DT. Shrinkage of uterine fibroids during therapy with goserelin (Zoladex): a luteinizing hormone-releasing hormone agonist administered as a monthly subcutaneous depot. Fertil Steril 1987; 48:45–51.

5 Bozzini N, Messina ML, Borsari R, Hilario SG, Pinotti JA. Comparative study of different dosages of goserelin in size reduction of myomatous uteri. J Am Assoc Gynecol Laparosc. 2004;11:462–3.

6 Hardt W, Schmidt-Gollwitzer M, Schmidt-Gollwitzer K, Genz T, Nevinny-Stickel J. Erste Ergebnisse bei der Behandlung der Endometriose mit dem LH-RH-Analogon Buserelin. Geburtshilfe Frauenheilkd 1986;46:483–9.

7 Mettler L, Steinmüller H, Schachner-Wunschmann E. Experience with a depot GnRH agonist (Zoladex) in the treatment of genital endometriosis. Hum Reprod 1991; 6:694–8.

8 Reichel RP, Schweppe KW. Goserelin (Zoladex) depot in the treatment of endometriosis. Fertil Steril 1992;57:1197–202.

9 Shaw RW. An open randomized comparative study of the effect of goserelin depot and danazol in the treatment of endometriosis. Zoladex Endometriosis Study Team. Fertil Steril 1992;58:265–72.

37 Transvaginal Ultrasound in Planning the Radiotherapy of Gynecologic Cancers

An essential goal in radiotherapy is to deliver the highest possible radiation dose to the targeted tissue while minimizing the damage to healthy adjacent tissues. Collateral damage can be reduced by fractionating the radiation to allow for better tissue recovery between doses and also by accurately defining and calculating the target volume that is to be irradiated.

With percutaneous irradiation, the optimum shape and number of radiation portals are calculated by computer programs on the basis of an analysis of digitized computed-tomographic images and, more recently, magnetic resonance images. This makes it possible to tailor the treatment regimen to the individual anatomy.

The planning of local contact irradiation, which has proven to be effective for cancers of the uterus and vagina in the form of radium therapy, was long based on the extent of disease assessed by palpation. However, the afterloading technique, as well as developments in ultrasound and especially endosonography, have made it possible to adapt the radiotherapy better to individual requirements. *Afterloading* begins by inserting a guide tube into the region that has been targeted for treatment. In the case of the uterus, this means that one or more uterine applicators are inserted. The radiation source, laser-welded to a guide wire, is then advanced through a tubing system to the applicator tip and is either moved back and forth over a prescribed distance or is retracted at prescribed intervals, as previously programmed, in order to achieve a desired isodose distribution. Today, the most commonly used radiation sources are cesium-137 and iridium-192. Owing to the high dose rate of iridium (*HDR irradiation*), the treatment times with this isotope are measured in minutes. Due to its greater biological effectiveness, however, a high-dose rate source requires greater fractionation than a low-dose rate source such as radium-226 (*LDR irradiation*).

The main advantages of afterloading are shorter dwell times in the patient, significantly better safety for the patient and staff, and better accuracy in dose control.

Endosonography, or intracavitary ultrasound, is already being used in the planning of radiotherapy for various cancers, such as esophageal ultrasound in the afterloading of esophageal carcinoma and transrectal ultrasound for rectal and prostatic carcinoma, which can be irradiated by tumor spiking.

Transuterine ultrasound, also known as hysterosonography, has been described in radiation dose planning for gynecologic cancers [1], but it requires preliminary cervical dilation and carries a greater risk of infection. A simpler option is transvaginal ultrasound, in which the high frequency of the endovaginal probe and its proximity to the uterus can provide detailed images of the internal genitalia, making it possible to define the extent of disease both inside and outside the uterus. Detecting infiltration of the bladder, rectum, and parametria, particularly with cervical carcinoma, is an important aid in devising a treatment strategy and planning a specific radiotherapy protocol.

The transducer used in *transvaginal ultrasound* should have a sufficiently large field of view (> 150°). The transducer frequency should be at least 5 MHz, but this is a less important consideration than the field of view. The transvaginal scans can be supplemented if necessary by *transrectal ultrasound*, which is also useful for evaluating rectal and parametrial infiltration [2] and if necessary can even replace transvaginal ultrasound in patients with vaginal stenosis. For spatial reasons, transrectal ultrasound can define cervical carcinoma better than endometrial carcinoma. The technique requires additional practice, however, and a biplanar probe is needed that can be switched from axial to longitudinal scan planes.

The images presented in this chapter were acquired with a Combison 310 scanner (Kretztechnik, Austria) using a 5-MHz or 7-MHz endovaginal probe (with a 240° field of view) and a 7.5-MHz endorectal probe.

The first step in radiotherapy dose planning is to measure the uterus in longitudinal section, determining its overall length, endometrial thickness, and the anteroposterior dimensions of the cervix and uterine corpus. The cavity length, especially in a straight uterus, should be verified by a direct probe measurement. Axial scans are then acquired by placing the vaginal probe in the anterior fornix (with an anteflexed uterus) or the posterior fornix (with a retroflexed uterus) and measuring the transverse dimensions of the cervix and corpus. The vaginal cylinder, which maintains a specified distance from the probe to the vaginal surface, is selected in accordance with clinical criteria.

For ultrasound measurements of the parametria, which we believe to be easier and just as reliable as measurements with computed tomography or magnetic resonance imaging [3], the cervix is imaged in axial section and the probe is then moved laterally by approximately 45° and rotated externally by about the same amount (Fig. 37.**1**). This gives a transverse section of the parametrium that will directly display any parametrial infiltration (Fig. 37.**2**). A comparable plane can be defined with transrectal ultrasound. Thickening of the homogeneous parametrium to 10 mm or more is interpreted as *infiltration*, which of course may be inflammatory rather than neoplastic (transvaginal Fig. 37.**3**, transrectal Fig. 37.**4**, hysterosonography Fig. 37.**5**).

It is also important to examine the bladder wall for tumor invasion, which may (Fig. 37.**6**) or may not extend through the mucosa, and to evaluate the ureters, which may show dilation in some cases (Fig. 37.**7**). In addition, the kidneys should always be visualized.

Vaginal carcinoma and vaginal metastases can also be defined with ultrasound. The depth of tumor invasion is a particularly important concern in treatment planning, so that an optimum trade-off can be made between penetration depth and tissue conservation. It is advantageous to use a higher-frequency probe (7 MHz), and a rectal probe with a water standoff may be a helpful accessory. Ultrasound also makes it possible to estimate the depth to which the tumor can be safely removed (e.g., by laser ablation) as a prelude to radiotherapy.

The measurements are entered into the isodose computation software. Generally, an inferiorly weighted "pear-shaped" distribution pattern is used for cervical cancers and a superiorly weighted "inverted pear" pattern for endometrial cancers. Curved uterine applicators (20° or 40°) can be used in patients with pronounced anteflexion or retroflexion of the uterus, but a straight applicator introduced along a horizontal axis is advantageous for maintaining reasonably equal clearance from the bladder and bowel.

If the desired tumor dose is 8 Gy, for example, the corresponding isodose line in the cervical region should have at least a 2-mm clearance laterally (near the ureter) and anteriorly (near the bladder) and at least a 5-mm clearance in the upper corpus region adjacent to the small bowel. A higher or lower dose may be advisable, depending on the size of the tumor and the purpose of the radiotherapy (i.e., palliative or curative). A sample isodose calculation for cervical carcinoma is shown in Fig. 37.**8**.

After the uterine applicator has been inserted and measuring probes have been placed in the bladder and bowel, the placement is checked radiographically in two planes. Ultrasound (abdominal or transrectal)

can be added to confirm the placement, but cannot replace biplanar radiographs. The dose delivered to the bladder and rectum is measured online during each therapy session.

The goal of afterloading therapy is to deliver a total dose of at least 48 Gy to the tumor (fractionated to 8 Gy in each of six applications). This is supplemented by percutaneous irradiation of the true pelvis with shielding of the bladder and rectum after 20 Gy (effective: approximately 22 Gy). We also treat patients with purely palliative cases with afterloading therapy alone (64 Gy fractionated to 8×8 Gy), using the GammaMed 12i Afterloader (Sauerwein) with GammaDot software.

Transvaginal ultrasound scans should be repeated after every two or three fractions so that the dose calculation can be adjusted for rapid tumor shrinkage; this is particularly important with cervical cancers. The definitive response can be assessed sonographically at 6–8 weeks after the completion of radiotherapy.

In all of our patients to date (n = 90), we have been able to document at least a local tumor response to the radiotherapy on the basis of clinical and ultrasound criteria. The cervical carcinomas, most of which initially appeared sonographically as heterogeneous tumors (Fig. 37.**9** axial, Fig. 37.**10** longitudinal) separated from the uterine corpus by an echogenic border, showed increased homogeneity and decreased echogenicity following radiotherapy (Fig. 37.**11**). We also noted a decrease in uterine size, accompanied by an approximately one-fourth reduction in cervical diameter. Previously involved parametria also showed an approximately 50% decrease in their initial thickness (Fig. 37.**12**).

With endometrial carcinomas, detected as an echogenic thickening of the endometrial echo, we also observed increased homogeneity and less echogenicity in the tumor area, although it was common to find a residual intracavitary echo at the end of treatment consistent with an inflammatory reaction. Six weeks after the conclusion of treatment, the uterus appeared uniformly hypoechoic.

Serometra or hematometra commonly develops as a late sequela of radiogenic cervical stenosis. In the absence of other criteria, this does not necessarily signify a recurrence.

To date, we have observed one rectovaginal fistula 10 months after palliative afterloading therapy (the patient had received combined radiotherapy 27 years previously) and one urethrovaginal fistula 2 years after combined radiotherapy (and external biopsy). We cannot yet state definitively that the incidence of fistulas is lower that that associated with radium therapy (3–5%).

On the whole, the use of ultrasound data in radiotherapy planning makes it possible to design an individualized protocol for delivering a total of 70 Gy to the tumor (48 Gy by afterloading and 22 Gy by percutaneous irradiation). This approach is particularly effective in protecting the ureters, which are located in the overlap region between the percutaneous and intracavitary radiation fields. In the fundal region, the 8 Gy isodose line can be safely confined to the uterus while sparing adjacent loops of small bowel. On the basis of the clinical and sonographic results and calculations to date, an efficient treatment protocol can be designed that will keep the risks (especially of fistula formation) within reasonable limits, particularly in the treatment of small tumors that have a good prognosis.

In addition to supplying data for treatment planning, transvaginal ultrasound can also provide criteria that are helpful in deciding between treatment modalities: surgery versus radiotherapy. It is reasonable to expect that therapeutic efficacy can be improved and a better isodose distribution achieved in complex calculations through the use of multiple probes (for endometrial cancers) or ultrasound-guided tumor spiking (for cervical carcinoma) [4].

References

1 Hötzinger H. Durch Intrauterinsonographie optimierte intrakavitäre Strahlentherapie bei Korpuskarzinomen. Strahlentherapie 1984;160:600–4.
2 Bernaschek G, Janisch H. Eine Methode zur Objektivierung des Parametrienbefundes beim Zervikalkarzinom. Geburtshilfe Frauenheilkd 1983;43:498–500.
3 Jaspers V, Spätling L. Vaginosonography in staging of cervical carcinoma. Ultrasound Obstet Gynecol 1991;1(Suppl):50.
4 Weitmann HD, Knocke TH, Waldhausl C, Potter R. Ultrasound-guided interstitial brachytherapy in the treatment of advanced vaginal recurrences from cervical and endometrial carcinoma. Strahlenther Onkol. 2006;182:86-95.

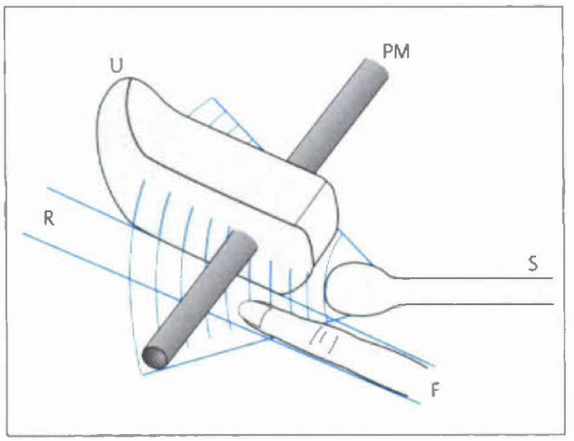

1

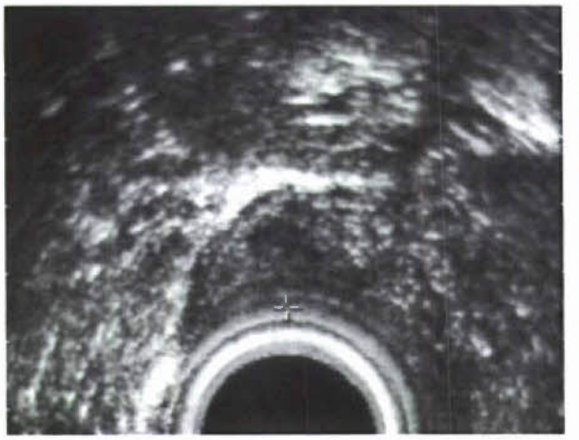

2

Fig. 37.1 Parametrial measurement with ultrasound. P: endovaginal probe; F: finger; R: rectum; U: uterus; PM: parametria.

Fig. 37.2 Direct infiltration of the right parametrium by cervical carcinoma. Transvaginal coronal scan.

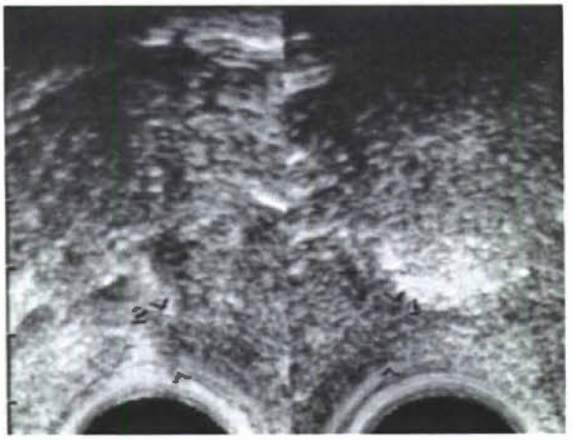

3

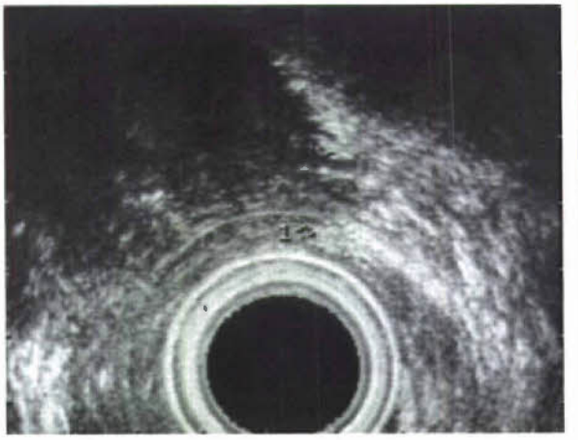

4

Fig. 37.3 Bilateral thickening of the parametria (> <). Transvaginal coronal scans.

Fig. 37.4 Thickened parametrium on the right side (> <). Transrectal ultrasound.

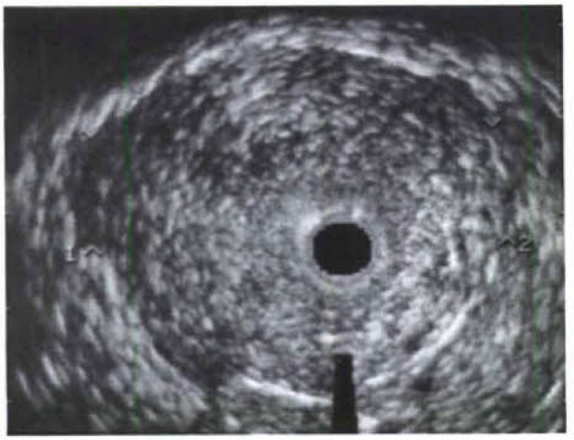

5

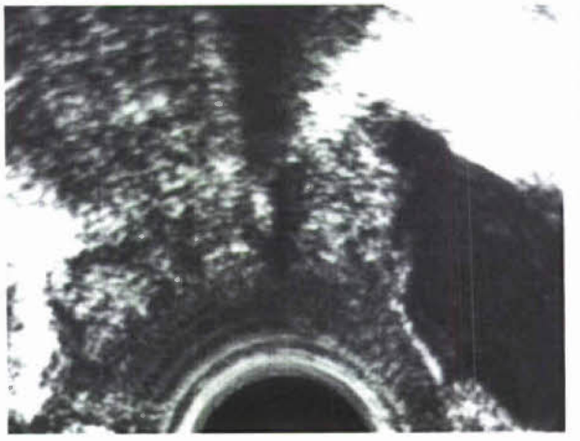

6

Fig. 37.5 Bilateral thickening of the parametria (> <). Hysterosonography.

Fig. 37.6 Infiltration of the posterior bladder wall by cervical carcinoma.

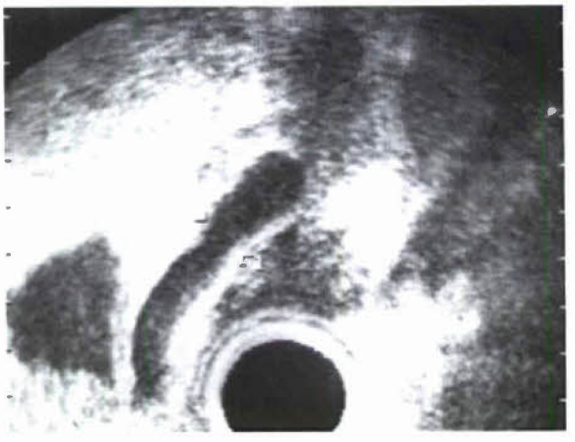

7

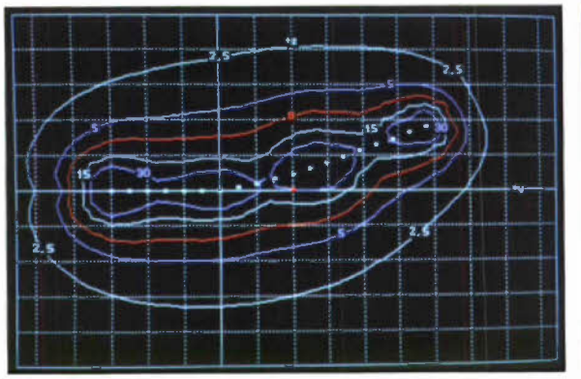

8

Fig. 37.7 Right hydroureter secondary to cervical carcinoma (> <).

Fig. 37.8 Example of an isodose calculation for the radiotherapy of cervical carcinoma.

Fig. 37.**9** Transverse scan of cervical carcinoma. Transrectal ultrasound.

Fig. 37.**10** Cervical carcinoma with an echogenic rim, demonstrated by transvaginal ultrasound. Longitudinal scan.

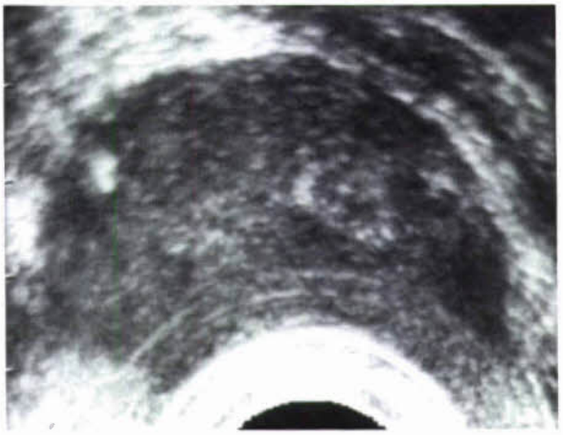

9

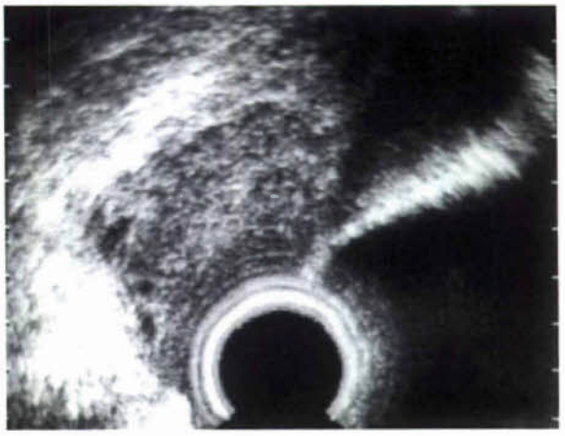

10

Fig. 37.**11** The same uterus as in Fig. 37.**10**, 6 weeks after radiotherapy.

Fig. 37.**12** Normal-appearing parametria (> <) 6 weeks after radiotherapy for cervical carcinoma (primary thickness 22 mm).

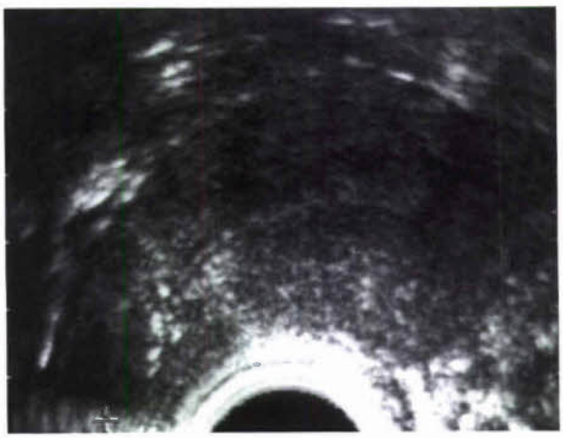

11

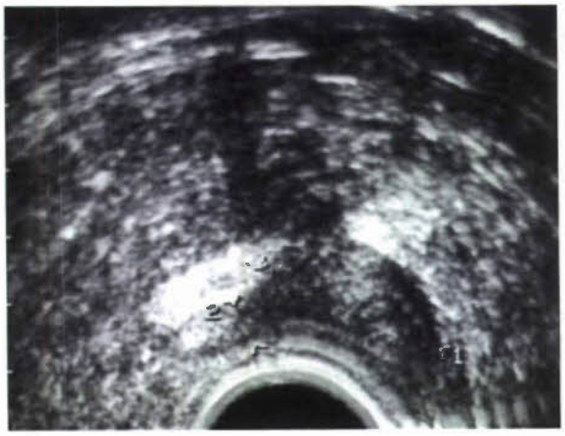

12

Transvaginal Doppler Ultrasound (Color Doppler and Pulsed Doppler)

38 Basic Principles and Practical Application of Transvaginal Doppler Ultrasound in Gynecology

Transvaginal Doppler ultrasound is still a relatively new diagnostic technique in gynecology. The first transvaginal Doppler examinations employed *continuous-wave Doppler* technology. In recent years, however, *pulsed color Doppler ultrasound* has become an established tool in the evaluation of normal and abnormal Doppler waveforms in the true pelvis owing to its numerous advantages [1,2]. Through rapid technological advances in color Doppler instrumentation, it is now possible to measure blood flow velocities less than 1 cm/s.

Doppler Effect

The Doppler effect, named after the Austrian physicist Christian Johann Doppler (1805–1853), is based on the motion-dependent frequency modulation of waves [3]. In the Doppler systems used in medicine, an ultrasound beam emitted by a transmitter is scattered by corpuscular elements moving in a blood vessel, thereby altering the frequency of the reflected ultrasound beam in proportion to the velocity of the moving elements. The resulting frequency shift is called the *Doppler frequency spectrum* or *Doppler shift* [4] (Fig. 38.**1**).

The Doppler spectrum that is recorded from a blood vessel has a waveform characterized by a maximum systolic flow velocity (A), a maximum end-diastolic flow velocity (B), and a mean flow velocity (V_{mean}). The systolic part of the waveform reflects the force of cardiac contraction, while the end-diastolic flow reflects the level of peripheral vascular resistance. When the flow velocity, wavelength, and insonation angle of the ultrasound relative to the interrogated vessel are known, the frequency shift can be used to calculate the flow velocity of the blood.

The Doppler effect is described mathematically by the Doppler equation (Fig. 38.**2**). This equation can be used to calculate the blood flow velocity from the magnitude of the frequency shift between the transmitted frequency and the received frequency. According to the Doppler equation, the angle of incidence of the Doppler beam relative to the vessel being examined, called the *beam–vessel angle* or *Doppler angle*, is of critical importance. When the beam–vessel angle is 90°, for example, no frequency shift is detected because the cosine of 90° is equal to zero. Figure 38.**3** shows the Doppler shift as a function of blood flow velocity. The graph indicates that, for a constant flow velocity, the Doppler shift increases as the beam–vessel angle decreases. When the Doppler angle is greater than 60°, the ±5% error is approximately 20% or more [5] (Fig. 38.**4**). The measurement errors are smallest in the range of angles from 30° to 60°, and the resistance index is the parameter that is least sensitive to angle-related errors [6].

Pulsed Doppler Ultrasound, Pulsed-Wave (PW) Doppler

In pulsed Doppler systems, a specific range can be selected at which Doppler spectra are sampled and recorded [7,8]. This is achieved by using a single piezoelectric element that alternately transmits and receives short ultrasound pulses.

The pulses are received only from a designated region of interest, called the *sample volume* (or *Doppler gate*). The location of the Doppler beam and sample volume can be freely selected in both the vertical and transverse directions (Fig. 38.**5**).

The number of pulses transmitted per second is called the *pulse repetition frequency* (*PRF*) and is indirectly proportional to the penetration depth. The maximum measurable Doppler frequency is limited to one-half the PRF. This physical limit is termed the *Nyquist limit*:

$$Fd_{max} = \frac{PRF}{2}$$

In a pulsed Doppler system, flow velocities up to the Nyquist limit are displayed in one direction in graphic form. When a high flow velocity exceeds this limit, a phenomenon called *aliasing* occurs. This causes the highest frequency spectra to be cut off and displayed below the zero baseline (Fig. 38.**6**). Aliasing can be prevented either by shifting the position of the baseline (*baseline shift*) or increasing the pulse repetition frequency.

Aliasing rarely occurs in gynecologic transvaginal Doppler ultrasound due to the low flow velocities and is generally caused by a faulty setting of the Doppler parameters.

A *high-pass filter*, called also a wall filter, can be used to eliminate the extraneous low-frequency signals caused by the movement of vessel walls. Care should be taken that the wall filter is not set too high, as this can simulate the absence of end-diastolic flow (Fig. 38.**7**). This error may also be caused by making the sample volume too small.

Doppler Parameters

The qualitative description of Doppler waveforms has become an established technique in ultrasound interpretation owing to its simplicity and good reproducibility. The waveform is evaluated in a freeze-frame image by an integrated software program that permits both automated and manual *waveform analysis* (Fig. 38.**8**).

The parameters that are analyzed are the maximum systolic (A) and diastolic (B) frequency shift and the mean flow velocity (V_{mean}). The Doppler parameters in Fig. 38.**9** have proven most useful in clinical and office settings for the qualitative analysis of Doppler waveforms (Fig. 38.**1**).

The waveform data can be documented on thermoprinter paper, video media, or diskettes.

Color Doppler Ultrasound

Color Doppler ultrasound, known also as *color duplex* and *color flow imaging* [9–11], is a pulsed Doppler technique in which a large number of sample volumes are superimposed over a conventional B-mode image in a defined area called the *region of interest*. Multiple sample volumes are interrogated along each Doppler scan line, and numerous Doppler lines are assembled to produce a color-encoded Doppler image. This display method is also known as *multigate pulsed Doppler* [12] (Fig. 38.**10**). The received Doppler signals are not displayed as frequency spectra, however, but are simultaneously superimposed over the gray-

scale image as intensity-weighted, color-encoded mean blood flow velocities. Components moving away from the transducer are encoded in shades of blue, and components moving toward the transducer are encoded in shades of red (Figs. 38.**11**, 38.**15**). The higher the blood flow velocity relative to the transducer, the brighter the color shade. This is particularly evident in laminar flows, where the central portion of the blood vessel appears brighter due to the higher flow velocities in that region. The color encoding of blood flow is not accessible to qualitative analysis, and therefore a conventional Doppler spectrum is displayed next to the color flow image.

The color-encoded display of *blood flow* depends both on the Doppler angle and on the flow velocity in the insonated vessel (Fig. 38.**11**). As in pulsed Doppler ultrasound, velocity information is limited by the pulse repetition frequency (PRF), which depends on the penetration depth of the color box. If the measured Doppler frequency is greater than one-half the PRF (the Nyquist limit), a *color reversal* occurs, with red changing to blue and blue changing to red. In extreme cases, this results in a multicolored mosaic pattern (Fig. 38.**12**). This phenomenon, called *aliasing*, can be corrected by increasing the PRF or shifting the baseline color scale. The *color gain* can be adjusted to increase or reduce the sensitivity level for detecting blood flow. For an optimum color display, the PRF should first be adjusted for the expected flow velocity, and then the color gain should be optimized. Setting the color gain too low leads to poor color filling of the vessel, while setting the color gain too high causes extraneous color signals to "bleed through" the vessel wall and create color noise in the surrounding tissue.

The *wall filter* suppresses velocities below the defined filter setting and keeps them from being displayed as color signals. The *frame rate* also influences the quality of the color image. The frame rate is the frequency at which a color-encoded ultrasound image is refreshed each second. Slow frame rates are necessary for the display of slow flow velocities like those encountered in tumor vessels.

Specific Vessels

External Iliac Artery and Vein

The external iliac vessels appear in coronal section as an elongated, double vascular bundle. The artery can be identified by its pulsations and by its position above the vein. The Doppler waveform of the *external iliac artery* is triphasic, consisting of a sharp systolic upstroke, a reversal of flow in early diastole, and low end-diastolic flow (Fig. 38.**13**). The *external iliac vein*, on the other hand, shows a flat, continuous waveform that varies with respirations (Fig. 38.**14**). Blood flow in the external iliac artery is generally directed toward the endovaginal probe and is encoded red in the color flow image, while flow in the external iliac vein is directed away from the probe and is encoded in blue (Fig. 38.**15**). The color display of the vessels is dependent on the position of the endovaginal probe relative to the vessel axis (Fig. 38.**11**).

One clinical application of transvaginal Doppler scanning of the external iliac vessels is in the evaluation of deep iliac vein thrombosis.

Ovarian Artery

The vaginal probe is positioned in the lateral fornix to evaluate blood flow velocity in the ovarian artery. With normal anatomical relationships, the ovary can be imaged medial to the external iliac artery and vein (Fig. 38.**15**). The ovarian artery is very difficult to define in the B-mode image and with gray-scale Doppler, but is relatively easy to identify lateral to the ovary with color Doppler. After the color mode is switched on, the color box is positioned over the region of interest. Care should be taken to keep the sector angle of the color box as small as possible. Next, the PRF is adjusted for the expected flow velocity, and the color gain is adjusted to obtain an optimum color display. Generally the color gain should be kept very low to avoid obscuring the vessel by extraneous color signals. Manipulations of the vaginal probe during the examination should be slow and gentle to avoid motion artifacts. When the ovarian artery has been identified in cross section, the vaginal probe can be gently rotated to define the vessel in longitudinal section (Fig. 38.**16**).

Because the blood flow in the ovarian artery is generally directed toward the ultrasound probe, the vessel appears red in the color flow image, and high velocities are encoded in yellow. When the vessel has been identified, the Doppler beam is positioned over the ovarian artery and the Doppler gate (sample volume) is opened to fully encompass the vessel lumen. The angle is then adjusted in the direction of the vessel, and the Doppler mode is activated to record frequency shifts in the real-time or freeze-frame B-mode image (Fig. 38.**17**). Good-quality waveforms should be recorded over at least three cycles, whereupon the Doppler parameters and blood flow velocities can be automatically or manually evaluated.

It should be noted that the waveforms sampled from the ovarian vessels show significant changes during the menstrual cycle and are also dependent on menopausal status [1]. Besides ultrasound folliculometry and the determination of hormonal parameters, transvaginal color Doppler studies of the ovarian artery as well as intraovarian vessels are being used in the evaluation of infertility patients and in monitoring therapeutic response (Figs. 38.**18**, 38.**19**) (Chapter 39).

Uterine Artery

The uterine vessels should be evaluated following the transvaginal ultrasound examination of the uterus. Any endometrial abnormalities, uterine masses, and uterine anomalies should first be carefully described and documented. Accurate uterine waveform analysis also requires a knowledge of the cycle phase and menopausal status and whether the patient is receiving hormone replacement therapy. The uterine artery is defined sonographically at the isthmocervical junction in a transverse scan of the paracervical region. The uterine artery can be identified by its pulsations in the B-mode image. While it can be very difficult and time-consuming to locate the uterine vessels with conventional transvaginal Doppler ultrasound, color Doppler allows for rapid orientation and localization of the vessels. Given the tortuous course of the ascending and descending branches of the uterine artery, color Doppler shows an alternation of blue and red luminal areas consistent with the changing direction of the blood flow. The uterine artery waveform is characterized by a steep systolic upstroke followed by an early diastolic notch and low flow at end diastole [13] (Fig. 38.**20**).

Power Doppler Imaging

In 1993, the Acuson Corporation (Mountain View, California) introduced an ultrasound technology in which the energy of the Doppler signal produced by blood flow is detected and displayed as a color-encoded image. The key advantages of this technology, known as power Doppler imaging or color Doppler energy (CDE), are that it can detect considerably lower flow velocities than conventional color flow Doppler and is largely unaffected by the beam–vessel angle, or the position of the vessel in relation to the ultrasound probe.

It is expected that this technology will become particularly important in the diagnosis of inflammatory processes with tissue hyperemia [14] and of neoplasms. The angiogenesis that is frequently induced by tumors [15] can be demonstrated more clearly with power Doppler than with conventional color Doppler (Figs. 38.**21**, 38.**22**). Power Dop-

pler can define even the tiniest blood vessels, like those occurring in cyst walls, which cannot be seen in a conventional color flow image (Figs. 28.**42**, 28.**64**). Although this technique has interesting diagnostic aspects, its true value cannot be assessed until large-scale studies become available. At present, the main limitation of power Doppler is its inability to quantify the recorded color signals.

The differences between conventional color Doppler and power Doppler imaging are outlined in Table 38.**1**.

Table 38.**1** Comparison of conventional color Doppler and power Doppler

Color Doppler imaging (conventional color Doppler)	Power Doppler imaging (color Doppler energy)
• Detection of blood flow velocity and variance	• Energy of the Doppler signal produced by blood flow is color-encoded
• Cannot detect very low velocities	• Can detect even very low flow velocities
• Vascular imaging depends on vessel position	• Vascular imaging does not depend on vessel position
• Dependence on beam–vessel angle	• No dependence on beam–vessel angle
• Aliasing	• No aliasing
• Can detect blood flow direction	• Cannot detect blood flow direction
• Few motion artifacts	• Conspicuous motion artifacts

References

1 Bourne TH. Transvaginal color Doppler in gynecology. Ultrasound Obstet Gynecol 1991;1:359–73.
2 Kurjak A, Shalan H, Kupesic S, Predanic M, Zalud I, Breyer B, et al. Transvaginal color Doppler sonography in the assessment of pelvic tumor vascularity. Ultrasound Obstet Gynecol 1993;3:137–54.
3 Doppler C. Über das farbige Licht der Doppelsterne und einiger anderer Gestirne des Himmels. Abh K Böhm Ges 1843;2:465–82.
4 Wells PN. Doppler ultrasound in medical diagnosis. Br J Radiol 1989;62:399–420.
5 Griffin D, Cohen-Overbeek T, Campbell S. Fetal and utero-placental blood flow. Clin Obstet Gynecol 1983;10:565–602.
6 Schmidt W, Rühle W, Braun W, Auer L. Verlässlichkeit der Duplex-Sonographie zur nichtquantitativen Messung des Durchflusses im Vergleich zur induktiven Flugmessung einer in vitro-Studie. Z Geburtshilfe Perinatol 1988;192:19–23.
7 Taylor KJ, Holland S. Doppler US. Part I. Basic principles, instrumentation, and pitfalls. Radiology 1990;174:297–307.
8 Scoutt LM, Zawin ML, Taylor KJ. Doppler US. Part II. Clinical applications. Radiology 1990;174:309–19.
9 Klews PM. Einführung in die farbkodierte Duplexsonographie (FKDS). In: Wolf KJ, Fobbe F, editors. Farbkodierte Duplexsonographie. Grundlagen und klinische Anwendung. Stuttgart: Thieme, 1993: 1–13.
10 Strauss, AL. Farbduplexsonographie der Arterien und Venen. Leitfaden und Atlas. Berlin: Springer, 1994.
11 Wolf KJ, Fobe F. Farbkodierte Duplexsonographie. Grundlagen und klinische Anwendung. Stuttgart: Thieme, 1993.
12 Mitchell DG. Color Doppler imaging: principles, limitations, and artifacts. Radiology 1990;177:1–10.
13 Schulman H, Fleischer A, Farmakides G, Bracero L, Rochelson B, Grunfeld L. Development of uterine artery compliance in pregnancy as detected by Doppler ultrasound. Am J Obstet Gynecol 1986;155:1031–6.
14 Newman JS, Adler RS, Bude RO, Rubin JM. Detection of soft-tissue hyperemia: value of power Doppler sonography. AJR Am J Roentgenol 1994;163:385–9.
15 Folkman J, Watson K, Ingber D, Hanahan D. Induction of angiogenesis during the transition from hyperplasia to neoplasia. Nature 1989;339:58–61.
16 Gosling RG, King DH. Ultrasound angiology. In: Marcus W, Adamson L, editors. Arteries and veins. Edinburgh: Churchill Livingstone, 1975: 61–9.
17 Pourcelot L. Applications cliniques de l'examen Doppler transcutané. In: Pourcelot L, ed. Velocimetric Ultrasonore Doppler. Paris: Inserme, 1974:212–218.
18 Stuart B, Drumm J, FitzGerald DE, Duignan NM. Fetal blood velocity waveforms in normal pregnancy. Br J Obstet Gynaecol 1980;87:780–5.

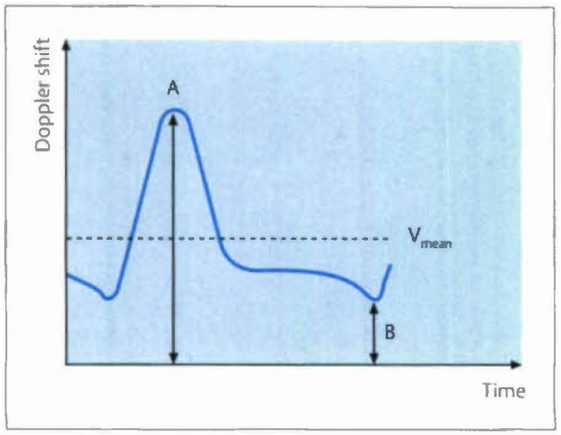

1

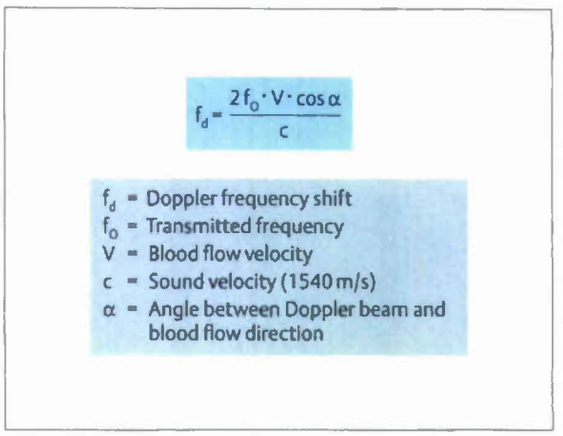

2

Fig. 38.1 Schematic representation of the Doppler frequency shift.

Fig. 38.2 The Doppler equation.

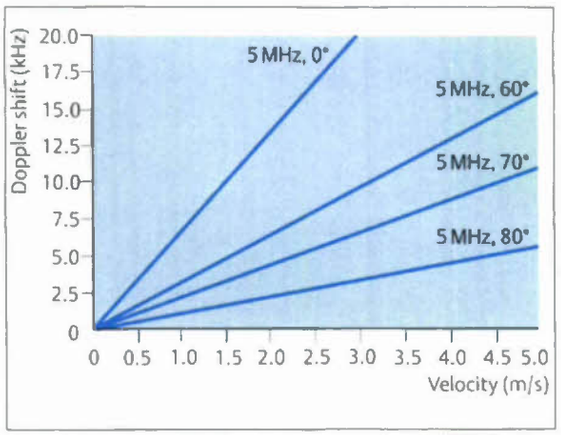

3

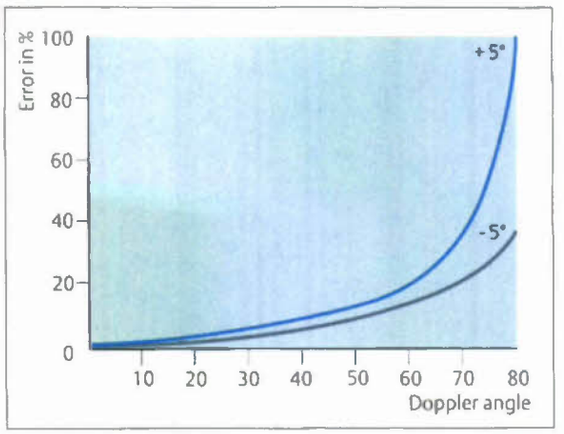

4

Fig. 38.3 Doppler shift versus blood flow velocity for various Doppler angles (adapted from Klews [9]).

Fig. 38.4 Effect of the Doppler angle. Percentage error in flow velocity calculation for an angle setting error of ± 5 % (adapted from Griffin et al. [5]).

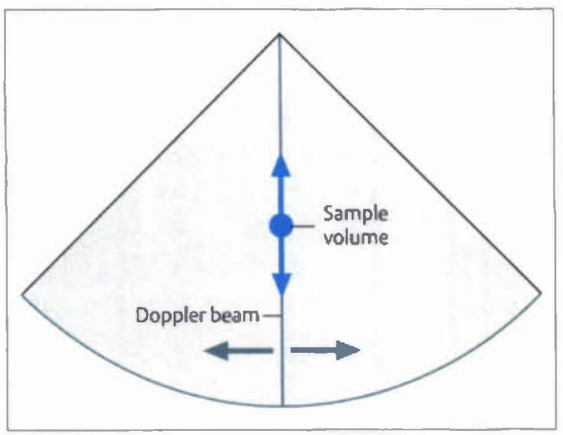

5

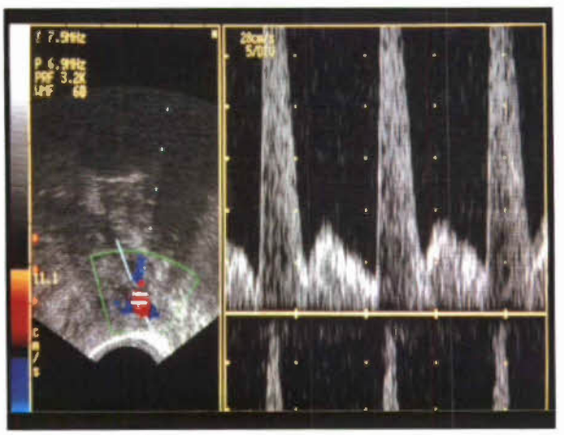

6

Pulsed Doppler Ultrasound, Pulsed-Wave (PW) Doppler

Fig. 38.5 PW Doppler with sample volume.

Fig. 38.6 Aliasing in the left uterine artery. The pulse repetition frequency setting, at 3.2 kHz, is definitely too low.

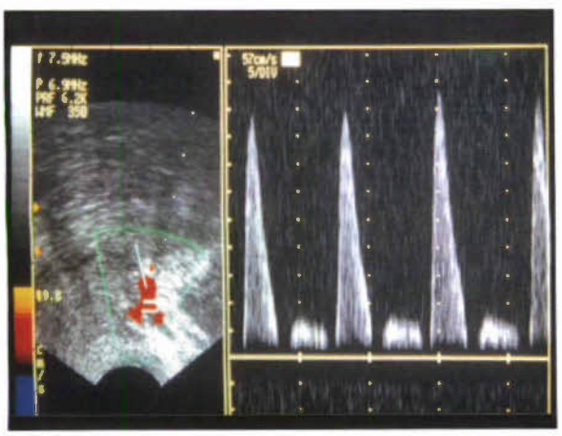

7

Fig. 38.7 The wall filter has been set at 350 Hz. This is too high, as it suppresses the low-frequency components in the left uterine artery.

Doppler Parameters

Fig. 38.8 Automated waveform analysis. The spectral waveforms were sampled from an intraovarian artery in the presence of a corpus luteum cyst.

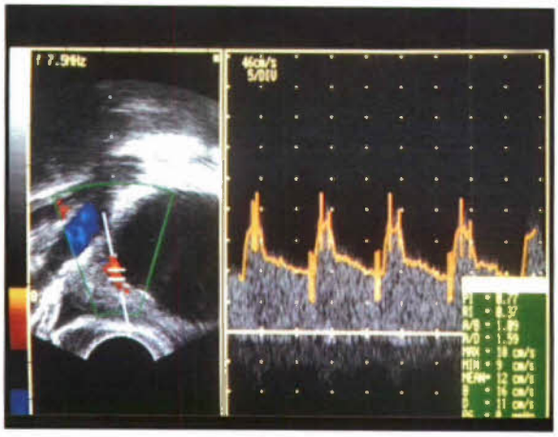

8

Fig. 38.9 Indices used in qualitative analysis of the Doppler waveform.

$$\text{Resistance index} = \frac{A-B}{A} \quad \text{(Pourcelot, 1974)}$$

$$\text{Pulsatility index} = \frac{A-B}{V_{mean}} \quad \text{(Gosling and King, 1975)}$$

$$\text{A/B-ratio} = \frac{A}{B} \quad \text{(Stuart et al., 1980)}$$

9

Fig. 38.10 Principle of multigate Doppler.

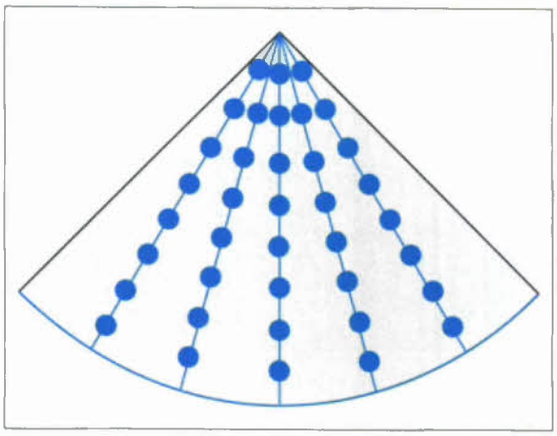

10

Fig. 38.11 Directional dependence of color encoding, illustrated for the external iliac artery and vein. The color reversal from red to blue, and vice-versa, is caused by the relative change in flow direction. Blood flow toward the transducer is encoded in shades of red, flow away from the transducer in shades of blue. Flow at the center of the vessel is not detected, due to the unfavorable 90° beam–vessel angle.

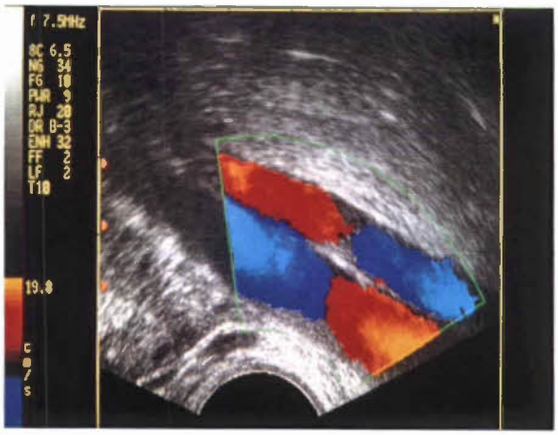

11

Fig. 38.12 Aliasing. The pulse repetition frequency, and thus the sampling rate, has been set too low for the flow velocity in the pelvic wall vessels.

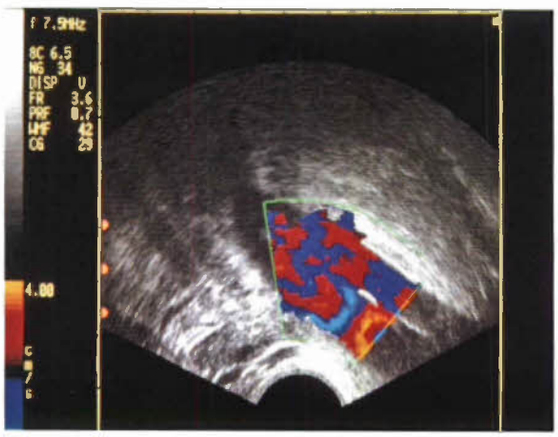

12

Fig. 38.13 A typical waveform recorded from the external iliac artery, indicating a high peripheral vascular resistance.

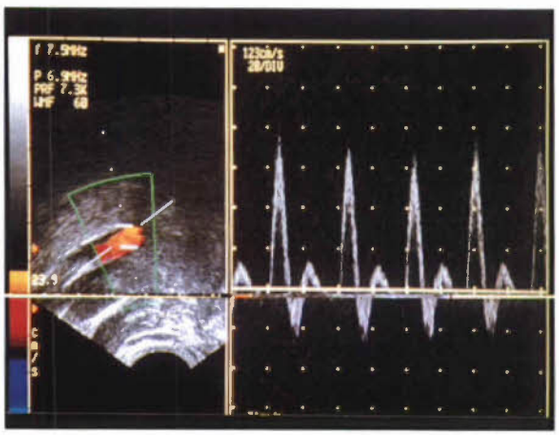

13

External Iliac Artery and Vein

Fig. 38.14 Color Doppler image and spectrum recorded from the external iliac vein. The blue color indicates blood flow directed away from the vaginal probe. The sample volume encompasses the entire vessel.

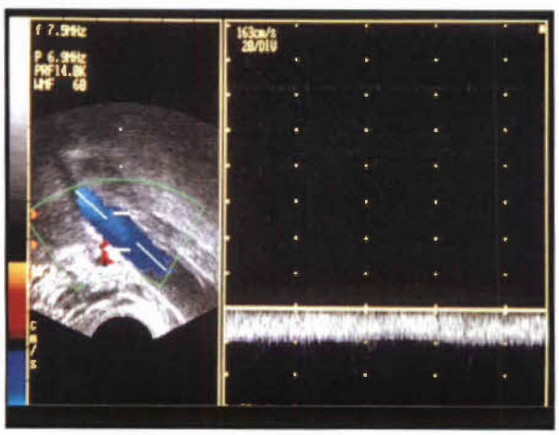

14

Fig. 38.15 Transvaginal color Doppler image of the right external iliac artery (red) and external iliac vein (blue). The right ovary appears medial to the iliac vessels.

15

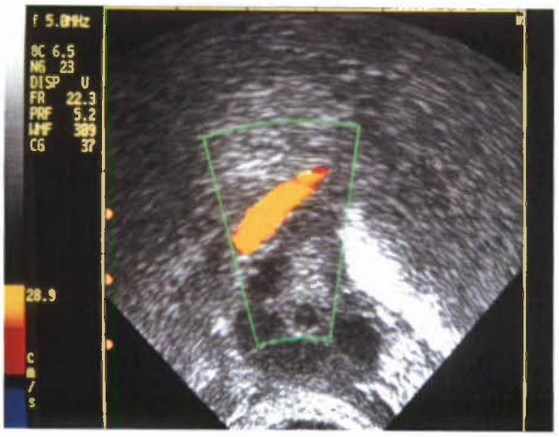

16

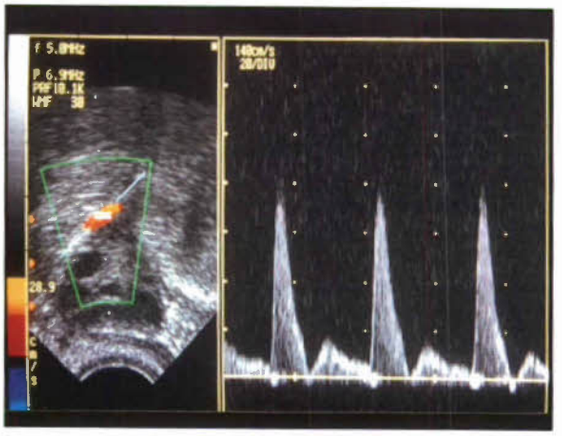

17

Ovarian Artery

Fig. 38.16 Transvaginal color Doppler image of the right ovarian artery. The pulse repetition frequency has been set at 5.2 kHz, which is too high for this flow velocity and causes yellow encoding of the artery lumen.

Fig. 38.17 Color Doppler image and spectrum of the right ovarian artery on day 7 of the menstrual cycle.

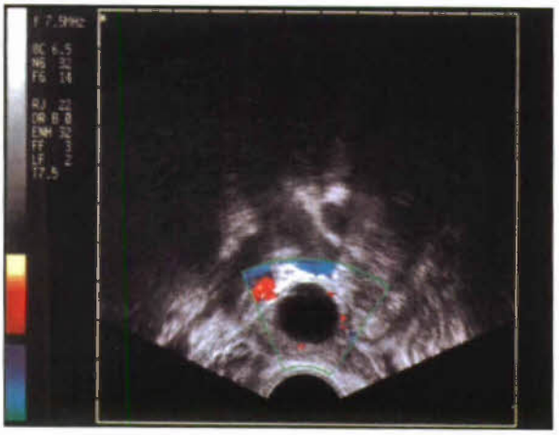

18

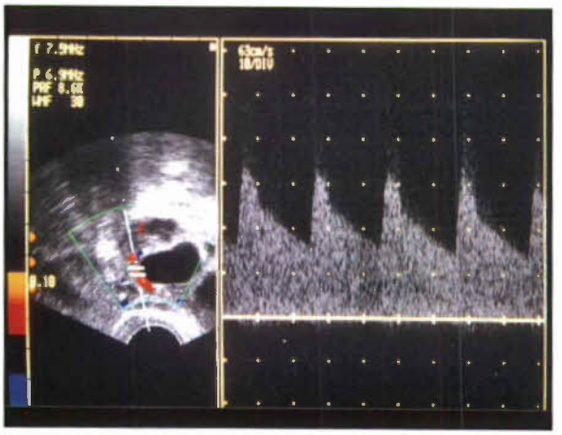

19

Fig. 38.18 Transvaginal color Doppler image of an ovary on day 7 of the menstrual cycle.

Fig. 38.19 Color Doppler image and spectrum of an intraovarian artery on day 14 of the menstrual cycle.

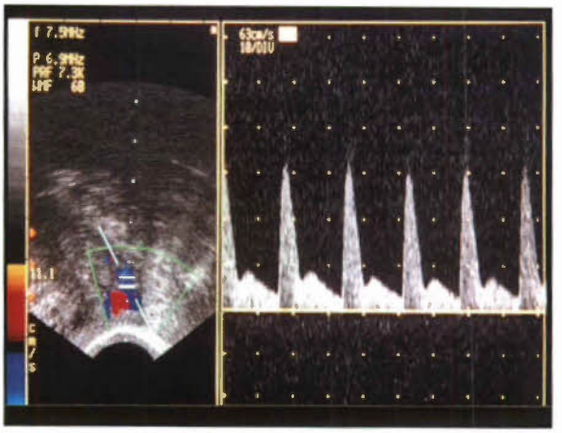

20

Uterine Artery

Fig. 38.20 Transvaginal color Doppler scan of the left uterine artery, demonstrating the uterine artery waveform.

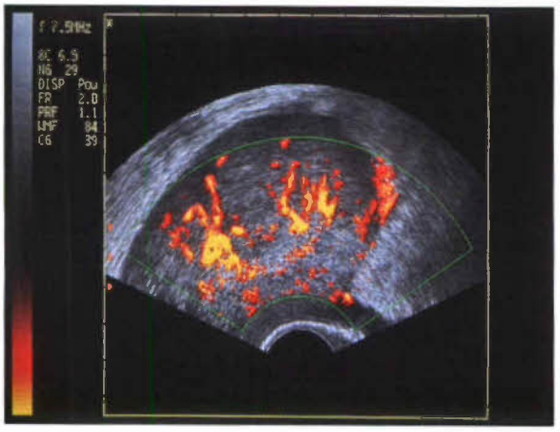

21

22

Fig. 38.21 A malignant solid ovarian tumor. Power Doppler reveals an irregular vascular distribution within the mass.

Fig. 38.22 A small, solid, malignant ovarian tumor with markedly irregular vascularity (power Doppler image).

39 Transvaginal Doppler Ultrasound in the Evaluation of Infertility and Gynecologic Tumors

Transvaginal pulsed Doppler and color Doppler ultrasound provide a qualitative impression of blood flow in the vessels of the true pelvis. The information supplied by color Doppler can potentially influence the clinical management of patients in a variety of situations:

- Identifying patients whose masses can be treated by a minimally invasive approach (laparoscopy, microsurgery) and distinguishing them from patients who require a standard laparotomy and extensive cancer surgery.
- Establishing the diagnosis of hemorrhagic ovarian cysts that will resolve without treatment.
- Confirming the sonographic diagnosis of ovarian torsion, which requires immediate operative intervention.
- Verifying a pelvic congestion syndrome.

Ovary

A growing number of studies on normal and abnormal ovarian blood flow have been published during the past 5 years. These studies have documented the capabilities of transvaginal color Doppler ultrasound in detecting and understanding the physiologic and pathophysiologic changes that can occur in ovarian blood flow.

Vascular Anatomy of the Ovaries

An accurate knowledge of ovarian vascular anatomy is important for the proper application of Doppler technology in hemodynamic studies. The vascular anatomy of the ovary consists of an arterial, venous and lymphatic system. At present Doppler technology is not useful for lymphatic examinations, although this may become possible in the near future. The venous system is accessible to Doppler scanning, but a standard technique for this examination has not yet been established. The main focus of current interest is the arterial system.

The vascular system of the ovaries can be subdivided into two parts:

- The *extrinsic vascular system*, consisting of arteries that arise from the major abdominal vascular trunks and pass to the ovary, along with their accompanying veins.
- The *intrinsic vascular system*, consisting of vessels that enter the ovary from the ovarian hilum and sustain the microcirculation before terminating at the veins [1].

Although both of these vascular systems comprise a common system, it is functionally helpful to make a topographic distinction between the two subsystems.

The cyclic changes in ovarian vascularity are manifested most clearly in the intrinsic vascular system. The basic pattern of the ovarian blood supply is comparable in all mammals, but becomes increasingly complex toward the top of the phylogenetic pyramid [1].

Arteries

The ovaries derive their arterial supply from two sources: the ovarian artery and the utero-ovarian branches of the uterine artery [2]. These arteries anastomose in an arch parallel to the ovarian hilum and form the genital vascular arcade. The *ovarian artery* arises from each side of the abdominal aorta below the level of the renal arteries. From there, it runs obliquely downward, crosses over the ureter and iliac vessels, and enters the ovarian suspensory ligament. The artery approaches the ovary at its upper pole. The external ovarian artery arises in this plane but does not contribute to the ovarian blood supply. The second arterial branch, which does contribute to ovarian perfusion, is the *ovarian branch* of the uterine artery. This vessel arises from the uterine artery at the cornual level and passes to the lower pole of the ovary. Both of these arteries anastomose directly or via branches that enter the ovary from the front or from the hilum. While embryonic development clearly indicates that the ovary receives most of its blood supply from the ovarian artery, the importance of the ovarian branch of the uterine artery appears to depend on the type of anastomosis that is formed. Topographically, four types of anastomosis may develop between the two arteries and are characterized by a balanced supply or a dominant supply from one of the arteries.

Veins

The ovarian veins leave the ovary at the level of the hilum and form the *pampiniform plexus*, characterized by its numerous plexus-like connections. Together with the veins that drain the uterus, this plexus is continued in the paired utero-ovarian veins, which are interlinked by numerous cross-connections [3]. Both channels pass obliquely upward and unite to form a single ovarian vein, which empties into the renal vein on the left side and into the vena cava on the right side.

Intrinsic Vascular System (Microcirculation)

The intrinsic vascular system (microcirculation) of the ovary has an arterial supply that is known for its specialized pattern and functional changes. Arterial branches radiate into the stroma from the ovarian hilum [1] and acquire a tortuous, spiraled course as they coil about their own axis. Because of this special arrangement, they are termed the *spiral arteries*. They undergo numerous divisions in the ovarian stroma, steadily diminishing in caliber until their diameters in the cortical zone are in the range of 40–60 µm. Branching from the main vessel at an acute or right angle, they form a succession of arterioles at the first capillary level [3]. The abundant spiral arteries in the ovarian stroma form a true medulla at this level [1]. The arterial vessel drains through a venous system (> 80 µm in diameter) that forms a tangled coil called the *ovarian bulb*. The spiral pattern of the ovarian arteries plays an important role in hemodynamic adaptations during the ovarian cycle. The spiral course of the arteries enlarges the frictional surface area during blood flow, thereby increasing the vascular resistance and lowering the blood pressure. This is necessary in order to maintain an elevated pressure in the initial portion of the ovarian artery [1]. The specialized shape of these arteries creates zones of turbulence within the vascular system, while the angled branching pattern of the arterioles helps to maintain the stability of blood flow with minimal loss of energy. This type of vascular structure also facilitates adaptation to the size changes that are necessary in relation to follicular development and corpus luteum formation. As follicular growth proceeds, the arteries become larger and less coiled. With follicular atresia and regression of the corpus luteum, the arteries return to their initial state [4].

Uterus

Uterine Blood Supply

The blood flow changes that occur in the large uterine arteries and their intrauterine branches during the menstrual cycle are important prerequisites for implantation and the development of early pregnancy. The uterine artery and its small arterial branches can be visualized by transvaginal color Doppler imaging, and the blood flow changes in those vessels can be analyzed with pulsed Doppler [5]. The color signal of the uterine arteries can be identified at the level of the uterine isthmus. The uterus is supplied by the two uterine arteries, which are branches of the internal iliac artery [6]. In the lower part of the uterus the *uterine artery* divides into the vaginal artery and an ascending branch from which the *arcuate arteries* arise. The latter run parallel to the uterine cavity and anastomose with one another to form a vascular ring around the uterine cavity. The small *radial arteries* arise from the arcuate arteries and penetrate the myometrium at right angles to the uterine cavity. As these arteries continue into the endometrium, they give off lateral branches that supply the basal lamina. These basal arteries continue toward the endometrial surface and acquire a corkscrew-like configuration in their terminal portions. These coiled arterial segments, called the *spiral arteries*, are very sensitive to hormonal changes. One reason for the delicacy of the functional layer of the endometrium is the absence of anastomoses among the spiral arteries. The glands of the endometrium and the stromal tissue are supplied by capillaries that arise from the spiral arteries at the level of the endometrium. The capillaries drain the blood into a venous plexus and, to a degree, into the arcuate veins of the myometrium and the uterine veins. This unique vascular architecture represents an important adaptation to cyclical changes and enables implantation and placentation to occur. The blood flow parameters of the uterine vessels correlate with ovarian hormone levels in the peripheral venous blood [7,8]. During the menstrual cycle, the endometrium is subject to structural and functional changes that relate mainly to the development of the spiral arteries [9–13]. The increase in the vascularity of the endometrium is based on blood flow changes in the uterine arteries, arcuate arteries, and radial arteries.

Color Doppler Examination of the Ovary and Uterus and its Value in Infertile Patients

Blood Flow in the Ovarian Artery

The ovarian artery branches from the abdominal aorta and reaches the ovary by way of the ovarian suspensory ligament [1]. This vessel cannot be clearly visualized in some patients, but it can be identified by placing the Doppler sample volume over the ligament and then over the ovarian tissue until an arterial signal is detected. Signals from the ovarian artery show the characteristic spectral pattern of small vessels with low-velocity flow. The waveform changes with the state of ovarian activity. Studies of ovarian artery waveforms have shown differences in vascular resistance between the two ovarian arteries depending on the presence of a dominant follicle or corpus luteum [14,15]. A longitudinal study of ovarian artery waveforms during the course of an ovarian cycle (conducted at the Ultrasonic Institute, University of Zagreb, Croatia) showed increased blood flow with decreased pulsatility and resistance indices in the ovarian artery on the side with the dominant follicle or corpus luteum (Figs. 39.**1**, 39.**2**). By contrast, the ovarian artery of the "inactive" ovary was found to have little or no end-diastolic flow. The rise of end-diastolic flow velocity in the "active" ovary is most apparent on day 21 of the cycle and indicates that the corpus luteum functions as a low-resistance shunt.

Various invasive and noninvasive techniques have already been used for ovarian blood flow measurements in mammals. They include the use of microspheres [16], selective blood sampling [17], the implantation of Doppler flowmeters [18], and the implantation of electromagnetic flowmeters in the cow [19]. These techniques have shown that 80–90% of the blood flow in the ovarian arteries supplies the corpus luteum [20]. The increased blood supply to the functioning corpus luteum is essential for the release of substances that are involved in steroid synthesis and for the elimination of progesterone [16,19,21]. Studies in animal models have shown a rapid decline in ovarian blood flow during regression of the corpus luteum [17]. Prostaglandin $F_{2\alpha}$ has been identified as an active luteolysin in this process. A 90% reduction of luteal flow has been reported following the local administration of $PGF_{2\alpha}$ [22]. In patients who had been treated with clomiphene citrate and/or human menopausal gonadotropin (HMG) and were found to have multifollicular growth on both sides, both ovarian arteries exhibited the low-pulsatility waveforms typical of low vascular resistance.

With the onset of pregnancy, the corpus luteum continues to function and the active-type waveforms persist. Studies have confirmed that Doppler ultrasound is a good method for monitoring the activity of the corpus luteum.

Intraovarian Blood Flow

Doppler waveforms sampled from the ovarian artery (high-pressure system) are radically different from the waveforms recorded from intraovarian branches. Near the ovarian hilum the penetrating vessels are coiled and tortuous. This type of vascular supply demonstrates a high-resistance flow pattern (high resistance index).

Each month in a woman of reproductive age, a single mature ovarian follicle releases one oocyte. A variety of biochemical, morphological and vascular changes occur during this process. Color Doppler can demonstrate well-vascularized zones at the periphery of a dominant follicle that has reached a diameter of 10 mm or more. The resistance index (RI) prior to ovulation is approximately 0.54 (Fig. 39.**3**). The index begins to decline two days before ovulation and reaches its lowest value at the time of ovulation ($RI = 0.44 \pm 0.04$) [23]. The rise of maximum systolic flow velocity in the vessels of the follicular wall accompanied by a relatively constant RI is a particularly interesting discovery that may signify impending ovulation. Increased vascularity in the innermost ring of the follicular wall [24] could represent the dilation of new vessels that develop between the relatively vascular theca cell layer and the normally hypoxic granulosa cell layer of the follicle. The disruption of these vascular changes has profound effects on the oxygen concentration in the follicular epithelium [25,26].

We are hopeful that a more detailed knowledge of ovarian perfusion will be useful not only in predicting ovulation but also in detecting ovarian dysfunction. We did not observe a rise of maximum blood flow velocity during the preovulatory period in 12 women with LUF (luteinized unruptured follicle) syndrome. Study data support the hypothesis regarding changes of oxygen partial pressure in the follicular wall that are necessary in order for follicular rupture to occur [24–26]. If the process of oogenesis or ovulation can be inhibited independently of the main pathways of steroid synthesis, new methods of contraception could become available. Steroids that inhibit angiogenesis in the presence of heparin have already been identified [27]. It is clear that transvaginal color Doppler ultrasound could be used to monitor the changes that take place within the framework of these new contraceptive methods.

A similar approach can be used to monitor the progression of intraovarian blood flow changes in patients with polycystic ovary (PCO) syndrome. Hormonal parameters—luteinizing hormone (LH)/follicle-stimulating hormone (FSH) ratio > 3, elevated androgen values—and intraovarian blood flow were measured in 34 oligomenorrheic or amen-

orrheic women with bilaterally enlarged ovaries, a thickened ovarian capsule, and numerous cystic structures 2–8 mm in diameter. No changes were found in the resistance indices of the ovarian arteries or intraparenchymal ovarian vessels during the menstrual cycle. Continuously high diastolic flow velocities were sampled from the ovarian stroma, showing a mean resistance index of 0.54 (Fig. 39.**4**). These vascular changes may be the product of a local hyperandrogenism and/or LH stimulus on the (vascularized) theca cells.

It is easiest to record color Doppler signals from ovarian tissue during the luteal phase of the cycle. The qualitative postovulatory changes in the intraovarian waveforms are striking, as zones of increasing turbulence accompany morphologic changes in the intraovarian vascular network [28] and numerous arteriovenous shunts develop during the luteal phase [29]. The postovulatory resistance index differs significantly from the preovulatory values. Every women with confirmed ovulation was found to have an RI of 0.43±0.04 shortly after ovulation (Fig. 39.**5**). The RI remains at this low level for 4–5 days and then rises to 0.50, which is lower than the RI in the early follicular phase. Luteal transformation can be detected in all normal ovulatory cycles without having to identify the corpus luteum [23]. Altered blood flow signals persist throughout the luteal phase and are not observed on the nondominant contralateral side. The same findings have been reported in patients with an anovulatory cycle or LUF syndrome [30]. The perfusion pattern of the corpus luteum, characterized by low resistance and high flow, is easily detectable by transvaginal color Doppler scanning in a normal pregnancy, in an ectopic pregnancy, and in the nonpregnant subject [31]. At present, it is still uncertain whether inadequate vascularization plays a role in luteal phase defect and whether luteal flow can be interpreted as a prognostic sign.

Uterine Blood Flow During the Menstrual Cycle

During the *proliferative phase* of the cycle, blood flow in the uterine artery shows a resistance index of 0.88±0.04 (SD) (Fig. 39.**6**). The flow resistance begins to decline on the day before ovulation, reaching its lowest value on day 18 (RI 0.84±0.04) (Fig. 39.**7**). The RI remains at that level for the rest of the cycle. Because the changes begin before ovulation, it is reasonable to assume that they are caused by other factors than the muscle-relaxing effect of progesterone. The persistently low resistance index during the luteal phase suggests that these effects on the uterine arteries continue until the onset of menstruation. It is interesting that the lowest resistance is observed when luteal function is highest, at the time when implantation is most likely to occur [2,12,27]. Some authors, such as Kurjak et al. [32], Goswamy et al. [7,33], Steer et al. [34], and Battaglia et al. [35], have reported high blood flow to the uterus during the late luteal phase. These changes are not seen in anovulatory cycles, which are marked by a steady rise in the resistance index [32]. In most women, low end-diastolic flow is detected in the uterine arteries during the proliferative phase. A rapid rise of end-diastolic flow velocity occurs between the proliferative and secretory phases [32]. The absence of end-diastolic blood flow that has been seen in some infertile women may relate to their infertility or diminished reproductive function [7,32–34] or may simply be a variant that disappears after pregnancy [32] (Fig. 39.**8**). Steer et al. [34] observed a rising RI and increasing S/D ratio during the postovulatory fall of the serum estradiol level. An increase in resistance in the uterine arteries was reported 3 days after the LH peak, while Scholtes et al. [15] found that the pulsatility index (PI) in the uterine arteries was highest on day 16 of the cycle. These observations can perhaps be explained by the increase in uterine contractility causing compression of the uterine wall vessels [36]. This compression narrows the vascular diameter, increasing the resistance to blood flow.

In an earlier study, we analyzed the RI of the uterine arteries during the periovulatory phase in one group of women with spontaneous cycles and another group with stimulated cycles [37]. In the women with spontaneous cycles, the resistance index in the uterine arteries began to decline on the day before ovulation, with a subsequent increase in uterine blood flow. In the group of women with stimulated cycles, no changes were observed during the same period.

With transvaginal color Doppler, it is possible to investigate blood flow changes in the radial and spiral arteries under physiologic and pathophysiologic conditions. Changes in the Doppler spectra of the radial and spiral arteries in cycles with spontaneous ovulation are accompanied by changes in the flow dynamics of the uterine arteries. The resistance index of the *radial arteries* during the proliferative phase is 0.78±0.10. It begins to fall at midcycle and reaches its low point of 0.68±0.04 in the mid-luteal phase (Fig. 39.**9**). We were the first to describe the changes in the Doppler spectra of the *spiral arteries* that occur during a normal cycle [37]. On the day before ovulation, the blood flow velocity in the spiral arteries begins to increase with a RI of 0.54±0.03 (Fig. 39.**10**). The RI reaches its low point of 0.49±0.05 between days 16 and 18. In stimulated ovarian cycles, however, we found that the flow resistance rose on the day before ovulation. It may be that ovulation induction interferes with the uterine changes, and this should be investigated by Doppler studies prior to in-vitro fertilization (IVF). The noninvasive monitoring of endometrial perfusion permits a more reliable assessment of uterine receptivity than the perfusion of the uterine artery alone. For this reason, waveform changes in the spiral arteries can be used to predict the success rate of implantation in order to detect undisclosed infertility problems and screen out patients in whom abnormal endometrial perfusion may be correctible by appropriate treatment. Goswamy et al. [33] and Goswamy and Steptoe [7] showed that the administration of estradiol can improve the uterine response in patients with poor uterine blood flow [37]. It is important to understand the blood flow changes in the endometrium in order to predict the optimum timing for implantation and embryo transfer. It would then be possible to deep-freeze embryos in patients with unfavorable uterine conditions, or reduce the number of transferred embryos when conditions are optimal.

Color Doppler Studies in Tumors

The vascularization of tumors is not a process that can be calculated or predicted. Conventional angiography and color Doppler ultrasound are the only modalities that can supply information on tumor vascularization. While angiography is an invasive study, transvaginal color and pulsed Doppler ultrasound is a noninvasive method that is considerably more comfortable for the patient.

Neovascularization of Tumors

The vascular network of tumors generally develops from preexisting vessels in the affected organ [38] and from vessels that form as an angiogenic response to cancer cells [39]. Although tumor vessels may arise from the vessels of the affected organ, their organization may be completely different depending on the type, growth rate, and location of the tumor. The vascular architecture of tumors varies not only between different tumor types but also between a tumor and its metastases [40]. Tumors can be grossly subdivided into two ideal categories: tumors with *peripheral vascularity* and tumors with *central vascularity*. In tumors with peripheral vascularity, the central portions of the lesion tend to be poorly perfused. The opposite would be expected in tumors with central vascularity, but in reality a tumor is composed of various regions in which one or the other type of vascularity predominates. At the macroscopic level, tumor vascularity is very heterogeneous and does not obey normal rules of vascular organization. An essential dif-

ference between normal vessels and tumor vessels is that tumor vessels are expanded, saccular, and tortuous and may contain tumor cells within the endothelial lining of the vessel wall [41]. Also, in contrast to normal tissues which have reasonably predictable connections between arterial and venous vessels, the blood flow in a tumor may pass from one venule to another via multiple interposed vessels or may flow directly through an arteriovenous shunt. Given the peculiar nature of the vascular system, the organization of tumor blood vessels can vary by location and by time of observation. As a result, we would expect to find different blood flow pathways in the well-perfused peripheral zone, the seminecrotic zone, and the necrotic zone. Tumors are commonly divided into four regions based on differences in perfusion:

- Avascular region (necrotic)
- Seminecrotic region (ischemic)
- Region with a stable microcirculation
- Invasive peripheral region (hyperemic)

As tumors grow larger, the surface area of the vessels generally decreases while the intercapillary distances increase, and necrotic areas may develop. Newly formed tumor vessels are large, endothelium-lined, capillary-like channels or sinusoids, whose walls contain fibrous connective tissue instead of smooth muscle. Because most of the flow resistance is caused by arterioles, the absence of muscular elements in the tumor vessels leads to a decrease in flow resistance and an increase in volume flow compared with higher-resistance vessels. The microcirculation appears to play an important role in growth, in metastasis, and in the detection and treatment of tumors. Transvaginal color and pulsed Doppler ultrasound provides a qualitative picture of blood flow in the vascular system and its microcirculation in relation to the surrounding anatomy (Figs. 39.**11**, 39.**12**). Extensive studies of normal and abnormal uterine and adnexal structures can be performed with ultrasound scanners presently available, and they have already yielded a number of important discoveries [40,42].

Angiogenesis in Benign Ovarian Tumors

Functional cysts are the most frequent type of adnexal mass in women of childbearing age. The two main types, follicular cysts and corpus luteum cysts, are benign and result either from an unruptured follicle or the cystic degeneration of a corpus luteum [43]. Typically these cysts are unilateral and smaller than 6 cm in diameter. They have a smooth, rubbery consistency when palpated in the manual pelvic examination. At ultrasound, the cysts are unilocular and fluid-filled, show no evidence of solid components, and do not transcend organ boundaries [44] (Fig. 39.**13**). Neovascularity was detected in 17.8% of our study population and showed a peripheral or pericystic location. As for the Doppler indices, we determined a resistance index (RI) of 0.52 for follicular cysts and 0.46 for corpus luteum cysts.

It appears that transvaginal color Doppler ultrasound is helpful in the differential diagnosis of an *acute abdomen* and can also be used to detect the *torsion of a functional cyst*. This torsion restricts the blood supply to the ovary, affecting both the ovarian artery and the ovarian branch of the uterine artery. In three patients with symptoms of an acute abdomen, we observed color Doppler signals and a moderate flow resistance (RI = 0.47–0.52) at the periphery of the cyst in front of the torsion site. No blood supply was detected past the morphologic torsion site.

Bleeding from a *ruptured corpus luteum cyst* may be so profuse that it is mistaken for a ruptured ectopic pregnancy. Color Doppler ultrasound enhances our ability to distinguish between the two disorders and identify the patients who should be referred for operative intervention.

Mature teratomas (dermoid cysts) most commonly occur in women of childbearing age. They contain elements of mature structures that are derived from all three embryonic germ layers: the endoderm, mesoderm, and ectoderm [43]. Thus, dermoid cysts may contain hair, teeth, bone, skin, and calcified areas that can produce circumscribed high-level echoes with associated acoustic shadows. Unfortunately, these hyperechoic foci may be obscured by overlying bowel gas, so that even large masses may go undetected by ultrasound. In our study, peripheral arteries were found in 22.2% of these tumors (Fig. 39.**14**), with an average RI of 0.48. We obtained a false-positive result in 18 dermoid cysts examined. Each of these cases involved a dermoid cyst with active cell division that showed a low blood flow resistance with a diastolic notch.

Serous and *mucinous cystadenomas* are also common tumors. *Serous cystadenomas* may be unilocular but are usually multilocular, and some may present with an internal papillary growth [43,45]. A large stromal component was found in 19% of benign serous ovarian tumors, and papillary structures were found on the cyst wall in 4.5% of cases [45]. Mucinous cystadenomas may reach a tremendous size; weights of 45 to 90 kg have been reported in the literature. They most often appear as round or ovoid masses with a smooth, usually transparent or bluish gray-white capsule. *Mucinous cystadenomas* have thin walls and are usually multilocular (Fig. 39.**15**). Papillary projection may be present but are less common than in serous cystadenomas. An ultrasound examination, either alone or combined with tumor markers [46,47], cannot provide benign-malignant discrimination unless Doppler is also used. This is not surprising, as it can be difficult to distinguish a benign ovarian tumor from a malignant or borderline tumor even by gross visual inspection. Sometimes this is even difficult on microscopic examination. It appears that transvaginal color Doppler can increase the reliability of the sonographic diagnosis of serous and mucinous cystadenomas [48,49]. We found seven cases (15.5%) of vascularity in this group of ovarian tumors (n = 45). The location of the vascularity was an important criterion for differentiating the lesion from a malignant tumor. Peripheral vessels that were derived from preexisting branches of the adnexal vessels had an average resistance index of 0.52 (0.48–0.58). Vessels that coursed within septa had an average RI of 0.48 (0.45–0.54).

Fibromas, *theca cell tumors*, and *Brenner tumors* are solid benign tumors that occur in premenopausal women (Fig. 39.**16**). Small, solid tumors are difficult to detect by ultrasound because their echo texture is similar to that of a normal ovary [44]. When a solid mass is found in the adnexal region of a premenopausal woman, it is more likely to be a pedunculated or intraligamentous leiomyoma than a solid ovarian tumor. Transvaginal color Doppler is helpful in these cases, as uterine myomas can be distinguished from solid ovarian masses by their pattern of vascularization. Color Doppler sampling from the interior or periphery of a uterine mass (even if the mass is outside the uterine contour) can demonstrate the undulating signal pattern that is typical of the uterine vascular system. The blood flow in these cases is usually similar to the normal myometrial perfusion derived from the terminal branches of the uterine artery. By contrast, the small vessels that supply a growing ovarian tumor are derived from the vessels of the ovary.

In rare cases solid benign ovarian tumors are associated with ascites or pleural effusion (*Meigs syndrome*) [45].

Serum levels of CA-125 are elevated in approximately 82% of patients with epithelial ovarian carcinoma [47]. Elevated levels have also been found in a variety of benign disorders such as pelvic inflammatory disease, endometriosis, leiomyomas, and benign stromal tumors with ascites [46,47]. Jones and Surwit [50] postulated that the elevated CA-125 levels in patients with Meigs syndrome related more to a peritoneal reaction and ascites formation than to an ovarian tumor. Other reports [46,47] of CA-125 determinations in patients with benign stromal tumors without ascites described levels below 35 IU/mL. It is noteworthy that in our study of 680 confirmed adnexal tumors, we observed low Doppler resistance indices (RI = 0.42, PI = 0.78) in one patient with a benign stromal lesion and elevated CA-125 levels (318 IU/mL). Transvaginal ultrasound demonstrated a complex mass in the adnexal region with large solid parts, and transabdominal scans showed copious ascites. Histopathology confirmed that the tumor was benign.

Ovarian Vascular Changes During the Menstrual Cycle

Fig. 39.1 Blood flow in the ovarian artery over the course of the menstrual cycle.

Fig. 39.2 Ovarian artery waveforms recorded during the periovulatory phase of the menstrual cycle.

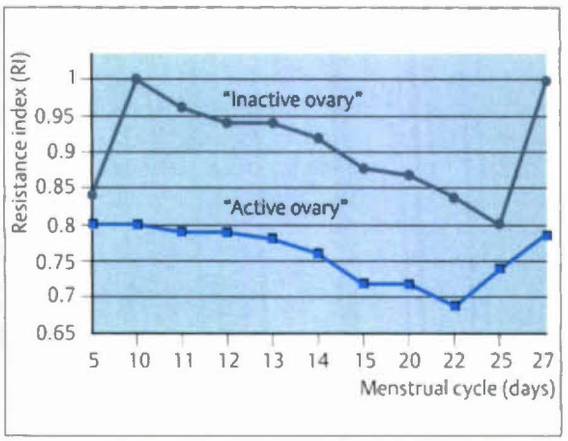

1

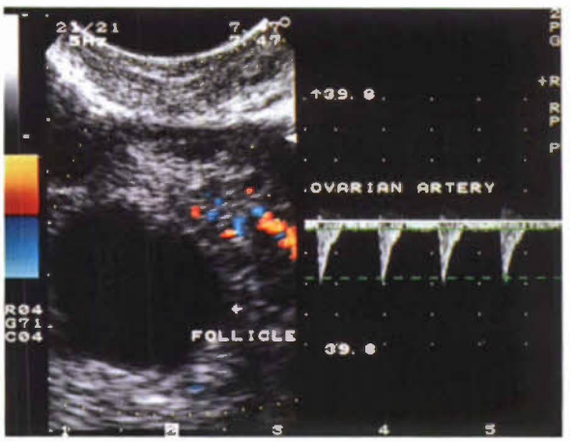

2

Fig. 39.3 Transvaginal ultrasound demonstrates an angiogenic ring around two follicles at the time of presumed ovulation (left half of image). The resistance index just before ovulation is 0.54 (right half of image).

Fig. 39.4 Transvaginal color Doppler scan of a polycystic ovary with multiple small peripheral cysts (left half of image). Waveforms with high diastolic flow are recorded from the ovarian stroma. Mean RI = 0.54 (right half of image).

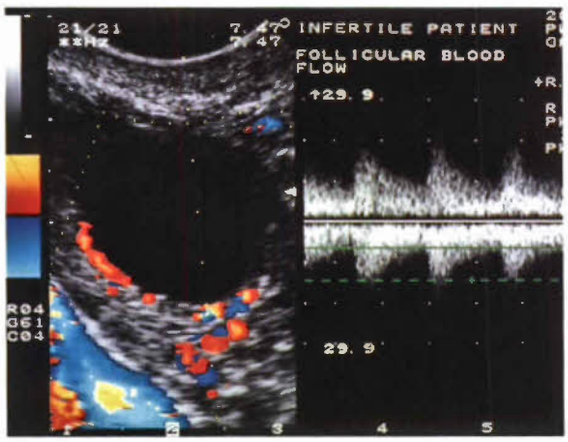

3

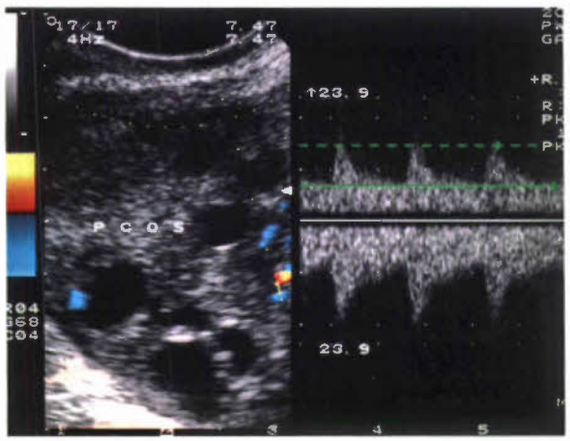

4

Fig. 39.5 High blood flow velocity and low RI (0.43) characterize the typical flow pattern of a mature corpus luteum.

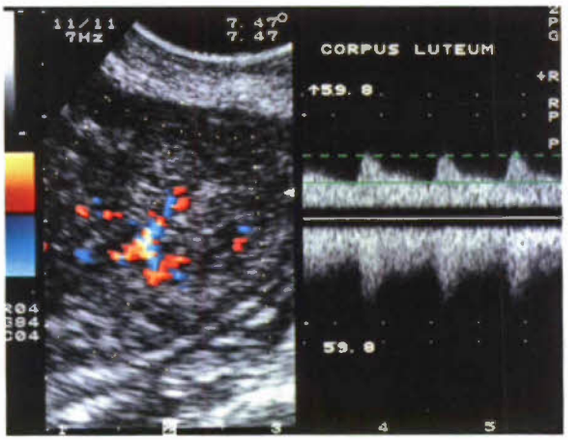

5

Uterine Vascular Changes During the Menstrual Cycle

Fig. 39.6 Blood flow velocity in the uterine artery over the course of the menstrual cycle.

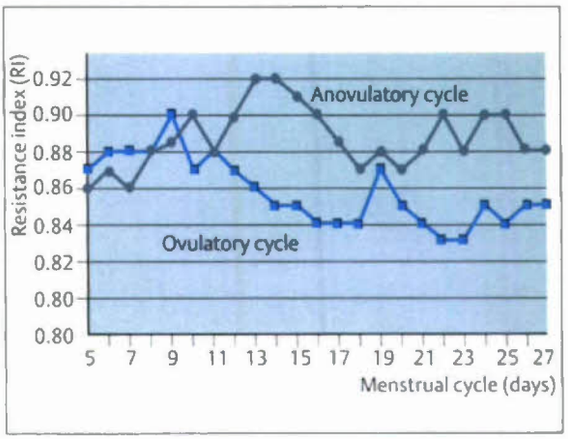

6

Fig. 39.7 Uterine artery waveforms during the secretory phase of the cycle are characterized by an increased end-diastolic flow velocity (RI = 0.81).

Fig. 39.8 Absence of diastolic blood flow in the uterine artery may be associated with infertility. * = Preovulatory follicle in the right ovary.

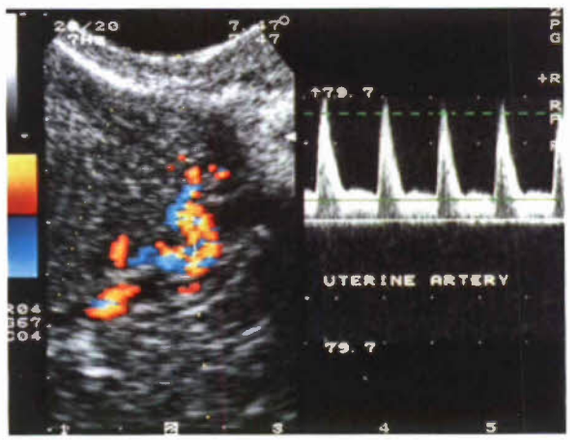

7

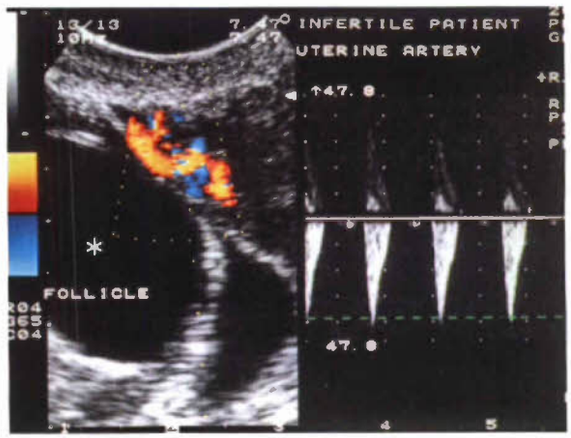

8

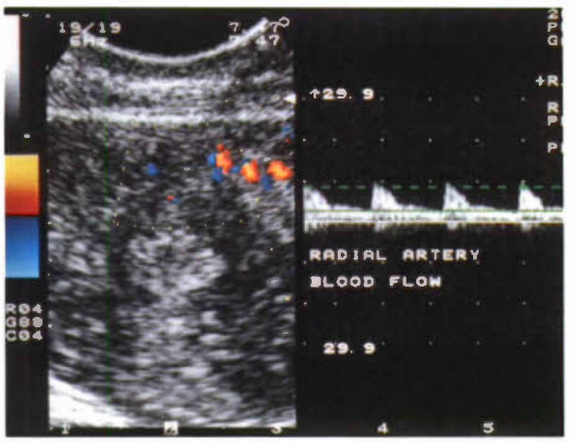

9

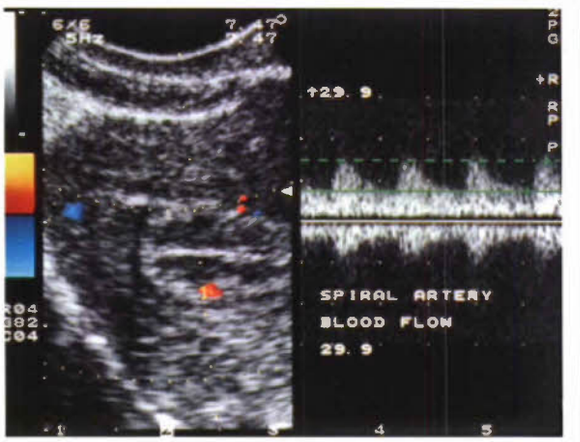

10

Fig. 39.9 Radial artery waveforms (right half of image). Note the position of the sample volume within the myometrium for blood flow detection (left half of image).

Fig. 39.10 Spiral artery waveforms during the periovulatory phase of the cycle. A low resistance index (RI = 0.51) and increased flow velocity are observed on the day of ovulation.

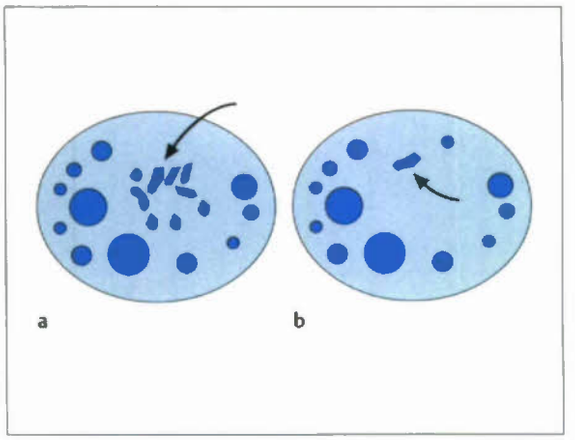

11

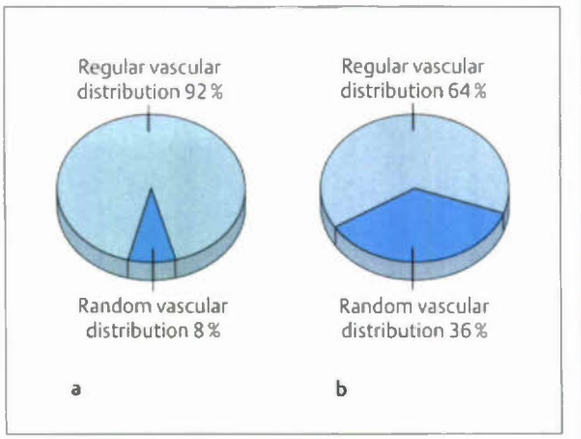

12

Angiogenesis in Benign Ovarian Tumors

Fig. 39.11 Schematic representation of the vascular patterns seen in benign and malignant ovarian tumors.
a Randomly scattered vessels.
b Isolated vessel.

Fig. 39.12 Percentage distribution of the vascular patterns seen in benign ovarian tumors (**a**) and malignant ovarian tumors (**b**).

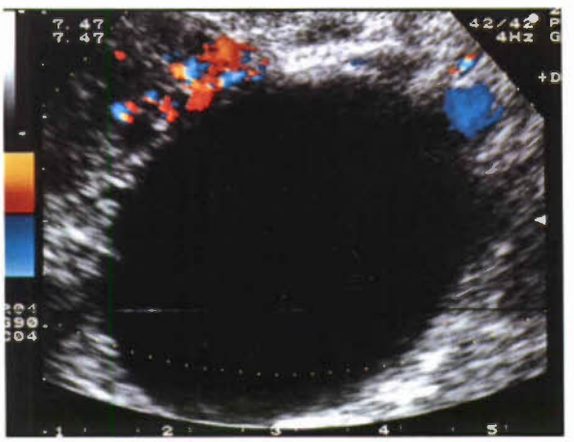

13

14

Fig. 39.13 Solitary ovarian cyst. The pericystic vascularized zone is typical of benign lesions.

Fig. 39.14 Transvaginal color Doppler scan of a complex tumor. Note the echogenicity of the solid tumor components and the color-encoded area. This blood flow pattern is typical of cystic teratomas with active cell division.

15

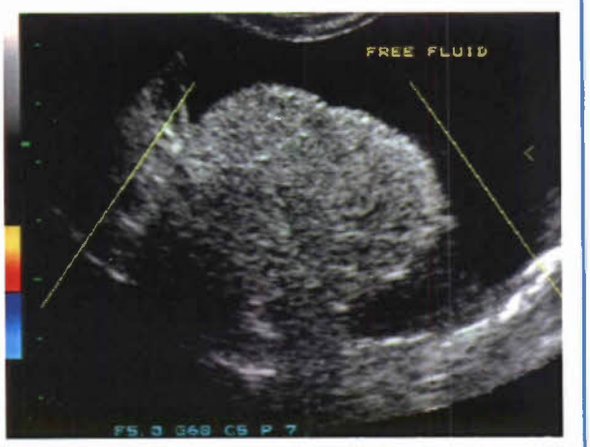

16

Fig. 39.15 Large, oval, multicystic mucinous cystadenoma containing echo-free fluid.

Fig. 39.16 Transvaginal scan of a solitary, avascular ovarian tumor with associated ascites. Histology: ovarian fibroma.

Fig. 39.**17** Chocolate cyst with homogeneous, high-level internal echoes. The hilar type of vascularity is typical of ovarian endometriosis.

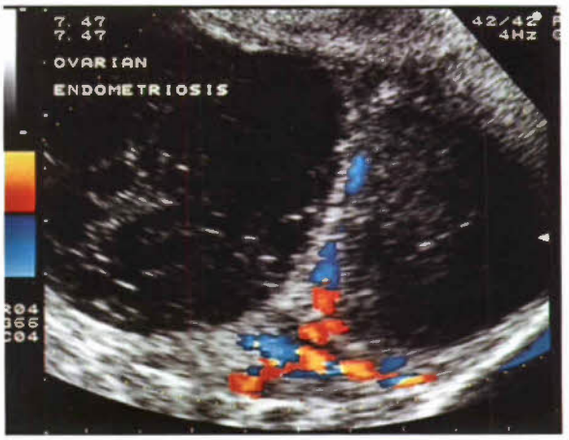

17

Fig. 39.**18** Endometriosis. Color Doppler shows conspicuous vascularity in the area of the ovarian hilum (left half of image). Pulsed Doppler (right half of image) demonstrates high-velocity blood flow with a low resistance index (RI = 0.40) during menses.

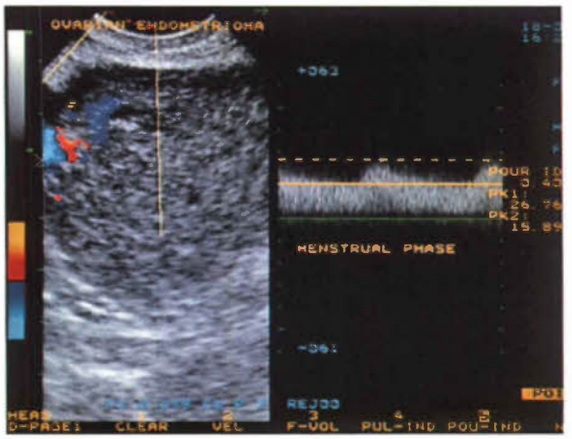

18

Fig. 39.**19** Complex adnexal mass in the cul-de-sac in a patient with acute pelvic inflammatory disease. The increased vascularity has developed in response to various bacterial antigens and substances.

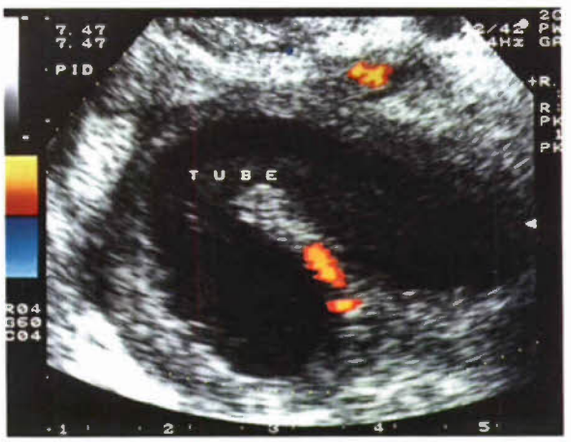

19

Fig. 39.**20** Chronic adnexitis with laparoscopically confirmed chronic salpingitis. Flow sampling within the complex mass indicates an absence of diastolic flow. The high resistance index (RI = 1.0) is a result of irreparable scarring.

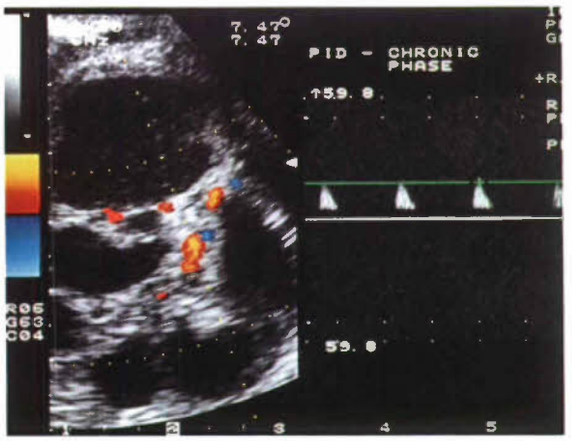

20

Angiogenesis in Borderline Tumors

Fig. 39.**21** Color Doppler image of neovascular signals within septa.

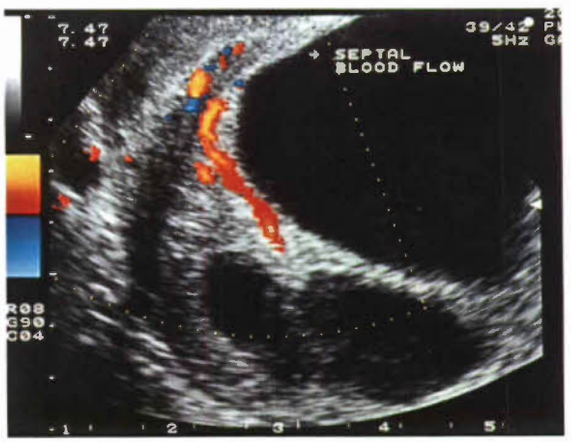

21

Fig. 39.**22** Pulsed Doppler ultrasound (right half of image) indicates a low to moderate flow resistance (RI = 0.42). Histopathology: mucinous borderline tumor.

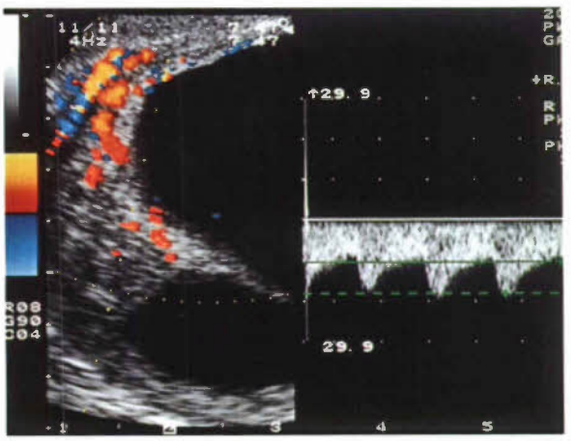

22

Angiogenesis in Malignant Ovarian Masses

Fig. 39.**23** Randomly distributed vessels in a large adnexal mass.

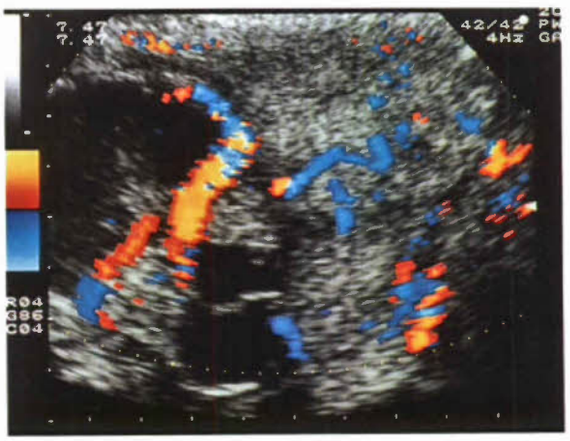

23

Fig. 39.**24** The blood flow in the central portion of a cystic-solid malignant tumor shows a very low vascular resistance (RI = 0.28).

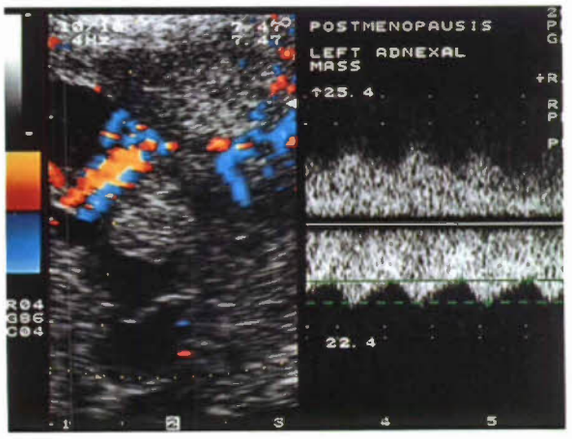

24

Endometriosis is a disease marked by heterotopic endometrial implants occurring at sites outside the uterus, such as the surface of the bowel or bladder or the abdominal wall [51]. The ovary is a relatively favorable site for implantation because its steroid levels exceed those in the peripheral blood, making it an ideal milieu for the implantation of endometrial tissue. It appears that the superficial epithelium and the proximity of the tubal ostium are favorable for transplantation. When endometrial cells invade the ovarian stroma, they may form large endometriotic cysts that contain a viscous, chocolate-colored fluid. Usually the wall of the endometriotic cyst is clearly demarcated from the normal adjacent ovarian stroma. The most conspicuous vascularized zone in these typically benign cysts is found at the level of the ovarian hilum (Fig. 39.**17**). This type of neovascularity was found in 78.6% of endometriotic cysts. The RI values at that site were usually greater than 0.45. Nevertheless, the flow indices ranged from low values (RI 0.41–0.45) in 20.4% of the cases (Fig. 39.**18**) to elevated values (RI 0.51–0.60) in 79.6%. It appears that high diastolic flow and low resistance values can be detected at the onset of menstrual bleeding. We therefore recommend the late follicular phase as the best time for evaluating the vascular supply of an endometriotic cyst. It is postulated that the response to pharmacologic therapy depends largely on the degree to which metabolically active substances can reach their sites of action through a competent circulatory system. Conservative therapy offers encouraging possibilities and can be successfully used in patients with an optimum vascular supply. Perifocal inflammation or fibrotic changes that might interfere with this process can be detected by transvaginal color Doppler scanning. It has been our experience that avascular lesions of the ovary should be surgically removed.

Pelvic inflammatory disease (PID) is a nonspecific term for a number of diseases of the female upper genital tract that are characterized by an inflammatory reaction [52]. Entities that fall under the heading of PID include endometritis, salpingitis, peritonitis, and tubo-ovarian abscess. It is believed that tubo-ovarian abscess results from a bacterial invasion of the tubal epithelium with associated tissue destruction and necrosis. This creates an ideal culture medium for the invasion and growth of anaerobes [53]. Bacteria produce various compounds such as lysosomal enzymes, exotoxins, surface virulence factors, and antigens that can incite a pronounced inflammatory response and increased vascularization (Fig. 39.**19**). The resulting edema eventually compromises blood flow, leading to ischemia and necrosis of the fallopian tube wall. Later, an inflammatory exudate or purulent discharge develops which drains from the fimbriated end of the infected tube. Finally, a tubo-ovarian abscess forms when the infectious secretions incite an inflammation that spreads to the fallopian tube and other adnexal structures such as the ovaries and broad ligament. Laparoscopy is the gold standard for diagnosis but is costly and entails surgical and anesthesiological risks [54]. Color Doppler ultrasound is an effective alternative in these cases owing to the structural and vascular changes that result from the inflammatory process in the ovary.

The early stage of inflammation is characterized by edema of the fallopian tube and dilation of the blood vessels in the tubal wall. The mean RI of the arterial blood flow in the fallopian tubes of 112 patients with PID was equal to 0.55. The inflamed ovaries are enlarged and display multiple cysts that represent infected follicles or corpus luteum cysts. The intraovarian vessels are easily defined with color Doppler ultrasound and have a mean RI of 0.52.

It is known that the sonographic appearance of complex adnexal masses should always be interpreted within the context of the clinical presentation. For example, a thick-walled mass containing echogenic fluid in a febrile patient is probably an abscess. With this advanced and severe form of PID, it is difficult to identify pelvic anatomy. The ovaries are usually adherent to the pelvic wall or uterus, and cicatrizing processes can compromise their endocrine function and blood flow. In the group of 57 patients with PID in this study, the blood flow in the ovarian parenchyma showed a significantly higher vascular resistance (mean RI = 0.68) or even an absence of diastolic flow (Fig. 39.**20**). In our experience, the dynamic use of color Doppler ultrasound in patients with PID is important in making an accurate diagnosis, monitoring progression, and evaluating ovarian function and blood flow.

Angiogenesis in Borderline Tumors

Serous borderline tumors of the ovary account for 21–23% of all serous ovarian carcinomas. These neoplasms have a relatively good prognosis compared with other ovarian cancers [55]. They show varying degrees of atypia but no evidence of infiltrative growth [56]. Nevertheless, this type of tumor may be associated with peritoneal deposits in 30–40% of affected women [57]. They also have a greater propensity for bilateral occurrence. The majority of serous borderline tumors present as unilocular or multilocular cysts with an endophytic, confluent type of papillary growth. They are distinguished from serous carcinomas by an absence of significant necrosis or hemorrhage. Mucinous borderline tumors are usually thin-walled and multilocular and do not differ significantly from benign cystomas. They generally have a large volume and a smooth surface. Approximately 25–60% of lesions contain solid areas and papillary projections [58]. Ultrasound is used for the detection, characterization, and evaluation of ovarian tumors. The principle of diagnosis is based on the assessment of gross pathologic features. Thick septa, irregular solid components within the mass, ill-defined margins, the presence of ascites, and matted bowel loops are considered criteria of malignancy (Fig. 39.**21**) [59]. Some authors have reported that low-grade ovarian malignancies exhibit the same patterns as higher-grade malignant tumors [60]. At the same time, Achiron et al. [61] noted that borderline tumors are difficult to distinguish from benign tumors because of their similar appearance. Consequently, the detection of vascular changes and the measurement of blood flow resistance (RI) are necessary in these ovarian tumors in order to show evidence of a malignant or benign lesion. The spectral waveforms of borderline tumors in our study were characterized by relatively high diastolic flow velocities and a low resistance index (0.43 ± 0.07) (Fig. 39.**22**). It is our assumption that abnormal Doppler waveforms result from large arterioles or sinusoids that lack a muscular wall. This may be the hemodynamic response to tumor angiogenesis factors that are produced by cells of low malignant potential. For this reason, the preoperative ultrasound evaluation of adnexal masses should take into account the size and consistency of the mass as well as its blood flow in order to assess the probability of malignancy. Based on our experience, transvaginal color Doppler ultrasound supplies diagnostic information that is useful in differentiating benign ovarian tumors from malignant or borderline tumors.

Angiogenesis in Malignant Ovarian Masses

Vessels can be demonstrated in all portions of malignant ovarian tumors: within the sonographically nonhomogeneous central region of the mass, in its peripheral portion (Fig. 39.**23**), at the base or interior of large papillary outgrowths, in pericystic regions, and even within septa. A tumor may consists of different areas that present different vascular patterns. The abnormal vascular architecture of malignant tumors leads to abnormal waveforms detectable by pulsed Doppler ultrasound. Compared with pulsed Doppler findings in normal tissues and organs, the Doppler sonograms of malignant tissues are distinguished by low vascular resistance resulting in a low resistance index and low pulsatility index (Fig. 39.**24**). These observations also correlate with the findings in malignant breast tumors, which are characterized by abnormal Doppler spectra with very high flow velocities at the periphery of malignant tumors [62–64]. The high flow velocities that were observed in breast malignancies led to the hypothesis that these signals were caused by

arteriovenous anastomoses [64]. These results were later confirmed by various groups of authors [65–67]. The advantages of transvaginal pulsed and color Doppler ultrasound in ovarian tumors were first documented in 1989 by groups of investigators from Zagreb and London. The Zagreb group [68] studied the vascularity of pelvic masses and observed intratumoral blood flow with low resistance in malignant ovarian tumors as well as other pelvic tumors. The RI in five malignant tumors averaged 0.33 ± 0.08 (SD). These results indicate that an increase in the blood supply to a tumor is strongly suspicious for malignancy. The London group [69] corroborated these findings. Eight of 18 ovarian tumors in their study were malignant. The pulsatility indices in seven of the eight malignant tumors were less than 1.0 (0.3–0.9). This led the authors to conclude that a high vascular flow resistance excludes invasive ovarian cancer. False-positive results were obtained with bilateral dermoid cysts, which had PI values of 0.4 and 0.8.

In a large study conducted at our institute, 14317 asymptomatic or minimally symptomatic women were examined for ovarian carcinoma [70]. A total of 680 adnexal masses were detected, 624 of which were benign and 56 malignant. Taking RI < 0.41 as the cut-off point for discriminating between malignant and benign ovarian tumors, the sensitivity was 97% and the specificity was 100%. Numerous publications in 1993 and 1994 dealt with the detection of adnexal masses. Bromley et al. [71] examined 33 postmenopausal women and found 12 malignant and 21 benign adnexal masses. Based on morphologic criteria alone, the sensitivity in the detection of malignancy was 91% and the specificity was 52%. When pulsed Doppler ultrasound was used with an RI cut-off of 0.6, the sensitivity was 66% and the specificity was 81%. When the RI cut-off was increased to 0.8, the sensitivity and specificity rates were the same as those based on morphologic criteria alone. These authors used a 3.5-MHz abdominal transducer to detect masses in the upper pelvis. They did not indicate how many tumors were detected with the abdominal transducer, nor did they explore the differences between the transvaginal and transabdominal examinations. The use of a 3.5-MHz abdominal transducer should be avoided, however, due to the low frequency and relatively poor sensitivity.

Valentin et al. [72] examined 149 women (86 premenopausal, 63 postmenopausal) with 121 benign and 28 malignant ovarian masses. The ultrasound morphology of the tumors was found to be a better discriminator between benign and malignant tumors than any of the Doppler variables. Ultrasound morphology correctly identified all of the malignant tumors, with a false-positive rate of 27%. The quality of the discrimination improved slightly when the PI and blood flow velocity were used to distinguish between benign and malignant multilocular cysts with solid parts. With this approach, all malignant multilocular tumors with solid parts were diagnosed. The false-positive rate of 17–23% depended on which Doppler variable and which cut-off level were used. The authors emphasized that the entire tumor should be examined in order to determine the maximum and minimum PI or RI values. They also reported that the flow velocities (V_{max} and V_{mean}) were better for discriminating between benign and malignant tumors than the PI or RI values alone—a finding that conflicts with results published earlier [73,74]. The authors also found that gray-scale B-mode imaging provided very good discrimination of tumors, whereas color Doppler made only a limited contribution to the differential diagnosis. Based on this publication, it appears that the same cut-off value cannot be used to distinguish benign masses from malignant cystic, cystic-solid or solid adnexal masses. However, this study did not specify the phase of the menstrual cycle in which the transvaginal examinations were performed. Also, the authors reported a higher detection rate with color Doppler than with pulsed Doppler. This is somewhat puzzling, because color Doppler signals that cannot be verified by pulsed Doppler sampling should be interpreted as artifacts, not as blood flow signals. Carter et al. [75] found that when color flow Doppler was used alone, it provided high specificity but lacked sensitivity and predictive value as a predictor of malignancy. This led them to conclude that color Doppler was useful only as an adjunct to the gray-scale morphology of pelvic tumors. Unfortunately, the authors furnished no data on the menopausal status or menstrual phase of the women examined. They also presented the results of uterine, cervical, and ovarian benign and malignant tumors in the same table. Because of this, their results cannot be compared with those of other authors.

Schneider et al. [76] compared the results of color Doppler ultrasound, two-dimensional ultrasound, and tumor marker determination (CA-125) in 22 premenopausal and 33 postmenopausal women who had previously been diagnosed with an adnexal mass by ultrasound and/or computed tomography. Although they determined RI values for every tumor, they did not provide any data on tumor morphology (cystic, cystic-solid) or tumor size. It is possible that the majority of malignant tumors with false-negative RI values were large, cystic adnexal masses. If this is true, it may be that neovascular signals were easily missed or that normal pericystic vessels with high RI values were erroneously interpreted as malignant signals.

In a study by Weiner et al. [77], 18 women who had completed their treatment for pelvic cancer underwent a follow-up examination by ultrasonography, computed tomography, and serum CA-125 determination. The results were compared with transvaginal color flow Doppler, which provided a 100% specificity and 86% sensitivity in the detection of recurrent pelvic tumors. Intratumoral blood flow was detected in all cases with color Doppler, but the PI was high in only one of those cases.

Fleischer et al. [78] compared the specificity of color Doppler ultrasound with two-dimensional transvaginal ultrasound in a consecutive series of 96 women 16–84 years of age who had undergone surgical excision and pathologic examination of a pelvic mass. They found that color Doppler was more specific than two-dimensional ultrasound in 43% of cases, both were equally specific in 41%, neither was more specific in 10%, and two-dimensional ultrasound was more specific than color Doppler in 6%. Also, the positive and negative predictive values of color Doppler were found to be higher in postmenopausal women than in premenopausal women.

Aleem et al. [48] examined adnexal vascularity with a 10-MHz continuous Doppler probe in 24 patients undergoing laparotomy for benign gynecologic disease. They analyzed the tubal arteries, the ovarian hilar arteries, and the ovarian artery in the ovarian suspensory ligament to determine their RI and PI values. They found that these values were significantly lower in the tubal arteries than in the ipsilateral ovarian arteries and their hilar branches. The authors concluded that the tubal artery flow signals were characteristic and were distinct from the ovarian artery signals, and that tubal artery signals might be erroneously sampled during transvaginal color Doppler scanning of the ovaries, especially in the presence of conditions causing decreased resistance to blood flow in the pelvis, such as ovarian tumors. It was concluded that identifying the tubal artery flow signal could be helpful in differentiating ovarian and tubal vessels detected during color Doppler scanning. Unfortunately, the authors did not compare the values determined by intraoperative continuous-wave Doppler with the findings of preoperative transvaginal pulsed Doppler ultrasound. This would have allowed a very reliable assessment of the degree to which blood flows could be accurately detected by transvaginal pulsed Doppler ultrasound.

The report by Prömpeler et al. [79] introduced the concept of using complex flow velocity measurements based on the sum of the systolic, end-diastolic and time-averaged maximum velocities. This increased the sensitivity to 95%, with a specificity of 86% and an accuracy of 91%.

In earlier studies by Fleischer et al. [73] and Kurjak et al. [74], no significant difference was found between the flow velocities of benign and malignant tumors. Moreover, the maximum systolic blood flow velocity, end-diastolic flow velocity, and time-averaged maximum flow velocity may also be increased at the periphery of certain benign diseases such as ovarian endometriosis and tubo-ovarian abscess. The same phenomenon occurs within the vascular system of malignant tumors due

to the presence of arteriovenous shunts. For this reason, a combined morphological and pulsed color Doppler sonographic evaluation should include an analysis of flow impedance (measured by RI and PI), flow velocity (with appropriate angle correction), vessel location (peripheral, pericystic, intraseptal, central, or intrapapillary), and the detection of abnormal vascularity (a regular or random arrangement of vessels). The arrangement of the vessels and the quantification of blood flow should be interpreted in relation to tumor morphology and to the size and location of the vessels. Based on the experience of Fleischer et al. [73], this multiparameter analysis may be able to distinguish masses with growth potential from masses that will undergo spontaneous regression. In addition, most errors in diagnosis can be reduced by conducting a color Doppler follow-up. The data from the study by Schulman et al. [49] are encouraging. This study clearly showed that the morphological features of adnexal masses defined by conventional transvaginal ultrasound can be used to evaluate the histopathology of most lesions. With nonspecific complex tumors that contain solid and cystic areas, the adjunctive use of color Doppler ultrasound can help to clarify tumor etiology. The same method proved indispensable for the detection of ovarian carcinoma in normal-size ovaries. In this study as in our own, the Doppler flow velocity for the ovary was defined as abnormal when the resistance index was less than 0.41. When this value was used as the cut-off, 15 histologically confirmed benign cysts were corrected predicted and one stage Ib ovarian cancer was successfully detected.

In the study published by Jeng et al. [80], 801 patients with adnexal tumors were examined preoperatively by transvaginal color Doppler ultrasound. Seven hundred forty of the tumors were identified as benign by pathologic examination, 55 as malignant, and six as borderline tumors. All the benign tumors had an RI of more than 0.4, most had an RI of more than 0.6, and 354 cases (47.8%) had no detectable arterial blood flow within the tumor. Five cases with borderline tumors had an RI between 0.5 and 0.6, and the others exhibited no blood flow. All except three of the malignant tumors had an RI of less than 0.4.

Numerous papers were presented at the Seventh World Congress of Ultrasound in Medicine and Biology. Most of the authors recommended transvaginal color Doppler ultrasound as a very helpful examination. The most widely used RI cut-off value was 0.41. A number of publications on color Doppler studies of malignant ovarian tumors are reviewed in Table 39.**1** [71,72,75,76,79–93].

Table 39.**1** Blood flow characteristics of ovarian carcinoma

First author, ref.	Patients (n)	Malignant/ benign	Cut-off	Sensitivity	Specificity
Bromley [71]	33	12/21	RI = 0.60	66%	81%
			RI = 0.80	91%	52%
Valentin [72]	149	28/121	PI = 1.23	95%	80%
Carter [75]	228	88/140	PI = 1.00	57%	78%
			RI = 0.40	13%	97%
Schneider [76]	55	6/49	RI = 0.80	94%	59%
Natori [81]	90	37/183	PI = 1.15	70%	79%
Hsieh [82]	222	39/183	RI = 0.39		
Sohn [83]	51				
Prömpeler [79]	83	42/41	RI = 0.4		
Jeng [80]	801	55/740	RI = 0.4	100% PPV	
Zhang [84]	57		RI = 0.38	100% PPV	
Brown [85]	44	8/36	RI = 0.4	50%	96%
			PI = 1.0	100%	46%
Sengoku [86]	28	16/12	PI = 1.0	43.8%	91.7%
			PI = 1.25	68.8%	91.7%
			PI = 1.5	81.3%	83.3%
			PI = 2.0	81.3%	58.3%
Chou [87]	114	25/83	RI = 0.5	88%	82%
Wu [88]	410	103/307	RI = 0.4	68%	97%
Zanetta [89]	80	33/47	RI = 0.56	85%	91%
			PI = 1.0	97%	87%
Salem [90]	102	13/89	PI = 1.0	79%	77%
Bonilla-Musoles [91]	10				
Hamper [92]	31	6/24	PI = 1.0		
			RI = 0.5		
Wu [93]	222	79/152	RI = 0.4		

PPV: positive predictive value.

Vascularization of Uterine Tumors

Uterine Myomas

Uterine myoma is the most commonly diagnosed pelvic tumor in women of childbearing age [94–96]. Myomas arise from the smooth muscle and connective tissue of the uterine corpus and fundus. Only 3% are of cervical origin [97]. Myomas are usually multiple and of varying size. Intramural myomas are located within the uterine wall, while submucous tumors project into the uterine lumen. External tumor growth can result in a pedunculated or subserous myoma. Intramural myomas are the most common, while submucous tumors are the least common [95]. Patients with submucous myomas often present with metrorrhagia, dysmenorrhea or infertility, whereas patients with subserous myomas are frequently asymptomatic. The presence and severity of symptoms generally depend on the number, size, and location of the myomas. The ultrasound diagnosis of a uterine leiomyoma is based on an irregular uterine contour, uterine enlargement, and a change in echo texture, which may be hypoechoic to echogenic depending on the relative amount of smooth muscle or connective tissue. Secondary changes such as necrosis, hemorrhage, degeneration, or calcification lead to a broad spectrum of sonographic characteristics. Central ischemia, which develops when tumor growth outstrips the blood supply, leads to various stages of degeneration. Approximately 25% of myomas contain calcifications, which range from small foci to large mural calcifications or global calcification [98]. With their protean appearance, some myomas are apt to be mistaken for solid ovarian tumors, endometrial polyps, blood, or mucus.

The small vessels that supply a growing tumor are easily detected with transvaginal color Doppler ultrasound (Fig. 39.**25**). Transvaginal color Doppler has been used to detect the vascularity of uterine myomas as well as to assess the physiologic and pathophysiologic characteristics of blood flow in the uterine arteries. This method has shown considerable potential for the in-vivo differentiation of benign and malignant uterine tumors [99].

Benign uterine masses are vascularized by preexisting vessels such as the normal myometrial vessels that arise from the terminal branches of the uterine artery. When color Doppler ultrasound is used, analysis of the spectral waveforms shows that the vascular resistance is slightly less than or equal to the normal myometrial perfusion from the terminal branches of the uterine artery. Scans in premenopausal women can usually detect a higher level of diastolic flow than is found in the uterine artery. Color flow Doppler signals can be recorded at the periphery or center of a myoma. The myoma vessels have a mean resistance index of 0.54 (Fig. 39.**26**) and a mean pulsatility index of 0.89. Very low RI values have been found in cases with necrosis or secondary degenerative and inflammatory changes within the tumor. Uterine artery flowmetry studies in myoma patients have documented increased blood flow velocities and decreased RI and PI values in both uterine arteries. The blood supply of a myoma may perhaps provide an index for predicting its growth rate. Color Doppler ultrasound appears to be helpful in the identification of well-vascularized myomas that are responsive to treatment with gonadotropin-releasing hormone analogs [99]. This technique can also help determine the optimum timing for operative treatment.

A very interesting observation has been made in women with postmenopausal regression of myomas. The blood flow detected at the periphery of the myomas showed a different pattern (higher RI) than that

observed in premenopausal women. In some cases there was even an absence of end-diastolic flow. This method also provides a means of discriminating between intraligamentous fibromas and solid ovarian tumors. Transvaginal color Doppler ultrasound is the method of choice for evaluating myomas that enlarge during pregnancy.

Uterine myomas cause hemodynamic changes in uterine perfusion, marked by a rise of blood flow velocity and a fall of vascular resistance in both uterine arteries. The blood flow characteristics in vessels at the tumor periphery are not very different from those in the uterine arteries. Moreover, the presence of diastolic flow is always detectable in the main arteries that supply the leiomyomas. On the whole, the vascularity of benign uterine masses is dependent on tumor size and location and on the extent of secondary degenerative changes. Large and laterally situated myomas, especially those with necrotic, degenerative and inflammatory changes, are usually characterized by rising diastolic flow values and a low resistance index.

Uterine myomas with secondary changes display a number of vascular changes. A marked decrease in the impedance to blood flow has been observed, similar to that found in association with malignant tumors.

Endometrial Carcinoma

A number of recent Doppler studies have attempted to improve the sensitivity and specificity of transvaginal ultrasound in the diagnosis of endometrial carcinoma [100–105]. Pulsed and color Doppler ultrasound can supply information on tumor vascularity, providing an additional criterion for the detection of uterine malignancies (Fig. 39.**27**). We conducted a color Doppler study [104] in 750 postmenopausal women who had undergone hysterectomy for various gynecologic indications. Endometrial carcinoma was diagnosed histologically in 35 of these cases. Thirty-two of those tumors (91%) were successfully detected by transvaginal color Doppler ultrasound. The mean resistance index of the detectable vessels was 0.42 ± 0.02 (SD) (Fig. 39.**28**). The maximum systolic velocities in the vessels were relatively high. The mean velocity in intratumoral vessels was 12.04 ± 3.1 cm/s, and the mean velocity in peritumoral vessels was 17.12 ± 2.7 cm/s. The difference between the two velocities was statistically significant ($P < 0.05$). Endometrial carcinoma was detected in three asymptomatic women (two stage IA and one stage IB based on the classification of the International Federation of Gynecologists and Obstetricians). These tumors presented in the B-mode image as a thickened (> 10 mm), nonhomogeneous endometrium with an intact subendometrial halo. Color Doppler ultrasound detected vascularized areas within the endometrium with low vascular resistance (RI = 0.42).

We concluded from this study that transvaginal pulsed and color Doppler ultrasound can detect endometrial carcinoma even in asymptomatic women.

Merce et al. [106] examined 45 patients with metrorrhagia and compared their findings with 19 normal women. The authors used a duplex system with a transvaginal ultrasound probe. They recorded Doppler signals in both uterine arteries and the myometrium in a region which they ascribed to the radial arteries or arcuate arteries. They found a significant decrease in the RI of the uterine and intramyometrial arteries in women with endometrial pathology. This led the authors to conclude that the RI of the intramyometrial arteries (arcuate and radial arteries) correlates strongly with the prediction of positive findings. By comparison, the RI of the uterine arteries was less accurate and less specific in predicting endometrial pathology.

Bourne et al. [101] investigated uterine artery blood flow in patients with endometrial carcinoma and in patients with normal uterine morphology. They reported a significant difference in PI values between both groups and defined a cut-off value of 2.0. The positive predictive value in this study was 80.9% while the negative predictive value reached 99.9%. In a later publication, Bourne et al. [107] reported an arbitrarily defined PI cut-off of 1.5 for the uterine artery as the basis for a positive test result. This would result in a 94% predictive value for a positive outcome in postmenopausal women with bleeding. Presumably, the predictive value could be increased even further by the selection of smaller vessels. It appears that the uterine artery is too large to detect hemodynamic changes produced by small areas of neovascularization in an early stage of endometrial carcinoma.

On the other hand, a marked fall in uterine artery resistance is found in more advanced stages where some tumor vessels can no longer be identified due to massive necrosis. Hata et al. [108] determined the resistance index in the arcuate arteries of 10 patients with endometrial carcinoma and compared it with the RI values measured in healthy women of the same age group and parity. Significantly lower values were found in the arcuate arteries of women with endometrial cancer (RI = 0.53 ± 0.15) than in the control group (RI = 0.76 ± 0.17). The same authors reported a 100% success rate (all of nine patients) for detecting the feeding arteries and a 77% success rate (seven of nine patients) for detecting intratumoral vessels. The blood flow within the tumor was characterized by low resistance in the arterial and venous systems. The same method was used to investigate intratumoral hemodynamic changes before and after intra-arterial chemotherapy [103]. The mean maximum systolic velocity during intra-arterial chemotherapy was significantly higher (58.9 ± 29.3 cm/s) than before the chemotherapy (16.0 ± 6.3; $P < 0.05$). A significant difference was also noted between the RI value during chemotherapy (0.61 ± 0.09) and before the therapy (0.64 ± 0.12; $P < 0.05$). These results show that intra-arterial chemotherapy induces a significant, selective increase of blood flow in uterine carcinoma.

Bonilla-Musoles et al. [100] reported a 97% detection rate of intratumoral vessels in 67 patients with histologically confirmed endometrial carcinoma. The authors concluded that the sensitivity and specificity in the detection of uterine adenocarcinoma could be significantly increased by color Doppler ultrasound compared with the B-mode evaluation of endometrial thickness alone.

Rudigoz and Gaucherand [105] suggested that morphologic criteria (ratio of endometrial to uterine thickness) be combined with Doppler sonographic criteria in the detection of endometrial carcinoma. An abnormal blood flow pattern was found in six of seven endometrial carcinomas with an RI of 0.47–0.60. This contrasted sharply with the results of Sladkevicius and Valentin [109], who found that color Doppler analysis did not yield additional information that was useful in discriminating between benign and malignant endometrial tumors.

The high resolution of modern endovaginal ultrasound probes makes it possible to detect endometrial pathology and determine the depth of myometrial invasion. It has been our experience [104] that the following features are strongly suspicious for endometrial carcinoma: endometrial thickness > 10 mm, nonhomogeneous or hyperechoic endometrial echo pattern, and the detection of intrauterine fluid. When the subendometrial halo was disrupted, myometrial invasion was usually present. Resistance measurements in intratumoral and peritumoral vessels showed statistically lower values in endometrial carcinoma than in benign endometrial changes ($P < 0.05$). Intratumoral vessels were also found to have lower velocities compared with peritumoral vessels. It appears, then, that peritumoral vascularity develops as a direct response to the angiogenic activity of tumor cells and represents an area of intense tumor growth. Three of 95 patients were misdiagnosed. All three of these women had undergone curettage one week before the color Doppler examination, and this may have altered the hemodynamics of the endometrium. For this reason, a transvaginal color Doppler ultrasound examination should always be completed before the patient undergoes dilation and curettage. Three patients with endometrial carcinoma (two stage IA and one stage IB based on the classification of the International Federation of Gynecologists and Obstetricians) were asymptomatic. The color Doppler diagnosis in these cases was based on

a thickened endometrium (> 20 mm) and the detection of intratumoral and/or peritumoral blood flow with a low resistance index (< 0.42). "Dense vascular arrangements" were noted in these cases. A survey of color Doppler studies of endometrial carcinoma is presented in Table 39.**2** [101–105,107]. Although the results vary with regard to RI and PI values, it is clear that pulsed and color Doppler ultrasound is a useful adjunct in the differentiation of benign, suspicious and malignant endometrial changes. This applies to sites of endometrial thickening in symptomatic as well as asymptomatic postmenopausal women.

Another useful application of pulsed and color Doppler ultrasound is in the detection of *uterine sarcoma*. In a previously unpublished study, we determined the blood flow indices of primary vessels (intratumoral neovascularity) in 10 patients with uterine sarcoma. Irregular, thin, and randomly distributed blood vessels were typically found in peripheral and/or central areas of the sarcomas (Fig. 39.**29**) with very low-resistance shunts. Additionally, both uterine arteries in the sarcoma group showed low resistance indices compared with a group of patients of comparable age with a normal or myomatous uterus. Color Doppler was able to detect areas of neovascularity (at the periphery and/or center of the tumor) in all patients with sarcoma (100%), while only 61% of the myomas were vascularized. Diastolic flow was seen in all of the uterine tumors and was increased compared with the flow in the uterine artery. The mean RI in the sarcoma group was 0.37 ± 0.03 (SD) (Fig. 39.**30**). The difference relative to the myoma group (0.54 ± 0.08 [SD]) was statistically significant ($P < 0.05$). The mean RI of intramyometrial blood flow was 0.68 in the healthy patients and was significantly higher ($P < 0.05$) than in the other two groups examined.

Kurjak et al. [110] showed that the vascularity of benign uterine tumors was strongly dependent on tumor size, tumor location, and the extent of degenerative changes. Large and laterally situated leiomyomas, particularly those with necrosis and inflammatory changes, may show increased diastolic flow resulting in low RI values. Thus, in three patients with uterine myomas we observed an overlap with the values for uterine sarcoma based on an RI cut-off of 0.40. This observation warrants further study. A low RI value could be caused by a fast-growing myoma or may signify a premalignant condition. The meticulous transvaginal color Doppler examination of a uterine tumor should therefore include an assessment of morphologic changes as well as an analysis of tumor vascularity (color brightness, location and type of vascularity). Malignant uterine tumors are characterized by bright color signals with randomly branching vessels. Analysis with pulsed Doppler ultrasound indicates a low vascular resistance (mean RI = 0.37 ± 0.03).

In large and necrotic leiomyomas, central areas of neovascularity usually show low resistance values caused by the release of vasoactive substances, while peripheral angiogenesis is characterized by moderate resistance values. The vascular resistance, measured as RI and PI values, and the maximum systolic flow velocity in the uterine arteries can serve as additional parameters for the diagnosis of leiomyosarcoma, which is marked by significantly lower values than in uterine leiomyomas. It appears that an ultrasound evaluation based on multiple parameters (tumor morphology and size plus neovascularity) can help to make the diagnosis of uterine sarcoma in a high-risk group such as postmenopausal women with a rapidly enlarging uterus.

Table 39.**2** Blood flow characteristics of endometrial carcinoma

First author, ref.	Uterine artery		Intratumoral blood flow	
	Mean RI	Mean PI	Mean RI	Mean PI
Bourne [101]		0.89		0.49
Bourne [107]		0.91		
Hata [102]	0.53*			
Hata [103]			0.64	
Kurjak [104]			0.42	
Rudigoz [105]			0.47–0.60	

RI: resistance index; PI: pulsatility index; * = arcuate arteries.

False-Positive Findings

Even an experienced examiner working with good equipment is not immune to errors of interpretation in difficult cases. Increased vascularity may be found not only in pathological conditions but also in certain physiological states. Increased diastolic blood flow, which indicates a significantly decreased resistance to blood flow distal to the sampling site, may also be found in a preovulatory follicle or corpus luteum. For this reason, the vascular information obtained in a premenopausal ovary should always be correlated with the menstrual cycle.

The *corpus luteum* can be demonstrated as a cystic structure with an irregular wall that sometimes occupies more than half of the ovary. Color Doppler ultrasound can define numerous capillaries and intervening blood vessels that supply the corpus luteum. An echogenic fluid inside the mass, an increased blood flow velocity, and a decreased resistance index (RI = 0.04) may cause the examiner to make an erroneous interpretation. The *physiological angiogenic activity* of the ovary should be excluded by performing the examination during the early proliferative phase (between days 3 and 10 of the menstrual cycle). There are a number of lesions that exhibit low vascular resistance and high diastolic flow. They include inflammatory masses such as tubo-ovarian abscess, an active hemorrhagic corpus luteum cyst, and a dermoid cyst. All of these masses normally present with enlarged and dilated vessels that can simulate the flow pattern of ovarian tumors.

Most ultrasound scores that have been devised for the detection of malignant ovarian tumors are based on morphologic features such as internal wall structure, wall thickness, septal thickness, and tumor echogenicity. The main problem with morphologic scores is that some benign tumors have features similar to malignant tumors. We are hopeful that a scoring system that incorporates transvaginal pulsed and color Doppler ultrasound can avoid these pitfalls.

Some examples: It is not uncommon to find a large ovarian mass with thick internal septa and papillary components that is suspicious for a malignant ovarian tumor. If color Doppler scanning does not show areas of increased vascularity, it is reasonable to assume that histopathologic examination will indicate a benign lesion. Figure 39.**31** shows an excellent example of a large, morphologically suspicious ovarian mass. Color Doppler in this case showed no increase in vascularity, and the lesion was identified histopathologically as a mucinous cystadenoma. Endometriotic cysts are the most common source of false-positive findings. In a series described by Campbell and his group (at the Ultrasound World Congress in Japan), endometriosis was responsible for five of 13 false-positive findings.

A new scoring system that includes transvaginal pulsed and color Doppler ultrasound in addition to serum CA-125 determination could reduce the number of false-positive ovarian findings in screening examinations. It appears that the location of the intratumoral vessels that can be detected with color Doppler is extremely helpful in differentiating ovarian endometriosis from ovarian carcinoma. With *ovarian endometriosis*, the most conspicuous vascularized zone is found in the hilar region. This contrasts with malignant tumors, which tend to show central vascularity with low RI values. Our group found that menstrual bleeding was associated with low vascular resistance and high diastolic flow (RI = 0.36–0.40), indicating that ultrasonography to distinguish a malignant ovarian tumor from endometriosis should be performed during the late follicular and early luteal phase of the cycle. It is helpful to repeat the color and pulsed Doppler examination in doubtful cases.

In patients with endometriosis, the degree of vascularity can be used as a basis for directing further management. The success of pharmacologic therapy depends on metabolically active substances being able to reach their intended site of action. The pharmacologic treatment of ovarian endometriosis with fibrotic plaques, inflammatory processes or scar formation is never successful due to the changes in vascularity. This explains why avascular lesions are an indication for operative

Vascularization of Benign Uterine Tumors

Fig. 39.**25** Uterine myoma with the same echogenicity as the adjacent myometrium. Color Doppler signals are detected at the tumor periphery.

Fig. 39.**26** Doppler spectrum sampled from a myoma vessel indicates a moderate vascular resistance (RI = 0.57). Histopathology: benign tumor.

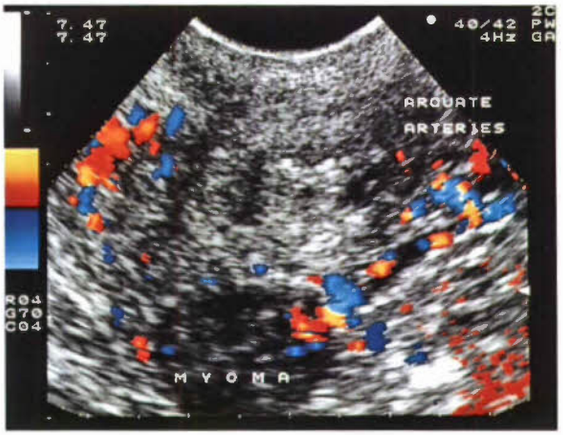

25

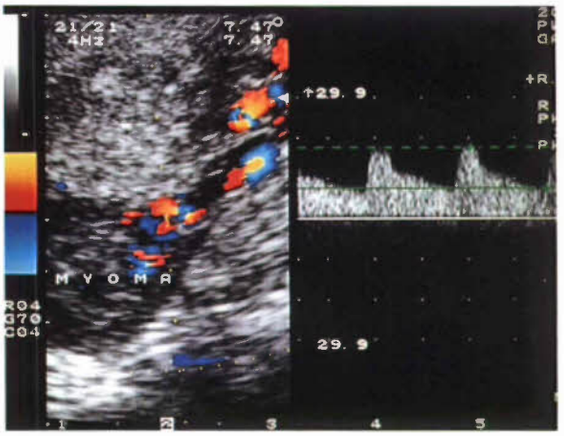

26

Endometrial Carcinoma

Fig. 39.**27** Color Doppler shows a thick, nonhomogeneous endometrium with a stellate pattern of peripheral and intratumoral vascularity.

Fig. 39.**28** Spectral analysis in the same patient reveals a low resistance index (RI = 0.41). Histopathology: endometrial carcinoma.

27

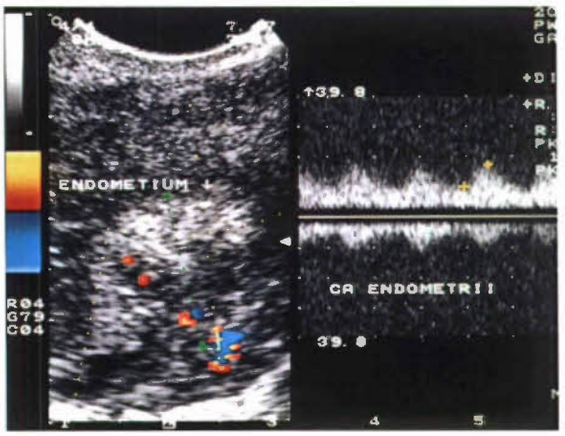

28

Fig. 39.**29** Uterine tumor with areas of high vascularity. Histopathology: sarcoma.

Fig. 39.**30** Areas of neovascularization with low vascular resistance (RI = 0.37) signify a malignant process. Histopathology: uterine sarcoma.

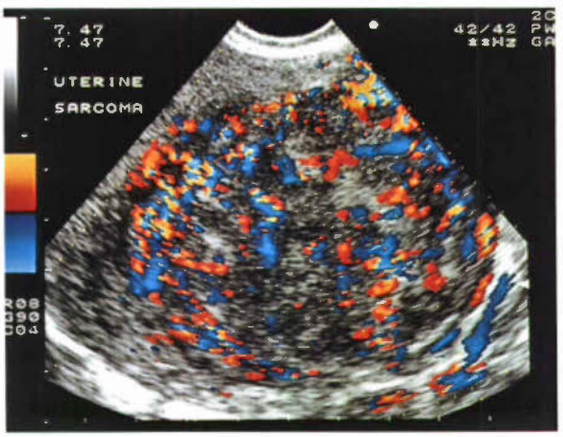

29

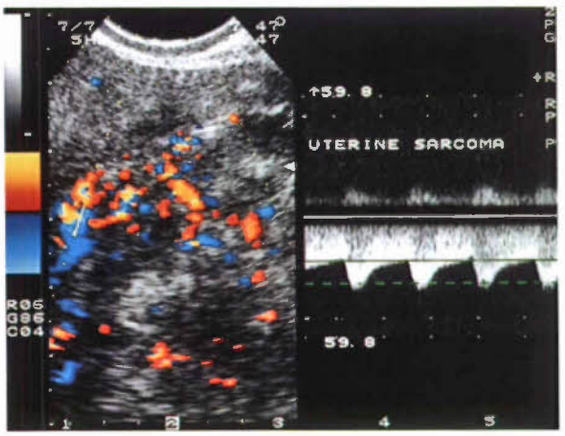

30

treatment. *Dermoid cysts* are another possible source of misdiagnosis. A low vascular resistance may be detected in dermoid cysts that contain actively dividing cells.

In patients with *chronic inflammatory adnexal masses*, the morphologic findings revealed by transvaginal ultrasound can easily mimic the appearance of a malignant ovarian tumor. Wall irregularities and thick septa are the usual cause of false-positive findings in these cases. On the other hand, color Doppler ultrasound can demonstrate the fine vascularity of the septa in a sactosalpinx while pulsed Doppler can detect a high vascular resistance (RI = 0.65). These findings can aid the examiner in concluding that the lesion is most likely a benign adnexal mass.

Real-time ultrasound scanning will sometimes reveal multiple tortuous, echo-free zones within the pelvis. These areas may represent a hydrosalpinx, a multilocular ovarian cyst, fluid-filled bowel loops, or matted veins. Color Doppler ultrasound is particularly effective in defining the dilated varices that result from venous stasis within the pelvis (Fig. 39.**32**).

All of these examples show that color Doppler ultrasound can critically influence the management of pelvic masses.

Several of our illustrations deal with the *vascularization of uterine tumors*. Figure 39.**33** shows a solid, heterogeneous mass arising from the posterior uterine wall. Color Doppler displays a peripheral type of vascularity arising from preexisting vessels (the radial and arcuate arteries), which form a regular angiogenic ring. When the vessels with color signals are interrogated by pulsed Doppler, significant blood flow is detected even in diastole, with a resistance index of 0.50. Well-perfused myomas are likely to undergo rapid growth. They may also respond well to pharmacologic therapy.

Figure 39.**34** shows another example of a well-vascularized myoma. The Doppler waveform indicates low vascular resistance within the tumor (RI = 0.40). Histopathology confirmed the presence of necrotic, degenerative and inflammatory changes within the myoma. If an RI of 0.40 were taken as the cut-off for discriminating between benign and malignant uterine tumors, it would result in a false-positive diagnosis for this tumor.

Another example is shown in Fig. 39.**35**. A transvaginal ultrasound examination in a postmenopausal patient revealed a large mass arising from the posterior wall of the uterus. Though it resembled a myoma, it was exhibiting rapid growth. The tumor presented a generally nonhomogeneous echo pattern with an irregular vascular network. Pulsed Doppler sampling of the randomly branching vessels indicated high-velocity blood flow with a low resistance index (RI = 0.37). The bright color signals and low resistance values of the vessels accompanied by rapid tumor growth helped to identify the lesion as a uterine sarcoma.

False-Negative Findings

At the present stage of development, caution is required, as more is known about false-positive findings than about false-negative findings. It is necessary to learn more about false-negative results. Unfortunately, false-negative cases are rarely analyzed in the setting of prospective, randomized studies, as it is too time- and labor-intensive and has a relatively small yield.

To determine the actual sensitivity of color Doppler ultrasound, we need studies that compare preoperative and postoperative findings in women who have been operated for a nonovarian disease. The incidence of false-negative results can be determined only in patients who undergo surgery or are found to have a clinically unsuspected malignancy.

Future Challenges

Today, we can predict in many cases whether a pelvic tumor is malignant or benign with a high degree of confidence. No single parameter is pathognomonic, however, and future studies should therefore be based on a multiparameter analysis. This requires the more precise determination of blood flow characteristics, flow velocities, and the location of suspicious vessels (a central versus scattered arrangement). In characterizing pelvic masses, moreover, we should evaluate the intensity and distribution of blood flow, analyze the Doppler spectral waveform, and also make an analysis of volume flow, which is currently imprecise. It may be that the actual perfusion, relative vascular density, and selective tumor perfusion can be evaluated more accurately with the aid of ultrasound contrast agents.

Kurjak et al. [111] proposed a screening test for ovarian carcinoma based on color Doppler ultrasound (Table 39.**3**; Figs. 39.**36**, 39.**37**).

Transvaginal color Doppler ultrasound is no longer in its infancy. There are still controversies that are helping to advance the critical and objective evolution of this technique. Disappointments cannot be attributed entirely to examination technique. It is important to standardize the ultrasound equipment (objective measurements) as well as the Doppler measurements themselves (subjective measurements). For the present, this standardization is only a dream. Precise knowledge of the physics of Doppler ultrasound and its appropriate use; a knowledge of pelvic anatomy, physiology, and hemodynamics; and an awareness of the varying nature and behavior of pelvic tumors can definitely help to minimize subjective errors in color Doppler examinations.

On the whole, transvaginal color Doppler ultrasound can be considered a reliable method for the early detection of ovarian carcinoma. Published data suggest that this method has a high detection rate and an acceptably low false-positive rate. For women with a high risk of ovarian cancer, transvaginal color Doppler ultrasound is currently the best method available for detecting a malignant tumor in an early stage.

Table 39.**3** Doppler classification of ovarian masses

Mass	Fluid		Inner margins	
Unilocular	Clear	(0)	Smooth	(0)
Multilocular	Internal echoes	(1)	Irregular	(2)
Cystic-solid	Clear	(1)	Smooth	(1)
	Internal echoes	(1)	Irregular	(2)
	Clear	(1)	Smooth	(1)
	Internal echoes	(2)	Irregular	(2)
Papillary growths	Suspicious	(1)	Definitive	(2)
Solid area	Homogeneous	(1)	Echogenic	(2)
Peritoneal fluid	Not present	(0)	Present	(1)
Unilateral/bilateral	Unilateral	(0)	Bilateral	(1)
	Ultrasound score ≤ 2 Benign 3–4 Questionable > 4 Suspicious			
	RI (resistance index)			
Color Doppler		(0)	> 0.40	(1)
• No detectable vessels		(0)	≤ 0.40	(2)
• Uniformly distributed vessels		(1)		
• Randomly distributed vessels		(2)		
	(If a corpus luteum is suspected, repeat the examinations during the proliferative phase of the next cycle.)			
	Color Doppler score ≤ 2 Benign 3–4 Questionable > 4 Suspicious			

Errors of Interpretation

Fig. 39.**31** Large, multilocular tumor with thick septa, papillary projections, and multiple solid areas. Color Doppler showed no evidence of increased vascularity. Histopathology: benign cyst.

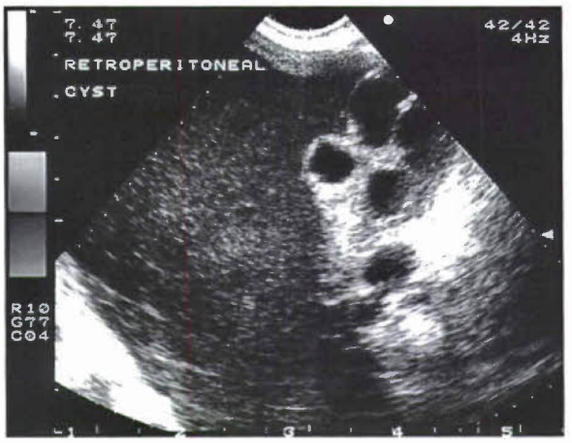

31

Fig. 39.**32a** Transvaginal sonogram shows a mass in the right adnexal region that may be interpreted as a multilocular cystic mass. **b** Color Doppler settles the question of whether the mass is a multilocular cyst or dilated veins. Pelvic congestion syndrome was confirmed by laparoscopy.

32a

32b

Fig. 39.**33** Transvaginal sonogram of a small, nonhomogeneous nodule within the myometrium. It may represent a submucous myoma or other pathologic finding.

33

Fig. 39.**34** Color Doppler defines the nutrient vessels supplying a submucous myoma.

34

Fig. 39.**35** The bright color signals recorded from a small submucous nodule are helpful in differentiating it from other diseases. Pulsed Doppler reveals high flow velocities and a low resistance index (RI = 0.35). Histopathology: uterine sarcoma.

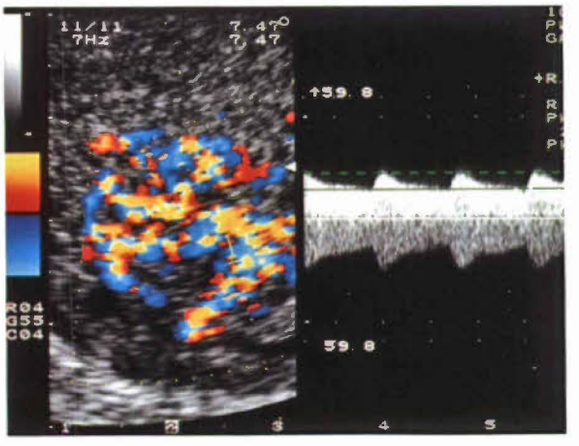

35

Fig. 39.**36** Schematic representation of the various types of vascularity that are associated with ovarian pathology. **a** Central, **b** peripheral, **c** pericystic, **d** septum, **e** papilla.

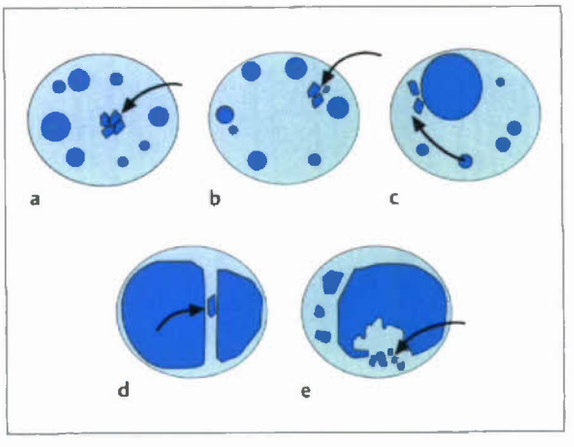

36

Fig. 39.**37** Percentage distribution of the vascular patterns associated with benign (**a**) and malignant (**b**) ovarian lesions.

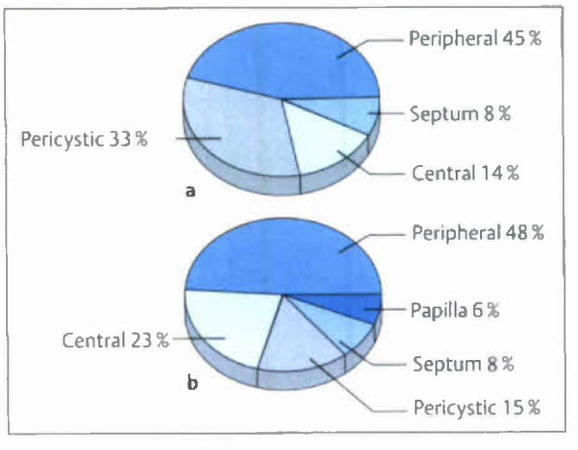

37

Pitfalls and Artifacts

It is known that artifacts occur during ultrasound examinations, including color and pulsed Doppler. It is important for these artifacts to be recognized, so that they are not mistaken for pathology and so that they can be eliminated if possible by modifying the examination technique or equipment settings. In color Doppler ultrasound, as in any new technology, it is necessary to know how to adjust the equipment settings to obtain the best possible diagnostic information. The examiner has to know which controls will worsen or improve the color display and how the various controls are related to one another. The examiner should also know the physics of Doppler ultrasound and have a basic knowledge of image generation and blood flow hemodynamics to ensure that pulsed and color Doppler technology are optimally utilized.

The artifacts that arise in color and spectral Doppler imaging can lead to the misinterpretation of blood flow information. Faulty equipment settings, anatomical factors, and the physical and technical limitations of the examination technique are the most important factors. An incorrect time gain compensation setting or an improper wall filter or velocity-range setting can significantly distort the flow velocity waveform and lead to faulty conclusions. Reflections of the Doppler signal from highly reflective interfaces can produce a mirror-image artifact. Vascular motion can simulate velocity changes because the sample volume will encounter different velocities within the laminar blood flow. Unintended motion can sometimes cause a generalized Doppler shift. Increasing the scanning angle during the Doppler examination will degrade the quality of the waveform, and increasing the Doppler angle to 90° will mimic bidirectional flow (see Fig. 38.**11**).

The detection of these artifacts is essential for the correct interpretation of Doppler waveforms. With the various controls and their interactions, there is no question that color and pulsed Doppler ultrasound is a complicated and sometimes confusing technology. The examiner has to be familiar with the functioning of each control and the effect that is produced by each change in equipment settings. He or she must also know the equipment settings that are appropriate for different pelvic vessels. When all of these factors are taken into account, optimum Doppler information can be obtained.

References

1 Reynolds S. Blood and lymph vascular systems of the ovary. In: Greep SR, editor. Female reproductive system, part I. Washington, DC: American Physiological Society, 1973: 261–316.
2 Ginther OJ, Diersche DKJ, Walsh SW, Del Campo CH. Anatomy of arteries and veins of uterus and ovaries in rhesus monkeys. Biol Reprod 1974;11:204–19.
3 Gillet JY, Koritke JG, Muller P, Juliens C. [On the microvascularization of rabbit ovary; in French.] C R Séances Soc Biol Fil 1968;162:762–6.
4 Merce L. Bases anatómicas de la circulation utero-ovarica. In: Merve LTA, editor. Ecografia Doppler en obstétrica y ginecologia. Madrid: Interamericana McGraw-Hill, 1993: 1–7 .
5 Jurkovic D, Jauniaux E, Kurjak A, Hustin J, Campbell S, Nicolaides KH. Transvaginal color Doppler assessment of utero-placental circulation in early pregnancy. Obstet Gynecol 1991;77:365–8.
6 Speroff L, Glass RH, Kase NG. The uterus. In: Speroff L, Glass RH, Kase NG, editors. Clinical gynecologic endocrinology and infertility, 5th ed. Baltimore: Williams & Wilkins, 1994.
7 Goswamy RK, Steptoe PC. Doppler ultrasound studies of the uterine artery in spontaneous ovarian cycles. Hum Reprod 1978;3:721–4.
8 Long M, Boultbee JE, Hanson ME, Begent R. Doppler time velocity waveform studies of the uterine artery and the uterus. Br J Obstet Gynaecol 1989;96:588–90.
9 Fleischer A, Herbert CM, Hill GA, Keppler D. M, Worrell JA. Transvaginal sonography of the endometrium during induced cycles. J Ultrasound Med 1991;10:93–7.
10 Glissant A, de Mouzon J, Frydman R. Ultrasound study of the endometrium during in vitro fertilization cycles. Fertil Steril 1985;44:786–9.
11 Gonen Y, Casper RF, Jacobson W, Blankier J. Endometrial thickness and growth during ovarian stimulation: a possible predictor of implantation in in vitro fertilization. Fertil Steril 1989;52:446–9.
12 Jauniaux E, Jurkovic D, Campbell S. In vitro investigation of the anatomy and the physiology of early human placental circulations. Ultrasound Obstet Gynecol 1991; 1:5–9.
13 Smith B, Porter R, Ahuja K, Craft I. Ultrasonic assessment of endometrial changes in stimulated cycles in an in vitro fertilization and embryo transfer program. J In Vitro Fert Embryo Transf 1984;1:233–8.
14 Kurjak A, Kupesic-Urek S, Schulman H, Zalud I. Transvaginal color Doppler in the assessment of ovarian and uterine blood flow in infertile women. Fertil Steril 1992;56:870–3.
15 Scholtes M, Wladimiroff J, van Rijen H, Hop W. Uterine and ovarian flow velocity waveforms in the normal menstrual cycle: a transvaginal color Doppler study. Fertil Steril 1989;52:981–5.
16 Janson P, Damber B, Axen C. Luteal blood flow and progesterone secretion in pseudopregnant rabbits. J Reprod Fertil 1981;63:491–3.
17 Bruce NW, Hillier K. The effect of prostaglandin $F_{2\alpha}$ on ovarian blood flow and corpora lutea regression in the rabbit. Nature 1974;249:176–7.
18 Brown B, Emery M, Mattner E. Ovarian artery blood velocity measured with Doppler ultrasonic transducers in conscious ewe. J Reprod Fertil 1980;58:295–300.
19 Ford S, Chenaluit J. Blood flow to the corpus luteum bearing ovary and ipsilateral uterine horn of cows during oestrus cycle and early pregnancy. J Reprod Fertil 1981;62:555–9.
20 Wary M, Cook M. Redistribution of blood flow by prostaglandin F2-α in the rabbit ovary. Am J Obstet Gynecol 1973;117:381–5.
21 Taylor K, Burns PN. Duplex Doppler scanning in the pelvis and abdomen. Ultrasound Med Biol 1985;11:643–7.
22 Nell T, Niswender G. Luteal blood flow and receptors for LH during PGF2-α–induced luteolysis: production of PGF2-α during early pregnancy. Acta Vet Scand 1981; 77:117–30.
23 Kurjak A, Kupesic-Urek S. Infertility. In: Kurjak A, editor. Transvaginal color Doppler: a comprehensive guide to transvaginal color Doppler sonography in obstetrics and gynecology. Carnforth, Lancashire: Parthenon, 1991: 33–8.
24 Bourne TH, Jurkovic D, Kurjak A, Campbell S. Intrafollicular blood flow during human ovulation. Ultrasound Obstet Gynecol 1991;1:53–9.
25 Collins W, Jurkovic D, Bourne TH, Kurjak A, Campbell S. Ovarian morphology, endocrine function and intra-follicular blood flow during the preovulatory period. Hum Reprod 1991;6:319–24.
26 Sladkevicius P, Valentin L, Marsal K. Blood flow velocity in the uterine and ovarian arteries during the normal menstrual cycle. Ultrasound Obstet Gynecol 1993;3: 199–201.
27 Inger DE, Madri JA, Folkman JA. Possible mechanism for inhibition of angiogenesis by angiostatic steroids: induction of capillary basement membrane dissolution. Endocrinology 1986;119:1768–75.
28 Reynolds S. Morphological determinations of the flow characteristics between an artery and its branch with special reference to the ovarian spiral artery in the rabbit. Acta Anat 1948;5:1–6.
29 Niswender GD, Reiners TJ, Diekmann MA, Nett Y. Blood flow: a mediator of ovarian function. Biol Reprod 1976;14:64–81.
30 Merce LT, Andrino R, Barco MJ, de la Fuente F. Cyclic changes of the functional ovarian compartments: echographic assessment. Acta Obstet Gynecol Scand 1990; 69:327–32.
31 Zalud I, Kurjak A. The assessment of luteal blood flow in pregnant and non-pregnant women by transvaginal color Doppler. J Perinat Med 1990;18:215–8.
32 Kurjak A, Kupesic-Urek S, Schulman H, Zalud I. Transvaginal color flow Doppler in the assessment of ovarian and uterine blood flow in infertile women. Fertil Steril 1991;56:870–4.
33 Goswamy RK, Williams S, Steptoe P. Decreased uterine perfusion: a cause of infertility. Hum Reprod 1988;3:955–9.
34 Steer CV, Mulls CL, Campbell S. Vaginal colour Doppler assessment on the day of embryo transfer accurately predicts patients in in vitro fertilization programme with suboptimal uterine perfusion who fail to become pregnant. Ultrasound Obstet Gynecol 1991;1:79–82.
35 Battaglia C, Larocca E, Lanzani A, Valentini M, Genanzzani AR. Doppler ultrasound studies of the uterine arteries in spontaneous and IVF cycles. Gynecol Endocrinol 1990;4:245–8.
36 Hauksson A, Akerlund M, Melin P. Uterine blood flow and myometrial activity at menstruation and the action of vasopressin and a synthetic antagonist. Br J Obstet Gynecol 1988;95:898–901.
37 Kupesic S, Kurjak A. Uterine and ovarian perfusion during the preovulatory period assessed by transvaginal color Doppler. Fertil Steril 1993;3:439–39.
38 Cohen H, Tice H, Mandel F. Ovarian volumes measured by ultrasound: bigger than we think. Radiology 1990; 77:189–93.
39 Goswamy RK, Campbell S, Royston JP, Bhan V, Battersby RH, Hall VJ, et al. Ovarian size in postmenopausal women. Br J Obstet Gynaecol 1988;95:795–9.
40 Strickland B. The value of arteriography in the diagnosis of bone tumors. Br J Radiol 1959;32:705–9.
41 Jain RK, Ward-Harley K. Tumor blood flow characterization, modifications and role in hyperthermia. Trans Sonics Ultrason 1984;31:504–9.
42 Gamill SL, Shipkey FH, Himmelfarb EH, Parvey LS, Rabinowitz JG. Roentgenology–pathology correlative study of neovascularity. AJR Am J Roentgenol 126 (1976) 376–385.
43 Granberg S, Nostrom A, Wikland M. Tumors in the lower pelvis as imaged by vaginal sonography. Gynecol Oncol 1990;37:224–6.
44 Hermann U, Locher G, Goldrich A. Sonographic patterns of ovarian tumors: prediction of malignancy. Obstet Gynecol 1987;69:777–80.
45 Luxman D, Bergman A, Sagi J, David M. The postmenopausal adnexal mass: correlation between ultrasonic and pathologic findings. Obstet Gynecol 1991;77:726–9.
46 Inoue M, Fujita M, Nakazawa A, Ogawa H, Tanizawa O. Sialyl-Tn, sialyl-Lewis Xi, CA 19-9, CA 125, carcinoembryonic antigen, and tissue polypeptide antigen in differentiating ovarian cancer from benign tumors. Obstet Gynecol 1992;79:434–40.
47 Jacobs I, Basr R. The CA 125 tumor-associated antigen: a review of literature. Hum Reprod 1989;4:1–5.
48 Aleem F, Zeitoun K, Calame R, Trinca D, Zalud I, Schulman H. The characterization of flow signals from tubal and ovarian arteries using intraoperative continuous wave Doppler. Ultrasound Obstet Gynecol 1994;4:304–9.

49 Schulman H, Conway C, Zalud I, Farmakides G, Haley J, Cassata M. Prevalence in a volunteer population of pelvic cancer detected with transvaginal ultrasound and color flow Doppler. Ultrasound Obstet Gynecol 1994;4:34–8.
50 Jones OWI, Surwit EA. Meigs syndrome and elevated CA 125. Obstet Gynecol 1989;73:520–1.
51 Donez J, Nissole M, Casabas-Roux F, Grandejan P. Endometriosis: pathogenesis and pathophysiology. In: Shaw RW, editor. Endometriosis. Carnforth, Lancashire: Parthenon, 1990: 11–31. (Advances in reproductive technology, 1.)
52 Landers DV, Sweet RL. Current trends in the diagnosis and treatment of tuboovarian abscess. Am J Obstet Gynecol 1985;151:1098–2001.
53 Paavoren J, Teisala K, Heinonen PK. Microbiological and histopathological findings in acute pelvic inflammatory disease. Br J Obstet Gynaecol 1987;94:454–7.
54 Reich H, McGlynn F. Laparoscopic treatment of tuboovarian and pelvic abscess. J Reprod Med 1987;3:747–5.
55 Nation JG, Krepart GV. Ovarian carcinoma of low malignant potential: staging and treatment. Am J Obstet Gynecol 1986;154:290–3.
56 Russel P, Merkur H. Proliferating ovarian "epithelial" tumors: a clinico-pathological analysis of 144 cases. Aust N Z Obstet Gynaecol 1979;19:45–51.
57 Julian CG, Woodruf JD. The biologic behavior of low-grade papillary serous carcinoma of the ovary. Obstet Gynecol 1972;40:860–7.
58 Russel P. Borderline epithelial tumors of the ovary: a conceptual dilemma. Clin Obstet Gynaecol 1984;11:259–77.
59 Bell DA, Weinstock MA, Scully RE. Peritoneal implants of ovarian serous borderline tumors: histologic features and prognosis. Cancer 1988;62:2212–22.
60 Buy JN, Ghossain MA, Sciot T, Bazot M, Guinet C, Prevot C. Epithelial tumors of ovary: CT findings and correlation with US. Radiology 1991;178:811–8.
61 Achiron R, Schejter E, Malinger G, Zakud H. Observation on the ultrasound diagnosis of ovarian neoplasms. Arch Gynecol Obstet 1987;241:183–90.
62 Burns PN, Halliwell M, Wells PNT, Webb AJ. Ultrasonic Doppler studies of the breast. Ultrasound Med Biol 1982;8:127–32.
63 Minasian M, Bamber JC. A Preliminary assessment of an ultrasonic Doppler method for the study of blood flow in human breast cancer. J Ultrasound Med Biol 1982;8:357–62.
64 Wells PNT, Halliwell M, Skidmore R, Webb AJ, Woodcock JP. Tumor detection by ultrasonic Doppler blood flow signals. Ultrasonics 1977;15:231–4.
65 Hata H, Hata K, Yamane Y, Kitao M. Real-time two-dimensional and pulsed Doppler ultrasound detection of intrapelvic neoplastic tumor and abnormal pathogenic changes: preliminary report. J Cardiovasc Ultrasonogr 1988;7:135–9.
66 Jellins J, Kossoff G, Boyd J, Reeve TS. The complementary role of Doppler to the B-mode examination of the breast. J Ultrasound Med 59 (1983) 89–93.
67 Taylor KJW, Ramos L, Carter D, Morse SS, Snower D, Fortune K. Correlation of Doppler ultrasound tumor signals with neovascular morphologic features. Radiology 1988;166:57–61.
68 Kurjak A, Zalud I, Jurkovic D, Alfirevic Z, Miljan M. Transvaginal color Doppler for the assessment of pelvic circulation. Acta Obstet Gynecol Scand 1989;68:131–5.
69 Bourne T, Campbell S, Steer C, Whitehead MI, Collins WP. Transvaginal color flow imaging: a possible new screening technique for ovarian cancer. Br Med J 1989;299:1367–70.
70 Kurjak A, Zalud I, Alfirevic A. Evaluation of adnexal masses with transvaginal color ultrasound. J Ultrasound Med 1991;10:295–7.
71 Bromley B, Goodman H, Benacerraf BR. Comparison between sonographic morphology and Doppler waveform for the diagnosis of ovarian malignancy. Obstet Gynecol 1994;83:434–7.
72 Valentin L, Sladkevicius P, Marsal K. Limited contribution of Doppler velocimetry to the differential diagnosis of extrauterine pelvic tumors. Obstet Gynecol 1994;83:425–33.
73 Fleischer AC, Rodgers WH, Kepple DM, Williams LL, Jones H. Color Doppler sonography of ovarian masses: a multiparameter analysis. J Ultrasound Med 1993;12:41–8.
74 Kurjak A, Predanic M, Kupesic-Urek S, Jukic S. Transvaginal color and pulsed Doppler assessment of adnexal tumor vascularity. Gynecol Oncol 1993;50:3–9.
75 Carter J, Saltzman A, Hartenbach E, Fowler J, Carson L, Twiggs LB. Flow characteristics in benign and malignant gynecologic tumors using transvaginal color flow Doppler. Obstet Gynecol 1994;83:125–30.
76 Schneider VL, Schneider A, Reed KL Hatch KD. Comparison of Doppler with two-dimensional sonography and CA-125 for prediction of malignancy of pelvic masses. Obstet Gynecol 1993;81:983–8.
77 Weiner Z, Beck D, Brandes JM. Transvaginal sonography, color flow imaging, computed tomographic scanning and CA 125 as a routine follow up examination in women with pelvic tumor: detection of recurrent disease. J Ultrasound Med 1994;13:37–41.
78 Fleischer AC, Cullinan JA, Kepple DM, Williams LL. Conventional and color Doppler transvaginal sonography of pelvic masses: a comparison of relative histologic specificities. J Ultrasound Med 1993;12:705–12.
79 Prömpeler HJ, Madjar H, Sauerbrei W, Lattermann U, Pfleiderer A. Quantitative flow measurements for classification of ovarian tumors by transvaginal color Doppler sonography in postmenopausal patients. Ultrasound Obstet Gynecol 1994;4:406–13.
80 Jeng CJ, Lin SY, Wang KL, Yang YC, Wang KG. Transvaginal color Doppler sonography in the prediction of adnexal malignancy. Ultrasound Med Biol 1994;20:180.
81 Natori M, Kohno H, Saitou M, Udagawa Y, Nozawa S. Doppler velocity waveform and ovarian tumor diagnosis. Ultrasound Med Biol 1994;20:56–9.
82 Hsieh FJ. Color Doppler ultrasound study on gynecologic malignancies: the clinical assessment and histopathologic correlation. Ultrasound Med Biol 1994;20:179–83.
83 Sohn C. Diagnosis of blood flow in tumors of uterus and ovary by ultrasound. Ultrasound Med Biol 1994;20:180–3.
84 Zhang QP, Xu XH. The study of correlation of color Doppler flow imaging ovarian tumor signals with neovascular morphologic features. Ultrasound Med Biol 1994;20:180–4.
85 Brown DL, Frates MC, Laing FC, DiSalvo DN, Doubilet PM, Benson CB, et al. Ovarian masses: can benign and malignant lesions be differentiated with color and pulsed Doppler US? Radiology 1994;190:333–6.
86 Sengoku K, Satoh T, Saitoh S, Abe M, Ishikawa M. Evaluation of transvaginal color Doppler sonography and CA 125 for prediction of ovarian malignancy. Int J Obstet Gynecol 1994;46:39–43.
87 Chou CY, Chang CH, Yao BL, Ko HC. Color Doppler ultrasonography and serum CA-125 in the differentiation of benign and malignant ovarian tumors. J Clin Ultrasound 1994;22:491–6.
88 Wu CC, Lee CN, Chen TM, Lai JI, Hsieh CY, Hsieh FJ. Factors contributing to the accuracy of detection of endometrial cancer. J Ultrasound Med 1994;2:23–35.
89 Zanetta G, Vergani P, Lissoni A. Color Doppler ultrasound in the preoperative assessment of adnexal masses. Acta Obstet Gynecol Scand 1994;73:637–41.
90 Salem S, White L, Lai J. Doppler sonography of adnexal masses: the predictive value of the TVCD. Radiology 1994;34:23–5.
91 Bonilla-Musoles F, Ballester MJ, Simon C, Serra V, Raga F. Is avoidance of surgery possible in patients with premenopausal ovarian tumors using transvaginal ultrasound and duplex color Doppler sonography? J Ultrasound Med 1993;12:33–9.
92 Hamper UA, Sheth S, Abbs FM, Rosenshein NB, Aronson D, Kurman RJ. Transvaginal color Doppler sonography of adnexal masses: differences in blood flow impedance in benign and malignant lesions. AJR Am J Roentgenol 1993;160:1225–8.
93 Wu CC, Lee CN, Chen TM, Shyu MK, Hsieh CY, Chen HY, et al. Incremental angiogenesis assessed by color Doppler ultrasound in the tumor genesis of ovarian neoplasms. J Ultrasound Obstet Gynecol 1993;33:45–9.
94 Fleischer AC, Entman SS, Porrath SA, James AE. Sonographic evaluation of uterine malformations and disorders. In: Sanders RC, James AE Jr, editors. The principles and practice of ultrasonography in obstetrics and gynecology. Norwalk, CT: Appleton-Century-Crofts, 1985: 531–44.
95 Kurjak A. Sonography of the uterus. In: Kurjak A, editor. An atlas of ultrasonography in obstetrics and gynecology. Carnforth, Lancashire: Parthenon, 1986: 245–53.
96 Tureck RW. Uterine leiomyomata. In: Garcia CR, Mastroianni L, Amelar RD, Dubin L, editors. Current therapy of infertility. Toronto: Decker, 1988: 80–9.
97 Kurjak A, Zalud I. Uterine masses. In: Kurjak A, editor. Transvaginal color Doppler: a comprehensive guide to transvaginal color Doppler sonography in obstetrics and gynecology. Carnforth, Lancashire: Parthenon, 1991: 123–30.
98 Gross BH, Silver TM, Jaffe NH. Sonographic features of uterine leiomyomas: analysis of 41 proven cases. J Ultrasound Med 1983;2:401–4.
99 Matta WM, Stabile L, Shaw RW, Campbell S. Doppler assessment of uterine blood flow changes in patients with fibroids receiving the gonadotropin-releasing hormone agonist buserelin. Fertil Steril 1988;49:1083–5.
100 Bonilla-Musoles F, Ballesteros A, Ballester MJ. Transvaginal color Doppler in the diagnosis of endometrial adenocarcinomas. Ultrasound Obstet Gynecol 1993;3:23–5.
101 Bourne TH, Campbell S, Whitehead MI, Royston P, Steer CV, Collins WP. Detection of endometrial cancer in postmenopausal women by transvaginal ultrasonography and color flow imaging. Br Med J 1990:301:369–74.
102 Hata K, Hata T, Manabe A, Makihara K, Kitao M. New pelvic sonography for detection of endometrial carcinoma: a preliminary report. Gynecol Oncol 1992;45:179–84.
103 Hata K, Hata T, Manabe A, Kitao M. Transvaginal Doppler ultrasound assessment of intratumoral hemodynamic charge before and during hypertensive intraarterial chemotherapy for uterine cancer. Obstet Gynecol 1992;80:801–4.
104 Kurjak A, Shalan H, Sosic A, Benic S, Zudenigo D, Kupesic S, et al. Endometrial carcinoma in postmenopausal women: evaluation by transvaginal color Doppler ultrasonography. Am J Obstet Gynecol 1993; 69:1597–603.
105 Rudigoz RC, Gaucherand P. Vaginal sonography and color Doppler in postmenopausal normalities. Ultrasound Obstet Gynecol 1993;3:42–6.
106 Merce LT, Garcia L, de la Fuente F. Doppler ultrasound assessment of endometrial pathology. Acta Obstet Gynecol Scand 1991;70:525–30.
107 Bourne TH, Campbell S, Steer CV, Royston P, Whitehead MI, Collins WP. Detection of endometrial cancer by transvaginal ultrasonography with color flow imaging and blood flow imaging and blood flow analysis: a preliminary report. Gynecol Oncol 1991;40:253–9.
108 Hata K, Makihara K, Hata T. Transvaginal color Doppler imaging for hemodynamic assessment of reproductive tract tumors. Int J Gynecol Obstet 1991;36:301–8.
109 Sladkevicius P, Valentin L. Transvaginal color Doppler examination of women with postmenopausal bleeding. Ultrasound Obstet Gynecol 1993 3:25–9.
110 Kurjak A, Kupesic-Urek S, Miric D. The assessment of benign uterine tumors by transvaginal color Doppler. J Ultrasound Med Biol 1992;18:645–9.
111 Kurjak A, Schulman H, Sosic A, Zalud I, Shalan H. Transvaginal ultrasound, colour flow and Doppler waveform of the postmenopausal adnexal mass. Obstet Gynecol 1992;80:917–21.

Transvaginal 3D and 4D Ultrasound

40 Transvaginal 3D/4D Ultrasound and its Applications in Gynecology

Development of Transvaginal 3D Ultrasound

While three-dimensional visualization of structures was achieved during the 1980s using techniques in computed tomography (CT) and magnetic resonance imaging (MRI) [1–3], the development of three-dimensional ultrasonography proved much more difficult. This was because, unlike the automated techniques in CT and MRI, scanning freehand with an ultrasound probe did not enable the examiner to acquire a coordinated sequence of sectional images spaced at equal intervals. Although initial reports on three-dimensional (3D) in-vitro ultrasound studies were published during the 1980s [4–6], several years passed before the initial clinical applications of 3D ultrasound took place. The first commercially available ultrasound system with mechanical 3D transducers (the Combison 310) was marketed by the Austrian firm Kretztechnik in 1989 [7].

In designing an endovaginal 3D transducer, it was necessary to create a device that did not differ significantly from a conventional two-dimensional (2D) endovaginal probe. The control unit that uniformly deflects the scan plane had to be housed in a considerably smaller space than in a 3D abdominal transducer. The first acceptable imaging results were achieved with a side-scanning probe (Kretztechnik, Austria) in which the B-mode plane was rotated around the probe axis (360° panoramic scan) [8] (Fig. 40.**1**). The disadvantage of this design was that the probe was limited to lateral volume acquisition [9,10] (Fig. 40.**2**). Frontal volume acquisition is much more favorable for scanning the true pelvis, however, and efforts were therefore directed toward developing an end-firing type of 3D scanner. The result was a forward-scanning sector probe (Fig. 40.**1**) in which the two-dimensional image plane was rotated by a motor 180° about the longitudinal probe axis. This sweeps out a volume shaped like a truncated cone extending forward from the end of the probe (Fig. 40.**3**) [9,11–13]. One disadvantage of this system, however, was that the overlapping of image planes along the axis of rotation tended to degrade the image quality at the center of the image. As a result, this concept was eventually abandoned in favor of a different forward-scanning technique. The end-firing 3D vaginal probes in current use (Fig. 40.**1**) have a motor that deflects the beam in a fan-shaped pattern, similar to the function of 3D abdominal transducers (Fig. 40.**4**). Acquisition rates of up to 35 volumes per second can now be achieved, making real-time 3D imaging—or "four-dimensional" (4D) imaging—a reality.

In addition to 3D/4D systems with special 3D probes for volume acquisition, freehand systems [14,15] have also been developed. In these systems, an electromagnetic sensor mounted on the transducer can accurately detect the position and movements of the transducer on the basis of changes in an applied magnetic field. The sectional images acquired with this technique are coordinated in computer memory by a graphic program and assembled into a volume. The advantage of the freehand technique is that the sensor can be mounted on any commercially available transducer, eliminating the need to purchase a costly 3D transducer. One disadvantage, however, is that freehand scanning leads to volume acquisition with irregular slice intervals. Interpolative computer software has to fill in the gaps, resulting in poorer image quality. Another drawback is that manual volume acquisition is not compatible with real-time (4D) imaging [16].

Technical Aspects of 3D Ultrasound

The basic principle of three-dimensional ultrasound is that multiple adjacent two-dimensional planes of section are acquired, assembled into a volume, and digitally stored in an electronic memory. Because three-dimensional ultrasound is based on two-dimensional ultrasound, a high-quality 2D image is the foundation for a good 3D image.

A 3D ultrasound examination generally consists of four basic steps [16,17]:

- Volume acquisition
- Volume rendering
- Volume manipulation and image processing
- Digital storage of volumes or rendered images

Volume Acquisition

As in conventional 2D vaginal ultrasound, the patient can be examined on an examination table or a gynecologic chair. Before the 3D probe is inserted into the vagina, it is sheathed in a condom (without a reservoir) that has been smeared inside and outside with ultrasound coupling gel.

The transvaginal 3D ultrasound examination begins in the same way as a conventional 2D examination. When the organ of interest has been optimally visualized, the region of interest (the region that has been targeted for volume acquisition) is outlined with a variable-size volume box in the B-mode image. A button is then pushed to activate volume acquisition. The transducer automatically scans the outlined region in a period of 0.5–2.0 seconds, and the volume data are digitally stored at spatially encoded sites in the volume memory. After all the data have been loaded into memory, the individual contiguous 2D scan planes are assembled into a volume. The transducer has to be held stationary during volume acquisition in order to avoid motion artifacts.

A total of three volume acquisitions can completely cover the true pelvis (Fig. 40.**5**). If an abnormally enlarged uterus or a high-sited ovarian mass is found, the 3D transvaginal examination should be followed by a 3D abdominal examination.

Volume Rendering

Volume rendering may involve pure gray-scale rendering, pure color rendering, or a combination of gray-scale and color modes called glass-body rendering. The principal rendering modes used in gynecologic ultrasound are described below.

Gray-scale rendering modes. In the gray-scale modes, only gray-scale information is used in rendering the image. Three main options are available: multiplanar rendering, surface rendering, and transparent rendering.

Multiplanar (= triplanar) rendering. As soon as the volume has been loaded into memory, the three mutually perpendicular (orthogonal) image planes that encompass the scanned region are rendered and displayed simultaneously on the monitor (multiplanar display, Fig. 40.**6**).

The corresponding scan planes are marked by lines at the borders of the images, while the center of rotation appears as a dot at the center of the image. A fourth image can be displayed in the form of a graphic model showing the location of the outlined reference plane within the stored volume or even in the form of a surface-rendered image (Fig. 40.**6**). Any of the three planes can also be displayed separately or may be composited to produce a cutaway "niche mode" display (see Fig. 40.**36**).

Surface rendering is used to reconstruct surface views of designated regions, such as the inner wall of a cyst (see Fig. 40.**45**). It can also be used to reconstruct cut surfaces (see Figs. 40.**7**–40.**15**). For this purpose, the desired subvolume has to be outlined in all three planes. Various modes are available for surface rendering, and any two of the modes can be combined in one display.

Transparent rendering preferentially displays echogenic structures such as calcifications (see Fig. 40.**16**).

Color rendering modes. *Pure color rendering.* This mode renders only the color information acquired by color or power Doppler scanning. This permits the isolated visualization of blood flow within vessels.

Glass-body rendering. The glass-body mode combines transparent rendering with color or power Doppler flow mapping [18–21] to provide a transparent, three-dimensional view of the vascular system in an organ (see Figs. 40.**32**, 40.**34**, 40.**38**, 40.**56**, 40.**57**). This makes it possible to detect abnormal patterns of vascularity, as well as vascular abnormalities such as stenoses and dilated vascular segments.

Volume Manipulation and Image Processing

Multiplanar reformatting. The *multiplanar (triplanar) display* allows interactive volume manipulation, making it an easy matter to display image planes in all three dimensions (multiplanar reformatting). Standard planes of section can be displayed as well as planes that are not accessible to conventional 2D ultrasound, such as oblique sections. All three planes can be pieced together in the *niche mode* to render a cutaway view (see Fig. 40.**36**).

Tomographic survey. The multiplanar display also permits a tomographic survey of the stored volume in millimeter increments. The examiner should first display the object in a "textbook" position before proceeding with the survey [22].

Relatively new technologies for displaying a series of two-dimensional image planes are the multi-slice view (MSV; Medison) and tomographic ultrasound imaging (TUI; GE-Kretz) (see Fig. 40.**31**). Both the desired image plane and the interval between slices can be defined in these modes.

Image animation (cine mode). To obtain an even clearer spatial impression of an object, multiple adjacent or overlying three-dimensional images can be computed and displayed on the monitor in the form of a rotating sequence. This animation may be done in the surface mode, transparent mode, or glass-body mode. The operator defines the starting and end points of the sequence (i.e., the total rotation angle) and the angle between the individual cine images (see Fig. 40.**46**). When the calculations are completed, the 3D images can be viewed as an animated sequence on the monitor. The object can be rotated around the x or y axis. The speed of rotation is influenced by the total rotation angle and the number of cine images.

Electronic scalpel. The electronic scalpel [23] can be used to selectively remove overlying structures that are unfavorable for surface rendering. Various cut modes are available for this purpose. The electronic scalpel is also used to remove portions of an organ such as the anterior or lateral half of the uterus or ovary (see Figs. 40.**17**–40.**30**). Gray-scale and color echoes in the glass-body mode can be removed independently of one another.

Filtering. Internal echoes in cystic lesions create unwanted signals that can be troublesome in surface rendering. These unwanted echoes can be filtered out with the *threshold control.* The control is adjusted until it just suppresses the extraneous echoes (see Fig. 40.**49**) [16]. The threshold should not be set too high, as this will also remove echoes of normal tissue and produce iatrogenic defects. Threshold filtering is unnecessary in the transparent mode.

Contrast and brightness. Image brightness and contrast are fully adjustable in all display modes, and all changes are immediately displayed on the monitor. This interactive control makes it possible to display any object with optimum brightness and contrast [16]. In glass-body rendering, the color and gray-level components can be adjusted independently of one another.

Color selection. Besides the simple gray-scale display, various color modes can be selected for the display of 3D images. In some cases, an abnormality in the image can be brought out more clearly by assigning specific color values (see Fig. 40.**10**).

Measurements. Measurement can be taken in all three planes of the multiplanar display. Measurements are not available in rendered images, however.

Volumetry. Using the Virtual Organ Computer-Aided Analysis (VOCAL) volume calculation program (GE-Kretz), the volumes of organs or masses can be calculated manually or semiautomatically and displayed as a separate three-dimensional image on the screen (see Fig. 40.**47**).

Histogram. With this feature, the gray-scale and color components within a designated volume can be plotted as a separate graphic display (see Fig. 40.**54**).

Archiving

Volumes as well as three-dimensional images can be written onto an external hard drive, a magneto-optical disk (MO disk), a CD, or a DVD for permanent digital archiving.

Advantages of Transvaginal 3D Ultrasound

Automatic scanning of the pelvis with an endovaginal 3D probe for the acquisition and storage of selected volumes opens up new diagnostic possibilities in the true pelvis (Table 40.**1**) [11,12,24,25]. The main advantage is the ability to generate transverse sections of the true pelvis in addition to conventional sagittal and coronal scans. Also, the examiner can scroll through a stored volume millimeter by millimeter in all three planes and can rotate the volume in all three directions. This makes it possible not only to determine the maximum extent of an abnormal finding, but also to define the precise topographic location of the lesion in all three planes. The ability to display all three orthogonal planes simultaneously on the monitor also enables a precise volumetric analysis [26,27]. This is particularly important in the determination of tumor volumes [28,29].

Moreover, the ability to render a three-dimensional surface view or transparent view can produce a direct, lifelike image or organs such as

Table 40.1 Advantages of transvaginal three-dimensional ultrasound over conventional two-dimensional ultrasound

- Simultaneous visualization of all three image planes (sagittal, coronal, and transverse)
- Ability to rotate the volume so that abnormal findings can be displayed in the optimum plane
- Ability to make a tomographic survey of the stored organs
- Three-dimensional surface rendering and transparent views
- Surface rendering of cut surfaces
- Three-dimensional color display of organ or tumor blood flow
- Accurate volumetry
- Less total scanning time in the patient
- Digital volume storage without data loss
- Ability to access and evaluate the stored volumes at any time
- Volume available for analysis by a second reader (telemedicine)
- New training opportunities

the uterus or adnexa. Adding color Doppler signals can also provide a three-dimensional display of tumor perfusion. All of these capabilities have opened up a world of new possibilities in gynecologic diagnosis.

The automatic acquisition of a designated volume in 0.5–4.0 seconds can significantly reduce the total time spent scanning the patient. Once the optimum volume has been stored, it can be explored in various planes of section as often as desired, even after the patient has left [16,17,19]. Additional measurements can be taken, and new three-dimensional images can be rendered. This may be done immediately after the ultrasound examination or at a later time. A second reader can also access and evaluate the volume, which is stored with digital image quality. If a second opinion is needed, a compression program can be used to send the volume data via the internet to a consulting expert, who can load the volume into his ultrasound system or computer for evaluation [30]. Stored volumes can also be a resource for continuing education and training: multiple copies can be made of a selected volume so that different readers can view the same volume on multiple screens at the same time [31]. Finally, the ability to archive a volume without data loss provides an opportunity for retrospective volume analysis at a later date.

When Merz et al. [12] conducted comparative 2D and 3D ultrasound examinations in 223 gynecologic patients with various conditions, they found that three-dimensional ultrasound offered advantages over traditional two-dimensional ultrasound in 61% of the cases studied. The advantages resulted from the selective visualization of the desired plane, the precise volumetry of pelvic masses, and the ability to generate lifelike surface-rendered and transparent views.

Problems in Transvaginal 3D Ultrasound

Every examiner who changes from transvaginal 2D ultrasound to transvaginal 3D ultrasound will require an initial learning period, during which he or she has to practice selective volume acquisition, orientation within the stored volume, and the rendering of three-dimensional images. Because a volume can be arbitrarily rotated in space, concepts such as cranial, caudal, left, and right no longer relate to the image borders as in 2D ultrasound, but rather to the object under study [12]. As a result, the examiner has to have a good sense of the way in which a three-dimensional object is situated in space. Ultimately, the only scan plane that is important for the examiner is the one that displays the finding with greatest clarity. This may be a longitudinal, coronal, horizontal, or arbitrary oblique plane of section.

The simultaneous acquisition of gray-scale and color Doppler signals may take as long as 10 seconds, during which time the transducer must be held still. Any motion of the transducer during the acquisition will cause nonuniform entry of volume data into the memory, leading to motion artifacts.

During surface rendering, the threshold control should not be set too high to suppress unwanted echoes, as this could lead to the appearance of iatrogenic structural defects.

A medium with a high storage capacity is still essential for storing volume data sets. A capacity of up to 20 megabytes per volume may be necessary, depending on the size of the volume.

Technical Aspects of 4D Ultrasound

To date, 4D ultrasound has played a much smaller role in gynecology than in obstetrics because gynecologic ultrasound deals mainly with nonmoving objects. Nevertheless, there have been some interesting initial applications that may become important in the future. They include the evaluation of intestinal and endometrial movements, the assessment of tubal perfusion by hysterosalpingo-contrast sonography, and the use of color Doppler for the three-dimensional assessment of tumor blood flow.

Unlike static 3D ultrasound, up to 35 volumes/second are acquired in 4D ultrasound. Various acquisition modes are available for this purpose.

4D Volume Cine

4D ultrasound may be done as an adjunct to 3D ultrasound, or it may be done first to define the precise region of interest, which is then evaluated further in the 3D mode. Since multiple volumes have already been stored in memory, it is easy to scroll back through the volumes in a cine sequence until the optimum volume is found.

Two main 4D technologies are available for gynecologic applications: volume contrast imaging and spatiotemporal image correlation.

Volume contrast imaging (VCI), known also as the "thick-slice" technique, is a special 4D technique in which relatively thin volumes are displayed in rapid sequence with improved contrast.

The *VCI-A technique* displays the same anatomical region as the 2D image, but the low thickness of the volume results in enhanced tissue contrast (Fig. 40.**7**).

In the *VCI-C technique*, a thin coronal volume is acquired perpendicular to the 2D image plane (Fig. 40.**8**). The desired level of volume acquisition is defined by a green indicator line in the two-dimensional image. The VCI-C technique provides morphologic information on planes that are not accessible with conventional 2D scanning.

Spatiotemporal image correlation. Much as in fetal echocardiography [32], it is now possible to demonstrate the blood flow to gynecologic organs and tumors in three dimensions. By adding color or power Doppler, it is possible not only to define the three-dimensional pattern of vascularity but also observe vascular pulsations over time. This technique, like fetal echocardiography, does not require external triggering. While observing the spatial distribution and pulsation of the vessels, the examiner can simultaneously rotate the volume in all directions, so that it can be viewed from various angles.

Applications of 3D and 4D Ultrasound

A number of applications already exist for transvaginal 3D and 4D ultrasound (Table 40.**2**).

Table 40.**2** Applications of 3D/4D ultrasound

Uterus
• Endometrial evaluation • Investigation of uterine anomalies • Localization of intrauterine devices • Myoma diagnosis • Carcinoma diagnosis • Uterine blood flow
Ovary
• Folliculometry • Investigation of ovarian masses • Ovarian blood flow
Fallopian tube
• Assessment of tubal patency • Investigation of postinflammatory tubal changes and tubal masses
Rest of the true pelvis
• Investigation of endometriotic lesions
Pelvic floor
• Surface rendering of the pelvic floor

Uterus

The uterus can always be rotated in the stored image to display the organ in exact sagittal, coronal, and transverse planes of section (Fig. 40.**6**). With the four-dimensional VCI-A technique, the uterus can be viewed much as in a 2D image but with an enhanced contrast that clearly delineates the endometrium from the myometrium (Fig. 40.**7**). With the VCI-C technique, the examiner can mark the endometrium in the sagittal 2D image to generate an immediate 3D coronal image in which the cornual region is clearly displayed (Fig. 40.**8**).

When the uterus is rotated to an upright position and its anterior surface is removed with the electronic scalpel, the 3D surface mode can be activated to render a three-dimensional view of the endometrium in coronal section (Figs. 40.**10**, 40.**17**)).

Endometrial volumetry may be done within the framework of in-vitro fertilization therapies [33–36] and in patients with suspected tumors [28].

3D power Doppler is an effective mode for the visualization of subendometrial blood flow [35,37,38].

3D technology also facilitates the localization of intrauterine devices [39–43]. The ability to rotate the stored uterine image to display an exact coronal section makes it possible not only to check the position of the vertical stem of a Copper-T intrauterine device (IUD) in the uterine cavity, but also to confirm that the side arms of the device are properly deployed (Figs. 40.**12**, 40.**13**). Endometrial calcifications that mimic an IUD can be quickly identified by rotating the volume to a coronal section in the transparent mode (Fig. 40.**16**).

In patients in whom palpable findings raise a suspicion of a uterine anomaly, the coronal section is excellent for detecting a uterine anomaly and even classifying the anomaly type (Figs. 40.**18**–40.**22**) [44,45].

Abnormalities in the uterine cavity (Fig. 40.**23**) or an abnormal echo pattern in the endometrium (Fig. 40.**24**) can be investigated by selectively defining the suspicious area in all three planes or in the surface-rendered view.

In the investigation of uterine tumors, myomas can be accurately localized and their volume can be precisely determined (Figs. 40.**25**–40.**27**).

In the uterine corpus, a coronal display of the endometrium in surface mode can provide a fast, clear impression of endometrial pathology (Fig. 40.**28**). When endometrial carcinoma is present, the coronal view is excellent for evaluating myometrial invasion and detecting tumor extension in the caudal direction (Fig. 40.**29**). Abnormalities can also be detected in the sagittal surface image (Fig. 40.**30**). The multislice view (MSV; Medison) and tomographic ultrasound imaging (TUI; GE-Kretz) are new technologies that can display changes in all three planes as in computed tomography (Fig. 40.**31**).

By combining the transparent mode with color or power Doppler (glass-body rendering), it is possible for the first time to obtain three-dimensional views of uterine vascularity and neovascularization. Besides the course of the vessels, the glass-body mode can clearly demonstrate areas of vascular stenosis and dilation (Figs. 40.**23**, 40.**33**).

Both benign and malignant lesions of the uterine cervix can be diagnosed with 3D ultrasound. Abnormalities can be recognized in the lateral surface image (Fig. 40.**34**), coronal surface image (Fig. 40.**35**), and niche mode (Fig. 40.**36**). Chou et al. [29] have described the use of 3D ultrasound in the volumetry of cervical carcinomas.

With 3D power Doppler ultrasound, the neovascularization of cervical carcinomas can be clearly visualized in three dimensions (Figs. 40.**37**, 40.**38**) [18,20,21].

3D ultrasound has been applied not only in the diagnosis of gynecologic malignancies, but also in evaluating their response to treatment [46].

Ovary

The simultaneous display of all three planes can provide a comprehensive overview of the entire ovary and its volume (Fig. 40.**39**) [47]. Ovarian blood flow can be evaluated by combining 3D power Doppler with the transparent mode (glass-body rendering, Fig. 40.**40**).

The multiplanar mode and surface-rendering mode can both be used to evaluate follicular maturation in spontaneous and stimulated cycles and to evaluate the ovaries in hyperstimulation (Figs. 40.**41**–40.**43**). Both modes are also useful in the investigation of cystic ovarian masses [48] (Figs. 40.**44**–40.**55**). The surface mode can be used for the selective visualization of smooth wall contours as well as wall irregularities. Proliferative foci on the inner cyst wall are detected by using the threshold control to eliminate extraneous echoes within the cyst (Fig. 40.**49**). With a properly adjusted image, surface rendering can open up new possibilities in the benign-malignant discrimination of ovarian tumors.

The glass-body mode can provide impressive three-dimensional views of the vascularity and neovascularity of borderline and malignant ovarian tumors (Figs. 40.**54**, 40.**56**, 40.**57**).

The surface mode can be used in the investigation of solid ovarian tumors, as well as cystic masses. A portion of the tumor can be removed with the electronic scalpel, and the cut surface can then be viewed in surface mode, displaying structural nonhomogeneities more clearly than a conventional 2D image (Fig. 40.**58**). 3D power Doppler and the glass-body mode are also useful for detecting areas of neovascularization (Fig. 40.**59**). Several groups of authors have reported on the value of 3D power Doppler ultrasound in the investigation of ovarian masses [49–51].

Fallopian Tubes

Hysterosalpingo-contrast sonography (HyCoSy) is a procedure for evaluating tubal patency with 2D ultrasound. One drawback of this technique is that the scan plane must be repeatedly adjusted to follow the tortuous course of the tubes. With 3D/4D ultrasound, however, the uterine cavity [52] and fallopian tubes can be demonstrated in three dimensions [53], providing a clearer assessment of tubal patency (Fig. 40.**60**).

Postinflammatory tubal changes such as hydrosalpinx are clearly visualized in the surface mode and are easily distinguished from an ovarian cyst (Fig. 40.**61**). Glass-body rendering can rapidly detect any abnormal varicosity in the adnexal region (Fig. 40.**62**).

Other Findings in the True Pelvis

Besides primary uterine and adnexal tumors, transvaginal 3D/4D ultrasound can also be used in the investigation of intestinal tumors or recurrent tumors in the true pelvis. The glass-body mode can be used to investigate tumor blood supply and is particularly effective for the detection of tumor-feeding vessels (Fig. 40.**63**).

3D/4D ultrasound is also useful for the selective exclusion of a tumor. For example, the orthogonal display or 4D technique can quickly determine that a questionable adnexal mass is actually a distended bowel loop (Figs. 40.**64**, 40.**65**).

Pelvic Floor

For the first time, 3D ultrasound makes it possible to obtain sonographic views of the pelvic floor [54–57]. By using a curved volume box in the surface mode, the examiner can generate a curved surface-rendered image of the pelvic floor (Fig. 40.**66**).

Reports have also been published on the use of 3D ultrasound in examinations of the urethral sphincter [58], in urinary incontinence [59], and for evaluating the anal sphincter [60].

Critical Appraisal and Outlook

Despite the learning curve that is involved in handling the 3D endovaginal probe and rendering three-dimensional images, transvaginal 3D ultrasound is setting new standards in gynecologic diagnosis owing to the simultaneous display of all three image planes and the ability to generate surface-rendered, transparent and glass-body images. With the development of high-speed, high-capacity computers and the use of fast endovaginal probes, transvaginal 4D ultrasonography has now become a reality.

With regard to the future of transvaginal 3D/4D ultrasound, it is reasonable to expect that there will be further improvements of image quality accompanied by even faster image generation, simpler methods of automatic volume calculation, and perhaps the development of new display modes. It would be desirable for the various ultrasound manufacturers to adopt the Digital Imaging and Communication in Medicine (DICOM) standard for the storage of volume data and for image displays.

Ultimately, the widespread use of transvaginal 3D/4D ultrasound will become a reality only when the equipment costs fall sufficiently for the technology to be affordable for office practitioners.

References

1 Levin DN, Hu X, Tan KK, Galhotra S. Surface of the brain: three-dimensional MR images created with volume rendering. Radiology 1989;171:277–80.
2 Rusinek H, Mourino MR, Fironoznia H, Weinreb JC, Chase NE. Volume rendering of MR images. Radiology 1989;171:269–72.
3 Vannier MW, Hildeboldt CF, Marsh JL, Pilgram TK, McAlister WH, Shackelford GD, et al. Craniostenosis: diagnostic value of three-dimensional CT reconstruction. Radiology 1989;173:669–73.
4 Brinkley JF, Muramatsu SK, McCallum WD, Popp RL. In vitro evaluation of ultrasonic three-dimensional imaging and volume system. Ultrason Imaging 1982;4:126–39.
5 Fredfelt KE, Holm HH, Pedersen JF. Three dimensional ultrasonic scanning. Acta Radiol Diagn 1984;25:237–41.
6 Sohn C, Grotepass J, Schneider W, Funk A, Sohn G, Jensch P, et al. Erste Untersuchungen zur dreidimensionalen Darstellung mittels Ultraschall. Z Geburtshilfe Perinatol 1988;192:241–8.
7 Wiesauer F. Methodology of three-dimensional ultrasound. In: Kurjak A, Kupesic S, editors. Clinical application of 3D sonography. New York: Parthenon, 2000: 1–6.
8 Merz E, Weber G, Macchiella D, Bahlmann F. 3D-Volumensonographie in der transvaginalen Diagnostik. Ultraschall Klin Prax 1993;8:154.
9 Kirbach D, Whittingham TA. 3D ultrasound: the Kretztechnik Voluson approach. Eur J Ultrasound 1994;1:85–9.
10 Merz E, Bahlmann F, Weber G. Volume scanning in the evaluation offetal malformations: a new dimension in prenatal diagnosis. Ultrasound Obstet Gynecol 1995;5:222–7.
11 Feichtinger W. Transvaginal three-dimensional imaging. Ultrasound Obstet Gynecol 1993;3:375–8.
12 Merz E, Weber G, Macchiella D, Bahlmann F. 3D-Volumensonographie in der transvaginalen Diagnostik. Gynäkologe 1995;28:270–5.
13 Steiner H, Staudach A, Spitzer D, Graf AH, Wienerroither H. Bietet die 3D-Sonographie neue Perspektiven in der Gynäkologie und Geburtshilfe? Geburtshilfe Frauenheilkd 1993;53:779–82.
14 King DL, King DL Jr, Shao MY. Three dimensional spatial registration and interactive display of position and orientation of real-time ultrasound images. J Ultrasound Med 1990;9:525–32.
15 Watkin KL, Khalifé S, Nuwayhid B, Baer L, Mathur S, El-Hakim S, et al. Three dimensional reconstruction of freehand abdominal and vaginal ultrasonic images. Ultrasound Obstet Gynecol 1993;3(Suppl 2):185.
16 Merz E. 3D ultrasound in prenatal diagnosis. In: Merz E, editor. Ultrasound in obstetrics. Stuttgart: Thieme, 2004: 516–528.
17 Merz E. 3-D ultrasound in prenatal diagnosis. Curr Obstet Gynaecol 1999;9:93–100.
18 Hsu KF, Su JM, Huang SC, Cheng YM, Kang CY, Shen MR, et al. Three-dimensional power Doppler imaging of early-stage cervical cancer. Ultrasound Obstet Gynecol 2004;24:664–71.
19 Muniz C, Fleischer A, Donnelly E, Mazer M. Three-dimensional color Doppler sonography and uterine artery arteriography of fibroids. J Ultrasound Med 2002;21: 129–33.
20 Suren A, Osmers R, Kuhn W. 3D color power angio imaging: a new method to assess intracervical vascularization in benign and pathological conditions. Ultrasound Obstet Gynecol 1998;11:133–7.
21 Testa AC, Ferrandina G, Distefano M, Fruscella E, Mansueto D, Basso D, et al. Color Doppler velocimetry and three-dimensional color power angiography of cervical carcinoma. Ultrasound Obstet Gynecol 2004;24:445–52.
22 Merz E, Weber G, Bahlmann, Miric-Tesanic D. Application of transvaginal and abdominal three-dimensional ultrasound for the detection or exclusion of malformations of the fetal face. Ultrasound Obstet Gynecol 1997;9:237–43.
23 Merz E, Miric-Tesanic D, Welter C. Value of the electronic scalpel (cut mode) in the evaluation of the fetal face. Ultrasound Obstet Gynecol 2000;16:564–8.
24 Bega G, Lev-Toaff A, O'Kane P, Becker E, Kurtz A. Three-dimensional ultrasonography in gynecology. J Ultrasound Med 2003; 22:1249–69.
25 Merz E. Three-dimensional transvaginal ultrasound in gynecological diagnosis. Ultrasound Obstet Gynecol 1999;14:81–6.
26 Gregg A, Steiner H, Staudach A, Weiner CP. Accuracy of 3D sonographic volume measurements. Am J Obstet Gynecol 1993;168:348.
27 Steiner H, Gregg AR, Bogner G, Weiner CP, Staudach A. First trimester 3-D ultrasound volumetry of the gestational sac. J Ultrasound Obstet Gynecol 1993;3(Suppl 2):168.
28 Alcazar JL, Merce LT, Manero MG, Bau S, Lopez-Garcia G. Endometrial volume and vascularity measurements by transvaginal 3-dimensionalultrasonography and power Doppler angiography in stimulated and tumoral endometria: an interobserver reproducibility study. J Ultrasound Med 2005;24:1091–8.
29 Chou CY, Hsu KF, Wang ST, Huang SC, Tzeng CC, Huang KE. Accuracy of three-dimensional ultrasonography in volume estimation of cervical carcinoma. Gynecol Oncol 1997;66:89–93.
30 Kratochwil A, Lee A, Schoisswohl A. Networking of three dimensional sonography volume data. Ultrasound Obstet Gynecol 2000;16:335–40.
31 Merz E, Bahlmann F, Weber G, Macchiella D. Three-dimensional ultrasonography in prenatal diagnosis. J Perinat Med 1995;23:213–22.
32 Goncalves LF, Lee W, Chaiworapongsa T, Espinoza J, Schoen ML, Falkensammer P, et al. Four-dimensional ultrasonography of the fetal heart with spatiotemporal image correlation. Am J Obstet Gynecol 2003;189:1792–802.
33 Child TJ, Sylvestre C, Tan SL. Endometrial volume and thickness measurements predict pituitary suppression and non-suppression during IVF. Hum Reprod 2002; 17:3110–3.
34 Raga F, Bonilla-Musoles F, Casan EM, Klein O, Bonilla F. Assessment of endometrial volume by three-dimensional ultrasound prior to embryo transfer: clues to endometrial receptivity. Hum Reprod 1999;14:2851–4.

35 Schild RL, Holthaus S, d'Alquen J, Fimmers R, Dorn C, Van Der Ven H, Hansmann M. Quantitative assessment of subendometrial blood flow by three-dimensional-ultrasound is an important predictive factor of implantation in an in-vitro fertilization programme. Hum Reprod 2000;15:89–94.
36 Yaman C, Sommergruber M, Ebner T, Polz W, Moser M, Tews G. Reproducibility of transvaginal three-dimensional endometrial volume measurements during ovarian stimulation. Hum Reprod 1999;14:2604–8.
37 Ng EH, Chan CC, Tang OS, Yeung WS, Ho PC. Comparison of endometrial and subendometrial blood flow measured by three-dimensional power Doppler ultrasound between stimulated and natural cycles in the same patients. Hum Reprod 2004; 19:2385–90.
38 Raine-Fenning NJ, Campbell BK, Kendall NR, Clewes JS, Johnson IR. Quantifying the changes in endometrial vascularity throughout the normal menstrual cycle with three-dimensional power Doppler angiography. Hum Reprod 2004;19:330–8.
39 Bonilla-Musoles F, Raga F, Osborne NG, Blanes J. Control of intrauterine device insertion with three-dimensional ultrasound: is it the future? J Clin Ultrasound 1996; 24:263–7.
40 Bonilla F, Martinez-Molina V, Blanes J, Raga F, Villabos A. Three-dimensional ultrasound investigation for identification and control of uterine devices. In: Merz E, editor. 3-D ultrasound in obstetrics and gynecology. Philadelphia: Lippincott Williams & Wilkins, 1998: 31–36.
41 Hösli I, Holzgreve W, Tercanli S. [Use of three-dimensional ultrasound for assessment of intrauterine device position: in German.] Ultraschall Med 2001;22:75–80.
42 Jurkovic D, Aslam N. Three-dimensional ultrasound for diagnosis of congenital uterine anomalies. In: Merz E, editor. 3-D ultrasound in obstetrics and gynecology. Philadelphia: Lippincott Williams & Wilkins, 1998: 27–29.
43 Lee A, Eppel W, Sam C, Kratochwil A, Deutinger J, Bernaschek G. Intrauterine device localization by three-dimensional transvaginal sonography. Ultrasound Obstet Gynecol 1997;10:289–92.
44 Jurkovic D, Geipel A, Gruboeck K, Jauniaux E, Natucci M, Campbell S. Three-dimensional ultrasound for the assessment of uterine anatomy and detection of congenital anomalies: a comparison with hysterosalpingography and two-dimensional sonography. Ultrasound Obstet Gynecol 1995;5:233–8.
45 Woelfer B, Salim R, Banerjee S, Elson J, Regan L, Jurkovic D. Reproductive outcomes in women with congenital uterine anomalies detected by three-dimensional ultrasound screening. Obstet Gynecol 2001;98:1099–103.
46 Yaman C, Fridrik M. Three-dimensional ultrasound to assess the response to treatment in gynecological malignancies. Gynecol Oncol 2005;97:665–8.
47 Hata T, Yanagihara T, Hayashi K, Yamashiro C, Ohnishi Y, Akiyama M, et al. Three-dimensional ultrasonographic evaluation of ovarian tumours: a preliminary study. Hum Reprod 1999;14:858–61.
48 Weber G, Merz E, Bahlmann F, Macchiella D. Sonographische Beurteilung von Ovarialtumoren. Vergleich zwischen transvaginaler 3D-Technik und konventioneller zweidimensionaler Vaginosonographie. Ultraschall Med 1997;18:26–30.
49 Cohen LS, Escobar PF, Scharm C, Glimco B, Fishman DA. Three-dimensional power Doppler ultrasound improves the diagnostic accuracy for ovarian cancer prediction. Gynecol Oncol 2001;82:40–8.
50 Kurjak A, Kupesic S, Sparac V, Kosuta D. Three-dimensional ultrasonographic and power Doppler characterization of ovarian lesions. Ultrasound Obstet Gynecol 2000;16:365–71.
51 Kurjak A, Kupesic S, Sparac V, Prka M, Bekavac I. The detection of stage I ovarian cancer by three-dimensional sonography and power Doppler. Gynecol Oncol 2003; 90:258–64.
52 Weinraub Z, Herman A. Three-dimensional hysterosonography. In: Merz E, editor. 3-D ultrasound in obstetrics and gynecology. Philadelphia: Lippincott Williams & Wilkins, 1998: 57–64.
53 Sankpal R, Confino E, Matzel A, Cohen L. Investigation of the uterine cavity and fallopian tubes using three-dimensional saline sonohysterosalpingography. Int J Gynecol Obstet 2001; 73:125–9.
54 Dietz H, Steensma A, Hastings R. Three-dimensional ultrasound imaging of the pelvic floor: the effect of parturition an paravaginal support structures. Ultrasound Obstet Gynecol 2003;21:589–95.
55 Dietz HP. Ultrasound imaging of the pelvic floor. Part II: three-dimensional or volume imaging. Ultrasound Obstet Gynecol 2004;23:615–25.
56 Dietz HP, Steensma AB. Posterior compartment prolapse on two-dimensional and three-dimensional pelvic floor ultrasound: the distinction between true rectocele, perineal hypermobility and enterocele. Ultrasound Obstet Gynecol 2005;26:73–7.
57 Wisser J, Schar G, Kurmanavicius J, Huch R, Huch A. Use of 3D ultrasound as a new approach to assess obstetrical trauma to the pelvic floor. Ultraschall Med 1999;20: 15–8.
58 Robinson D, Toozs-Hobson P, Cardozo L, Digesu A. Correlating structure and function: three-dimensional ultrasound of the urethral sphincter. Ultrasound Obstet Gynecol 2004;23: 272–6.
59 Defreitas GA, Wilson TS, Zimmern PE, Forte TB. Three-dimensional ultrasonography: an objective outcome tool to assess collagen distribution in women with stress urinary incontinence. Urology 2003;62:232–6.
60 West RL, Dwarkasing S, Briel JW, Hansen BE, Hussain SM, Schouten WR, et al. Can three-dimensional endoanal ultrasonography detect external anal sphincter atrophy? A comparison with endoanal magnetic resonance imaging. Int J Colorectal Dis 2005; 20: 328–33.

1a

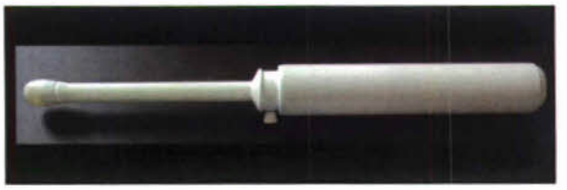

1b

1c

Fig. 40.1 3D endocavitary probes.
a The first 3D endocavitary probe with lateral volume acquisition (used mainly for endorectal scanning).
b 3D vaginal probe with frontal volume acquisition.
c 3D vaginal probe with a fan-shaped frontal beam.

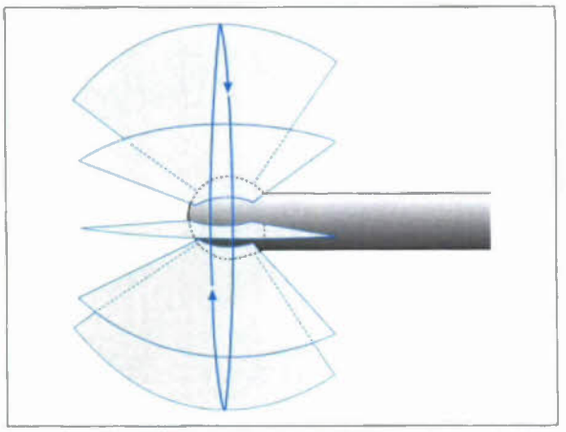

2

Fig. 40.2 Schematic representation of a side-firing endocavitary probe. Volume data are acquired by rotating the lateral B-mode plane around the probe axis.

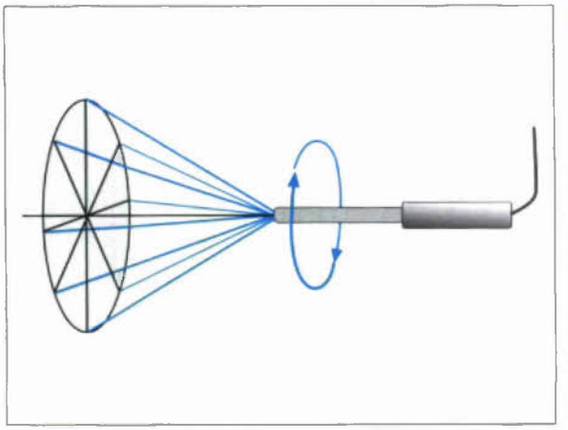

3

Fig. 40.3 Schematic representation of an end-firing transvaginal 3D probe. Volume data are acquired by rotating the B-mode plane through a 180° angle.

4

Fig. 40.4 The scanning principle of the transvaginal 3D/4D probe. With an end-firing probe, a motor sweeps the 2D plane from point 0 to point 1 and then back to point 2.

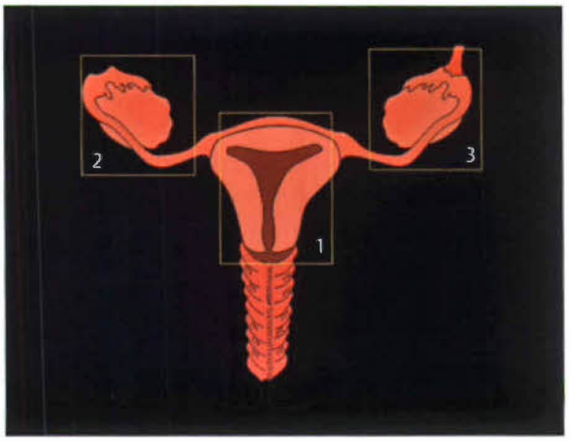

5

Fig. 40.5 Volume acquisition. Three volumes can cover the entire true pelvis.
Volume 1: uterus;
volume 2: right ovary;
volume 3: left ovary.

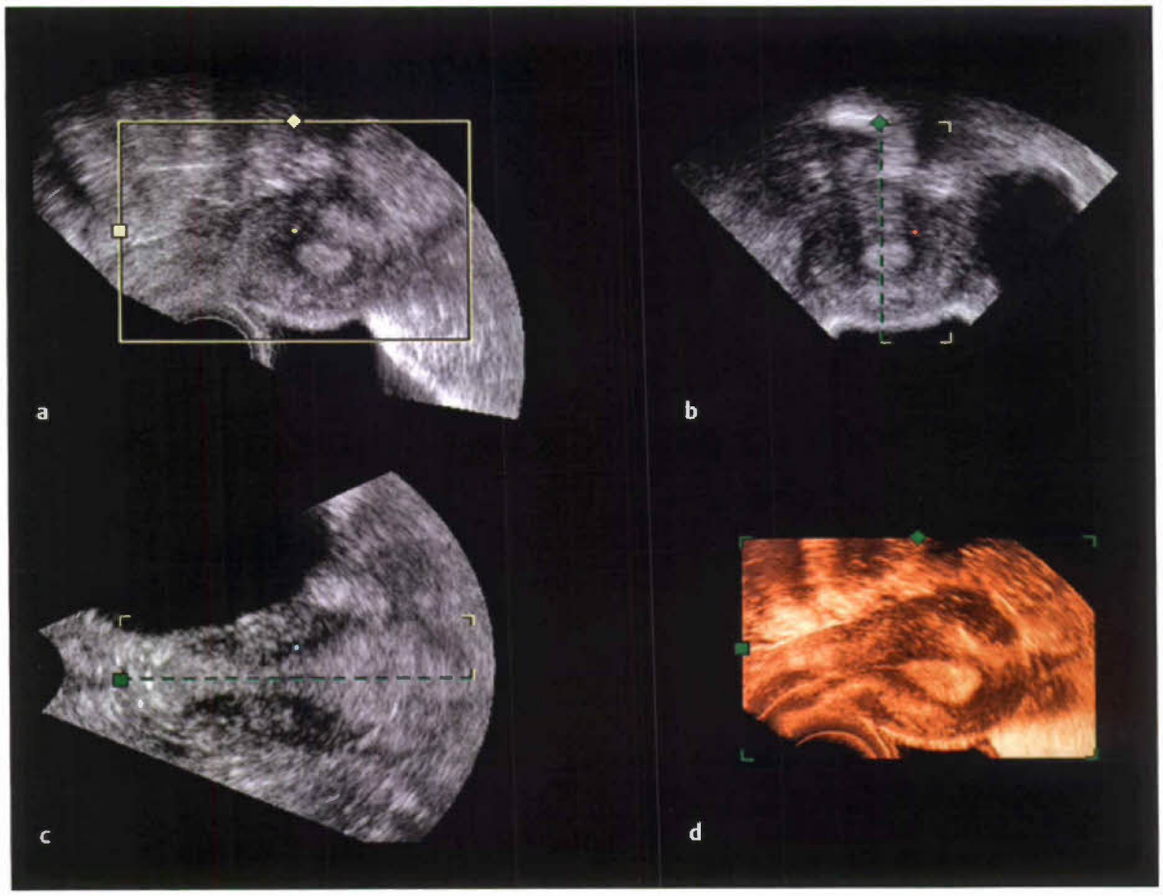

6

Fig. 40.6 The endometrium, displayed in the three orthogonal planes of section and by surface rendering.
a Sagittal section through the uterus.
b Transverse section through the uterus.
c Coronal section through the uterus.
d A surface-rendered image of the endometrium in longitudinal sagittal section.

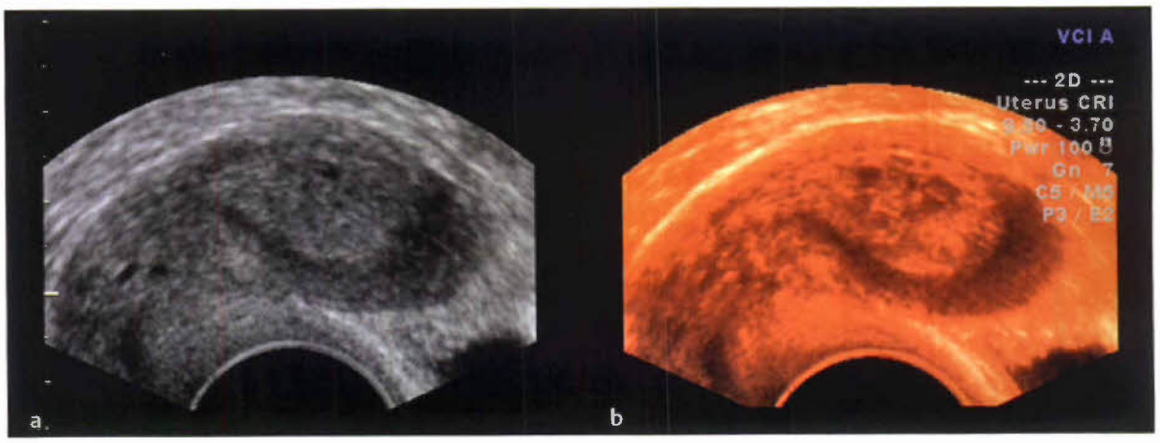

7

Fig. 40.7 VCI-A imaging of an anteflexed uterus with a large endometrial polyp.
a The conventional 2D image.
b The VCI-A image provides significantly better contrast.

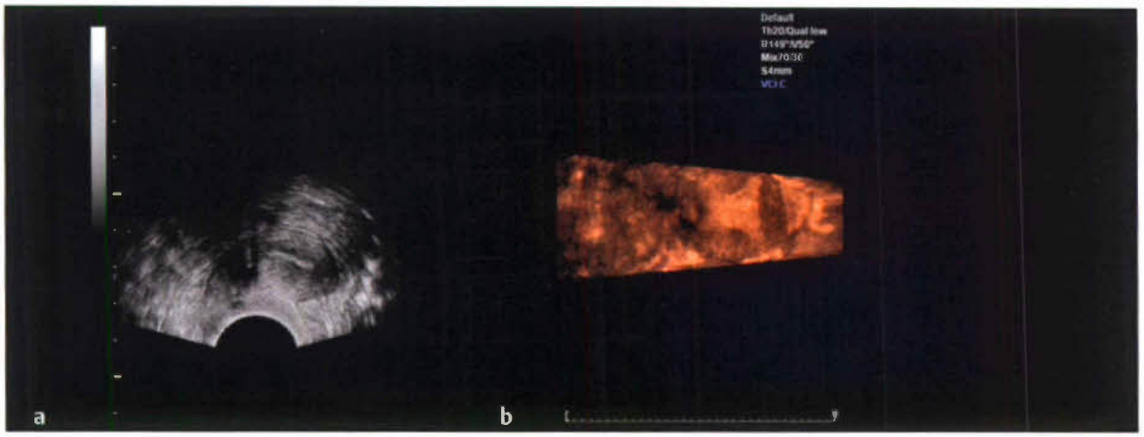

8

Fig. 40.8 VCI-C imaging of the endometrium.
a The 2D image of a normal anteflexed uterus with a flat endometrium.
b When a selected portion of the endometrium is marked with a green line (see Fig. 40.**8a**), a coronal endometrial image immediately appears on the right side of the screen. The coronal section provides a good overview of the cornual region.

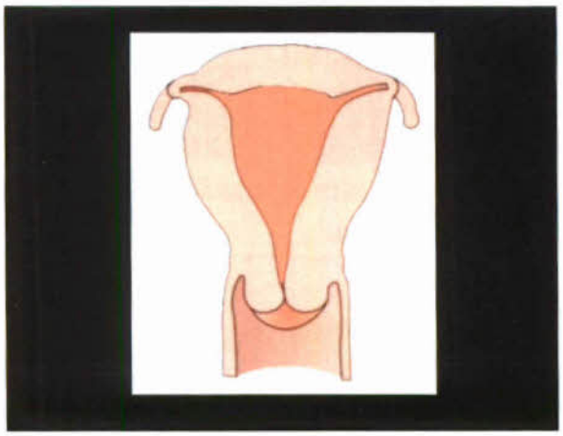

9

Fig. 40.9 Schematic diagram of the endometrium in coronal section.

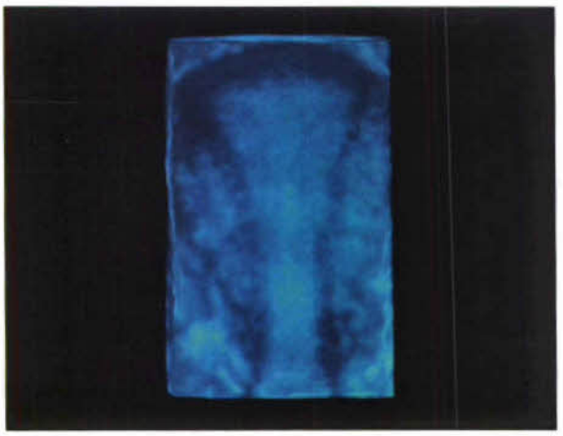

10

Fig. 40.10 Surface-rendered image of the endometrium in an anteflexed uterus.

11

Fig. 40.11 Surface-rendered image of the endometrium in a retroflexed uterus.

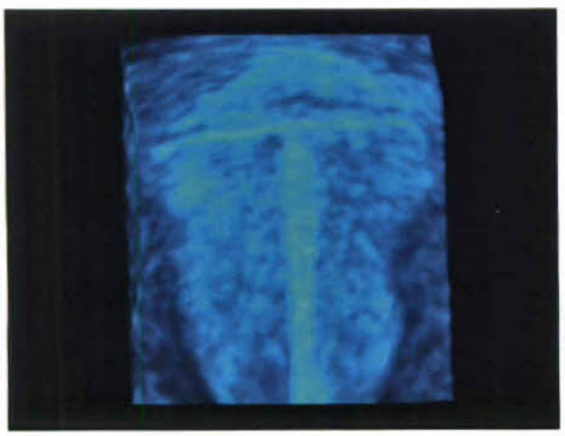

12

Fig. 40.12 Coronal surface-rendered image of a Copper-T intrauterine device (IUD) in a straightened anteflexed uterus

13

Fig. 40.13 A normally positioned Copper-T IUD in an enlarged retroflexed uterus. Surface-rendered view.

Fig. 40.**14** + 40.**15** Incorrect (oblique) position of an intrauterine device. Surface-rendered view.

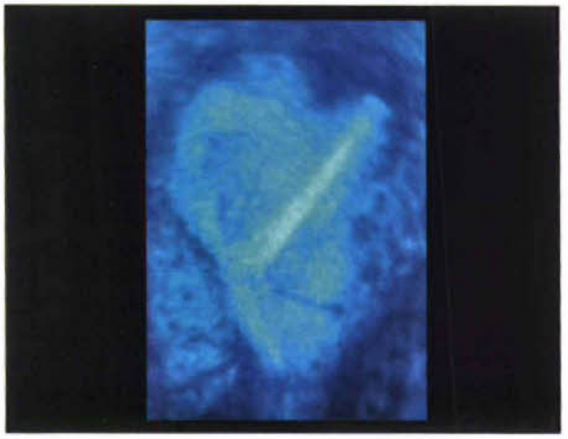

14

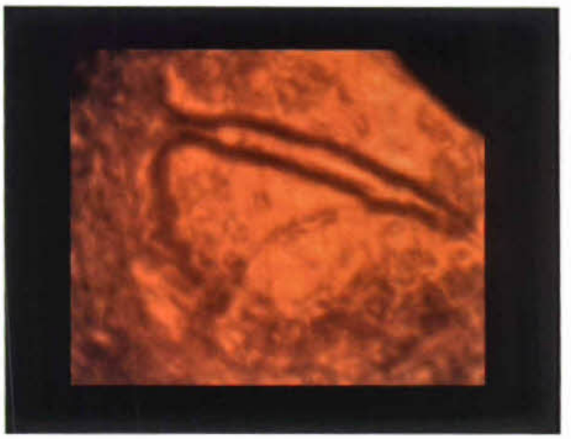

15

Fig. 40.**16**
a The uterus in midsagittal section. An oblong area of ossification in the endometrium mimics an intrauterine device.
b A transparent view of the uterus in coronal section clearly demonstrates the area of ossification.

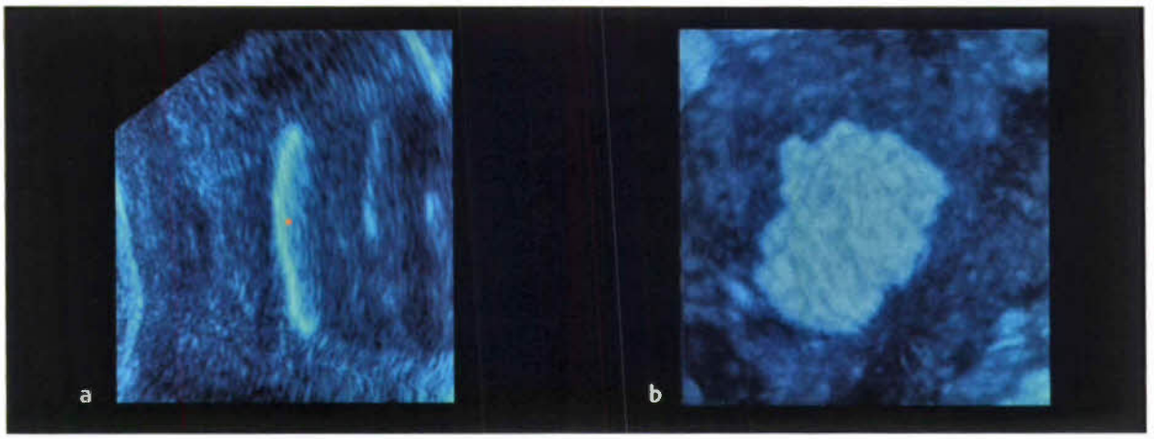

16

Fig. 40.**17** Surface-rendered imaging of the endometrium in coronal section. Normal endometrium with a convex fundus.

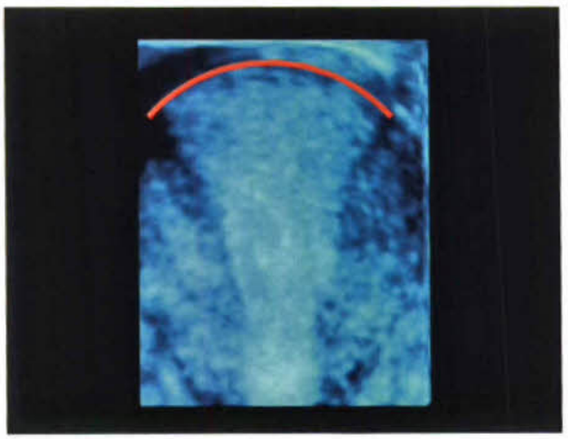

17

Fig. 40.**18** Surface-rendered imaging of the endometrium in coronal section. Arcuate uterus with a concave fundus.

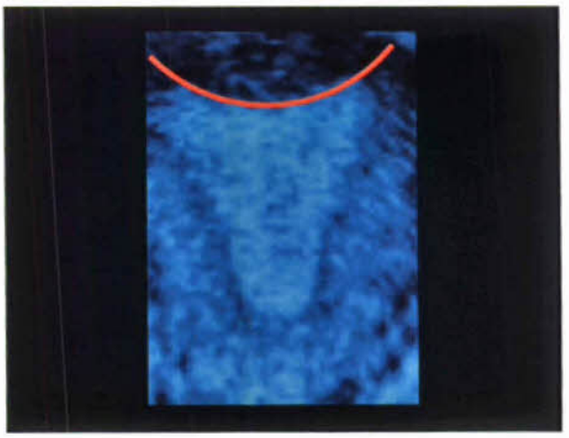

18

Fig. 40.**19** + 40.**20** Subseptate uterus.

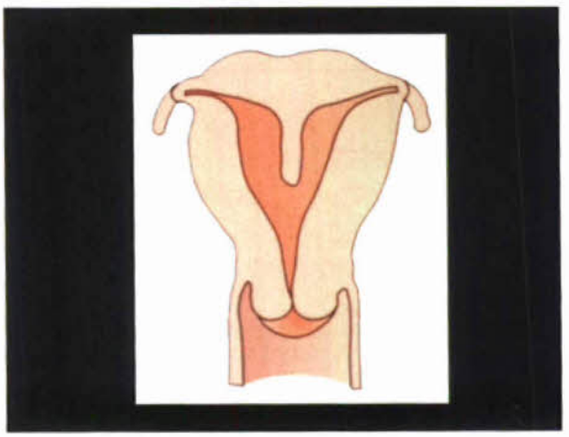

19

20

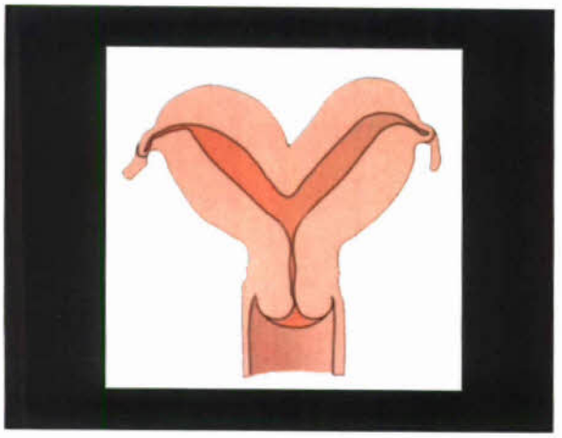

21

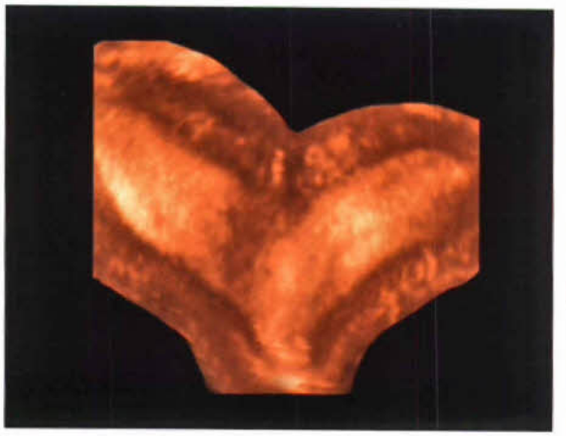

22

Fig. 40.**21** + 40.**22** Uterus bicornis unicollis.

23

Fig. 40.**23** This coronal surface-rendered image of the uterus demonstrates a fluid collection in the uterine cavity.

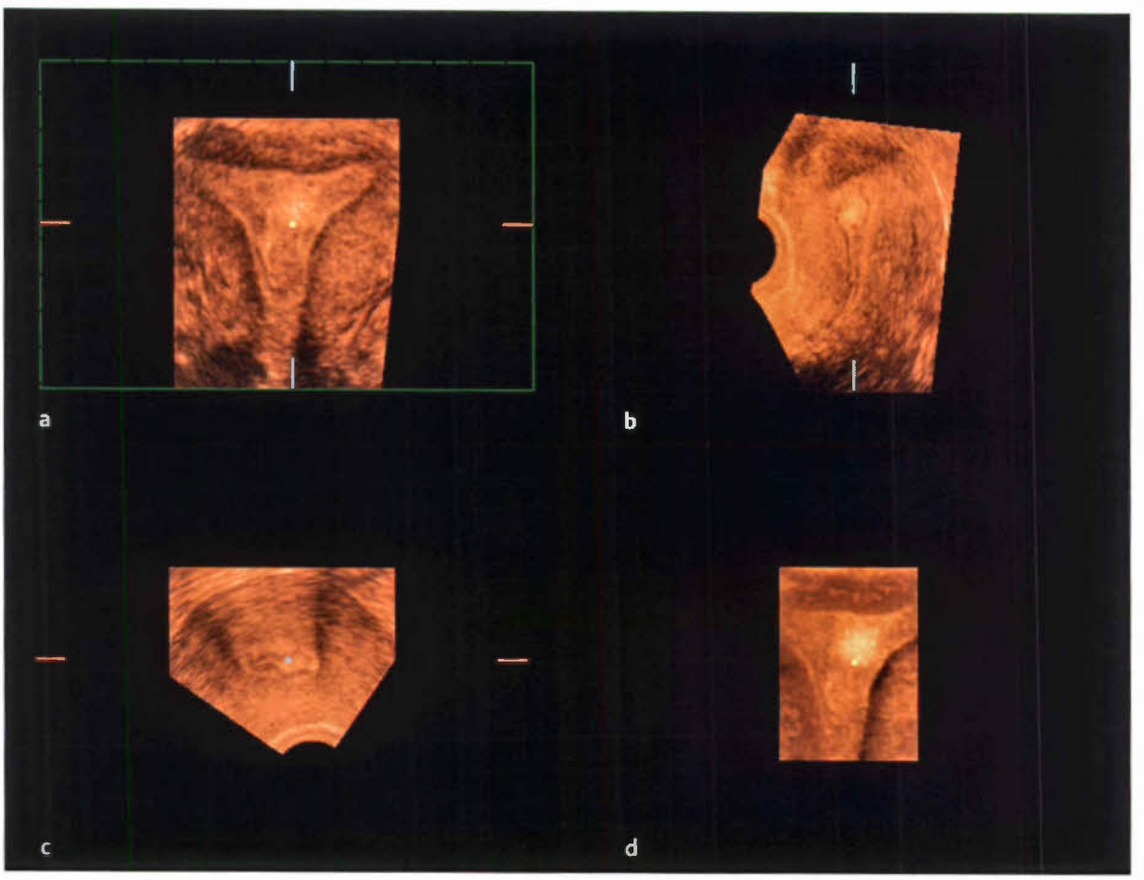

24c

24d

Fig. 40.**24** Multiplanar display and surface-rendered imaging of an endometrial polyp.
- **a** Coronal section.
- **b** Sagittal section.
- **c** Transverse section through the uterus.
- **d** Surface-rendered image of the hyperechoic polyp within the endometrium (longitudinal coronal section).

25

Fig. 40.**25** Surface-rendered image of a hypoechoic submucous myoma (25 × 20 × 23 mm).

26

Fig. 40.**26** Surface-rendered image of the endometrium in coronal section. An intramural myoma (23 × 20 × 20 mm) is visible on the left side.

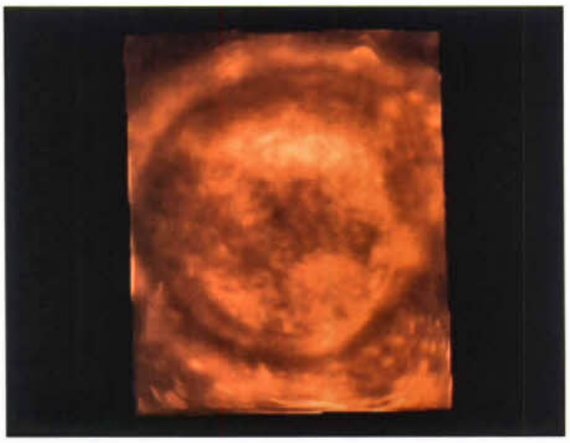

27

Fig. 40.**27** Coronal surface-rendered image of a large submucous myoma (54 × 58 × 55 mm).

28

Fig. 40.**28** Coronal surface-rendered image of a thickened macrocystic and microcystic endometrium in a patient receiving tamoxifen therapy.

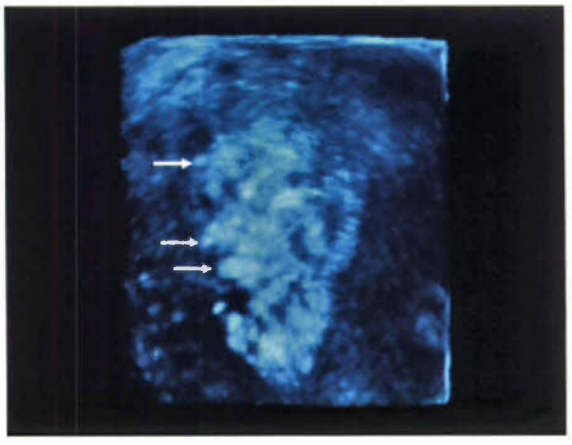

29

Fig. 40.**29** Coronal section of a uterus with an abnormal endometrial structure and irregular endometrial boundaries with myometrial infiltration (arrows).

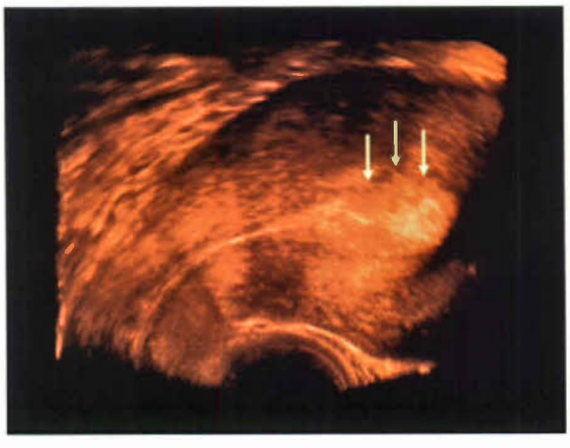

30

Fig. 40.**30** Lateral surface rendering of early endometrial carcinoma with incipient myometrial infiltration in the posterior wall of the uterine corpus (arrows).

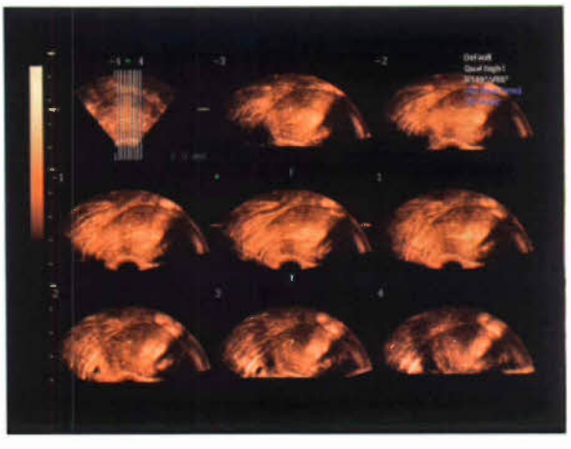

31

Fig. 40.**31** Tomographic ultrasound imaging survey of the early endometrial carcinoma in Fig. 40.**30**.

32

33

Fig. 40.**32** Glass-body rendering (combined transparent and color Doppler display) of an endometrial carcinoma shows conspicuous neovascularization, predominantly on the right side of the uterine corpus.

Fig. 40.**33** Glass-body rendering (combined transparent and power Doppler display) of an extensive endometrial carcinoma shows marked neovascularization throughout the uterine corpus (truncated just above the cervix). The tumor vessels show areas of stenosis and dilation.

34

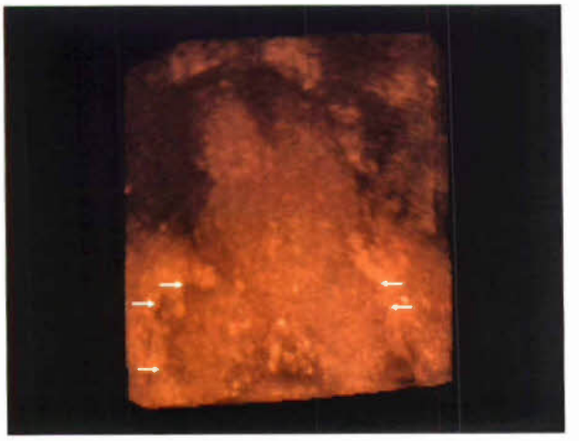

35

Fig. 40.**34** Surface rendering of a longitudinal section of the uterus, showing a cystic area in the cervical region.

Fig. 40.**35** This surface rendering of a coronal uterine section shows a barrel-shaped distension of the cervix by cervical carcinoma with incipient bilateral parametrial invasion (arrows).

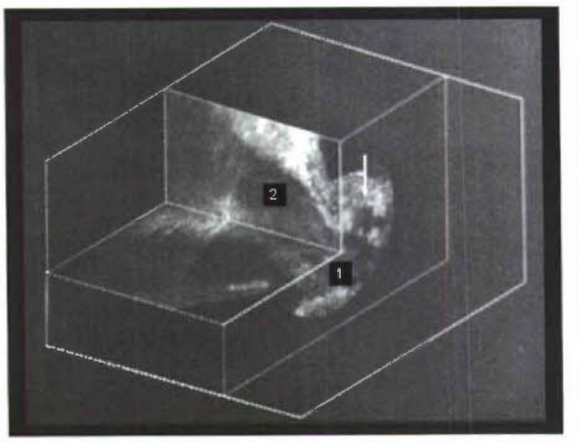

36

Fig. 40.**36** Three-dimensional niche display of cervical carcinoma with involvement of the left parametrium (arrow). The right anterior quadrant of the uterus has been removed.
1 Cervix
2 Uterine corpus

37

38

Fig. 40.**37** Surface-rendered image of a large cervical carcinoma in the gray-scale mode.

Fig. 40.**38** Glass-body rendering (combined transparent and power Doppler display) of the same tumor shows conspicuous neovascularization throughout the cervix.

Fig. 40.**39**
a–c Multiplanar display of a normal ovary.
d A surface-rendered image of the sectioned ovary.

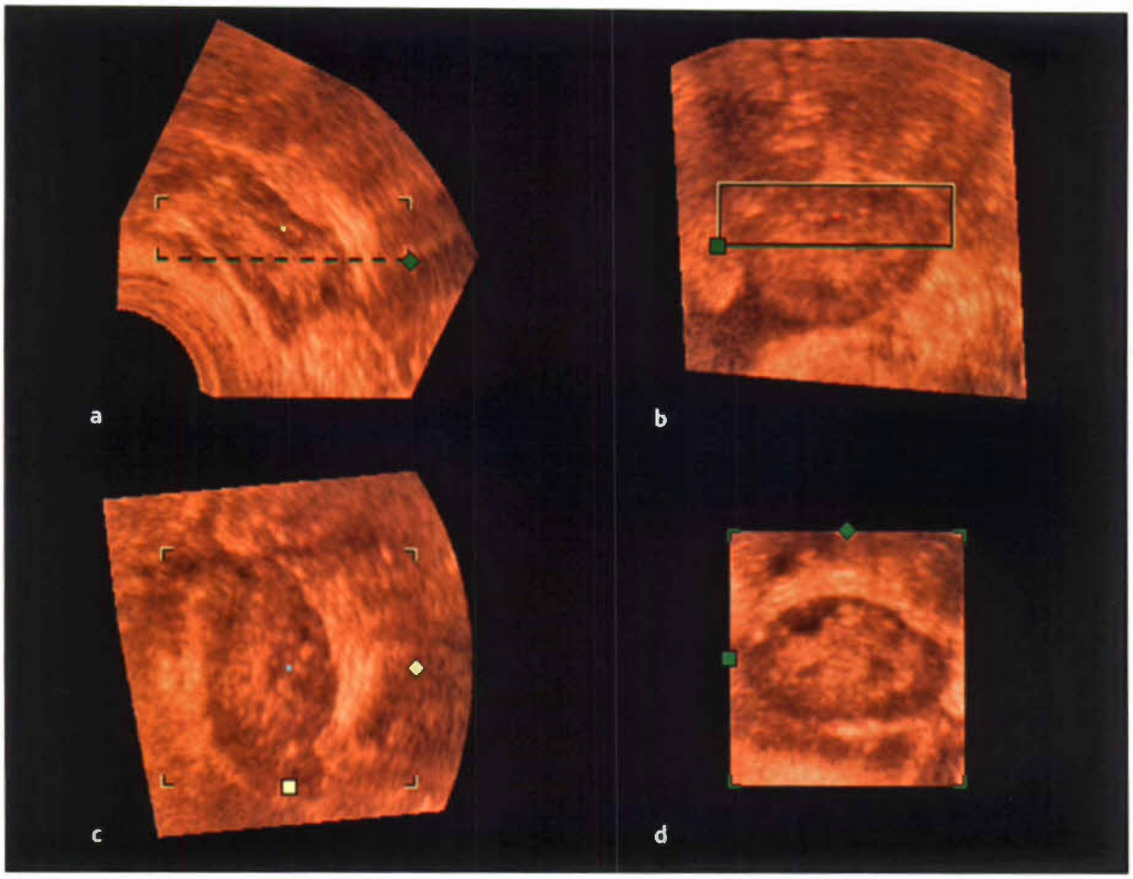

39

Fig. 40.**40** Glass-body display of a normal ovary with normal blood flow.

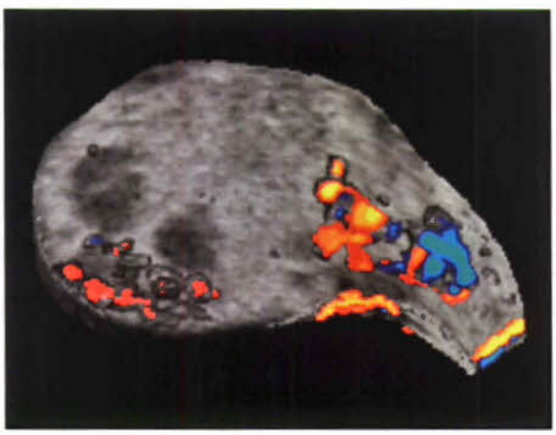

40

Fig. 40.**41** Surface-rendered image of an ovary with a mature follicle.
a Oblique view.
b Viewed from above.

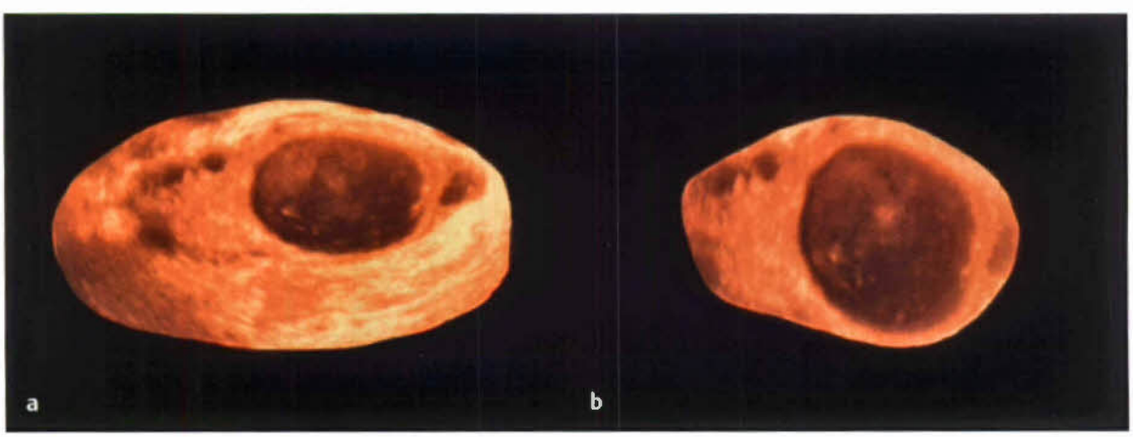

41

42

43

Fig. 40.**42** A stimulated ovary following human menopausal gonadotropin therapy (surface-rendered image).

Fig. 40.**43** Surface-rendered image of a hyperstimulated ovary, with large lutein cysts.

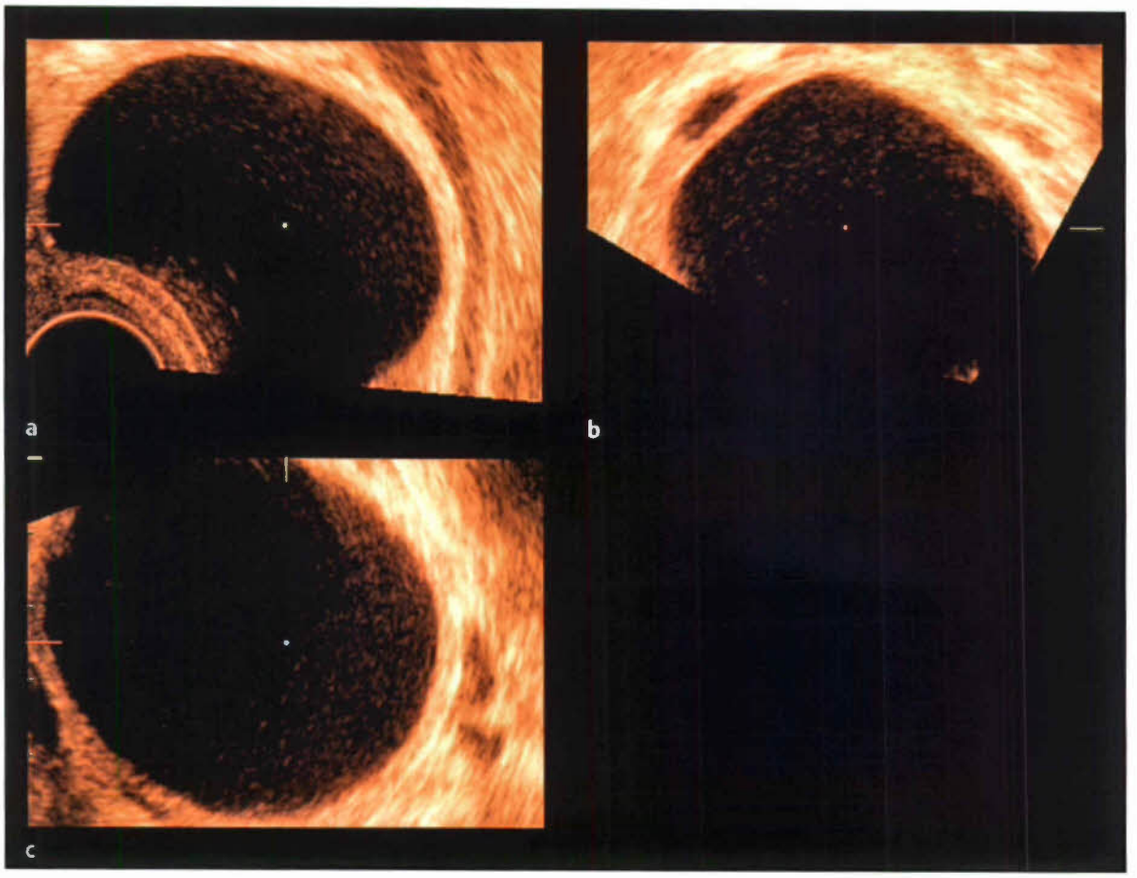

44

Fig. 40.**44** Multiplanar display of a smooth-walled cystic mass.

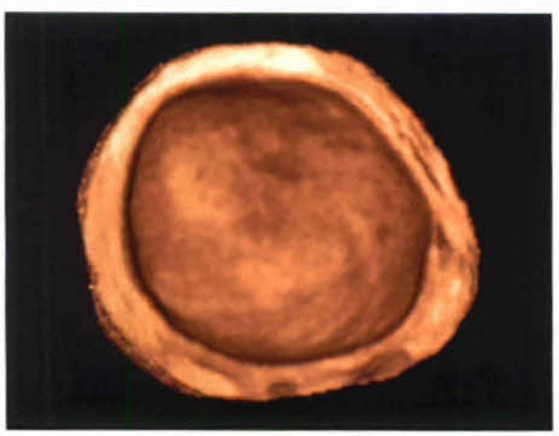

45

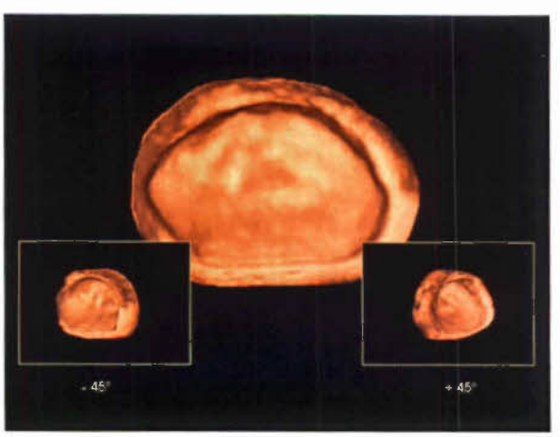

46

Fig. 40.**45** The same lesion as in Fig. 40.**44**. The surface-rendered image clearly demonstrates the smooth margins of the cyst wall.

Fig. 40.**46** Setup for generating a cine sequence. The operator defines the starting point (−45°) and end point (+45°) of the rotating sequence and the angle between the cine images.

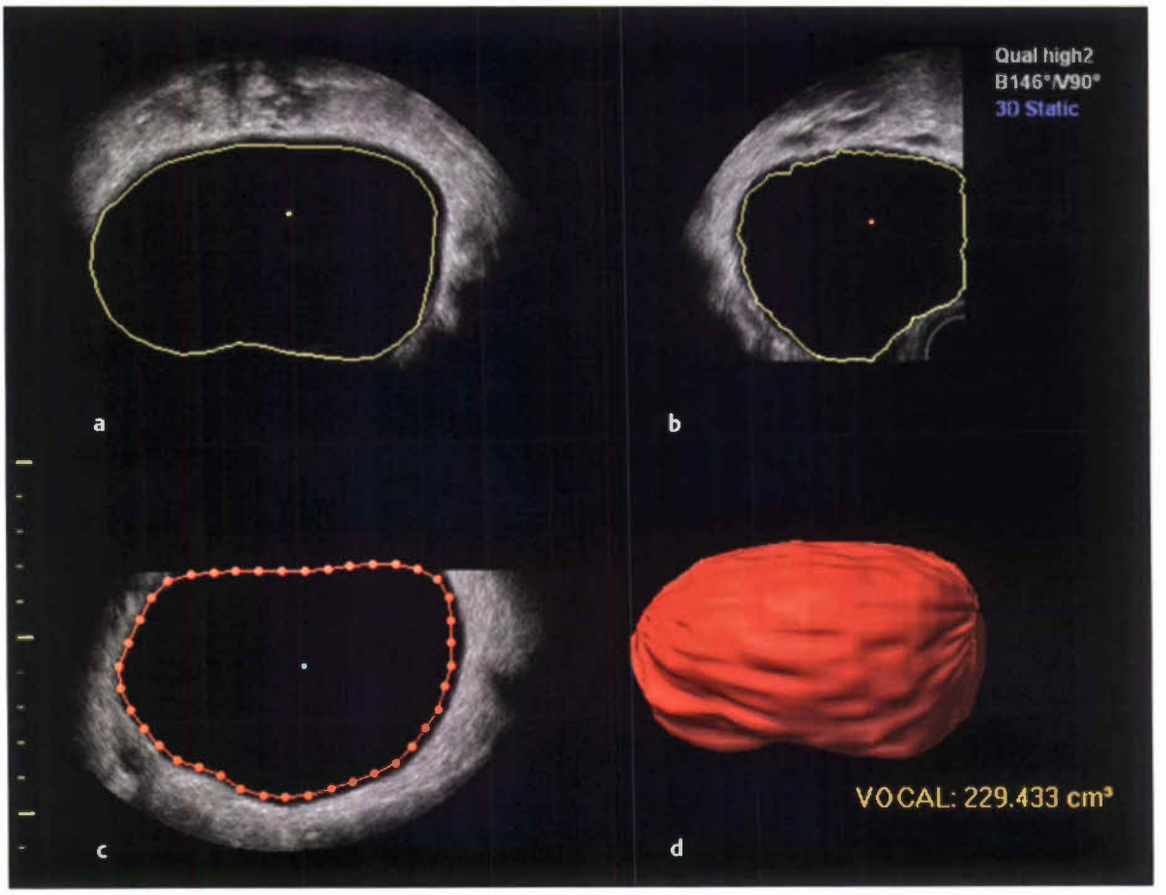

47

Fig. 40.**47** Determining tumor volume with the VOCAL program. The tumor volume is displayed as a three-dimensional color figure.

48

Fig. 40.**48** Surface-rendered image of a loculated cystic mass with a smooth inner wall.

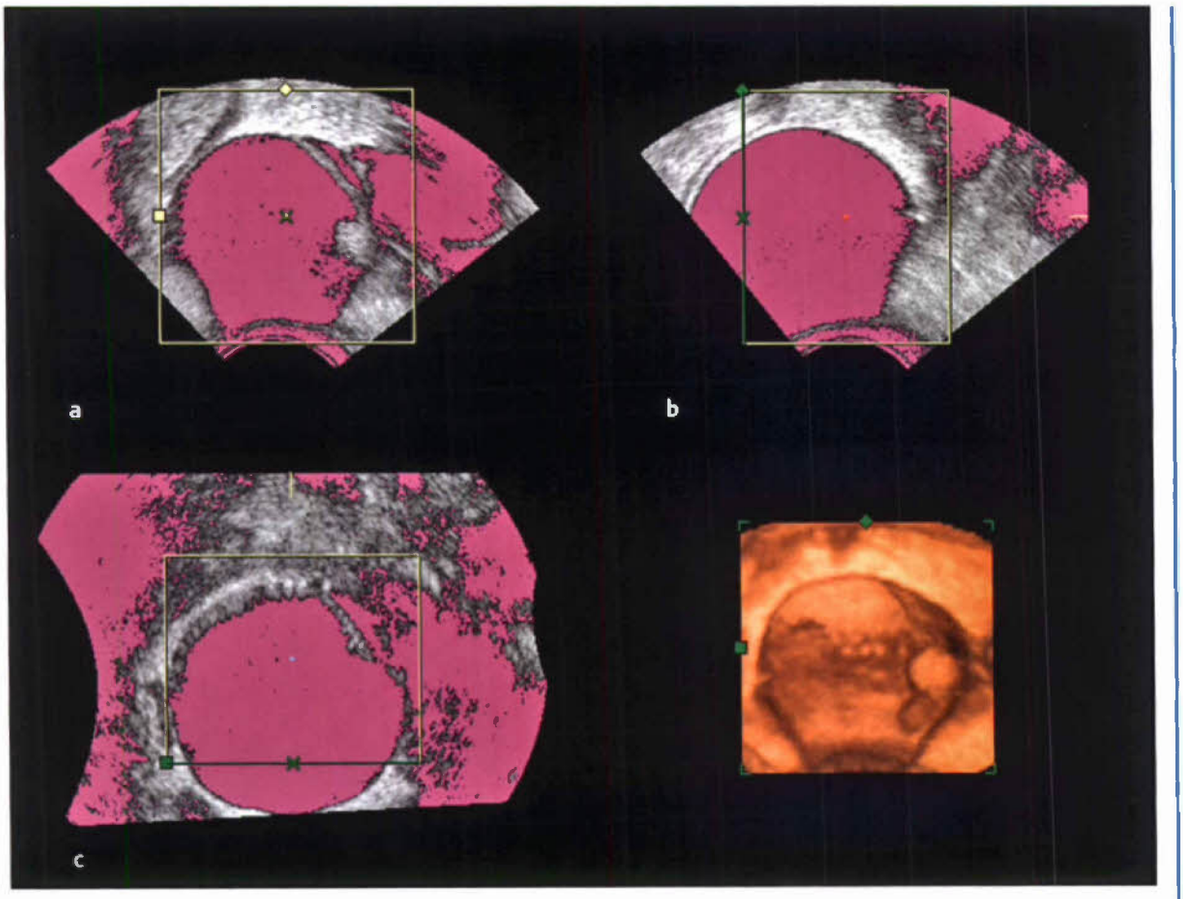

49

Fig. 40.**49a–c** A proliferative focus on the inner wall of a cystic ovarian mass. The purple zones within the cyst are areas in which the threshold control was used to filter out fine extraneous echoes.
Lower right: Surface-rendered image of the proliferative focus.

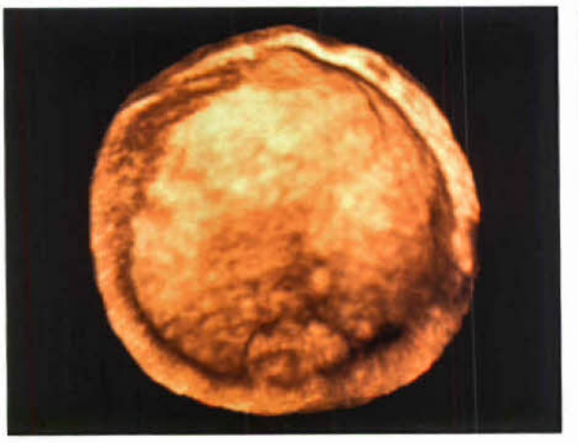

50

Fig. 40.**50** A sectional surface-rendered image of a cystic borderline tumor with a proliferative focus on the inner wall of the cyst floor.

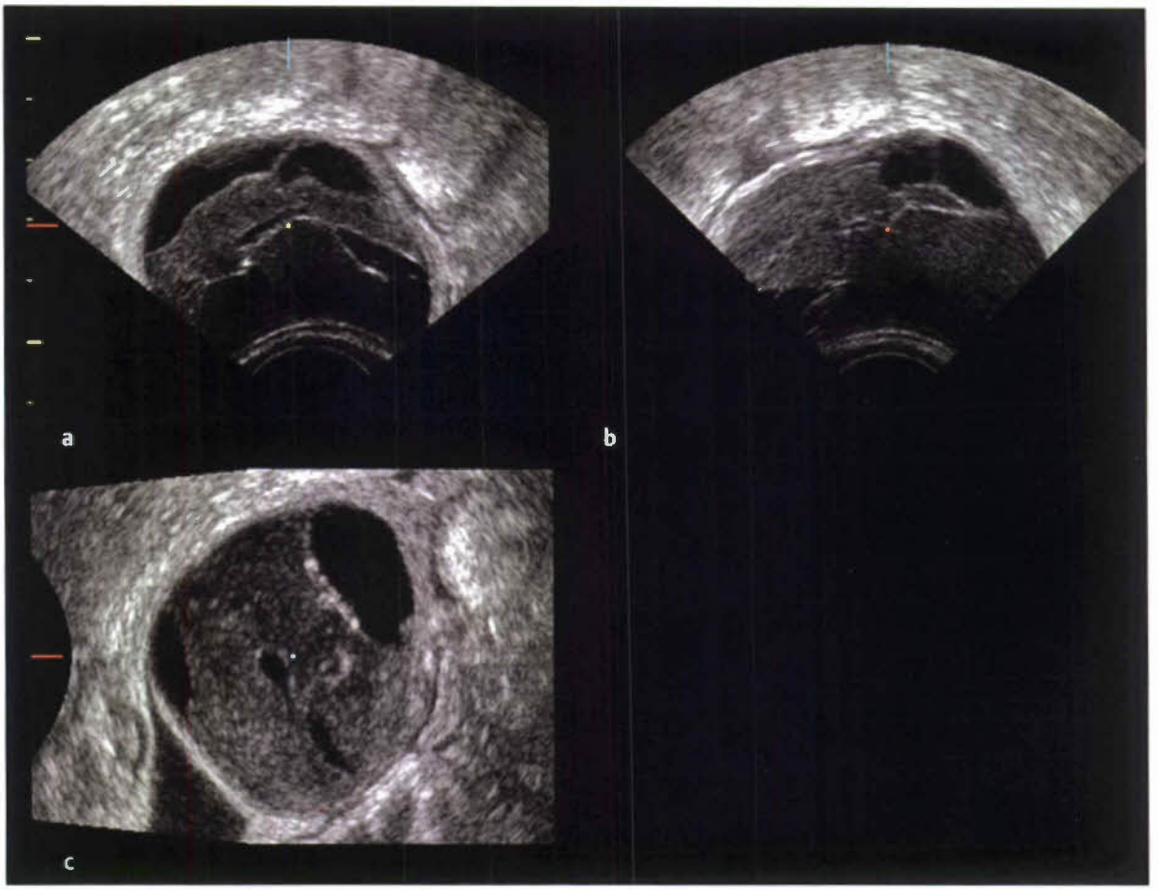

51

Fig. 40.**51** A multiplanar display of a mixed cystic-appearing and solid-appearing mass with smooth margins: a corpus luteum cyst with intracystic hemorrhage. Typically, color Doppler will not show color-flow signals within the hematoma.

52

Fig. 40.**52** A surface-rendered image of a cystic ovarian mass, with fine, high-level internal echoes and a thick wall: an endometriotic cyst.

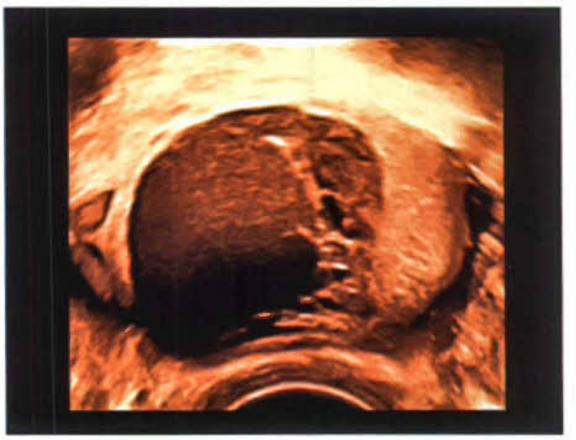

53

Fig. 40.**53** A surface-rendered image of a mixed cystic and solid ovarian mass with hyperechoic components. Histology: dermoid cyst.

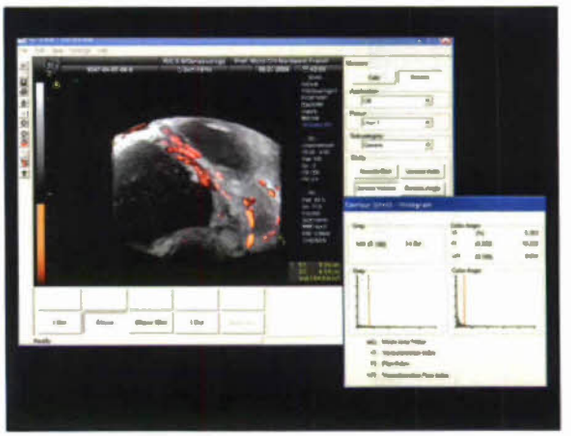

54

Fig. 40.**54** 3D display of a loculated cystic ovarian mass. The histograms show the distribution of gray-scale and color components in the power Doppler mode.

55

Fig. 40.**55** A surface-rendered image of an ovarian carcinoma, which has a cauliflower-like surface structure.

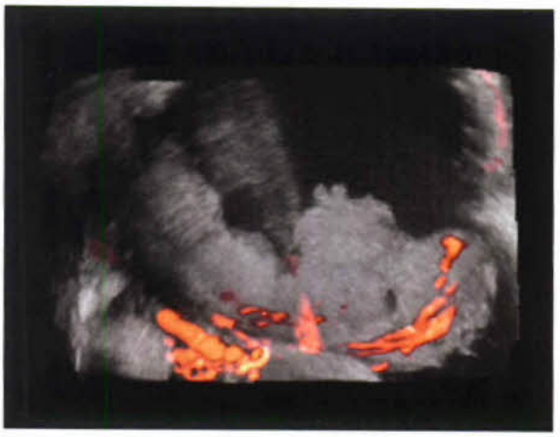

56

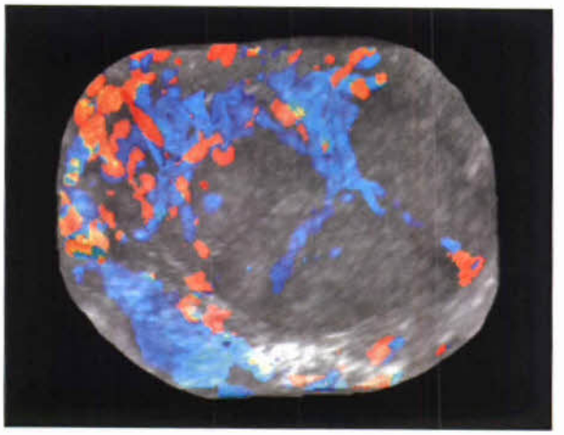

57

Fig. 40.**56** Glass-body rendering of ovarian carcinoma shows an irregular proliferative lesion on the tumor wall and provides a three-dimensional display of the blood vessels at the tumor base (power Doppler mode).

Fig. 40.**57** Glass-body rendering of ovarian carcinoma shows an abnormal three-dimensional vascular pattern marked by dilated, stenotic, and irregular vascular channels.

58

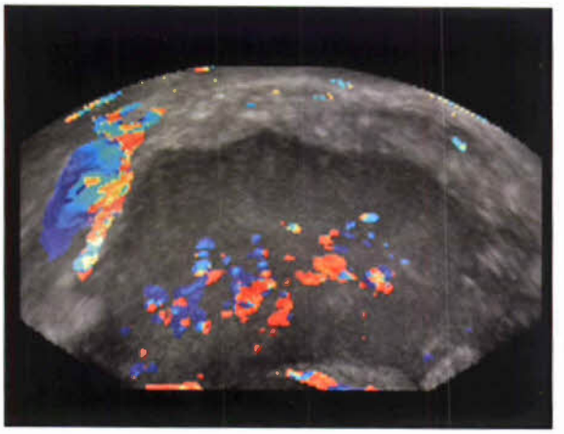

59

Fig. 40.**58** A solid ovarian tumor (metastatic breast carcinoma). The sectional surface-rendered image clearly demonstrates the irregular tissue structure of the tumor.

Fig. 40.**59** Glass-body rendering shows conspicuous neovascularization in a solid ovarian tumor.

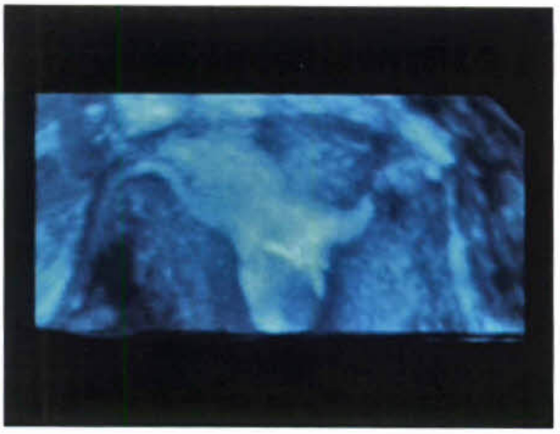

60

61

Fig. 40.**60** Three-dimensional transparent display of tubal patency using hysterosalpingo-contrast sonography.

Fig. 40.**61** Surface-rendered image of hydrosalpinx. The three-dimensional display clearly distinguishes this lesion from an ovarian cyst.

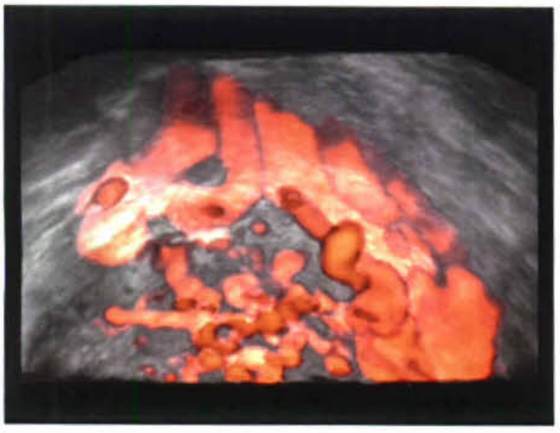

62

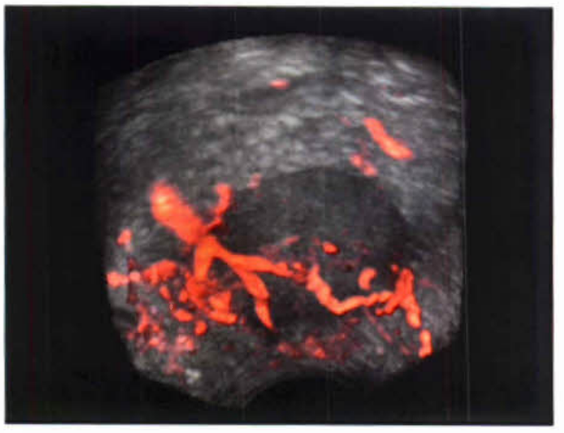

63

Fig. 40.**62** Adnexal varicosity demonstrated by glass-body rendering with power Doppler.

Fig. 40.**63** Glass-body rendering of a central recurrence of cervical carcinoma. The three-dimensional color display clearly demonstrates the tumor-feeding vessels, which are entering the upper right and lower left aspects of the tumor.

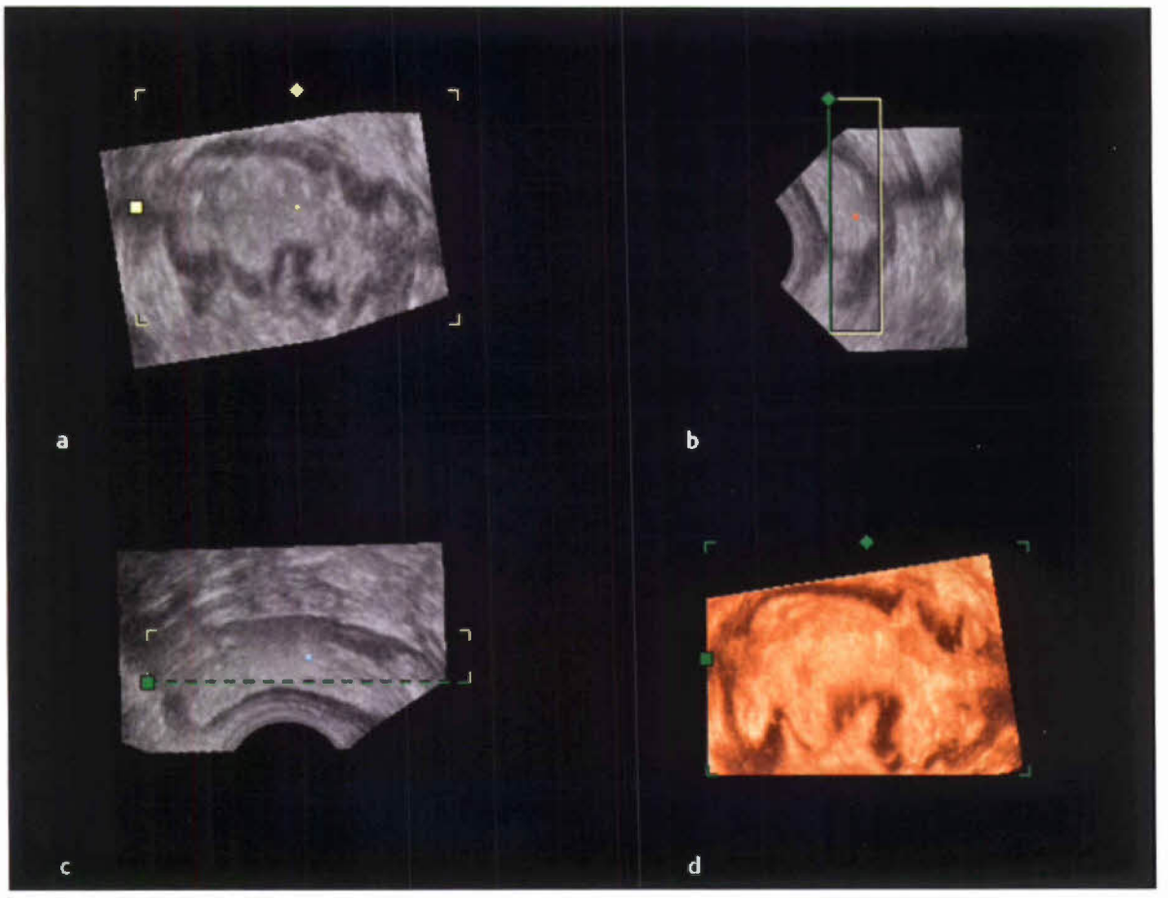

64

Fig. 40.**64** Multiplanar and surface-rendered views of sigmoid diverticulosis (lower tight).

65

Fig. 40.**65** An abdominal 3D surface-rendered image of floating bowel loops in ascites.

66

Fig. 40.**66** A three-dimensional surface-rendered image of the pelvic floor, viewed from below.
1 Urethra
2 Vagina
3 Rectum

Transrectal Ultrasound

41 Transrectal Ultrasound: Technique and Applications

Although transrectal ultrasound has limited applications in gynecology, there are cases in which it can provide a helpful adjunct or alternative to transvaginal or conventional transabdominal ultrasound scanning of the lower abdomen.

As in all sonographic techniques, it is important in transrectal ultrasound to take into account palpable findings and laboratory data to ensure that an abnormal finding is interpreted correctly.

Development of Transrectal Ultrasound

Among the pioneers of transrectal ultrasound are Wild and Reid [1], who published initial diagnostic results as early as 1956, and Watanabe et al. [2], who used the method in the 1970s for imaging the prostate. The real breakthrough came in the 1980s following the development of hand-held real-time ultrasound probes. These probes were most commonly used in surgery and urology. Today, rectal probes are used surgically in the evaluation of rectal tumors [3–13], recurrent tumors [14,15], and perirectal disease [16], and they are used in urology mainly for imaging the prostate and seminal vesicles [17,18].

As transrectal ultrasound can demonstrate not only the bowel wall and pararectal tissue, but also the vagina, paravaginal tissue, uterus, and pelvic walls (provided the transducer frequency is not too high), this technique has also found limited applications in gynecologic diagnosis [19–22].

Probes

Most endorectal ultrasound probes are side-scanning transducers that rotate through an arc of up to 360°. While earlier rectal probes required a fluid standoff in the form of a water-filled balloon catheter (Fig. 41.**1a**), this is unnecessary with more modern probes (Fig. 41.**1b**). One problem with the water balloon method was that small air bubbles often entered the balloon when it was filled, significantly degrading the ultrasound image. The only way to eliminate the air bubbles was by repeatedly emptying and refilling the balloon.

Side-scanning rectal probes provide transverse sectional images of the true pelvis. Some probes can also provide longitudinal scans of the true pelvis (90° sector angle) by deflecting their scan plane forward. The probes operate at a frequency of 5–10 MHz and have both near-field and far-field focusing. High-frequency probes that transmit at 10 MHz are most useful for evaluating the rectal wall, while probes in the 5–7 MHz range are better for evaluating the cervix, parametria, and pelvic walls, owing to their greater penetration depth.

Preparation

Most patients do not require special preparation. A Fleet enema can be given if the rectum is distended with stool, particularly if the rectal mucosa is to be evaluated. If there is insufficient clearance between the probe and rectal wall, it can be increased by using a water balloon filled to approximately 30 mL.

Table 41.**1** Standard image orientation in transrectal ultrasound

Top of image	Posterior
Bottom of image	Anterior
Right side of image	Left side of patient
Left side of image	Right side of patient

In principle, there is no absolute need for rectal palpation before transrectal ultrasound. Rectal palpation is indicated, however, whenever there is suspicion of tumor invading the rectal wall. It allows the examiner to assess the consistency of suspicious areas and also detect any narrowing of the rectal lumen. If luminal narrowing is present, the examiner has to be particularly careful when manipulating the endorectal probe.

The patient can be placed in the supine or left lateral decubitus position. With a supine patient, the buttocks should be elevated on a cushion to facilitate downward angulation of the probe handle.

As in transvaginal ultrasound, the probe is sheathed in a condom that has been filled at the tip with ultrasound coupling gel. Lubricating gel is smeared over the front end of the condom, and the probe is carefully inserted into the rectum and advanced by several centimeters (Figs. 41.**2**, 41.**3**). The insertion can be aided by having the patient bear down as if passing stool. The probe should be advanced gently, not forcibly, to reduce the risk of injury. Generally, the lower 15 cm of the rectum can be evaluated with this technique.

A small amount of urine in the bladder is helpful but not essential for establishing orientation in the true pelvis.

When a rotary transducer is used, the image produced by transrectal ultrasound has the same left–right and anteroposterior orientation as a transverse scan in abdominal ultrasound: anterior is at the top of the image, posterior is at the bottom, the right side of the image corresponds to the patient's left side, and the left side of the image corresponds to the patient's right side (Fig. 41.**4**, Table 41.**1**).

Normal Anatomy

When the tip of the probe has passed through the anal ring, the anatomical layers of the bowel wall can be seen encircling the probe, which appears as an echo-free round area (Fig. 41.**5**). The mucosa and the muscularis propria appear as hypoechoic rings that are less echogenic than the submucosa and serosa [5].

Just anterior to the bowel is the vagina, which appears as a slightly curved, transverse oval structure (Fig. 41.**6**). The urethra is displayed in cross-section anterior to the vagina. Its muscular coat appears as a hypoechoic outer layer, its mucosa as an echogenic inner layer. The central urethral canal is hypoechoic (Fig. 41.**6**). As the probe is advanced farther into the rectum, it displays a transverse scan through the cervix and lateral parametria (Fig. 41.**7**). When the probe is advanced further, the uterine corpus is defined in cross section if it occupies a straight or retroflexed position. With an anteflexed uterus, the corpus is usually too far away from the transducer to be seen with transrectal ultrasound. The same applies to the ovaries, which can be imaged clearly only if they are located in the cul-de-sac. If they occupy a relatively anterior position, they cannot be imaged by transrectal scanning.

Table 41.2 Applications of transrectal ultrasound

- Palpable abnormality in the rectal examination
- Investigation of a rectal tumor (polyp, carcinoma)
- Suspected recurrence of a rectal tumor
- Pelvic evaluation in Mayer–Rokitansky–Küster syndrome
- Hematocolpos secondary to hymenal atresia
- Pelvic evaluation following colpectomy
- Pelvic evaluation in patients with atrophic or post-radiotherapy vaginal stenosis
- Evaluation of parametrial infiltration in patients with cervical carcinoma
- Investigation of retroperitoneal masses or ovarian masses located in the cul-de-sac or sacral hollow
- Detecting recurrences of gynecologic tumors

Applications in Gynecology

Transrectal ultrasound has found a variety of applications in recent years (Table 41.2). Its main surgical indication is in the investigation of rectal tumors [3–5,7,8], particularly tumors that have not yet penetrated the rectal mucosa and therefore cannot be evaluated by proctoscopy.

There are various gynecologic indications for transrectal ultrasound (Table 41.2). It can be used in very young patients to detect *hematocolpos* secondary to hymenal atresia (Figs. 41.**8**, 41.**9**). Its principal use in older women is for the diagnosis of *pelvic tumors*, especially cervical carcinoma. Besides defining the extent of cervical involvement, transrectal ultrasound can also detect *parametrial infiltration* [19,21]. It is easiest to make this assessment by imaging and comparing both sides. Although gross parametrial infiltration can be clearly recognized in most cases by noting an irregular, hypoechoic structure extending toward the pelvic wall (Figs. 41.**10**, 41.**11**), even transrectal ultrasound cannot detect microscopic tumor spread in the lymphatics. Nor has it been possible to distinguish confidently between inflammatory and neoplastic infiltration of the parametria [19].

On the other hand, it is an easy matter to detect the extension of larger tumor masses from the cervix toward the vagina (Fig. 41.**12**) or rectum (Fig. 41.**13**). The same applies to tumor-involved pararectal lymph nodes, which are conspicuous by their size and their nonhomogeneous echo pattern (Fig. 41.**14**).

Transrectal ultrasound can also be used to define the extent of endometrial carcinoma (Figs. 41.**15**, 41.**16**) in cases in which postmenopausal atrophy or radiotherapy has caused the vagina to become so narrow that it can no longer accommodate an endovaginal probe. Transrectal scans are of limited value in patients with a strongly anteflexed uterus, however.

Transrectal ultrasound can also be useful in the investigation of retroperitoneal masses, the detection of recurrent pelvic wall neoplasms [20], and the investigation of ovarian masses located in the cul-de-sac or sacral hollow (Fig. 41.**17**).

The endorectal probe can also be fitted with a needle guide for the fine-needle aspiration biopsy of recurrent tumors [23].

Obstacles in Transrectal Ultrasound

Large, painful hemorrhoids, a narrow, scarred sphincter, and a tumor causing high-grade rectal stenosis are significant limiting factors that may even preclude transrectal ultrasound in some patients. Caution is advised in all patients who have had previous surgery involving the lower rectum. It should never be necessary to advance the rectal probe forcibly against resistance. Gentle insertion is essential in order to avoid iatrogenic perforation.

References

1 Wild JJ, Reid JM. Diagnostic use of ultrasound. Br J Phys Med 1956;19:248–57.
2 Watanabe H, Igari D, Tanahashi Y, Harada K, Saitoh M. Development and application of new equipment for transrectal ultrasonography. J Clin Ultrasound 1973;2:91–8.
3 Boscaini M, Moscini PL, Montori A. Transrectal ultrasonography: interpretation of normal intestinal wall structure for the preoperative staging of rectal cancer. Scand J Gastroenterol 1986;21:87–98.
4 Dragsted J, Gammelgaard J. Endoluminal ultrasonic scanning in the evaluation of rectal cancer: a preliminary report of 13 cases. Gastroinest Radiol 1983;8:367–9.
5 Feifel G, Hildebrandt U, Dhom G. Die endorectale Sonographie beim Rectumcarcinom. Chirurg 1985;56:398–402.
6 Heintz A, Buess G, Frank K, Kunz C, Strunck H, Junginger T. Endoluminal ultrasonic examination of sessile polyps and early carcinomas of the rectum. Surg Endosc 1989; 3:92–5.
7 Lindmark G, Elvin A, Pahlman L, Glimelius B. The value of endosonography in preoperative staging of rectal cancer. Int J Colorect Dis 1992;7:162–6.
8 Orrom WJ, Wong WD, Rothenberger DA, Jensen LL, Goldberg SM. Endorectal ultrasound in the preoperative staging of rectal tumors. Dis Colon Rectum 1990;33: 654–9.
9 Otto R, Engeler V. Transrektale Sonographie bei Raumforderungen des weiblichen Beckens. In: Otto RC, Jann FX, editors. Ultraschall-Diagnostik 82. Stuttgart: Thieme, 1983: 458–63.
10 Roubein LD, David C, DuBrow R, Faintuch J, Lynch P, Fornage B, et al. Endoscopic ultrasonography in staging rectal cancer. Am J Gastroenterol 1990;85:1391–4.
11 Shimizu S, Tada M, Kawai K. Use of endoscopic ultrasonography for the diagnosis of colorectal tumors. Endoscopy 1990;22:31–4.
12 Wang KY, Kimmey MB, Nyberg DA, Mack LA, Haggitt RC, Shuman WP, et al. Colorectal neoplasms: accuracy of US in demonstrating the depth of invasion. Radiology 1987;165:827– 9.
13 Zainea GG, Lee F, McLeary RD, Siders DB, Thieme ET. Transrectal ultrasonography in the evaluation of rectal and extrarectal disease. Surg Obstet Gynecol 1989;169: 153–6.
14 Beynon J, Mortensen NJ, Foy DM, Channer JL, Rigby H, Virjee J. The detection and evaluation of locally recurrent rectal cancer with rectal endosonography. Dis Colon Rectum 1989;32:509–17.
15 Charnley RM, Heywood MFG, Hardcastle JD. Rectal endosonography for the visualization of the anastomosis after anterior resection and its relevance to local recurrence. Int J Colorect Dis 1990;3:127–9.
16 St Ville EW, Jafri SZH, Madrazo BL, Mezwa DG, Bree RL, Rosenberg BF. Endorectal sonography in the evaluation of rectal and perirectal disease. AJR Am J Roentgenol 1991;157:503–8.
17 Gammelgaard J, Holm HH. Transurethral and transrectal ultrasonic scanning in urology. J Urol 1980;124:863–8.
18 Watanabe H, Igari D, Tanahashi Y, Harada K, Saitoh M. Transrectal ultrasonotomography of the prostate. J Urol 1975;114:734–9.
19 Bernaschek G, Janisch H. Eine Methode zur Objektivierung des Parametrienbefundes beim Zervikalkarzinom. Geburtshilfe Frauenheilkd 1983;43:498–500.
20 Bernaschek G, Tatra G, Janisch H. Die rektale Sonographie. Eine Erweiterung der Rezidivdiagnostik zervikaler Neoplasien. Geburtshilfe Frauenheilkd 1984;44:495–7.21 Gitsch G, Deutinger J, Bernaschek G. Der diagnostische Wert der Rektosonographie bei der Beurteilung der parametranen Infiltration beim Zervixkarzinom. Geburtshilfe Frauenheilkd 1992;52:412–4.
22 Zaritzky D, Blake D, Willard J, Resnik, M. Transrectal ultrasonography in the evaluation of cervical carcinoma. Obstet Gynecol 1979;53:105–8.
23 Squillaci E, Salzani MC, Grandinetti ML, Auffermann W, Marsella A, Maresca G, et al. Recurrence of ovarian and uterine neoplasms: diagnosis with transrectal ultrasound. Radiology 1988;168:355–8.

Fig. 41.1 Transrectal ultrasound probes.
a Old probe, with a balloon standoff.
b New probe, without a standoff.

1a

1b

Fig. 41.2 Schematic diagram of the ultrasound probe inserted into the rectum.

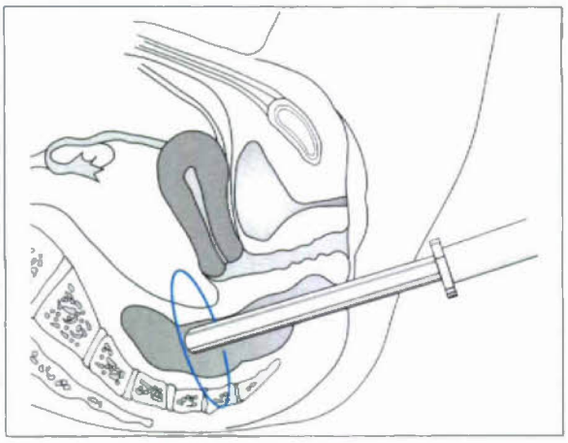

2

Fig. 41.3 Probe in place within the rectum. Transabdominal longitudinal scan. The transducer rotates at the tip of the rectal probe within a fluid-filled balloon, which is directly below the cervix in this image.

3

Fig. 41.4 Image orientation in transrectal ultrasound.

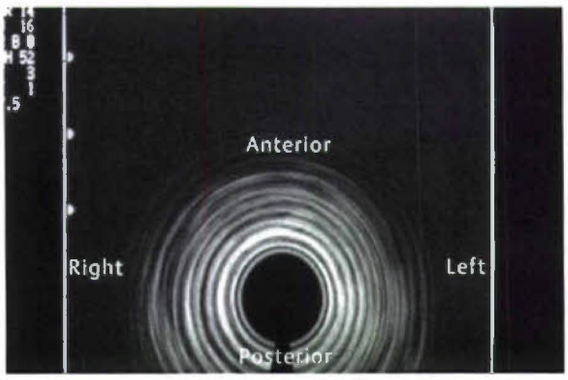

4

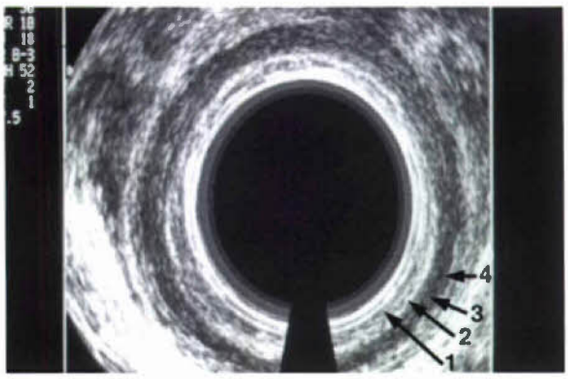

5

Normal Anatomy

Fig. 41.5 Appearance of the anatomical layers of the rectum.
1 Mucosa
2 Submucosa
3 Muscularis propria
4 Serosa

Fig. 41.6 The vagina (*) and urethra (→) are displayed in cross-section.

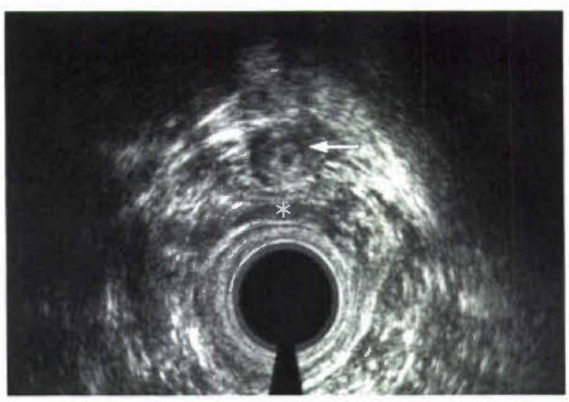

6

Fig. 41.7 Transrectal scan through the cervix demonstrates normal parametrial tissue on both sides.

7

Applications in Gynecology

Fig. 41.8 Moderate hematocolpos secondary to hymenal atresia (*). Transverse scan of the vagina.

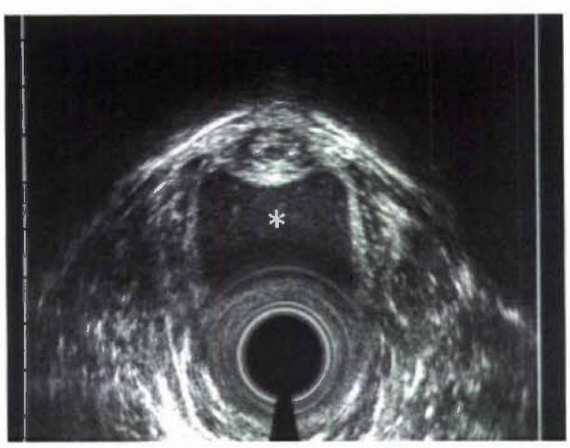

8

Fig. 41.9 Pronounced hematocolpos in a patient with hymenal atresia. Transverse scan of the vagina.

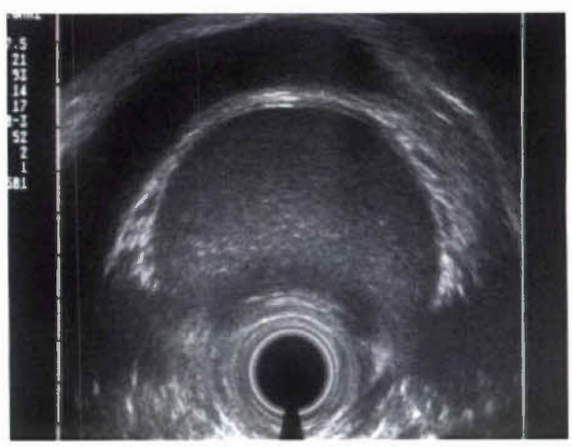

9

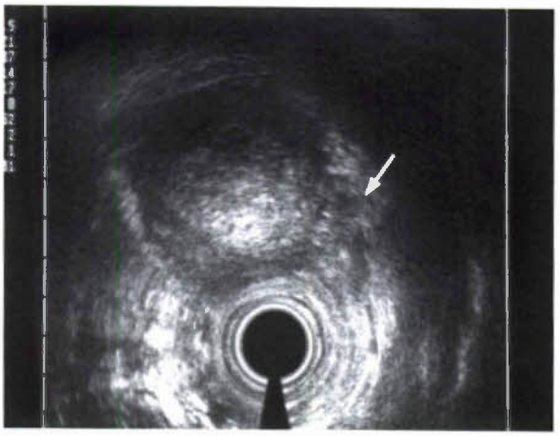

10

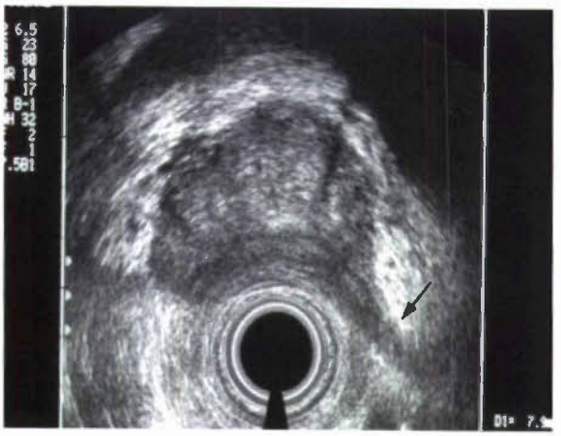

11

Fig. 41.10 Cervical carcinoma with incipient parametrial infiltration on the left side (—).

Fig. 41.11 Cervical carcinoma with definite parametrial infiltration on the left side extending to the pelvic wall (—).

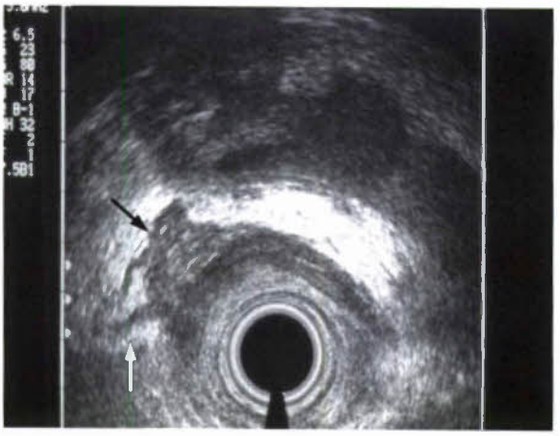

12

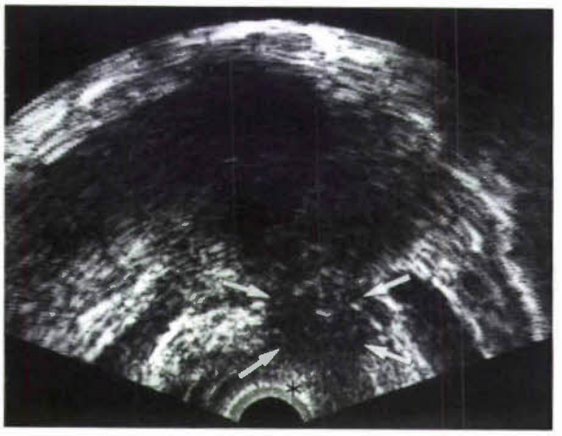

13

Fig. 41.12 Cervical carcinoma infiltrating the vagina and right paracolpium (→).

Fig. 41.13 Transrectal ultrasound demonstrates a stage IV cervical carcinoma with extensive posterior infiltration (—), extending to the rectal wall (*).

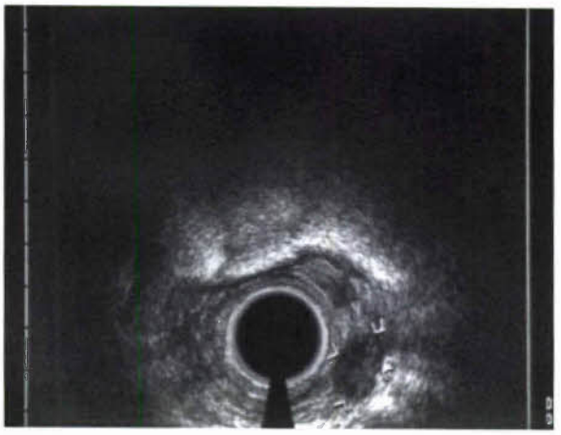

14

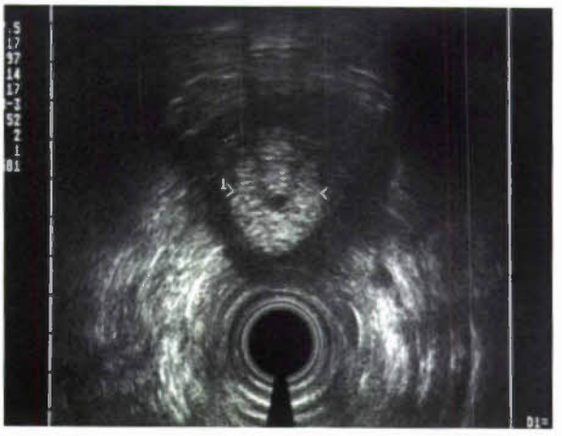

15

ig. 41.14 Enlarged, tumor-involved pararectal lymph node on the left side (> <).

Fig. 41.15 Endometrial carcinoma (> <) with involvement of the inner half of the myometrium.

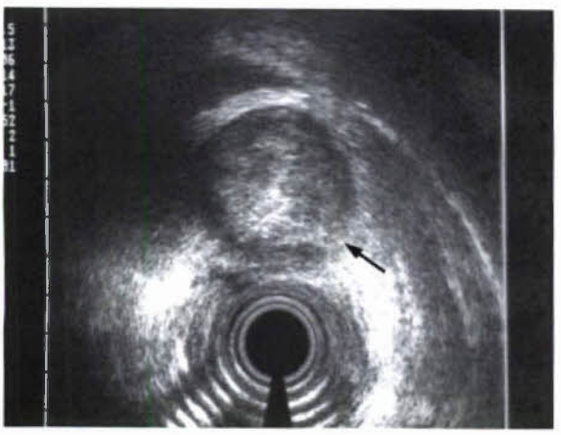

16

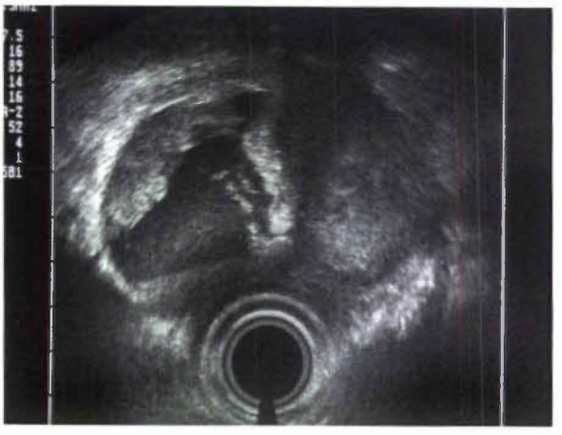

17

Fig. 41.16 Endometrial carcinoma permeating the entire myometrium (—).

Fig. 41.17 Transrectal scan of a mixed solid and cystic ovarian mass in the cul-de-sac.

Transuterine Ultrasound

42 Transuterine Ultrasound: Technique and Applications

Transuterine ultrasound, known also as hysterosonography [1–5], is an imaging procedure in which a narrow ultrasound probe is introduced through the dilated cervical canal into the uterine cavity (Fig. 42.**1**). Because dilation of the cervical canal is painful, the examination requires either local anesthesia or brief general anesthesia, thereby limiting the ambulatory use of this technique. To prevent cervical and endometrial injury, the intracavitary probe is sheathed in a metal tube so that only the scatter tip rotates freely in the uterine cavity.

The frequencies used in transuterine ultrasound are generally higher (7–10 MHz) than those used in transvaginal ultrasound. The higher frequencies provide excellent near-field resolution, but also greatly limit the penetration depth of the beam, especially when a 10-MHz probe is used. In these cases, it may not be possible to evaluate the outer uterine boundary if the myometrium is thickened.

The rotating transducer is mounted at the tip of the probe and provides transverse scans of the uterus (Figs. 42.**1**–42.**4**). The endometrium, myometrium, and perimetrium are clearly visualized. The uterotubal junction can also be displayed (Fig. 42.**5**). The uterine fundus can be accurately evaluated only if the intrauterine probe has a forward-scanning capability.

Transuterine ultrasound is useful for the specific exclusion of intrauterine pathology and for the selective detection of small submucous myomas (Fig. 42.**6**) and other endometrial abnormalities (Fig. 42.**7**).

In patients with uterine malignancies, transuterine scanning can define the shape of the tumor, the direction of its spread, and the lateral extent of tumor infiltration (Figs. 42.**8**–42.**10**).

The possible applications of transuterine ultrasound are listed in Table 42.**1**.

Table 42.1 Applications of transuterine ultrasound

- Detection of submucous myomas
- Detection of mucosal polyps
- Assessment of invasion depth by endometrial carcinoma
- Assessment of invasion depth by cervical carcinoma including parametrial involvement
- Planning of intracavitary radiotherapy

Given the constant improvements in the resolution of endovaginal probes and the noninvasiveness of transvaginal ultrasound, there is no longer a compelling reason to favor transuterine ultrasound as a diagnostic procedure. An exception to this is in radiotherapy, in which precise evaluation of the tumor extent allows more accurate planning of intracavitary radiotherapy [2].

References

1 Hötzinger H, Becker H, Becker V. Intrauterine Ultraschalltomographie (IUT): Vergleich mit makroskopischen Präparateschnitten. Geburtshilfe Frauenheilkd 1984;44: 219–24.
2 Hötzinger H. Durch Intrauterinsonographie optimierte intrakavitäre Strahlentherapie bei Korpuskarzinomen. Strahlentherapie 1984;160:600–4.
3 Hötzinger H. Hysterosonography and hysterography in benign and malignant diseases of the uterus: a comparative in vitro study. J Ultrasound Med 1991;10:259–63.
4 Popp LW, Lueken RP, Lindemann HJ. Hysterosonographie. Diagn Intensivther 1982; 4:69–73.
5 Popp LW, Lueken RP, Müller-Holve W, Lindemann HJ. Gynäkologische Endosonographie: erste Erfahrungen. Ultraschall 1983;4:92–7.

Fig. 42.**1** Transuterine ultrasound. Schematic diagram.

Fig. 42.**2** Normal cervix in transverse section.

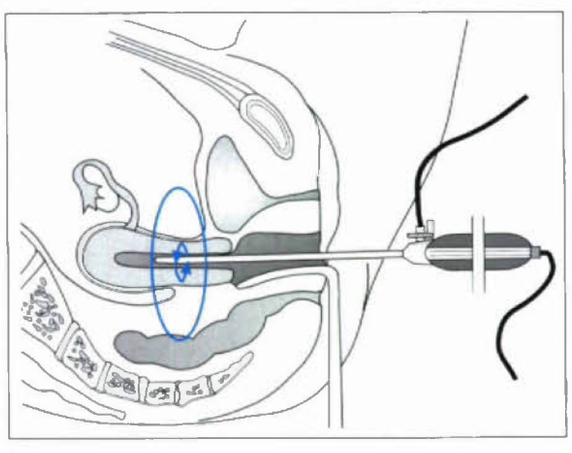

1

2

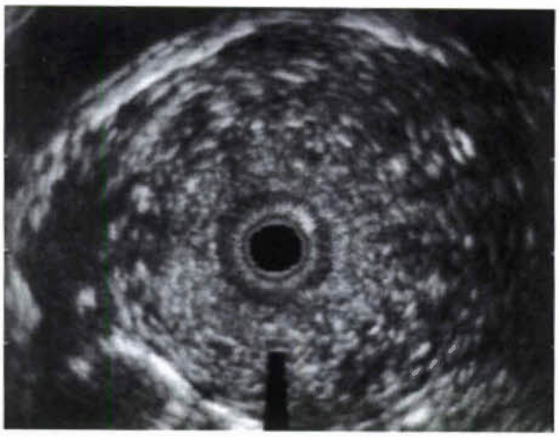

3

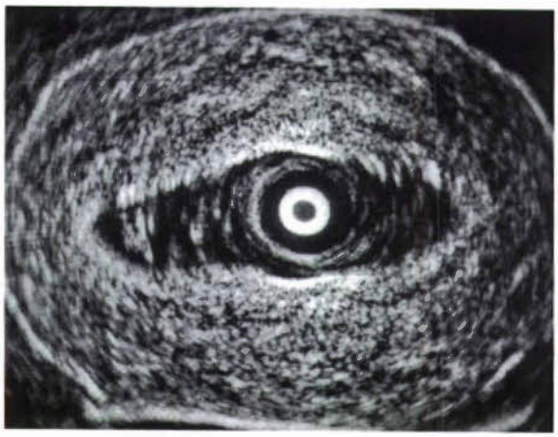

4

Fig. 42.3 Normal uterine corpus in transverse section.

Fig. 42.4 Normal-appearing uterine fundus (image courtesy of Prof. H. Hötzinger).

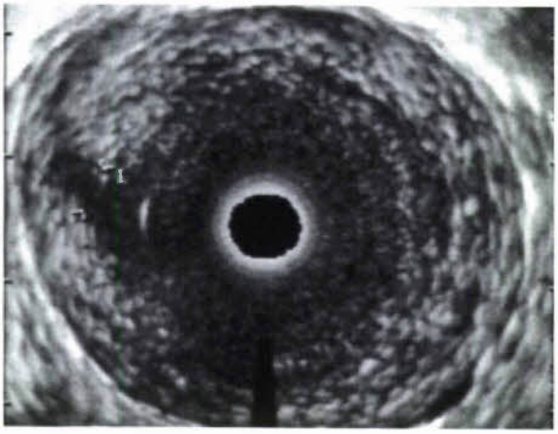

5

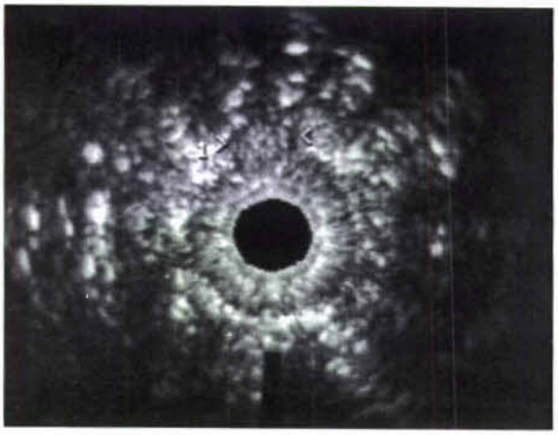

6

Fig. 42.5 Appearance of a normal uterotubal junction on the right side (> <).

Fig. 42.6 Small submucous myoma (6 mm in diameter).

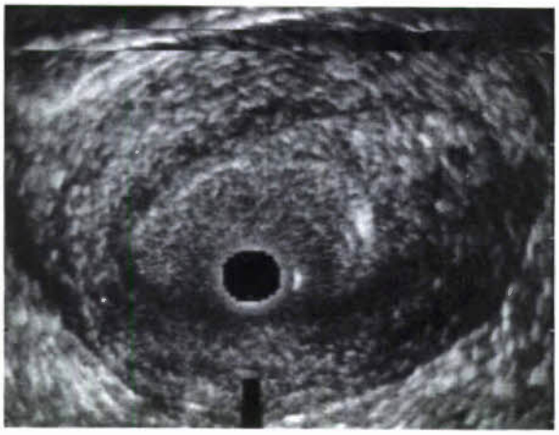

7

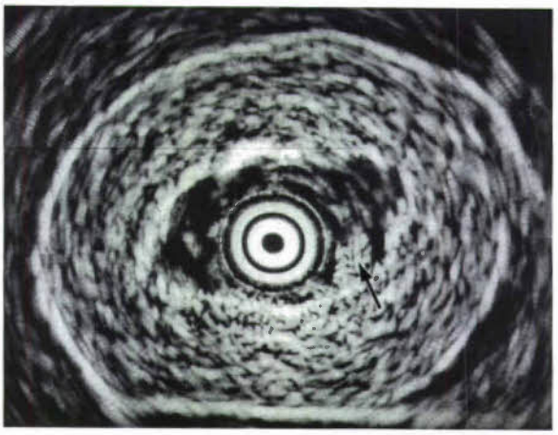

8

Fig. 42.7 Adenomatous hyperplasia.

Fig. 42.8 Exophytic endometrial carcinoma at the 4-o'clock position (→) (image courtesy of Prof. H. Hötzinger).

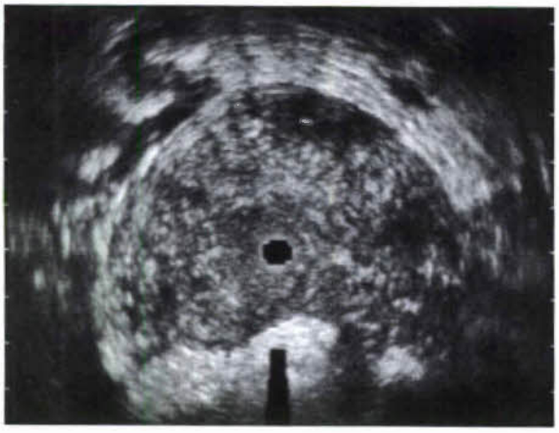

9

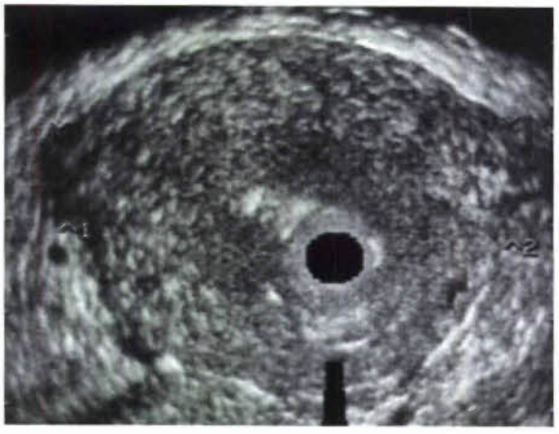

10

Fig. 42.9 Extensive carcinoma of the uterine corpus, penetrating all of the wall layers.

Fig. 42.10 Cervical carcinoma with infiltration of both parametria (> <).

Breast Ultrasound

43 Ultrasound Diagnosis of Breast Diseases

Epidemiology of Breast Cancer

The epidemiological impact of breast cancer is reflected in the fact that it is the most common cancer in women. It accounts for 22% of cases in Germany and is the leading cause of cancer deaths. To date, there has been no nationwide compilation of breast cancer statistics in Germany, but data from the Saarland Cancer Registry are considered representative of the country as a whole. These data clearly indicate that there has been a gradual rise in the incidence of breast cancer during the past 20 years. Moreover, there has been no decline in the mortality from breast cancer, despite the availability of improved treatment options [1]. Our own studies indicate an overall 5-year survival rate of 72% and a 10-year survival rate of 55%. The prognosis depends mainly on the stage of the tumor [2]. For the present, then, it appears that the only effective way to lower breast cancer mortality is to detect the disease at an earlier stage.

Results of Mammographic Screening

Since the 1960s, more than 500000 women worldwide have had a mammographic screening examination [3–6]. Studies have shown that the tumor stages detected in the screened population were less advanced than in comparable control groups. When all the results are taken into account, the studies show that screening can lower the mortality rates from breast cancer by 25–30%. It should be noted, however, that the follow-up period in most studies is still too short to make a definitive evaluation. Another problem in screening examinations is that the results vary with age. The participants in most studies averaged 40 years of age. When the results for premenopausal and postmenopausal women are considered separately, it is found that the mortality rates in younger women have shown little or no decline, according to most studies [6]. The sensitivity of mammographic screening measured entirely on the basis of clinically detected cancers was also lower in the younger age groups, and a higher incidence of interval cancers was documented in the younger women. This is due to the fact that conventional mammograms are less sensitive for detecting tumors in the dense glandular breasts of younger women. It is also important to note that 25–30% of breast cancers occur in premenopausal women.

Role of Ultrasound

The earliest attempts to diagnose breast tumors with ultrasound were made in the early 1950s [7]. However, effective soft-tissue discrimination has been possible only since the advent of gray-scale imaging [8]. A major advantage of ultrasound over radiography is its ability to penetrate the dense glandular tissue in the young breast [9]. In years past, the principal role of breast ultrasound was in differentiating between cystic and solid masses that presented as palpable focal lesions or mammographic densities [10]. Today, the indications for breast ultrasound have been dramatically expanded by rapid advances in ultrasound technology [11–13]. It is surprising, then, that even some recent publications still limit the role of ultrasound to investigating palpable breast masses and differentiating between cystic and solid masses [14]. This limited perspective may have made sense in the early 1980s, given the imaging quality available at that time (Fig. 43.**1**) [15], although even then there were several groups of authors who had achieved significantly better results in breast cancer diagnosis [11,13,16]. However, the limitations that were still being debated over a decade ago are no longer valid today. With the high resolution provided by modern ultrasound scanners, it is now possible to detect early tumors smaller than 1 cm in diameter and even to detect lesions in the lactiferous ducts [17–20].

Mammograms still have an essential role in the detection of occult breast lesions, especially in postmenopausal women. Ultrasound is indispensable for selective preoperative investigations, however. The sectional imaging format of ultrasound and its excellent soft-tissue characterization, combined with high structural and contrast resolution, often allow more accurate differentiation between benign and malignant lesions than is possible with mammograms. Ultrasound is definitely superior to mammograms for determining tumor size, owing to the absence of superimposed shadows [9,21]. The main problem with using mammograms alone is that they may prompt an ill-conceived decision to carry out breast-conserving therapy. In a large histopathological study of breast cancer patients, it was found that 30–40% of the cancers were associated with diffuse or multifocal disease that was occult on conventional mammograms [22]. Magnetic resonance mammography has recently been advocated for the detection of multifocal breast cancer [23]. However, we have shown that multifocal lesions can also be reliably detected with high-resolution real-time ultrasound [18].

In addition, ultrasound-guided fine-needle aspiration biopsies and core biopsies, plus the preoperative localization of nonpalpable focal lesions, are playing an ever-expanding role in the perioperative management of women with breast lesions [24]. Several indications for breast ultrasound have also been established (Table 43.**1**). It is important, however, to distinguish between the use of a simple scanner that meets basic technical requirements but cannot satisfy higher quality standards, and scanning with a high-resolution system. The experience of the examiner plays an equally important role. Given the lack of uniform standards for examiner training and proficiency, many of the statements made in this chapter may not be fully applicable to every situation.

Table 43.**1** Diagnosis of breast cancer

Basic work-up
• Investigation of palpable focal lesions
• Investigation of mammographic densities
• Differentiation of cystic and solid lesions
• Ultrasound-guided percutaneous biopsy
Specialized examinations
• Improved tumor differentiation
• Accurate measurement of tumor size
• Detection of multifocal lesions
• Examination of high-risk patients to detect occult tumors
• Detection of early abnormalities

Examination Technique

A systematic examination routine should be followed in order to fully utilize the advantages of high-resolution breast ultrasound. The tissue layer through which scanning is carried out should be thin enough to allow optimum focusing over a short distance and to minimize sound absorption. The breast itself should be stabilized in order to facilitate movements of the transducer probe and ensure better reproducibility. This is most easily accomplished with the patient lying supine, as this position allows the breast to flatten against the chest wall. Also, the patient should extend both arms above the head and interlock the fingers behind the neck to further flatten the breast and stabilize it by pectoralis muscle tension. This position also provides access for axillary scanning in the same session. Another advantage of this position is that it is very similar to the position used on the operating table, making it easier to locate the tumor intraoperatively. For patients with large breasts, we recommend placing a small cushion beneath the shoulder on the examined side to shift the breast volume medially and flatten the outer quadrants.

The transducer probe should be moved over the breast in a meandering pattern that results in a series of overlapping scan planes. This is more easily accomplished in sagittal planes than in horizontal planes (Figs. 43.**2**, 43.**3**). Some examiners scan in a concentric pattern, working from the periphery of the breast toward the alveolar region. This technique requires considerably more scanning movements, however, to ensure that all of the breast parenchyma is visualized.

The probe should be held perpendicular to the skin to facilitate optimum penetration of the sound waves. Just enough pressure should be applied to obtain uniform acoustic coupling between the probe and skin. Too much pressure can be painful and may distort the breast parenchyma, making it more difficult to evaluate normal breast anatomy (Fig. 43.**4**). Also, uneven probe pressure may displace tumors out of the scan plane, causing them to be missed at examination. If sound penetration is insufficient, the probe pressure can be increased slightly to obtain better penetration (43.**5**). This is often necessary in the subareolar region and in parenchymal areas affected by fibrosis, which increases sound absorption (Fig. 43.**6**). The compression effect flattens the acoustic interfaces and improves the scanning angle; this promotes sound transmission and makes it easier to bring out structural details [25]. The *compression technique* is an important aid in identifying tumors. The most common problem for beginners is distinguishing between fatty tissue infiltration and true neoplasms, since both appear as hypoechoic lesions in the breast (Figs. 43.**7**, 43.**8**). Fatty tissue is soft, however, and will change its shape or even disappear when probe pressure is applied. By contrast, true neoplasms (other than lipomas, lipomatous adenomas, and fibrolipomas) are firm and show little or no compressibility. This makes it easy to distinguish them from fat, despite their similar echogenicity (Fig. 43.**8**).

Evaluation of Breast Masses

Cysts

Cysts are the most common breast lesions. Cysts with a diameter of 1–2 cm or more may present clinically as nodules with a rubbery consistency, although many cysts are difficult to palpate due to diffuse induration of the breast parenchyma. Cysts may occasionally appear as rounded densities on mammograms, especially when they are relatively large. But since these lesions occur predominantly in premenopausal women with dense, fibrous breasts, they are often obscured by the parenchyma and are not visualized, or may create superimposed shadows that appear as ill-defined or spiculated densities that require further investigation. These doubts can be quickly resolved by ultrasound, while formerly the only other options were percutaneous biopsy or surgery. Women with cysts occasionally complain of breast pain, prompting them to see a physician. Most breast cysts are asymptomatic, however, and many are detected incidentally during an ultrasound examination. Their sonographic characteristics are listed in Table 43.**2**.

Table 43.**2** Sonographic criteria for cysts

Shape	Round or oval
Margins	Sharp or smooth
Echo pattern	Homogeneous
Echogenicity	Echo-free to hypoechoic
Through-transmission	Increased
Acoustic shadowing	Lateral edge shadows

When a cyst has no internal echoes, has well-circumscribed margins, and shows posterior acoustic enhancement, there should be no difficulty in making a confident diagnosis (Fig. 43.**9**). However, if the cyst has been present for some years, its contents may become inspissated and slightly echogenic, despite the fact that there have been no actual proliferative changes (Fig. 43.**10**). It is common to encounter microhemorrhages and hemosiderin deposits within cysts, resulting in increased echogenicity. However, echogenic cysts may also result from proliferative foci on the inner cyst wall and increased cellularity of the cyst fluid. Occasionally the cysts become so echogenic that they are difficult to distinguish from fibroadenomas. Given this uncertainty, these cysts should be investigated by aspiration cytology.

The presence of wall irregularities (Fig. 43.**11**) or intracystic tumors (Fig. 43.**12**) also warrants further investigation. Traditionally, a suspicious breast cyst was aspirated with a percutaneous needle, filled with air, and then examined by mammography (*pneumocystography*), so that the cyst contents could be evaluated. With ultrasound, however, it is generally possible to evaluate the cyst walls so reliably that there is no need to proceed with pneumocystography. If a definite intracystic tumor is detected, aspiration cytology is no longer appropriate, as there is a compelling indication for surgical excision (Fig. 43.**12**). If the cyst contents were percutaneously aspirated, it would be extremely difficult to find the tumor again by mammography or ultrasound for preoperative localization. Occasionally, puncture of a suspected carcinoma may be indicated in the immediate preoperative period in order to help plan the surgical excision. The same rules apply to proliferative lesions on the cyst wall. Of course, the mammographic findings should also be taken into account when planning the operation. It is common for these patients to have varying degrees of proliferative fibrocystic breast changes, which are commonly associated with indeterminate microcalcifications. If this is the case, the operation provides an opportunity to investigate all equivocal findings.

Prosthetic Implants

Prosthetic breast implants are a special type of iatrogenic cystic mass. Silicone-filled implants are most widely used. Close ultrasound follow-up is particularly important in patients who have had a prosthetic breast reconstruction following cancer surgery. Mammograms are of very limited value after prosthetic reconstructions, as the implant obscures the residual breast tissue (Fig. 43.**13**). Occasionally this prompts recommendations for magnetic resonance mammography in patients with breast implants, but this modality is too costly for use in routine follow-ups. Also, each examination would require the administration of a paramagnetic contrast agent to produce enhancement of the hypervascular lesion. Ultrasound is excellent for the examination of prosthetic breast implants (Fig. 43.**14**), as silicone is transparent to ultrasound waves. The implant has smooth outer margins and an echo-free interior, like a large cyst. Due to the strong reflectivity of the implant shell, however, it is common for reverberations to arise in the region near the

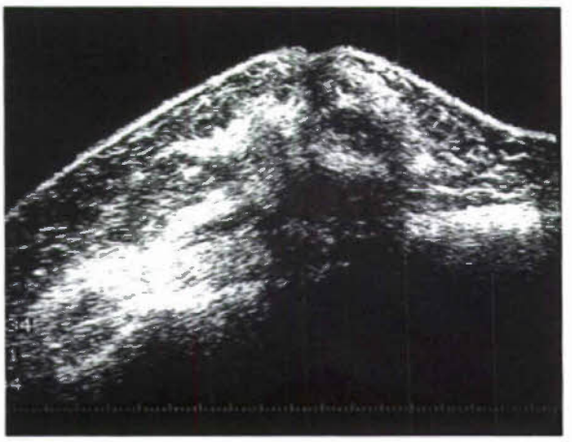

1

Fig. 43.1 Sagittal ultrasound scan through the center of a breast with extensive invasive ductal carcinoma. The scan was acquired with a 4-MHz water-path compound scanner of the type used in the early 1980s (system 1, Ausonics, Sydney). This technique provides a good survey of breast anatomy, although the resolution is considerably poorer than that obtained with modern high-frequency real-time scanners with short-range focusing.

Examination Technique

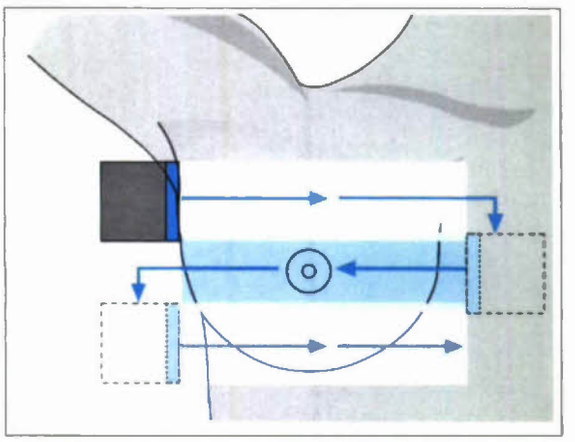

2

Fig. 43.2 Diagram of the meandering pattern of probe movements used to examine the breast in sagittal sections. The breast is scanned in three or four horizontal passes, depending on the size of the breast and the length of the probe. The scan planes should overlap to ensure complete coverage of the breast parenchyma.

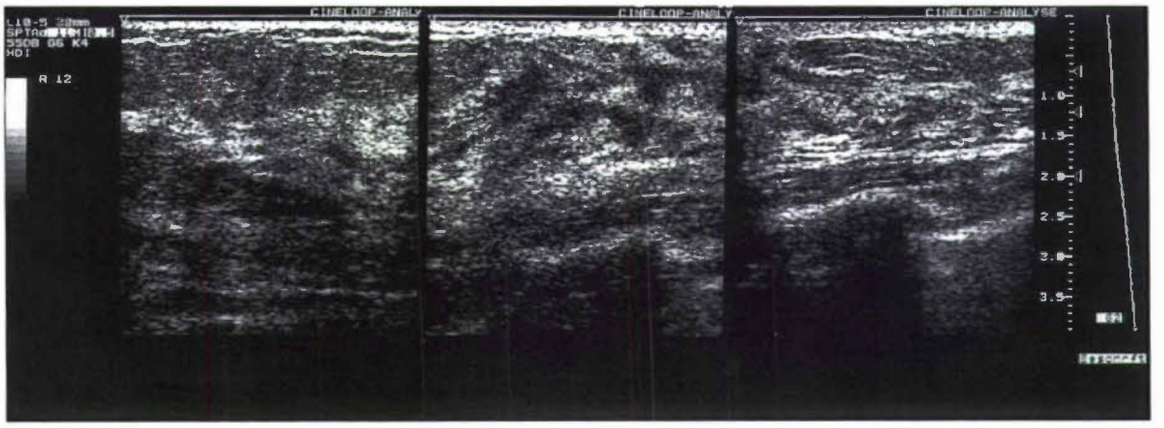

3a 3b 3c

Fig. 43.3 Normal sonographic anatomy of the breast in sagittal scans through the center of the breast.
- **a** Cranial extension of breast parenchyma.
- **b** Central region.
- **c** Caudal extension of parenchyma.

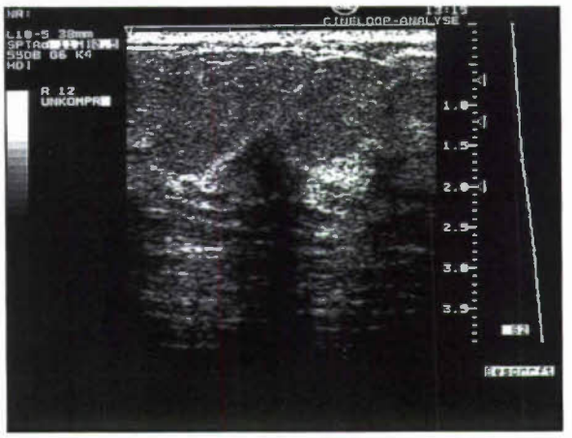

4a

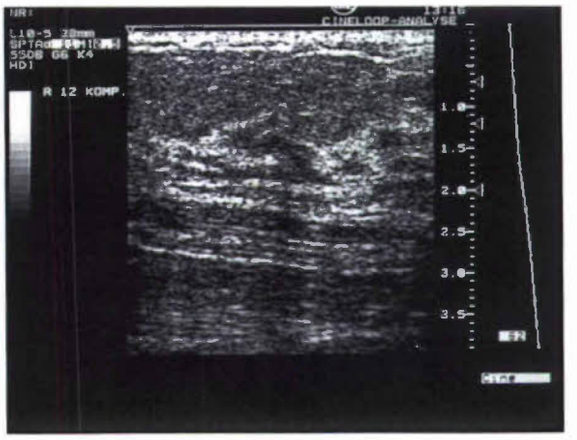

4b

Fig. 43.4 The appearance of breast structures in the supine position.
- **a** Without compression. The probe is placed lightly on the skin, applying just enough pressure for uniform acoustic coupling.
- **b** Compression is applied with the probe, deforming the soft fatty tissues and glandular structures. The breast parenchyma now appears denser and more compact. Some anatomical details are lost, but sound penetration is improved.

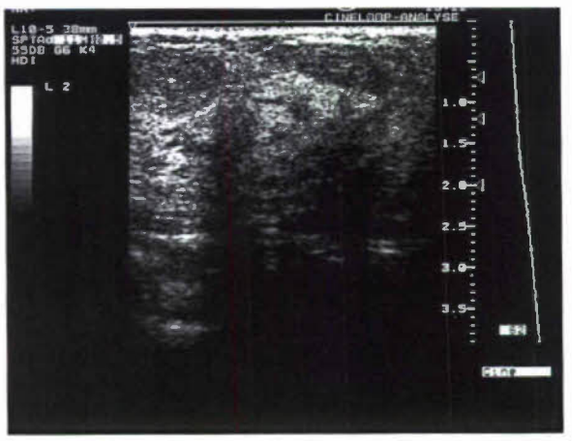

5a

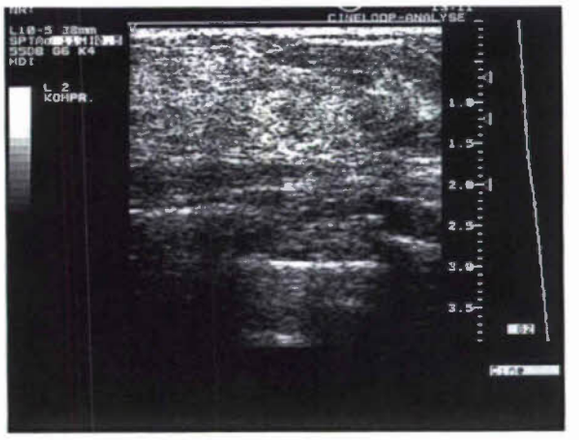

5b

Fig. 43.5 Sound absorption in the subareolar region.
- **a** Without compression, the breast fibers that project anteriorly into the nipple region cause significant sound attenuation (posterior acoustic shadowing).
- **b** Compression with the probe flattens the fibers. This improves sound transmission, provides better visualization of the fibers, and eliminates the acoustic shadows.

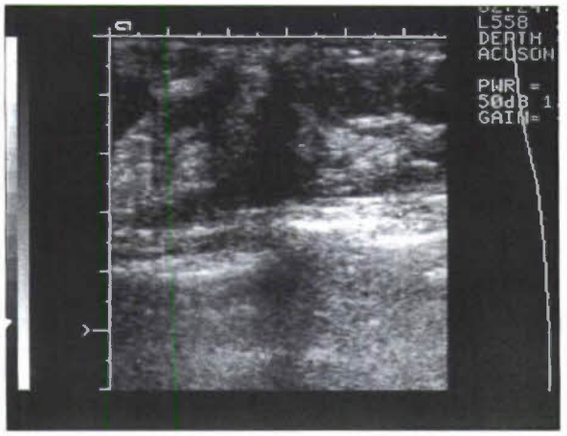

6a

6b

Fig. 43.6 Increased parenchymal density in the periphery of the breast.
a Without compression.
b With compression. Structures that impede ultrasound transmission at unfavorable scanning angles may cast acoustic shadows that appear as indeterminate focal lesions, not just in the critical subareolar region but anywhere in the breast parenchyma. Applying light pressure with the probe can flatten the structures and improve sound penetration.

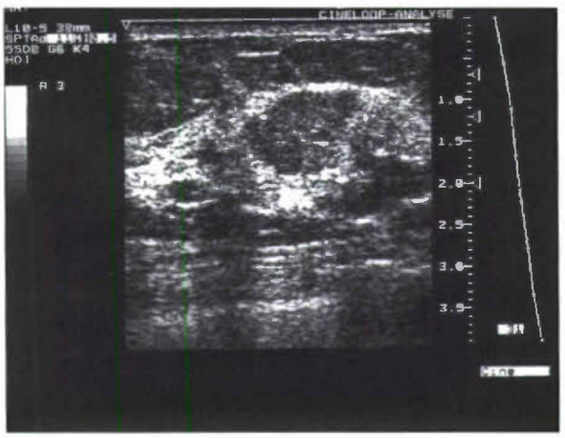

7a

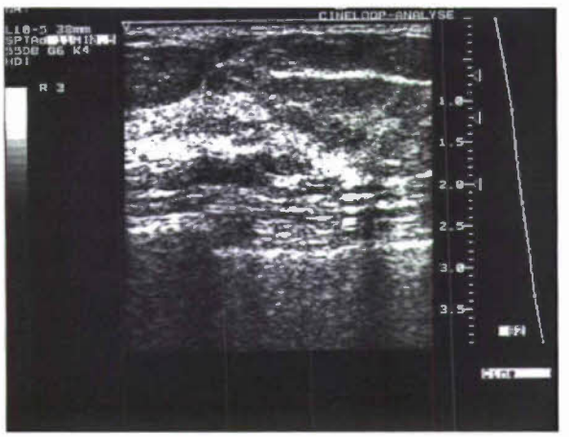

7b

Fig. 43.7 Fatty infiltration of the breast. Areas of fatty infiltration appear as hypoechoic foci when they are surrounded by echogenic parenchyma. Beginners in particular may have trouble distinguishing these foci from true tumors, which are also hypoechoic.
a Without compression.
b With compression. Again, applying the proper amount of pressure can yield important diagnostic information. Fatty tissue is soft and compliant, whereas solid tumors show little or no compressibility.

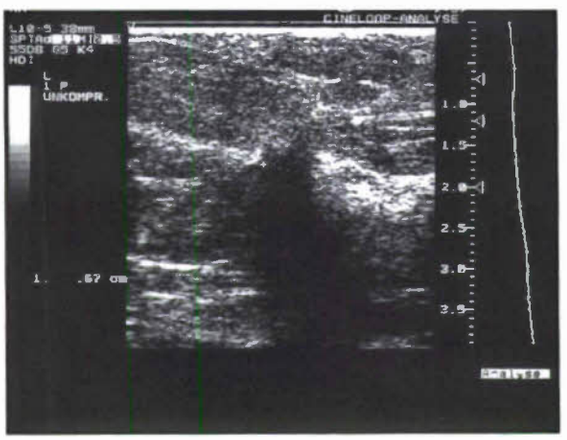

8a

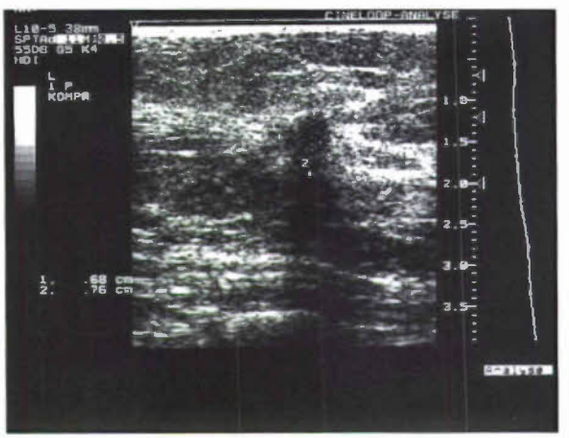

8b

Fig. 43.8 Breast carcinoma, 8 mm in diameter.
a Without compression.
b With compression. Unlike the case in Fig. 43.7, probe pressure does not alter the shape of the mass. It flattens the surrounding tissue and improves sound penetration, resulting in better visualization of the tumor.

Cysts

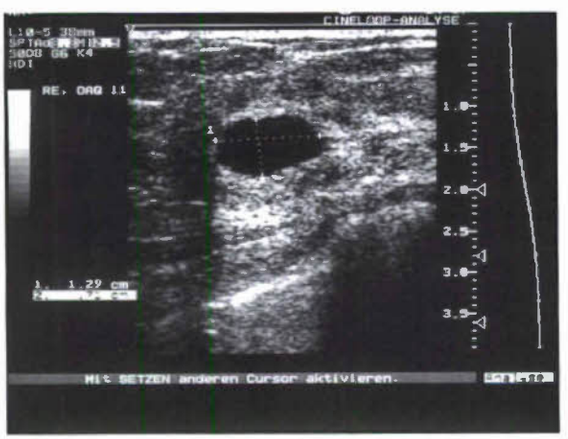

9

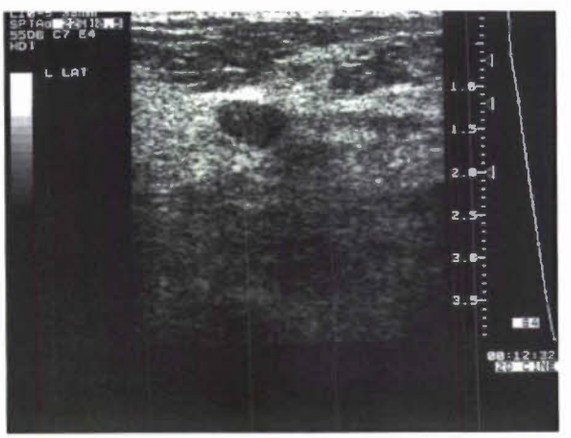

10

Fig. 43.9 A typical cyst appears as an echo-free focal lesion with smooth, sharp margins and posterior acoustic enhancement.

Fig. 43.10 This complicated cyst appears as a uniformly hypoechoic, sharply circumscribed focal lesion with slightly increased through-transmission of sound. This appearance is also consistent with fibroadenoma. Often the only way to distinguish these lesions is by ultrasound-guided percutaneous biopsy.

Fig. 43.11 This complicated cyst displays the characteristic features of a cystic mass. Its lateral wall shows a definite area of irregular thickening, however. This lesion was identified histologically as proliferative fibrocystic change.

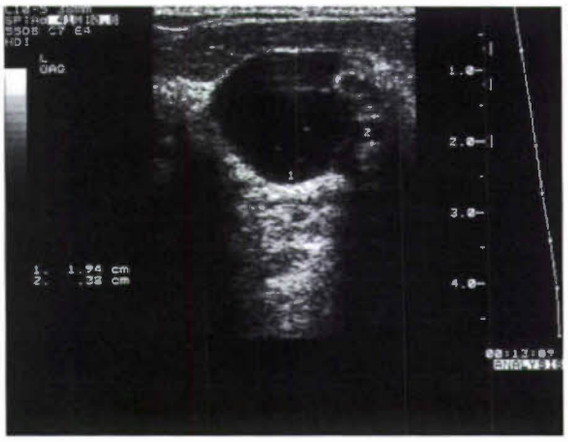

11

Fig. 43.12 Intracystic papilloma. This example shows that it is not sufficient to detect a cyst with ultrasound. Every lesion should be closely scrutinized for wall changes and suspicious internal structures. Owing to the high contrast between the cyst fluid and tissue, even the smallest intracystic tumors can be reliably detected. This type of lesion requires histopathological investigation.

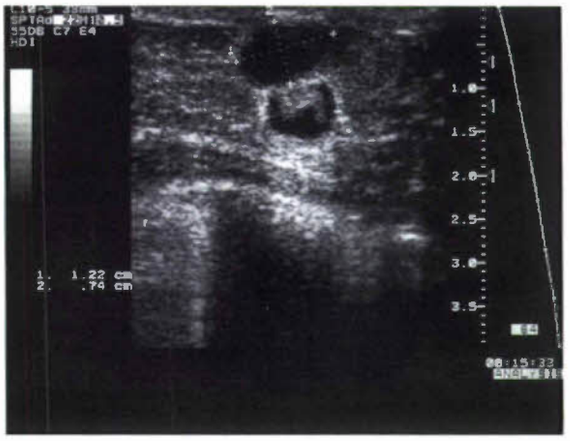

12

Prosthetic Breast Implants

Fig. 43.13 Mammogram of a silicone breast implant. The implant obscures the underlying residual tissue, making it necessary to supplement mammography with ultrasound.

13

Fig. 43.14 Ultrasound scan of a silicone breast implant. Careful ultrasound follow-up is particularly important in patients who have undergone a prosthetic breast reconstruction after mastectomy.

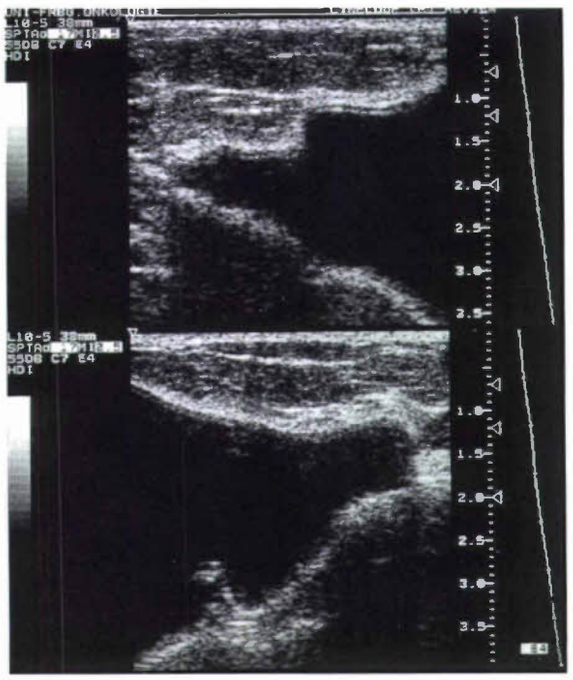

14

Inflammatory Breast Disease

Fig. 43.15 Mastitis with abscess formation.

- **a** The first scan shows a diffuse inflammatory process with edematous hypoechoic tissue. Purulent liquefaction has already begun at the center of the inflammatory process.
- **b** Complete liquefaction. This abscess is sharply demarcated from its surroundings by its almost capsule-like border and its doughy-cystic contents.

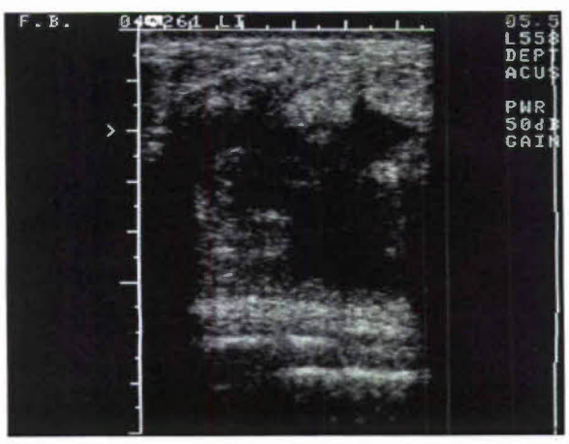

15a

15b

transducer. These artifacts move in response to compression and decompression, however, and this serves to distinguish them from true internal echoes. The breast should be surveyed twice during each examination: first with *near-field focusing* to evaluate the tissue anterior to the implant, and then with a *deep focal zone* to evaluate the chest wall. Implants usually appear considerably thicker in the ultrasound image than they actually are. This is because sound travels more slowly in silicone than in normal body tissues, creating a distorted image that may hamper accurate interpretation at the periphery of the implant.

Inflammatory Breast Disease

In patients who present with the clinical manifestations of mastitis, it should first be determined whether there is a diffuse inflammatory process in the tissue or whether an abscess has already developed, as this will critically influence management: should the condition be treated with antibiotics and a dopamine agonist, or by surgical evacuation? *Diffuse inflammation* is characterized by simple edematous swelling of the breast parenchyma with a slight decrease in echogenicity, whereas *abscess formation* is characterized by an architectural tissue distortion that increases from the periphery toward the center. The hypoechoic lesion has irregular, ill-defined margins and a nonhomogeneous pattern of low-level internal echoes (Fig. 43.**15a**). There may also be circumscribed areas of liquefaction, however, producing a doughy cystic mass with relatively sharp margins (Fig. 43.**15b**; Table 43.**3**).

Fibroadenomas

These tumors are a common occurrence between puberty and 30 years of age. They often grow in response to hormonal stimulation during late thelarche and also during pregnancy. Many fibroadenomas stop growing spontaneously after reaching a size of 1–2 cm, only to be detected many years later during mammographic screening. Given their homogeneous structure, the tumors have a uniformly hypoechoic sonographic appearance, with increased through-transmission of sound. Tumors that enlarge (pregnancy, proliferative fibroadenomas) tend to show increasing echogenicity as they grow larger. The well-defined, capsule-like margins of the tumors account for their smooth, sharply marginated appearance on sonograms (Fig. 43.**16a, b**). Coarse specks of calcification typically develop in fibroadenomas that have been present for many years or decades, and these calcifications are pathognomonic on mammograms when they are associated with a smooth tumor mass. At ultrasound, however, these gross calcifications cast dense acoustic shadows that obscure the tumor margins. This results in a suspicious-looking hypoechoic mass with irregular margins and a posterior acoustic shadow (Fig. 43.**16c**, Table 43.**4**).

Fibrolipomas, lipofibromas, and adenofibrolipomas (named for their histological components) display sonographic features similar to those of fibroadenomas. A very compressible tumor is assumed to contain a large proportion of fat. This should be confirmed by fine-needle aspiration or core biopsy, however, because carcinomas may occasionally mimic this appearance, although this occurs in fewer than 1% of cases. If cytology is negative, follow-up examinations should be scheduled at 6-month intervals to exclude a proliferative tendency.

Table 43.**3** Sonographic criteria for abscesses

Shape	Variable, occasionally round or oval
Margins	Irregular, ill-defined; rarely smooth and sharp
Echo pattern	Usually nonhomogeneous
Echogenicity	Hypoechoic
Through-transmission	Increased

Table 43.**4** Sonographic criteria for fibroadenoma

Shape	Round, oval, or lobulated
Margins	Sharp and smooth
Echo pattern	Homogeneous, occasionally nonhomogeneous
Echogenicity	Hypoechoic, occasionally hyperechoic
Through-transmission	Indifferent or increased
Acoustic shadowing	Lateral edge shadows

Table 43.**5** Sonographic criteria for intramammary scars

Shape	Bizarre
Margins	Ill-defined
Echo pattern	Homogeneous to nonhomogeneous
Echogenicity	Hypoechoic, increasingly echogenic toward the periphery
Through-transmission	Decreased
Acoustic shadowing	Central shadow (decreases on compression)

Scars

These iatrogenic changes are discussed separately, as they may cause differential-diagnostic problems. Large architectural defects are present during the early period after a breast operation. Usually the scarred area will regenerate over the next 3–6 months and should resolve almost completely in about 1 year, often leaving no visible evidence of a scar within the breast parenchyma. Occasionally, however, the regenerative process is delayed, or heavy collagen proliferation may occur. This causes increased sound absorption in the affected region, appearing sonographically as a hypoechoic focal lesion with a posterior acoustic shadow. Often these lesions are palpable as firm nodules, and mammograms show suspicious spiculated densities (Fig. 43.**17a**) that may prompt a recommendation for repeated biopsies in some women. In most cases, however, the hypoechoic focal lesion is easily identified with ultrasound by applying pressure to the scar tissue with the probe. This flattens the diffuse connective-tissue fibers, improving sound penetration and generally causing the architectural defect to disappear in the ultrasound image (Fig. 43.**17b, c**; Table 43.**5**).

Carcinomas

Malignant breast tumors have a very diverse imaging appearance and consistently raise problems of differential diagnosis. Owing to its sectional imaging format and good soft-tissue characterization, ultrasonography is superior to mammography in the differentiation of focal lesions. Technical refinements, moreover, have made it possible to detect increasingly small tumors, requiring a more refined interpretation of ultrasound findings in order to fully utilize the information contained in the images. With carcinomas, it is important to distinguish the primary criteria that describe the tumor itself from secondary features that result from the interaction of the cancer with its surroundings. The various diagnostic criteria are weighted differently, and none of the criteria is sufficient in itself to establish a diagnosis of cancer. Multiple criteria have to be met before a lesion is characterized as suspicious and in need of pathological evaluation. In the absence of these criteria, the lesion is classified as indeterminate and is referred for further investigation or follow-up. This means that suspicious ultrasound findings have major implications even in cases in which the clinical and mammographic findings are normal.

Figure 43.**18a** illustrates a typical breast lesion that meets all the criteria for a malignant tumor. An acoustic shadow that does not disappear in response to compression is considered a strong criterion. This is not a reliable indicator of malignancy, however, as it is seen in only about half of malignant tumors (Fig. 43.**18b, c**; Tables 43.**6**, 43.**7**).

Irregular, ill-defined margins are also considered a reliable criterion. Although nearly half of all malignant tumors have relatively sharp mar-

Table 43.6 Primary sonographic criteria for breast carcinoma

Shape	Bizarre, variable
D/W ratio	Ratio of depth to width > 1
Margins	Irregular and ill-defined
Echo pattern	Nonhomogeneous
Echogenicity	Echo-free to hypoechoic
Through-transmission	Decreased or increased
Acoustic shadowing	Central shadow
Compressibility	Noncompressible

Table 43.7 Secondary features of breast carcinoma

- Architectural distortion
- Perifocal reaction, infiltration zone (echogenic rim)
- Retraction and thickening of Cooper ligaments
- Little mobility relative to surroundings
- Skin thickening
- Dilated milk ducts
- Microcalcification echoes
- Regional lymph-node enlargement and texture change

gins, the margins are almost always irregular. A nonhomogeneous internal echo pattern is also typical of malignancies but is seen in only about half of cases. This is because heavy shadowing from the hypoechoic tumor often gives the mass a relatively homogeneous appearance. The most reliable secondary feature of breast cancers is a distortion of the normal breast architecture. An *echogenic rim* is also a fairly common and specific criterion for malignancy. The variability in the appearance of malignancies emphasizes the need to look at all the features when evaluating a tumor.

Owing to constant improvements in the quality of ultrasound equipment, sonographers are able to detect increasingly small subclinical tumors (Fig. 43.**19**). Ultrasound has thus become an essential adjunct to mammograms, especially for the optimum evaluation of premenopausal high-risk patients. Another important role of breast ultrasound is in preoperative planning. Because of superimposed shadows, mammograms often cannot accurately define the extent of tumors or detect multifocal lesions [22]. Ultrasound is a valuable adjunct in these cases, because it provides sectional images that are free of superimposed structures [18] (Fig. 43.**20**).

The accuracy of differential diagnosis is inherently limited in clinical examinations, as well as in mammography and ultrasound, by the small number of breast cancers that present smooth, sharp margins (1–4%). For this reason, all solid tumors should be investigated by cytological or histological examination. Ultrasound-guided fine-needle aspiration biopsy and even core-needle biopsies are simple procedures that are relatively safe in experienced hands and allow an immediate outpatient investigation of most indeterminate breast lesions [24]. In cases in which there is a very high index of suspicion for malignancy, however, we dispense with percutaneous biopsy confirmation, as the biopsy finding would not eliminate the need for a surgical diagnosis.

Tumor Blood Flow

Given the diagnostic problems described above, it must be concluded that there are no definite, specific criteria that can be applied in diagnostic imaging. Current efforts are therefore focusing on ways of improving the diagnosis by various means. Studies of tumor pathology and biology have shown that the development of an invasive malignancy and its further growth are mediated by growth factors that induce the formation of new, abnormal blood vessels [26–29]. Recent histological studies on angiogenesis have shown that the degree of tumor vascularity correlates strongly with the metastatic behavior of the tumor [30].

Thermography

Various diagnostic methods are based on the detection of increased tumor blood flow. One such method is thermography, in which temperature differences measured on the surface of the skin provide clues to the presence of metabolically active and hypervascularized lesions within the breast [31,32]. Thermography is rarely used nowadays due to its low specificity, but this modality did provide evidence that tumors with a copious blood supply have a less favorable prognosis [33].

Angiography and Magnetic Resonance Imaging

Some authors have successfully used angiography in the differentiation of breast masses [34–36], but the procedure is not widely utilized for this application. However, magnetic resonance imaging (MRI) has acquired a rapidly expanding role in the diagnosis of breast diseases [37]. MRI without paramagnetic contrast agents was initially found to have no advantages over mammography because of its poor spatial resolution. However, intravenous injection of gadolinium diethylenetriaminepentaacetic acid (Gd-DTPA) was found to produce rapid signal enhancement in hypervascularized tissues, and this sparked a breakthrough in MRI of the breast [23,38].

Continuous-Wave Doppler Ultrasound

This method has become popular owing to the development of new color Doppler systems, but the technology is not new. As early as 1977, researchers described a method with which a simple continuous-wave (CW) Doppler technique could be used to detect increased vascularity associated with breast tumors [39]. The procedure was increasingly refined during subsequent years [40–45]. It was also found that the level of tumor blood flow measured with CW Doppler correlated with prognostic factors [46], although long-term follow-up is still needed to draw definite conclusions. The main advantage of CW Doppler using an 8–10-MHz pencil-shaped probe is its high sensitivity for detecting small blood vessels. The main disadvantages of CW Doppler are that it does not produce an image and is basically limited to the examination of palpable masses [47]. In any case, statistical analyses of various flow parameters showed that the level of tumor blood flow was the most useful parameter for tumor differentiation, whereas the frequency spectral waveform and the indices derived from it were not reliable as differentiating criteria. Normal variations also have to be taken into account in interpreting CW Doppler findings. Blood flow is subject to small fluctuations during the normal menstrual cycle. The average frequency shifts detected by CW Doppler are in the range of 500–1000 Hz [48], but these values are substantially increased during pregnancy and lactation. The frequency shifts detected in malignant tumors are two to five times higher on average than in normal tissues.

Color Doppler Ultrasound

Because CW Doppler does not produce an image, duplex scanning was used in an attempt to locate and evaluate tumor vessels [49,50]. This is a very tedious process, however, as small tumor vessels cannot be visualized in the gray-scale image. Moreover, most older duplex systems used relatively low Doppler frequencies (2–3 MHz), which cannot detect flow in microscopic tumor vessels [49]. The real breakthrough in Doppler ultrasound came with the introduction of color Doppler technology, in which areas of color-encoded blood flow are superimposed over the gray-scale image [51–53]. The sensitivity of color Doppler systems is highly variable, however. All systems are not of the same quality [54], although constant improvements by manufacturers have produced significant advances in recent years.

The color Doppler imaging of breast lesions is still a new field, and it is difficult to compare the results of different studies due to differences

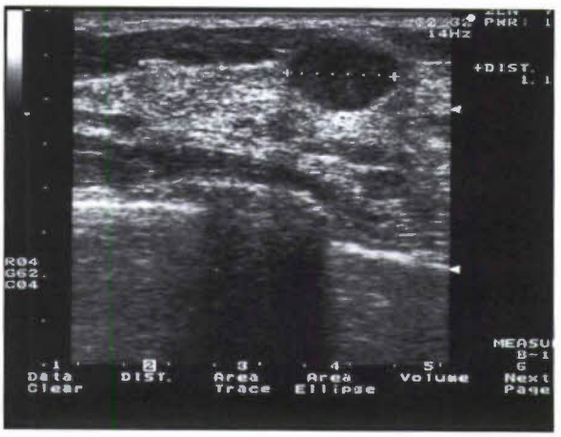

16a

16b

16c

Fibroadenomas

Fig. 43.16 Fibroadenomas.

- **a** A typical fibroadenoma appears as a smooth, sharply circumscribed, homogeneous, solid tumor with increased through-transmission and a faint lateral edge shadow.
- **b** Proliferative fibroadenoma. This tumor resembles the one in **a**, except for its nonhomogeneous internal echo pattern.
- **c** Calcified fibroadenoma. This tumor has a suspicious ultrasound appearance due to the sound-attenuating effect of the macrocalcifications. This results in a hypoechoic lesion with posterior acoustic shadowing.

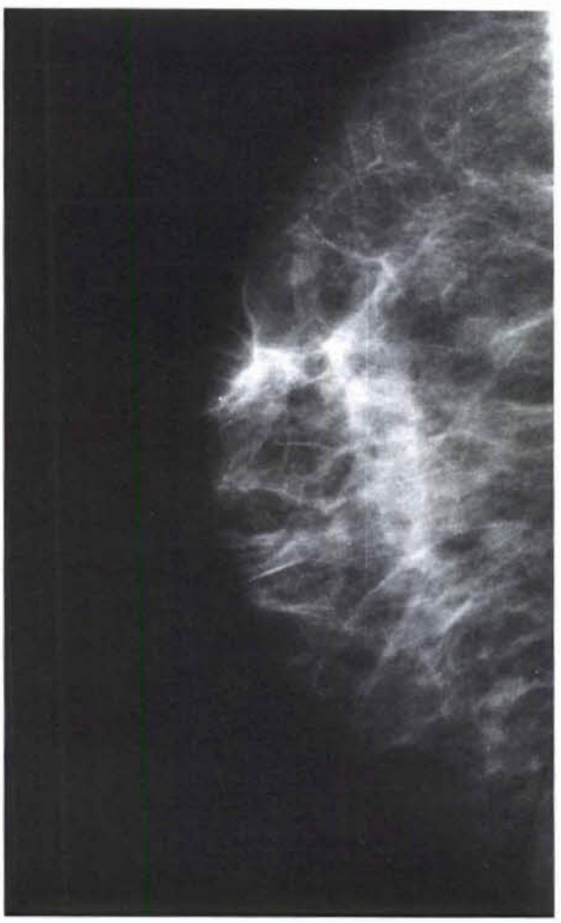

17a

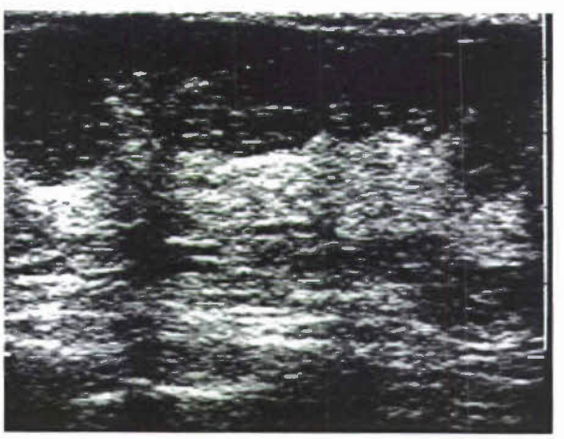

17b

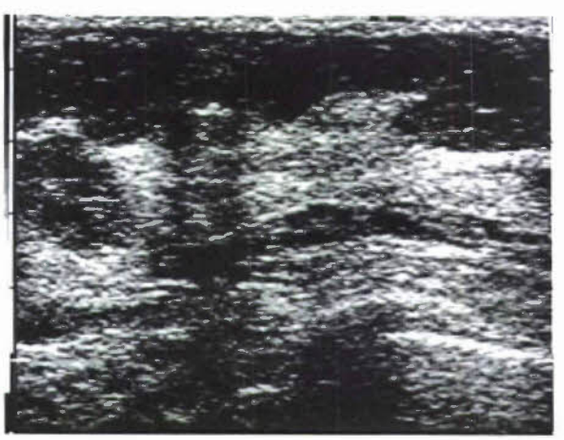

17c

Scars

Fig. 43.17 Scars.

- **a** Mammogram shows a suspicious spiculated density.
- **b** Ultrasound shows a hypoechoic mass with irregular margins and posterior acoustic shadowing.
- **c** When probe compression is applied, the structural distortion caused by the scar disappears as a result of improved sound penetration in the diffuse scar tissue.

Carcinomas

Fig. 43.18 Examples of invasive breast carcinomas.

a This lesion meets all the criteria for malignancy. It is nonhomogeneous and hypoechoic with irregular, ill-defined margins and a posterior acoustic shadow. It is noncompressible, and its D/W ratio (the ratio of the anteroposterior tumor diameter to the horizontal diameter) is greater than 1. Other suspicious features are an echogenic rim and architectural distortion.

b In contrast to **a**, this tumor does not cast a posterior acoustic shadow. Its outlines are irregular but sharply defined.

c Sonodense carcinoma. This lesion is an invasive lobular carcinoma. With its high sonodensity, this tumor is poorly delineated from the surrounding parenchyma. On closer scrutiny, however, the tumor is found to cause architectural distortion and presents irregular, ill-defined margins.

d This tumor has a nonhomogeneous internal echo pattern, good through-transmission of sound, and smooth, sharp margins. While these features are consistent with fibroadenoma, the tumor is actually an invasive carcinoma.

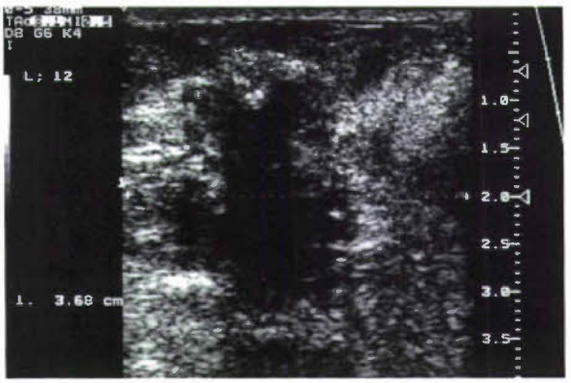

18a

18b

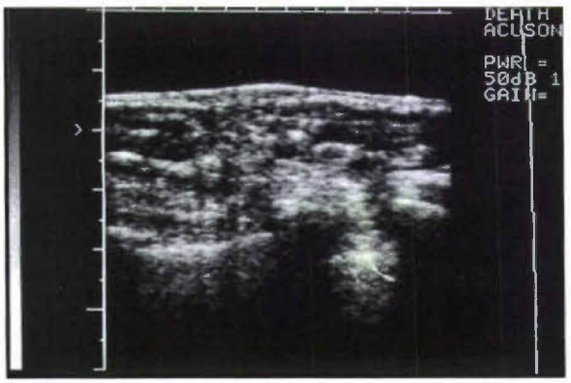

18c

18d

Fig. 43.19 Small breast cancers imaged with high-resolution ultrasound (10-MHz linear array).

a An invasive ductal carcinoma, 6 mm in diameter. This tumor is irregular but has well-defined margins. It is hypoechoic and shows marked architectural distortion.

b An early invasive breast carcinoma, 6 mm in diameter, with an intraductal component. The architectural distortion and the combination of well-defined and ill-defined margins create a high index of suspicion for carcinoma.

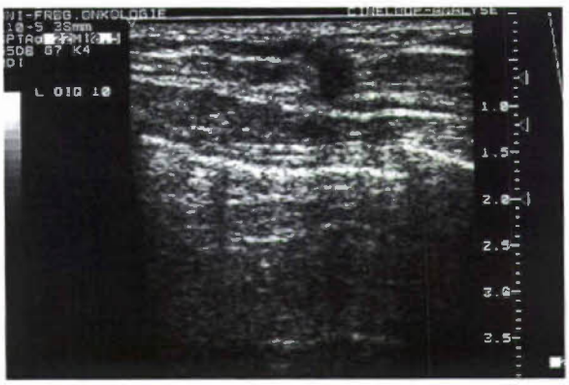

19a

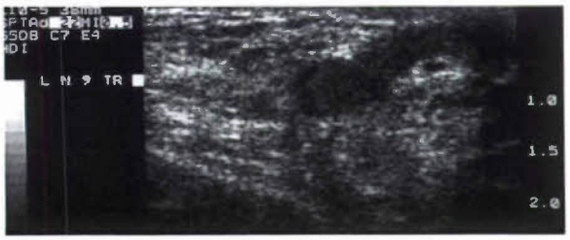

19b

Fig. 43.20 Multifocal breast cancers.

a Invasive ductal carcinoma appears as two irregular, hypoechoic foci with a combination of well-defined (left) and ill-defined margins (right).

b Invasive lobular carcinoma with predominantly ill-defined margins. Some of the lesions are hypoechoic (above) and some are more echogenic (below).

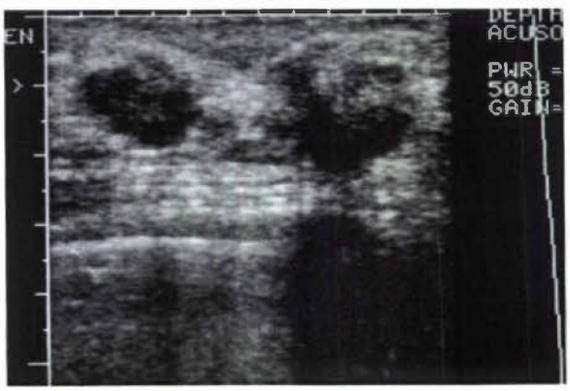

20a

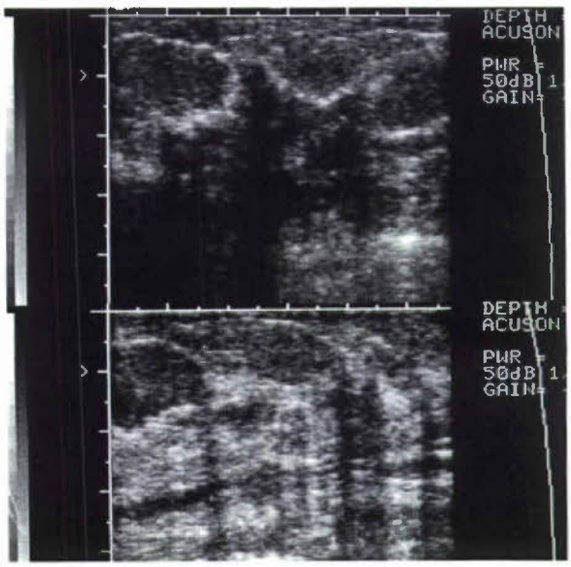

20b

Color Doppler Ultrasound

21a

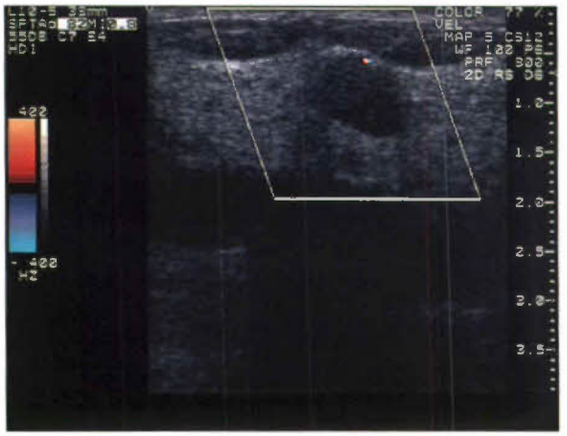

21b

Fig. 43.21 Invasive ductal breast carcinoma.
- **a** The color Doppler image shows a hypoechoic lesion, 10 mm in diameter, with irregular margins and several tumor vessels.
- **b** Quantitative analysis in the duplex mode shows a markedly increased flow velocity of 26.2 cm/s.

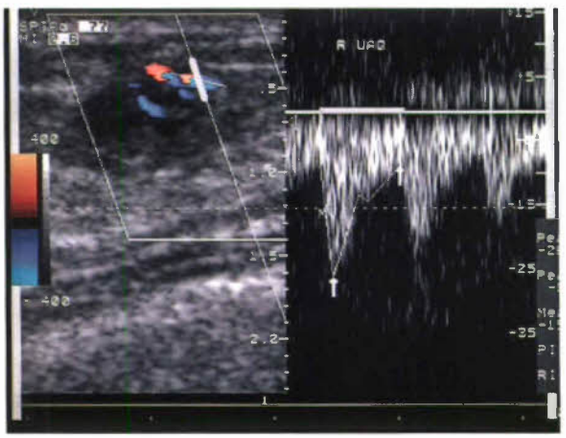

22a

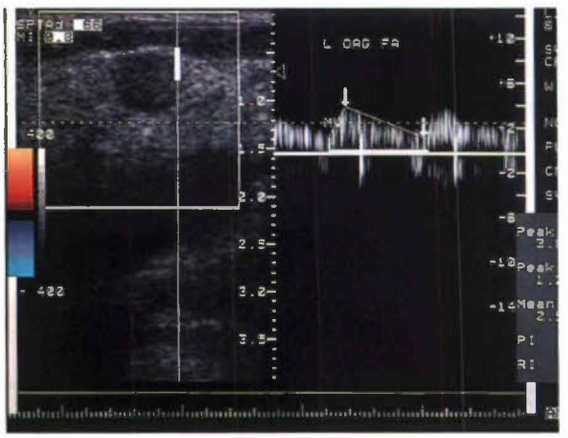

22b

Fig. 43.22 Fibroadenoma, 10 mm in diameter.
- **a** Color Doppler demonstrates a tiny vessel at the superior tumor margin.
- **b** Analysis in the duplex mode indicates a low flow velocity of 3.8 cm/s.

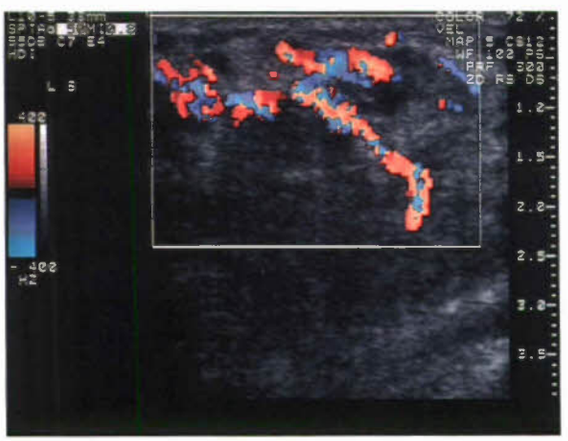

23a

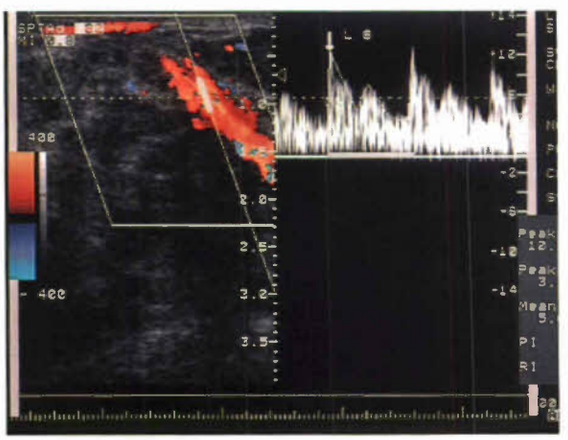

23b

Fig. 43.23 Mastitis with abscess formation.
- **a** The inflammatory process shows a rich vascular supply in the color Doppler image.
- **b** The flow velocity is 10.3 cm/s, which is still within normal limits.

24a

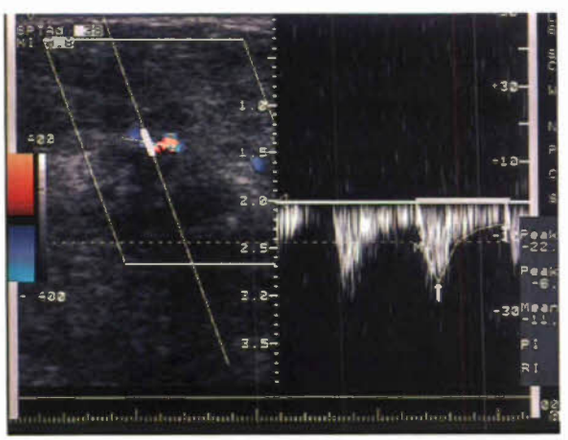

24b

Fig. 43.24 Hypovascular invasive ductal carcinoma.
- **a** Color Doppler shows scant vascularity, with only one demonstrable blood vessel.
- **b** Spectral analysis still indicates a high flow velocity of 22.5 cm/s.

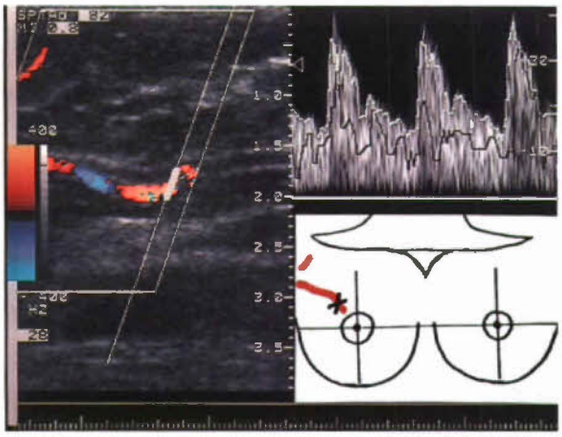

25

Fig. 43.**25** A large vascular trunk running from the axilla to the center of the breast. The flow velocity in this vessel is very high (34.6 cm/s). If these vessels were sampled near a (benign) tumor, they could be misinterpreted as a suspicious finding.

26

Fig. 43.**26** Color Doppler artifact caused by microcalcifications in an area of proliferative fibrocystic change. Mammography showed clustered calcifications in this area. B-mode ultrasound demonstrates several faint punctate echoes. Color Doppler shows a fluctuating color signal that could easily be mistaken for a vessel. Duplex analysis shows that it is not a flow signal, but a reverberation artifact caused by sound reflections from the microcalcifications. This case illustrates the rule that duplex should always be used for color analysis, in order to avoid errors.

in equipment, examination technique, and the selection of diagnostic criteria. Some groups of authors have limited their work to the qualitative analysis of color patterns [51,55,56]. This approach is unsatisfactory, as the subjective interpretation of color patterns does not allow findings to be quantified. A good Doppler system can detect blood flow not just in cancers but also in benign tumors and normal tissues, making it necessary to apply quantitative criteria when formulating a differential diagnosis. The simplest quantitative flow parameter was described by Cosgrove [52], who calculated the area of contiguous color pixels per unit tumor area. This technique, which was developed in England, is a greatly simplified form of blood flow measurement, but systems in current use are not programmed for this type of calculation.

Due to lingering uncertainties about the diagnostic importance of various Doppler parameters, we conducted an analysis of all known parameters in a prospective study of 258 patients with 176 benign lesions and 82 malignant lesions [54,57]. The results are summarized in Table 43.**8**. They basically indicate that Doppler spectral indices are not reliable predictors of whether a tumor is malignant or benign. It is noteworthy, however, that the resistance index (RI) values and A/B ratios are higher in malignancies than in benign tumors, and that all the parameters that reflect flow volume are significantly increased in malignant tumors.

Malignant tumors are typically supplied by a greater number of blood vessels, and the flow velocities in these vessels are higher than normal (Fig. 43.**21**). Benign tumors have very little vascularity, and the flow velocities are low (Fig. 43.**22**). An increase in the basal metabolic rate, such as that occurring during pregnancy, also leads to a significant increase in blood flow. Inflammatory changes may cause a similar effect, but are marked by profuse vascularity with a significant increase in venous flow but very little increase in arterial flow (Fig. 43.**23**). Differential-diagnostic problems result from the fact that a small percentage of malignancies (approximately 10%) are relatively hypovascular, and this can lead to false-negative results (Fig. 43.**24**). False-positive results may stem from a physiological rise in the metabolic rate or from unintended scanning of large, richly perfused vascular trunks in the breast (Fig. 43.**25**). This error can be avoided by tracing the scanned vessels back to their origins. Color reverberation artifacts from microcalcifications are also a common occurrence and may simulate a blood vessel (Fig. 43.**26**). This equivocal finding can be quickly resolved by attempting to sample a frequency spectrum from the "vessel" in the duplex mode.

Although the results have been very encouraging, color Doppler ultrasound cannot yet be recommended as a routine study for clinical breast imaging. The results still depend strongly on the equipment and the examiner. Other obstacles are the physiological variations in normal breast perfusion and the fact that some breast cancers have a scant vascular supply. Also, there is still some doubt as to the validity of using Doppler measurements as prognostic parameters. Nevertheless, our studies have demonstrated a correlation between the level of tumor blood flow and the presence of lymph-node metastases. Another potential application of color Doppler is for monitoring the response to the pharmacological treatment of fibrocystic breast changes [58] and cancer chemotherapy [59].

It appears, then, that Doppler ultrasound of the breast is a method of great scientific interest, but that further research is needed before it can

Table 43.**8** Comparison of the blood flow characteristics of benign and malignant tumors. The following Doppler parameters were analyzed: number of arterial tumor vessels (Art); average (V_{av}), maximum (V_{max}) and minimum (V_{min}) flow velocity; sum of flow velocities (V_{sum}); average (RI_{av}), maximum (RI_{max}) and minimum (RI_{min}) resistance index; and average (A/B_{av}), maximum (A/B_{max}) and minimum (A/B_{min}) A/B ratio (ratio of systole to diastole). The median (50% value) and the 25% and 75% quartiles were calculated. The differences between the two groups were tested for statistical significance using the Wilcoxon test (*P* and *z* values).

	Benign tumors (n = 176) Quartiles			Malignant tumors (n = 82) Quartiles			Wilcoxon test	
	25%	50%	75%	25%	50%	75%	*P*	*z*
Art (n)	1	2	2	5	8	14	0.0001	11.675
V_{av}	6.4	11.1	14.9	13.7	18.8	25.1	0.0001	7.733
V_{sum}	7	18.9	34.2	71.3	147.3	266.7	0.0001	11,152
V_{max}	6.7	12.5	18	22.5	32.5	47.3	0.0001	9.581
V_{min}	5.4	8.9	12.1	6.3	9.0	11.3	0.5698	0.568
RI_{av}	0.62	0.68	0.72	0.67	0.75	0.81	0.0001	4.801
RI_{max}	0.65	0.71	0.78	0.78	0.88	0.99	0.0001	7.881
RI_{min}	0.57	0.64	0.68	0.53	0.64	0.71	0.6942	0.393
A/B_{av}	2.7	3.1	3.7	3.2	4.3	7.7	0.0001	5.773
A/B_{max}	2.9	3.4	4.6	4.5	8.4	9.9	0.0001	8.819
A/B_{min}	2.3	2.8	3.2	2.2	2.9	3.5	0.8691	0.165

be recommended for routine examinations. Current work on the development of new ultrasound contrast agents holds considerable promise for the future, as the peripheral intravenous injection of these agents produces rapid Doppler signal enhancement in regions with abnormal vascularity [60]. This concept requires more rigorous clinical investigation, however, with the ultimate goal of using color Doppler in much the same way as contrast-enhanced MRI for the noninvasive discrimination of indeterminate breast lesions.

References

1 Statistisches Landesamt. Krebsregister Saarland. Saarbrücken: Statistisches Landesamt, 1991.
2 Schmidt-Matthiesen H, Basted G. Gynäkologische Onkologie. In: Schunemann H, Beaufort F, editors. Gynäkologische Malignome: Tumortherapie und Nachsorge bei Mamma- und Genitalmalignom. 3rd ed. Munich: Zuckschwert, 1989.
3 Milder AB. The Canadian National Breast Screening Study. In: Day NE, Milder AB, editors. Screening for Breast Cancer. Berne: Huber, 1988: 51–8.
4 Strax P, Venet L, Shapiro S. Mass screening in mammary cancer. Cancer 1969;23:875–8.
5 Tabar L, Fagerberg CJG, Day NE. The results of periodic one-view mammography screening in a randomized, controlled trial in Sweden. In: Day NE, Milder AB, editors. Screening for Breast Cancer. Berne: Huber, 1988: 33–44.
6 Verbeek ALM, Straatman H, Hendriks JHCL. Sensitivity of mammography in Nijmegen women under age 50: some trials with the Eddy model. In: Day NE, Milder AB, editors. Screening for Breast Cancer. Berne: Huber, 1988: 29–32.
7 Wild JJ, Reid JM. Echographic visualization of lesions of the living intact human breast. Cancer Res 1954;14:277–82.
8 Jellins J, Kossoff G, Reeve TS, Barraclough BH. Ultrasonic gray-scale visualization of breast disease. Ultrasound Med Biol 1975;1:393–404.
9 Harper AP, Kelly-Fry E, Noe JS. Ultrasound breast imaging: the method of choice for examining the young patient. Ultrasound Med Biol 1981;7:231–7.
10 Jellins J, Kossoff G, Reeve TS. Detection and classification of liquid-filled masses in the breast by gray scale echography. Radiology 1977;125:205–12.
11 Harper AP, Kelly-Fry E, Noe JS, Bies JR, Jackson VP. Ultrasound in the evaluation of solid breast masses. Radiology 1983;146:731–6.
12 Jellins J. Ultrasonic examination of the breast: international perspective. In: Kasumi F, Ueno E, editors. Topics in breast ultrasound. Tokyo: Shinohara, 1991.
13 Leucht W, Rabe D, Boos R, Humbert KD, von Fournier D, Schmidt W. [Value of high-resolution real-time sonography in Breast Cancer; in German.] Geburtshilfe Frauenheilkd 1984;44:557–62.
14 Jokich PM, Monticciolo DL, Adler YT. Breast ultrasonography. Radiol Clin North Am 1992;30:993–1009.
15 Sickles EA, Filly RA, Callen PW. Breast cancer detection with sonography and mammography: comparison using state-of-the-art equipment. AJR Am J Roentgenol 1983;140:843–5.
16 Madjar H, Jellins J, Schillinger H, Picker R, Kossoff GG. Ergebnisse der Mammasonographie am Ultrasonics-Institute in Sydney in der Krebsdiagnostik von 1980 bis 1983. In: Judmaier G, Frommhold H, Kratochwil A, editors. Ultraschalldiagnostik 84. Stuttgart: Thieme, 1985: 5.361–2.
17 Kamin T, Kameoka, S, Muraki H, et al. Significance of ductal findings in ultrasonic examination of the breast: diagnosis of intraductal tumor and intraductal spreading of breast cancer. In: Kasumi F, Ueno E, editors. Topics in breast ultrasound. Tokyo: Shinohara, 1991: 200–5.
18 Madjar H, Ladner HA, Sauerbrei W, Oberstein A, Prömpeler H, Pfleiderer A. Preoperative staging of breast cancer by palpation, mammography and high-resolution ultrasound. Ultrasound Obstet Gynecol 1993;3:185–90.
19 Madjar H, Makowiec U, Mundinger A, Du Bois A, Kommoss F, Schillinger H. [Value of high-resolution sonography in breast cancer screening; in German.] Ultraschall Med 1994;15:20–3.
20 Teboul M. A new concept in breast investigation: echo-histological acino-ductal analysis or analytic echography. Biomed Pharmacother 1988;42:289–95.
21 Fornage BD, Toubas O, Morel M. Clinical, mammographic, and sonographic determination of preoperative breast cancer size. Cancer 1987;60:765–71.
22 Holland R, Veling SH, Mravunac M, Hendriks JH. Histologic multifocality of Tis, T1–2 breast carcinomas: implications for clinical trials of breast-conserving surgery. Cancer 1985;56:979–90.
23 Kaiser WA, Zeitler E. MR imaging of the breast: fast imaging sequences with and without Gd-DTPA. Preliminary observations. Radiology 1989;170:681–6.
24 Fornage BD, Sneige N, Faroux MJ, Andry E. Sonographic appearance and ultrasound-guided fine-needle aspiration biopsy of breast carcinomas smaller than 1 cm3. J Ultrasound Med 1990;9:559–68.
25 Kremkau FW. Diagnostic ultrasound: physical principles and exercises. New York: Grune and Stratton, 1981.
26 Blood CH, Zetter BR. Tumor interactions with the vasculature: angiogenesis and tumor metastasis. Biochim Biophys Acta 1990;1032:89–118.
27 Folkman J, Watson K, Ingber D, Hanahan D. Induction of angiogenesis during the transition from hyperplasia to neoplasia. Nature 1989;339:58–61.
28 Samejima N, Yamazaki K. A study on the vascular proliferation in tissues around the tumor in breast cancer. Jpn J Surg 1988;18:235–42.
29 Plate KH, Breier G, Weich HA, Risau W. Vascular endothelial growth factor is a potential tumour angiogenesis factor in human gliomas in vivo. Nature 1992;359:845–8.
30 Weidner N, Semple JP, Welch WR, Folkman J. Tumor angiogenesis and metastasis: correlation in invasive breast carcinoma. N Engl J Med 1991;324:1–8.
31 Dodd GD, Wallace JD, Freundlich IM, Marsh L, Zermino A. Thermography and cancer of the breast. Cancer 1969;23:797–802.
32 Gautherie M, Haehnel P, Walter JP, Keith LG. Thermovascular changes associated with in situ and minimal breast cancers: results of an ongoing prospective study after four years. J Reprod Med 1987;32:833–42.
33 Sterns EE, Zee B. Thermography as a predictor of prognosis in cancer of the breast. Cancer 1991;67:1678–80.
34 Feldman F. Angiography of cancer of the breast. Cancer 1960;23:803–10.
35 Fuchs HD, Strigl R. [Diagnosis and differential diagnosis of breast cancer using intravenous DSA; in German.] RöFo 1985;142:314–20.
36 Maeda M. [New angiographic knowledge regarding the female breast; in German.] RöFo 1979;130:711–5.
37 Powell DE, Stelling CB. Magnetic resonance imaging of the human female breast: current status and pathologic correlations. Pathol Annu 1988;23:159–94.
38 Stack JP, Redmond OM, Codd MB, Dervan PA, Ennis JT. Breast disease: tissue characterization with Gd-DTPA enhancement profiles. Radiology 1990;174:491–4.
39 Wells PT, Halliwell M, Skidmore R, Webb AJ, Woodcock JP. Tumour detection by ultrasonic Doppler blood-flow signals. Ultrasonics 1977;15:231–2.
40 Bamber JC, Sambrook M, Minasian H, Hill CR. Doppler study of blood flow in breast cancer. In: Jellins J, Kobayashi T, editors. Ultrasonic Examination of the Breast. New York: Wiley, 1983: 371–8.
41 Burns PN, Halliwell M, Wells PN, Webb AJ. Ultrasonic Doppler studies of the breast. Ultrasound Med Biol 1982;8:127–43.
42 Madjar H, Jellins J, Schillinger H, Hillemanns HG. Differenzierung von Mammakarzinomen durch CW-Doppler Ultraschall. Ultraschall 1986;7:183–4.
43 Minasian H, Bamber JC. A preliminary assessment of an ultrasonic Doppler method for the study of blood flow in human breast cancer. Ultrasound Med Biol 1982;8:357–64.
44 Schild R, Fendel H. [Doppler ultrasound differentiation of benign and malignant breast tumors; in German.] Geburtshilfe Frauenheilkd 1991;51:969–72.
45 Srivastava A, Webster DJ, Woodcock JP, Shrotria S, Mansel RE, Hughes LE. Role of Doppler ultrasound flowmetry in the diagnosis of breast lumps. Br J Surg 1988;75:851–3.
46 Madjar H, Giese E, Schillinger H. Durchblutungsmessungen an Mammatumoren. Vergleich mit Prognosefaktoren. Arch Gynecol Obstet 1989;245:697–8.
47 Madjar H, Sauerbrei W, Münch S, Prömpeler H, Schillinger H. [Analysis of a method for Doppler study of the female breast; in German.] Ultraschall Med 1990;11:196–201.
48 Madjar H, Vetter M, Prömpeler HJ, Wieacker P, Schillinger H. [The normal vascularization of the female breast in Doppler ultrasound; in German.] Ultraschall Med 1992;13:171–7.
49 Madjar H, Sauerbrei W, Munch S, Schillinger H. Continuous-wave and pulsed Doppler studies of the breast: clinical results and effect of transducer frequency. Ultrasound Med Biol 1991;17:31–9.
50 Schoenberger SG, Sutherland CM, Robinson AE. Breast neoplasms: duplex sonographic imaging as an adjunct in diagnosis. Radiology 1988;168:665–8.
51 Adler DD, Carson PL, Rubin JM, Quinn-Reid D. Doppler ultrasound color flow imaging in the study of breast cancer: preliminary findings. Ultrasound Med Biol 1990;16:553–9.
52 Cosgrove DO, Bamber JC, Davey JB, McKinna JA, Sinnett HD. Color Doppler signals from breast tumors: work in progress. Radiology 1990;176:175–80.
53 Madjar H, Prömpeler H, Kommoss F, Göppinger A. [Does color Doppler complement breast examination? In German.] Radiologe 1992;32:568–75.
54 Madjar H, Prömpeler HJ, Bauknecht T, Göppinger A, Pfleiderer A. CW- und Farbdoppler zur Blutflusserfassurig von Mammakarzinomen. In: W. Schmidt, editor. Jahrbuch der Gynäkologie und Geburtshilfe, 1994. Zülpich, Germany: Biermann, 1994: 87–93.
55 Luska G, Lott D, Risch U, von Boetticher H. [The findings of color Doppler sonography in breast tumors; in German.] RöFo 1992;156:142–5.
56 Ueno E, Tsunoda-Shimizu H, Nakamura N, Hirano M, Imanura A. Colour Doppler imaging for the diagnosis of solid breast masses. In: Kasumi F, Ueno E, editors. Topics in Breast Ultrasound. Tokyo: Shinohara, 1991.
57 Madjar H, Prömpeler HJ, Sauerbrei W, Wolfarth R, Pfleiderer A. Color Doppler flow criteria of breast lesions. Ultrasound Med Biol 1994;20:849–58.
58 Madjar H, Vetter M, Prömpeler H, Breckwoldt M, Pfleiderer A. Doppler measurement of breast vascularity in women under pharmacologic treatment of benign breast disease. J Reprod Med 1993;38:935–40.
59 Madjar H, Du Bois A, Kommoss F, Meerpohl HG, Pfleiderer A. Implementation of Doppler ultrasound for therapy control of breast malignancies treated with chemotherapy. Onkologie 1993;16:183–8.
60 Schlief R. Diagnostic potential of intravenous contrast enhancement in various areas of cardiovascular Doppler ultrasound: efficacy results of a multinational clinical trial with the galactose-based agent SHU 508 A. Echocardiography 1993;10:665–82.

Breast Ultrasound

44 3D and 4D Breast Ultrasound

Introduction

The tremendous advances that have been made in three-dimensional (3D) and four-dimensional (4D) ultrasound technology since the 1990s have greatly expanded the diagnostic capabilities available not just in the field of obstetrics and gynecology in general, but also in breast ultrasound. The incorporation of 3D breast ultrasound into clinical practice was a relatively slow process, however, in comparison with 3D prenatal ultrasound. This was due largely to the fact that the development of high-resolution 3D transducers for breast imaging lagged behind the development of abdominal and endovaginal 3D probes.

However, in the hands of an experienced examiner, 3D breast ultrasound can provide impressive images and outstanding diagnostic results that are entirely comparable to those in prenatal ultrasound. The tomographic analysis of a breast lesion and its surroundings in the three orthogonal planes and in surface-rendered views can yield a wealth of radically new information. The main advantages of this technology are improved benign–malignant discrimination, owing to the presence of a third (coronal) plane of section, the ability to scrutinize vascular structures in the glass-body mode, volumetry, and safe, precise guidance of percutaneous breast biopsies [1].

Examination Technique

Technical Requirements: Equipment for 3D Breast Ultrasound

The basic difference between 2D and 3D ultrasound is that 3D ultrasound acquires and stores not just individual images, but whole volumes made up of multiple adjacent two-dimensional slices, which can then be processed and analyzed in numerous ways. Whereas the examiner using conventional 2D ultrasound has to mentally assemble the individual sectional images in order to visualize an anatomical structure in three dimensions, 3D ultrasound can actually render a three-dimensional view of a structure and display it on the monitor.

Two main types of system are used in 3D breast ultrasound: the internal (integrated) 3D system and the external system. With an *internal 3D system*, a special 3D transducer is used that sweeps the scan plane through the tissue at the touch of a button, automatically acquiring a complete set of volume data (Fig. 44.**1**). The scan plane is swept through the "acquisition angle" by a small motor inside the transducer casing. The beam is swept through the region of interest in a fan-shaped pattern (Fig. 44.**2**). The sectional images captured during volume acquisition are spaced at equal intervals, encoding the exact location of each image slice and allowing for precise signal processing of the digitally stored image series [2]. The advantages of an integrated system include excellent image quality and a very short acquisition time for tissue volumes. This type of system is essential for 4D (real-time) volume imaging.

With an *external system*, a special 3D transducer is not required. A sensor is mounted on a standard 2D transducer. When used within a magnetic field, the sensor can accurately determine the position of the transducer in space. For volume acquisition, the transducer is swept through the tissue using a *freehand technique*. Special computer software is used to assemble the 2D images into a volume of interest [1,3]. The freehand technique causes some variability in the intervals between the individual 2D slices, and this has a negative effect on the precision and quality of the images, making it necessary to use interpolation software. Unlike an internal system, this method cannot be used for 4D imaging.

Table 44.1 Technical criteria for three-dimensional breast ultrasound

- Homogeneous image with high B-mode resolution
- Geometrical precision
- Short acquisition time with no motion artifacts
- Operator convenience

The technical criteria listed in Table 44.**1** should be followed in the routine practice of 3D breast ultrasound.

Planning and Protocol: Basic Steps in a 3D Breast Ultrasound Examination

Good two-dimensional image quality is a prerequisite for the successful 3D ultrasound examination of a breast lesion or region of the breast. Generally, the examination begins with a seamless 2D ultrasound examination of both breasts using the traditional technique. If this survey detects a focal abnormality or a suspicious area that requires further scrutiny with 3D ultrasound, that lesion or area is marked as a *region of interest* (ROI) or *volume of interest* (VOI) and is acquired as a volume block (3D data set).

A 3D ultrasound examination of the breast consists of *four basic steps* [3,4]:

- Volume acquisition (= data acquisition)
- Volume rendering
- Volume manipulation and image processing (= postprocessing)
- Storage of the volumes or rendered images

Volume Acquisition

First, the object of interest (e.g., an indeterminate breast lesion) is viewed in the two-dimensional B-mode image. A volume box of adjustable size is superimposed on the B-mode image so that it encompasses the entire lesion plus a margin of surrounding tissue. A button is then pushed to activate volume acquisition. It is important to select an optimum size and shape for the volume box. If the box is too small, it will not allow adequate evaluation of the lesion margins or perifocal tissue reaction. The operator also selects the size, shape, and orientation of the volume box when surface-rendering a lesion within the stored volume. In this case, the box should conform to the lesion in a way that yields an optimum surface-rendered image (Figs. 44.**3**, 44.**4**). For the same reasons, the value of the *acquisition angle* (the current maximum is 29°) should be tailored to the size of the VOI and is set on the scanner *before* volume acquisition. Another important aspect of planning the examination is to define the *acquisition axis*. Correct anatomical orientation (e.g., right/left orientation) can be established in the stored volume only if the transducer position at the time of volume acquisition is precisely known.

The *acquisition of volume data* takes from 0.5 to 3.0 seconds to complete, depending on the size of the VOI and the selected sweep speed of the transducer. To avoid motion artifacts, the transducer and patient should be as motionless as possible during this very brief time window. When the volume block has been acquired, it is digitally stored without loss or degradation in an electronic volume memory, from which the volume can be retrieved at any time after the examination is completed. The stored volume is shown on the monitor in a multiplanar display (Fig. 44.**5**).

3D/4D Visualization

3D visualization. The object of interest can be accessed from the stored volume and displayed in a variety of modes. The following display modes or *visualization modes* are most commonly used in 3D breast ultrasound:

- Multiplanar (= orthogonal) mode (see Figs. 44.**5**, 44.**6**)
- Niche mode (see Fig. 44.**7**)
- Surface mode (see Figs. 44.**8**, 44.**9**)
- Transparent mode (see Fig. 44.**10**)
- Minimum mode (see Fig. 44.**34**)
- Inversion mode (see Figs. 44.**29**, 44.**35**)
- Color mode (see Fig. 44.**69**)
- Glass-body mode (a combination of transparent mode and color mode; see Figs. 44.**31** and 44.**68**)

Vascular imaging in the glass-body mode or color mode requires volume acquisition using a combination of 3D and color Doppler or 3D and power Doppler.

4D visualization. In 4D ultrasound, a designated volume is continuously scanned at a high acquisition rate (up to 35 volumes/second). This provides a dynamic, real-time 3D display that can be used to evaluate the compressibility of a breast mass or guide a minimally invasive percutaneous biopsy.

Volume Manipulation and Image Processing

Various postprocessing options are available in each mode for optimizing the B-mode image quality and the 3D/4D display. These options include compound resolution imaging (CRI), focus frequency composite (FFC), tissue harmonic imaging (THI), and volume contrast imaging in the A or C planes (VCI-A, VCI-C). These new functions are used with varying frequency, depending on the nature of the investigation and the examiner's level of experience.

The 3D image can be optimized in various ways during postprocessing. The *color*, *brightness*, and *contrast* of the image can be directly adjusted on the monitor, and the image can be stored in this optimized form (Fig. 44.**10**). In the examination of cysts, the *threshold control* can be used to filter out echoes from material floating in the cyst fluid, making it easier to detect and evaluate any mural structures within the cyst. Setting the threshold too high (> 70) leads to iatrogenic wall defects, while setting it too low (< 20) does not allow optimum structural evaluation.

The "electronic scalpel" that is commonly used in 3D prenatal ultrasound to remove extraneous tissue areas can also be used for volume manipulation in 3D breast ultrasound. In actual practice, however, the removal of "extraneous" glandular breast tissue is usually carried out by adjusting the size and position of the volume box.

In the *rotation mode*, multiple surface-rendered or transparent images are rapidly computed and displayed at a designated interval. The first and last images in the desired animation sequence are preset on the monitor, and a satisfactory rotation angle is defined. Depending on the selected axis of rotation (x or y), the object can be viewed on the monitor from various angles while rotating about the x or y axis (Fig. 44.**11**).

The *VOCAL* program can be used to calculate the volume of breast masses (Figs. 44.**12**, 44.**13**).

Storage of Volumes and 3D Images

Original volumes can initially be stored digitally in the scanner memory (digital scanning eliminates problems of data loss or degradation). From there, selected volumes can be accessed and transferred onto various storage media such as CD, DVD, magneto-optical disk (MO disk), or removable hard disks for permanent archiving. For *documentation*, selected images can be transmitted as Digital Imaging and Communication in Medicine (DICOM) files from the scanner to the picture archiving and communication system (PACS) department of the office or hospital, or they may be printed out in traditional fashion.

The ability to store complete volumes without data loss makes it possible to conduct a complete examination of the stored volume block at any time while taking advantage of all the display options listed above. In addition, necessary *measurements* that the sonographer may have forgotten to take during the actual examination can be carried out in the stored volume. Another advantage is the ability to review and reevaluate certain findings.

Special software can be used to transfer the stored data from the scanner to a desktop computer for evaluation. It is also possible to send one or more volumes per data transmission to a second reader.

Display Options in 3D and 4D Breast Ultrasound

In the *multiplanar (triplanar) display*, all three mutually perpendicular image planes are displayed on the monitor immediately after volume acquisition (Fig. 44.**5**). The coronal (C) plane has special significance, as it is very difficult to visualize this plane with conventional 2D ultrasound. The individual scan planes are marked by lines and dots that help the examiner maintain orientation when the planes are moved or rotated.

A *tomographic survey* of the stored volume is among the most important options that are available in 3D ultrasound. The examiner can explore the tissue volume in detail like a pathologist, viewing millimeter-thin sections of the lesion and scrolling through it from top to bottom, front to back, or side to side.

The latest technical development in 3D technology is tomographic ultrasound imaging (TUI), in which a designated volume can be viewed dynamically in thin sections ("multi-slicing"). This principle, already familiar from other sectional imaging modalities such as computed tomography (CT) and magnetic resonance imaging (MRI), makes it possible to display a lesion on the monitor in multiple parallel planes. The examiner can freely select the direction of the analysis and the interval between slices (Figs. 44.**14**, 44.**66**, 44.**67**).

Another mode for taking a "virtual tour" of a lesion or tissue is the *niche display* (Fig. 44.**7**). The niche image can be uniformly adjusted by *translation* in all three planes. This mode not only provides a cutaway view of the breast lesion, but can also display its relationship to the nipple and duct system.

Another goal of 3D ultrasound is to generate a lifelike view of the object in three dimensions. This is accomplished by *volume rendering* (three-dimensional image reconstruction) [5]. Two modes of volume rendering are used in 3D breast ultrasound: the surface mode and the transparent mode.

In the *surface mode*, rendering is limited to the voxels (the smallest volume units), which are scanned *first* in the volume block. This process can provide a photorealistic view of surfaces (Figs. 44.**8**, 44.**9**).

1

Fig. 44.1 Volume transducer for three-dimensional/four-dimensional ultrasound examination of the breast 6–12 MHz (GE-Kretztechik, Austria).

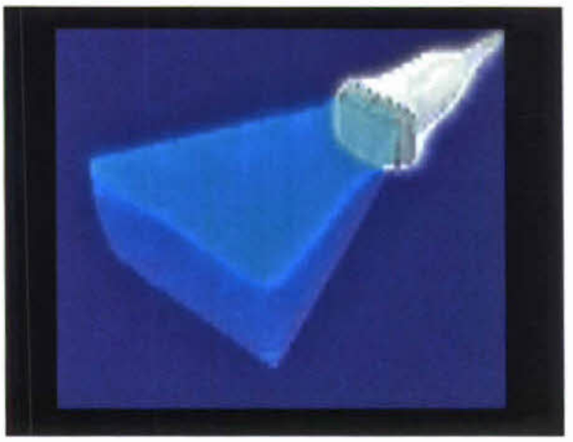

2

Fig. 44.2 Schematic representation of volume acquisition with an end-firing probe. A motor inside the transparent casing sweeps out the two-dimensional plane in a fan-shaped pattern, acquiring and digitally storing a volume block.

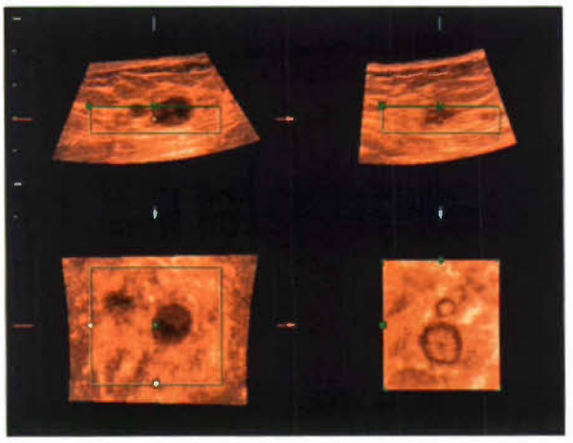

3

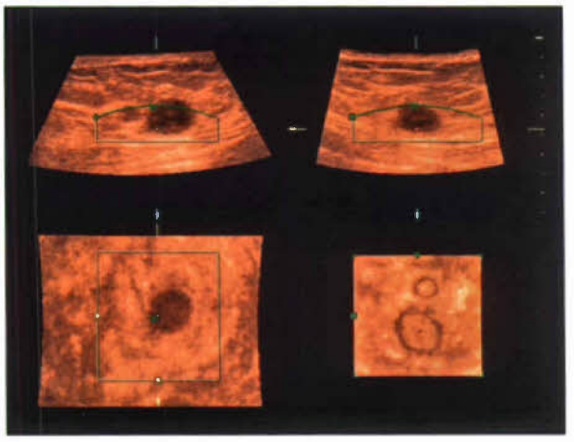

4

Fig. 44.3/44.4 Visualization of two small breast cysts. The volume box is adjusted to the lesion for optimum surface rendering of the region of interest (ROI). The operator can freely define the position, size, and shape of the box.

Fig. 44.3 Volume box with a straight green line.

Fig. 44.4 Volume box with a curved, convex green line.

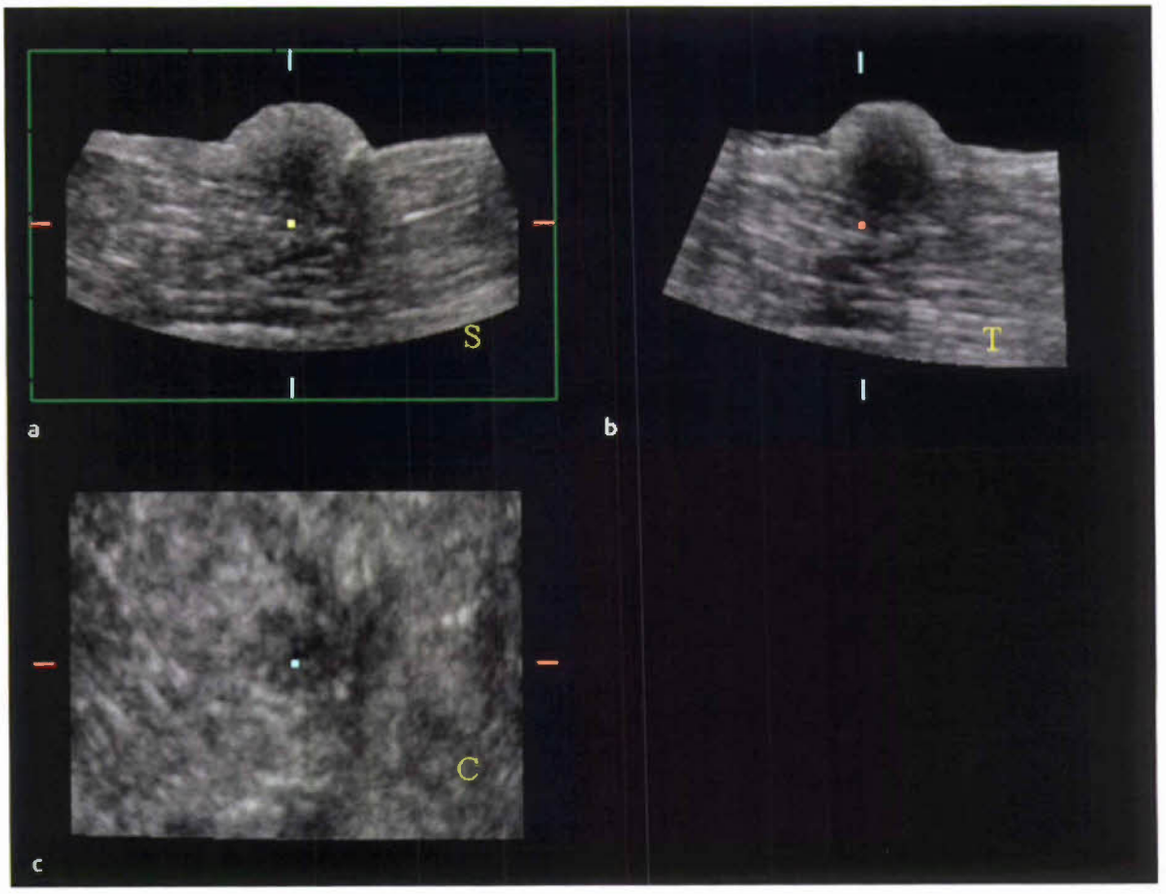

5

Fig. 44.5 Multiplanar (orthogonal) display of the nipple.
Sagittal (S) plane of section.
Transverse (T) plane.
Coronal (C) plane. The C plane is directed parallel to the chest wall.

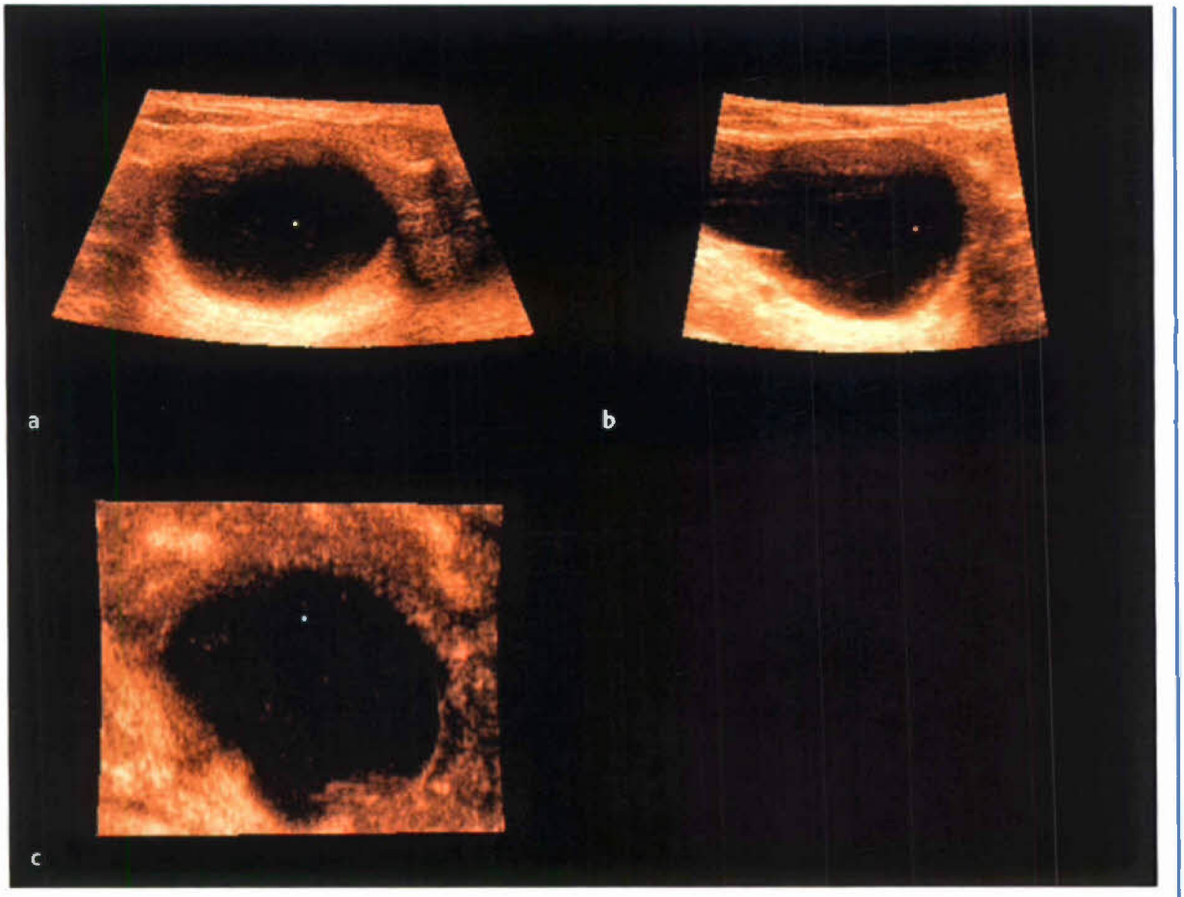

6

Fig. 44.6 Multiplanar display of a conglomerate cystic mass in the breast.

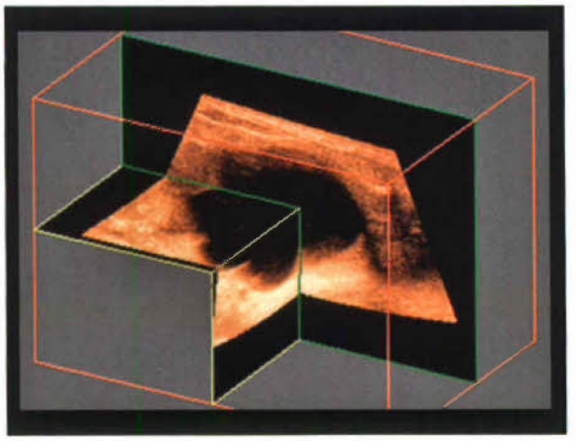

7

Fig. 44.7 Niche display of the tumor from Fig. 44.6. The three planes of section (sagittal, transverse, coronal) can be arbitrarily assembled in the niche mode to create a three-dimensional cutaway view.

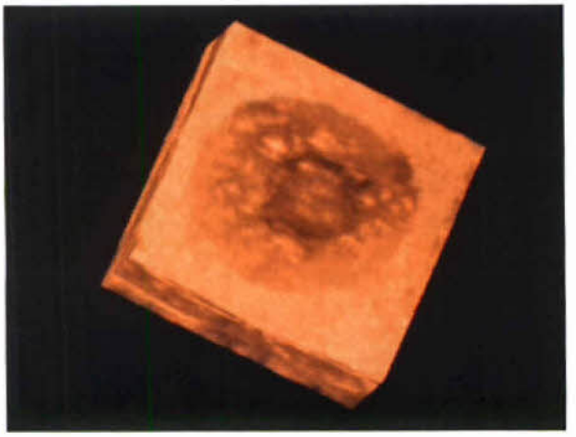

8

9

Fig. 44.8 Surface-rendered image of the nipple-areola complex viewed from the outside.

Fig. 44.9 The inner surface of a smooth-walled cyst.

Fig. 44.**10a–c** Postprocessing. Parameters such as brightness, contrast, and color selection can be varied as desired following volume acquisition. Here, an area of retroareolar fibrosis is displayed in different colors.

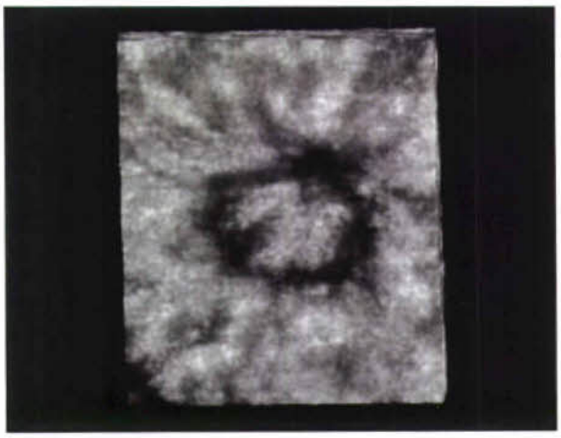

10a

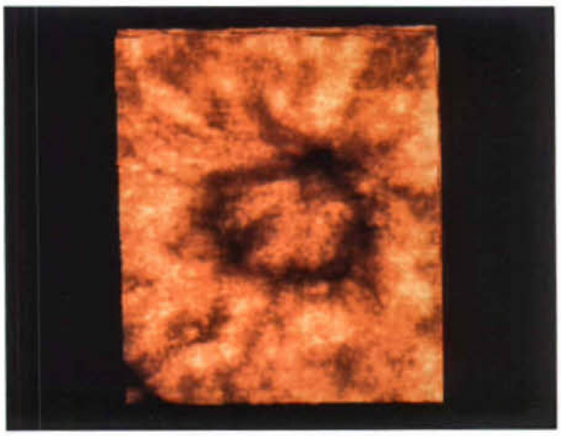

10b

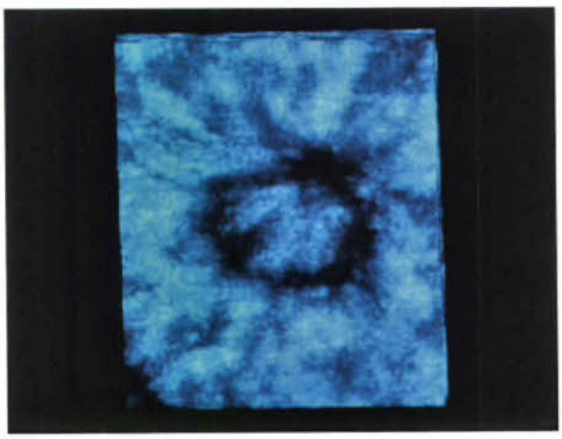

10c

Fig. 44.**11** In the rotation mode, multiple surface-rendered images are rotated through a total angle of 60° so that the lesion can be inspected from various angles. Also, a tumor can be rotated on the monitor to convey a better impression of its three-dimensional geometry. This image shows the inner wall of a smooth-bordered breast cyst.

Fig. 44.**12** The three-dimensional ultrasound system incorporates a computer program (VOCAL), with which the volume of a mass can be automatically or manually determined with fairly high precision.

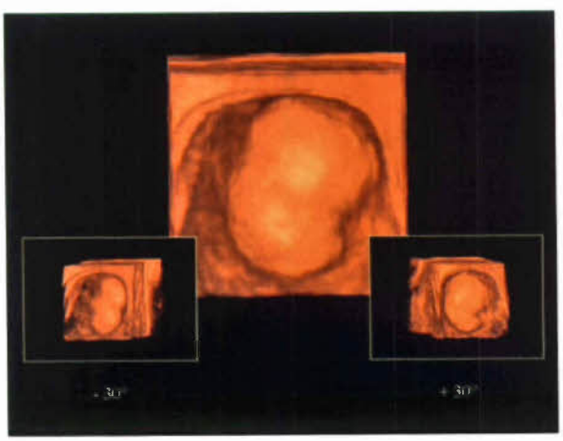

11

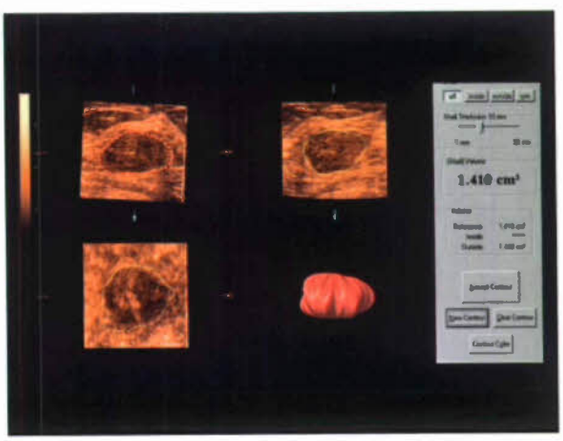

12

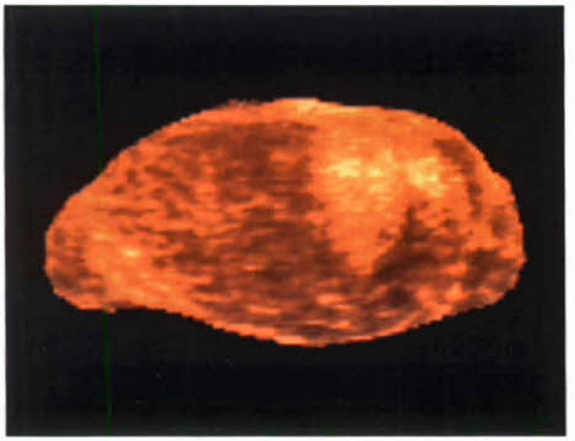

13a

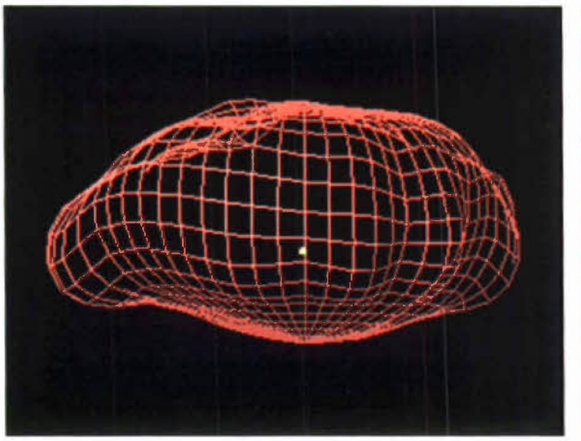

13b

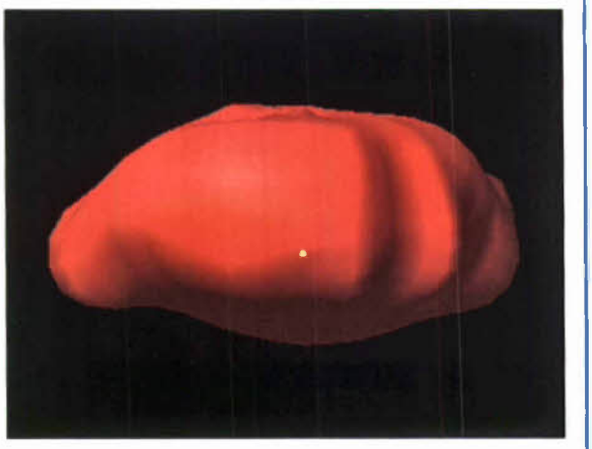

13c

Fig. 44.13a–c A breast mass can be electronically isolated and displayed in the form of a three-dimensional grid-lined or solid figure.

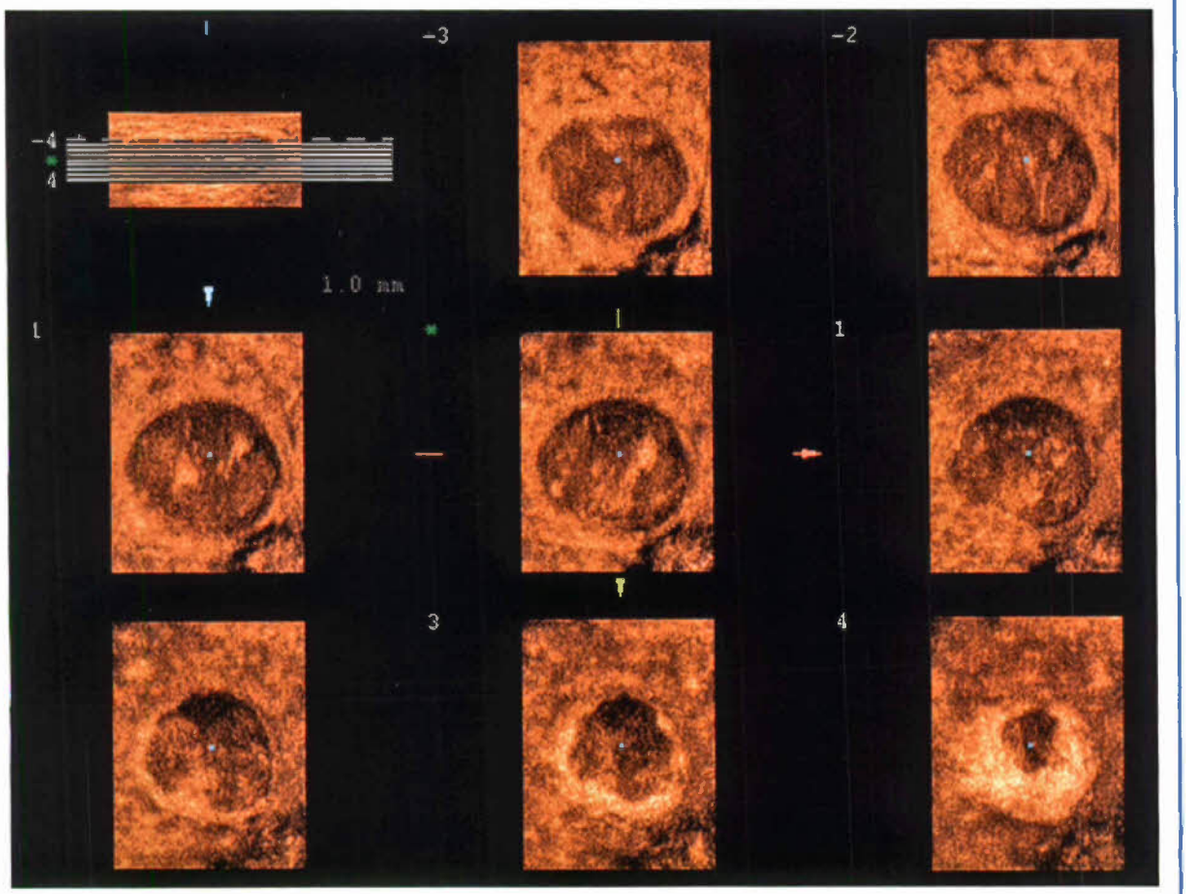

14

Fig. 44.14 Tomographic ultrasound imaging (TUI). This program allows the operator to scroll through a tumor in various dimensions and at designated slice intervals, similar to magnetic resonance imaging.

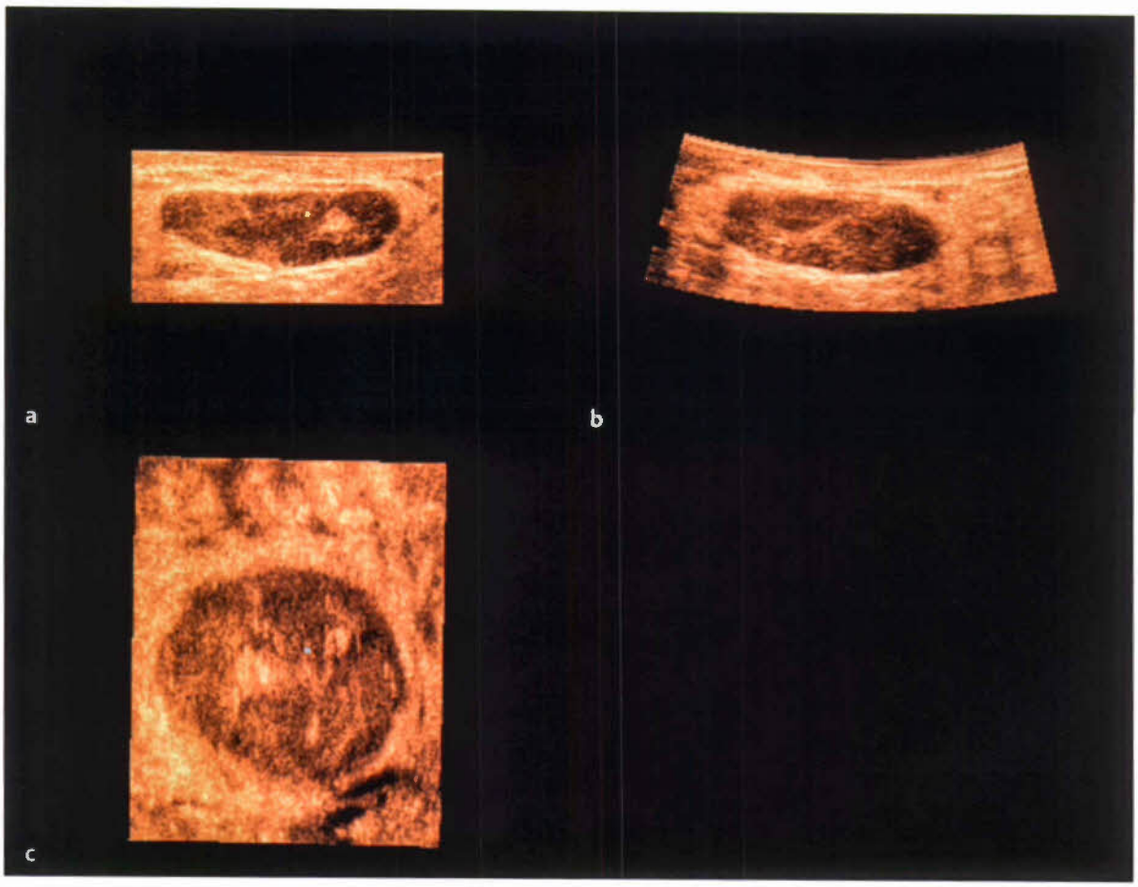

15

Fig. 44.15 Multiplanar display of a benign lesion. The coronal plane (lower left) shows a typical expansile type of tumor growth that compresses the surrounding parenchyma, forming a kind of "growth ring" around the tumor (= compression pattern).

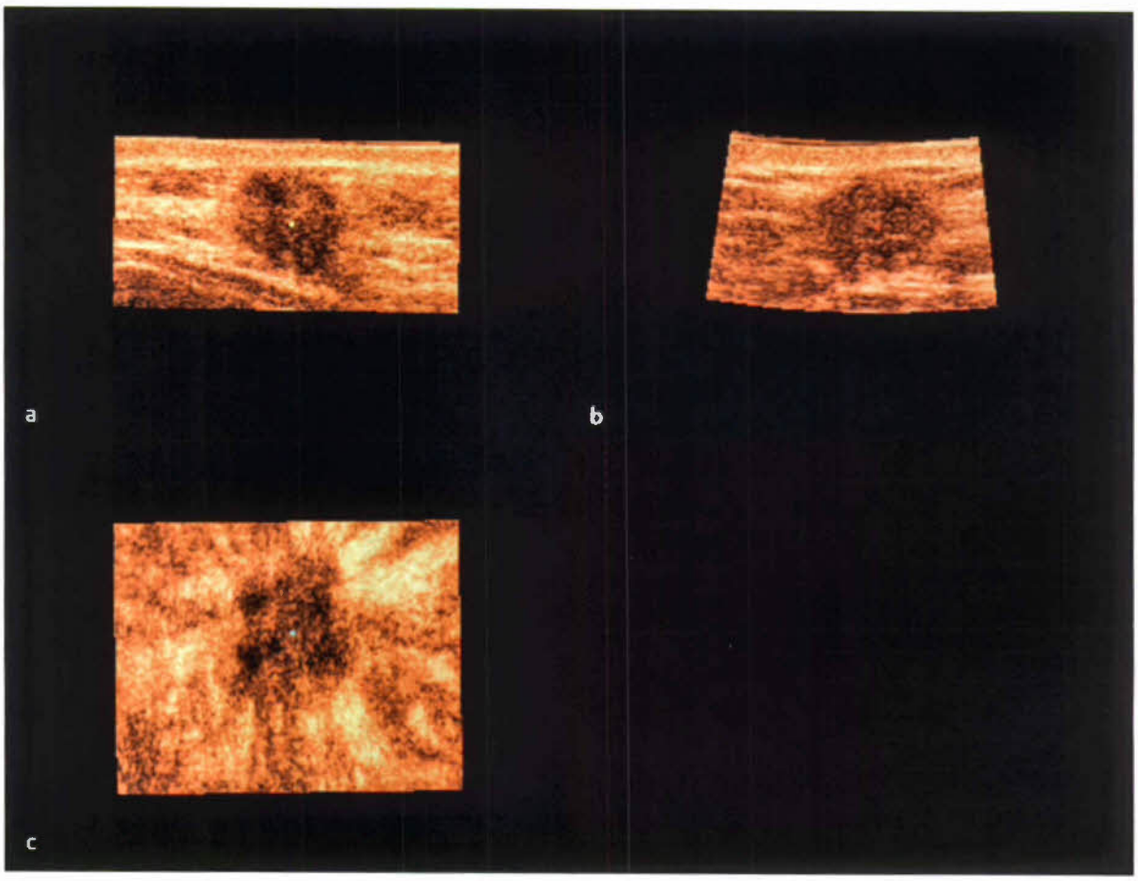

16

Fig. 44.16 Multiplanar display of a malignant lesion (in this case, an invasive ductal carcinoma 11 mm in diameter). The coronal plane (lower left) demonstrates a typical stellate pattern around the malignant tumor (retraction pattern).

In the *transparent mode*, the rendering algorithm generates a "see-through" display of the object. Extremely sonodense structures are displayed in the maximum mode, intermediate gray levels in the x-ray mode (Fig. 44.**70**), and echo-free masses (cysts, lactiferous ducts) in the minimum mode [2] (Fig. 44.**35**) or in the *inversion mode* (Figs. 44.**29**, 44.**35**).

An interesting variant of the transparent mode is *glass-body rendering*, in which the gray levels in the transparent view are combined with color Doppler or power Doppler signals. This can provide a three-dimensional display of blood flow, giving a detailed view of the blood vessels and their calibers inside a tumor (Fig. 44.**68**). The gray-level scale can even be switched off to provide an isolated view of tumor perfusion (ultrasound angiography) (Fig. 44.**69**).

The same modes that are available in 3D ultrasound can also be used in *4D ultrasound* (real-time 3D ultrasound).

Applications

Benign–Malignant Differentiation of Breast Lesions

During the past 30 years, the diagnostic criteria used for the differentiation of breast lesions in conventional 2D ultrasound have been rigorously analyzed and described in numerous publications [6–8]. When improved B-mode image quality became available in the late 1970s, the criteria of shape and sound transmission [8] were supplemented by other parameters such as margins, echogenicity, internal echo pattern, edge shadowing, and the L/T ratio [6,7]. Even today, however, there are no single criteria in 2D ultrasound that can reliably discriminate between benign and malignant lesions, and this differentiation is always based on a combination of parameters.

The triplanar view in 3D breast ultrasound displays the coronal plane of section in addition to the sagittal and transverse planes, providing an entirely new source of information. This makes it possible to scroll through all of the breast parenchyma from the nipple to the chest wall, proceeding in individual sections that are exactly parallel to the body surface. This method can detect breast lesions with a previously unknown degree of clarity.

As early as 1991, Rotten et al. [9] described the different appearances of benign and malignant benign lesions in the coronal plane and in surface-rendered images. In another study, Rotten et al. [10] investigated 186 solid breast tumors and analyzed the pattern of the surrounding tissue. Benign tumors such as fibroadenomas *grow by expansion*, displacing the surrounding tissue and producing a *compression pattern* (Figs. 44.**15**, 44.**17**). By contrast, malignant tumors *grow by infiltration* and incite a fibroplastic reaction; this creates a *retraction pattern* that is strongly suggestive of malignancy (Figs. 44.**16**, 44.**18**). Both growth patterns can be detected during volume acquisition in the coronal (C) plane. They are appreciated even more clearly in surface-rendered views of the C plane.

Statistically, the compression and retraction patterns have a high specificity (0.938), high sensitivity (0.914), and high positive and negative predictive values (PPV 0.869, NPV 0.960) for discriminating between benign and malignant tumors [10,11]. In a recent study investigating the growth patterns of 263 solid tumors, Weismann [12] found similarly high efficacy values for these diagnostic criteria. With a sensitivity of 0.995 and a specificity of 0.842 (PPV 0.919, NPV 0.991), the compression and retraction patterns were found to be strong predictors of the benignancy or malignancy of a circumscribed lesion.

Thus, characterizing a lesion in the coronal plane in 3D breast ultrasound is a valuable criterion in the differentiation of malignant and benign breast tumors. It should be emphasized, however, that it is not possible to assign all circumscribed breast lesions to one of the two main groups. According to Weismann [12], this third group comprises a total of 26% of all breast masses. It should be added that 83% of these *indifferent* lesions are benign.

Benign Breast Lesions

Fibroadenomas. When imaged by conventional 2D ultrasound, a typical fibroadenoma appears as a round, oval or lobulated mass with smooth, sharp margins (Figs. 44.**19**–44.**24**). Most fibroadenomas are uniformly hypoechoic and show distal acoustic enhancement. Older fibroadenomas frequently undergo regressive changes over time, making sonographic evaluation considerably more difficult. Sclerosing processes and the formation of macrocalcification clusters can transform an older fibroadenoma into a suspicious-appearing, hypoechoic, irregular, nonhomogeneous tumor with a distal acoustic shadow. Often, it is no longer possible to define the posterior tumor margin.

With 3D ultrasound, the tumor shape and margins can be displayed in the coronal plane and surface-rendered image without interference from macrocalcifications (Figs. 44.**17**, 44.**18**). The *compression pattern* typical of benign tumors, especially fibroadenomas, is produced when the expanding mass pushes against its surroundings. The tissue surrounding the nodule is compressed into an annular, echogenic "pseudocapsule" of variable thickness (Fig. 44.**15**).

Even with fibroadenomas that have undergone regressive changes, 3D ultrasound can exclude an infiltrative growth pattern, especially when the volume is also viewed in the rotation mode (Fig. 44.**25**).

Cysts and intracystic structures. Although cysts can be accurately evaluated with conventional 2D ultrasound, surface rendering can do more than display the cyst in just one plane. It can provide a complete, three-dimensional view of the inner cyst wall as if the examiner were looking into a cut-open specimen (Figs. 44.**26**–44.**28**). A detailed exploration of the inner cyst wall is particularly important for the confident detection or exclusion of small proliferative areas (Fig. 44.**30**). In cysts with protein-rich or inflammatory contents, 2D ultrasound cannot always positively distinguish intracystic debris from an excrescence on the cyst wall. 3D ultrasound can be particularly useful in these cases, as the threshold control can eliminate unwanted echoes and give a clear surface-rendered view of the inner cyst wall, making it possible to exclude proliferative changes.

Surface-rendered imaging of the subareolar region is an interesting new approach to the investigation of unexplained nipple discharge. It can demonstrate ectatic lactiferous ducts and detect any small mural papillomas that may be present (Figs. 44.**32**, 44.**33**). The minimum mode can clearly define hypoechoic structures like the lactiferous ducts, and the "inversion mode" can provide a three-dimensional view of the entire duct system, similar to a casting, which may eliminate the need for conventional ductography (Fig. 44.**35**).

Fibrocystic changes. Circumscribed areas of microcystic change are a common problem in breast diagnosis. They are almost always associated with irregular margins and with micro- and/or macrocalcifications. These features limit the value of conventional ultrasound for benign-malignant discrimination, and a biopsy is often required.

Again, imaging in the coronal plane will often reveal the true significance of these irregular margins, showing at once that the lesion is not infiltrating its surroundings, even though isolated broad but short spicules may be seen (Figs. 44.**36**, 44.**37**).

Scars. The diagnostic limitations of 2D ultrasound become even more apparent in the evaluation of scars. The distal acoustic shadow is a significant factor in this regard. The exclusion of a local recurrence is challenging in these cases and may be accomplished by reviewing previous mammograms, obtaining a core needle biopsy, performing color Doppler scans, or by using 3D ultrasound. Surface-rendered images can display the entire course of the scar from the skin surface to its posterior extremity (Fig. 44.**38**).

Fig. 44.**17** Example of a typical compression pattern in the surface-rendered image. Fibroadenoma.

Fig. 44.**18** Example of a typical retraction pattern. Invasive ductal carcinoma.

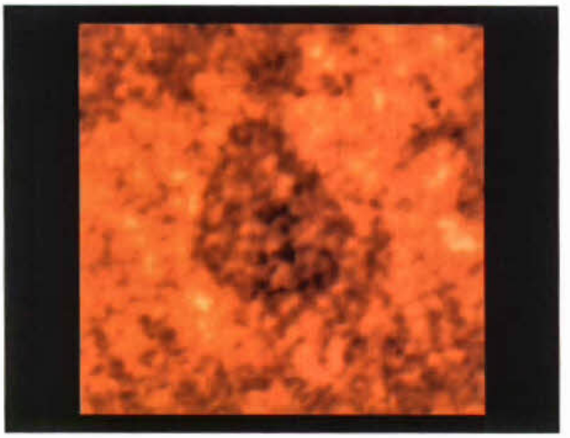

17

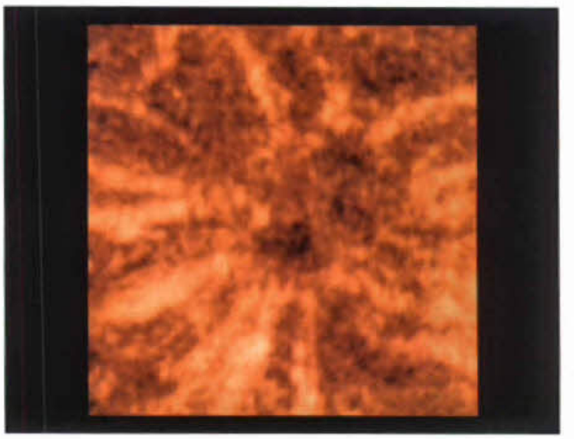

18

Figs. 44.**19**/44.**20** Two adjacent fibroadenomas in the surface-rendered image.

44.**19** This image shows only the anterior cut surface.

44.**20** This image shows the entire volume block after 60° of rotation. The obvious smooth margins and the relationship of the tumors to the skin and chest wall can be documented in a single image.

19

20

Figs. 44.**21**–44.**24** A lobulated juvenile fibroadenoma, displayed in the surface mode (Fig. 44.**21**) and glass-body mode (Fig. 44.**22**).

Fig. 44.**23** External view of the surgical specimen.

Fig. 44.**24** Cut-open view of the surgical specimen.

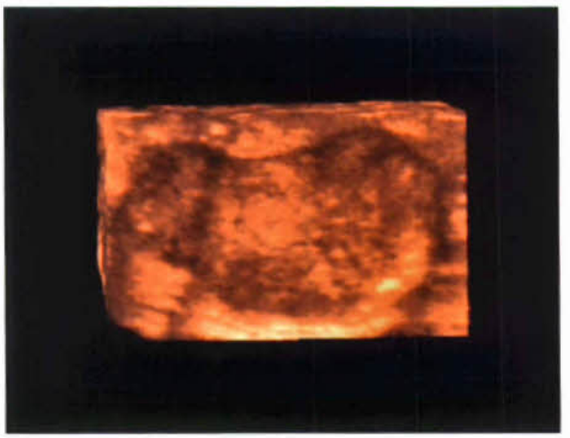

21

22

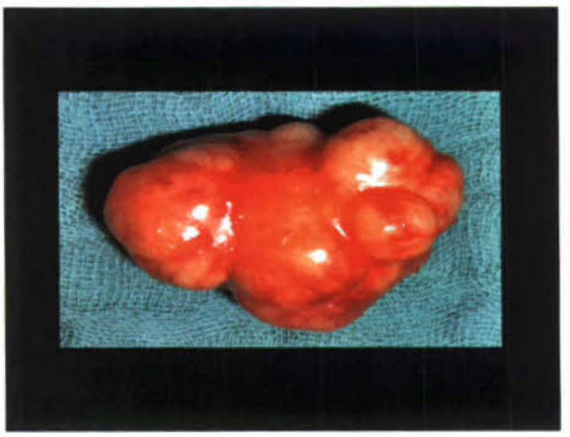

23

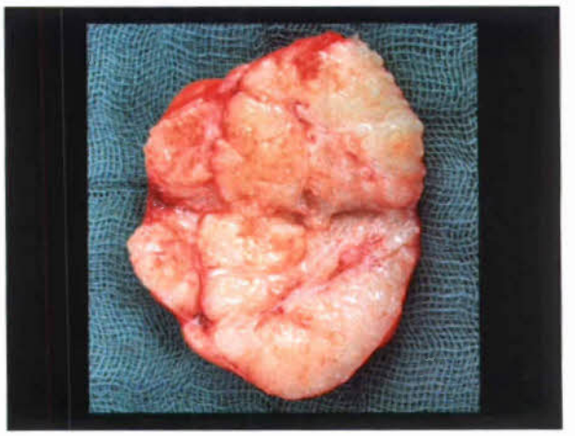

24

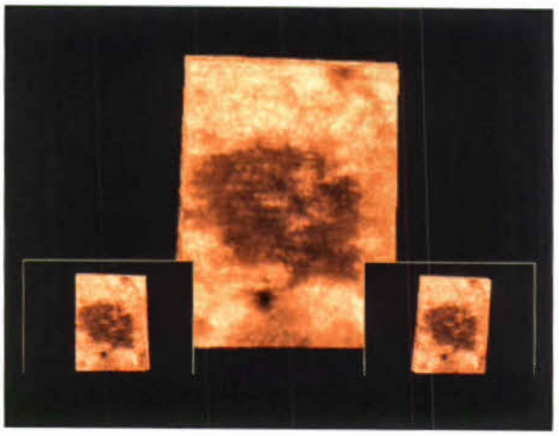

25

Fig. 44.25 Rotated views of a fibroadenoma that has undergone regressive changes. When the lesion and perifocal reaction are viewed from different angles, the external boundaries can be evaluated much more accurately than with conventional two-dimensional ultrasound. This makes it easier to exclude infiltrating margins.

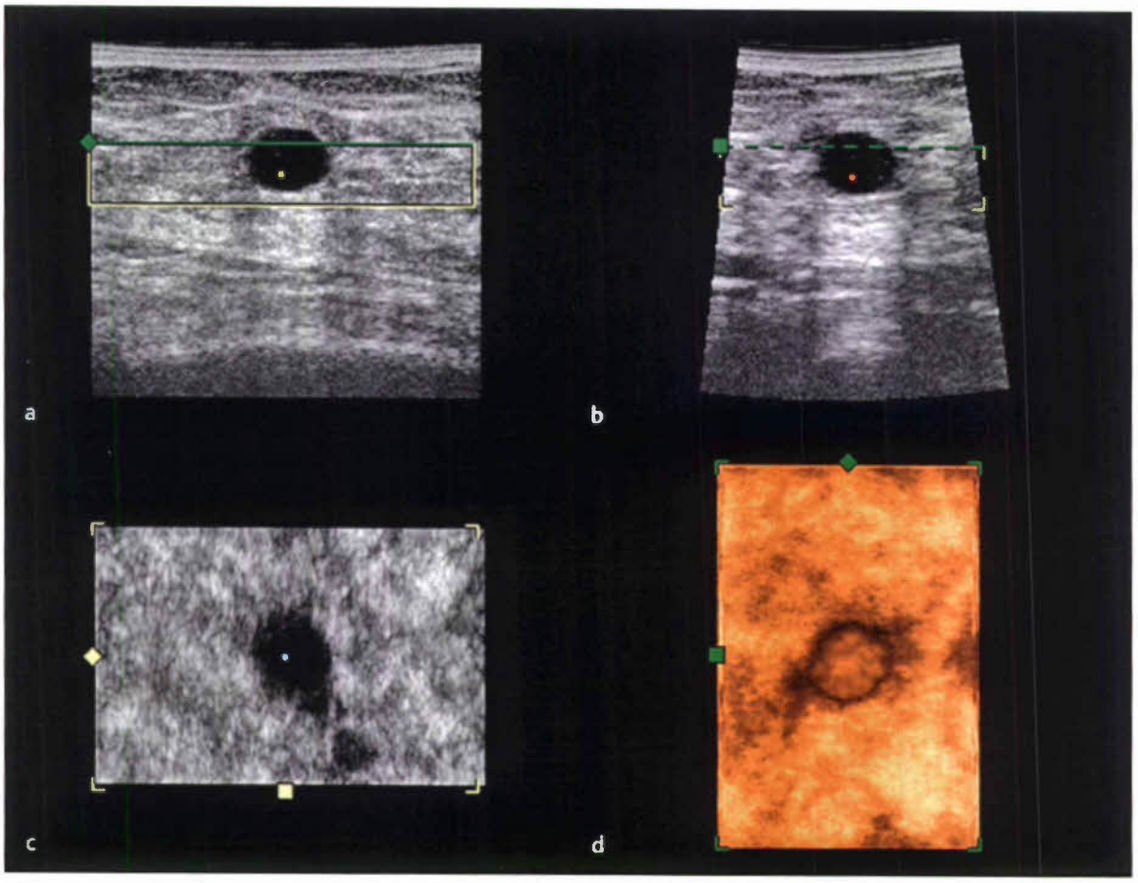

26

Fig. 44.26 Multiplanar display (**a**–**c**) and surface-rendered image (**d**) of a 6-mm breast cyst. The interior views demonstrate a completely smooth inner cyst wall.

Fig. 44.**27** Multiplanar display (**a**–**c**) and surface-rendered image (**d**) of a breast cyst 28 mm in diameter. As with fibroadenomas, a compression pattern can be seen when a large cyst is imaged in the coronar plane. The surface-rendered image displays a smooth cyst wall with no proliferative irregularities.

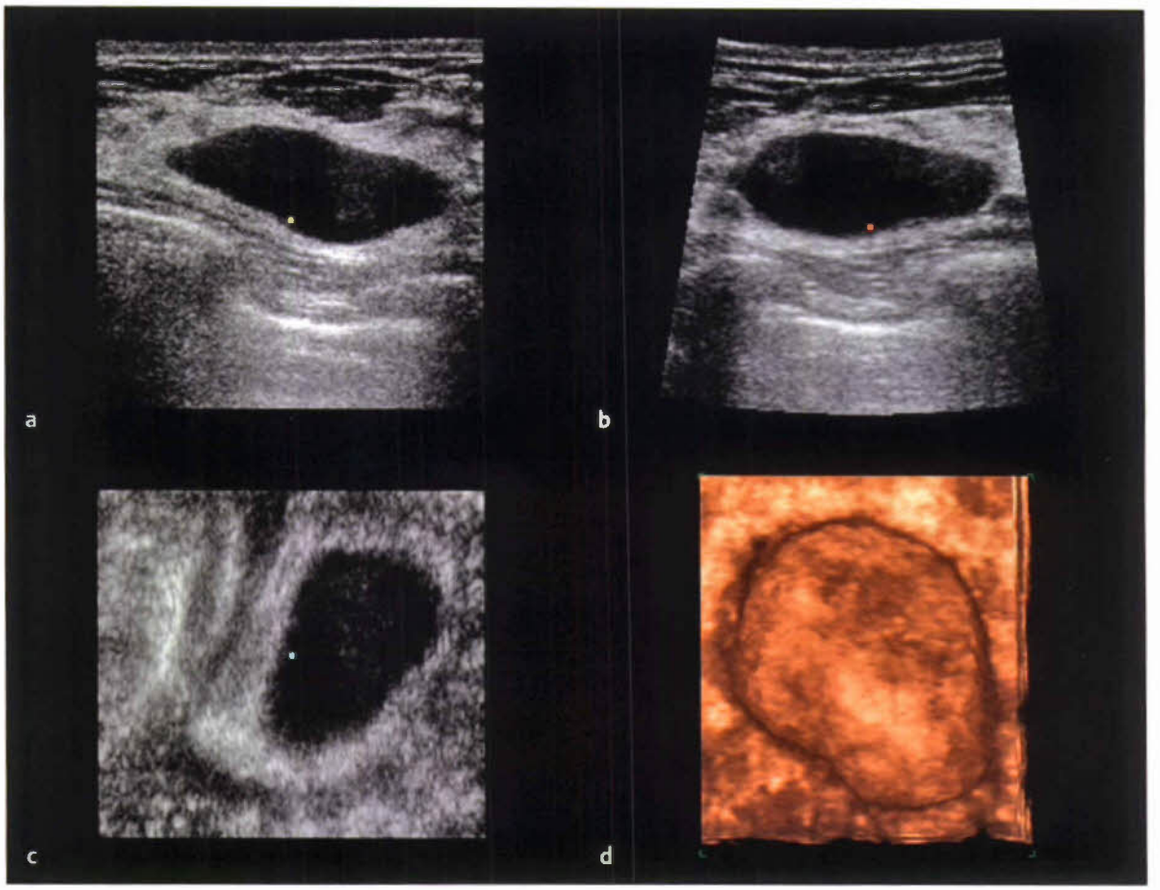

27

Fig. 44.**28** Surface-rendered image of aggregated breast cysts (sagittal section).

Fig. 44.**29** The same cysts, viewed in the inversion mode, which transforms the hypoechoic cysts into solid hyperechoic structures.

28

29

Figs. 44.**30**/44.**31** Ductectasia with a 4 mm papilloma on the duct wall.

44.**30** Surface-rendered image.

44.**31** Spatial configuration of the feeding vessels in the glass-body mode.

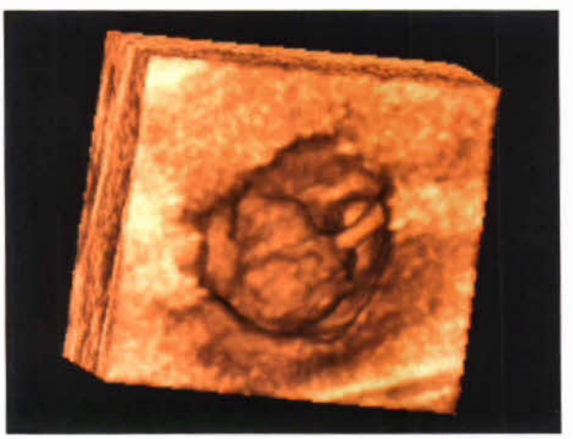

30

31

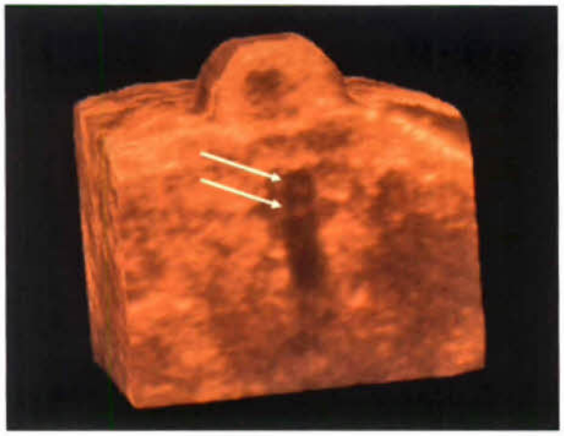

32

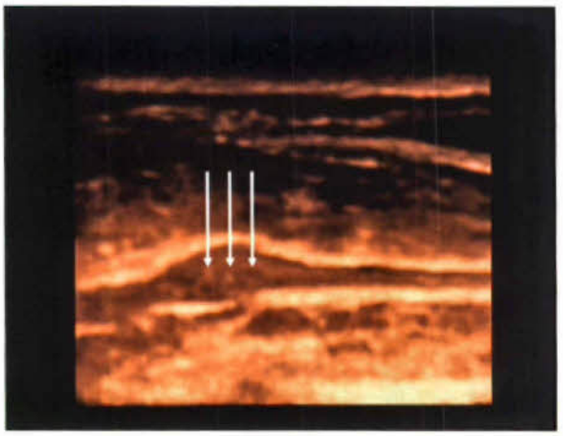

33

Fig. 44.32 Cut-open view (sagittal section) of the retroareolar region in a surface-rendered image. The patient presented clinically with a scant, bloody nipple discharge. The image shows two tiny papillomas (arrows) inside the smooth mammary duct, which is dilated to 4 mm.

Fig. 44.33 Three 1-mm papillomas (arrows) within a mammary duct. Surface-rendered image of the cut surface (sagittal section).

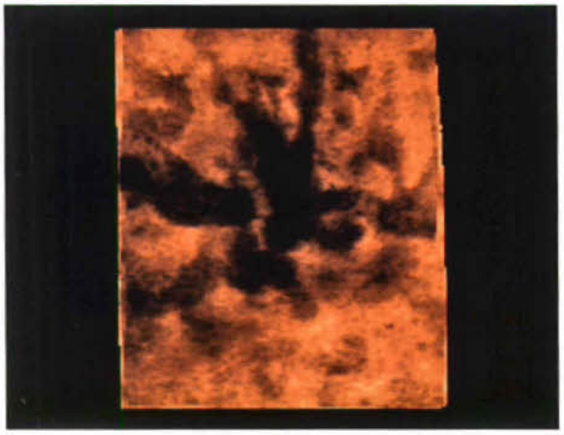

34

35

Fig. 44.34 Hypoechoic display of partially dilated ducts in the minimum mode.

Fig. 44.35 The immersion mode displays the duct system as a hyperechoic, solid-appearing figure that resembles a casting.

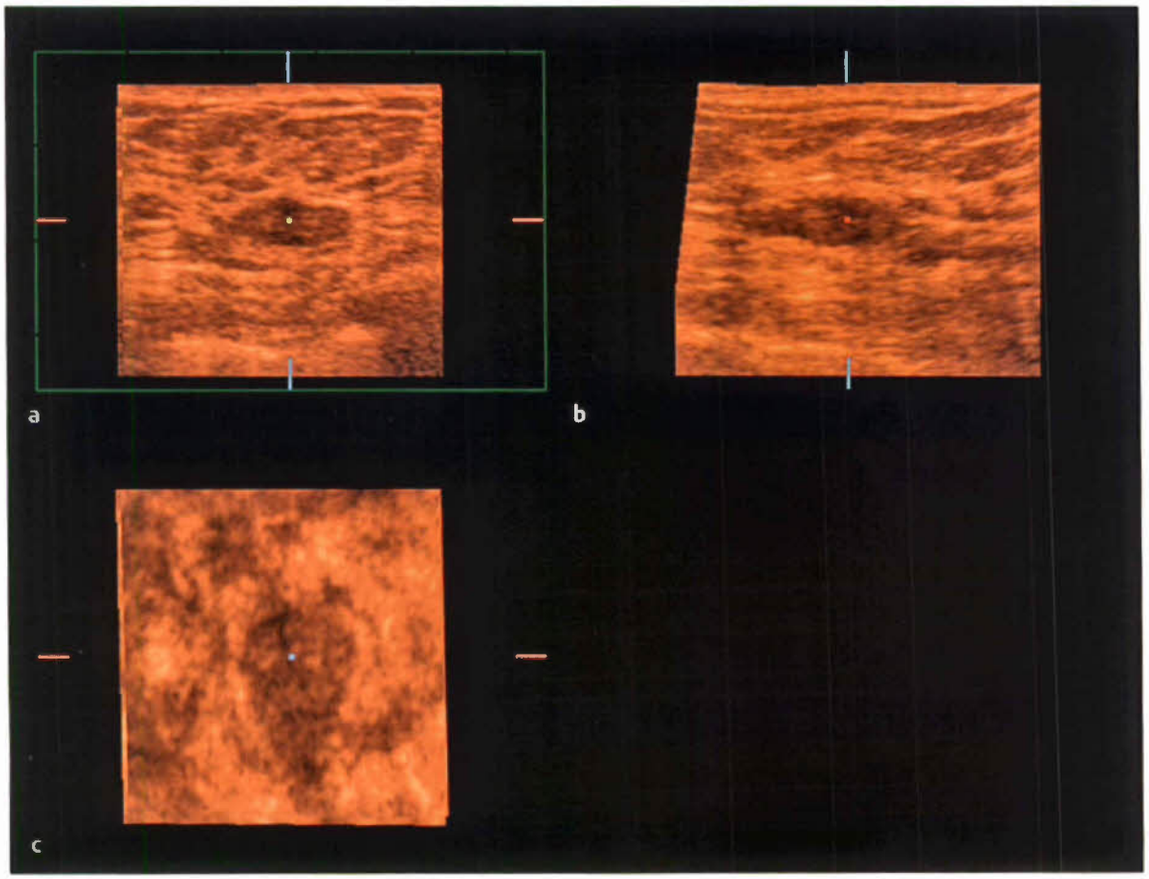

36

Fig. 44.36 Multiplanar display of a hypoechoic area of microcystic change. The two-dimensional images in the sagittal and transverse planes do not always allow a definitive diagnosis. The lesion can be evaluated more clearly in the coronal plane (coronal plane, lower left).

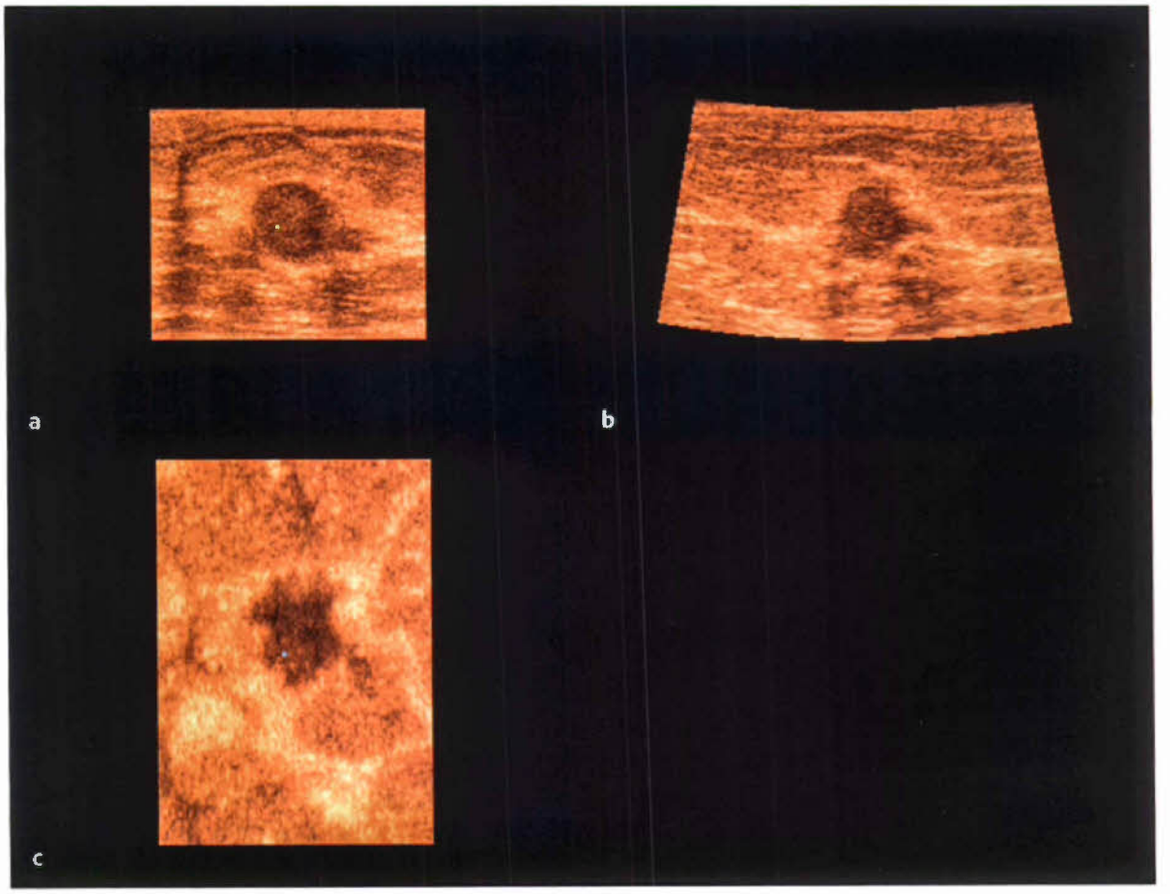

37

Fig. 44.37 Multiplanar display of a hypoechoic round nodule (7 mm in diameter). While the sagittal plane (**a**) and transverse plane (**b**) show only a tapered extension arising from the nodule, the coronal plane (**c**) reveals multiple short, broad-based spicules. We do not see the stellate pattern typical of a malignancy, however. Core biopsy identified the lesion as a fibrocystic change.

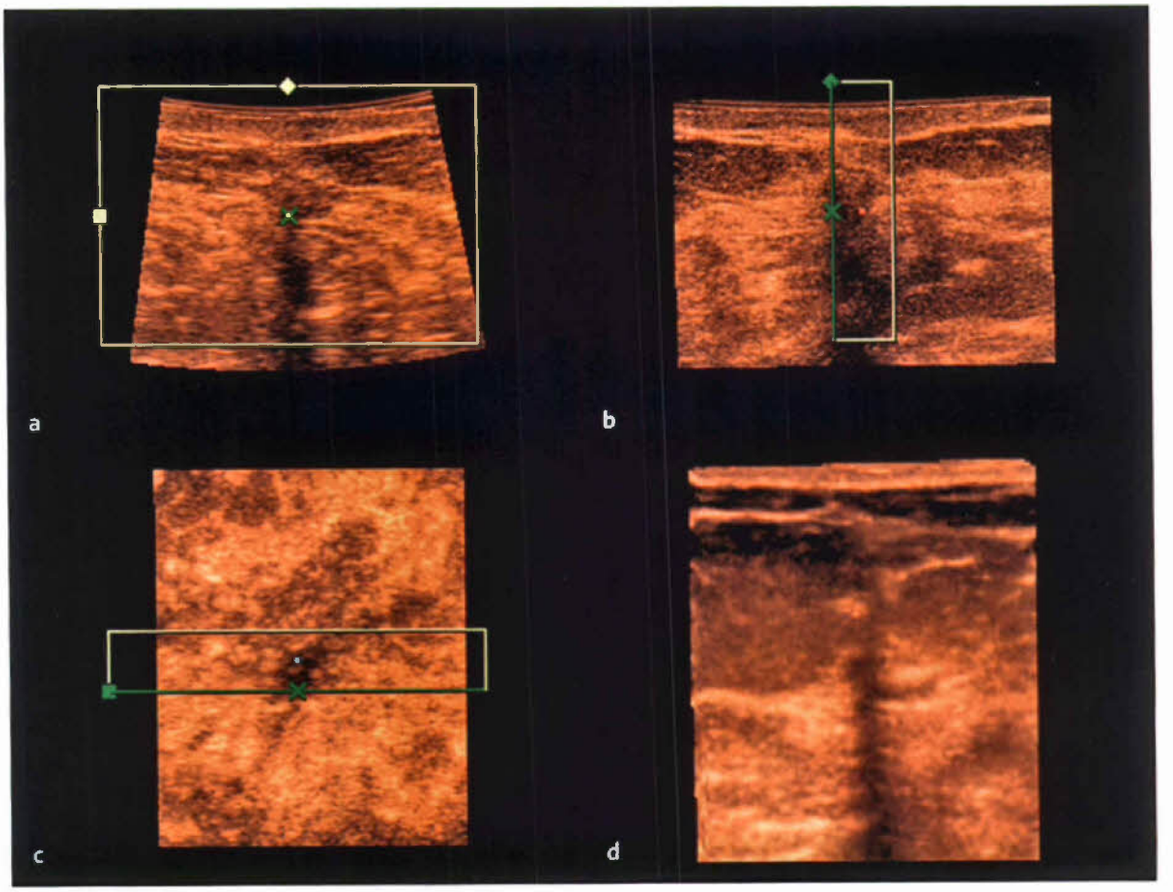

38

Fig. 44.38 Multiplanar display (**a**–**c**) of a normal-appearing scar from a previous breast biopsy.
d A surface-rendered image in sagittal section clearly demonstrates a continuous scar extending deep into the breast from the skin.

Malignant Breast Tumors

The correct interpretation of 3D images requires a detailed knowledge of the gross morphology of malignant breast tumors. Breast cancers have a protean appearance ranging from round masses with almost smooth margins (mostly medullary, tubular or mucinous carcinomas) and diffusely infiltrating lesions or ductal carcinoma in situ (DCIS), which may involve large areas of the breast and show a variety of growth patterns, to rare intracystic malignancies. This diversity is reflected in the variety of appearances that may be seen with 3D ultrasound.

Because most breast malignancies arise from the terminal duct system (75% of invasive breast cancers are ductal carcinomas), the coronal plane in 3D ultrasound offers excellent opportunities for analysis. For example, the narrow spicules that radiate from the lesion can be demonstrated from all sides and are not obscured by shadowing effects due to microcalcifications. Combined with the desmoplastic response and architectural distortion, this 3D view conveys the unmistakable impression of a *stellate* or *retraction pattern* (Figs. 44.**39**–44.**47**).

Invasive lobular carcinomas (10–15% of breast cancers), which arise in the epithelial layer of the lobules and grow diffusely along the ducts, vessels, and Cooper ligaments, may cause architectural distortion and create a *retraction pattern* in 3D ultrasound (Fig. 44.**46**).

A *retraction pattern* therefore creates a high index of suspicion for a malignant lesion. Tumor size has no bearing on the importance of this valuable diagnostic criterion. Among our own patients, we have been able to identify several small malignant masses 3–7 mm in diameter based solely on the presence of a retraction pattern (Fig. 44.**47**).

Noninvasive carcinomas (ductal carcinoma in situ, lobular carcinoma in situ) usually exhibit numerous broad extensions in the coronal plane with little or no evidence of a stellate pattern (Fig. 44.**48**). There are cases of DCIS, however, that already exhibit a definite stellate pattern (Fig. 44.**49**).

Among our own patients (n = 183), we also observed a retraction or stellate pattern in association with five benign lesions. One patient had retroareolar fibrosis (Fig. 44.**50**), two had fat necrosis, one had a postoperative seroma, and one had very circumscribed fibrosis (7 mm). We have also observed a pseudoretraction pattern caused by a radial scar and by one case of sclerosing adenosis.

Although most carcinomas show a characteristic retraction pattern of variable degree, malignant tumors are occasionally found that do not exhibit this typical stellate pattern (Figs. 44.**51**–44.**59**).

The detection of *multifocality* or *multicentricity* is of major importance in the preoperative planning of breast-conserving surgery. High-resolution breast ultrasound is definitely superior to mammography in this regard, as we showed in a 1993 study of 100 breast cancer patients [13].

With its capability for multiplanar views and detailed tomographic analysis, *3D ultrasound* adds an extra dimension to the detection of intraductal spread and multifocal disease (Figs. 44.**60**–44.**62**). The ability to define the spatial relationships of the tumors to one another and accurately measure their distances from one another and from the nipple are of great practical value in *treatment planning*.

Although ultrasound is the modality of choice for *oncologic follow-up*, there are situations in which 2D ultrasound has its limits. A prime example is differentiation between a scar and a recurrence (Figs. 44.**63**–44.**65**). The diagnosis can be significantly improved by color Doppler scanning, especially when it is combined with 3D ultrasound. The ability to define the entire course of a scar in the surface-rendered image in itself makes it easier to interpret the stellate density found in the 2D image (Fig. 44.**65**).

Tomographic Tumor Analysis

For the first time, 3D ultrasound provides a CT-like imaging modality that can be repeated as often as desired and can display thin slices of a tumor or organ segment from the skin to the chest wall. Through tomographic tumor analysis in the coronal plane, the *boundaries of the tumor* can be completely and accurately defined. A slice-by-slice survey is particularly rewarding in the analysis of nonhomogeneous masses (benign and malignant tumors) and of tumors with microcalcifications or macrocalcifications or necrotic components. Like CT and MRI, tomographic ultrasound imaging (TUI) can simultaneously display multiple contiguous slices on the monitor. This makes it possible to analyze lesions along various axes and at varying slice intervals (Figs. 44.**66**, 44.**67**).

3D Vascular Imaging

The 3D volume acquisition of a breast mass, combined with color or power Doppler imaging (*glass-body rendering*), can provide a precise, three-dimensional display of tumor vascularity and feeding vessels (Figs. 44.**31**, 44.**68**, 44.**69**).

Qualitative and quantitative differences in the neovascularization of malignant tumors compared with the vascularity of normal tissue and benign tumors have been investigated by 2D ultrasound in numerous studies [14–16]. Criteria such as vessel count, flow velocity, and intralesional vascular resistance do not allow a definitive differentiation of malignant and benign tumors. Despite a tendency for malignant tumors to have greater vascularity, a considerable overlap is found between avascular carcinomas and hypovascular benign tumors such as fibroadenoma. The results have been somewhat improved by the use of ultrasound contrast agents [17].

The visualization of vessels within a tumor and about its periphery is an important suggestive sign in the diagnosis of malignant tumors (Figs. 44.**68**, 44.**69**). The great majority of carcinomas (95%) show an irregular configuration of confluent vessels with stenoses and dilatations, constituting a typical *basic pattern (type 3a/b)* (Fig. 44.**71**). This pattern is distinguished from the *benign type (type 2a/b)*, which is characterized by scant vessels of equal size in the peripheral part of the tumor. There is also an *avascular type* in which no tumor vessels can be visualized [18] (Fig. 44.**71**).

The different vascular patterns have proven helpful not only in tumor differentiation but also in difficult problems such as distinguishing between a scar and a local recurrence. It is also possible to determine the vascularity of a tumor at different times, such as before, during and after neoadjuvant chemotherapy, and compare the findings by reviewing the stored volumes. Parameters such as the vascularity index (VI), flow index (FI), and vascularization flow index (VFI) are available for the quantitative analysis of vascularity in a volume [19].

Glass-body rendering is an optimum mode for the *visualization of perfusion*. Unlike two-dimensional vascular imaging, which displays only individual sections and is thus limited to isolated vascular segments (which may not be representative), 3D ultrasound can demonstrate *all of the tumor blood supply*. In the rotation mode, where multiple planes in the glass-body mode are rendered at a designated angle, the rotation of the tumor on the monitor allows the overall tumor vascularity to be scrutinized from various angles.

Occasionally, we see cases in which color Doppler must be added in order to make a correct diagnosis. One sharply circumscribed tumor that was classified as benign by mammography and by 2D/3D ultrasound showed a malignant type of vascularity when viewed in the glass-body mode (Fig. 44.**57**). Investigation by core biopsy identified the tumor as a soft-tissue manifestation of plasmacytoma.

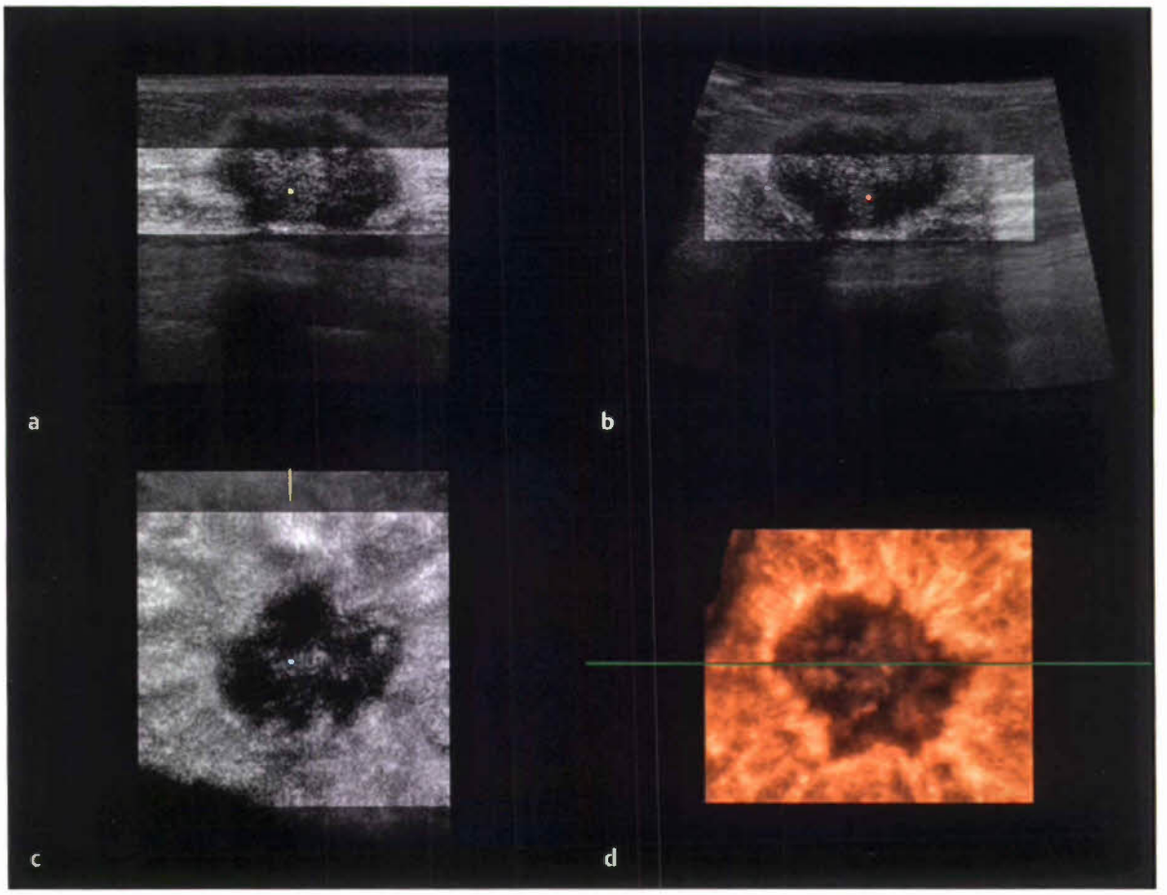

Fig. 44.**39** Multiplanar display (**a**–**c**) of a 22-mm, hypoechoic, transverse oval breast mass in a 40-year-old woman. While the mass appears fairly innocuous in the sagittal and transverse planes, the coronal plane demonstrates a retraction pattern that is suspicious for carcinoma.

d The same pattern appears in the surface-rendered image. Histology confirmed that the lesion was invasive ductal carcinoma.

39

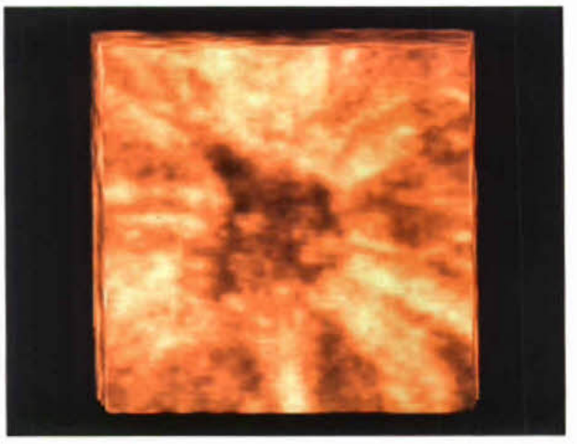

40

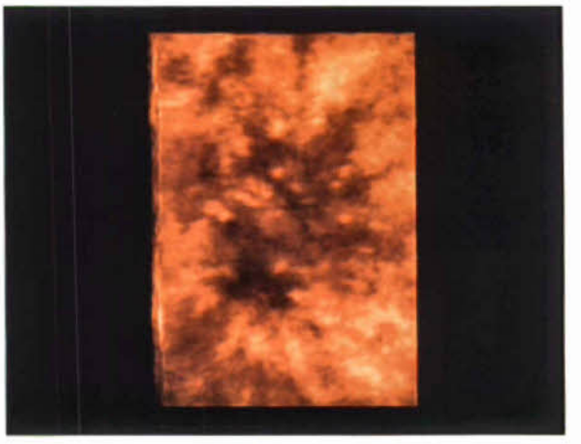

41

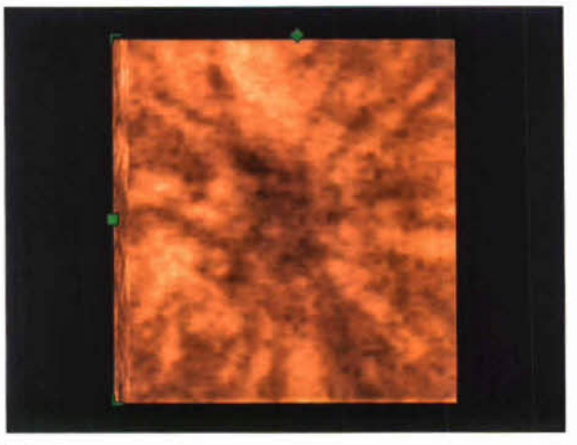

42

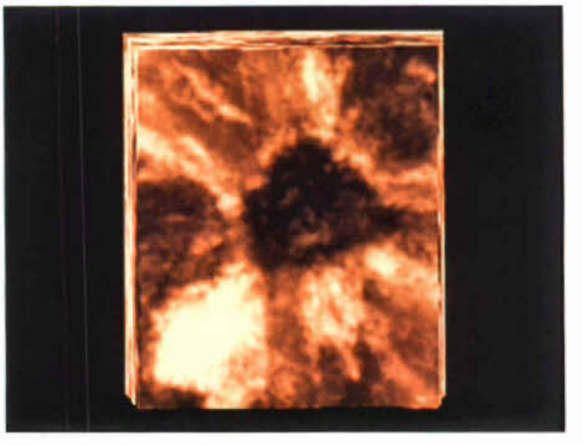

43

Figs. 44.**40**–44.**46** Typical retraction patterns associated with different invasive ductal breast carcinomas (Figs. 44.**40**–44.**45**) and an invasive lobular carcinoma (Fig. 44.**46**). The stellate pattern is appreciated particularly well in the coronal surface-rendered image. Surface views.

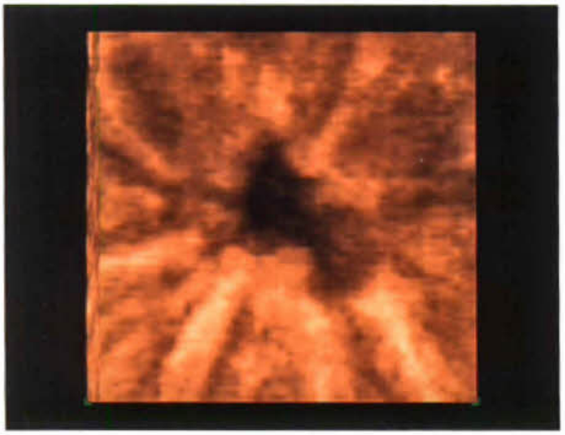

44

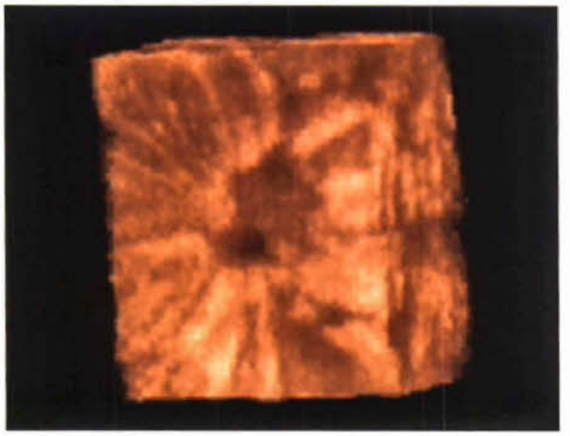

45

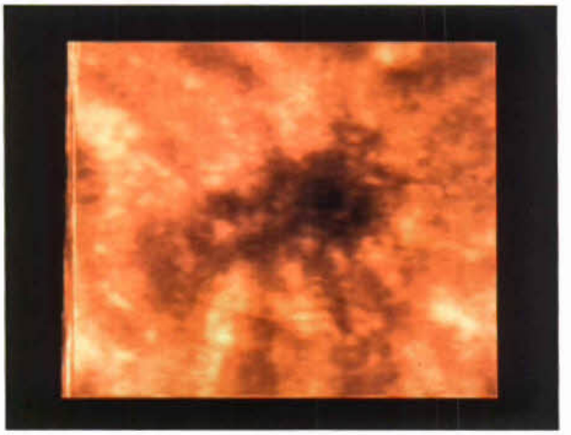

46

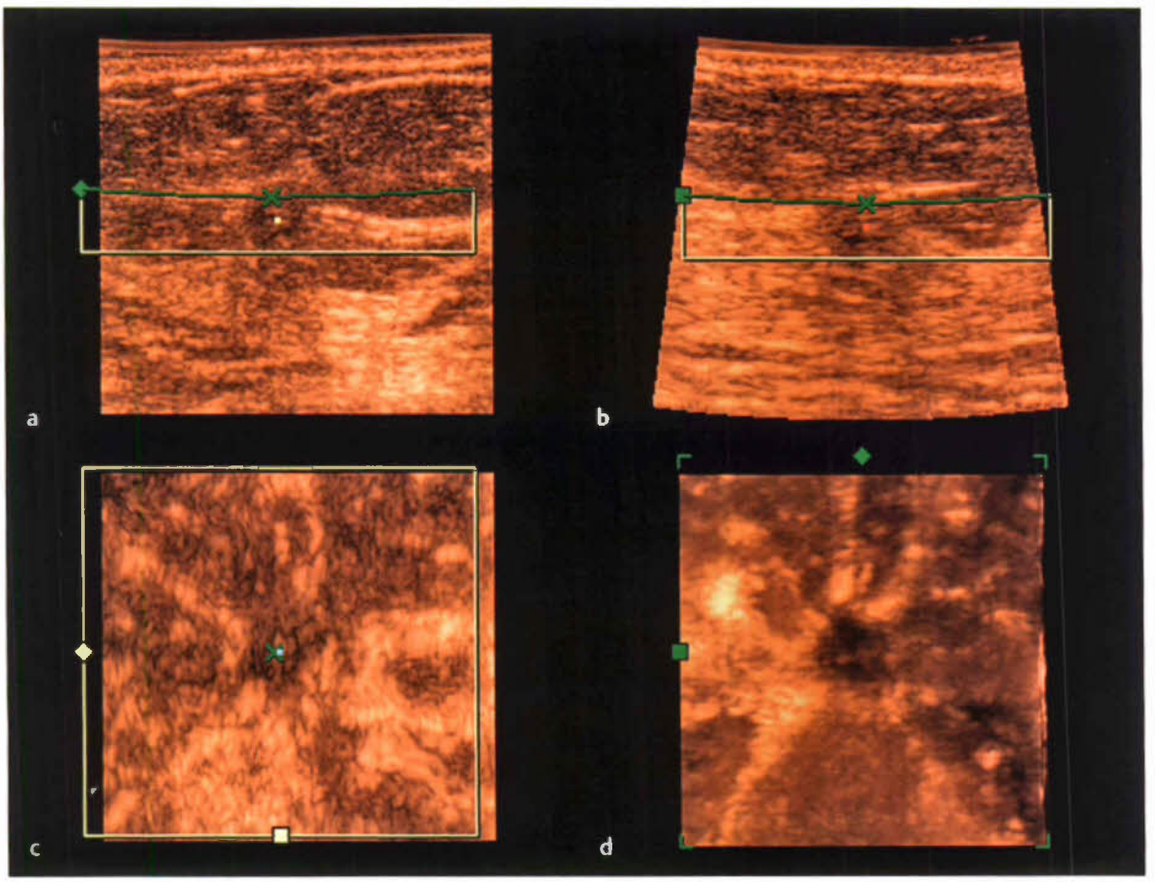

47

Fig. 44.**47** Invasive ductal carcinoma 5 mm in diameter. Even a lesion this small can produce a retraction pattern that is visible in the coronal plane of the multiplanar display (**c**) and in the coronal surface-rendered image (**d**).

Figs. 44.**48**/44.**49** Surface-rendered images of ductal carcinoma in situ. Surface rendering in coronal section may show irregular hypoechoic structures with macrocalcification and irregular margins (Fig. 44.**48**) or may reveal a subtle stellate pattern (Fig. 44.**49**), depending on the level of the section.

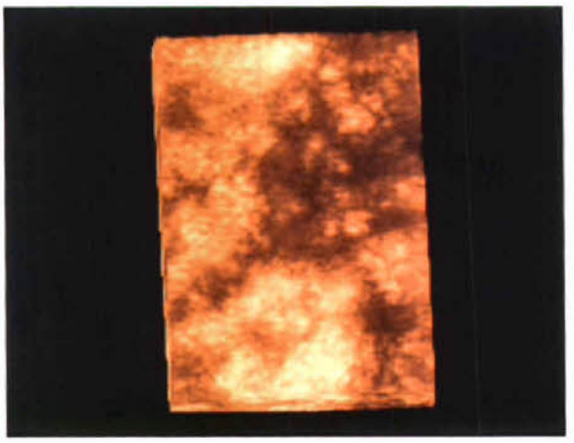

48

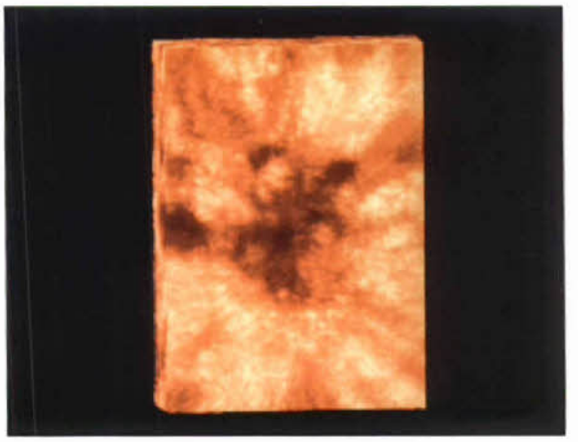

49

Fig. 44.**50** The coronal plane in the multiplanar display and its surface-rendered image show a subtle stellate pattern associated with an oblong retroareolar mass. Mammography and magnetic resonance imaging raised a suspicion of a malignant process. Open breast biopsy and histology identified the lesion as fibrosis. (Compare with Fig. 44.**37**.)

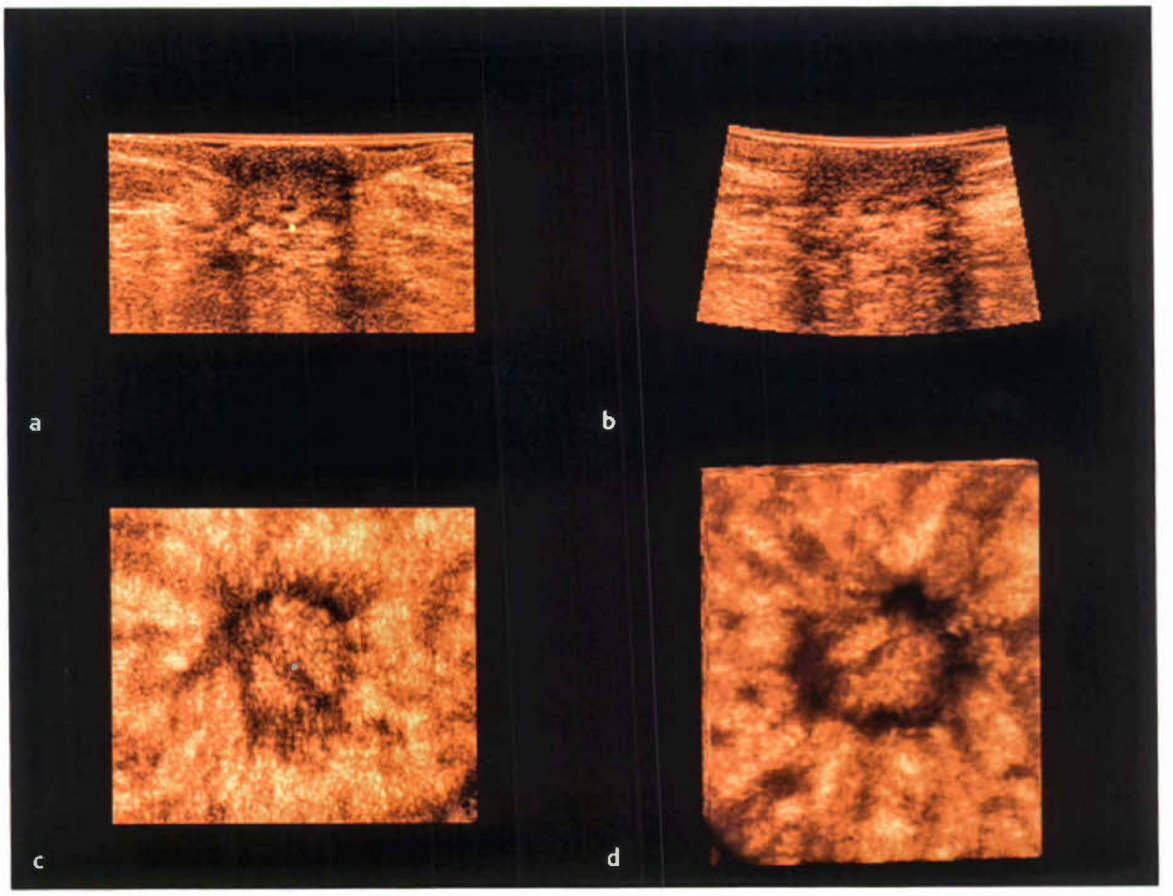

50

Fig. 44.**51** Surface-rendered image of a transverse oval breast mass with microlobulated margins and a non-homogeneous internal echo pattern in a 36-year-old woman. The short spicules at the periphery of the mass were not clearly seen until the tumor was rotated. The lesion had been misinterpreted as fibroadenoma by two-dimensional ultrasound. Histology: grade III tubular breast carcinoma, 31 × 24 × 28 mm.

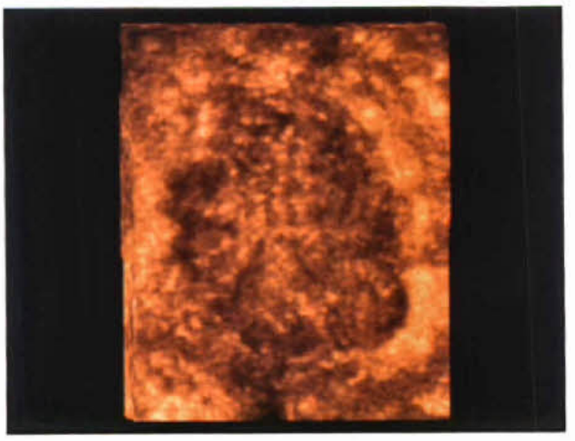

51

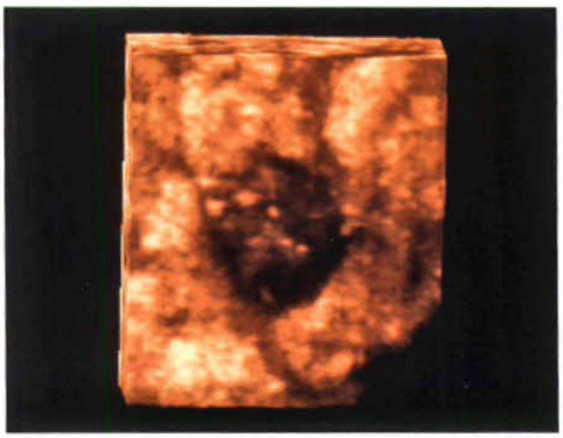

52

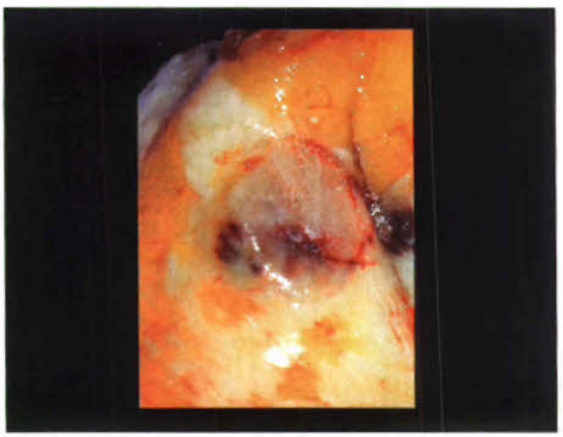

53

Fig. 44.**52** Surface-rendered image of a small, round breast mass (15 mm in diameter) with a nonhomogeneous internal echo pattern (macrocalcifications) but no appreciable retraction pattern. Histology: invasive ductal carcinoma.

Fig. 44.**53** The same tumor as in Fig. 44.**52** cut open.

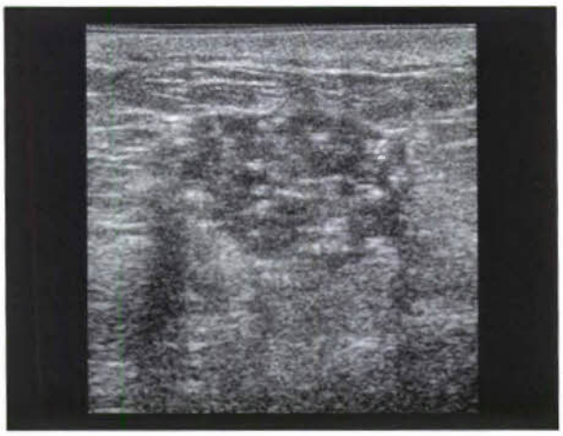

54

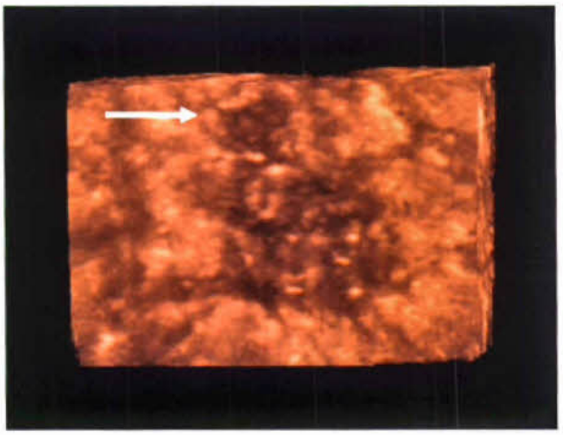

55

Figs. 44.**54**/44.**55** Transverse oval breast mass (22 mm in diameter) with macrocalcifications and microcalcifications in a 36-year-old woman.

44.**54** The two-dimensional ultrasound scan showed no definite malignant criteria in sagittal section.

44.**55** The three-dimensional coronal surface-rendered image does not show a typical stellate pattern, but several long, thin radial extensions are observed. A 4-mm satellite lesion (arrow) also appears close to the main tumor. Histology: invasive ductal carcinoma.

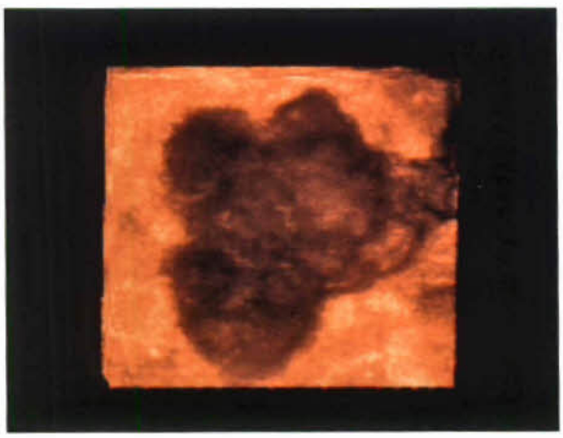

56

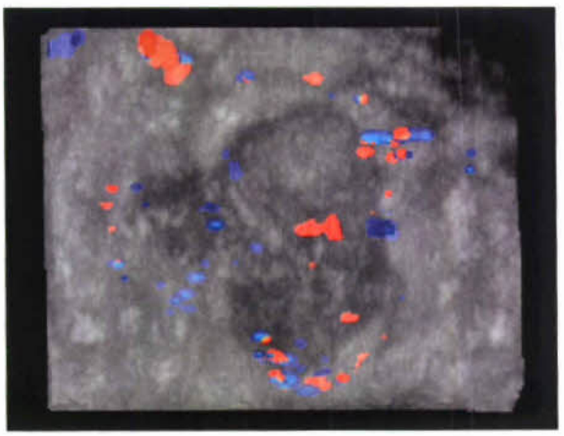

57

Figs. 44.**56**/44.**57**

44.**56** A lobulated breast mass with smooth margins that appeared benign in this surface-rendered ultrasound image and in the mammogram.

44.**57** However, the glass-body mode demonstrates a vascular pattern that is suspicious for malignancy. Histology: intramammary plasmacytoma.

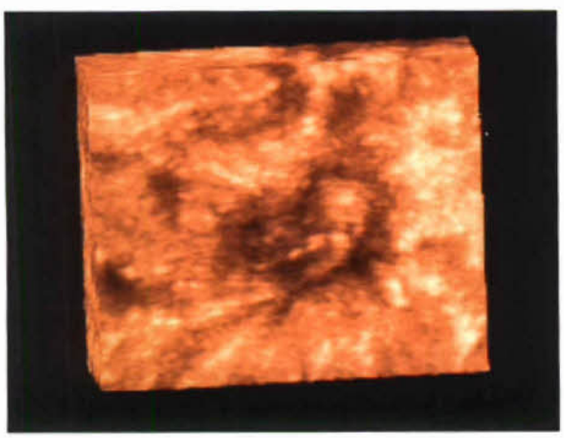

58

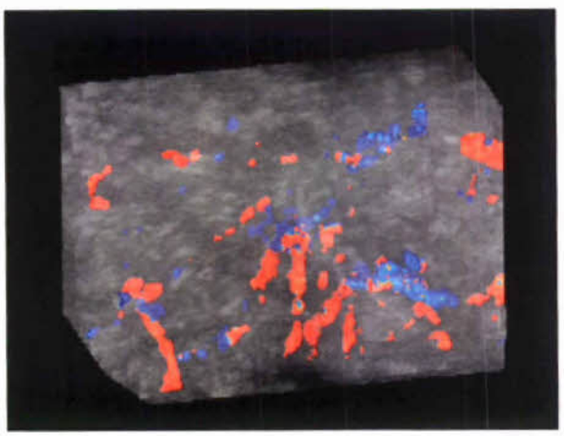

59

Figs. 44.**58**/44.**59** A small breast carcinoma (12 × 8 mm).

44.**58** Surface-rendered image in the coronal plane shows isolated peripheral spicules, but does not show a definite retraction pattern.

44.**59** The glass-body mode shows an abnormal pattern of peripheral tumor vascularity.

Fig. 44.**60** Multiplanar display (**a**–**c**) and surface-rendered image (**d**) of multifocal breast carcinoma.

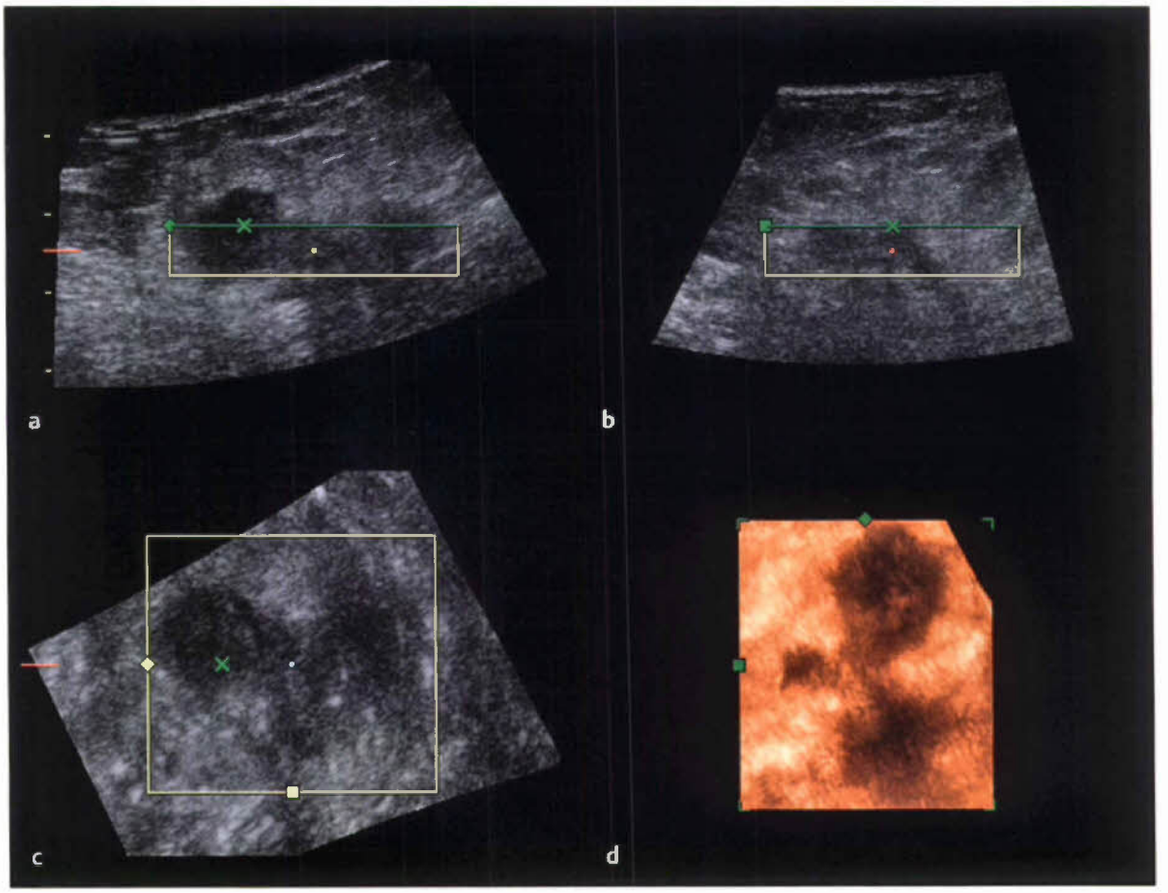

60

Fig. 44.**61** Coronal surface-rendered image of an 11-mm invasive ductal carcinoma with a 4-mm satellite lesion.

Fig. 44.**62** The same tumor as in Fig. 44.**61**. The surface-rendered image in a different coronal plane shows a definite retraction pattern associated with the main lesion.

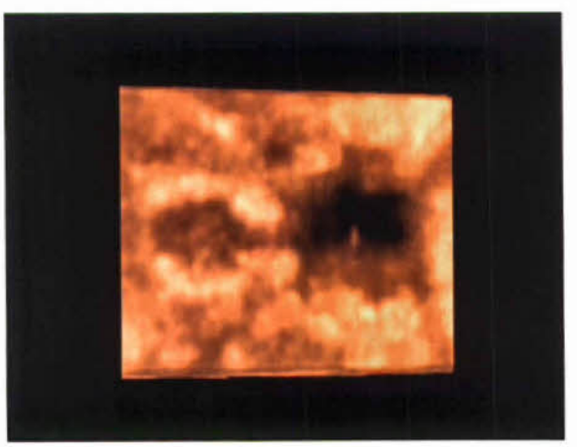

61

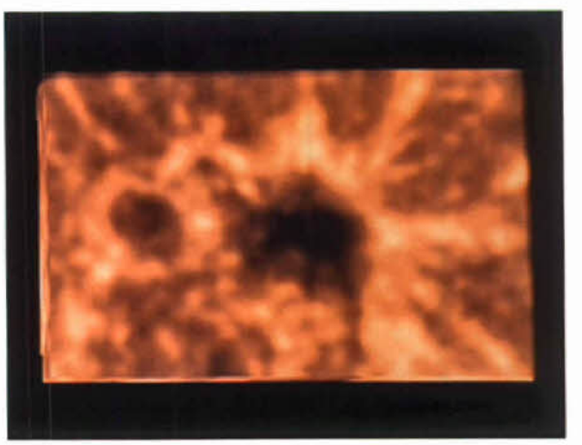

62

Figs. 44.**63**/44.**64** Scar versus tumor recurrence.

44.**63** The sagittal surface-rendered image shows the scar as a narrow hypoechoic zone extending deep into the breast from the skin (arrows).

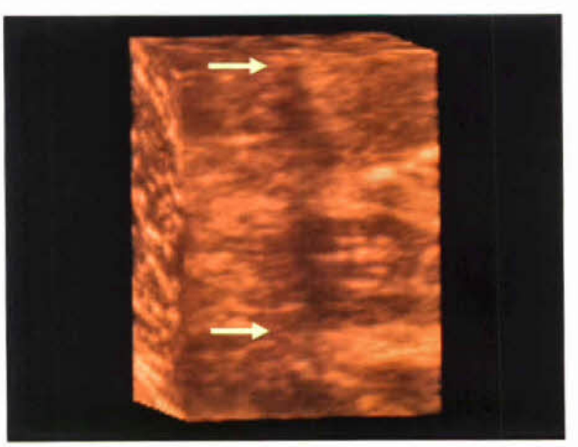

63

44.**64** An elliptical breast carcinoma (arrows), with normal breast tissue appearing between the skin and tumor.

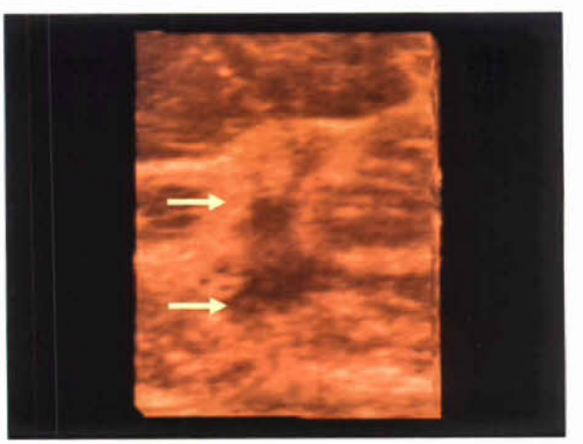

64

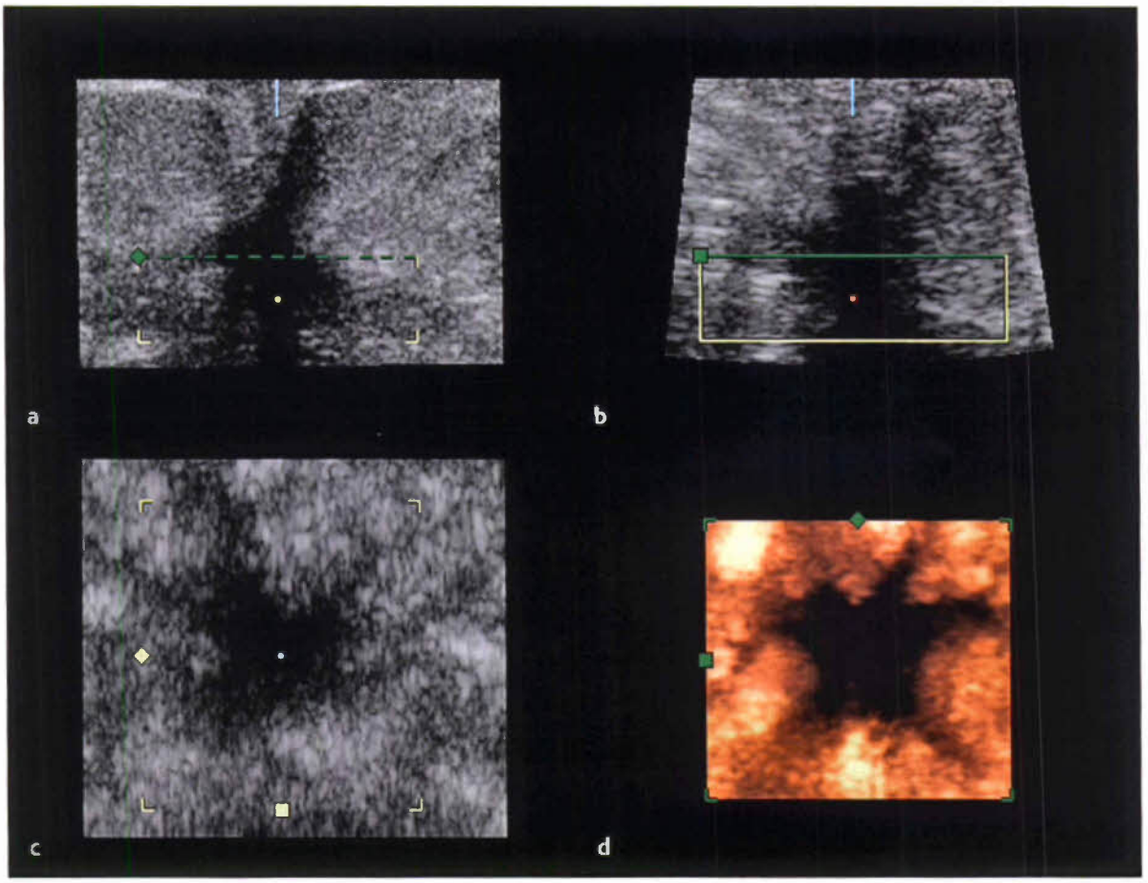

65

Fig. 44.65 Multiplanar display (**a**–**c**) and surface-rendered image (**d**) of a hypoechoic recurrence of invasive ductal carcinoma. The recurrence developed in the surgical scar.

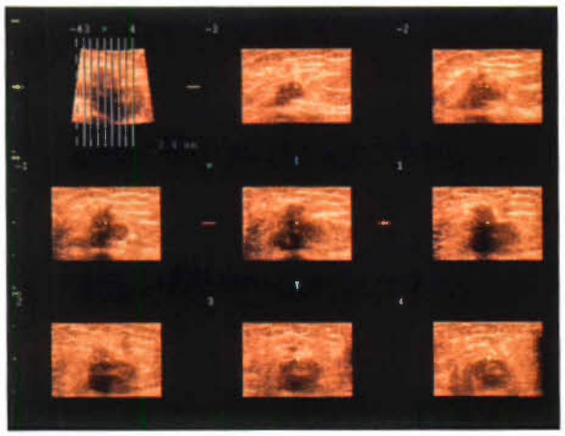

66

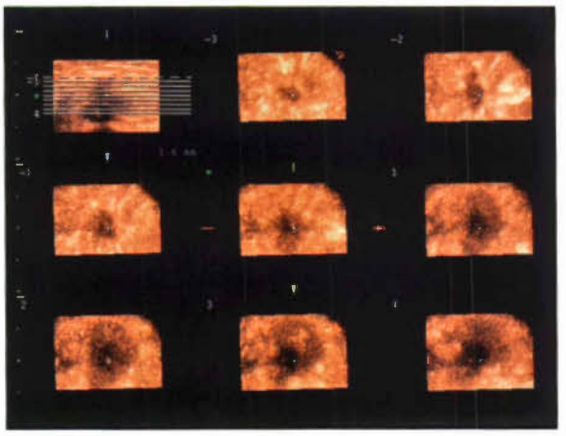

67

Fig. 44.66 Tomographic ultrasound imaging. The simultaneous display of multiple parallel sagittal planes of section on the monitor (with a slice interval of 2.4 mm) illustrates how the appearance of a nonhomogeneous malignant breast tumor (16 mm in diameter) can vary in different planes.

Fig. 44.67 The same tumor as in Fig. 44.66. The simultaneous tomographic display of multiple parallel coronal planes of section demonstrates a stellate pattern only in selected planes.

Fig. 44.**68** Glass-body rendering yields a combined display of gray levels and color Doppler signals.

68

Fig. 44.**69** The same tumor as in Fig. 44.**68**. The gray-scale components can be removed to obtain an isolated three-dimensional color display of the tumor blood supply. While the tumor appears benign in the sagittal two-dimensional image, the abnormal vascular pattern is suspicious for malignancy. Histology: invasive ductal carcinoma.

69

Fig. 44.**70** Transparent view of the tumor (see Figs. 44.**68** and 44.**69**).

70

Fig. 44.**71** Schematic representation of different vascular patterns associated with breast tumors. According to Stuhrmann et al. [18], 95 % of carcinomas show a basic type-3a/3b pattern (Modified with permission from Weismann [12]).

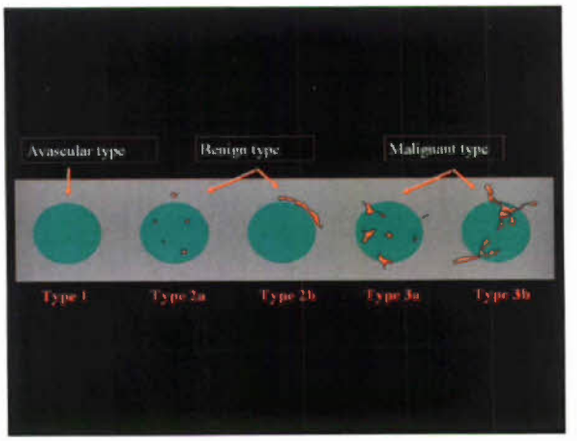

71

Tumor Size Determination and Volumetry

Accurate determination of tumor size is a basic and important task in breast ultrasonography, both for preoperative planning and for the follow-up of benign lesions. Ultrasound is superior to mammography in the determination of tumor size (with respective correlation coefficients of 0.91 and 0.78) [13].

In 3D ultrasound, the tumor dimensions are measured in the three mutually perpendicular image planes. Because all three planes are displayed simultaneously on the monitor, the measurement can be reproduced at any time and can be done more accurately than with conventional 2D ultrasound, in which two different images are measured. 3D ultrasound also eliminates the pitfall of an oblique measurement in 2D ultrasound when the transducer position is changed to measure the third plane.

Another important advantage of 3D ultrasound is that all of the masses contained in the volume can still be measured retrospectively at any time. 3D systems have integrated Virtual Organ Computer-Aided Analysis (VOCAL) computer software that allows automatic or manual volumetry of a circumscribed lesion (Fig. 44.**12**). The geometry of the tumor surface is determined by rotating the volume about a fixed axis, and focal volumetry can be carried out using the formula for a rotational ellipsoid ($V = L \times W \times D \times 0.523$). The three-dimensional shape of a tumor can be represented schematically in the form of a grid-lined or solid color figure (Fig. 44.**13**).

Focal volumetry is used primarily to monitor the growth progression of sharply circumscribed benign tumors (e.g., fibroadenomas). A variant of this technique, residual volumetry, can be used to evaluate the result of a vacuum biopsy [20].

Tissue Evaluation after Implant Surgery (Figs. 43.45, 43.46)

In patients who have undergone breast reconstruction with an implant, high-resolution ultrasound is the method of first choice for evaluating the residual parenchyma, since mammography is not possible in most cases (Figs. 44.**72**–44.**74**).

3D ultrasound is useful not only in evaluating the integrity of the implant but also in excluding a local recurrence. With older implants, analysis of the coronal planes and surface rendering of the surrounding tissue make it possible to exclude a leak. Often this cannot be done confidently with 2D ultrasound alone because of troublesome scattered echoes. Cost-intensive MRI can often be avoided with the aid of 3D ultrasound.

Axilla

High-resolution ultrasound is practically the only imaging modality that allows even very small (4–5 mm), hypoechoic (suspicious) lymph nodes to be detected and investigated by needle biopsy during postoperative follow-up and in patients with clinical suspicion of lymph node metastases.

The adjunctive use of 3D ultrasound in the axillary region facilitates differentiation between benign and malignant nonhomogeneous lymph nodes. These structures can be analyzed in the multiplanar mode, in the surface mode, and by tomographic ultrasound imaging (Figs. 44.**75**–44.**78**).

3D Ultrasound Guidance of Needle Biopsies

It is increasingly common for screening mammograms to detect very small lesions that require further (histologic) investigation. High-resolution breast ultrasound is also detecting indeterminate focal lesions with increasing frequency. To ensure that this diagnostic progress will not lead to unnecessary breast surgery, an updated diagnostic concept is needed that includes the option of core needle biopsy for histologic analysis. Two points are essential in this concept: safety and accuracy.

Ultrasound is the imaging modality of choice for the guidance of needle biopsies (Table 44.**2**). This presumes that the lesion can be visualized with ultrasound. Most lesions, including very small lesions in the 2–3 mm range, can be successfully visualized and percutaneously biopsied with high-resolution breast ultrasound.

Various biopsy needles are available for the investigation of benign lesions, and all of them can be used under ultrasound guidance (Fig. 44.**79**). Microcalcifications not associated with a tumor are the only lesions that require investigation by stereotactic mammographic biopsy.

A *core biopsy* with a 14-gauge or 16-gauge needle is the most commonly used technique for obtaining percutaneous histologic samples (Fig. 44.**79**). The needle is fired into the lesion at high speed with a biopsy gun (e.g., Bard Magnum System), which can be set to a range of 15 or 22 mm. This provides a tissue core approximately 10 mm long (see Fig. 44.**81**). From three to five tissue cores are usually obtained.

In cases in which a larger tissue volume is needed for histologic examination (e.g., in patients with diffuse tissue changes, microcalcifications, or suspected DCIS), an 8-gauge or 11-gauge *vacuum biopsy needle* can be used (Fig. 44.**79**). *Fine-needle aspiration* (FNA) is useful only for cytologic examination and uses a 20-gauge or 22-gauge needle (Fig. 44.**79**).

Any type of needle should always be introduced *parallel to the chest wall* in order to minimize the risk of injury (Fig. 44.**80**). It is essential to maintain clear and continuous ultrasound visualization of the needle during the insertion.

In conventional 2D breast ultrasound, the relationship of the needle to the target lesion (after firing) is first evaluated in a transverse plane. This view cannot show whether the needle is actually within the lesion, and it cannot exclude needle placement is in front of or behind the lesion. The examiner must then rotate the transducer 90° (this may be difficult with a large breast or small lesion) to define the needle as a point in the sagittal plane and document a correct needle placement.

With the multiplanar display in 3D breast ultrasound, the examiner can directly visualize the needle in all three planes on the monitor without having to change the transducer position. This provides immediate confirmation that the biopsy needle is correctly positioned in all three planes (Figs. 44.**82**–44.**86**). This also guides the decision on how many core biopsy samples should be obtained.

The simultaneous visualization of the needle and lesion in all three planes is a domain of 3D breast ultrasound and is called *3D targeting*.

The needle position in relation to the lesion is described as *central*, *eccentric*, *marginal*, or *outside the lesion* (Figs. 44.**82**–44.**86**).

Weismann [21] investigated the role of 3D ultrasound guidance in a study of 188 core biopsies and 24 fine-needle biopsies. After the completion of a conventional 2D-guided biopsy, a corresponding volume was acquired and evaluated in 3D. It was found that a central or eccentric (satisfactory) needle position had been achieved in only 82% of the cases. Multiplanar 3D analysis showed a marginal needle placement in 10% of the cases, and in 8% of cases the needle had been placed outside the lesion. This study showed an overall sensitivity of 98% and specificity of 100% for 3D ultrasound biopsy guidance, and these figures have been confirmed in various other studies [22–24].

The question of how many core biopsy samples are needed to make an accurate, definitive histologic diagnosis has been addressed in several large-scale studies [25–27]. Most authors recommend taking five tissue cores. By enabling the precise control of needle position, 3D breast ultrasound can make a significant contribution to reducing the number of needle passes that are necessary for an accurate diagnosis [22].

There are cases in which more than five passes may be needed, depending on the size and structure of the lesion. It is extremely impor-

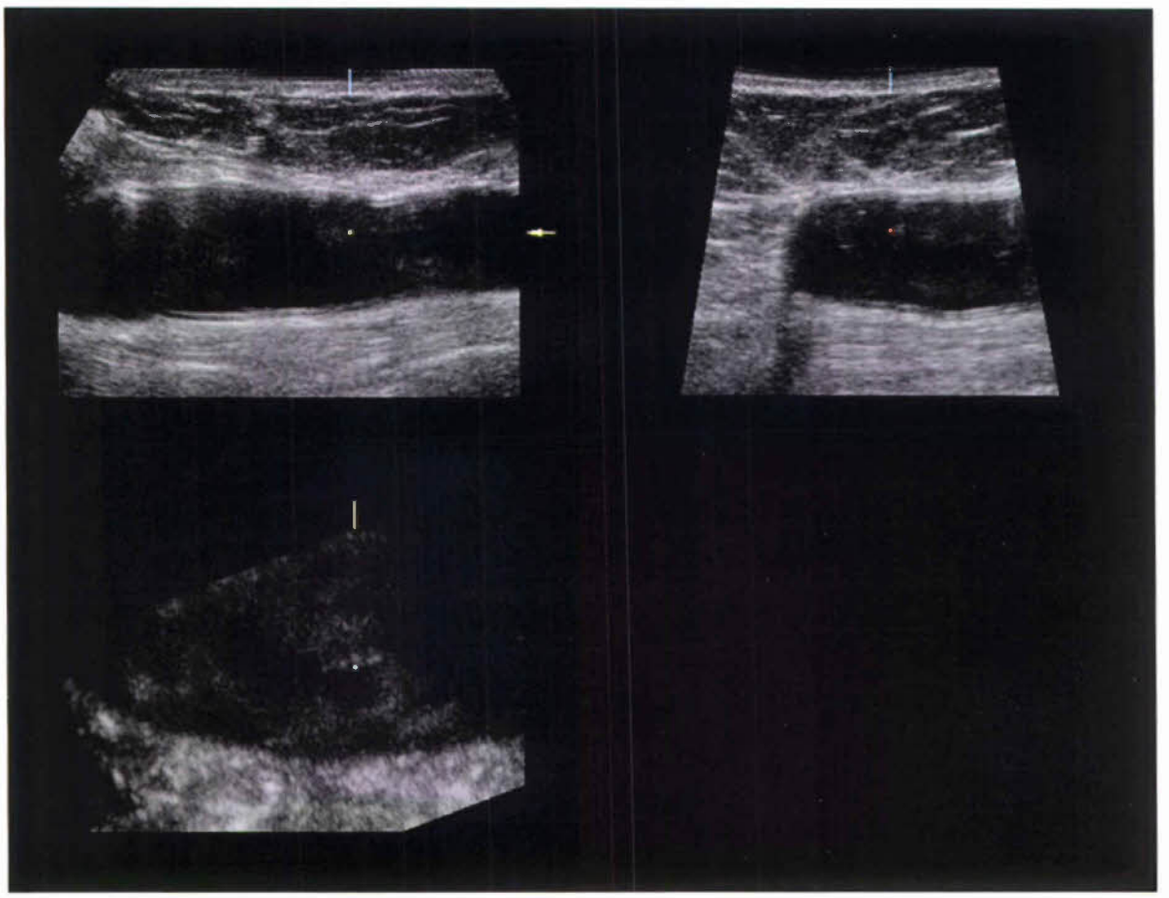

72

Fig. 44.72 Multiplanar display of a silicone breast implant. The walls of the implant and the surrounding parenchyma can be clearly evaluated in all three planes.

73

Fig. 44.73 A typical smooth-walled silicone breast implant.

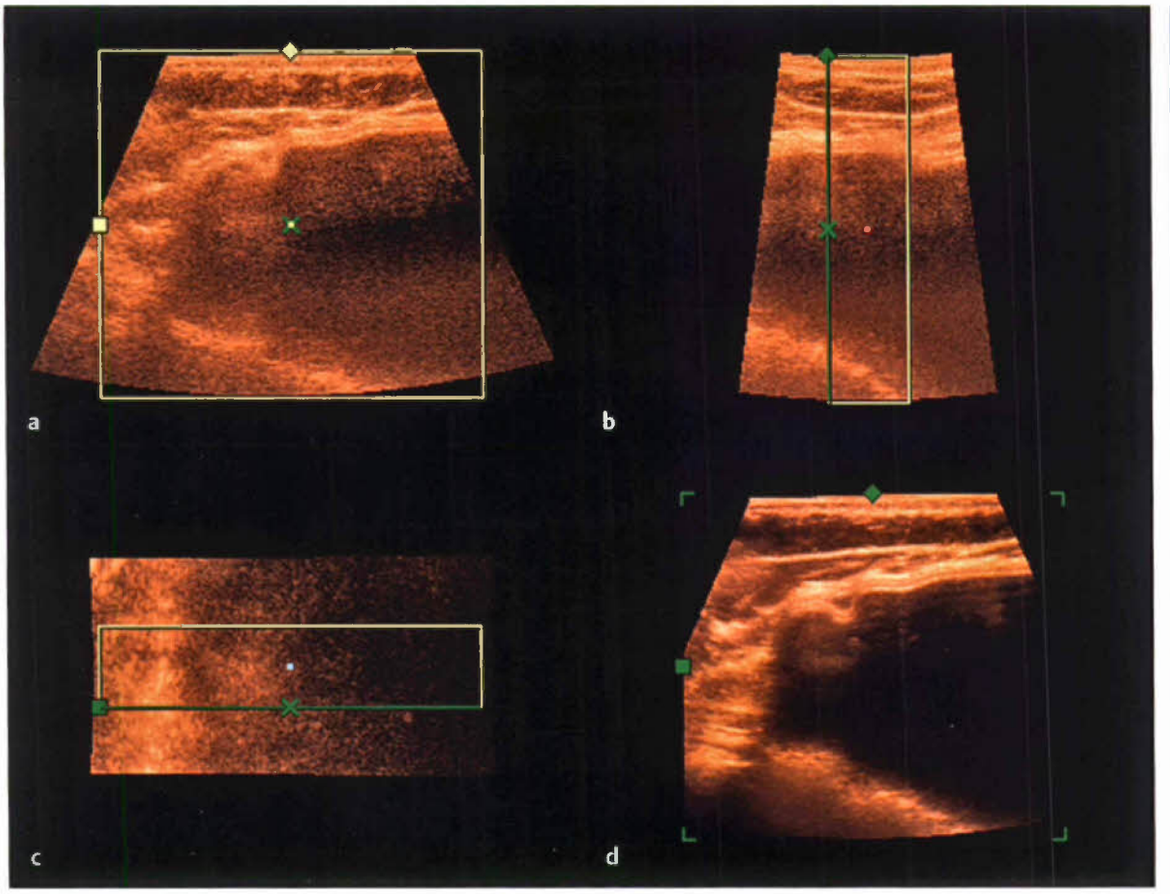

74

Fig. 44.74 Excluding rupture of an older breast implant. The multiplanar display and surface-rendered image both show crumpling of the implant surface. It is easier to exclude a rupture in the surface-rendered image (**d**) than in the multiplanar display (**a**–**c**), as the surface mode defines the walls of the implant with greater clarity.

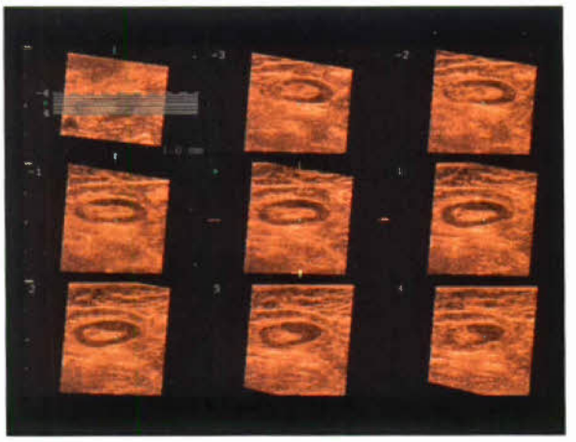

75

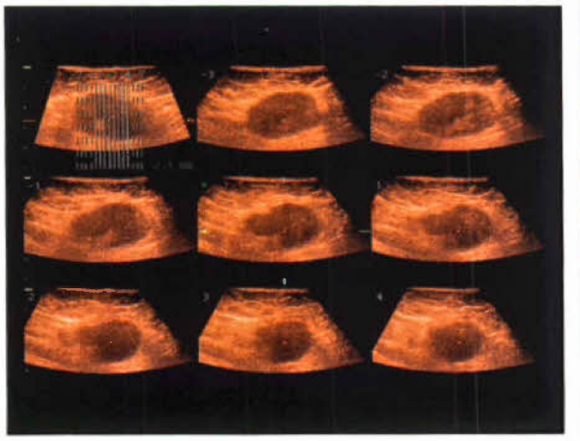

76

Fig. 44.75 Tomographic ultrasound imaging (TUI) of an enlarged axillary lymph node. The serial examination of coronal slices at 1 mm intervals shows no evidence of lymph node metastasis. Histology: reactive lymphadenopathy.

Fig. 44.76 Tomographic ultrasound imaging (TUI) of a hypoechoic lymph node involved by metastasis. The lesion is explored in transverse slices spaced at 2.3 mm intervals. Varying degrees of nonhomogeneity are seen in different slices.

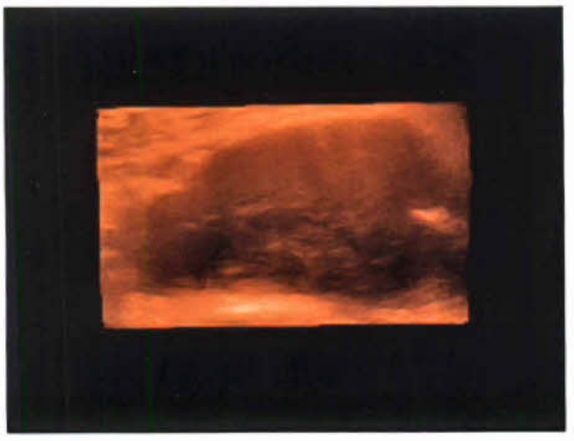

77

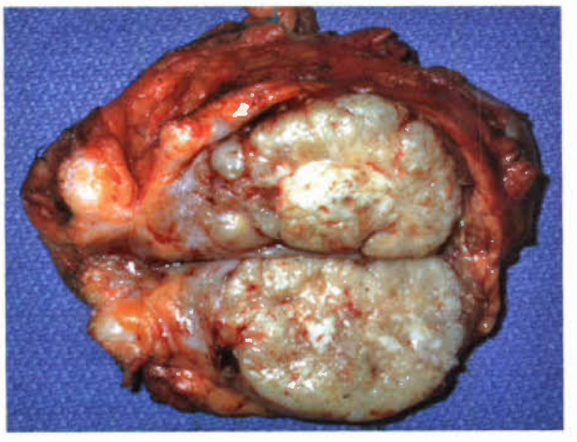

78

Fig. 44.77 Sectional three-dimensional surface-rendered image of a lymph-node metastasis.

Fig. 44.78 Surgical specimen of Fig. 44.77.

79

Fig. 44.**79** Instrumentation for minimally invasive breast biopsy.
1, Fine-needle aspiration biopsy: 20-gauge needle on an ordinary syringe;
2, biopsy gun with a 14-gauge core biopsy needle;
3, an open high-speed biopsy needle with a 20-mm-long collection chamber;
4, biopsy drill, also formerly used for "blind" tissue sampling from palpable breast masses;
5, a vacuum biopsy needle (11 gauge) for use with a hand-held mammotome device–a single-use instrument, with tubing attached.

80

Fig. 44.**80** Hand-held vacuum breast biopsy with three-dimensional ultrasound guidance. The needle is directed parallel to the transducer face and to the chest wall.

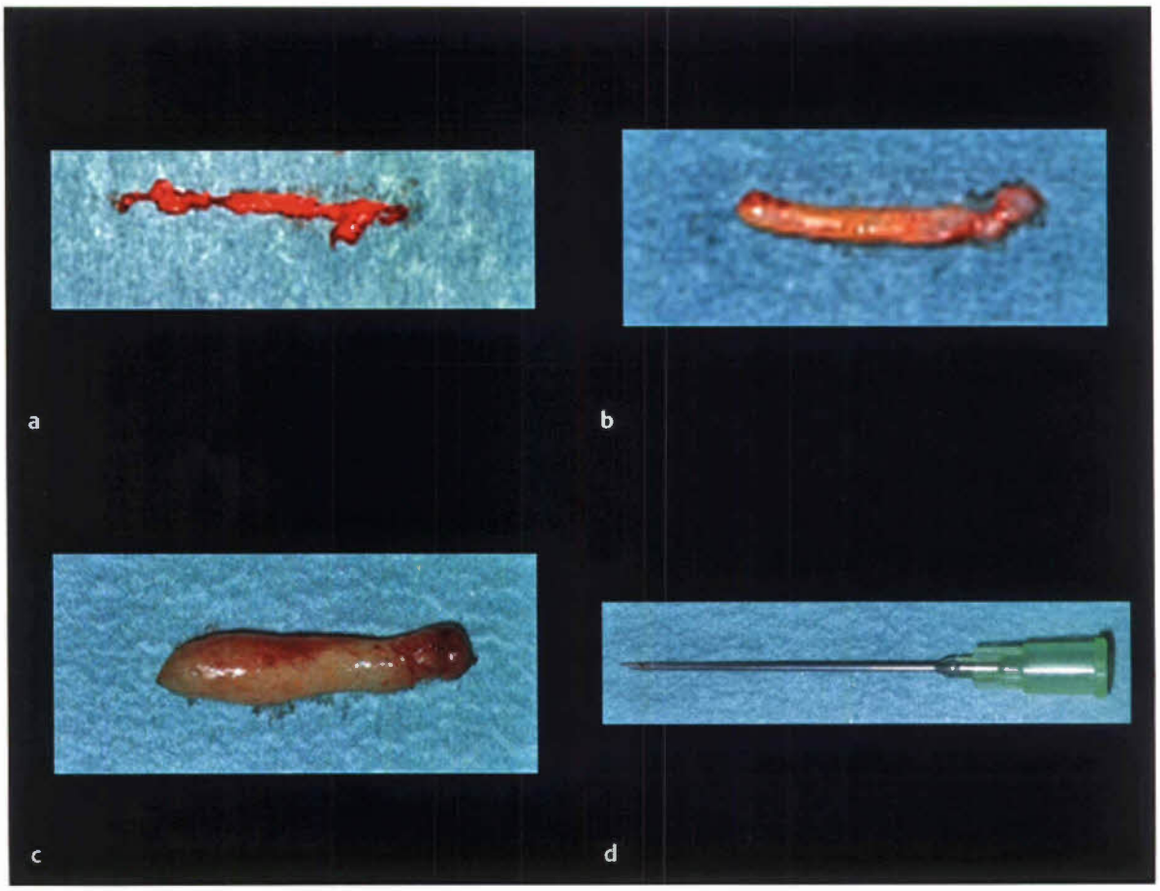

81

Fig. 44.**81** Tissue cores obtained with needles of different diameters. Vacuum biopsy provides the best tissue samples, owing to the vacuum effect and the large needle lumen. Injection needle for companson.

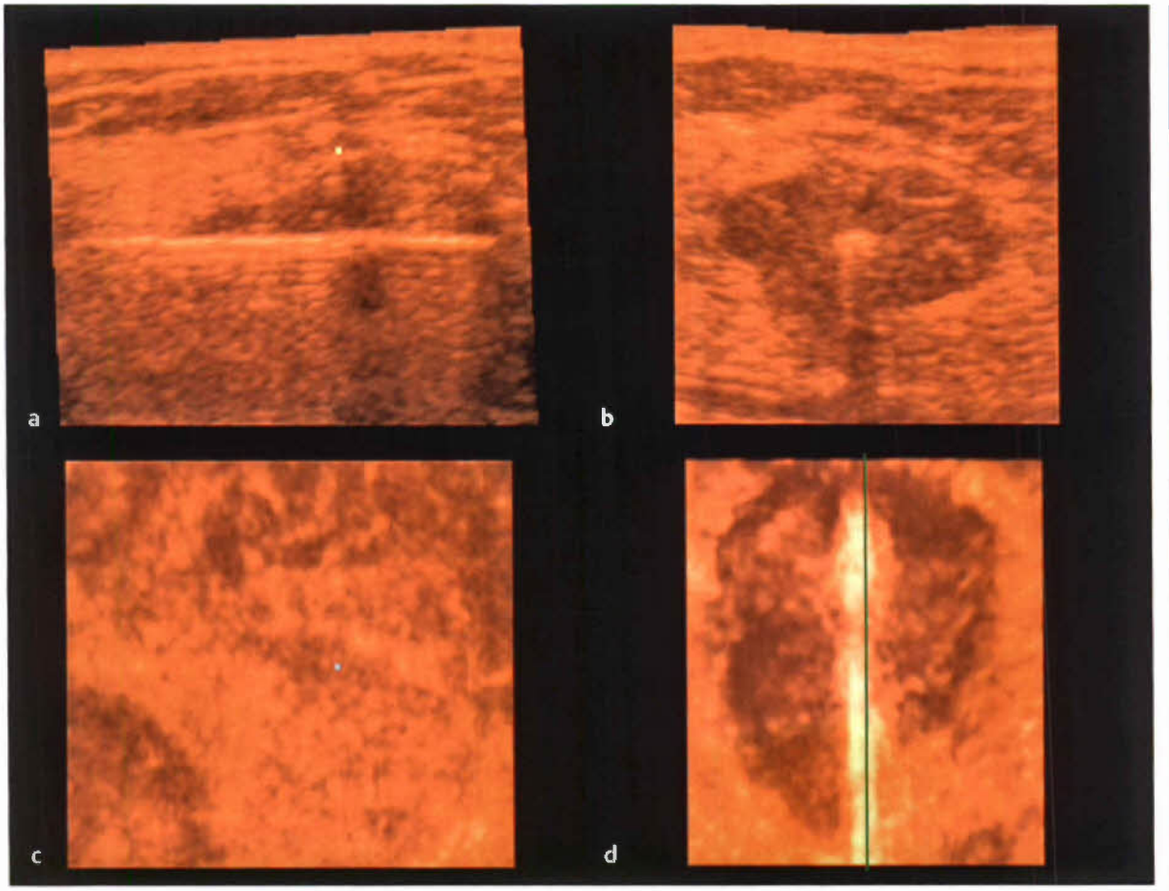

82

Fig. 44.82 Biopsy needle placement checked with three-dimensional ultrasound (multiplanar and surface modes). A central needle position can already be confirmed during volume acquisition in the sagittal and transverse planes. Lower right: Surface image of the needle at the center of the lesion.

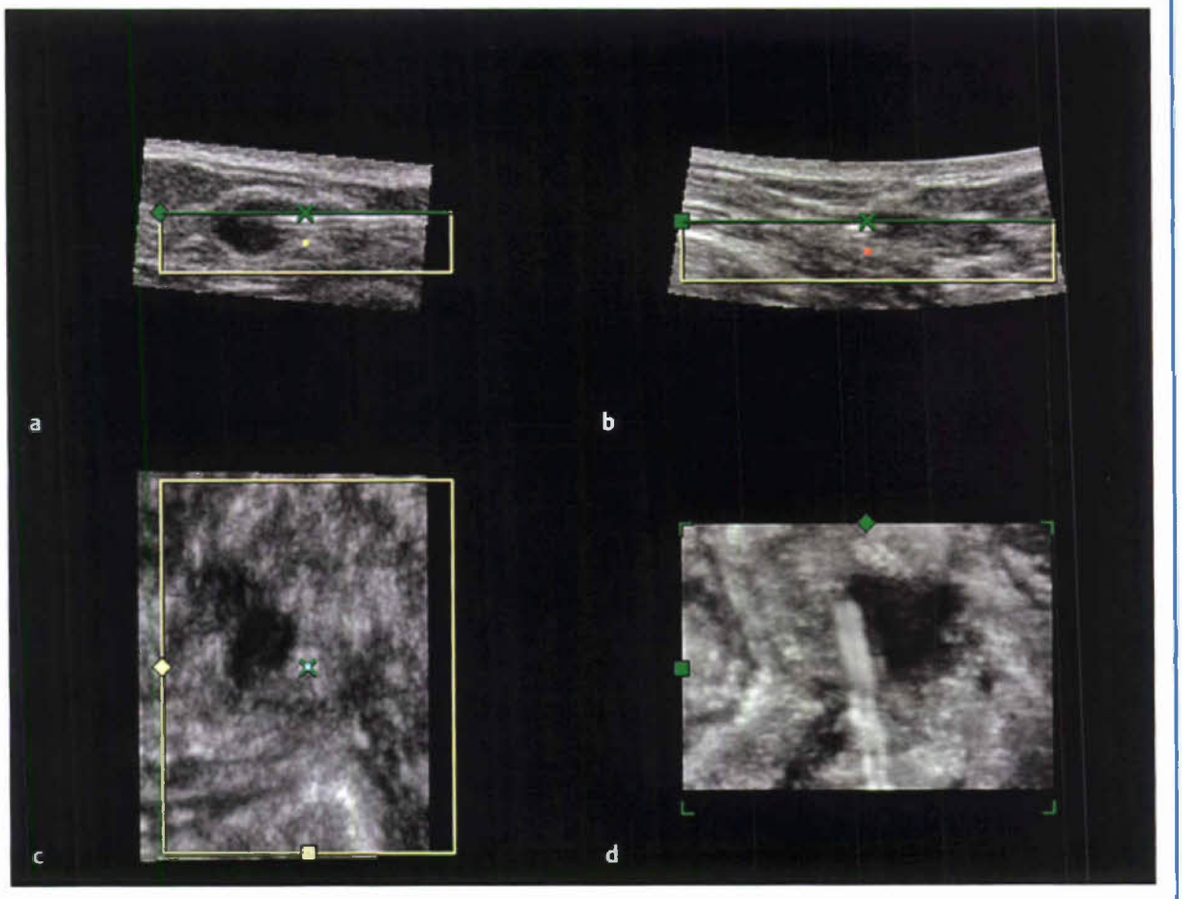

83

Fig. 44.83 Three-dimensional assessment of needle placement during biopsy of a 6-mm cyst shows a marginal needle position. Despite the peripheral needle position, it was still possible to aspirate the cyst contents for cytologic study. Lower right: Surface rendered image.

tant to document the individual cores in these cases because different histologic patterns may be found within the same lesion and thus in different tissue cylinders (Fig. 44.**85**). In cases in which a vacuum biopsy device is used for complete removal of a benign lesion, the needle is placed *below* the lesion (unlike the core needle used in suspected malignancies), and the target tissue is excised in layers from back to front, with one skin entry site (Figs. 44.**87**, 44.**88**).

The success of 3D ultrasound-guided needle biopsy, as in 2D-guided biopsies, depends critically on the *experience of the examiner* and on his or her technique. The most common factors underlying a failed ultrasound-guided needle biopsy include the following: the lesion is very small and is roughly isoechoic to its surroundings (e.g., fibrocystic nodules); the target and/or the needle are outside the volume box; and the needle cannot be visualized because it has been introduced too steeply or is masked by echogenic structures.

The routine use of 3D ultrasound for the guidance of minimally invasive biopsies can provide levels of sensitivity and specificity comparable to those achieved with open breast biopsy. It is not only a fast and *accurate* method for the histologic investigation of indeterminate breast lesions but is also associated with very low morbidity. 3D ultrasound also provides an ideal form of documentation (a complete volume block with the needle in the lesion), enabling a retrospective review of the puncture site in the lesion. This gives the examiner greater confidence in interpreting the histologic findings in problem cases and in evaluating extremely small lesions (Fig. 44.**86**).

Table 44.**2** reviews the basic protocol for performing a needle breast biopsy under 3D ultrasound guidance.

4D Ultrasound

4D breast ultrasound is a three-dimensional ultrasound examination of the breast in real time (up to 35 volumes/second). Besides allowing the selective evaluation of tumor structure, this technology also makes it possible to observe the compressibility of a breast tumor in response to transducer pressure.

4D ultrasound is also used in needle breast biopsies, enabling the real-time tracking of needle movements in the multiplanar display and in rendered views. A very narrow volume window should be used to ensure accurate visualization of the needle. In addition, the needle should be introduced exactly parallel to the skin so that it can be visualized over its entire length. Visualization can be somewhat difficult in biopsies of deep-seated lesions, because the needle cannot always be advanced parallel to the skin. Orientation and navigation in the deeper portions of the breast may prove particularly challenging for examiners who have had little experience with breast biopsies.

Volume contrast imaging (VCI) is a special "thick slice" 4D technique in which relatively thin volumes are imaged in rapid sequence with enhanced contrast. This basically amounts to selective ultrasound sectional imaging in which the slice thickness can be freely varied over a range from 3 to 20 mm. Advantages are that the transducer is the same type used in 2D scanning and that the image resembles a conventional 2D image even though it is actually a thin volume.

In the *VCI-A technique*, the same anatomical region is displayed as in the 2D image, but the narrow three-dimensional display results in better tissue contrast (Fig. 44.**89**).

In the *VCI-C technique*, a thin volume is acquired perpendicular to the 2D image plane. The desired level of volume acquisition is selected by manipulating a green indicator line in the 2D image. The VCI-C technique provides morphologic information on planes that are not accessible to conventional 2D scanning. This makes it easy to define coronal planes of section in the breast (Fig. 44.**90**).

With *spatiotemporal image correlation* (STIC) technology, which incorporates power Doppler imaging, the examiner can evaluate and store not only the course of blood vessels within tumors but also the perfusion of the tumor including vascular pulsations.

Table 44.**2** Basic protocol for three-dimensional ultrasound-guided needle breast biopsy

- Preliminary 3D ultrasound analysis of the lesion (location, morphology, benign or malignant characteristics)
- Under continuous 2D ultrasound guidance (in the "conventional" transverse plane), the needle is manually introduced parallel to the skin and advanced to the lesion without entering it
- A narrow volume box is selected, and the multiplanar view is displayed to check the needle position in relation to the lesion (the entire needle length is defined)
- The needle position is adjusted as needed
- The needle is advanced into the lesion and left in place
- Volume acquisition of the needle and lesion
- Multiplanar analysis of the needle position. (Except in a vacuum biopsy, the needle must be within the lesion)
- The volume is digitally stored to document correct needle position

Advantages and Problems of 3D Breast Ultrasound

Advantages of 3D Breast Ultrasound

The main advantages of 3D breast ultrasound are the ability to acquire and store tissue volumes and the various options the are available for displaying and manipulating objects that have been digitally stored in memory.

In the multiplanar mode, which displays all three orthogonal planes of section, the third (coronal) plane represents a particularly important addition in the diagnosis of breast lesions.

Surface rendering supplements the examiner's ability to "reconstruct" a three-dimensional mental picture from conventional 2D images by providing an actual 3D image. This image is then available for viewing on the monitor by other examiners and by the patient herself.

For the first time, 3D vascular imaging in the glass-body mode has made it possible to analyze patterns of vascularity in three dimensions. This technique is becoming particularly important for evaluating the neovascularization of malignant tumors.

When 3D technology is used routinely in the setting of minimally invasive biopsy procedures, it is possible not only to monitor and direct the needle placement in all three planes, but also to document and store the needle position in all dimensions after the needle has been placed within the lesion.

The clinically significant advantages of 3D breast ultrasound are summarized in Table 44.**3**.

Problems in 3D and 4D Breast Ultrasound

The procedural aspects of 3D breast ultrasound, especially volume acquisition, may seem cumbersome at first. For example, the larger, box-shaped transducer used in 3D ultrasound "handles" differently from a narrow, conventional 2D linear probe. Another problem is that volume acquisition requires a certain degree of planning to ensure that the volume can be optimally stored and processed.

Moreover, the variety of display options, orientation within the volume, dealing with artifacts, and various other issues cannot be mastered at the "touch of a button." All of this places greater initial demands on the examiner. Nevertheless, all of these problems are a matter of training, which generally is not a lengthy process for examiners already experienced in 2D breast ultrasound—and is certainly worthwhile when measured by the results. It should be added, however, that the ability to interpret three-dimensional images, along with spatial orientation in

Table 44.3 Advantages of three-dimensional/four-dimensional breast ultrasonography for specific applications

• **Availability of the third (coronal) plane**	– New criteria for benign–malignant discrimination – Better evaluation of the duct system (intraductal spread)
• **Tomographic survey of tissue volumes**	– Photorealistic sectional images of benign lesions – Accurate visualization of the desired plane (multislicing, tomographic imaging) – Detailed evaluation of intraductal and cystic structures – Detection of multifocal and multicentric lesions
• **Visualization of inner cyst walls**	– View the interior of cystic structures and detect or exclude tiny proliferative lesions on the cyst wall
• **Observation of breast lesions from various angles**	– Optimum visualization of lesion margins
• **Accurate volumetry of breast lesions**	– Follow-up
• **Three-dimensional evaluation of vascular systems**	– Analysis of vascular patterns, luminal characteristics, and tumor perfusion
• **Accurate guidance of needle biopsies with simultaneous visualization of the lesion and needle in three orthogonal planes**	– Maximum diagnostic accuracy – Fewer passes – Accurate, definitive histologic diagnosis
• **Ability to store complete volumes without data loss**	– Allows multiple analyses (retrospective and second reads), reproducibility – New training opportunities, especially by correlating ultrasound findings with the pathology report – Optimum documentation
• **Reevaluation and postprocessing of stored volumes can be done at any time**	– Operator convenience – Quality improvement – Shorter examination time
• **Ability to transmit volumes electronically**	– Telemedical consulting and conferencing

Table 44.4 Potential problems in three-dimensional and four-dimensional breast ultrasound

- The examiner has to become accustomed to the size and shape of the transducer
- The successful use of 3D breast ultrasound requires a solid grasp of 2D ultrasound
- During the learning period, the examiner may have orientation problems in the stored volume
- 4D-guided needle biopsy of small lesions should be reserved for experienced examiners (orientation and simultaneous visualization of the needle and lesion in a narrow volume window may be difficult in some circumstances)
- Technical flaws (e.g., acquisition angle too small, threshold set too high or too low, motion artifacts, inadequate use of the electronic scalpel) may lead to difficult or erroneous interpretation of the image, resulting in a misdiagnosis
- 3D and 4D breast ultrasound, like conventional 2D ultrasound, are very examiner-dependent, although they do allow for retrospective evaluation (without time or space constraints)
- The ability to perform state-of-the-art 3D and 4D breast ultrasound depends on the availability of proper equipment
- Large-scale clinical studies are still needed on the diagnostic efficacy of the method

minimally invasive procedures, are subject to marked interexaminer differences.

Table 44.4 lists potential problems that may be encountered in 3D and 4D ultrasound examinations.

Critical Appraisal and Outlook

At present, the greatest problem in 3D/4D breast ultrasound relates to a lack of qualified examiners and large-scale studies. The success of this promising technology is heavily dependent on the skills of the examiner and the quality of the equipment used. This explains the variability in the results of smaller studies that have been published to date [28].

In a 2005 study, in which Watermann et al. [29] examined and evaluated 100 breast lesions with an older-generation 3D system (Voluson 530), the authors mainly applied 2D-based diagnostic criteria and used very few of the 3D criteria for lesion characterization that are known today. For example, the "retraction pattern" was found to have a 95% specificity. Parameters such as the "compression pattern" and advanced 3D techniques such as glass-body rendering were disregarded. Thus, the belief that the diagnostic accuracy of 3D breast ultrasound is no better than that of 2D ultrasound is apparently rooted in outdated technology.

It is our view that 3D/4D breast ultrasound is visually and diagnostically superior to conventional 2D ultrasound. For example, tomographic analysis of breast lesions (including lesion margins), topographic visualization of breast lesions, and three-dimensional analysis of tumor vascularity offer new capabilities for distinguishing between benign and malignant breast lesions. 3D breast ultrasound has undisputed value in the monitoring and guidance of core biopsies.

When we look back on the development of 3D ultrasound systems during the past 15 years, it is clear that the progress made has been closely linked to advances in computer technology. Rapid data acquisition, the rapid display and processing of volumes in different modes, and the electronic transfer of volume data have already become a reality. When we look at the innovations that have occurred in 3D/4D breast ultrasound during the last 3 years, there can be no doubt that these developments will continue.

Meanwhile, there is an urgent need for further prospective studies using up-to-date 3D systems. As 3D/4D ultrasound becomes more widely practiced, it is reasonable to expect that larger scientific studies will be forthcoming and will confirm the clinical importance of this technology on a broad basis.

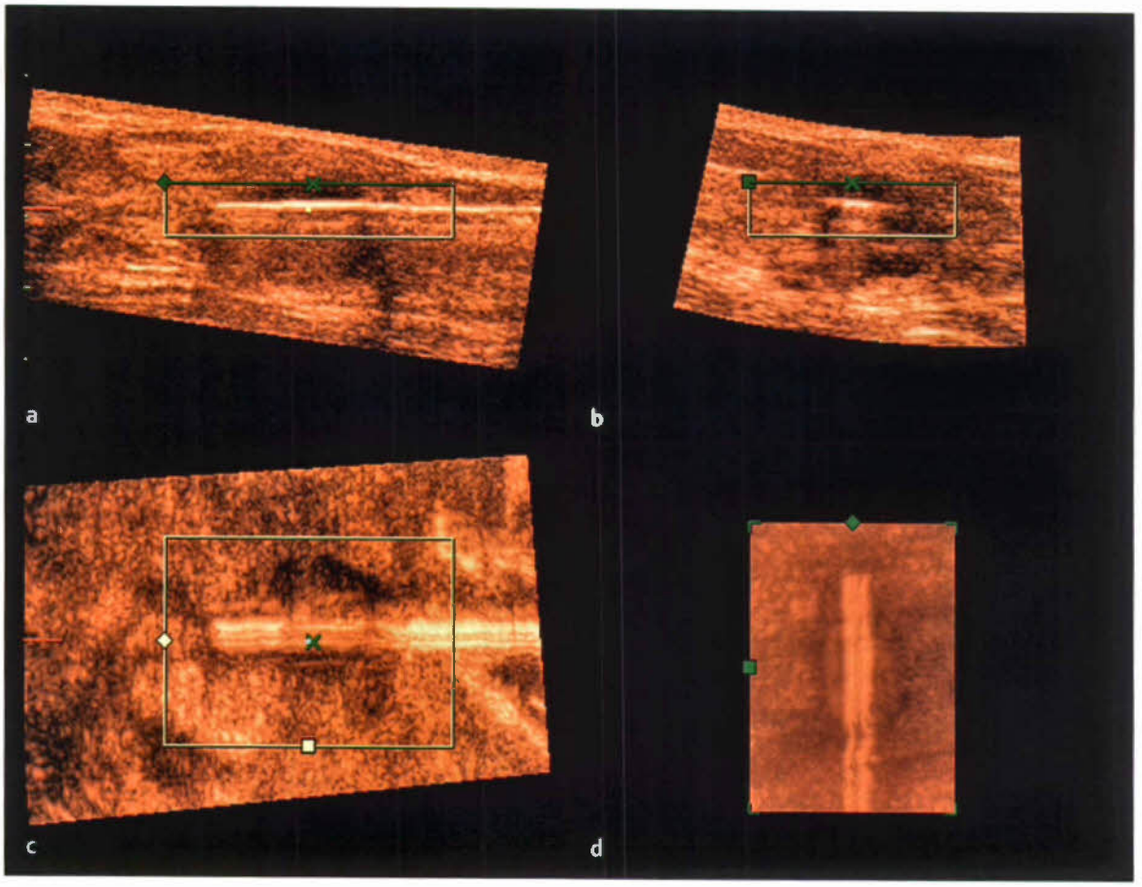

84

Fig. 44.**84** Three-dimensional assessment of biopsy needle placement in a breast carcinoma. The needle can be defined within the tumor in three planes (**a**–**c**) and in the surface-rendered image (**d**).

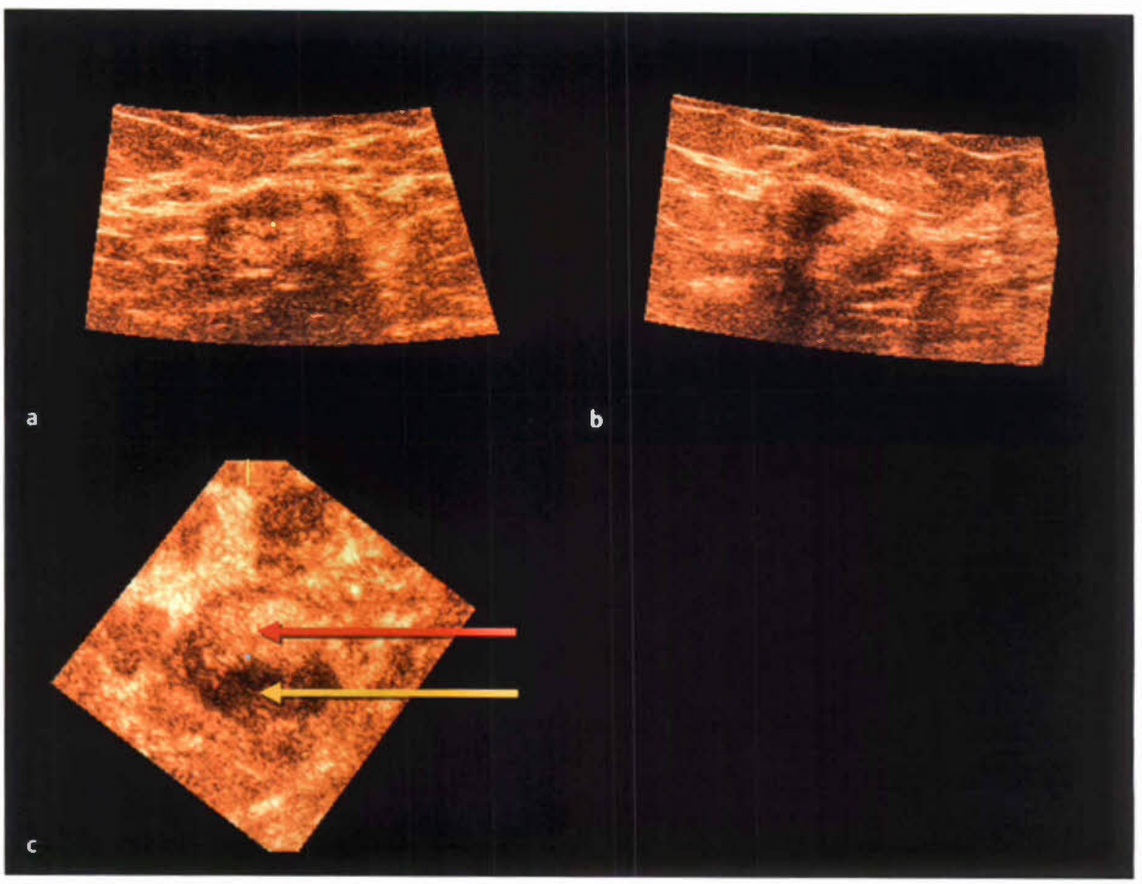

85

Fig. 44.**85** With nonhomogeneous breast lesions, different tissue areas can be selectively sampled under three-dimensional ultrasound guidance. Red arrow: sclerosing adenosis; yellow arrow: fibrocystic change.

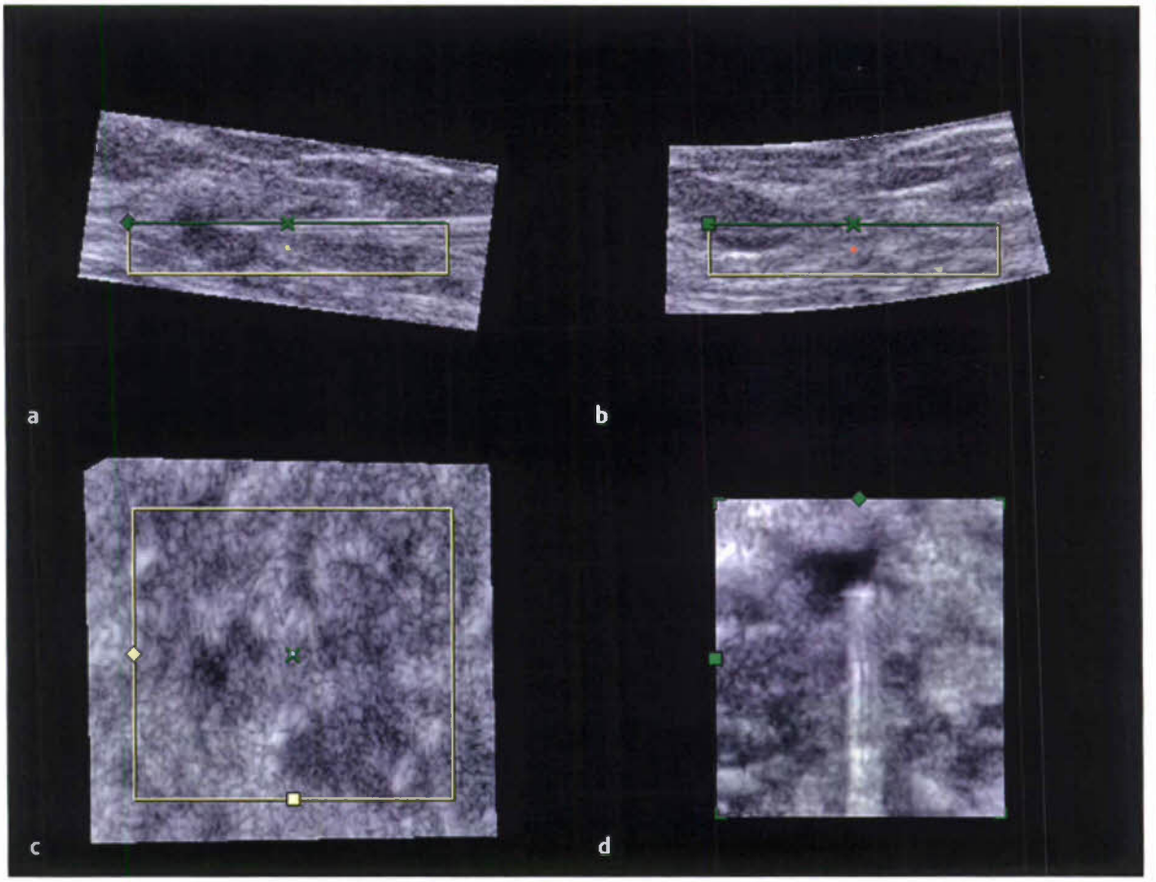

86

Fig. 44.**86**
a–c Even small focal lesions 5 mm in diameter can be safely evaluated by core biopsy under three-dimensional ultrasound guidance.
d The needle position is checked in the surface mode before definitive tissue sampling.

87

Fig. 44.**87**
The mammotome unit for ultrasound-guided vacuum biopsy (hand-held biopsy).

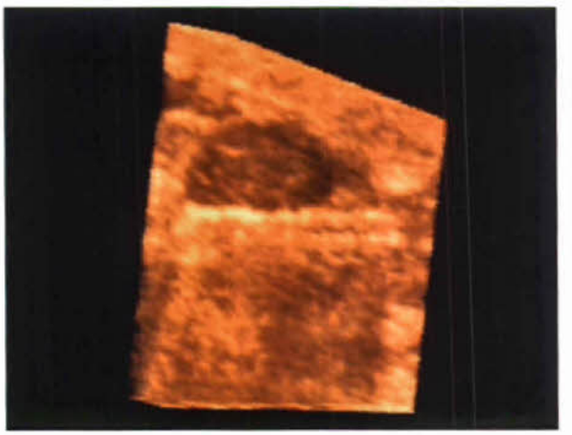

88

Fig. 44.**88** In the mammotome technique, the needle is positioned below the lesion, and tissue samples are taken in layers in the posterior-to-anterior direction.

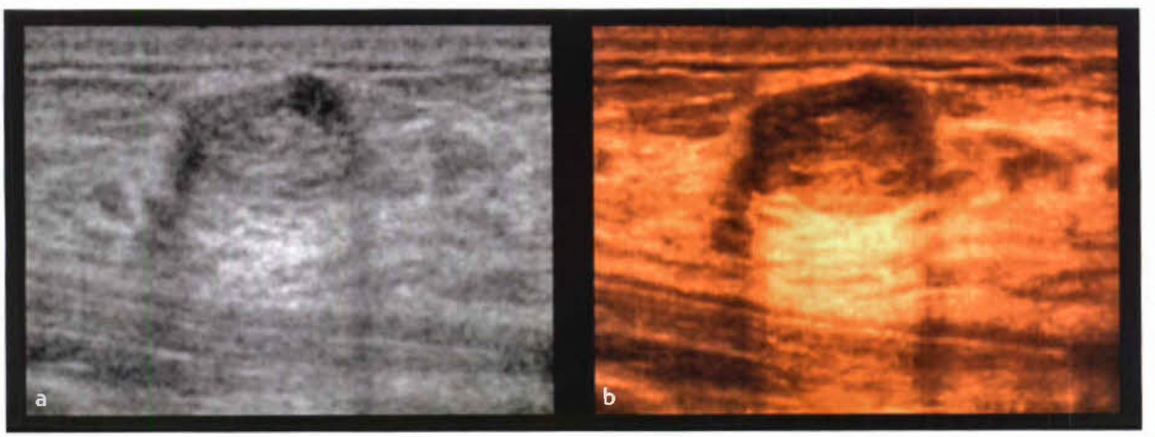

89

Fig. 44.**89** A circumscribed area of fibrocystic change. In comparison with conventional two-dimensional ultrasound (**a**), volume contrast imaging in the A plane (VCI-A, **b**) more clearly demonstrates the contours and internal echo pattern of the lesion.

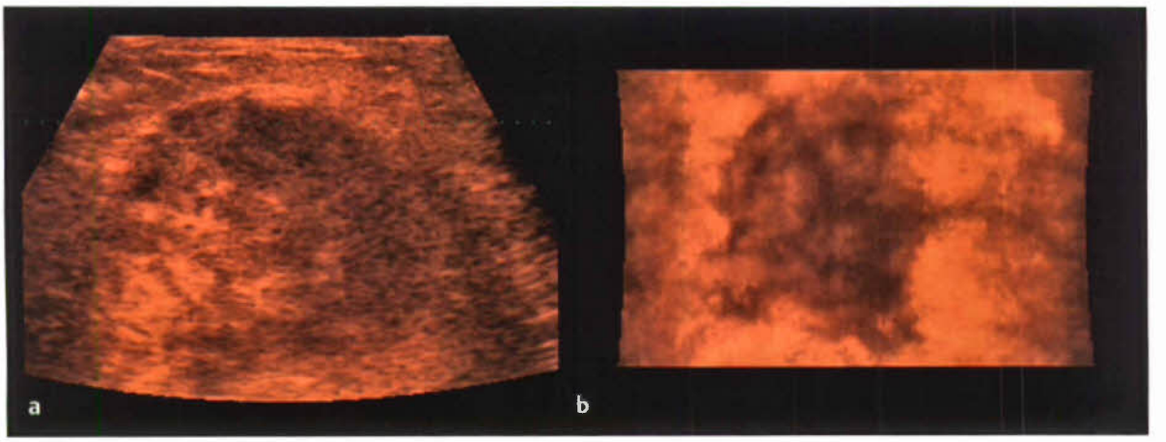

90

Fig. 44.**90** Medullary breast carcinoma demonstrated by volume contrast imaging in the C plane (VCI-C). The green line in the two-dimensional image (**a**) identifies the C plane for surface rendering (**b**), which clearly demonstrates the tumor spicules.

References

1 Downey, DB Fenster, A Williams, JC. Clinical utility of three-dimensional US. RadioGraphics 2000;20:559–71.
2 Gritzky A, Brandl H. The VoluSon (Kretz) Technique. In: In: Merz E, editor. 3D-ultrasonography in obstetrics and gynecology. Philadelphia: Lippincott Williams & Wilkins, 1998: 9–15.
3 Merz E. 3D Ultrasound in prenatal diagnosis. In: Merz E, editor. Ultrasound in obstetrics. Stuttgart: Thieme, 2004.
4 Merz E. 3-D ultrasound in prenatal diagnosis. Curr Obstet Gynaecol 1999;9:93–100.
5 Baba K. Development of three-dimensional ultrasound in obstetrics and gynecology: technical aspects and possibilities. In: Merz E, editor. 3D-ultrasonography in obstetrics and gynecology. Philadelphia: Lippincott Williams & Wilkins, 1998: 3–8.
6 Cole-Beuglet C, Kurtz AB, Rubin CS, Goldberg BB. Ultrasound mammography. Radiol Clin North Am 1980;18:133–43.
7 Kasumi F, Fukami A, Suno A, Kajitani T. Characteristic echographic features of circumscribed cancer. Ultrasound Med Biol 1982;8:369–75.
8 Kobayashi T. Review ultrasonic diagnosis of breast cancer. Ultrasound Med Biol 1975;1:383–91.
9 Rotten D, Levaillant JM, Constancis E, Collet Billon A, Le Guerinel Y, Rua P. Three-dimensional imaging of solid breast tumors with ultrasound: preliminary data and analysis of its possible contribution to the understanding of the standard two-dimensional sonographic images. Ultrasound Obstet Gynecol 1991;1:384–90.
10 Rotten D, Levaillant JM, Zerat L. Analysis of normal breast tissue and of solid breast masses using three-dimensional ultrasound mammography. Ultrasound Obstet Gynecol 1999;14:114–24.
11 Rotten D, Levailland JM, Zerat L. Use of three-dimensional ultrasound mammography to analyze normal breast tissue and solid breast masses. In: Merz E, editor. 3D-ultrasonography in obstetrics and gynecology. Philadelphia: Lippincott Williams & Wilkins, 1998: 73–8.
12 Weismann CF. Three- and four-dimensional breast imaging and vascularity assessment. In: International Breast Ultrasound Seminar. Copenhagen: 2003: 60–6.
13 Madjar H, Ladner HA, Sauerbrei W, Oberstein A, Prömpeler H, Pfleiderer A. Preoperative staging of breast cancer by palpation, mammography and high-resolution ultrasound. Ultrasound Obstet Gynecol 1993;3:185–90.
14 Blohmer JU, Oellinger H, Schmidt C, Hufnagl P, Felix R, Lichtenegger W. Comparison of various imaging methods with particular evaluation of color Doppler sonography for planing surgery for breast tumors. Arch Gynecol Obstet 1999;262:159–71.
15 Cosgrove DO, Kedar RP, Bamber JC, Al Murrani B, Davey JBN, Fisher C, et al. Breast diseases: colour Doppler US in differential diagnosis. Radiology 1993;189:99–104.
16 Svensson W, Hashimoto H, Forouhi P, Lynn J, Falzon M. Differences of vascular pattern demonstrated by colour Doppler ultrasound allow differentiation of fibroadenomas from cancer in the breast. Eur J Ultrasound 2000;11(Suppl 1):5–6.
17 Svensson WE. Use of colour Doppler to improve diagnostic accuracy. In: International Breast Ultrasound Seminar. Copenhagen: 2003: 54–9.
18 Stuhrmann M, Aronius R, Schietzer M. Tumor vascularity of contrast enhanced Doppler sonography. AJR Am J Roentgenol 2000;175:1585–9.
19 Weismann CF. Three-dimensional sonography of the breast. In: Kurjak A, Kupesic S, editors. Clinical application of 3D sonography. New York: Parthenon, 2000: 215–28.
20 Baez E, Huber A, Vetter M, Hackeloer B. Minimal invasive complete excision of benign breast tumors using a three-dimensional ultrasound-guided mammotome vacuum device. Ultrasound Obstet Gynecol 2003;21:267–72.
21 Weismann CF, Forstner R, Prokop E, Rettenbacher T. Three-dimensional targeting: a new ultrasound technique to evaluate needle position during breast biopsy. Ultrasound Obstet Gynecol 2000;14:359–64.
22 Delle Chiaie L, Terinde R. Three-dimensional ultrasound-validated large-core needle biopsy: is it a reliable method for the histological assessment of breast lesions? Ultrasound Obstet Gynecol 2004;23:393–7.
23 Lell M, Wenkel E, Aichinger U, Schulz-Wendtland R, Bautz W. [3D ultrasound in core breast biopsy: in German.] Ultraschall Med 2004;25:126–30.
24 Sauer G, Deissler H, Strunz K, Helms G, Remmel E, Koretz K, et al. Ultrasound-guided large-core needle biopsies of breast lesions: analysis of 962 cases to determine the number of samples for reliable tumour classification. Br J Cancer 2005;92:231–5.
25 Liberman L, Dershaw DD, Rosen PP. Stereotactic 14-gauge breast biopsy: how many core biopsy specimen are needed? Radiology 1994;192:793–5.
26 Parker SH, Burbank F, Jackman RJ, Aucreman CJ, Cardenosa G, Cink TM, et al. Percutaneous large-core breast biopsy: a multi-institutional study. Radiology 1994;193:359–64.
27 Philpotts LE, Hooley RJ, Lee CH. Comparison of automated vs vacuum-assisted biopsy methods for sonographically guided core biopsy of the breast. AJR Am J Roentgenol 2003;180:347–51.
28 Kotsianos D, Wirth S, Fischer T, Hiltawsky K, Sittek H, Reiser M. [3D ultrasound in the diagnosis of focal breast lesions: in German.] Radiologe 2005;45:237–44.
29 Watermann DO, Foldi M, Hanjalic-Beck A, Hasenburg A, Lughausen A, Prömpeler H, et al.. Three-dimensional ultrasound for the assessment of breast lesions. Ultrasound Obstet Gynecol 2005;25:592–8.

Appendix

45 Normal Organ Dimensions and Hemodynamic Values in Gynecologic Ultrasound

Uterus

Table 45.1 Normal abdominal uterine dimensions as a function of age (adapted from Bundscherer and Freundl [1])

Age group	n	Length (mm) (SD)	Height (mm) (SD)	Width (mm) (SD)
1–4 weeks	26	40 (5)	11 (2)	16 (4)
2–6 months	14	35 (4)	9 (2)	12 (3)
7–12 months	5	28 (5)	7 (1)	11 (1)
Year 2	9	28 (3)	8 (2)	11 (3)
Year 3	8	30 (2)	7 (2)	9 (3)
Years 4–5	10	29 (3)	7 (2)	12 (2)
Years 6–7	11	29 (4)	7 (1)	11 (1)
Year 8	17	33 (5)	7 (1)	12 (1)
Year 9	13	36 (6)	7 (1)	12 (2)
Year 10	19	37 (4)	7 (2)	11 (2)
Year 11	28	41 (7)	9 (3)	15 (4)
Year 12	16	47 (9)	11 (4)	18 (6)
Year 13	26	57 (11)	17 (5)	28 (9)
Year 14	11	70 (10)	22 (5)	29 (6)
Year 15	18	70 (8)	25 (5)	35 (9)
> 15 Years	20	67 (9)	23 (5)	37 (10)

Table 45.2 Uterine dimensions measured by transvaginal ultrasound in women of childbearing age and in postmenopausal women as a function of parity and years after menopause (adapted from Merz et al. [2])

Parity and menopausal status	0-para Mean (SD) cm	1-para Mean (SD) cm	> 2-para Mean (SD) cm	MP ≤ 5 years Mean (SD) cm	MP > 5 years Mean (SD) cm
Uterine length	7.3 (0.8)	8.3 (0.8)	9.2 (0.8)	6.7 (0.7)	5.6 (0.9)
Corpus length	4.4 (0.6)	4.9 (0.6)	5.6 (0.9)	3.8 (0.5)	3.3 (0.6)
Corpus width	4.0 (0.6)	4.6 (0.5)	5.1 (0.5)	3.6 (0.5)	3.1 (0.5)
Corpus height	3.2 (0.5)	3.9 (0.5)	4.3 (0.6)	3.1 (0.4)	2.5 (0.4)
Cervical length	2.9 (0.5)	3.4 (0.5)	3.7 (0.6)	2.9 (0.4)	2.4 (0.5)
Cervical width	2.9 (0.5)	3.3 (0.5)	3.4 (0.5)	2.7 (0.5)	2.3 (0.4)
Cervical height	2.6 (0.4)	2.7 (0.4)	3.0 (0.6)	2.4 (0.4)	2.1 (0.4)
Corpus–cervix ratio	1.6 (0.3)	1.6 (0.4)	1.5 (0.3)	1.4 (0.2)	1.4 (0.2)

MP, menopause; SD, standard deviation.

Table 45.3 Maximum endometrial thickness (double-layer measurement) in premenopausal women and in postmenopausal women not on hormone replacement therapy (adapted from Merz et al. [2])

Premenopausal women	Postmenopausal women
1.5 cm	0.5 cm

Ovaries

Table 45.4 Ovarian volume determined by transvaginal ultrasound in women of childbearing age and in postmenopausal women as a function of parity and years after menopause (after Merz et al. [2])

Parity and menopausal status	0-para Mean (SD)	1-para Mean (SD)	≥ 2-para Mean (SD)	MP ≤ 5 years Mean (SD)	MP > 5 years Mean(SD)
Volume of right ovary (cm^3)	7.8 (2.6)	7.8 (2.3)	7.8 (2.6)	3.4 (1.3)	2.5 (1.3)
Volume of left ovary (cm^3)	7.4 (2.4)	7.7 (2.3)	7.5 (2.3)	3.8 (1.6)	2.5 (1.1)

MP, menopause; SD, standard deviation.

Formula for calculating the approximate ovarian volume:

$$V = \tfrac{1}{2} \times \text{length (cm)} \times \text{height (cm)} \times \text{width (cm)}$$

Normal Doppler Indices in the Vessels of the Internal Genitalia

Uterus

Table 45.5 Resistance index (RI) of various vessels in different phases of the menstrual cycle (adapted from Kupesic and Kurjak [3])

Phase of cycle	Uterine artery RI	Radial artery RI	Spinal artery RI
Proliferative phase	0.88 ± 0.04	0.78 ± 0.10	0.54 ± 0.03
Postovulatory phase	0.84 ± 0.094 (day 18)	0.68 ± 0.04 (midluteal phase)	0.49 ± 0.05 (day 16–18)

Table 45.6 Range of mean pulsatility index (PI) values in the uterine arteries at different points in the menstrual cycle (adapted from Steer et al. [4])

Phase of cycle	Observations (n)	PI Mean (SD)	PI Minimum	PI Maximum
Days 1–6	26	3.8 (0.9)	2.0	5.6
Day 7–LH peak	50	3.0 (0.8)	1.2	2.9
LH peak +1 to menstruation −1	56	2.5 (0.9)	0.5	4.7

Ovaries

Table 45.7 Periovulatory resistance index (RI) values measured in the region of the dominant follicle (adapted from Kurjak and Kupesic-Urek [5])

Phase of cycle	Intraovarian RI Mean ± SD
Proliferative phase	0.54
Time of ovulation	0.44 ± 0.04

References

1 Bundscherer F, Freundl K. Die Uterusentwicklung im Kindesalter. Sonographische Normalwerte und Vergleich mit klinischen Zeichen der pubertären Entwicklung. Ultraschall Klin Prax 1992;7:32–6.
2 Merz E, Miric-Tesanic D, Weber G, Bahlmann F. Sonographic size of the uterus and ovaries in pre- and postmenopausal women. Ultrasound Gynecol Obstet 1996;7:1–5.
3 Kupesic S, Kurjak A. Uterine and ovarian perfusion during the preovulatory period assessed by transvaginal color Doppler. Fertil Steril 1993;3:439–42.
4 Steer CV, Campbell S, Pampiglione JS, Kingsland CR, Mason BA, Collins WP. Transvaginal colour flow imaging of the uterine arteries during the ovarian and menstrual cycles. Hum Reprod 1990;5:391–5.
5 Kurjak A, Kupesic-Urek S. Infertility. In: Kurjak A, editor. Transvaginal color Doppler: a comprehensive guide to transvaginal color Doppler sonography in obstetrics and gynecology. Carnforth, Lancashire: Parthenon, 1991: 33–8.

Index

A

abdominal pain 127
abdominal ultrasound 6–7, 169
  abnormalities 60–62, *63–66*
  needle procedure guidance 70, *71*
abdominal wall 11, *16*
  hematoma 72, *73*
  metastases 57, *58–59*, 169
abscesses
  hepatic *65*
  inflammatory breast disease *256*, 257, *261*
  perityphlitic 166
  in PIDs 25, *28–29*
  postoperative 189
  preuterine 25, *29*
acoustic enhancement 4
acoustic shadowing 4, 6
adenocarcinomas 132–136, 143
adenofibromas 42, *51*
adenoid carcinomas *52*
adenomatous hyperplasia 32, *37*, 132, *249*
adenomyosis 132, *133*
adenopapillary carcinomas *52*, *53–55*
adhesions
  ascites and 169, *170*
  follicular definition 17
  in PID 127, *129*
  visualization 25, *29*
adnexal masses 2, 207, *209–210*, 217
  benign 149–153, *150–151*
adnexal torsion 164, *165*
adnexitis 25, *26*, 127, *128*
afterloading therapy 193–194
age, uterine dimensions 10, 298
aliasing 198, *201*
amenorrhea 149
ampullary patency 176–180, *179*
angiogenesis
  benign tumors 207–211, *209–210*
  malignant tumors
    breast 262, 279, *286*, 292
    endometrial 214–215, *216*
    ovarian 148, 159, *162*
angiography, breast tumors 258
anovulatory cycles 18, 121
anteflexed uterus 10, *14*, 101, *103–104*
  3D/4D sonography *228–229*
aorta, intraoperative ultrasound 80, *82–83*
appendicitis 61, 62, *66*
appendix *12*
  mucocele 166, *167*, *168*
archiving records 223–224, 267, 292
arcuate arteries 205, 214
arcuate uterus 124, *125*, *126*
  HyCoSy evaluation 176, *178*
  3D/4D sonography *230*
areolar region 273, *277*
arrhenoblastoma (Sertoli-Leydig cell) tumors 42, *52*, 159, *160*
artefacts, ultrasound 219, 224, 262, *263*
arteries, ovarian 204
arteriovenous shunts 212–213
ascites 6
  aspiration 70, *71*, 184, *186*
  cancer follow-up 169, *170*
  hepatic metastases 61, *65*, 159
  hyperstimulation syndrome 121, *123*
  ovarian tumors 159
    benign 207, *209*
    malignant 42, 57, *58*
  tubal carcinoma 164, *165*
Asherman syndrome 176, *179*
aspiration cytology, cysts 253
assisted conception *see* in-vitro fertilization (IVF)
automatic needle puncture device 183, *185*
axillary region 287, *289*

B

benign-malignant differentiation 4, 6
benign masses
  adnexal 149–153, *150–151*
  breast 261, *262*
    3D sonography *272*, 273, *274–278*
  ovarian 41–42, *44–51*, 152–153, *156*
    angiogenesis in 207–211, *209–210*
  tubal 56, 164, *165*
  uterine 32, *34–37*, 132–136, *133–135*, *137–138*
    vascularization 213–215, *216*
  vaginal 130, *131*
bicornate uterus 124, *125*, *126*
biometry
  ovarian 105
  uterine 101, *104*, 105, 298
biopsy, ultrasound-guided percutaneous 253
biopsy needle placement *294–295*
bladder 10, *11–15*, 105, *107*
  distension 6–7, 17
  shielding 193–194
bladder carcinomas 166, *167*
  invasion from cervix 33, *39*, 193, *195*
bladder dysfunction
  neurogenic 42, *47*
  overdistended 152, *155*
bladder endometriosis 166, *167*
bladder neck descent (BND) 86–87, *89–90*
bleeding
  postmenopausal 140, 214
  postoperative 188–189, *190*
blood flow
  breast tumors 259–262
  Doppler effect 198–199, *201–203*, 205
  ovarian arteries 204, 205
borderline tumors
  angiogenesis *210*, 211
  3D/4D sonography *237–238*
botryoid sarcoma 136
bowel 108, *109*, 242, *244*
  obstruction 62, *74*
  shielding in radiotherapy 193–194
bowel loops 7, 43, *55*, 166, *168*
  differential diagnosis 42, *50*, 226, *240*
breast biopsy 287, *290*
breast cancer, screening 252–253
breast carcinomas 253, *255*, 257–258, *260*
  hepatic metastases 56, *59*, 61, *65*
  noninvasive 279, *282–285*
  3D sonography 279, *280–281*, *282*, *283–284*
  ultrasound 253, *255*, 257–258, *260*
  volume contrast imaging (VCI) *296*
  see also ductal carcinoma; ductal carcinoma in situ (DCIS)
breast cysts 253, *255–256*
  aspiration *291*
  3D sonography *268–270*, 273, *275–277*
breast diseases, ultrasound diagnosis 252–261, *254–256*, *259–260*, *262–263*
  false-positive 261, *263*
breast fibroadenomas 257, *259*, *272*, 273, *274–275*
  differential diagnosis 253, *255*, *260*, 261, *262*
breast implants
  prosthetic 253–257
  residual tissue evaluation 287, *288–289*
breast reconstruction *see* breast implants
breast tumors
  benign 261, *262*
  differential diagnosis *272*, 273
  malignant 279, *280–281*
  see also breast cancer; breast carcinomas
breast ultrasonography, problems 292–293
Brenner tumors 158, 207

C

CA-125 levels 207
calcification
  in breast lesions *282*, *283*
    fibroadenomas 257, *259*, 273
  in uterine lesions 136, *138*
    myomas 132, *133–134*, 213
    3D/4D imaging 225, *230*
cancer treatment
  follow-up care 169, *170*
  radiotherapy planning 193–194, *195–196*
carcinomas
  bladder *see* bladder carcinomas

breast *see* breast carcinomas
cervical *see* cervical carcinomas
endometrial *see* endometrial carcinomas
ovarian *see* ovarian carcinomas
tubal *see* tubal masses, carcinomas
uterine *see* uterine carcinomas
cardinal ligaments 101, *102*
cervical carcinomas 33, *39–40*, 130, *131*, 143–147, *145–146*
differential diagnosis 32
recurrence 33, *40*
squamous cell 80, *82*, 143
3D/4D ultrasound 225, *233*, *239*
transrectal ultrasound 243, *245*
transuterine ultrasound 248, *249*
treatment response 75, *76*
cervical cysts 136, *139*
cervical myomas 32, *37*, 132, 136, *141*
cervical polyps 136, *139*
cervix
anatomy *11*, 101, *102–104*
atrophic occlusion 136, *138*
benign masses 136, *139*, *141*
endometrial carcinoma in 140, *142*
menstrual cycle changes 114, *118*
structural anomalies 124, *125*, *126*
3D/4D ultrasound 225, *233*
transrectal ultrasound 243, *245*
uterine vessels *111*
cesium-137 radiation 193
chemotherapy, change in tumor RI 214
childhood, uterus 10, *12*, *13*
chocolate cyst *210*
cholecystolithiasis 61, *65*
chromolaparoscopy 174, 175, *177*, 180–181
cine mode (animation) 223, 224, *235*
clear-cell carcinomas *53*
clomiphene citrate therapy 17, *20*
CO_2 pertubation 174
coccygeus muscle 108, *109*
color Doppler ultrasound 198–200, *202–203*
artefacts 219
breast tumors 258–261
endometrial carcinomas 143, *144*
false results 215–217
hemorrhagic corpus luteum cysts 149, *150*
myometrial vessels *103*
ovarian malignant masses 211–213
ovarian vessels 108, *111*
tubal patency 180, *181*
tumor-induced angiogenesis 148, 159, *164*, 206–215, *209–210*, *216*
color duplex *see* color Doppler ultrasound
color flow imaging *see* color Doppler ultrasound
color mode 267, *286*
color selection *229*
colposuspension, postoperative evaluation 88, *90*
complex mass 3, 4
compressibility, of mass 4
compression pattern, benign tumors *272*, 273, *274*, *276*
compression technique, in breast ultrasound 253, *254–255*
congenital uterine anomalies 23, *24*, *125–126*, *230–231*
connective tissue tumors 130, *131*, 153
continuous-wave (CW) Doppler ultrasound 258
contraception
new developments 205
see also intrauterine devices (IUDs)
contractions, subendometrial 114
contrast and brightness 223
contrast medium, Echovist 174–176, *177*, 180–181
Copper T IUD 67, *68*, 171–172, *173*
3D/4D imaging 225, *229*
core biopsy 287, *290*
corpus, of uterus 101, *102*, *104*
corpus albicans 115, *119*
corpus-cervix ratio 101
corpus hemorragicum 115, *119*
corpus luteum 17, *19*
blood flow velocity 215
endometrial changes and 18, *22*
formation 114–115, *118*, *119*
ovarian artery waveforms and 205, *208*
corpus luteum cysts 41, *44*, 149, *150–151*
hemorrhagic *95*, 149, *150–151*
transvaginal aspiration *186*
treatment response 75, *76*
ruptured 207
criteria
sonographic *2*
ultrasound mass 2–4
Crohn's disease 25, *28*, 61, 62, *66*
cul-de-sac *11*, *107*, 108
abscess in 25, *29*, 127, *129*
endometriosis 169, *170*
fluid in 25, *26*
postoperative bleeding 188, *190*
cumulus oophorus 17, *19*, 115, *119*
cystadenocarcinomas 42, *54*
cystadenomas
mucinous 42, *49*, *51*, 152, *156*
serous 42, *47–49*, *51*, 152, *155*
angiogenesis 207
potential malignancy *156–157*, 158
cystadenopapillary carcinoma *54*
cystic and solid mixed tumors 42, *52–53*, 159, *160–161*
cystic glandular hyperplasia 132, *135*, *137*
cystic kidney 166, *166*
cystic masses 3
fallopian tube 164, *165*
malignant transformation *156–157*, 158, *160*
ovarian 42, *52–53*, 148–159, *150–151*, *154–156*
3D/4D ultrasound 225, *235–238*
sound conductivity 6
vaginal 130, *131*
see also dermoid cysts; ovarian cystic masses; ovarian cysts
cystic teratomas *see* dermoid cysts
cystocele 87, *90*
cystomas
mucinous *95*
proliferative mucinous *157*, 158
unilocular 149, *150*
cystourethrography 86–88, *89–90*
cysts
breast 253, *255–256*, 273, *275–277*
aspiration *291*
3D sonography *268–270*
cervical 136, *139*
functional 207, *209–210*
hepatic 61, *65*
transvaginal aspiration 184, *186*
vaginal 30, *30–31*
see also corpus luteum cysts; lymph cysts

D

delineation, of mass 4
dermoid cysts 41, *46–47*, 152, *154–155*
angiogenesis 207, *209*, 217
intraoperative ultrasound 80, *82*
3D/4D sonography *238*
desquamation 113, *116*
diagnostic applications of ultrasonography 6–7
diffuse myomatosis 132, *133*
display, 3D/4D ultrasound 267–273, *268*, *271*, *285*
Doppler compatability, in probes 96
Doppler effect 198, *201*
Doppler parameters 198, *202*
Doppler ultrasound 198–200, *201–203*
see also color Doppler ultrasound; continuous-wave (CW) Doppler ultrasound; power Doppler imaging
double uterus 176, *178*
ductal carcinoma *260*, *262*
invasive *272*, *280–281*, *283–286*
ductal carcinoma in situ (DCIS) 279, *282*
ductal lesions *277*
ductectasia *276*

E

echo patterns 3, *3*, 4–5
Echovist, contrast medium 174–176, *177*, 180–181
ectopic pregnancy 56, 69
electronic scalpel 223, *230–232*
embryo transfer, timing 206
embryonic development 124, *125*
endometrial carcinomas 32–33, *38–40*, 136–143, *141–142*, *144*
angiogenesis 214–215, *216*
color Doppler ultrasound 143, *144*
invasion depth 140, *142*, *144*
metastases from 140
prognosis 140, *142*
radiotherapy planning 193–194
tamoxifen and 132–136
3D/4D sonography *232–233*
transrectal ultrasound 243, *245*
transuterine ultrasound 248, *249*
endometrial polyps 32, *37*, 38, 136, *137–138*

differential diagnosis 143, *144*
HyCoSy 176, *179*
malignant transformation 143, *144*
3D/4D sonography *231*
endometrial ring sign 18, *22*, 113, *117*
endometrial stromal sarcomas 143, *145*
endometriosis 41, 215
bladder 33, *40*, 166, *167*
cul-de-sac 169, *170*
differential diagnosis 32, 33, *37*, *40*
neovascularity *210*, 211
treatment response 75, *76*, 191, *191*
endometriotic cysts 44, *45*, 149–152, *154*, 215, *218*
3D/4D sonography *238*
transvaginal aspiration *186*
endometrium 101, *102*, *104*
anomalies 248, *249*
calcifications in 136, *138*
cyclical changes 18, *20–22*, 113–114, *116–118*, 205
functional disturbance 132, *135*
HyCoSy evaluation 176, *179*
IUD mimic 171, *173*
stimulated cycle 120, *122*
tamoxifen-associated changes 132–136, *137*
thickness *104*, 105, 225, *229*, *230*
carcinoma and 140, *141*, 214–215
hyperplasia 32, *37*, 132
cystic glandular 132, *135*, *137*
3D/4D imaging 225, *228–230*, *231–232*, *232–233*
endometroid sarcoma of the ovary 42, *54*
endomyometritis 127, *128*
endosonography, in radiotherapy 193
enhancement, acoustic 4
epithelial tumors, classification 153
estrogen, in endometrial changes 113, *116*, 132
exophytic carcinomas, cervical 143, *145–146*
external iliac vessels 199, *202*
extragenital masses 166, *167–168*

F

fallopian tubes *11*, *12*, 105, *106*
cystic masses 164, *165*
HyCoSy 176–180, *179*
inflammation in 127, *128*
in PIDs 25, *26–28*
3D/4D ultrasound 226, *239*
see also tubal masses; tubal patency
fatty tissue, breast ultrasound 253, *255*
female pelvis *see* pelvic anatomy
fibroadenomas 257, *259*, *272*, 273, *274–275*
differential diagnosis 253, *255*, *260*, 261, *262*
fibrocystic breast changes *278*, *294*, *295*
3D sonography 273, *277–278*
fibroids *see* myomas (leiomyomas)
fibroleiomyomas, vaginal 130, *131*
fibromas, ovarian 152–153, *156*, 207, *209*
fibrosis, retroareolar *270*, 279, *282*
filtering, unwanted signals 223, *237*
fine needle aspiration 287, *290*
fistulas, postoperative 189
fluid
conductivity of 6
in cul-de-sac 25, *26*
intrauterine 136, *138*, *231*
focal volumetry 287
follicles, graafian 114, *118*, *119*
follicular aspiration, transvaginal 183, *185*
follicular cysts 17, 149, *150*
see also ovarian cysts, simple
follicular growth 114–115, *118–119*
endometrial changes 18, *21–22*
menstrual cycle 17, *19*
stimulated cycle 17–18, *20*, 120–121, *122–123*
follicular monitoring 17
follicular phase, menstrual cycle 114–115, *116*
follow-up care 169, *170*, 279, *284–285*
4D ultrasound
breast 266, *268*, 292, *295–296*
problems 292–293
transvaginal 224–226
tubal patency assessment 180
visualization modes 267
frequency, endovaginal probes 96
functional cysts 207, *209–210*
fundal-IUD distance 67, *68*

G

gallbladder 61, *65*
gallstones 61, *65*, *83*
Gartner duct cysts 30, *31*, 130, *131*
genital tract anomalies 23, *24*, 124, *125–126*, *230–231*
germ cell tumors, ovarian 152, 153, *154–155*
glass-body rendering 223, *234*, 267
breast masses *276*, 279, *283*, *286*
cervical carcinomas *233*
endometrial carcinomas *233*
ovarian masses 225, *239*
GnRH therapy *see* gonadotropin-releasing hormone (GnRH) therapy
gonadoblastomas 153
gonadotropin-induced cycles 17–18, *20*
gonadotropin-releasing hormone (GnRH) therapy *122*, 191, *191*, 213
graafian follicles 114, *118*, *119*
granulosa-cell tumors 42, *51*, 159
gray-scale imaging 6, 212
gray-scale rendering 222–223, *228*, *233*
greater omentum 57, *58*
gynecologic chair *94*, 97

H

HDR irradiation 193
hematocolpos 23, *24*, 30, *31*
transrectal ultrasound 243, *244*
hematomas
in corpus luteum cyst 149, *150*
intrauterine 143, *144*
post-traumatic 130, *131*
postoperative 72, *73*, 188, *190*
hematometra 33, *38*, 136, *138*
hematosalpinx 25, 164, *165*
hemorrhage, postoperative 72, *73*
hemorrhagic corpus luteum cysts *see* corpus luteum cysts, hemorrhagic
hemorrhagic ovarian cysts 41, *44*
hepatic metastases 6, 57
echogenicity 56, *59*, 169
histograms 223, *238*
hormonally active tumors 158–159
hormone replacement therapy (HRT), endometrial thickness *104*, 105
human menopausal gonadotropin-human chorionic gonadotropin (HMG-HCG) treatment 17, *20*
HyCoSy *see* hysterosalpingo-contrast sonography (HyCoSy)
hydatid cyst, hepatic *65*
hydronephrosis 60, *63*
hydrosalpinx 127, *129*
in PIDs 25, *26*
postinflammatory 164, *165*
3D/4D ultrasound 225, *239*
hymen, imperforate 23, *24*
hymenal atresia 30, *31*, 243, *244*
hyperandrogenemia 121
hyperechoic metastases 169
hyperstimulation (ovarian) 17, *20*, 42
syndrome 120, 121, *123*
hypoechoic metastases 169
hysterectomy complications 72, *73*, *74*
postoperative bleeding 188, *190*
hysterosalpingo-contrast sonography (HyCoSy) 174–176, *177–179*, 180–181, *181*

I

ileus, postoperative 72, *74*, 189
iliac lymph nodes 108, *112*
iliac vessels *16*, 108, *110*
external 199, *202*
thrombosis 25, *27*
visualization 11
image orientation 7, *8*, 97, *100*
image processing, 3D/4D display 223, 267, *270–271*
implant surgery *see* breast implants
in-vitro fertilization (IVF) 17–18, *20*
embryo transfer 206
oocyte maturation 120–121
tubal patency 175
inclusion cysts, cervical 136, *139*
incontinence *see* urinary stress incontinence
infections, postoperative 189
infertility
amenorrhoea 149
investigations 174–175
ovarian artery waveforms 199, *203*
transvaginal Doppler ultrasound 204
see also tubal patency
inflammatory bowel changes 25, 61–62, *66*

inflammatory breast disease *256*, 257, 261, *262*
inflammatory masses 25, 56
  vascular resistance 215, 217
  see also pelvic inflammatory diseases (PIDs)
intensity, of echoes 3
internal echo pattern 3–4
internal iliac artery 108, *110*
intestinal tract 61–62, *66*, 166
intracystic papilloma *256*
intraligamentous myomas 32, *36*, 132, *133*, *135*
intramural myomas 32, *34*, 132, *133–134*, 213
intraoperative ultrasound 75, *77*, 80, *81–83*
intrauterine devices (IUDs)
  displaced 172, *173*
  localization 67, *68–69*, 171–172, *173*
    3D/4D imaging 225, *229–230*
intrauterine fluid 136, *138*, *231*
intrinsic vascular system, ovaries 204
introital ultrasound 87–88, *89–90*
invasion depth, endometrial carcinoma 140, *142*, *144*
invasive ductal carcinoma *272*, *280–281*, *283–286*
invasive lobular carcinoma 279, *280*
inversion mode, 3D sonography 267, 273, *276*, *277*
iridium-192 radiation 193
IUDs *see* intrauterine devices (IUDs)
IVF *see* in-vitro fertilization (IVF)

K

kidneys
  cystic 166, *166*
  normal 60, *63*
  pelvic 42, *50*, 166, *166*
Krukenberg tumors 169

L

lateral sacral lymph nodes 108, *112*
LDR irradiation 193
leiomyomas *see* myomas (leiomyomas)
leiomyosarcomas 143, *145*
levator ani 108, *109*
ligaments
  pelvic *110*
  uterine 101, *102*
    intraligamentous myomas 132, *133*, *135*
lipid (lipoid) cell tumors 153
Lippes Loop IUDs 67, *68*, 171, *172*
liver 61, *65*
  see also hepatic metastases
lobular carcinomas *260*
  invasive 279, *280*
  in situ 279
local contact irradiation 193–194
lower urinary tract 86–88, *89–90*
LUF (luteinised unruptured follicle) syndrome 17, 121, 205
luteal phase, menstrual cycle 113, 114, *118*
luteinized unruptured follicle (LUF) syndrome 17, 121, 205
lymph collection, postoperative 189, *190*
lymph cysts 70, *71*, 72, *73*
lymph node metastases 57, *58*, 169
  cervical carcinomas *146*, 147
  endometrial carcinomas 140
  intraoperative ultrasound 80, *82*
  3D sonography 287, *289*
lymph nodes 108, *110*, *112*
  transrectal ultrasound *245*
  TUI imaging *289*

M

magnetic resonance imaging (MRI), breast tumors 258
malignant breast tumors 257–258, *260*
  criteria in 257–258, *260*
  3D sonography *272*, 273–279, *280–285*
malignant cervical tumors 33, *39–40*
malignant masses
  differentiation 4
  false-positive findings 215–217
  secondary changes 57, *58–59*
  treatment response 75
malignant melanomas, metastases 80, *82*, 130, *131*
malignant ovarian tumors 42–43, *52–55*, 159–162, *160–162*
  potentially malignant 42, *51–52*, 153–159, *156–157*
  power Doppler 199–200, *203*
  3D/4D ultrasound 225, *238–239*
malignant renal tumors 61, *64*
malignant transformation 42, *51–52*, 153–159, *156–157*
malignant uterine tumors 32–33, *38*, 136–147, *141–142*, *144–146*
malignant vaginal tumors 130, *131*
mammographic screening 252
mammotone *295*
manual needle puncture 183, *185*
masses
  sonographic findings 2–4
  see also specific organs
mastitis *256*, 257, *262*
Mayer-Rokitansky-Küster syndrome 23, *24*
Meig's syndrome 42, 153, 207, *209*
melanomas, metastatic 80, *82*, 130, *131*
menstrual cycle
  disorders 121, *123*
  endometrial changes 18, *20–22*, 113, *116*
  normal Doppler indices 299
  ovarian changes 17–18, *19*, 114–115, *118–119*
  ovarian vascular changes 199, *203*, 204, 205, *208*
  uterine changes 10, 113–114, *116–118*
  uterine vascular changes 206, *208–209*
mesenchymal malignant mixed tumors 143
metastases
  classification 153
  follow-up care 169
  intraoperative ultrasound 80, *82*
  see also hepatic metastases; ovarian tumors, metastastatic
metastatic tumors *see* metastases
midsagittal scan *8*
minimum mode 267, *277*
mixed solid and cystic tumors 159, *160–161*, 166, *168*
mobility, of mass 4
mucinous borderline tumors *210*, 211
mucinous cystadenocarcinomas 42, *54*
mucinous cystadenomas 42, *49*, *51*
  angiogenesis 207, *209*
  diagnosis 215, *218*
  ovarian 152, *156*
mucinous cystomas *95*
mucocele of the appendix 166, *167*, *168*
müllerian ducts 124, *125*
  anomalies 23, *24*
müllerian epithelial cysts 130, *131*
multi-slice view (MSV) 225
multigate pulsed Doppler 198–199, *202*
Multiload IUD 67, *68*
multiplanar reformatting 223, *233*
multiplanar 3D display 267
  benign lesions *268–269*, *272*, *275–278*
  malignant masses *272*, *280*, *282*, *284–285*
myomas (leiomyomas) 32, *34–37*, 132, *133–135*
  angiogenesis 207, 215, 217, *218*
  HyCoSy evaluation 176, *179*
  intraligamentous 32, *36*, 132, *133*, *135*
  intramural 32, *34*, 132, *133–134*, 213
  medical reduction 191, *191*
  pedunculated 132, *133–134*, *141*
    subserous 32, *36*
  subserous 32, *35–36*, 132, *133–134*
  3D/4D imaging 225, *232*
  transabdominal *vs* transvaginal ultrasound *95*
  transuterine ultrasound 248, *249*
  vascularization 213–215, *216*
  see also cervical myomas; submucous myomas; tubal masses, myomas
myometrium 101, *102–103*
  carcinoma invasion depth 140, *142*, *144*

N

nabothian cysts 101, 136, *139*
needle procedure guidance
  abdominal ultrasound 70, *71*
  3D ultrasound 287–292, *291–292*, *294–295*
  transvaginal ultrasound 92, 183–184, *185–187*
neovagina construction 75, *77*
neovascularization 206–207, *209*
  see also angiogenesis
nephrolithiasis 60, *63*
neurinoma, retroperitoneal 166, *168*
niche display mode 267, *269*
nipples
  disorders 273

3D sonography *268*, *269*
noninvasive carcinomas, breast 279, *282–285*
nulliparous uterus 10, *12*, *13*
Nyquist limit 198

O

obesity 6, 17
oblique scan *8*
oblique tendons, abdominal *16*
obturator internus 108, *109*
oocyte maturation, monitoring 120–121
oocyte retrieval 17–18, 183, *185*
organ pathology, postoperative 189
orientation, 3D ultrasound 224
ovarian abscesses *186*
ovarian arteries 108, 204, 205
color Doppler 199, *203*, 205
ovarian biometry 105
ovarian carcinomas 42–43, *52–55*, 159–162, *160–162*
ascites with 57, *58*
hepatic metastases 56, *59*, 61, *65*
prognosis 159, *160*
screening 162, 217, *218*
3D/4D sonography *238–239*
ovarian cycle, vascular changes 204
ovarian cystic masses 148–159, *150–151*, *154–156*
with solid structures 42, *52–53*
3D/4D ultrasound 225, *235–238*
ovarian cysts
hemorrhagic 41, *44*
hydrosalpinx compared 25
simple 41, *44*, 149, *150–151*, *155*
string-of-beads 121, *123*
3D/4D sonography *235–237*
torsion 25
transvaginal aspiration 184, *186*
see also dermoid cysts
ovarian endometriosis 215
ovarian fibromas 42, *50–51*
ovarian follicles *106*
ovarian masses 41–43, *44–55*, 148–162, *150–151*, *154–157*, *160–162*
echo pattern 148–149
evaluation criteria 148–149, 158, 159
scoring system 42–43, *55*
transrectal ultrasound 243, *245*
ovarian suspensory ligament *11*, *12*
ovarian tumors
benign, angiogenesis in 207–211, *209–210*
borderline 211
differential diagnosis 32, *36*
evaluation 148, 158, 159
malignant 159–162, *160–162*
angiogenesis *210*, 211–213
power Doppler 199–200, *203*
see also ovarian carcinomas
metastastatic 159, *161*
potentially malignant 42, *51–52*, 153–159, *156–157*
scoring system 158, 159
3D/4D ultrasound 225, *238–239*
ovarian veins 204
ovaries *11*, *12*, *15–16*, 105, *106*
anatomy 10–11
HyCoSy 176–180, *179*
hyperstimulation 17, *20*, *49*
syndrome 120, 121, *123*
3D/4D ultrasound 225, *235*
menstrual cycle changes 17–18, 114–115, *118–119*
normal dimensions 298
normal Doppler indices 299
3D/4D ultrasound 225, *234*, *234–239*
vascular supply *16*, 108, *110*, *111*, 204
ovulation 115, *119–120*
endometrial changes 113, *117*
lateralization issues 120
vascular changes 205–206, *208*
ovulatory cycle 113, *116–118*
endometrial changes 18, *21–22*
stimulated 120–121, *122–123*
uterine dimensions 10

P

palliative care, radiotherapy planning 193–194
pampiniform plexus 204
papillary cystadenocarcinoma *54*
papillary cystadenomas 42, *51*
papillomas, breast *256*, *276*, *277*
paracervical varicosities 136, *141*
parametrium
cervical carcinoma 146
radiotherapy planning 193–194, *195*
paraovarian cysts 41, *44*, 149, *150*
parasagittal scan *8*
paraurethral gland cysts 130
parenchymal density, breast 253, *254–255*
parity, uterine biometry 101, 298
patient monitor
HyCoSy 180
transvaginal ultrasound 97, *100*
PCO syndrome *see* polycystic ovary (PCO) syndrome
pedunculated myomas 132, *133–134*, *141*
pedunculated polyps 136, *139*
pedunculated subserous myomas 32, *36*
pelvic anatomy 10–11, 101, *102–104*, 105, *106–107*, 108, *109–112*
pelvic floor, 3D/4D ultrasound 226, *240*
pelvic floor anatomy, coordinate system 87, *89*
pelvic inflammatory diseases (PIDs) 25–29, 127, *128–129*
IUDs and 69, 172
vascular changes *210*, 211, 215
pelvic kidney 166, *166*
pelvic lymph nodes 108, *112*
pelvic masses 223–224
pelvic venous thrombosis 25, *27*
pelvic vessels 11, 108, *110*
pelvic wall hematomas 188, *190*
pelvic walls 108, *109*
percutaneous ultrasound 193–194
perimenopausal women, endometrial hyperplasia 132
perineal ultrasound 86–87, *89*
peritoneum *16*
carcinomatosis 169, *170*
cysts 149, *154*
metastases 57, *58*
PIDs *see* pelvic inflammatory diseases (PIDs)
piriformis muscle 108, *109*
plasmacytoma, intramammary 279, *283*
pneumocystography 253
polycystic kidneys 60, *64*
polycystic ovary (PCO) syndrome 17, *19*, 121, *123*
intraovarian blood flow 205–206, *208*
polyps
cervical 136, *139*
endometrial *see* endometrial polyps
pedunculated 136, *139*
porcelain gallbladder 61, *65*
posterior acoustic effects 6, 148
posterior vesicourethral angle (PUV) 86–87, *89*
postinflammatory changes 127, *129*
cervical occlusion 136, *138*
fallopian tubes 225, *239*
postmenopausal women
bleeding 140
endometrium
carcinoma 140, *141*
hyperplasia 132
endovaginal ultrasound 92
intrauterine fluid 136, *138*
myoma regression 213–214
normal Doppler indices 298
ovaries 105, *106*
carcinoma screening 162
uterus 10, *12*, *13*
biometry 101, *104*, 105, 298
postoperative complications 70, *71*, 72, *73–74*
transvaginal ultrasound 188–189, *190*
potentially malignant tumors 42, *51–52*, 153–159, *156–157*
power Doppler imaging *157*, 159, *162*, *164*, 199–200, *203*
pregnancy
assisted conception 120–121
ectopic 56, 69
endovaginal ultrasound 92
myomas in 132
ovarian artery waveforms 205
spontaneous after HyCoSy 180–181
pregnancy termination, complications 72, *73*
probes *see* ultrasound probes
progesterone, in endometrial changes 113, *116*
proliferative fibroadenomas 257, *259*
proliferative mucinous cystomas *157*, 158
proliferative phase of menstrual cycle
endometrial changes 113, *116–117*
uterine blood flow 206
proliferative serous cystadenomas *156–157*, 158
proliferative serous papillary cystadenomas 42, *51*

prostaglandin $F_{2\alpha}$ ($PGF_{2\alpha}$) 205
prosthetic breast implants 253–257, *256*
pseudocapsule *272*, 273
psoas muscle *15*, 108
psychological benefit, patient monitor in HyCoSy 180
pulsatility index (PI)
  endometrial pathology 214
  malignant tissues 211–212
  myomas 213, *216*
pulse repetition frequency (PRF) 198
pulsed Doppler ultrasound 198, 211–213
pulsed-wave (PW) Doppler *see* pulsed Doppler ultrasound
PUV *see* posterior vesicourethral angle (PUV)
pyometra 33, *39*
pyosalpinx 25, *27*, 127, *128*

R

radial arteries 205
  Doppler indices 206, *209*, 299
  endometrial pathology and 214
radiotherapy planning 193–194, *195–196*, 248
radium-226 radiation 193
record storage 223–224, 267, 292
recurrence detection
  breast lesions 279, *284–285*
  cancer care 169, *170*
  pelvic tumors 212
renal allograft, identification 166, *167*
renal anomalies 23, *24*, 61, 124
renal cell carcinoma 61, *64*
renal cysts 60, *64*
  giant 42, *49*
renal hypoplasia 61
renal masses 60–61, *64*
  cystic kidney 166, *166*
renal ultrasound
  technique 60
  see also kidneys
residual urine determination 72, *74*
resistance index (RI) *202*
  endometrial pathology 214
  intraovarian blood flow 205
    at ovulation 206, *208*
  malignant tissues *210*, 211–213
  myomas 213, *216*
retention cysts 149, *151*
retraction pattern, 3D sonography *272*, 273, *274*, 279, *280–281*
retroflexed uterus 10, *14*, 101, *103–104*
  3D/4D sonography *229*
retroperitoneal tumors 166, *168*
retropubic space 105, *107*
retrovaginal hematomas 188, *190*
Retzius cavity 105, *107*
Rokitansky-Küster syndrome 42, *50*, 61
rotation mode *270*
rotational bladder neck descent 87, *90*
round ligament *11*, *12*

S

sacrouterine ligaments 101, *102*
sactosalpinx 25, *26–27*, 176–180, *179*
  torsion 25, *28*
sarcomas
  ovarian 159, *161*
  uterine 136, 143, *145*
    blood flow indices 215, *216*, 217, *218*
scan planes 7, *8–9*
  transvaginal ultrasound 97, *99–100*
scanning angle, endovaginal probes 96, *98*
scars 169, *170*, 257, *259*
  HyCoSy evaluation 176, *179*
  3D sonography 273, *278*, 279, *284*, *285*
schwannoma, retroperitoneal 166, *168*
sclerosing adenosis *294*
scoring system, masses 42–43, *55*, 158, 159
screening
  breast cancer 252–253
  ovarian carcinoma 162, 217, *218*
secretory phase, menstrual cycle 113–114, *116–117*, *118*
septal thicknes, in cystic masses 3
septate uterus 124, *125*, *126*
  HyCoSy evaluation 176, *178*
serous adenopapillary ovarian carcinoma *52*
serous borderline tumors 211
serous cystadenomas 42, *47–49*, 152, *155*
  angiogenesis 207
  potential malignancy *156–157*, 158
Sertoli-Leydig cell (arrhenoblastoma) tumors 42, *52*, 159, *160*
sex cord stromal tumors 153, 158–159
shadow, acoustic 4
shrunken kidneys 61
sigmoid colon *11*, *12*
  carcinoma metastases 43, *55*
silicone breast implants 253–257, *256*
  multiplanar display *288–289*
simple mass 3
size and shape, mass 2
small bowel inflammation 62
solid echo complex 4
solid tumors
  echo pattern 4
  ovarian 148–149, 153–162, *156–157*, *160–162*
    with cystic areas 42, *52–53*
  sound absorption by 6
sonographic findings, mass 2–4
spacing, of echoes 3
spatiotemporal image correlation (STIC) 224, 292
spinal arteries, Doppler indices 299
spiral arteries 204, 205
  blood flow 206, *209*
spleen 61, *65*
Stein-Leventhal syndrome *see* polycystic ovary (PCO) syndrome
stellate pattern, malignancy 279, *280–282*, *285*
STIC (spatiotemporal image correlation) 224, 292
stimulated cycle
  follicular growth 17–18, *20*
  RI in uterine arteries 206
  sonographic changes 120–121, *122–123*
  3D/4D sonography of ovaries *235*
stones *see* cholecystolithiasis; gallstones; nephrolithiasis
straight uterus 101, *103*
string-of-beads ovarian cysts 121, *123*
subareolar region 273, *277*
subendometrial contractions 114
submucous myomas 32, *36–37*, 132, *133*, *135*, 213
  differential diagnosis 143, *144*
  3D/4D sonography *232*
subseptate uterus *230*
subserous myomas 32, *35–36*, 132, *133–134*
suprasymphyseal scan *8*
surface-rendered images 223, 267, *270*
  bowel *240*
  breast 266, *269*, *270*, *274*, *276–278*, *282–285*
  cervix *233*
  fallopian tubes *239*
  ovaries *234–239*
  uterus *228–232*

T

tamoxifen-associated endometrial changes 132–136, *137*, *232*
techniques
  abdominal ultrasound 6–7
  breast ultrasound 253, *254–255*
    3D imaging 266, *268*
  HyCoSy 175–176, *177*, 180
  intraoperative ultrasound 80, *81–83*
  introital ultrasound 87–88
  perineal ultrasound 86–87
  radiotherapy planning 193–194, *195*
  3D guided needle biopsies 287, *290–291*
  transrectal ultrasound 242
  transvaginal ultrasound 92–93, 97, *99–100*
theca-cell tumors 42, *52*, 207
theca lutein cysts 149, *151*
thecoma 159, *160*
therapeutic applications 6–7
thermography 258
3D ultrasonography 147
  breast 266–293, *268–272*, *274–278*, *280–286*, *288–291*, *294–296*
  image storage 223–224, 267
  problems 224, 292–293
  transvaginal 222–226, *227–240*
  vascular imaging *276*, 279, *283*, *286*
  visualization modes 267
tissue biopsy, transvaginal 184
tomographic survey 223, 267, *285*
tomographic ultrasound imaging (TUI) *232*, *271*
  breast tumors 279, *285*
  endometrium *232*
  lymph nodes *289*
torsion
  ovarian cyst 207

sactosalpinx 25, *28*
transabdominal puncture 70, *71*, 183
transabdominal *vs* transvaginal ultrasound 92–93, *95*
transducers 7, *8*
transparent visualization mode 267, *270*
transrectal ultrasound 193, 242–243, *244–245*
transuterine ultrasound 248, *249*
transvaginal cyst aspiration 184, *186*
transvaginal 4D ultrasound 224–226
transvaginal Doppler ultrasound 198–200, *201–203*
clinical uses 204–207, *208–210*, 211–215, *216*, 217, *218*, 219
transvaginal oocyte retrieval 183, *185*
transvaginal 3D ultrasound 222–226
transvaginal tissue biopsy *183*, 184
transvaginal ultrasound 92–93, *94–95*
examination technique 92–93, 97, *99–100*
needle procedure guidance 183–184, *185–187*
pelvic anatomy 101–112
postoperative complications 188–189, *190*
transversalis fascia *16*
traumatic epithelial cysts, vaginal 130
treatment planning, breast tumors 279
treatment response
monitoring 75, *76–77*
transvaginal ultrasound assessment 191, *191*
tubal artery flow signals 212
tubal masses 56, 164, *165*
carcinomas 56, *56*, 164, *165*
myomas 164, *165*
tubal patency 174–176, *177–179*, 180–181, *181*
3D ultrasound 180, *181*
3D/4D ultrasound 225, *239*
tubal spasm 176
tubal torsion 164, *165*
tuberculosis, genital *27*, 127
tubo-ovarian abscess 25, *28*
differential diagnosis 127, *129*
vascular changes 211
TUI *see* tomographic ultrasound imaging (TUI)
tumor-induced angiogenesis *see* angiogenesis
tumor marker CA-125 levels 207
tumor surgery, intraoperative ultrasound 80, *82*
tumors
benign *see* benign masses
color Doppler studies 206–215, *209–210*, *216*
malignant *see* malignant tumors
neovascularization 206–207, *209*
see also angiogenesis
perfusion 224
size determination *270–271*, 287
staging 140

U

ultrasonography
applications of 6–7
examination technique 6–7
liver and gallbladder 61
ovarian masses 148–149
transvaginal 92–93, 97, *99–100*
urinary tract 60
ultrasound evaluation criteria 148–149
ultrasound-guided needle biopsies, 3D sonography 287–292, *290–291*, *294–295*
ultrasound-guided percutaneous biopsy 253
ultrasound probes
endovaginal 92, *94*, 96, *98–99*
intraoperative use 80, *81*
placement 7, *8*
3D ultrasound 222, *227–228*
transrectal ultrasound 242, *244*
ultrasound screening *see* screening
umbilical ligaments *16*
unilocular cystoma 149, *150*
ureteral jet phenomenon 105, *107*
ureteral orifices 105, *107*
ureteral stones 60, *63*
ureters *107*, 108
postoperative complications 189
urethra *11*, *15*, 105, *107*
evaluation 86–87, *89–90*
transrectal ultrasound 242, *244*
urinary stasis
residual urine determination 72, *74*
tumor-related 33, *40*
urinary stress incontinence 87–88, *89–90*
urinary tract
abnormalities 23, *24*, 60–61, *63–64*, 124
examination technique 60
lower 86–88, *89–90*
urinary tract masses 166, *167*
urinary tract obstruction
hydronephrosis 60, *63*
by malignant tumor 56, *59*
postoperative 72, *73*, *74*
uterine arteries 108, *110*, 204, 205
Doppler indices 199, *203*, 299
menstrual cycle changes 205, 206, *208–209*
uterine carcinomas
hepatic metastases 56, *59*
transuterine ultrasound 248, *249*
uterine cervix *see* cervix
uterine corpus *11*, *12*
benign masses 132–136, *133–135*, *137–138*
transrectal ultrasound 242
uterine masses 32–33, *34–40*
3D/4D imaging 225, *232*
uterine myomas (leiomyomas) *see* myomas (leiomyomas)
uterine round ligaments 101, *102*
uterine sarcomas 143, *145*
blood flow indices 215, *216*
uterine tumors
benign
see also myomas (leiomyomas)
malignant 136–147, *141–142*, *144–146*
detection 214–215, *216*
local contact irradiation 193–194
radiotherapy planning *195–196*
see also cervical carcinomas; endometrial carcinomas; uterine carcinomas; uterine sarcomas
vascularization 213–215, *216*
uterine vessels
varicosities 136, *141*
see also uterine arteries
uterotubal junction 248, *249*
uterus
anatomy 10, *11–16*, 101, *102–104*
biometry 101, *104*, 105, 298
calcifications in 136, *138*
in childhood 10, *12*, *13*
congenital anomalies 23, *24*, 124, *125–126*, *230–231*
HyCoSy evaluation 176, *178*
3D/4D imaging 225, *230–231*
hematoma 72, *73*
HyCoSy evaluation 176, *177–179*
menstrual cycle changes 113–114, *116–118*
normal dimensions 298
normal Doppler indices 299
nulliparous 10, *12*, *13*
perforated by IUD 67, *69*
preuterine abscess formation 25, *29*
3D/4D ultrasound 225, *228–233*
transrectal ultrasound 243, *245*
transuterine ultrasound 248, *249*
vascular supply 108, *110*, *111*
uterus bicornis unicollis 23, *23–24*, 124, *125*
3D/4D sonography *231*
uterus didelphys 23, *23*, 124, *125*
HyCoSy 176, *178*

V

vacuum biopsy
mammotone *295*
needle 287, *290*, 292
vagina
anatomy 10, *11*, *13–15*, 101, *102–103*
aplasia 124
congenital anomalies 23, *24*
transrectal ultrasound 242, 243, *244*
vaginal arteries 108, *110*
vaginal cysts 30, *30–31*, 130, *131*
vaginal tumors 130, *131*
malignant, radiotherapy planning 193–194, *195–196*
varicose vessels
adnexal 17, *19*
paracervical 136, *141*
vascular anatomy, ovaries 204
vascular changes, ovulation 205–206, *208*
vascularity of tumors 206–207, *209*
breast 279, *286*
uterine 213–215, *216*
see also angiogenesis
VCI *see* volume contrast imaging (VCI)
vena cava, intraoperative ultrasound 80, *82–83*

venous thrombosis, pelvic 25, *27*
vermiform appendix *see* appendix
vestibular gland cysts 130
VOCAL program 223, *236*, *270*, 287
volume acquisition 222, *228*, *270*
  benign-malignant differentiation 273
  3D breast ultrasound 266–269, *268*
volume contrast imaging (VCI), 4D ultrasound 224, *228–229*, 292, *295–296*
volume manipulation 223
  3D/4D display 267, *270–271*
volume rendering 222–223, *228*
volumetry 223, *236*
  breast tumors *270–271*, 287
  pelvic masses 223–224

W

wall filter, in pulsed Doppler 198, 199, *201*
wall thicknes, cystic masses 3
waveform data, pulsed Doppler 198, 199, *202*
waveforms, ovarian artery 205, *208*